30th DANUBIA-ADRIA

DANUBIA ADRIA

Symposium on Advances in Experimental Mechanics

September 25-28, 2013 - Primošten, Croatia

CSM
CROATIAN SOCIETY OF MECHANICS
Zagreb
Rijeka
Osijek
Slav. Brod
Split

PROCEEDINGS

30th DANUBIA-ADRIA

Symposium on Advances in Experimental Mechanics

September 25-28, 2013 - Primošten, Croatia

PROCEEDINGS

www.danubia-adria2013.com

Publisher
CROATIAN SOCIETY OF MECHANICS
Ivana Lučića 5, HR-10000 Zagreb, Croatia
www.csm.hr

Editors
Ivo Alfirević
Damir Semenski

Graphic design, prepress and printing
STUDIO HRG, Hrvatske bratske zajednice 4,
HR-10000 Zagreb, Croatia
www.studiohrg.hr

Copies
250

Zagreb, September 2013

A CIP catalogue record for this book is available in the Online Catalogue of the National and University Library in Zagreb as 854973

ISBN 978-953-7539-17-7

CONTENTS

PREFACE

Dear participants and guests, dear colleagues,

We are happy to present the Proceedings of the thirtieth jubilee Danubia-Adria Symposium on Advances in Experimental Mechanics. At the first Danubia-Adria Symposium held in 1984, only 40 participants from 7 countries took part and submitted a total of 36 papers. On the occasion of this 30th jubilee, we expect more than 150 active participants and more than 150 contributions, authored and co-authored by more than 300 authors and coauthors from 23 countries.

As we can see, the delicate and fragile plant of the Danubia-Adria Symposium, that was planted by Rudolf Beer and Ivo Alfirević 30 years ago at the wonderful and enchanting Plitvice Lakes, has grown into a strong plant in full blossom. It would not be possible without an enormous effort of careful and diligent gardeners F. Thamm, I. Huszár, S. Jecić, A. Freddi and many others who have continuously promoted the Danubia-Adria idea. This jubilee symposium takes place in a colourful and picturesque small Dalmatian town of Primošten, with narrow streets and old stone houses. In the vicinity of Primošten there are several historical and interesting towns: Trogir, Šibenik, Split and others. In these towns one can find many beautiful palaces, churches, cathedrals, and museums. Two National Parks, Kornati Islands and Krka Waterfalls are also in the vicinity. We hope that you will enjoy the sightseeing.

We are happy to have among us our colleagues, the members of the EURASEM Council. Activities of the European Society for Experimental Mechanics (EURASEM) are compatible with the actions of the Danubia-Adria Society (DAS), undertaken to promote research in the magnificent field of Experimental Mechanics. Bearing in mind the great tradition of the EURASEM, established as early as in 1959, we shall use this opportunity to further spread the enthusiasm of DAS to strengthen future cooperation with this esteemed body.

To all of us we wish a lot of success in presenting our contributions that will hopefully incite vivid discussion and we do hope that you will be happy swimming in our clear, deep, blue sea.

Zagreb, September 10, 2013

Damir Semenski *Ivo Alfirević*

AIMS AND SCOPE

The Danubia-Adria Society on Experimental Methods (DAS) was founded in 1983. The objective of the Society is **to promote experimental mechanics, covering all aspects from the development to the applications of the methods, for the quality improvement of products and processes and for developing new models of education.**

The Danubia-Adria Symposium on Advances in Experimental Mechanics (DAS 2013) is intended to provide a forum for engineers, researchers, university teachers and students, scientists and industrial experts to present and discuss the current status and impact of modern technology and development in the field of experimental methods in mechanics. Focus will be on recent research and development of experimental and hybrid methods for quality enhancing of structures, service life, and technical safety.

Scientific Committee will support the publication of the best selected papers in distinguished journals.

Special issue of Transactions of FAMENA will be devoted to the DAS 2013.

TOPICS

Conventional and advanced experimental methods in mechanics

Measuring acquisition and data processing

Relations between experimental methods and numerical simulation

Experimental and applied biomechanics

Fatigue and reliability

Applications

ORGANIZER

Croatian Society of Mechanics (HDM)

CO-ORGANIZER

Austrian Society of Experimental Strain Analysis (ASESA)
Czech Society of Mechanics (CSM)
German Society of Experimental Structural Analysis (GESA)
Hungarian Scientific Society of MechanicalEngineering (GTE)
Italian Association for Stress Analysis (AIAS)
Polish Committee for Mechanics of the Polish Academy of Sciences (KMPAN)
Romanian Association for Stress Analysis (ARTENS)
Serbian Society of Mechanics (SSM)
Slovak Society of Mechanics (SSM)
Slovenian Society of Experimental Mechanics (SSEM)

SCIENTIFIC BOARD

Austria	J. Eberhardsteiner (Vienna) W. Eichlseder (Leoben)
Croatia	I. Alfirević (Zagreb) D. Semenski (Zagreb)
Czech Republic	F. Plánička (Plzen) M. Ružička (Prague)
Germany	W. Daum (Berlin)
Hungary	L. Borbás (Budapest) R. Kiss (Budapest)
Italy	F. Cosmi (Trieste) G. Nicoletto (Parma)
Poland	Z. Kowalewski (Warsaw) M. Szata (Wroclaw)
Romania	D.M. Constantinescu (Bucharest) S. D. Pastrama (Bucharest)
Serbia	M. Ognjanović (Belgrade) M. Živković (Kragujevac)
Slovakia	O. Bokůvka (Žilina) P. Palček (Žilina)
Slovenia	I. Emri (Ljubljana) A. Nikonov (Ljubljana)

Honorary Members of Scientific Board
R. Beer (Vienna)
S. Jecić (Zagreb)
S. Holý (Prague)
K. H. Laerman (Wuppertal)
F. Thamm (Budapest)
A. Freddi (Bologna)
R. Będziński (Wroclaw)
N. Iliescu (Bucharest)
J. Pastrav (Cluj-Napoca)

UNDER THE AUSPICES OF
Croatian Academy of Science and Arts
www.hazu.hr

PROCEEDINGS

30th DANUBIA-ADRIA
Symposium on Advances in Experimental Mechanics
September 25-28, 2013 - Primošten, Croatia

1G01 001

REFLECTIONS ON THE CORRELATION BETWEEN MATHEMATICAL AND EXPERIMENTAL ANALYSIS

Karl-Hans Laermann [1],

[1] Bergische Universität Wuppertal, FB **D**, Lehr- und Forschungsgebiet Statik und Dynamik der Tragwerke; Pauluskirchstr.7, 42825 Wuppertal, Germany.

Corresponding author: laermann@uni-wuppertal.de

1. Introduction

Pursuing the developments in experimental mechanics over the past century, remarkable progress and essential changes in measurement methods are to be noted, based on new achievements in physics. Laser-techniques had been invented and brought up new optical methods. Sensor- and fibre-optical techniques have widened the catalogue of measurement-techniques. CCD-cameras had revolutionised experimental mechanics. But the most effective influence on the experimental mechanics at all is to put on the introduction of computer-techniques. And soon scientists and engineers appreciated the advantages in math./numerical analysing their mechanical problems, rendering them into finite formulations and modelling the problems by means of numerical mathematics. And it looked as if with the possibility of FE-modelling of engineering problems for instance and related computer-programs any technical task - and not technical ones only -, could be solved. In this concern the question had been raised, whether one could refrain from experimental mechanics and analysis. But in the contrary it must be stressed that measurement and experimental mechanics has achieved extended importance just because of the advances in computer-techniques. Moreover it must be pointed out that analytical and experimental mechanics depend on each other. The one discipline cannot meet the challenges in mechanical engineering today to improve accuracy and reliability of results and even cannot exist without the other.

2 Review of mathematical/numerical analysis.

Mathematical/numerical analysis of technical problems based on theoretical mainly finite models turns out to be an idealisation- and a simulation process, which includes many uncertainties because of missing information on parameters, variability of variables, inaccurate knowledge on non-linear and time-depending responses of materials and structures as well as incorrect modelling of boundary conditions etc. Over and above important causes inherently responsible for biasing the results of numerical analysis are to mention [1]. i) Missing validation, i.e. the proving of the homomorphy between system and model, which includes the structure in addition to the input/output quantities. ii) Missing verification, i.e. the reconstruction of the information used for the construction of the model, which can concern the principles of mechanics and/or the measured data used. iii) Numerical uncertainty in the classical computer-arithmetic because of the error propagation in the solution, based on billions of arithmetic operations. vi) Unreflecting use of computer-programs, especially commercially available ones, without knowing their mathematical background and range of validity, withdrawn from any control of the codes and with that believe in the infallibility of computer calculations and in the correctness of results.

3 Review of experimental analysis

On the other hand experimental analysis and measurements provide a means of validating the mathematical/numerical model and immediately information on the object/structure responses like deformations, probably at least hints on non-linear, time-depending and other effects. This is advantageous, as some effects are difficult to simulate accurately if at all in mathematical modelling. But like in mathematical/numerical analysis, also in experimental analysis inaccuracies and uncertainties are to take into consideration. In principle all measured data are full of systematic and random errors. These may be caused e.g. by improper calibration of instruments in the experimental set-up and its mounting, neglecting the specific measuring range of the single instruments in the system,

their signal-to-noise ratio, the impedances along the path of signal transmission. Furthermore environmental influences on object and measurement system as well as interaction between both, improper inclusion of real boundary- and loading-conditions may be responsible for erroneous data. In experimental mechanics computer-techniques as well play a decisive role in connection with the improvements of the measurement methods and especially with regard to optical methods. The measurements yield optical signals in kind of grey-value-images, e.g. interferograms, which are recorded by high-dissolving CCD-cameras. For evaluation, these images have to pass through different mathematical processes, to obtain finally the information sought after. Because of the tremendous amount of data recorded in the images the performance of such processes requires proper computer programs and consequently some critical remarks referring to programs in mathematical analysis apply also to computer-aided evaluation of the recorded images.

4 Combination of mathematical and experimental processes

To overcome the disadvantages and uncertainties in structural analysis as mentioned above, i.e. to reduce the sources of errors, to validate and verify the mathematical model and to improve the accuracy and reliability of structural analysis to the best means is to combine mathematical and experimental concepts to a comprehensive procedure [2]. In this concern the heuristic as well as the iconic modelling must at least seem to yield the probable reactions of the object/system under the condition that the parameters are known only partly and are full of uncertainties. That is turning away from the as yet deterministic to the stochastic way of looking, from inductive and deductive procedures to a unite concept of experiment and simulation. This new paradigm meets in consequence the postulate "*to pay absolutely attention to the principle "praxis cum theoria" for all systems in the open nature"*[3]. From the mechanical point of view the combined procedure can be considered as the application of system identification. This immediately leads to inverse problems, the solutions of which require additional ambitious mathematically processes [4] and add a new chapter of mathematics in comprehensive analysis of mechanical problems.

The experimental analysis including the inverse solutions yield information on parameters, variables, assumptions and further more on stress- / strain-states, however depending on the initial mathematical model. These results are to compare with the results of the mathematical analysis to ascertain the degree of matching. Corresponding to this degree the parameters, variables, assumptions, constraints, boundary- and loading-conditions are updated, the numerical model modified and inconsistencies are eliminated. Thus the mathematical model will be improved till the final results are in acceptable correspondence. Then the model can be considered as validated and verified unless the applied computer-programs itself have proved their reliability. Such quantitative characterisation of uncertainties and their reduction play a central role in numerical simulation

5. Conclusion

A critical review has been undertaken on mathematical and experimental methods applied in projecting engineering structures and in identifying the actual state of already existing objects. It turns out that both these methods are full of different sources of uncertainties, inaccuracies and errors. Therefore the question had been raised, whether and how to overcome the problem to avoid and/or to reduce such sources. As recommended a satisfactory or at least best possible answer can be seen in combining the mathematical and experimental tracks because of the coherence between both.

6. References

[1] Natke, H., About the role of mathematics in engineering, GAMM-Mitteilungen, Heft 2, 1996. pp. 121-131.

[2] Laermann, K.-H., On the Coherence of Mathematical and Experimental Methods in Structural Analysis. In Proc. 50th Annual Conf.on Exp. Stress Analysis, ed.s M. Růžička et al., CVUT Prague, 2012. pp. 239-246.

[3] Anger, G., Zur Leistungsfähigkeit der Theorie in den Naturwissenschaften, der Technik und der Medizin. GAMM-Mittteilungen, Heft 1, 1997. pp. 19-36.

[4] Laermann, K.-H., Inverse Problems in Experimental Structural Analysis. Shaker-Verlag, Aachen, 2008. ISBN 978-3-8322-7257-9.

30th DANUBIA-ADRIA
Symposium on Advances in Experimental Mechanics
September 25-28, 2013 - Primošten, Croatia

1G02 030

THE PROGRESSIVE COLLAPSE OF MICRO LATTICE STRUCTURES MANUFACTURED USING SELECTIVE LASER MELTING

R.A.W.Mines[1], R.Hasan[1], M.Smith[1], W.J.Cantwell[1]

[1] School of Engineering, University of Liverpool, The Quadrangle, Liverpool, L69 3GH, U.K. E-mail: r.mines@liv.ac.uk , rafidah@liv.ac.uk , matt1982@liv.ac.uk, cantwell@liv.ac.uk

1. Introduction

Micro lattice structures, manufactured using the selective laser melting process, have potential for use in aerospace sandwich structures [1,2]. In this manufacturing process, metallic powders, such as Stainless Steel 316L (SS316L) or Titanium Alloy Ti-6Al-4V (Ti64), are selectively melted in a layering process [3] to form a Body Centred Cubic (BCC) structure with a strut diameter of 0.2mm and a cell size of 2.5mm (see Figure 1) [3]. Such structures are 'grown' in an SLM250 machine [3], and then used as core materials in sandwich panels [2]. The overall aim of this work is to quantify the foreign object impact performance of these structures, for potential use in fuselage and wing structures.

An important issue in this work is the progressive collapse of the BCC micro lattice structure. This paper compares the experimentally measured crush behaviour of a block of BCC lattice with a numerical simulation using ABAQUS.

2. Experimental Tests

20mm cubic BCC blocks were manufactured with a cell size of 2.5mm in SS316L and Ti64. These blocks were then placed between lubricated platens in an Instron servohydraulic machine, and compressed under static loading. Figure 2 shows the crush behaviour of the Ti64 specimen.

In the case of the SS316L specimen, block crush is dominated by plastic collapse at node hinges. This mode of failure has been analysed by Ushijima et. al. [4], and Gűmrűk and Mines [5], and they have shown that collapse behaviour is highly sensitive to block boundary conditions. Block collapse is controlled by parent material plasticity.

In the case of the Ti64 specimen, block crush is dominated by material rupture. Ti64 is a much more difficult material to work with using SLM, and the current state of manufacturing technology gives brittle parent material behaviour [2].

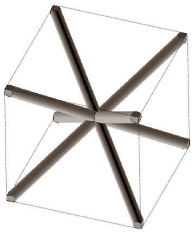

Fig. 1. Body Centred Cubic (BCC) geometry

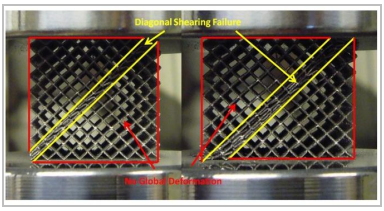

Fig. 2. Collapse of Ti64 blocks

3. Numerical Simulation using ABAQUS

In order to further investigate the above issues, a numerical simulation using the non linear finite element code, ABAQUS, was developed. In this, a single cell was modelled with solid elements. This approach was justified in terms of detailed modelling of parent material flow and rupture, with

detailed modelling of progressive collapse deformation. Figure 3 shows the model. The presence of surrounding unit cells was accounted for by ensuring that the faces, at the edge of the unit cell, all remain in the same plane during deformation.

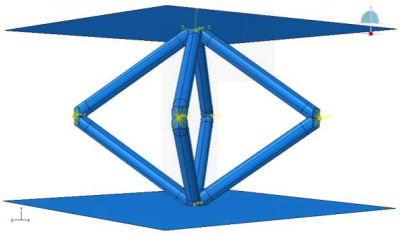

Fig.3. Abaqus unit cell model

An important issue in the numerical simulation is the quantification of the stress strain behaviour of parent material. This has been achieved by manufacturing micro struts individually, and testing them in a small tensile test machine [2,3]. Data for SS316L is given in [3] and for Ti64 is given in [2].

4. Comparison of experiment and simulation

The numerical simulation was validated for the SS316L case, as this material gives stable collapse. Figure 4 compares results for Ti64.

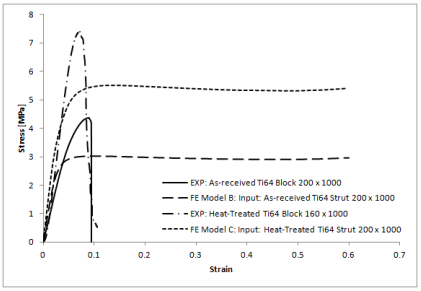

Fig. 4. Comparison of block compression for experiment and simulation for Ti64

Comparison of the experiment with simulation is not so good in this case, given the low ductility of the Ti64 SLM material and the complexity of rupture behaviour. The rupture approach of Hooputra et. al. [6] is being investigated for this case.

5. Conclusions

This experimental and numerical work has raised a number of interesting issues. In the case of SLM realized micro lattice structures there is an intimate relation between manufacturing parameters (laser power, laser exposure time), material mechanical properties (flow and rupture) and structural performance (progressive collapse) [2]. This work has identified the need for good quality mechanical property data, and the correct selection of flow and rupture finite element modelling. In this way, a rigorous approach is developed to realizing optimal micro lattice structures with associated quantified structural performance.

Acknowledgements

This research was funded by EU FP6 Celpact and EPSRC grants EP/009398/1 and EP/C009525/1. Ms Rafidah Hasan was supported by the Malaysian Government.

References

[1] Mines, R.A.W., On the characterisation of foam and micro lattice materials in sandwich construction, Strain **44** , 2008. pp71-83

[2] Mines, R.A.W., Tsopanos, S., Shen, Y., Hasan, R., McKown, S.T., Drop weight impact behaviour of sandwich panels with metallic micro lattice cores, To be published International Journal of Impact Engineering. DOI: 10.1016/j.ijimpeng.2013.04.007

[3] Tsopanos, S., Mines , R.A.W., McKown, S., Shen, Y., Cantwell,W.J., Brooks, W., Sutcliffe, C.J., The influence of processing parameters on the mechanical properties of selective laser melted stainless steel micro lattice structures, J. Manu. Sc. and Eng. **132** 2010. pp0410111 -12

[4] Ushijima, K.,Cantwell, W.J., Mines, R.A.W., Tsopanos, S., Smith M. , An investigation into the compression properties of stainless steel micro lattice structures, J. Sand. Struct. and Mat. **13:3** 2010. pp303-329

[5] Gűmrűk, R., Mines, R.A.W., Compressive behaviour of stainless steel micro-lattice structures, International Journal of Mechanical Sciences **68** 2013. pp125–139

[6] Hooputra, H., Gese, H., Dell, H., Werner, H., A comprehensive failure model for crashworthiness simulation of aluminium extrusions. International Journal of Crashworthiness, **9(5)** 2004. pp449-463.

30th DANUBIA-ADRIA
Symposium on Advances in Experimental Mechanics
September 25-28, 2013 - Primošten, Croatia

1G03 013

CRITICAL ASPECTS OF THE CRACKED BRAZILIAN-DISC TEST EXPLORED BY THE METHOD OF REFLECTED CAUSTICS

Stavros K. Kourkoulis[1]

[1] National Technical University of Athens, Department of Mechanics, Laboratory of Testing and Materials, Theocaris building, Zografou Campus, 157 73, Athens, GREECE. E-mail stakkour@central.ntua.gr

1. Introduction

The centrally cracked Brazilian-disc test (Fig.1) is widely used for the determination of fracture toughness of brittle rock-like materials since any combination of mode-I and mode-II loading types is achieved by adjusting the load-crack angle, ϕ_o. The test was standardized by ISRM in 1988 and it is since then under intensive study, however quite a few questions (for example the length of the contact arc at the disc-jaw interface) remain to be answered.

The stress intensity factors (SIFs) for a centrally cracked circular disc under uniform radial pressure were recently determined in closed form [1] for a short crack (with respect to the disc radius). Moreover the contact conditions at the disc-jaw interface were analytically explored by Kourkoulis et al. [2]. In the present study an attempt is described to experimentally assess the above analytic solutions with the aid of the reflected caustics technique [3].

2. Experimental procedure

2.1 The contact arc and the SIFs by caustics

The length, ℓ, of the contact arc in case an elastic disc is compressed between the jaws of the ISRM standardized device was recently determined as [4]:

$$\ell^2 + 2\left|C^*\right|^{\frac{2}{3}}\ell^{\frac{4}{3}} - \frac{\left[2W_{x'}(\alpha)\right]^4}{4\lambda_m^2} = 0 \qquad [1]$$

C^* is a constant (depending on the geometric characteristics of the disc, the mechanical properties of the disc's and jaw's materials and the experimental set-up), λ_m is the magnification factor and $W_{x'}$ is the characteristic dimension of the contact caustic.

Concerning the experimental determination of SIFs using the cracked Brazilian disc configuration the main difficulty is that the field around the crack-tips is of compressive nature. Therefore a distinction should be made between mathematical cracks and slits. In general the first stress invariant, on which the caustic's shape depends, at the tip of a crack is the same to that of a slit, independently more or less from the exact slit's shape [5]. Assuming stress-free lips the following formula for Mode-I and -II SIFs were proposed by Theocaris and Sakellariou [5]:

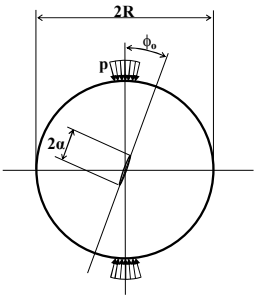

Fig. 1. The configuration of the problem

$$K_I = \frac{0.311}{Z_o t c \lambda_m^{3/2}}\left[D_{(-)}\right]^{5/2},\ K_{II} = K_I \cot\phi_o \quad [2]$$

In Eq.(2) t is the disc's thickness, c is the optical constant for reflection, Z_o is the distance between screen and specimen while $D_{(-)}$ is the diameter of the caustic in case of compressive stress fields.

2.2 Experimental procedure and results

The experimental set-up used consists of a He-Ne laser and two collimating lenses transforming the diverging laser beam to a collimated and then to a converging one with its focal point in front of the specimen, permitting thus control of the set-up's magnification factor λ_m. The beam impinges on the loaded specimen and the reflected rays are then driven with the aid of a semi-reflector, at an angle equal to 45° with respect to the specimen's plane, towards a screen forming the caustic [3].

The experiments were realized using the ISRM device and a 50 kN loading frame. The specimens, made of PMMA, were cylindrical discs with R=50 mm and t=10 mm. They were centrally cracked artificially. The slits had length 2α=10 mm while the distance between their lips was equal to 0.2 mm. Typical caustics from the disc-jaw contact region are shown in Fig.2a while in Fig.2b the caustics around the slit tips can be seen for ϕ_o=10°.

3. Experimental results and discussion

The contact angle according to the analysis of ref.[2], as a function of the force applied, is plotted in Fig.3a for a disc-jaw pair made of PMMA-steel, respectively. In the same figure the contact angle as obtained experimentally by measuring the distance W_x between the extreme points of the caustic curve (Fig.2a) and solving numerically Eq.(1) is plotted. It is clear that for low loads the agreement is quite satisfactory. For loads exceeding 60% of the fracture one the experimental data exceed those of the analytic solution. This is obviously due to deviation from linearity since the stress field at the vicinity of the disc-jaw interface is strongly amplified.

The respective analytic [1] and experimental data concerning the SIFs are plotted in Fig.3b for ϕ_o=10° and the same disc-jaw pair. Again the agreement is very satisfactory for low loads while discrepancies appear exceeding even 10% as the load level approaches that causing fracture. Again it is the deviation from linearity that can explain this behaviour.

Concluding it can be said that reflected caustics is a useful and flexible tool, permitting thorough experimental exploration of various critical aspects of the Brazilian-disc test. However the assumption of linearity (on which the present form of caustic's equations is based) is crucial. Taking into account the inevitable stress concentrations (both at the disc-jaw interface and also at the slit tips) the method

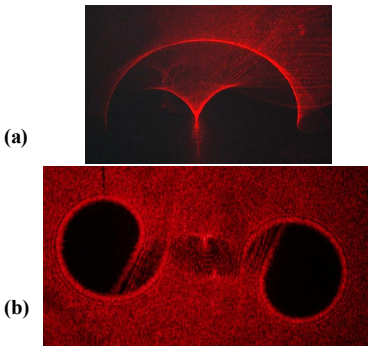

Fig.2. Caustics from the disc-jaw interface (a) and the tips of the slit for a specimen with ϕ_o=10° (b).

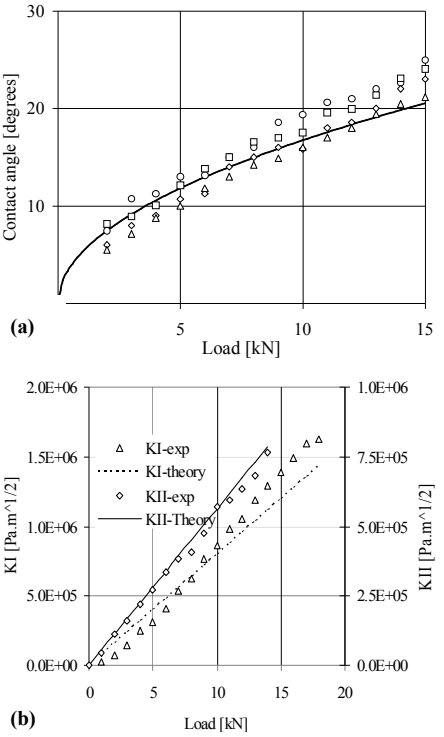

Fig.3 Experimental vs. analytic results for the contact length (a) and the SIFs (b).

should be applied very thoughtfully. Unfortunately, at least for the moment being, some interesting attempts to develop caustic's equations applicable in case of plasticity are not yet successful.

Acknowledgements

The author acknowledges the kind contribution of Prof. D.N. Pazis of the Dept. of Mechanics, NTUA.

References

[1] Markides Ch.F., Pazis D.N., Kourkoulis S.K., Appl. Math. Mod., **35**, pp. 5636–5651, 2011.

[2] Kourkoulis S.K., Markides Ch.F., Chatzistergos P.E., Int. J. Rock Mech. & Mining Sci., **57**, pp.132-141, 2012.

[3] Theocaris, P.S., J. Appl. Mech., **37**, 1970, pp. 409-415.

[4] Kourkoulis, S.K., Markides, Ch.F., Bakalis G., Smooth elastic contact of cylinders by caustics: The contact length in the Brazilian-disc test, Submitted for publication, 2013.

[5] Theocaris, P.S., Sakellariou, M., Acta Mechanica, **85**, pp. 55-70, 1990.

30th DANUBIA-ADRIA
Symposium on Advances in Experimental Mechanics
September 25-28, 2013 - Primošten, Croatia

1G04 033

EXPERIMENTAL CHARACTERISATION OF A VIBRATING SOURCE USING THE BLOCKED FORCE APPROACH

Goran Pavić

National Institute of Science, Vibration and Acoustics Laboratory, 25 avenue Jean Capelle, F-69621 Villeurbanne, FRANCE. E-mail: goran.pavic@insa-lyon.fr

1. Introduction

The current state of the art in vibration analysis does not allow yet the modelling of excitation by a vibrating source, such as a compressor, entirely by computation. This has to be done by measurement, but the task may prove to be a lot more difficult than it appears at first glance.

The usual way of characterising experimentally a vibration source is by employing a mechanical impedance (alternatively: mobility) approach. The source is characterised by a twin descriptor: its excitation is given by its blocked force vector and its resistance to motion by its impedance matrix. Both descriptors refer to the connection points between the source and its support and both are frequency-dependent. The experimental analysis has thus to be done in frequency domain.

As a rule, a characterisation approach requires an inverse technique which yields ill-conditioned matrices. This produces poor results even if some regularisation is applied. What is more, a typical impedance technique requires de-coupling of the source from its support. This may result in a considerable alteration of vibratory properties of the source in comparison to the coupled state. It thus appears that a characterization method which avoids decoupling of the source from its support and which is additionally free of inversion may display superiority over traditional methods.

2. Base relationships

2.1 The source descriptors

Assuming linearity, the frequency-dependent relationships between the coupling force vector F_c, and the blocked force vector F_b, reads:

$$F_c = Z_R (Z_S + Z_R)^{-1} F_b , \qquad (1)$$

Each symbol F in (1) stands for a generalized force vector, comprising both forces and moments, while Z stands for an impedance matrix. The indices S and R refer to the source and the receiver (support) respectively. F_c refers to the operational excitation between the source and the support: it represents usually the target of an analysis.

Eq. (1) shows that the full coupling conditions between a source and its support will be defined if the blocked force and impedance of the source as well as the support impedance are identified. Once the coupling conditions are known, the vibration transmission from the source to the support can be easily found by assuming that the support is uncoupled and externally driven by the coupling force. The identified blocked force and impedance can then be used in conjunction with any support in order to predict the transmission of vibration.

2.2 The blocked force

By extending the Thévenin's theorem [1] to linear vibration systems, a simple relationship can be found between the quantities involved, [2]:

$$F_b = -Z_c v_c , \quad Z_c = Z_S + Z_R \qquad (2)$$

where v_c, Z_c stand for the coupling velocity vector and the coupled impedance matrix respectively.

Eq. 2 provides a major practical result: the blocked force can be assessed by carrying out measurements in coupled conditions, moreover at no cost of matrix inversion. This result makes a basis of the novel characterization technique.

3. The characterization method

While the blocked force is provided explicitly by Eq. (2), this is not the case with the source impedance. In order to extract this impedance from the measured coupled impedance Z_c a convenient receiver has to be employed.

The simplest receiver which can fulfill the task is a free rigid mass, [3], one per connection point. In such a case a set of matrix equations can be readily obtained by computation, Eq. (3), which relates the coupling generalized force F_c to the generalized velocities of the coupling points v_c.

$$F_c = -Z_m v_c \tag{3}$$

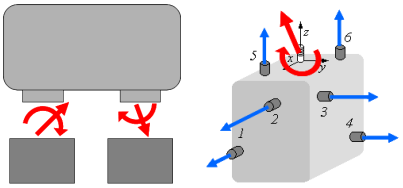

Fig. 1. Left: Source + mass receiver; right: loading mass equipped with sensors.

In practice the free conditions can be simulated by using a soft suspension of loading masses. If the masses are mutually decoupled the impedance Z_m will become a matrix of sub-matrices aligned along the diagonal which improves conditioning.

The 6 degree-of-freedom of each loading mass can be measured by 6 sensors as shown in Fig. 2. The velocity vector at the coupling point on the n^{th} loading mass, $v_{c,n}$, and the velocity vector at sensor positions, $v_{r,n}$, are interrelated via a transfer matrix Γ_n which depends only on the system geometry.

$$v_{c,n} = \Gamma_n v_{r,n} \tag{4}$$

An incomplete yet very suitable way of source characterisation consists of taking the resultant blocked force vector, which then contains only 6 components. The corresponding source impedance is a 6×6 matrix.

4. Example: oil pump characterization

A motor-driven oil gear pump unit has been characterized by its blocked force, using a single loading mass suspended by rubber mounts, Fig. 2.

Fig. 2. Motor-pump unit coupled to its loading mass.

The mass impedance matrix was identified by usual impact hammer measurements and 6 piezo accelerometers as sensors. The same sensors were used to measure the running vibration velocities of the pump. Using Eqs. (3) and (4) subjected to some further mathematical treatment, the blocked-force auto and cross spectra were established. Fig. 3 shows the auto rms spectra of force components; the moment components are of similar look.

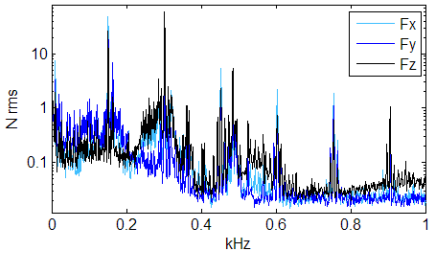

Fig. 3. Auto spectra of blocked-force components.

Using the measured blocked force data, the coupling force spectra were computed and then the vibration spectra at measurement points were re-computed using the theoretical values of loading mass impedances. Fig. 4 shows the measured and computed accelerations of measurement point 2.

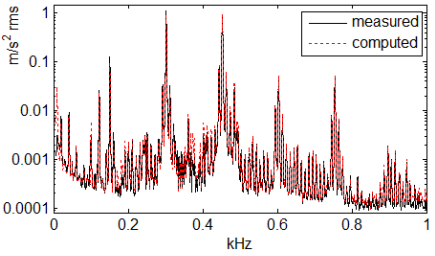

Fig. 4. Vibration accelerations at a measurement point.

Good matching demonstrates the robustness of the source characterization approach used.

References

[1] Thévenin, L.C., Sur un nouveau théorème d'électricité dynamique, Compte rendu des Séances de l'Académie des Sciences, 1883, pp. 159-161.

[2] Moorhouse, A.T., Elliott, A.S., Evans, T.A, In situ measurement of the blocked force of structure-borne sound sources, Journal Sound Vib. **325**, 2009, pp. 679-685.

[3] Pavić, G., Passive method for determination of vibration impedance of complex structures, Proc. Inter-Noise 93, 1993, pp. 1843-1846.

30th DANUBIA-ADRIA
Symposium on Advances in Experimental Mechanics
September 25-28, 2013 - Primošten, Croatia

1G05 056

MEASUREMENT OF CRACK DIRECTION AND STRESS FIELD AT BIFURCATED NOTCH TIP

Shinichi Suzuki[1], Takahiro Yabo[2], Tatsuya Fujishima[2], Yusuke Iwasaki[2]

[1] Toyohashi University of Technology, Department of Mechanical Engineering, Tempaku-cho, Toyohashi, Aichi, 441-8580, JAPAN. E-mail: shinichi@me.tut.ac.jp

[2] Graduate School of Toyohashi University of Technology, Department of Mechanical Engineering, Tempaku-cho, Toyohashi, Aichi, 441-8580, JAPAN. E-mail: s-m2@rm.me.tut.ac.jp

[3] Graduate School of Toyohashi University of Technology, Department of Mechanical Engineering, Tempaku-cho, Toyohashi, Aichi, 441-8580, JAPAN. E-mail: s-m1@rm.me.tut.ac.jp

1. Introduction

When a brittle material breaks under external forces, fast propagating cracks often appear whose speed is more than several hundred meters per second. The fast propagating crack bifurcates into two cracks when the crack speed is high enough. Since bifurcation is a characteristic feature of fast propagating cracks, many researchers have studied it [1-4], however, the mechanism is not fully understood.

One of the authors applied high-speed holographic microscopy to take microscopic photographs of fast propagating cracks at bifurcation [3]. They found that the bifurcation process is three dimensional and energy release rate increases continuously across the bifurcation point. The above results require us to carry out two dimensional experiments on bifurcated cracks that are more accurate than the previous ones [4].

Kalthoff [1] measured the propagation direction of cracks that arose at the tip of V shaped notches, which were used as a model of bifurcated cracks. He also measured the stress field around the notch tips with photoelasticity.

The present study measures the propagation direction of cracks that arise at the tip of Y shaped notches, which are much closer to real bifurcated cracks than V notches. The present study uses caustic method to measure the stress field at the tips of Y notches.

2. Methods

2.1 Specimen and crack direction

Specimens used in the present study are made of PMMA, and the size is 250mm in length, 250mm in width and 3mm in thickness. They have Y shaped notches of 125mm in length, and the notch tips are near the center of the specimen. Length l_b of two branch notches is 24mm, and the bifurcation angle ϕ are from 5 to 45° (Fig. 1).

Tensile force is applied to the specimen perpendicularly to the notch. A crack arises at one of the two tips of the bifurcated notch. Crack direction θ defined in Fig. 1 is measured.

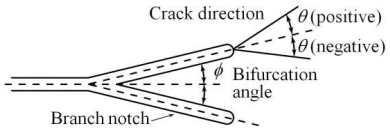

Fig. 1. Bifurcated notch and crack direction.

2.2 Caustic method

Caustic method [5] is applied to investigate the stress field in the vicinity of a notch tip. It can measure the ratio of stress intensity factor K_{II} of shearing mode to K_I of opening mode.

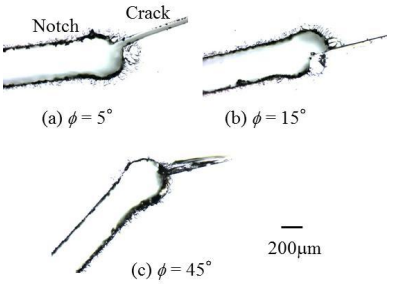

Fig. 2. Cracks that arise at the tips of the branch notches of length l_b=24mm.

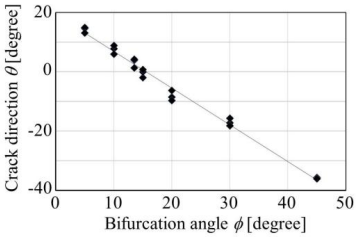

Fig. 3. Crack direction versus bifurcation angle. The length of the branch notch is 24mm.

3. Results

3.1 Crack direction

Figure 2 displays three photographs of the notch tip and crack. The photographs clearly say that the crack direction θ is positive when bifurcation angle ϕ is 5°, almost zero at ϕ=15° and negative at ϕ=45°.

Figure 3 shows the measurement result of crack direction θ as a function of bifurcation angle ϕ. The figure indicates that the crack propagates in the direction of the branch notch whose bifurcation angle is about 15°. This is very close to the bifurcation angle 13.5° of rapid crack bifurcation [3-5].

3.2 Caustic images

Figure 4 shows the caustic images of the notches with three bifurcation angles. The photographs of (a), (b) and (c) in Fig. 4 correspond to the notches (a), (b) and (c) in Fig.2 respectively. When the bifurcation angle ϕ is 5° or 45°, the caustic images are asymmetric, and the mode II stress intensity factor K_{II} is negative at ϕ=5°, and positive at ϕ=45°. When ϕ=15°, the caustic image

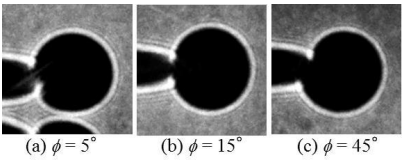

Fig. 4. Caustic image at the notch tips with three different angles of bifurcation.

is symmetric, thus K_{II} is zero.

4. Conclusions

(1) A crack propagates in the direction same as that of a branch notch of the Y shaped notch when the bifurcation angle ϕ is about 15°. The angle is very close to that of rapid crack bifurcation.

(2) The mode II stress intensity factor K_{II} is zero at ϕ=15°.

(3) These results are almost the same as those given by Kalthoff [1] with V shaped notches.

Acknowledgements

The research was supported by Grant-in-Aid for Scientific Research (24560097) of The Ministry of Education, Culture, Sports, Science and Technology, Japan.

References

[1] Kalthoff, J.F., On the Propagation Direction of Bifurcated Cracks, In Dynamic Crack Propagation: editor C. Sih, Nordhoff, 1972, pp. 449-458.

[2] Seelig, Th., Gross, D., On the Interaction and Branching of Fast Running Cracks – A Numerical Investigation, J. Mech. Phys. Solids, **47**, 1999, pp. 935-952.

[3] Suzuki, S., Sakaue, K., Iwanaga, K., Measurement of Energy Release Rate and Energy Flux of Rapidly Bifurcating Crack in Homalite 100 and Araldite B by High-Speed Holographic Microscopy, J. Mech. Phys. Solids, **55,** 2007, pp. 1487-1512.

[4] Suzuki, S., Miyashita, T., Measurement of Opening Displacement and Stress Intensity Factor of Bifurcated Notch by Moiré Interferometry, J. Solid Mech. Materials Eng., **2**, 2008, pp. 25-37.

[5] Kalthoff, J.F., Shadow Optical Method of Caustics, Handbook on Experimental Mechanics: editor A. Kobayashi, Prentice Hall, 1987, pp. 430-500

30th DANUBIA-ADRIA
Symposium on Advances in Experimental Mechanics
September 25-28, 2013 - Primošten, Croatia

1G06 008

EVALUATION OF STRUCTURAL NOISE IN THE CABIN AIRCRAFT VIBRATION INFLUENCE FROM THE NEW ENGINE GENERATION ON RESULTS OF EXPERIMENTAL INVESTIGATION

Viatcheslav Baklanov [1]

[1] Tupolev Design Bureau, Tupolev Embankment 17, 105005,Moscow, RUSSIA. E-mail: baklanov@tupolev.ru

1. Introduction

Compliance of aircraft to new noise standards defines the tendency to switch to extra-high bypass ratio engines. This direction development of power plants leads to increasing of fan diameter and the formation of shock waves at supersonic speed of blade tips.Fan shaft frequency reduction is one of the measures necessary for shockwaves control. Due to the decrease of frequency vibration spectrum shifts towards the low-frequency range. It is these components that will determine the power plant dynamic influence, transferred onto the airframe via mount points.

An airframe typically possesses dozens of oscillation modes in the low-frequency spectrum part. Interaction of some of them with the influence of power plant may cause low-frequency high-level noise generation in the cabin [1].
The acoustic field of the pressurized cabin has become a subject to essential changes since high by-pass engines were introduced.
Facilities for reduction engine vibration intensity and vibration transfer along structure come first by selecting of vibration protection for pressurized cabin and integration vibration protection units into engine mounting attachments seems to us the most effective.

But whatever vibration protection means (active or passive) are used to select parameters of vibration isolation units, calculated model is required which is based on real dynamic characteristics of engines and airframe in mounting points.

2. Experimental results

The long-term investigations directed to dynamical characteristics definition for bodies of several engines (with different by-pass ratio) and airframe constructions of main-line aircraft allow to significantly specify calculation models of modern aircraft constructions in engine's rotor frequency range [2].

The multi-connected dynamic model of the system «Engine-mount-airframe» can be studied by dividing it into independent subsystems, reaction forces being applied in the separation points, where the generalized dynamic characteristics (for example, dynamic compliance) are used as factors of proportionality between dynamic displacement and forces [3].

Although design models of the airframe, the pylon and the cabin take into account some thousands of freedom degrees, the engine is still considered to be a rigid body, its mass and moments of inertia taken into account only.

This is the due to an old tradition of successful flutter calculations, as the rigid-body engine model is still true in that range (low frequency range, below 15 Hz).
Generalization of performed investigations has revealed that dynamic behavior of advanced gas turbine engines casings corresponds to rigid state model up to 20…40 Hz according to pass-by ratio.

If pass-by ratio is increased up to estimated 8…12 we should expect that upper boundary of dynamic behavior of the engine, as a rigid body does not exceed 10 Hz.

Within wide range of rotor frequencies dynamic behavior of engine casing corresponds to model of elastic-inertial system or to elastic-dissipative element; differing substantially from idealized model of aircraft gas turbine engine as a rigid body both by value of dynamic compliance module and by type of dynamic behavior.

As evident from presented data, the dynamic behavior of the airframe (at engine brackets attachment points) depends on the frequency range. Elastic airframe's behavior accepted in many calculation models is limited by a rather narrow frequency range (30…100 Hz), which doesn't embrace the rotor frequency range of multi-shaft engine.

The obtained characteristics have allowed us to calculate the expected noise due to vibration impact of engine [4]. The calculation data have been confirmed by the results of experimental measurement (fig.1).

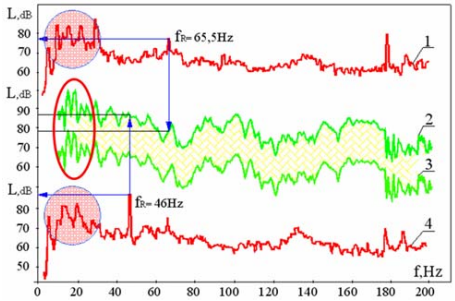

Fig. 1. The comparison of experimental and prediction data of the structure-borne sound in aircraft cabin. 1, 4 – experimental data V_E=10mm/s; 2, 3 – prediction data V_E=10mm/s, V_E=1mm/s accordingly.

The comparison of the expected noise and the experimental data yields both a good convergence of fan rotor harmonic level and a possibility of high-intensity low-frequency components generation at the operation level of engine vibration.

It was confirmed by new investigations on the airframe QTD-2 (Boeing-777 with engines GE-90-115B with bypass-ratio - 9), where low-frequency components rise over 30-40 dB [5].

Decreasing structure-borne noise will be an essential problem for providing comfortable conditions in the pressurized cabin, as its role increases with the introduction of high by-pass ratio engines.

The necessity of new vibroisolation mounting relates with: 1) extension of vibration spectrum of modern engines and its tendency to shift towards the low-frequency region; 2) insufficient efficiency of existing vibration protection, developed on basis of out-of-date computation models, especially in the low-frequency region; 3) change of dynamic characteristics of airframe and engine bodies at attachment points with the increase of engines by-pass ratio.

Acknowledgements

I am deeply grateful to the participants of the experimental investigations Zhukovsky Flight Test Center, Flight Institute by name M.M.Gromov and Vibroacoustic laboratory of A.N.Krylov Center (St.Petersburg).

References

[1] V.Baklanov.Interaction of power plant with airframe of new generation aircraft. 4th European Conference.for Airospace Sciences (EUCASS), S.Peterburq, 2011.

[2] Agafonov, V. K., Baklanov V. S., Vul V. M., Popkov V. I., Popov A. V. The Investigation of Dynamic and Vibroacoustic characteristics of Aircraft and an Engine by calibration Test Methods, VII Aero-acoustic Conference., TsAGI, Moscow, 1990, pp. 141-144.

[3] Baklanov V.S., Dynamic model of Engine-Mount-Airframe System of Trunk-Aircraft Basing on Results of Impedance Data Tests at Attachment Points, Ninth Congress on Sound and Vibration, Orlando, Florida, USA 2002.

[4] V.Baklanov, A. Zayakin, E. Orlenko, S. Postnov.The calculation of structural noise in cabin for aircraft with high-by-pass ratio engines. 11th AIAA/CEAS Aeroacoustic Conference, Monterey, California, May 23-25 2005, AIAA 2005-3034, pp. 1-9.

[5] E. Nesbitt, JiaYu and all, Quiet Technology Demonstrator 2 Intake Liner Design and Validation. 12th AIAA/CEAS Aeroacoustic Conference, 8-10 May, 2006, Cambridge, Massachusetts.

1G07 140

THE PARAMETRIC MODELING OF EXPERIMENTAL DATA

Alessandro Freddi [1]

[1] Academy of Science of the Institute of Bologna, Via Zamboni 31, I-40125 Bologna, ITALY. E-mail: alessandro.freddi@unibo.it

1. Introduction

Experiments must not be confused with tests: the last are only tools for hypotheses verification, but don't offer indications on the generalization of the conclusions. The Experimental Stress Analysis has the task of building models, even in case of incomplete data and of badly posed problems, in the belief that only the availability of a model is solution of a structural problem [1].

Since data are subjected to measurement uncertainties, they never exactly fit a model and adjusting the model parameters to a set of experimental results which are supposed to follow a theory, presumes the data are well determined with an acceptable level of experimental errors but also that the theory is sufficiently representative of the phenomenon [2]. These observations show the inverse value of the experimental activity and of the related techniques necessary for answering practical engineering problems. So concepts such as ill-posedness, regularization, stability, etc. have become familiar to the experimenters [3].

The typical approach needs the selection of an error function that represents the "distance" of experimental data to the previsions of theoretical (or numerical) models. The model parameters are then determined, adjusting their values to minimize this function, i.e. solving an optimization problem.

Numerical models are often expressed in discrete matrix algebra, but the majority of engineering inverse problems, however, can not be treated in matrix form, because they are too complex or the underlying theory is not formulate in this way. This is the case here presented, of the parametric identification by extrapolation when a singularity dominates the stress/strain field.

2. Methods

The extrapolation of experimental data in presence of a singularity, for linear and nonlinear cases, is performed utilizing the Elastic Fracture Mechanics theory, by the minimization of an error function for a variety of cracks geometries. The following examples are presented [4]:

- Photoelastic stress analysis of a single 3D crack and of two 3D interacting non-coplanar cracks in uniform state of stress
- Holographic interferometry displacements analysis of two 3D interacting coplanar cracks in uniform state of stress
- Strain gauges analysis around a single crack in uniform state of compressive stress.

A discussion on the adequacy of the model and on the nonlinear behavior is finalized to a practical estimation of stress intensity values in real engineering cases.

2.1 Photoelastic stress analysis of a single 3D crack with uniform state of stress

Fig.1 shows a photoelastic fringe pattern of a single circular crack in uniform state of stress.

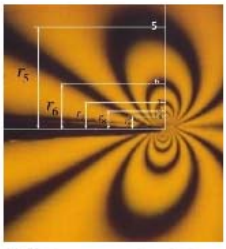

Fig. 1. Photoelastic fringe pattern of a single circular crack in uniform state of stress.

2.2 Photoelastic stress analysis of a two non-coplanar 3D cracks in uniform field of stress

Fig.2 shows the analysis for two interacting cracks. In this case both K_I and K_{II} factors are present and must be identified. The cracks are internally pressurized, that's equivalent to an uniform distribution of stress.

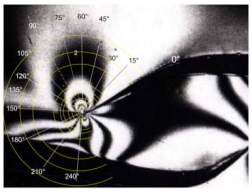

Fig. 2. . Photoelastic fringe pattern of two circular non coplanar cracks internally pressurized.

Since the problem is nonlinear, the Newton-Raphson iterative/incremental method is suitable for parameters identification, through the minimum of an error function.

2.3 Holographic interferometric displacements analysis of a two coplanar 3D cracks in uniform field of stress

Fig. 3 shows the displacements contour pattern of the deformed surfaces of two cracks very close one another. The parametric modeling (by the Stress Intensity Factors estimation) of the experimental data can be performed by the Least Square Method (LSM) applied to selected directions perpendicular to the crack front or by extra-polation of the Factors along these directions. The first method smoothes the local experimental errors but does not clearly point out differences on displacements, while the second magnifies the differences, even if is much more sensitive to experimental errors. For this reason, since the scope of the parametric modeling in this case was the discovering local differences in different crack tip points, the second method is seemed preferable, Fig. 4.

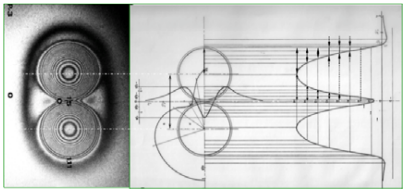

Fig.3. Holographic interferometry application to two co-planar cracks in an infinite medium. The cracks are internally pressurized.

2.4 Stress intensity Factor evaluation by the strain gauges technique.

The last example shows the parametric modeling of a crack of irregular shape in a huge steel column with a pre-compressive state of stress subjected to cyclic loads, through strain-gauges measurements. The difficulty in this case is due to the surface plastic zone that does not allow a direct determination of K_I by extrapolation at the radius zero. The measurements and the extrapolation must be done at a certain distance from the crack tip for avoiding to enter the plastic area, where K_I is not valid parameter, even if it controls the plastic zone size. For these reasons an iterative method was suggested for obtaining acceptable estimation, through a balance between the value of K_I and the border of the plastic zone.

3. Results

The results of the three examined cases are summarized in the following results: for the first case of Fig.1, (a linear problem) the solution is given by normal equations of the LSM: K_I=0.817 MPa√mm versus a theoretical value of K_I=0.825 MPa√mm. For the second problem of Fig. 2, a minimum of the error functional J is reached (=10.76) after 27 iterations, starting from two tentative values. The found values are: K_I=0.740 MPa√mm and K_{II}= 0.283 MPa√mm.

In the holographic analysis of Fig.3, the following diagram identifies the K parameter along the directions A and B:

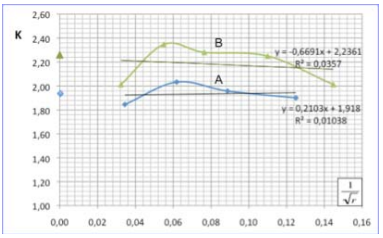

Fig.4. Stress intensity factor in directions A and B by local extrapolation.

The ratio $M=K_B/K_A$ =1.17 is much more insensitive to the errors than the single values, high dependent on the calibration of the material parameters (E, ν, etc).

References

[1] Doyle, J.F., Modern Experimental Stress Analysis, J.Wiley, 2004.

[2] Laermann, K.H., Inverse Problems in Experimental Structural Analysis. Shaker Verlag, Aachen, 2008.

[3] Liu, G.R., Han, X., Computational inverse techniques in nondestructive evaluation, CRC Press LLC. Boca Raton, London, New York. ISBN 0-8493-1523-9, 2003.

[4] Freddi, A., An Experimental Stress Analysis Syllabus and Course Design: 2012. "Giornata E. Funaioli". In press.

30th DANUBIA-ADRIA
Symposium on Advances in Experimental Mechanics
September 25-28, 2013 - Primošten, Croatia

1G08 004

INTRODUCING FRACTALS TO MECHANICS OF FRACTURE. INSTABILITIES IN VISCOELASTIC AND DUCTILE FRACTURE

Michael P. Wnuk [1]

[1] College of Engineering and Applied Science, University of Wisconsin – Milwaukee, USA. E-mail: mpw@uwm.edu

Classical mechanics including mechanics of fracture is often unsatisfactory when a solution predicts a singularity and the need arises to interpret the underlying physical meaning or lack thereof. A customary practice to deal with the singularity problem is to exclude a small region near the singular point, for which a different constitutive law – usually non-elastic – is postulated. This approach is adequate provided that the stress field outside the singular region is dominated by the elastic behavior. An alternative approach that successfully resolves problems containing singularities is the averaging process, also known as the quantization procedure – or – equivalently, application of the global criteria for the attainment of the critical state. Example of continuum theory of this kind is the J-controlled HRR asymptotic stress and strain fields embedded within the K-dominated asymptotic field. Here J stands for Rice's integral and K is Irwin's stress intensity factor used in linear elastic fracture mechanics (LEFM).

In last decade some new approaches such as quantized fracture mechanics and fractal fracture mechanics have been developed. These techniques necessitate implementation of the novel mathematical tools – as reviewed in the present paper.

Early stages of fracture and the pre-fracture deformation states associated with a stable propagation of a subcritical crack in viscoelastic and/or ductile solids are described in some detail. The initial stable growth of crack manifests itself as a sequence of the local instability states, while the onset of catastrophic fracture corresponds to attainment of global instability, following an analogy with the buckling phenomenon in shells.

2A01 010

SHAPE MEMORY ALLOYS AND POLYMERS STUDIED IN TENSION BY ADVANCED INFRARED TECHNIQUE

Elzbieta A. Pieczyska[1], Hisaaki Tobushi[2], Shunichi Hayashi[3], Michal Maj[1] and Maria Staszczak[1]

[1] Institute of Fundamental Technological Research, Polish Academy of Sciences, Warsaw, POLAND. E-mails: epiecz@ippt.gov.pl, mstasz@ippt.gov.pl, mimaj@ippt.gov.pl.

[2] Aichi Institute of Technology, Toyota, JAPAN. E-mail: tobushi@aitech.ac.jp

[3] SMP Technologies Inc., Tokyo, JAPAN. E-mail: hayashi@smptechno.com

1. Introduction and methods

In order to contribute to solving the problems of recourses, energy and environment of the earth, the development of multifunctional smart materials is required. In the intelligent materials, investigation of shape memory alloy (SMA) and shape memory polymer (SMP) has attracted high attention due to their functional properties and high potential in practical applications. In SMA, the shape memory property appears based on the martensitic transformation (MT) in which the crystal structure varies depending on the variation in stress or temperature [1]. In SMP, the elastic modulus and the yield stress are high at temperatures below the glass transition temperature T_g and low at temperatures above T_g. The shape memory property appears based on the glass transition in which the characteristics of molecular motion vary depending on the variation in temperature. Among the shape memory polymers, the polyurethane has been most often practically used [2, 3].

In this paper, investigation of stress-induced martensitic transformation in TiNi SMA and thermomechanical behavior of SMP (T_g = 19 °C) in tension at room temperature (≈22°C) are presented.

2. Experimental procedure

Shape memory materials were subjected to strain-controlled tension tests with various strain rates on Instron and MTS Testing machines. During the loading process, the infrared radiation from the specimens surface was recorded by fast (538 Hz) and sensitive (0.025 K) Phoenix infrared camera. The stress and strain quantities were related to the current values of the specimen cross-section, obtaining true stress and true strain values.

3. Shape memory alloys – Infrared imaging

Since the forward MT is exothermic whilst the reverse one exhibits endothermic property, the thermovision camera turned out to be very useful for investigation of SMAs. Infrared imaging of nucleation and evolution of macroscopic transformation bands, related to martensite forward (a) and reverse (b) transition is shown in Fig. 1.

a) Loading b) Unloading

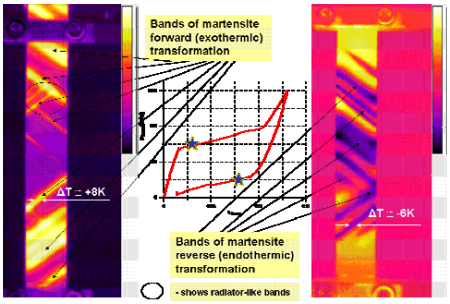

Fig. 1. Infrared imaging of transformation bands developing during a) loading and b) unloading of SMA.

At the certain level of the stress and strain state, the temperature starts to grow, indicating the homogeneous nature of the initial transformation process [5, 6]. At higher strains, inclined bands of higher temperature (ΔT≈8 K) are observed, starting usually in the specimen grip areas and developing towards the specimen center. They were called transformation bands or Luders-like deformation [6]. In the course of the SMA unloading, the specimen temperature decreases significantly and bands of lower temperature (ΔT ≈ - 6 K) nucleate, always from central part of the specimen [6].

4. Shape memory polyurethane - Effects of thermomechanical couplings.

Stress σ and temperature change ΔT versus strain obtained for SMP tensile test performed with various strain rates till rupture are presented in Fig. 2. The elongation limit of the SMP is over 180 % in case of true strain. The SMP turned out to be very flexible and it was not so easy to deform it till rupture. One can notice looking at Fig. 2 that the SMP exhibits a smooth, hardening-like behaviour at all the tested strain rates applied. This is probably a result of the reorientation of the polyurethane molecular chains that induces crystallization in the polymer structure [2, 3]. The higher strain rate, the higher temperature changes were obtained, since the process of the loading was more close to adiabatic conditions.

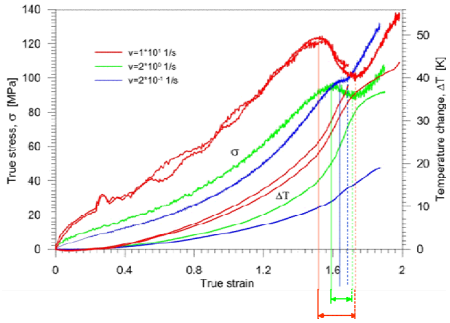

Fig. 2. Stress σ and temperature change ΔT versus strain for SMP tension with various strain rates.

At higher strains, a maximum of stress was recorded, especially pronounced at higher strain rates. Next, the stress drops are observed, followed by its increase, leading to the sample necking and rupture. The maximal temperature changes of the SMP, accompanying the specimen rupture, were quite significant; 18 K for $2x10^{-1}s^{-1}$, 38 K for $2x10^{0}s^{-1}$ and 44 K for $10^{1}s^{-1}$ of strain rate.

Stress and temperature changes related to particular stages of the SMP loading, namely the stress peak and the stress of the specimen rupture, are shown in Table 1.

Strain rate	Stress peak [MPa]	Temp. change str. peak [K]	Stress rupture [MPa]	Temp. change str. rupt. [K]
$2x10^{-1}s^{-1}$	128	25	139	44
$2x10^{0}s^{-1}$	100	20	132	38
$1x10^{1}s^{-1}$	102	14	108	18

Tab. 1. Stress and temperature changes related to the SMP stress peak and the specimen rupture.

5. Concluding remarks

- The obtained results emphasize high sensitivity and usefulness of the infrared camera to study the effects of thermomechanical couplings in shape memory alloys and shape memory polymers.
- Stress-induced martensitic transformation develops in TiNi SMA in tension via narrow bands of higher temperature. Nucleation of the localized martensitic forward transformation in shape memory alloy takes place either in the stress-concentrated area of the specimen grip or in any other area, whereas the reverse transformation always initiates in central part.
- The elongation limit of the shape memory polyurethane is over 180 % in the case of true strains. The higher strain rate, the higher temperature changes were obtained, since the process was more close to adiabatic conditions.

Acknowledgements

The research has been carried out with the support of the Polish National Center of Science under Grant No. 2011/01/M/ST8/07754. The assistance of Leszek Urbański in obtaining the experimental data is greatly appreciated.

References

[1] Yamauchi K., Ohkata I., Tsuchya K. and Miyazaki S. , Shape Memory and Superelastic Alloys, Woodhead Publishing Limited, 2011.

[2] Huang W.M., Young B. and Fu Y.Q., Polyurethane Shape Memory Polymers, CRC Press Taylor & Francis Group, 2012.

[3] Pieczyska E.A., Nowacki W.K., Tobushi H., Hayashi S., Thermomechanical properties of shape memory polymer subjected to tension in various conditions, QIRT J., **6**, 2010, pp. 189 - 205.

[4] Pieczyska E.A., Gadaj S.P., Nowacki W.K., Luckner J. and Tobushi H., Martensite and Reverse Transformation during Simple Shear of NiTi SMA, Strain, **45**, 2009, pp. 93-100.

[5] Pieczyska E.A., Activity of Stress-induced martensite transformation in shape memory alloy studied by infrared technique, J. Mod. Opt., **57**, 2010, pp. 1700-1707.

[6] Pieczyska E.A., Tobushi H, Kulasiński K., Development of transformation bands in TiNi SMA for various stress and strain rates studied by a fast & sensitive infrared camera, Smart Mater. Struct., **22**, 2013, 035007.

2A02 144

NUMERICAL MODELLING OF FATIGUE PROPERTIES OF COMPOSITES ON THE BASE OF EXPERIMENTS

Král, M.[1], Hraška, M.[1], Holý S.[2]

[1] Aerospace Research and Test Establishment (ARTE), Prague, Department of Composite Technology (DCT).

[2] Czech Technical University in Prague (CTU), Faculty of Mechanical Engineering. E-mail: stanislav.holy@fs.cvut.cz

The determination of dynamic strength and fatigue life of composite parts are becoming an integral part during design of composite structures. Right design is associated with experimental measurements on material samples to obtain the fatigue characteristics of materials.

The paper describes the methodology used in the DCT ARTE. Results are received in form of number of cycles to failure, residual strength and stiffness reduction. Technical realization of experiment is mentioned, too.

Fatigue life calculations is based mainly on the experimental data which are used to identifying the different degradation models and their implementation to finite element method software. This methodology has already been tested for continuous strand mat composite and the results of these calculations are also presented.

30th DANUBIA-ADRIA
Symposium on Advances in Experimental Mechanics
September 25-28, 2013 - Primošten, Croatia

2A03 046

ESPI AND SHEAROGRAPY THERMAL TEST FOR DEFECT DETECTION

M.J. Huang[1], Y.C. Hsu[1], Z.W. Huang[1]

[1] National Chung Hsing University, Faculty of Mechanical Engineering, 250, Kuo-Kuang Road, Taichung, Taiwan 40227, R.O.C. E-mail: mjhuang@dragon.nchu.edu.tw, okimo1013@gmail.com, domoqoo@gmail.com

1. Introduction

Holographic interferometry is a sub-wavelength high precision phase measurement technique [1], which is adopted in this article for defect detection of specimen heated by thermal radiation of halogen lamp. Among holographic interferometry, ESPI [2] and digital shearography [3] techniques, for their direct and excellent performance in sensing characteristics, are chosen herein for recording the thermal expansions and derivatives of the material surface after thermal heat flux.

Analyzing the deformation data, any non-smooth deformation with respect to their surroundings can be found and probably also the weak (e.g. defect) points of the tested sample, which very likely can cause failure of this working sample and endanger the environments and personals.

2. Sample and defects characteristics

Six artificially made defects are built on a 150 mm x 150 mm x 2 mm polyethylene plate, shown as Fig. 1. Different diameter defects are built to analyze the sensing ability of ESPI and shearography NDT techniques.

The depths of these defects are exactly the same (i.e. 1mm thick) but the diameters are quite different and are 1, 3, 5, 10, 15, and 20 mm respectively. Accordingly, these defects are all 1mm deep from the flat surface (i.e. the opposite side of the sample, also the detected surface we plan).

3. Thermal deformation simulation of sample subjected to heat flux

ANSYS FEM software is utilized for analyzing the 3D thermal deformation of the tested sample subjected to heat flux from the behind. The simulation results depict that when subjected to same heat flux radiation the bigger the simulating defect is, the higher the out-of-plan deformation of the surface at the defect center will be. Therefore, it is easier for the embedded defect to be sensed by the inspection technique.

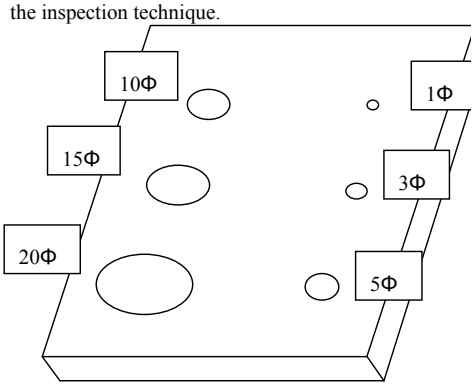

Fig. 1. Sample defects.

Tab. 1 lists the thermal deformations at surface points above different embedded defects. It is clearly shown from the simulated results that the out-of-plane deformation at surface point of large defect is higher than that of small defect. This data is also converted into the maximum fringe order of out-of-plane ESPI interferogram and shown in Tab. 2.

4. ESPI and shearography interferograms

The ANSYS out-of-plane deformation data are converted into ESPI and shearography interferograms shown as Fig. 2 and 3. Except for the smallest defect, the 1mm diameter case, the other five defects can be detected from the interferograms. For the low heat flux case, fringe-order two can be generated on the detected surface

directly above the 20mm-diameter defect center. As illustrated in the left bottom corner of Fig. 2 (, roughly at coordinate of (50, 40)), it is shown that fringe number 2 can be detected there.

	Low heat flux	Median heat flux	High heat flux
1mm	2.28E-05	2.23E-04	1.14E-03
3mm	7.75E-05	7.75E-04	3.88E-03
5mm	1.00E-04	1.00E-03	5.00E-03
10mm	2.71E-04	2.71E-03	1.36E-02
15mm	5.35E-04	5.35E-03	2.67E-02
20mm	6.32E-04	6.32E-03	3.16E-02

Tab. 1. Thermal deformation at surface points above different defect center when subjected to different heat flux (unit: mm).

	Low heat flux	Media n heat flux	High heat flux
1mm	0.07	0.71	3.60
3mm	0.25	2.45	12.25
5mm	0.32	3.16	15.80
10mm	0.86	8.58	42.88
15mm	1.69	16.89	84.47
20mm	2.00	19.97	99.85

Tab. 2. Thermal deformation at surface points above different defect center when subjected to different heat flux (unit: order).

Similarly, fringe number 1.69 and 0.86 at respectively the detected surface points directly above the 15mm-diameter and the 10mm-diameter defect centers will be generated there. Thus, the three big defects (20, 15, and 10 mm) are not difficult to be inspected by ESPI as the interferogram of Fig. 3 depicted around horizontal coordinate of 50. For the other three smaller defects (5, 3, and 1mm), the maximum fringe numbers are all less than 0.5 and the ESPI fringes are not obvious for inspection. However, the shearography interferogram provides displacement gradient signal and is thus easier to be detected.

5. Conclusions

ESPI and shearography are proved to be effective for the embedded defects detection. The defects size can be further achieved when provided with proper image processing techniques and criterions. Simulation and experimental results show that the defects near surface are more suitable to be detected than the deep ones. It is the limitation of the presented technique.

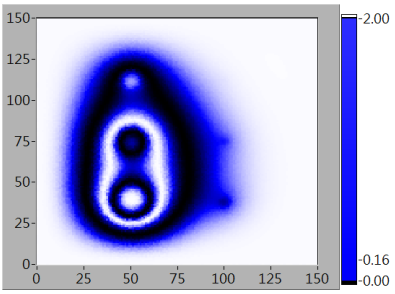

Fig. 2. Simulated ESPI interferograms.

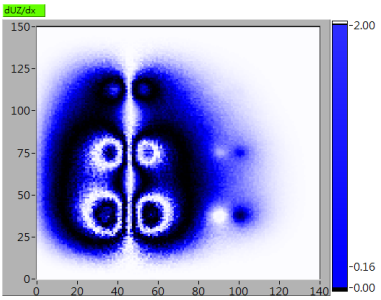

Fig. 3. Simulated shearography interferograms.

Acknowledgements

The authors would like to thank National Science Council of the Republic of China for financially supporting the research under Contract no. NSC101-2221-E-005-008.

References

[1] Vest, C.M., Holographic Interferometry. Wiley, NY, 1979.

[2] Jones, R., Wykes, C., Holographic and Speckle Interferometry. Cambridge University Press, 1989.

[3] Hung, Y.T., Shearography: a new optical method for strain measurement and nondestructive testing, Optical Engineering, **21**, 1982. pp. 391-395.

30th DANUBIA-ADRIA
Symposium on Advances in Experimental Mechanics
September 25-28, 2013 - Primošten, Croatia

2A04 108

CFRP DEFECTS DETECTION BY STEP HEATING THERMOGRAPHY

Terry Yuan-Fang Chen, Gang-Yu Lin

National Cheng Kung University, Department of Mechanical Engineering, No.1, University Road, Tainan City 701, Taiwan (R.O.C.). E-mail: ctyf@mail.ncku.edu.tw

1. Introduction

In recent years, the proportion of Carbon fiber reinforced polymers (CFRP) have been used more and more in commercial aircraft. However the nature of the CFRP materials is susceptible to internal defects, foreign bodies, and glued adverse effects the aviation safety.

In order to detect the defects inside CFRP, use of IR lock-in thermography[1] to detect CFRP materials has been reported., Finite element simulation of thermal diffusivity has also been used to explore and verify the feasibility of the method [2, 3]. In this report, an alternate method by step heating is studied from both experiment and finite element simulation. Test of the method on real CFRP specimens was carried out. The experimental results are compared to the simulated ones to validate the usefullness of step heating method.

2. Materials and Methods

2.1 Flat Composite specimens

Flat composite specimens contained four artificial defects of size 3x3 mm, 6x6 mm, 12x12 mm, 20x20 mm square shape. The defect depth is 0.3077mm from the surface (Layer 2). The defect was made by inserting different materials, such as Teflon film, centrifugal paper, centrifugal film into CFRP. Fig.1. shows the defect design of the flat composite specimens.

2.2 Finite Element simulation

Since the heating time of step heating is longer and the necessary of heat source is less. A proper heating time can be determined before the experimnt by finite element simulation.

Using one-dimensional heat conduction finite element simulation, and inputing thermodynamic properties for materials, and set the surface of the specimen be heated by a heat source with heat flux 4000 W/㎡ for 5 seconds. The temperature variation is analyzed continuously for 10 seconds.

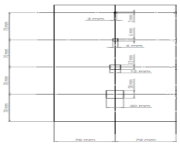

Fig.1. Flat composite specimens.

The simulated temperature difference between the defect and non-defect area vs. time is shown in Fig. 2. It can be observed that the centrifugal paper defects have the maximum temperature difference 3.77℃ and all are higher than 1.6℃ in 5s; Teflon film defects are all higher than 0.7℃ in 5s; the centrifugal film defects have the maximum temperature difference of 0.66℃, and difficult to identify defects.

2.3 Experimental test and results

Fig. 3 shows the photograph of experimental system. It contains an IR camera (TAS-G100EXD, NEC), a computer system, and protective box which have 4000 watts of heat source lamp at the top inside. The bottom of the box is set a shutter to extract after being heated uniformly.

After removing the shutter, the specimens was heated for 5s. Meanwhile, the IR image was recored and fed into computer for further examination and processing. Beacuse original image of defects are not clear, image enhancement process was applied. The tested IR images of the three types of defect, and after being enhanced are given in Fig. 4. The temperature difference between the defect and non-defect area from experimental results are showed in Fig.5.

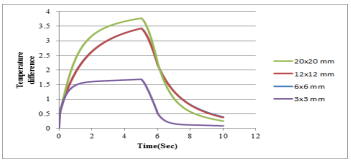

(a)

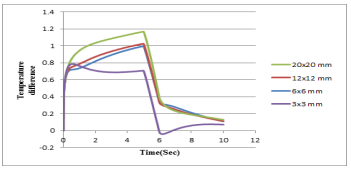

(b)

Fig. 2. Temperature difference of defects with time in layer 2. (a) Centrifugal paper defects. (b) Teflon film defects.

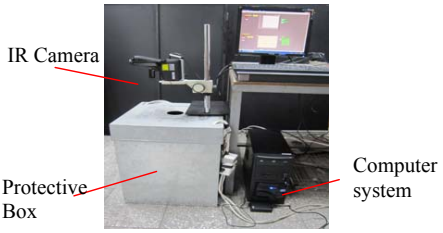

Fig. 3. Experimental system

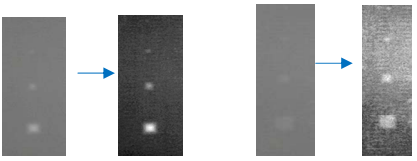

(a) (b)

Fig.4. Experimental and enhanced images of (a) centrifugal paper, and (b) Teflon film defects.

3. Discussion

The temperature difference of centrifugal paper defects in 5s are around 8℃ for 20x20 mm, 3.5℃ for 12x12mm, and 1.5℃ for 6x6 mm defect area. The temperature difference of Teflon film defects in 5s are all about 2.2℃. Those temperature can be detected by our system.

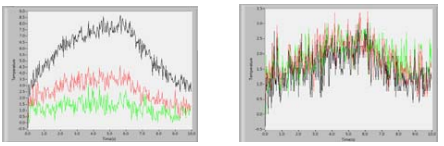

(a) (b)

Fig.5. Experimental temperature difference of various size of defects from: (a) Centrifugal paper and (b) Centrifugal film defects.

Comparing the Fig. 2 and Fig. 5, the tendency of temperature change in experiment are the same as the simulation ones for all kinds of defects. In centrifugal paper defects, the temperature difference between experiment and simulation of size 6x6 mm and12x12 mm are fairly close except for size of 20x20 mm which is 4□. For Teflon film defects a 1□difference between experiment and simulation is achieved. Therefore usefulness of step heating for IR detection of defects in composites are validated.

4. Conclusion

Use of IR step heating method to detect the defects in CFRP composite has been studied experimentally and simulated by finite element method. The temperature difference between experiment and simulation ones are fairly good. The applicability of step heating method in defect detection of CFRP composites is thus validated.

Acknowledgements

This study was supported by grant NSC 101-2221-E-006-101 from the National Science Council, Taiwan, Republic of China.

References

[1] Junyan Liu, Yang Wang, Hui Liu, Yinhang He, Research on CFRP Materials Nondestructive testing by IR Lock-in Thermography. Proc. of SPIE Vol. 7383, 73833U-1~9, 2009

[2] Pan, P.Y., Miller, R.A., Chu, T.P., Filip P., Thermal Diffusivity Measurements and NDE for C/C Composites Using Infrared Thermography. Proceedings of the SEM Annual Conference, 2009

[3] Bainbridge, B.G., Optimization of Transient Thermography Inspection of Carbon Fiber Reinforced Plastics. Thermomechanics and Infra-Red Imaging, Vol. 7, pp.75~82, 2010.

30th DANUBIA-ADRIA
Symposium on Advances in Experimental Mechanics
September 25-28, 2013 - Primošten, Croatia

2A05 043

ESTIMATION OF VELOCITY PROFILE AND PULSATILE WALL SHEAR STRESS IN ARTERIES USING THE MEASURED MAXIMAL VELOCITY

Ivan Korade[1], Zdravko Virag[1], Fabijan Lulić[2]

[1] University of Zagreb, Faculty of Mechanical Engineering and Naval Architecture, Ivana Lučića 5, HR-10000 Zagreb, CROATIA. e-mails: ivan.korade@fsb.hr, zdravko.virag@fsb.hr.

[2] University Clinic Rebro, Clinic for Pulmonary Diseases, Jordanovac 104, HR-10000 Zagreb, CROATIA. e-mail: fabijan.lulic@kbc-zagreb.hr.

1. Introduction

Blood flow in the arterial tree is essentially pulsatile. Time variation of the maximal velocity at certain points of the arterial tree may be obtained non-invasively, and used for tuning of 1D model parameters. In 1D models, it is convenient to assume a nearly flat velocity profile (blood flow rate is calculated as the product of maximal velocity and area) and Hagen-Poiuseuille friction model derived from a steady state flow condition. The goal of this paper is to estimate how good these two assumptions are.

We use the measured maximal velocity and the Womersley quasi two dimensional (Q2D) solution of pulsatile flow in a rigid pipe [1] to define the velocity profile at the considered cross-section. From this velocity profile, we calculated the actual flow rate (or mean axial velocity) and wall shear stress.

2. Womersley solution of Q2D flow

We consider an incompressible fluid flow in a rigid circular pipe of radius R, under a harmonic pressure gradient defined as:

$$\frac{\mathrm{d}p}{\mathrm{d}x} = S\sin(\omega t) + C\cos(\omega t), \qquad (1)$$

where $p(x,t)$ is the pressure, x is the space coordinate along the pipe axis, t is the time and ω is the circular frequency. If we assume an axial velocity $u(r,t)$, the linear momentum equation is:

$$\rho\frac{\partial u}{\partial t} = \mu\left(\frac{1}{r}\frac{\partial u}{\partial r} + \frac{\partial^2 u}{\partial r^2}\right) - \frac{\mathrm{d}p}{\mathrm{d}x}, \qquad (2)$$

where ρ is the fluid density, μ is the viscosity and r is the radial coordinate. Equation (2) is solved in the frequency domain, where the pressure gradient and axial velocity can be represented as real parts of:

$$\frac{\mathrm{d}p}{\mathrm{d}x} = \mathcal{R}e\left\{-i\hat{P}e^{i\omega t}\right\}, \quad u = \mathcal{R}e\left\{-i\hat{U}(r)e^{i\omega t}\right\} \qquad (3)$$

where $\hat{P} = S + iC$, and $\hat{U} = S_u + iC_u$ are complex amplitudes. The solutions for axial velocity, flow rate $Q = \int_0^R 2\pi u r\mathrm{d}r$ and wall shear stress τ_w are:

$$u = \mathcal{R}e\left\{\frac{\hat{P}}{\rho\omega}\left[1 - \frac{J_0(\Lambda y)}{J_0(\Lambda)}\right]e^{i\omega t}\right\} \qquad (4)$$

$$Q = \mathcal{R}e\left\{i\frac{2\pi\hat{P}\mu}{\rho^2\omega^2}\left[-\frac{\mathrm{Wo}^2 i}{2} - \frac{\Lambda J_1(\Lambda)}{J_0(\Lambda)}\right]e^{i\omega t}\right\} \qquad (5)$$

$$\tau_w = \mathcal{R}e\left\{\hat{P}\sqrt{\frac{\mu}{\rho\omega}}\frac{J_1(\Lambda)}{J_0(\Lambda)}e^{i\left(\omega t + \frac{3\pi}{4}\right)}\right\}, \qquad (6)$$

where $\mathrm{Wo} = R\sqrt{\rho\omega/\mu}$ is the Womersley number, $y = r/R$, $\Lambda = \mathrm{Wo}\,\exp(3\pi i/4)$, J_0 and J_1 are Bessel functions of the first kind and of zero and first order, respectively.

3. Method

The maximal velocity is defined by Eq. (4) for $y = 0$. We start from the measured maximal velocity $u_{\max}^{\mathrm{M}}(t)$ during one heart period T, which may be decomposed into Fourier series:

$$u_{\max}(t)=\sum_{n=0}^{N}\left(S_u^n\sin(n\omega_0 t)+C_u^n\cos(n\omega_0 t)\right) \quad (7)$$

where $\omega_0=2\pi/T$, and N is the number of harmonics. Using Eq. (4) for $u_{\max}$, it is possible to calculate the complex pressure gradient amplitudes at each frequency $\omega=n\omega_0$, and after that, to calculate $Q(t)$ and $\tau_w(t)$ from Eqs. (5) and (6) (as a sum of contributions of all N harmonics). The obtained average velocity $u_{\text{avg}}=Q(t)/(R^2\pi)$ will be compared with the measured maximal velocity, and obtained $\tau_w(t)$ with $\tau_{w,S}=4\mu Q/(R^3\pi)$ obtained from the Hagen-Poiusseuile formula.

4. Results

Simultaneous measurements of the pressure gradient and axial velocity $u^{\mathrm{M}}(y,t)$ at $y=(0;\ 0.5;\ 0.75$ and $0.95)$ in the femoral artery of a dog are given in [2]. We use $u^{\mathrm{M}}_{\max}(t)=u^{\mathrm{M}}(0,t)$ to calculate the pressure gradient and axial velocity at the other measurement locations. The assumed Womersley number associated with the heart frequency is Wo=3.8. To check the applicability of the proposed method, we compared measured and reconstructed values, which are depicted in Fig. 1.

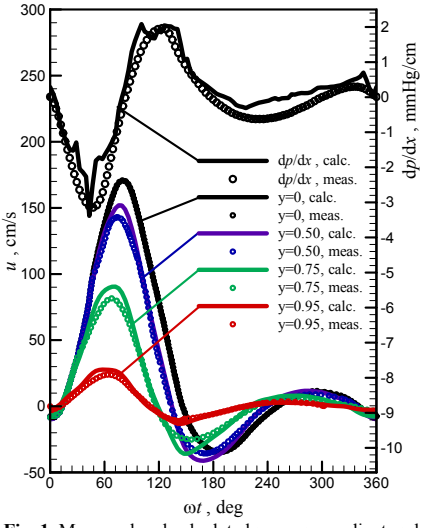

Fig. 1. Measured and calculated pressure gradient and axial velocity at different radii

Our results indicate that the proposed method could be used for estimating the axial velocity profile on the basis of the measured maximal velocity. Figure 2 shows the time variation of the measured maximal velocity and obtained mean axial velocity, as well as the wall shear stress τ_w and $\tau_{w,S}$.

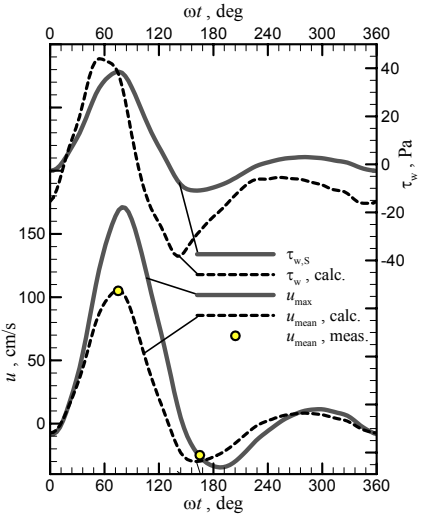

Fig. 2. Comparison of the two wall shear stresses, and the measured maximal velocity with calculated mean axial velocity. The two points denote the measured values of maximal and minimal mean axial velocity.

5. Remarks

- The proposed method for the calculation of the axial velocity using the measured maximal velocity requires the assumption of the Wo number associated with the heart frequency.
- The discrepancy of maximal and mean axial velocity is high, as a consequence of which the estimation of blood flow rate using the maximal velocity is poor.
- The proposed method offers a good estimation of the mean velocity and wall shear stress.

Acknowledgements

This research is funded by the Croatian Ministry of Science, Education and Sports.

References

[1] Womersley, J.R., "Method for the Calculation of Velocity, Rate of Flow and Viscous Drag in Arteries when the Pressure Gradient is Known, J. Phys. No.127, 1955, 553-563.

[2] Nichols, W.W; O'Rourke, M.F.: McDonald's Blood Flow in Arteries, (5th ed.) Oxford Univ. Press, New York, USA, 2005.

30th DANUBIA-ADRIA
Symposium on Advances in Experimental Mechanics
September 25-28, 2013 - Primošten, Croatia

2B01 029

USING ARTIFICIAL NEURAL NETWORKS FOR MODELLING OF TIME-DEPENDENT MATERIAL BEHAVIOR

Alexandra Aulova[1], Igor Emri[1]

[1] University of Ljubljana, Faculty of Mechanical Engineering, Aškerčeva ulica 6, 10000 Ljubljana, SLOVENIA. E-mail: alexandra.aulova@fs.uni-lj.si, ie@fs.uni-lj.si

1. Introduction

It is well known that in nature all existing processes are either "amplitude-" or "rate-dependent" (first or higher order derivatives). Any process represents interrelation between different physical quantities. The simplest case of such interrelation is response to a single quantity excitation. Let us assume an excitation in a form of displacement. Depending on the type of a system the force response may then assume three different forms that are known as basic physical laws, i.e., Hook's law, Newton's law of viscosity, and II law of Newton, Figure 1.

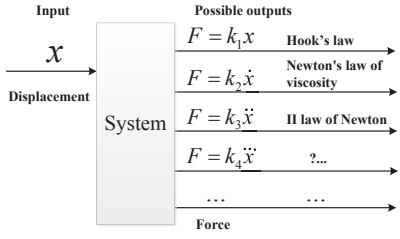

Fig. 1. Possible outputs on displacement excitation.

Dependencies on higher-order derivative also exist but are not well-elaborated yet. For example jolt, which is also known as jerk, surge, or lurch, is the third derivative of displacement in respect to time and is used in variety of applications: starting with transport and finishing with life safety in sports [1, 2]. Fourth (jounce or snap) and higher derivatives are used in calculation of orbits of space objects and in equations of state in cosmology [3]. So, it is obvious that all basic physical laws are either amplitude or rate dependent.

In viscoelastic materials both types of processes are present simultaneously and interact with each other: elastic response is amplitude dependent and viscous depends on the rate of excitation. This work proposes artificial neural network as a tool for modeling behavior of complex systems where several amplitude- and rate-dependent processes evolve in parallel. The network will be used first for observation of interactions between amplitude- and rate dependent processes that result in time-dependent behavior of viscoelastic materials.

2. Methods

In modeling of structural rearrangements on molecular level we may assume that we deal with amplitude- and rate dependent processes that interact with each other.

Most common simplification used in this modeling is utilization of the superposition principle. As the first step this approach assumes that all the processes in the system are independent or their interactions are negligible. Next it is assumed that these processes are additive, i.e., they can be added directly, with certain weights, or as their reciprocals, as shown in Figure 2.

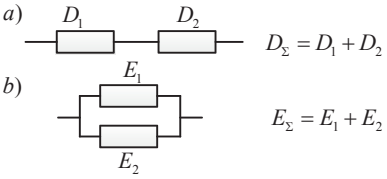

Fig. 2. a) Creep compliances in series and b) relaxation moduli in parallel.

It is obvious that in reality all processes, even if they are of different nature, interact with each other and have influence on each other. Hence,

utilization of the superposition principle is an efficient approach as shown by Ilya Prigogine [4].

This work proposes to use modified artificial neural networks as a tool for modeling the interaction between amplitude- and rate dependent processes within viscoelastic systems.

Since neural network (NN), defined by Aleksander and Morton [5], is a massively parallel distributed processor that has a natural propensity for storing experiential knowledge and making it available for use [6], it is a suitable tool for modeling processes that run simultaneously and interact with each other.

Neural networks have a lot of advantages such as possibilities to adapt and to be used in on-line monitoring, robustness, great generalization and approximation capabilities, etc. [6], in comparison to other modeling methods. But for the proposed particular application all these advantages are cancelled by necessity of training, to be more precise – necessity of large training data base.

It is obvious that obtaining experimental data for training takes enormous time and is expensive at the same time. Hence, it would be advantageous if we could use "artificially" generated data obtained from the closed-form solutions instead. Such possibilities are given, for example, in the field of viscoelasticity where many closed-from solutions for standard and non-standard excitations are known.

The main goal of this work is to create artificial neural network that will be capable of modeling interactions between amplitude- and rate dependent processes. Amplitude dependence is already well-implemented into neural network theory, however, rate-dependency is addressed at present only implicitly through recurrent networks, dynamic networks, etc.. Implementation of rate dependent structural (neural) elements into the conventional neural networks will allow modeling every complex system where multiple amplitude- and rate-dependent processes run simultaneously.

3. Results

Results of the described work may be used for modeling variety of problems connected to lifetime (durability) prediction of viscoelastic materials, particularly polymers and their composites. Polymers are widely used in different fields due to their superior properties (stiffness-to-mass ratio, processability, biocompatibility, corrosion resistance, etc.). However, time-dependent properties of polymers cause difficulties in prediction of their live-time and characterization of durability. In comparison to metals where failure is mostly caused by fatigue, polymer materials also exhibit strain accumulation [7] that cannot be monitored as easily as, for example, crack propagation.

Hence, newly developed neural network may be used for online monitoring of polymeric structures in order to predict their durability.

4. Remarks

- All processes in nature are either amplitude-, or rate-dependent as observed on examples of basic physical laws.
- We propose development of new artificial neural network that will be able to model and monitor interaction of parallel processes of different nature and, therefore, model behavior of complex systems. Proposed modeling technique may be later upgraded for online monitoring of polymeric structures durability and lifetime prediction.

5. References

[1] Villagra, J., et all., Smooth path and speed planning for an automated public transport vehicle, Robotics and Autonomous Systems, Elsevier, **60(2),** 2012, pp. 252–265.

[2] Emri, I., et al., Time-dependent behavior of ropes under impact loading: a dynamic analysis, Sports technology, John Wiley & Sons, **1(4/5)**, 2008, pp. 208-219.

[3] Visser, M., Jerk, Snap, and the Cosmological Equation of State, Classical and Quantum Gravity, **21 (11)**, pp. 2603–2616.

[4] Prigogine, I., Stengers, I., Order out of Chaos. Man's New Dialog with Nature, Bantam New Age Books; First Edition, 1984.

[5] Aleksander, I. and Morton H., An Introduction to Neural Computing, International Thomson, 1990.

[6] Haykin, S, Neural Networks. A Comprehensive Foundation, Prentice Hall, 2nd ed., 1999.

[7] Dao, K.C., Dicken, J.D., Fatigue Failure Mechanisms in Polymers. Polymer Engineering and Science, **27(4)**, 1987, pp. 271-27.

30th DANUBIA-ADRIA
Symposium on Advances in Experimental Mechanics
September 25-28, 2013 - Primošten, Croatia

2B02 068

MECHANICAL BEHAVIOUR OF PORCINE ZONULAR FIBRES

Z. Bocskai[1], Z. Kiss[2], G. L. Sándor[3], I. Bojtár [1], Z. Z. Nagy[3]

[1] Budapest University of Technology and Economics, Faculty of Civil Engineering, Department of Structural Mechanics, Műegyetem rkp. 3., 1111 Budapest, HUNGARY. E-mails: zbocskai@mail.bme.hu, ibojtar@mail.bme.hu

[2] Budapest University of Technology and Economics, Faculty of Mechanical Engineering, Department of Polymer Engineering, Bertalan L. u., 1111 Budapest, HUNGARY. E-mail: kiss@pt.bme.hu

[3] Department of Ophthalmology, Semmelweis University, Mária u. 39., 1085 Budapest, HUNGARY. E-mails: sandorgaborlaszlo@gmail.com, nz@szem1.sote.hu

1. Introduction

The mechanical properties of the zonular fibres affect the procedure of accommodation (*Burd et al. Bocskai and Bojtár, Hartridge*, *Liu et al.*). We developed a measuring process to obtain force-displacement diagram to estimate the mechanical parameters of porcine zonular fibres. With this method we can hold the integrity of zonular fibres between the ciliary body and the lens.

2. The applied measurement method

Figure 1 shows the basic idea of the measuring method. First of all we glued (with cyanoacrylate) the porcine eye globe to the dissecting ring (see Fig. 1), after then we cut off the anterior segment behind the posterior line of the dissecting ring. It can be seen the position of the remaining three rings (supporting ring and separating rings) on Figure 1. With the two separating rings we exclude the elasticity of the lens from the system. Between the supporting ring and the separating rings we have the conglomerate of zonular fibres.

The transducer overlies to the upper separating ring with its spherical surface, so the vertical displacement of the system is insured. We measured the vertical displacement of the transducer and the force. The applied installation was displacement-controlled.

It can be seen an upper view about an experimental sample in Figure 2 left side and a section cast filled by resin in Figure 2 right side. In Figure 3 shows the measurement process.

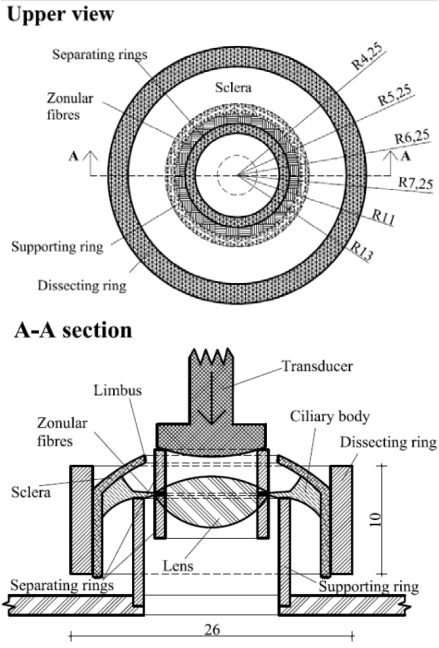

Fig. 1. Measurement sketch (upper view (left); A-A section (right))

3. Results

Figure 4 shows the force-displacement diagram obtained from one homogeneous sample group. We applied monotonically increasing force and cyclic load too. The unloading has started at displacement 0.5 mm and 0.3 mm. The diagrams also show the hysteresis loops. From the hysteresis

loop we can calculate the dissipated internal energy (*Bodor and Vas, Mark and Erman*). This behaviour is typical in fibrous biological materials and in viscoelastic materials such as polymers.

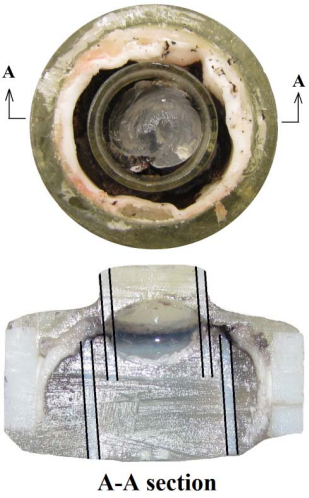

Fig. 2. Photos about an experimental sample (upper view (left); section view (right))

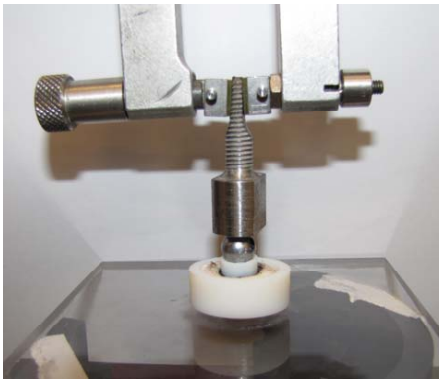

Fig. 3. The measurement process

4. Conclusion

Based on the measured values we are able to define a material model for zonular fibres what we can use to clarify the mechanics of the accommodation process. In the future, with minor modification this measuring procedure will be expansible for human specimens.

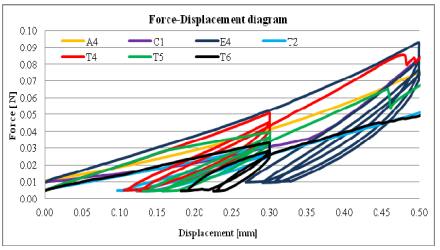

Fig. 4. Force-displacement diagram of zonular fibres

Acknowledgements

The work reported in the paper has been developed in the framework of the „Talent care and cultivation in the scientific workshops of BME" project. This project is supported by the grant TÁMOP-4.2.2.B-10/1--2010-0009.

References

[1] Bocskai, Z., Bojtár, I., Biomechanical modelling of the accommodation problem of human eye. Periodica Polytechnica - Civil Engineering, **57/1**, 2013. (accepted)

[2] Bodor, G., Vas, L.M., Polimer anyagszerkezettan. Műegyetem Kiadó, 2000.

[3] Burd, H.J., Judge, S.J., Flavel, N.J., Numerical modelling of the accommodating lens. Vision Research, **42**, 2002. pp. 2235-2251.

[4] Hartridge, H., Helmholtz's theory of accommodation. British Journal of Ophthalmology, **9**, 1925. pp. 521-523.

[5] Liu, Z., Wang, B., Xu, X.Z., Wang, C., A study for accommodating the human crystalline lens by finite element simulation. Computerized Medical Imaging and Graphics, **30**, 2006. pp. 371-376.

[6] Mark, J.E., Erman, B., Rubberlike elasticity – A molecular primer. Cambridge University Press. 2007.

30th DANUBIA-ADRIA
Symposium on Advances in Experimental Mechanics
September 25-28, 2013 - Primošten, Croatia

2B03 121

STATIC RESPONSE OF AN ANTI-TETRACHIRAL SANDWICH PANEL

Ştefan Sorohan[1], Marin Sandu[1], Dan M. Constantinescu[1], Adriana Sandu[1], Dragoş A. Apostol[1]

[1] University POLITEHNICA of Bucharest , Department of Strength of Materials, , Splaiul Independentei nr. 313, 060042 Bucharest, ROMANIA. E-mails: stefan.sorihan@upb.ro, marin.sandu@upb.ro, dan.constantinescu@upb.ro, adriana.sandu@upb.ro, apostolda@yahoo.com

1. Introduction

Chiral honeycomb is a particular form of honeycomb structure in which the ligaments are joined at chiral nodes. A chiral node is one which cannot be superimposed on its mirror image. The peculiar properties of the new developed material are largely due to their auxetic geometry. The term auxetic refers to a novel class of materials characterized by negative Poisson's ratio, that induce beneficial effects as: increased resistance to indentation, improved acoustic properties and a natural tendency to form dome-shaped surfaces [1-3]. The auxetic behaviour is a scale independent property and therefore the same mechanism can operate at macro, micro and nano level.

2. Chiral structure

The analyzed anti-tetrachiral panel (Fig. 1), assembled by adhesive bonding, was considered as simply supported on the edges of bottom face sheet and loaded with a lateral pressure p = 0.07 MPa, applied on the upper face sheet. The geometric parameters taken into account were the following: $a = 600$ mm, thickness of face sheets t_f =1 mm, thickness of the strips t_1 =2 mm, thickness of the bushes wall t_2 =1.8 mm, thickness of borders t_3 =3 mm, mean radius of bushes r =19.1 mm, total thickness of the sandwich panel t = 25 mm, b =75 mm, c=b/2. Linear and nonlinear geometric analyses are considered.

Physical properties of the materials that are involved in the analysis are given in Tab. 1. Because the PVC and the araldite AV 119 (Huntsman) have very close values of the elastic moduli and of the Poisson's ratios the adhesive will be not emphasized explicitly in the numerical model, being included into the PVC. The mass of the sandwich panel results as 3.309 kg.

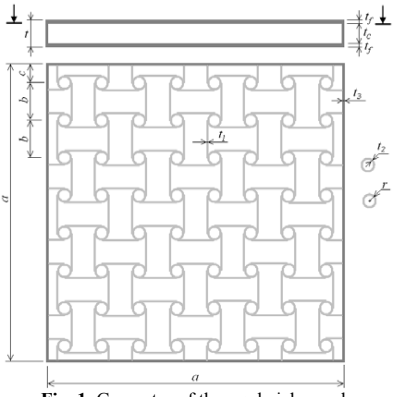

Fig. 1. Geometry of the sandwich panel.

Component	Face sheets	Bushes, Strips and Borders	Adhesive
Material	Aluminium 2024 T3	Rigid PVC	Araldite AV 119
Young's modulus [MPa]	72000	3200	3100
Poisson's ratio	0.33	0.35	0.34
Allowable stress [MPa]	300	40	45
Mass density [kg/m^3]	2700	1400	1380

Tab. 1. Properties of materials used in the finite element modelling of sandwich panels.

Only as an example, the FEA linear and nonlinear analyses are presented for the panel supported on: a) all four edges; b) the opposite edges (cylindrical bending) as in Fig. 2.

a)

b)

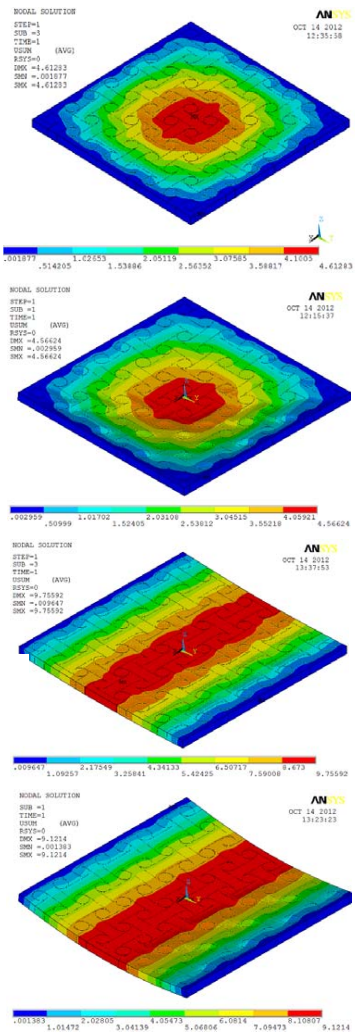

Fig. 2. Linear (first figure) and nonlinear (second figure) displacements on the top face sheet

Different types of cores as polymeric and metallic rigid foams, honeycomb structures made from different materials, corrugated plates, lattice type components and others are currently used.

It is to note that in the analytical evaluations of auxetic in-plane properties of 2-D chiral, anti-chiral and meta-chiral structures, two different approaches were used: a) rigid ligaments and nodes, connected together through ideal hinges; b) flexible ligaments connected with rigid or deformable nodes. Also, it is possible to evaluate the out-of-plane mechanical properties of a chiral lattice analytically or by means of finite element analysis (FEA).

This type of structure is superior to the honeycomb one, as the honeycomb cell generatrix is perpendicular to the face sheet and, therefore, the bonding between the honeycomb core and the face sheet can be achieved only by line contact. This is the major drawback of this type of sandwich structure, because the line-contact bonding between the honeycomb cross section and the face sheet can easily lose its bonding integrity as a result of corrosion.

Acknowledgements

This work was supported by a grant of the Romanian National Authority for Scientific Research, CNCS – UEFISCDI, Project number PN-II-PT-PCCA-2011-3.2-0068, contract 206/ 2012.

References

[1] J.P.M. Whitty, A. Alderson, P. Myler and B. Kandola, Towards the design of sandwich panel composites with enhanced mechanical and thermal properties by variation of the in-plane Poisson's ratios, Compos. Part A, **34**, 2003, pp. 525-534.

[2] J. Grima, A. Alderson and K. Evans, Negative Poisson's ratios from rotating rectangles, Comput. Meth. Sci. Tech., **10**, 2004, pp. 137-145.

[3] A. Spadoni and M. Ruzzene, Numerical and experimental analysis of the static compliance of chiral truss-core airfoils, J. Mech. Mat. Struct., **2**, 2007, pp. 965-981.

30th DANUBIA-ADRIA
Symposium on Advances in Experimental Mechanics
September 25-28, 2013 - Primošten, Croatia

2B04 064

ELASTIC RECOVERY AT MONTMORILLONITE AND CARBON NANOTUBE REINFORCED PA6 NANOCOMPOSITES

László Mészáros [1) 2)],

[1)] Department of Polymer Engineering, Faculty of Mechanical Engineering, Budapest University of Technology and Economics, Műegyetem rkp. 3, H-1111 Budapest, Hungary.

[2)] MTA–BME Research Group for Composite Science and Technology, Műegyetem rkp. 3, H-1111 Budapest, Hungary.

Corresponding author: meszaros@pt.bme.hu

1. Introduction

In technical life the utilization of polymer matrix nanocomposites gradually spreads because of their special characteristics like conductivity, enhanced gas-barrier properties, flame retardancy, etc. but their application as structural materials is still not reached the level that would be expected based on to their mechanical performance [1]. The main reason of it is the viscoelastic properties of the polymer matrix. At neat polymers and at polymer matrix microcomposites there is now sufficient knowledge to take the time-dependent behavior into account at the design of a new product. At nanocomposites - where the nanoparticles also can have strong effect on the viscoelasticity – this knowledge is still incomplete. As the viscoelastic properties of a polymer matrix composite depend on the applied loads on every load level there has to be made a one cycle test to characterize the instantaneous elastic, the time-dependent viscoelastic and the time-dependent viscous (or relaxation) deformation components. This characterization method can be quite long, therefore the researchers introduced rate of elastic recovery. At this cyclic measurement the tensile load increased by the cycles but between each cycle a certain time is applied for the recovery of the time-dependent viscoelastic deformations (elastic deformation). The elastic recovery can be calculated as the rate of the elastic deformation and the total deformation (Fig. 1.) [2].

In this study there were made cyclic tensile tests on polyamide 6 (PA6) matrix nanocomposites with 1 wt% nanoparticle content. The applied nanoparticles were: montmorillonite (MMT); montmorillonite modified by (2-hydroxyethyl)-methacrylate (HMMT) and multi-wall carbon nanotubes (MWCNT). The sample preparation was carried out according to a previous research [3].

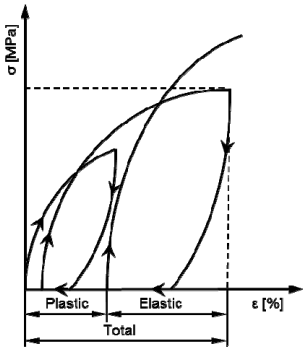

Fig. 1: Strain-stress curves for cyclic loading, at increasing load levels.

The cyclic tensile tests were performed on a Zwick Z020 (Germany) universal testing machine. The relaxation time was set to be 30 s and the load was increased by 100 N in each cycle. The machine was used in force-controlled mode, the up and the down load speed was set to 100 N/s. The measurement ended when close to the maximum force at least 1% additional elongation awaked and the force still could not achieve the maximum value. This phenomenon meant that the creeping behavior begun to be dominant that is far away from the elastic deformations.

2. Experimental Results

The residual strain measured after the relaxation time (plastic deformation) was marked as ε_{30s}. Fig. 2. shows the ε_{30s} values as a function of the cycles (viz. the stress: as there was no notable differences between the specimen geometries). It is visible that at

nanocomposites higher residual strains appear at higher cyclic numbers. That means the deformation behaviour is closer to the linear than at the neat matrix. It can also be concluded, that the HMMT containing nanocomposite showed the most elastic properties.

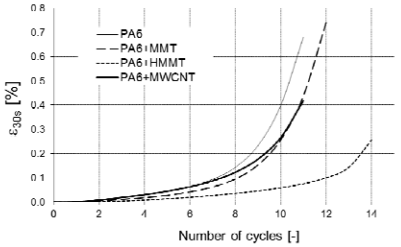

Fig. 2: The residual strain measured after the relaxation time (30 s).

Based on the measurements the percentages of the elastic recovery of the materials were calculated (Fig. 3.).

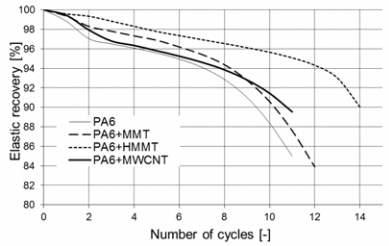

Fig. 3: Elastic recovery of nanocomposites

At the neat matrix and at the MWCNT containing one the elastic recovery decreases intensively at low cycles than gradually changed were observed. This can be explained by the orientation of the amorphous phase of the matrix. This phenomenon was less characteristic for the MMT containing composite and not occurred in case of the HMMT containing nanocomposite. Overall it means that in the last cases the amorphous region became more elastic, therefore the residual deformation was not considerable. At the HMMT containing nanocomposites after 10 cycles (i.e. 1000 N load) the elastic recovery was still around 95% while the others have remarkable residual deformations. At this nanocomposite the decrement of the elastic recovery is approximately linear in a wide cycle range that means the deformation can be relatively easily calculated. Based on the results it can be stated that by incorporating nanoparticles into the PA6 matrix at tensile loads the elastic region can be widen. This means that the nanocomposites can be used safely at higher loads compared to the neat matrix.

3. Acknowledgements

This research was realized in the frames of TÁMOP 4.2.4. A/1-11-1-2012-0001 „National Excellence Program – Elaborating and operating an inland student and researcher personal support system" The project was subsidized by the European Union and co-financed by the European Social Fund. This research was also supported by the Hungarian Research Fund (OTKA PD105564).

4. References

[1] F. Hussain, M. Hojjati, M. Okamoto and R. E. Gorga, Review article: Polymer-matrix Nanocomposites, Processing, Manufacturing, and Application: An Overview. Journal of Composite Materials, Vol. 40 (2006) 1511-1575.

[2] W. E. Morton and J. W. S. Hearle, Physical properties of textile fibers. Butterworth & Co. Ltd. and The Textile Institute, London and Colchester, 1962.

[3] L. Mészáros, T. Deák, G. Balogh, T. Czvikovszky and T. Czigány, Preparation and mechanical properties of injection moulded polyamide 6 matrix hybrid nanocomposite. Composites Science and Technology, Vol. 75 (2013) 22-27.

30th DANUBIA-ADRIA
Symposium on Advances in Experimental Mechanics
September 25-28, 2013 - Primošten, Croatia

2B05 034

NATURAL CONVECTION IN A BRIDGMAN CRYSTAL GROWTH

Mustapha Betrouni[1], Djamel Kalache[1]

[1] Houari Boumediene University of Algiers, Laboratoire de Mécanique des fluides théorique et appliquée, Faculté de Physique, USTHB, BP. 32, El Alia, Alger, Algérie. E-mail: mustapha.betrouni@yahoo.fr

1. Introduction

In any crystal growth process, we deal with no desired perturbations induced by convection in the fluid near the freezing front. Much work has been done to find the appropriate experimental conditions that would damp these perturbations. In the ideal case, we can proceed in a vanishing gravity level of space laboratories attempting to eliminate the source (gravity) of the convection.

Other experiments were made in a controlled gravity (under centrifugation) where rotation of the ampoule is expected to open specific domains for the existence of unsteady flows. In the "bottom seeded" Bridgman experiments performed in a large arm length centrifuge in presence of rotation, stabilizing thermal stratification and azimutal thermal torque, surprising results were found consisting of at least one gravity level for which the obtained ingots have crystalline properties comparable with those obtained in space laboratories.

As mentioned see (Regel, 1990), the Coriolis force might contribute quite significantly besides the buoyancy and drastically modify the flow structure from its pure thermoconvective state. In addition, the gravity field inhomogeneities must be taken into consideration, for they are coupled to the axial component of the "stabilizing" density gradient.

It is interesting to engage in a rough analysis of the melt phase hydrodynamics and in some numerical experiments to analyze separately the influence of the inhomogeneous gravity field and the Coriolis force in the crucible rotating with the centrifuge.

2. The experimental context

While rotating around a vertical axis ''Fig.1'' at the angular velocity **W** the experimental area container has its own axis of symmetry aligned with the resulting gravity $\mathbf{g_0}$ measured at its centre of mass situated at the distance $|\boldsymbol{L_0}|$ from $\mathbf{W} : \mathbf{g_0} = \mathbf{g_{00}} + \mathbf{W}^2 \boldsymbol{L_0}$ where $\mathbf{g_0}$ is called the mean resulting gravity.

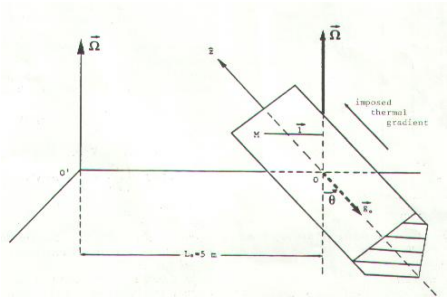

Fig. 1. Sketch of the experimental configuration of the crucible.

The angle $\theta = (\mathbf{g_{00}}, \mathbf{g_0})$ defines a parameter k which is convenient for the experimentalists:

$k = \cos^{-1}\theta = g_0 / g_{00}$.

The resulting gravity at a point M can be written as follows: $\mathbf{g} = \mathbf{g_0} + \delta\mathbf{g}$.

The thermal configuration is essentially characterized by an axial positive "stabilizing" gradient imposed by the furnace to the melt, trough the crucible, and an induced radial component trough the melt which triggers the convective flows when the growth is operated under natural gravity $\mathbf{g_{00}}$.

3. The dynamical configuration

First of all, from the existence of two preferred distinct directions, **Ω** and $\mathbf{g_0}$, the flows must have intrinsically 3D structures. The dimensionless Navier-Stokes and thermal equations are (with Boussinesq conditions assumed to be fulfilled):

$$\frac{D\vec{v}}{Dt} = -\vec{\nabla}p + T(\hat{z} - Fr\vec{l}) - \frac{2}{Ro}\hat{\Omega}\times\vec{v} + \left(\frac{\mathrm{Pr}}{Ra}\right)^{1/2}\nabla^2\vec{v},$$

$$\frac{DT}{Dt} = \left(Ra\,P_r\right)^{-1/2}\,\nabla^2 T \quad ,$$

$$div\ \vec{v} = 0 \quad ,$$

where the following dimensionless numbers appear: Rayleigh number, $Ra = V_{th}^2 / \{(\nu / H)\,(\kappa / H)\} = \beta\, g_0\, \Delta T\, H^3 / (\nu\,\kappa)$; Prandtl number, $Pr = \nu / \kappa$; Froude number, $Fr = \Omega^2\, H / g_0 = H \tan\theta / L_0$; Thermal Rossby number, $Ro = V_{co} / V_{th} = (\beta\, \Delta T / Fr)^{1/2}$, The free-fall velocity in the buoyancy field, $V_{th} = (\beta\, g_0\, \Delta T\, H)^{1/2}$ and the velocity obtained by the balance of the Coriolis and the thermal buoyancy forces, $Vco = \beta\, g_0\, \Delta T / 2\Omega$.

4. Numerical results

We have started by choosing not too strong convective conditions (β= 12.5 cm). The coefficient k is our experimental parameter from which the $\mathbf{g}_0$, $\boldsymbol{\Omega}$ and $\delta\mathbf{g}$ vectors are defined, once the arm length L_0 has been given.

4.1 The g_0 thermoconvective flow

The thermoconvective flow which is considered now is obtained with the mean gravity level g_0, by switching off, in the numerical code, the Coriolis and the δg contributions. This flow is taken as a reference flow. In ''fig.2'' are presented the isothermal lines in the horizontal plane z = -0.49H, illustrating the axisymetry of the thermal configuration.

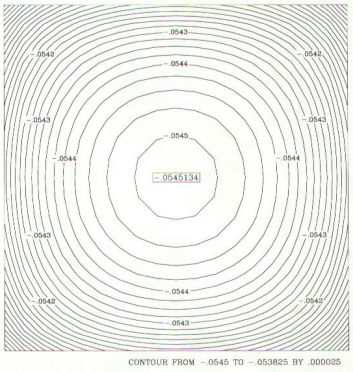

Fig. 2: Isothermal lines obtained in the horizontal plane z = -0.49H for the g_0 thermoconvective flow (Ra = 9 103)

4.2 The thermoconvective flow in the full resulting gravity field

We have taken k= 1.05 and L_0 = 5m, which gives Fr = 6 10^{-4}. the comparative orders of magnitude of the three dimensionless velocity components ($\vec{v} = u\,\hat{x} + v\,\hat{y} + w\,\hat{z}$) are presented in table 1.

Case	|u|	|v|	|w|
$g = g_0$	$0.96\ 10^{-3}$	$0.96\ 10^{-3}$	$0.53\ 10^{-2}$
$g = g_0 + \delta g$	$0.97\ 10^{-3}$	$0.97\ 10^{-3}$	$0.53\ 10^{-2}$

Table 1: Comparative orders of magnitude of the three dimensionless velocity components.

This case leads to two vertical rolls separated by the surface y = 0. This is what we observe in ''Fig.3''.

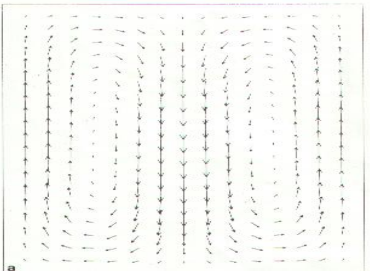

Fig. 3: thermoconvective flow. The flow velocity components (v, w) in the x = 0 plane

5. Conclusion

An ideal Bridgman furnace (i.e. with a pure constant axial thermal gradient in the melt) submitted to earth gravity will not anymore be ideal in a centrifuge, for the centrifugal acceleration field coupled to the axial thermal gradient generates thermoconvection, i.e. centrifugation prevents hydrostaticity of the melt phase.

The Coriolis force field plays a deflection role on the thermoconvective streamlines without altering significantly the orders of magnitude of the velocity.

No striking behavior is expected, in our chosen physical configuration, leading to some first explanation of the experimental results of crystal growth. Is it a good indication to look for an answer in the thermosolutal direction?

References

[1] M. Deville, and P.Haldenwang, in Proc. 4th GAMM Conf. on Numerical Methods in Fluid Mechanics, Ed. H. Viviand (Vieweg, Braunshweig, (1981)).
[2] W. W. Fowlis, and R. J. Hide, Atmospheric Sci. 22, 541, (1981)

3A01 133

INVESTIGATION OF RELATION BETWEEN SEVERITIES OF IMPACT DAMAGE TO FIBER REINFORCED PLASTIC AND HIDDEN FLAWS DETECTION BY THERMOCAMERA

Jaroslav Valach[1], Marek Žďárský[1], Daniel Kytýř[1]

[1] Czech Technical University, Faculty of Transportation Sciences, Konviktská 20, 11000 Prague 1, Czech Republic. Email: valach@fd.cvut.cz

1. Introduction

The role of composite materials in contemporary military and civil aircrafts steadily rose. The use of composites is implied by their mechanical performance, expressed e.g. in terms of their effective modulus and strength unsurpassable by any homogeneous material. Stiffness and strength tuned to excel in direction of expected loads in structure is associated with a trade off in relative weakness and proneness to damage in out-of plane direction. The damage can happen during maintenance of aircraft on land, as a result of collision with birds during take-off or landing or as a result of severe meteorological conditions – flight in hail storm. All these damages have in common fact that they are hard to detect and also can yield to decrease of material performance. Out-of-plane impact can cause permanent damage in as a dent, delamination of layers, it can cause partial breaking of fibers to full penetration of the component's material. Some of these damages can be only aesthetical while others can cause malfunction or be source of serious hazard. Delamination accompanying the defect can impair performance of material in terms of supporting shear stresses, but is also dangerous as potential site where condensation of moisture may occur leading to further degradation in positive-feedback process associated with freeze-thaw cycles during operation of aircraft.

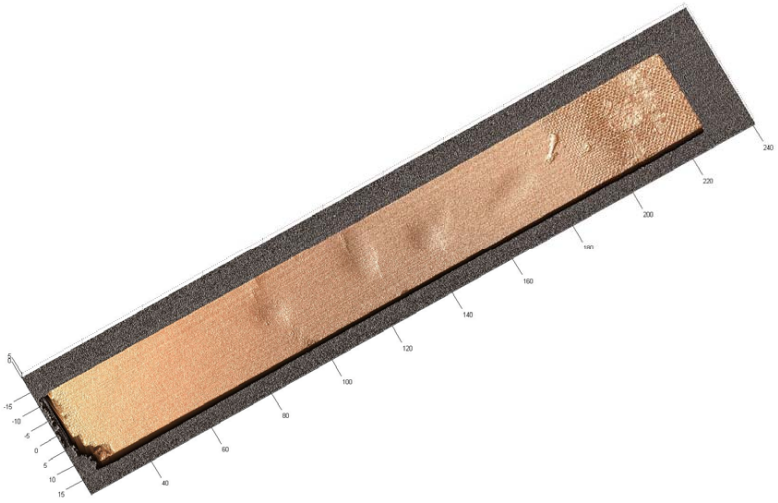

Fig. 1 Topography of CFRP specimen as captured by laser profilometer and enhanced by virtual illumination. Specimen width is 25mm and the deepest trace of impact is approximately 0.25mm deep.

Therefore a close attention is paid to improve understanding of relation between energy of impact collision and the level of damage it causes to the material, which can be measured as mechanical properties' degradation, on one hand, and to development of effective inspection methods for damage detection on the other hand.

2. Experimental procedure

In this paper, application of laser profilometry is demonstrated for surface geometry measurement and compared to results obtained by active thermography as a reference method for damage detection and assessment.

Specimens made of eight-ply carbon fiber reinforced PPS matrix laminate in the form of strips 25mm wide, 250mm long and 2mm thick were subjected to simulated impact damage. The damage comprised of hitting the specimen placed upon supporting material by steel ball at defined kinetic energy, most of which is transformed into permanent deformation. Defect's parameters, imprint size and depth were measured by custom-made laser profilometry device, centerpiece of which is computer controlled movement of a measuring head (Micro-Epsilon LLT2800–100 ScanControl system) performing laser triangulation distance measurement simultaneously for cca 1000 points in a line. Then followed thermography tests based on placing the specimens in contact with warmer body kept at constant temperature and measuring temperature using FLIR SC7600 camera.

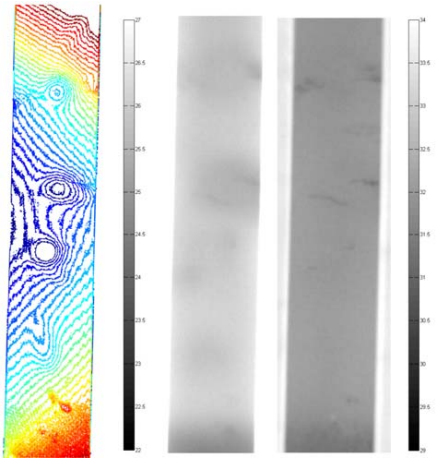

Fig. 2 Relation between impact depth (left, contour lines are 0.1 mm of height apart) in and variation in transient temperature field (center – early transient temperature field, right – final stage)

3. Results

Application of laser profilometer yields a detailed map of the specimen's surface and to measure impact imprints at a micrometer resolution as demonstrated on Fig. 1.

Among other non-destructive methods, thermography can be considered as the most suitable one. It is well known that internal discontinuity of material influence thermal conductivity and leaves discernible signature on surface otherwise with homogeneous temperature field. This effect can be seen when transient temperature field is induced by thermal pulse [1, 2]. The pulse creates heat flux which yields to rise of temperature, disrupting originally homogenous temperature field. As the heat flow transfers heat to colder parts of specimen, in places where subsurface defects occur, temperature difference can be detected. The phenomenon is illustrated on Fig. 2, where colder spots on specimen surface coincide with impact locations. In later stage of temperature field evolution, when heat flux becomes steady and constant in time, it also indicate presence of cracks.

4. Conclusions

The goal was to confirm that studied technique is capable detecting "smaller that serious" flaws. If one assumes that the damages detectable by thermography qualify as "serious", it can be concluded that profilometry can identify all of these damages. It can be concluded, that laser profilometry is also capable to detect impacts that do not leave discernible temperature signature, which is first sign of incurred damage of material. Therefore this method is suitable for monitoring of damage accumulation during fatigue process.

Acknowledgements

The research has been supported by Grant Agency of the Czech Technical University in Prague (grant No. SGS11/205/OHK2/3T/16), research plan of the Ministry of Education, Youth and Sports MSM6840770043.

References

[1] Ždárský M., Valach J., Kytýř D.: Evaluation of material's state during deformation process by means of thermographic measurement, The e-Journal of Nondestructive Testing, Vol.17, No.10, ISSN 1435-4934, (2012).

[2] Vollmer M., Möllmann K.-P.: Infrared Thermal Imaging, Wiley-VCH, ISBN 978-3-527-40717-0, (2010).

30th DANUBIA-ADRIA
Symposium on Advances in Experimental Mechanics
September 25-28, 2013 - Primošten, Croatia

3A02 049

OPTICAL 3D DYNAMIC DEFORMATION ANALYSIS OF A RAM CONTAINER DURING A DROP TEST

W. Daum, K.-P. Gründer, D. Kadoke, C. Protz, U. Zencker

BAM Federal Inst. for Materials Research and Testing, Unter den Eichen 87, 12205 Berlin, GERMANY

Corresponding author: werner.daum@bam.de

1. Introduction

Containers for interim storage and final disposal of radioactive material (RAM) have to meet certain requirements regarding mechanical stability and integrity. The assessment procedure applied by BAM is based on a series of full-scale drop tests with different drop heights and container orientations. In parallel dynamic FEM calculations are performed.

The container behaviour is monitored during the drop test by a large number of simultaneously triggered biaxial electrical strain gauges and uniaxial accelerometers in order to measure local strains at selected positions and to determine the kinematic behaviour and orientation of the container during the impact.

Within a research project a dynamic stereo photogrammetry approach was applied in a high-speed camera configuration to investigate the kinematic rigid body behaviour, relative local movements of the container or its structural parts in 3D, respectively. In the following the results of this approach are presented. A comprehensive description how to use optical methods in drop tests can be found in [2].

2. Test Set-up

The drop tests were performed at the BAM drop test facility by using KONRAD steel sheet containers of Type V [1]. The container dimensions are 3.2 m x 2.0 m x 1.7 m. The lid and bottom plates have a thickness of 5 mm, whereas the side ones are 3 mm thick. The container mass is approximately 1,840 kg. The experimental configuration covered a 0.4 m and a 5 m bottom-side drop test as well as a 5.0 m long bottom-edge drop test.

For rigid body and dynamic deformation analysis a stereo photogrammetry set-up with two calibrated synchronous triggered digital high-speed cameras have been used. This method is based on signalling points fixed on the object under test (Fig. 1). It provides 3D information about the dynamic behaviour of the container expressed by coordinates, displacement, distance, velocity, acceleration and deformation as a function of time.

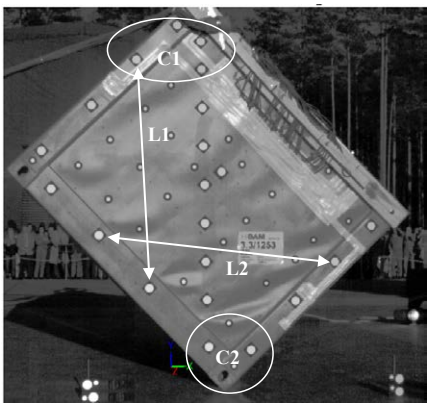

Fig. 1: Deformed steel sheet container during a long bottom-edge drop test with indicated measurement distances between points (L1, L2) and (C1, C2)

The cameras (PHOTRON FASTCAM-APX RS) were operated with a frame rate frequency of 10 kHz with a lateral resolution of 512 by 512 pixels approximately adapted to a field of view of 2.7 m by 2.7 m.

3. Experimental Results

3.1 Container Impact Speed

The calculation of the final container drop speed is based on the measurement data presented in Fig. 2. The final drop speed is calculated from all speed data up to about 57.6 ms before the impact using a linear fit function to be (9.78 ± 0.02) m/s. This value differs by 1.4 % from the ideal theoretical one.

3.2 Rigid Body Deceleration

Rigid body deceleration is another important parameter which has to be determined. This

parameter is needed to estimate the maximum container load or to design impact dampers for the container. This parameter cannot be calculated directly from stereo image data because of unavoidable noisy velocity values derived from the measured coordinates. An intermediate curve fitting step is necessary. In this case the height function is fitted using piecewise non-parametric splines. A maximum height coordinate difference below 0.15 mm relative to the observed vertical movement of about 550 mm (see Fig. 2) is achieved by this fitting process. The speed function calculated from this and starting 57 ms before impact is shown in Fig. 2. From this fitting function the deceleration is derived. A comparison of the results of the acceleration sensors and the stereo photogrammetry showed good agreement (Fig. 3).

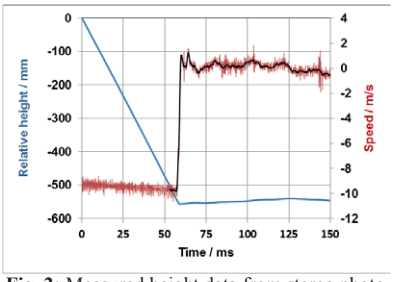

Fig. 2: Measured height data from stereo photogrammetry together with directly calculated and approximated drop speed

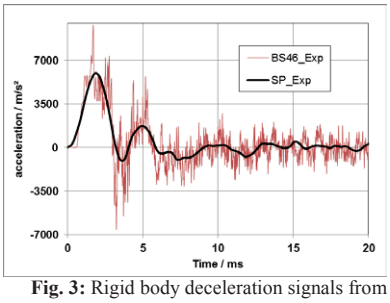

Fig. 3: Rigid body deceleration signals from a piezoelectric accelerometer (BS46) and stereo photogrammetry (SP)

The motion analysis is based not on single points but small groups of points (see markings C1 and C2 in Fig. 1). This averaging approach reduces the influence of the image noise. The maximum deceleration value determined at the upper container position away from the contact area is 6000 m/s², whereas the lower container part has a deceleration level of about 7550 m/s².

3.3 Elastic Deformation Analysis

Stereo photogrammetry can effectively be applied to study elastic deformation. The vertical and horizontal container deformations are determined by the analysis of time dependent changes of L1 and L2 (see Fig. 1).

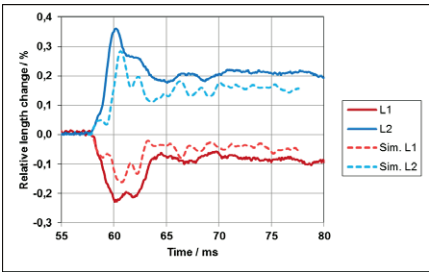

Fig. 4: Maximum elastic and remaining distance changes between surface points

The changes of L1 and L2 tend to opposite directions due to the spacious container bending and compression effects (Fig. 4). Changes in horizontal direction with a maximum at about 0.4 % are higher by a factor of 2 compared with the vertical direction. Nearly the same conclusion can be made from the FEM simulations. In both approaches significant inelastic remaining deformation up to 0.2 % is observed.

4. Conclusions

High-speed stereo photogrammetry is a highly suitable method to analyse the mechanical behaviour of a box-shaped container during drop tests. Comparison with FEM simulations and other measurement methods show a good degree of agreement. It is highly beneficial in order to validate numerical simulations and to get a deeper understanding of the dynamic mechanical behaviour of the container.

5. References

[1] Ellouz, M. et al: Container Safety Assessment for the Disposal of Non-Heat Generating Radioactive Waste …. In: Proc. of the INMM 53rd Ann. Meeting, Orlando / USA, July 15-19, 2012

[2] Gründer, K.-P. et al: Optical 3D Methods in Steel Sheet Container Drop Test Analysis. In: Proc. of OPTO 2013, Nürnberg / Germany, May 14-16, 2013 (to be published)

30th DANUBIA-ADRIA
Symposium on Advances in Experimental Mechanics
September 25-28, 2013 - Primošten, Croatia

3A03 017

DETECTION OF MATERIAL ANOMALIES BASED ON INFRARED THERMOGRAPHY IMAGE PROCESSING

Endri Garafulić [1], Lovre Krstulović-Opara [2], Željko Domazet [2]

[1] University of Split, Faculty of Science, Teslina 12, HR-21000 Split, CROATIA. E-mail: endri.garfulic@pmfst.hr

[2] University of Split, Faculty of Electrical Engineering, Mechanical Engineering and Naval Architecture, R. Boškovića 32., HR-21000 Split, CROATIA. E-mails: Lovre.Krstulovic-Opara@fesb.hr , domazet@fesb.hr

1. Introduction

Infrared thermography showed to be a reliable method for nondestructive testing (NDT) of polymer composites such as GRP and carbon reinforced composites (CRP). In our previous research [1,2] capabilities of gradient based thermography as a NDT method have been demonstrated. In this abstract the image processing based on Daubechies wavelets discrete transform is presented.

In order evaluate Daubechies wavelets image processing and compare results with gradient based method, the test sample made of GRP (97x97x 10.5 mm) is used (Fig. 1.). On the vacuum cured GRP sample several holes (diameter of 5 and 10 mm) with variable depth (2, 4, 6 and 8 mm) are machined. These holes are used to model anomalies with clear thermal response in order to compare various image processing methods.

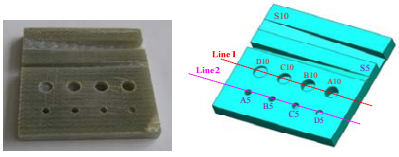

Fig. 1. GRP test sample

2. Pulsed IR thermography

The pulsed thermography PT is based on the fact that non-stationary heating is causing a heat response of material with different temperatures for zones where heat flow is changed by an obstacle, or due to changes in geometry.

Fig. 2 depicts infrared image taken from sane specimen side, 2 s after heat source was removed. In figure 3 green line depicts thermals contrast ΔT, i.e. difference between temperatures for lines where holes are drilled (red T_d line) and nearby line passing over material where no holes are drilled (blue T_{sa} line). The best thermal contrast was obtained for the case of 2 min pre-heating period (Fig. 2d). In Fig. 3 holes that can be distinguished are represented with dashed circles and named according to Fig. 1.

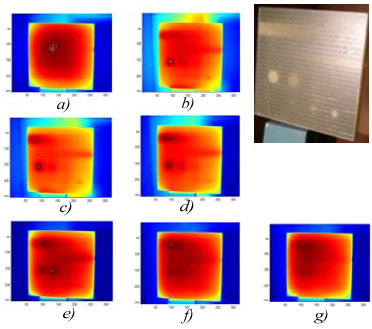

Fig. 2. Thermograms obtained for heating period of: a)1/4min, b) 1/2min, c) min, d) 2min, e) 4min, f) 6min and g) 8 min

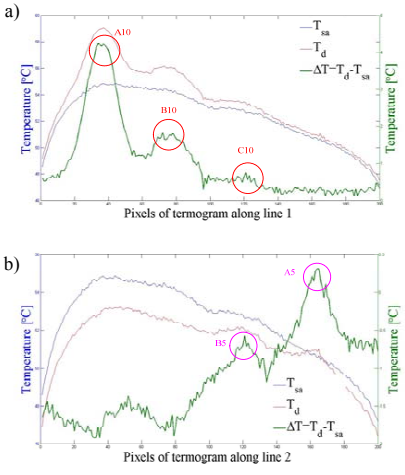

Fig. 3. Thermal contrast ΔT (green line) after 2 min heating for: a) line 1, and b) line 2

4. Image processing based on Daubechies wavelets

Based on [3], in this abstract the Matlab Wavelet Toolbox is used for wavelet decomposition. The algorithm is based on the signal is decomposition into 5 levels:

$$S = A_5 + D_5 + D_4 + D_3 + D_2 + D_1, \qquad (1)$$

where A is the approximation, and D is the detail of the signal. Experimenting with different wavelet families, the best results have been obtained with orthogonal Daubechies wavelets transform (DWT), i.e. Daubechie wavelet with 3 vanishing moments (Db3). Applying Daubechie wavelet transform (Db3, D5), all simulated defects of specimen, i.e. holes, can be detected (Fig. 5).

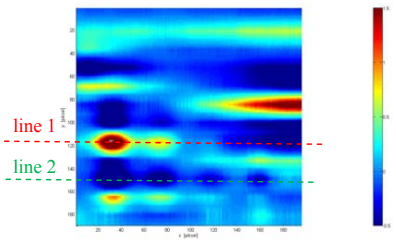

Fig. 4. Graphs of 1-D DWT of temperature field using wavelet Daubechies Db3, complete detail D5

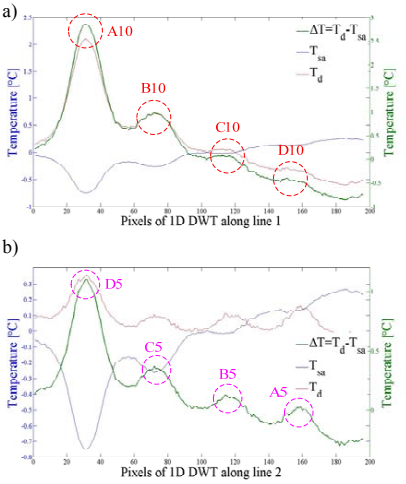

Fig. 5. Contrast of 1D DWT processed thermogram for: a) line 1, and b) line 2

5. Concluding remarks

The presented contribution demonstrated abilite of DWT as a powerful NDT. Although more powerful in detection, DWT can be confusing due to the jumps in level of detected anomlaies. Therefore, parralel usage of gradient based metod [3] is recommended.

Acknowledgements

Financial support from the Ministry of Science, Education and Sports project ‘‘Fatigue strength of constructions and materials‘‘ is gratefully acknowledged.

References

[1] Krstulović-Opara L., Klarin B., Neves P, Domazet Ž. Thermal imaging and Thermoelastic Stress Analysis of impact damage of composite materials. Engineering Failure Analysis, **18**, 2011. pp. 713-719.

[2] Krstulović-Opara, L., Klarin, B., Garafulić, E. and Domazet, Ž, Application of gradient based IR thermography to the GRP structures inspection. Key Engineering Materials, **489**, 2011. pp. 682-685.

[3] Ziopaja, K., Pozorski, Z., Garstecki, A., Damage detection using thermal experiments and wavelet transformation. Inverse Problems in Science and Engineering, **19**, **1**, 2011.

30th DANUBIA-ADRIA
Symposium on Advances in Experimental Mechanics
September 25-28, 2013 - Primošten, Croatia

3A04 077

APPLICATION OF DIGITAL IMAGE CORRELATION IN DENTISTRY

Milos Milosevic[1], Simon Sedmak[1], Uros Tatic[1], Radoslav Rajkovic[1], Jasmina Perović[1], Nenad Mitrović[2], Aleksandar Sedmak[2]

[1] University of Belgrade, Innovation center of Faculty of Mechanical Engineering, Kraljice Marije 16, 11000 Belgrade, SERBIA. E-mail: mmilosevic@mas.bg.ac.rs, ssedmak@mas.bg.ac.rs, utatic@mas.bg.ac.rs, rrajkovic@mas.bg.ac.rs, jasmina.perovic84@gmail.com

[2] University of Belgrade, Faculty of Mechanical Engineering, Kraljice Marije 16, 11000 Belgrade, SERBIA. E-mail: nmitrovic@mas.bg.ac.rs, asedmak@mas.bg.ac.rs,

1. Introduction

Digital image correlation (DIC) techniques have been increasing in popularity, especially in micro- and nano-scale mechanical testing appli–cations due to its relative ease of implementation and use. Advances in computer technology and digital cameras have been the enabling techno–logies for this method and while white-light optics has been the predominant approach, DIC can be and has been extended to almost any imaging technology. Digital image correlation method is becoming a common method in determining mechanical properties of biomaterials [1]. DIC using 3D optical measuring system has very broad application in dentistry research field.

The purpose of this paper will be, first, to give clearly the application of DIC in dentistry, in particular in determining the behavior of resto–rative composites under different load conditions.

The 3D optical strain and displacement analysis using DIC represents a useful experimental approach that helps to better understand full displacement/strain fields of loaded materials and structures [1-10]. The difference in strain at different positions between the two load stages is then calculated by comparing the two images. These changes are then detected by looking for anomalies in the strain field. The test will work by taking an image of the structure at its unloaded state, and then loading it. Another image is then taken and the two are compared [2]. DIC allows very accurate strain measuring, which is often difficult if not impossible to achieve by other methods [1-4].

2. Methods

This technique was principally developed by M.A. Sutton [5]. It is based on representing the displacement field as a function of two coor–dinates, x and y. Upon deformation, these two coordinates will have different values, x' and y' (Fig. 1). The difference between the two states gives displacements along both directions. These calculations are made for groups of pixels called patterns, whose size depends on the strain that is expected in the material in question.

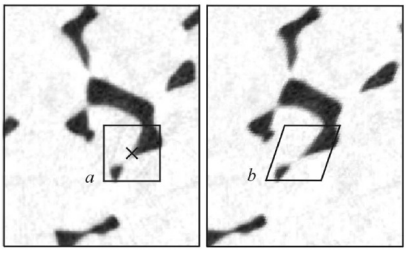

Fig. 1. The undeformed and deformed shapes of a material sample

This principle can be extended to three dime–nsions, by including an additional displacement, making the required function more complex.

3. Results

DIC can be combined with FEM, to provide experimental verification of numerical results [7].

Digital image correlation is also often used in various areas in biomaterial analysis, since the strains measured in this case are very small, as the samples are subjected to lower loads and stresses compared to the previous examples [2-4].

In this sense, DIC was used in determining the mechanical properties of various tissues, such as arteries and horns [8], and in a very creative paper, of the material that makes up the exoskeleton of lobsters [9].

Our focus, however will be on the application of DIC in dentistry, in particular in determining the behavior of restorative composites under different load conditions. One example is light-cured composite shrinkage analysis, leading to the appearance of strains in the composite and the tooth itself. In order for such an analysis to be made, it is necessary to know the mechanical properties of all materials used, i.e. the enamel, dentine, and the composite itself, along with an adhesive, in cases where it is used. As before, these results can be compared to the ones from numerical simulations using FEM. An example of results obtained by DIC is given in figure 2.

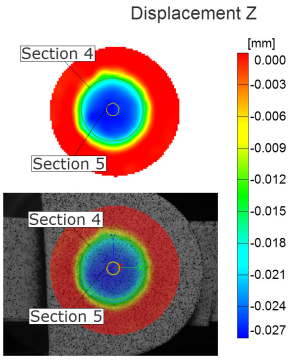

Fig. 2. Local displacement fields of dental composites after polymerization

4. Conclusion

Use of 3D Digital image correlation has shown great potential as a means as a tool for determining deformation fields in dental restorative composites. The main purpose of these tests is to compare the composites to each other in order to determine which one shows the best behavior, especially regarding light-cured shrinkage. The results obtained by this method have shown good compliance with numerical results.

Hence, by combining FEM and DIC in dentistry, it is possible to significantly improve the effectiveness of dental restorations.

Acknowledgements

The study was carried out within the Project TP - 36027 and Project TP – 35040, financed by the Ministry of Education, Science and Technological Development, Republic of Serbia.

References

[1] Mitrovic N., Milosevic M., Sedmak A., Petrovic A., Prokic-Cvetkovic R.: „Application and Mode of Operation of Non-Contact Stereometric Measuring System of Biomaterials“, FME Transactions, Vol. 39, No 2, page 55-60, 2011

[2] Milosevic M., Miletic V., Mitrovic N., Manojlovic D., Savic-Stankovic T., Maneski T.: “Measurement of local deformation fields in dental composites using 3D optical system”, Chemicke Listy 105, s751 - s753, 2011

[3] Miletic V., Manojlovic D., Milosevic M., Mitrovic N., Savic Stankovic T., Maneski T.: “Analysis of local shrinkage patterns of self-adhering and flowable composites using 3D digital image correlation“, Quintessence Int 2011;

[4] Ljiljana Tihacek Sojic, Aleksandra Milic Lemic, Ivan Tanasic, Nenad Mitrovic, Milos Milosevic and Aleksandar Petrovic, Compressive strains and displacement in a partially dentate lower jaw rehabilitated with two different treatment modalities, Gerodontology 2012, 29(2):e851-7;

[5] Sutton, M. A., Wolters, W. J., Peters, W. H., Ranson, W. F., McNeill, S. R. Determination of displacements using an improved digital correlation method, Image and Vision Computing, vol 1 n°3, août 1983, 133-139.

[7] Nenad Mitrovic, Milos Milosevic, Nikola Momcilovic, Aleksandar Petrovic, Aleksandar Sedmak, Tasko Maneski, Milorad Zrilic, Experimental and numerical analysis of local mechanical properties of globe valve housing, , Chemicke Listy 106, pp. 491-494, 2012.

[8] Zhang D., Arola D.D., Applications of digital image correlation to biological tissues, Journal of Biomedical Optics 9(4), (July/August 2004), pp. 691–699.

[9] Sachs C., Fabritius H., Raabe D., Experimental investigation of the elastic–plastic deformation of mineralized lobster cuticle by digital image correlation, Journal of Structural Biology 155 (2006), pp. 409–425.

[10] Sedmak A., Milosevic M., Mitrovic N., Petrovic A., Maneski T.: “Digital image correlation in experimental mechanical analysis”, Integritet i vek konstrukcija (Structural Integrity and Life), Vol.12, No1, pp.39–42, 2012.

30th DANUBIA-ADRIA
Symposium on Advances in Experimental Mechanics
September 25-28, 2013 - Primošten, Croatia

3A05 069

RAPID PROTOTYPING PRODUCTS MATERIAL LAW VALIDATION BY OPTICAL PHOTOELASTIC COATING METHOD

Peter Ficzere [1], Lajos Borbás[2]

1) PhD student; MSc in Mechanical Engineering; assistant professor; Department of Vehicle Parts and Structures Analysis; Budapest University of Technology. and Economics; H-1111 Budapest, Bertalan L. u. 2.; ficzere@kge.bme.hu
2) PhD in Mechanical Sciences, MSc in Mechanical Engineering; supervisor; Department of Vehicle Parts and Structures Analysis; Budapest University of Technology. and Economics; H-1111 Budapest, Bertalan L. u. 2.; borbas@kge.bme.hu

Corresponding author: ficzere@kge.bme.hu

1. Introduction

The number of products produced rapid prototyping technology has increased extraordinary over the last decade. This increase can increase the speed, that certain production technology patents expired last year. The technology is spreading more and more opportunities to develop their. As a result, we are able to produce more and better quality products. Thanks to the continuously improved quality, the RPT products are now not used for only marketing model, but also as a functional prototype when it has to be loadable. In the case of a certain number use this technology of economic reasons (Simply is not worth designed and manufactured tools in such a way as to) [1], which in this case, is called small-series production.

Moreover will increasing the number of medical applications (knee-, hip-, spine prostheses). We call this as unique mass production.

However in the case of functional prototypes and medical applications each item must be unique and loadable. In such cases, there is no way a preliminary trial, so you should know that whether the model will carry the applied loads. This can be determined by finite element analysis. To do this analysis, we need to have a 3D CAD model, we need to know the installation environment (constraints), expected loads, over and above we have to know the material properties too.

In this paper the OBJET FullCure720 material was investigated, which against our the preliminary assumption is not isotropic, but has an ortotrop material properties[2]. In the case of the application of new materials addition to defining the material models the measured material properties also should be validated.

2. Experimental Results

After determining the material properties of the material must be validate. This can be done in several ways. One of the very best method when comparing the results of finite element analysis performed using the measured material properties with a real part measured stress-distribution and stress values. One of the best methods the determination of the loads exactly on a given part on real models is the optical photostress method. This can help you get fast results when parts has complex geometry.

Further advantage that in the modeling may be incorrectly specified constraints using this clearly identifiable. We would like to validate our measured values such principle. To do this after the defining the material properties, we have to choose an arbitrarily complex geometry part with. In our case this is a special valve housing means. The valve housing are shown in fig. 1.

This part investigated under real loads, so that it is equipped with optical photoelastic coating and then after the assembly of the parts we loaded it. Investigated across the polymerization filters we recorded the observable stress distribution and fringe patterns.

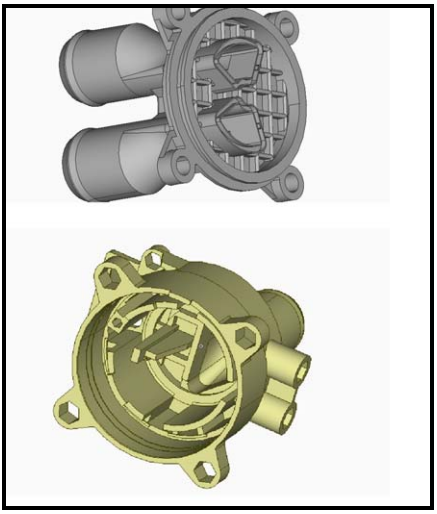

Fig. 1: Investigated valve houses

Then we compared the obtained results with results given by the finite element analysis on the 3D CAD model of the same part

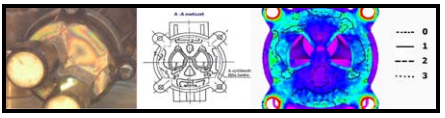

Fig. 2: Comparison of the results of optical photostress analysis with finite element analysis

Such a comparison is shown in fig. 2.

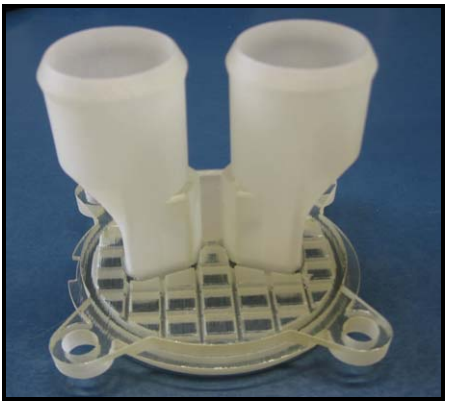

Fig. 3: RPT model

Fig. 2 shows well the similarities in addition, you can see that in case of known material properties the method is suitable for validating the material properties. After that we produced the examined valve housing by rapid prototyping method in two position/direction which are perpendicular to each other (these are the orthotropic principal directions). This is shown in fig. 3. We would like to this material properties validated. This model is also coated with test layer to optical phototstress test (only at the hypothetical critical areas). The model prepared to the optical photostress test can be seen in fig. 4.

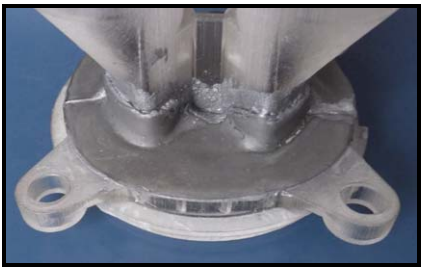

Fig. 4: Optical phototstress coating layered RPT valve housing

To carry out the investigation we assemblied the valve housing and then it was gradually loaded. Evaluation of the obtained results are currently in the process.

3. Acknowledgements

The research work is supported by Varinex Zrt, Hungary.

4. References

[1] P. Ficzere, Á. Török, Gyorsprototípus gyártás gazdasági előnyei. Key OGÉT 2013, Arad, Romania, pp. 113-117.(ISBN:2068-1267)

[2] P. Ficzere, L. Borbás: Investigation of material properties of rapid-prototyping products for finite element analysis [In Hungarian: Gyors-prototípus készítő eljárással gyártott termékek anyagtulajdonságainak meghatározása végeselemes analízis számára] GÉP 60:(10-11) pp. 36-39. (2009)

30th DANUBIA-ADRIA
Symposium on Advances in Experimental Mechanics
September 25-28, 2013 - Primošten, Croatia

3A06 065

RECONSTRUCTION OF LATERAL TIBIAL CONDYLE FRACTURES WITH PROSTHESIS AND BUTTRESS PLATE

L. Borbás [1], I. Bagi [1], R. Sződy [2]

[1] Budapest University of Technology and Economics, Research Centre of Biomechanics, H-1111 Budapest Műegyetem rkp.3-9. Hungary.

[2] Péterfy Sándor Hospital - Clinic and Traumatology Centre, H-1081 Budapest, Fiumei út 17., Hungary.

Corresponding author: borbas@kge.bme.hu

1. Introduction

Injuries of the proximal leg are frequently associated with fractures involving the joint surfaces of the lateral or medial tibia condyles. Primary treatment of these types of fractures consists of reconstruction of the joint surface and plate osteosynthesis with a so called buttress plate. These injuries heal often with destruction of the joint surface. However, pain upon weight bearing and the treatment of considerable unicompartmental posttraumatic osteoarthritis of the knee joint pose a real problem. According to the current protocol, implant removal and joint surface replacement with prosthesis is the solution. If the medial compartment is involved, total knee replacement or – if adequate – implantation of a medial unicondylar prosthesis is performed. According to the experiences gained so far, implantation of an unicondylar prosthesis was not advisable in case of injured lateral compartment, because it would be subject to adverse biomechanical effects, resulting in relaxation due to osteonecrosis and impaired stability of the cortical bone caused by the fracture. This creates a disadvantageous situation requiring repeated surgery very soon, furthermore, frequently implantation of a revision prosthesis. But if we remove only the proximal few screws and implant an unicondylar prosthesis in a minimally invasive manner, the buttress plate left in place reinforces the lateral cortex, and the unicondylar prosthesis makes up a solid biomechanical unit with the screws supported by the bone cement. Application of this method makes plate removal unnecessary. The aim of our experiments is to demonstrate the efficiency of the above method by the means of biomechanical measurements. Validation has been carried out with photostress analysis of experimental mechanics, in the Cooperation Research Centre of Biomechanics for Budapest University of Technology and Economics.

2. Experimental Results

Photostress analysis (photoelastic coating technic) has been used in this application to reveal the surface strain-stress distribution of the investigated specimen [1], [2], [3].

In case of the photostress analysis 1.6 mm coating was applied on the investigated surface.

The measurements have been carried out on the outer surface of the investigated bone. A network applied on the investigated surface, horizontally and on the generatrix, and on the circumference as well. The steps on horizontal way were plotted by 15 mm (originating from the top surface of the knee measured downwards), on the circumference by 90 degrees.

The investigated specimen shown in Fig. 1

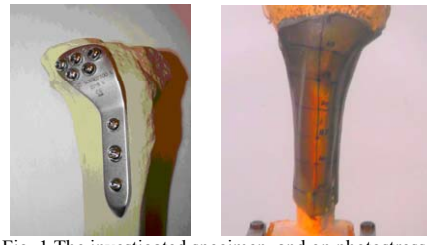

Fig. 1 The investigated specimen, and on photostress picture

In case of the photostress analysis for biomechanical application were introduced in some of our previous measurements [3]. In our case the sensitivity parameter of the coating material with calibration was $k = 680$ [μS] (that is $0.68 \cdot 10^{-6}$ [mm/mm]), in case of coating thickness $d = 1.6$ *mm* (on the basis of the calibration of the material of coating).

According to the basic equation of the photo-stress analysis the specific elongation of an investigated specimen glued with a sensitive coating is:

$$\varepsilon_1 - \varepsilon_2 = m \cdot k \,, \qquad (1)$$

where: m is fringe order at the investigated point,

ε_1, ε_2 the principal strain differences at the investigated point.

In case of the evaluation of the measurement results on specimen's fringe distributions drawn together from recorded polarisation pictures were prepared. From the fringe distribution principal strain differences were calculated (1). During the conversion of the strain results to stresses the elastic modulus E= 20.2 [GPa], and a Poisson ratio ν= 0.29 of the investigated specimen were calculated. Calculated by these values the stress level belonging to the unit fringe order (m=1, the colour of this in the fringe distribution pictures is purple) is the following equation:

$$\sigma = \sigma_1 = \frac{k \cdot E}{1+\nu} = \frac{0,68 \cdot 10^{-3} \cdot 2,02 \cdot 10^4}{1+0,33} = 10,3 \; MPa \qquad (2)$$

The FEM analysis carried out parallel [5] to experiments supported our assumptions. The buttress plate is a suitable solution to realise the injured knee.

3. Results

Biomechanical theoretical and experimental investigations have confirmed our assumptions that the applied buttress plate has really strengthened the lateral cortical "wall" and through the bone cement the screws and the plate prostheses constitute a unified biomechanical system.

Using this method makes the removal of the inserted plate unnecessary.

A traumatologic advantages are: minimum invasive procedure, loadable joint surface, painless condition, stable lateral wall, "reinforced concrete synthesis". Results for the patients are: painless condition, adequate function, loadable joint surface, no loosening. No total prosthesis is to be built in, in this way it is not necessary to sacrifice the whole joint.

4. Acknowledgements

Performing the measurements like to thank the Cooperation Research Centre of Biomechanics for Budapest University of Technology and Economics.

5. References

[1] L. Borbás, F. Thamm, M. Hagymási, G. Krakovits: Investigation of different design of femur head prosthesis with respect to the force transition to the femur shaft. XXV AIAS International conference on material engineering. Gallipoli-Lecce, 4...7 Szeptember, 1996. p.:245...248.

[2]. J. Gáspár, L. Borbás, , F. Thamm: Experimental tests on mandible and tooth prosthesis. XXII. DAS, Parma (Olaszország), 2005. szept. 28…okt. 1. p.: 130...131.(R. L.) (On Web: http://das.tuwien.ac.at)

[3] L. Borbás, F. Thamm, L. Oláh: Comparison of starin gage technique and photoelastic coating method in the investigation procedure of femur prosthesis. Journal of Computational and Aplied Mechancs, Vol. 7., No. 1. (2006), pp.: 3…12.

[4] N. Juhász: Tibia lateralis condylus lemez mellett behelyezett UCP. A Magyar Ortopéd Társaság és a Magyar Traumatológiai Társaság 2010. Évi Közös Kongresszusa, 2010. jún. 17-19, Pécs

[5] I. Bagi, R. Sződy, S. Ács: Tibia unicondiláris töréseinek csont necrosist követő ízfelszín pótlásának végeselemes anlízise. (FEM analysis of the unicordial brake of tibia) A Magyar Ortopéd Társaság és a Magyar Traumatológiai Társaság 2011. Évi Közös Kongresszusa, 2011. jún. 16-18, Debrecen

30th DANUBIA-ADRIA
Symposium on Advances in Experimental Mechanics
September 25-28, 2013 - Primošten, Croatia

3A07 024

INFLUENCE OF THE COLLAGEN AND ELASTIN FIBERS ON THE MECHANICAL RESPONSE OF BLOOD VESSEL WALL

Marta Kozuń[1,2], Magdalena Kobielarz[1,2], Agnieszka Chwiłkowska[2,4], Aleksandra Kuzan[2,4], Krzysztof Maksymowicz[2,3], Celina Pezowicz[1,2]

[1] Wrocław University of Technology, Division of Biomedical Engineering and Experimental Mechanics, Łukasiewicza 7/9, 50-371 Wrocław, Poland, marta.kozun@pwr.wroc.pl

[2] Regional Hospital in Wrocław, Research and Development Center, Kamieńskiego 73a, 51-124 Wrocław, Poland

[3] Wrocław Medical University, Department of Forensic Medicine, J. Mikulicza-Radeckiego 4, 50-368 Wrocław, Poland

[4] Wrocław Medical University, Department of Medical Biochemistry, Chalubinskiego 10, 50-368 Wrocław, Poland

1. Introduction

The two passive load bearing components of the arterial walls are collagen and elastin fibers [5]. Content of them in dry mass aorta is about 35% (collagen) and 50% (elastin) [4]. Collagen fibers have high failure strength. The value of ultimate strength of their ranges from 50-100MPa [1]. Elastin fibers are rubber-like structures. They can undergo uni-axial extensions of up 150% prior to breaking, whereas collagen fibers can only undergo less than 10% extension before breaking [1].

Mechanical properties of the arterial walls are mostly determined by its components [2]. Despite there are only a few analysis in a literature presented influence of collagen and elastin fibers on the mechanical response of human blood vessel walls. This knowledge is important for better understanding role of collagen and elastin fibers in biomechanics of blood vessel walls.

In this studies the mechanical properties of the native (N), elastin (E) and collagen (C) – digested specimens were determined.

2. Material and methods

The subject of the study were human thoracic aortas. The material consisted of 18 circumferential specimens of blood vessel walls coming from 11 corpses aged from 21 to 68. Aortas were obtained *post mortem* in cooperation with Department of Forensic Medicine, Wrocław Medical University.

In order to determine the function of elastin and collagen fiber of blood vessel walls, the technique of selective digestion was used. The specimens were treat with 2 enzymes: elastase and collagenase. After that uniaxial stretching until rupture was performed for native, elastin- and collagen digested specimens. The speed of loading was 2mm/min.

3. Results

For each type of specimens stress-strain curves were determined. The character of their is different. The stress-strain curves of collagen-digested specimens are quasi-linear. It's possible because stress-strain curves for elastin fibers are considered "the most linear elastic natural protein material". These fibers determine an isotropic properties of blood vessel walls [1]. Stress-strain curves of elastin-digested specimens aren't linear. It can be caused by step-by-step participation of collagen fibers in load-bearing process. The stress-strain curves of native specimens are non-linear.

In the next step the strength (σ_{max}) and Young's modulus (E) values were estimated on the base of stress-strain curves. The strength was defined as the maximum value of stress. For native specimens the Young's modulus was determined in the low (A) and high (B) strain phases (Fig.1.).

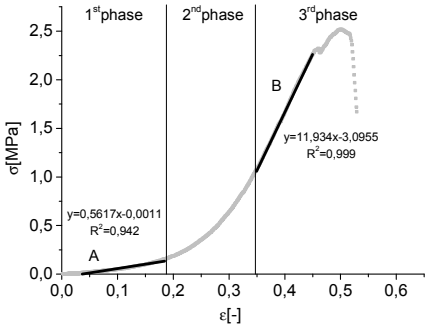

Fig.1. Stress-strain curve for native specimens with appointed 3 stages and the low (A) and the high (B) strain phases

Results indicate that the highest values of mechanical parameters (strength and Young's modulus) were obtained for native specimens (Tab.1.). The average value of strength of their is about 87% higher than collagen digested specimens and 61% higher than elastin-digested specimens. The high strain Young's modulus of native specimens can be associated with collagen fibers and the low strain Young's modulus can be connected with elastin fibers.

Based on the values of Young's modulus obtained for each specimen types, the stress-strain curves of native specimens were divided into 3 stages [3]. The 1st stage is refered as "elastin dominant stage". During loading in this stage collagen fibers are crimped, so elastin is load bearing component [3]. In the 2nd stage, when the load is increased, collagen fibers begin to bear load and two deformation mechanism are present. This stage is "stage of transition". In the 3rd stage refered as "collagen dominant stage" only collagen deformation mechanism is active [3].

type of specimens	E[MPa]		σ_{max}[MPa]
	A	B	
native	1,66±0,08	7,20±1,63	1,31±0,50
elastin-digested	3,62±1,16		0,51±0,07
collagen-digested	1,16±0,09		0,16±0,08

Tab. 1. The average values of strength and Young's modulus (A – the low strain phase, B – the high strain phase)

5. Conclusion

Results of our research confirm that the mechanical response of the blood vessel wall are mostly determined by its components [2]. The collagen fibers are responsible for the strength of blood vessel wall and they are load-bearing components in the 2nd and 3rd stages of stress-strain curve. The elastin fibers give extreme vessel wall elasticity and they are connected with the 1st stage of stress-strain curve [2].

Acknowledgements

This work is part of the project "WROVASC – Integrated Cardiovascular Centre", co-financed by the European Regional Development Fund, within Innovative Economy Operational Program, 2007-2013.

References

[1] Humphrey JD., Cardiovascular Solid, Mechanics: Cells, Tissues and organs. Springer: New York, 2002, pp. 386.

[2] Kobielarz M., Będziński R., Chwiłkowska A., et al., 27th Danubia-Adria Symposium on Advances in Experimental Mechanics, September 22nd-25th, Wrocław, Poland, 2010. pp. 97-98.

[3] Sheridan W.S., Duffy G.P., Murphy B.P., Mechanical characterization of a customized decellularized scaffold for vascular tissue engineering, Journal of the mechanical behaviour of biomedical materials 8, 2012, pp. 58-70.

[4] Silver F.H., Christiansen D.L., Buntin C.M., Mechanical properties of the aorta: A review. Critical Reviews in Biomed. Engr., 17, 1989, pp.323-358.

[5] Wulandana R., Robertson AM., An Inelastic Multi-Mechanism Constitutive Equation for Cerebral Arterial Tissue, Biomechanics and Modeling in Mechanobiology, 4, 2005, pp.235-248.

30th DANUBIA-ADRIA
Symposium on Advances in Experimental Mechanics
September 25-28, 2013 - Primošten, Croatia

3A08 066

NEW EXPERIMENTAL METHOD TO MEASURE METALLIC SURFACE AREA OF CORONARY STENTS

Dóra Károly[1], Miksa Kovács[1], Eszter Bognár[1,2]

[1] Budapest University of Technology and Economics, Faculty of Mechanical Engineering, Dept. of Materials Science and Engineering, Bertalan L. u. 7, 1111 Budapest, HUNGARY. E-mail: karoly.dora@gmail.com, miksa.kovacs@gmail.com

[2] MTA–BME Research Group for Composite Science and Technology, Műegyetem rkp. 3, 1111 Budapest, HUNGARY. E-mail: eszter@eik.bme.hu

1. Introduction

Endovascular stents, such as coronary stents, are widely used for the treatment of narrowed vessels caused by plaque formation in the arteries. The narrowing of expanded blood vessels (restenosis) is perhaps the major complication associated with endovascular stent implantation that is believed to be caused by insufficient metallic surface area (MSA) in some stent designs. The MSA is a ratio given as a percentage, of the stent's cylindrical surface to the covered surface of the blood vessel. For technical reasons a ratio too high is not recommended, because the contact area with the blood vessel wall is too large thus the risk of thrombus formation and restenosis increase. On the other hand, a ratio too small can lead to mechanical problems [1,2].

Most studies related to stent surface focus on stent coatings. They are looking for a material that meets mechanical requirements and generates an optimal biological response in the body. Because of this, knowing the exact size and geometry of the stent surface is very important. Furthermore, in the case of drug-eluting stents the stent pattern can also affect uniform dissolution [3].

2. Materials and methods

In the study we investigated 4 coronary stents. (A) and (B) stents have the same geometry, but different size. (C1) and (C2) stents have the same geometry and size too. The stents were expanded at nominal pressure. All measurements correspond to the MSZ EN ISO 25539-2 standard [4].

In our work we looked at a new experimental method to determine MSA. It was needed because of the previously used method's certain problems. The methods' efficiency was compared. Both methods, which were developed at our department, aimed at converting the cylindrical stent into a flattened two dimensional image in order to analyse the stent pattern with imaging software. With the stent pattern another useful stent properties can be easily determined, such as the largest and the smallest cell area, and the maximum achievable cell diameter in them.

2.1 The manual method

The first method was performed by manual stereo-microscopy. High-resolution digital images were taken of each segment of the stents' mantle. The pictures were taken with a stereo microscope fitted to a precision rotary unit. The stents were rotated by increments of 15° from the starting 0° position to 360° then the 24 pictures were joined to each other.

2.2 The new automatic method

The second method was done in an automated manner by a new configuration. The stents were pulled up to a shaft connected to a motor, so that the stents were rotating during the scanning process. In this case we get one whole picture of the stent pattern. The rotational speed and direction can be changed using the control panel buttons.

3. Results

Our findings showed that the first and the second methods gave similar results (Fig. 1). The locations of the largest and smallest cells are the same with the manual and the automatic method, except in the case of (C1) stent, where the location of the largest cell was different. Since the difference between the largest and the second

largest cell was negligibly small, the error might be due to inappropriate joining of images.

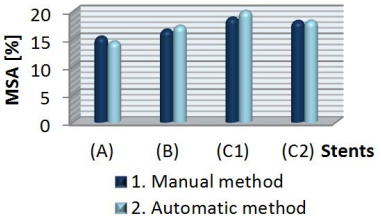

Fig. 1 MSA values with the two methods.

Fig. 2 shows the evaluated stent pattern of 3.0×12 mm, (B) stent. The largest cells are yellow, the smallest cells are green, and the circles with the maximum achievable diameter are red.

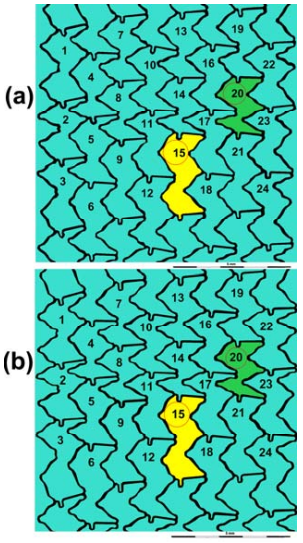

Fig. 2 The evaluated stent pattern of stent (A) (a) manual, (b) automatic method.

The largest differences between the methods were speed and accuracy. The automatic method needs less time (the difference is in hours), because the pictures did not need to be joined together. This is an important factor when the stent is too long to fit in the microscopic field. In that case separate images are taken of both ends of the stent, and then 48 images have to be joined up to create one big image. Resulting errors are multiplied during image editing, and time needed also increases.

In addition, Fig. 3 clearly shows that the struts reflect light in the microscope pictures of the metal stent surface. Bright and dark parts seem to have different strut widths which need to be corrected during evaluation. This both takes more time and causes inaccuracy. In contrast, reflective glare is eliminated in the images taken by scanner.

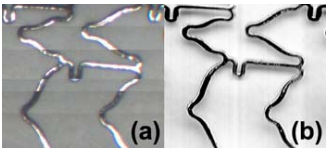

Fig. 3 Stent pattern (a) manual, (b) automatic method

4. Remarks

- Metallic surface area, the largest and the smallest cell sizes, and the maximum achievable cell diameter are stent properties which are important for the long-term effectiveness of the stent after implantation.
- We used two methods to measure MSA values. These results favour the new automatic method, which on the basis of this study seems to give the most accuracy in the shortest time.
- The collected experience and results of this study provide a basis for further research. We plan to use the obtained image data to create three-dimensional stent models and run finite-element simulations to predict mechanical properties of stents with given defined patterns.

Acknowledgements

First we would like to thank to our department and colleagues there for providing us with the environment and facilities to complete this project. Also, we would like to thank Vascular Venture Ltd. for providing us with stents.

This work is connected to the scientific program of the "Development of quality-oriented and harmonized R+D+I strategy and functional model at BME" project. This project is supported by the New Hungary Development Plan (Project ID: TÁMOP-4.2.1/B-09/1/KMR-2010-0002).

References

[1] Julio, L., et al. Intravascular stents in the last and the next 10 years, J of Endovascular Therapy. 2004, 11(2), pp. 200–206.
[2] Szabadits, P., et al. Flexibility and trackability of laser cut coronary stent systems. Acta of Bioeng and Biomech. 2009, 11(3), pp. 11-18.
[3] Seedial, S.M. et al, Local drug delivery to prevent restenosis. J Vasc Surg. 2013, 57(5). pp. 1403–1414.
[4] MSZ EN ISO 25539-2:2009 Cardiovascular implants. Endovascular devices. Part 2: Vascular stents (ISO 25539-2:2008).

30th DANUBIA-ADRIA
Symposium on Advances in Experimental Mechanics
September 25-28, 2013 - Primošten, Croatia

3A09 018

MECHANICAL PROPERTIES OF NICKEL-TITANIUM ORTHODONTIC WIRES WITH VARIOUS COATINGS

Višnja Katić[1], Jasna Leder Horina[2], Damir Semenski [2], Damir Ježek[3], Stjepan Špalj[4]

[1] Private dental practice, III. Podbrežje 39, HR-10020 Novi Zagreb, CROATIA. E-mail: visnja.katic@gmail.com

[2] University of Zagreb, Faculty of Mechanical Engineering and Naval Architecture, Ivana Lučića 5, HR-10000 Zagreb, CROATIA. E-mail: jasna.leder.horina@fsb.hr, damir.semenski@fsb.hr

[3] University of Zagreb, Faculty of Food Technology and Biotechnology, Pierottijeva 6, HR-10000 Zagreb, CROATIA. E-mail: djezek@pbf.hr

[4] University of Rijeka, Medical Faculty, Krešimirova 40, HR-51000 Rijeka, CROATIA. E-mail: stjepan.spalj@medri.uniri.hr

1. Introduction

Shape memory alloys (SMAs) made of nickel and titanium are used in fixed orthodontic treatment due to their superelasticity and memory retention [1]. Various coatings on nickel-titanium (NiTi) wires are manufactured to improve esthetics or reduce friction upon brackets. This study analyzes effect of coating on mechanical properties, and percentage of bending force action emitted to phase transformation during bending of NiTi orthodontic wires.

2. Methods

2.1 Material preparation

Three types of preformed rectangular (0.508 × 0.508 mm) BioForce Sentalloy (Dentsply GAC Int., NY, USA) orthodontic wires (nickel (50-51%) and titanium (49-50%)) were investigated in study:

- regular NiTi - with untreated surface

- rhodium coated NiTi (High Aestetic) – with rhodium, gold, tungsten and rubidium in 0.5 μm thin layer on surface

- nitrified NiTi (IonGuard) - with surface treated by nitrogen ion implantation, where nitrogen replaces nickel, forming titanium-nitride.

25 mm long specimens were cut from the straight ends of preformed archwires. Ten specimens were prepared for every wire type.

2.2 Mechanical testing

Specimens were subjected to the three-point bending test according to current standards [2, 3] in thermal chamber at 37°C. Support span of Texture Analyser TA.HD.plus (Stable Micro Systems, Godalming, UK) was set to 12 mm, and specimens loaded with low force cell (5 kg, factory calibrated) to a deflection of 3.1 mm and then unloaded to zero deflection at a cross-head speed of 0.0167 mm/s. Load, in newtons (N), and deflection, in millimeters (mm), were collected every 5 ms. Hysteresis loop gets generated from loading and unloading curves, and following data were read off from it: loading and unloading elastic modulus (E) and yield strength (YS), and percentage of bending force action emitted to phase transformation.

2.3 Statistical analysis

ANOVA and Student-Newman-Keuls post hoc test were used for analysis of differences in mechanical properties of each wire type in as-received condition. Statistical analysis were carried out using statistics software SPSS 10.0 (SPSS Inc., Chicago, USA), statistical significance was preset to $p<0.05$.

3. Results

3.1 Elastic modulus (E)

Rhodium coated NiTi wires showed statistically significant ($p<0.05$, marked with horizontal bars) increase in both loading and unloading E (Fig. 1),

and these wires appeared to be stiffest among three wire types tested.

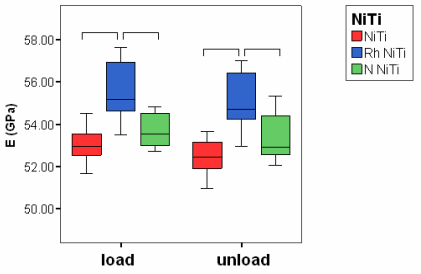

Fig. 1. Load and unload elastic modulus (*E*) of uncoated (NiTi), rhodium coated (Rh NiTi) and nitrified (N NiTi) orthodontic wires

3.2 Yield strength (YS)

Rhodium coated NiTi wires showed statistically significant ($p<0.05$, marked with horizontal bars) increase in loading YS (Fig. 2), and higher stress for plastic deformation was needed.

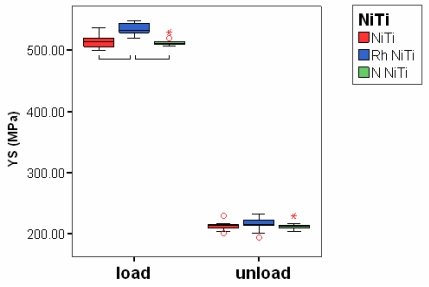

Fig 2. Load and unload yield strength (YS) of uncoated (NiTi), rhodium coated (Rh NiTi) and nitrified (N NiTi) orthodontic wires

3.3 Bending force action emitted to phase transformation

Bending force action emitted to phase transformation in crystal structure was calculated as difference between loading and unloading bending force. [4] The percentage of bending force action emitted to phase transformation in crystal structure represents portion of bending force applied for transformation, when compared to total bending force of the wire. Rhodium coated NiTi wires showed statistically significant ($p<0.05$, marked with horizontal bars) increase in percentage of bending force action emitted to phase transformation (Fig. 3). When larger part of total energy absorption is used for phase-transformation, less of action force remains for teeth movement.

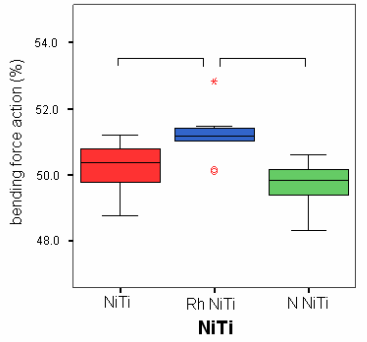

Fig. 3. Percentage of bending force action emitted to phase transformation of uncoated (NiTi), rhodium coated (Rh NiTi) and nitrified (N NiTi) wires

4. Remarks

- Type of coating dictates response of the wire.
- Rhodium coating caused increase in elastic modulus (*E*), yield strength (YS) and percentage of bending force action emitted to phase transformation of NiTi wires.

References

[1] Miura F, Mogi M, Ohura Y, Hamanaka H. The super-elastic property of Japanese NiTi alloy use in orthodontics, Am. J. Orthod. Dentofac. Orthop., **90**, 1986. pp. 1-10.

[2] American National Standard/American Dental Association. Specification No.32. Orthodontic wires. American Dental Association, Council on Scientific Affairs, Chicago, Ill. 2000.

[3] American Society for Testing and Materials. D790-10. Standard test methods for flexural properties of unreinforced and reinforced plastics and electrical insulating materials. American Society for Testing and Materials, West Conshohocken, Pa. 2010.

[4] Iijima M, Ohta M, Brantley WA, Naganishi A, Murakami T, Muguruma T and Mizoguchi I. Transformation behavior of nickel-titanium orthodontic wires under tensile load. Dent. Mater. J., **30**(3), 2011. pp. 398–403.

30th DANUBIA-ADRIA
Symposium on Advances in Experimental Mechanics
September 25-28, 2013 - Primošten, Croatia

3A10 016

FIELD EXPERIMENT ON BACTERIA TRANSPORT IN SAND

Masaharu Fukue[1], Satoshi Abe[2], Noriaki Jitsukata[3], Rie Takahashi[4], Tatsuya Shibata[5] Yuichi Fujimori[6]

[1] Tokai University, Faculty of Marine Science and Technology, 3-20-1 Orido, Shimizu-ku, Shizuoka, Japan. E-mail: fukue@scc.u-tokai.ac.jp

[2] Shizuoka River Office, Chubu Regional Bureau, Ministry of Land, Infrastructure, and Transport, 3-108 Tamachi, Aoi-ku, Shizuoka, Japan, E-mail, abe-s85aa@cbr.mlit.go.jp

[3] Ce Techno, Co., 16-50, 2-cho-me, Mabuchi, Suruga-ku, Shizuoka, Japan, E-mails: cet.jitsukata@forest.ocn.ne.jp

[4] Japanese Geotechnical Association for Housing Disaster Prevention, 600-6 Ikeda, Suruga-ku, Shizuoka, Japan, E-mail: takuchi-bousai@swan.ocn.ne.jp

[5] Geebec, Co., 1-17-34 Karase, Aoi-ku, Shizuoka, Japan, E-mail: tatu@geebec.co.jp

[6] Chubusokuchi-lab, Co., 801-1 Konan, Suwa, Nagano, Japan, E-mail: fujimori-yuichi@chubusokuchi-lab.co.jp

1. Introduction

Microbially induced carbonate precipitation will be one of the innovated rehabilitation techniques for construction materials, such as soil structure, concrete and rock [1]. For soil improvement, the transport of bacteria into soils is one of the most important subjects, because it governs the improved zone [2]. It was shown that the transport of bacteria is influenced by many factors, i.e., the interactions between bacteria and soil particles, permeability of soils, injection velocity, type of solution to be mixed with bacteria, etc. [2][3].

This study examines microbially induced carbonate precipitation in the field and the distribution of bacteria is evaluated by the carbonate content, CC., because carbonate precipitation is possible only where bacteria exist.

2. Experimentation

The field test was performed on the side of the Abe River in Shizuoka city. Natural beach sand was embanked as an experimental soil layer.

Ureolytic microbes (1.4×10^9 cfu/mL) were cultivated using liquid culture [2]. A cultivated solution of 0.12 m^3 was prepared. Prior to the injection, the cultivated bacteria solution (B solution) was mixed with the reactive solution (R solution). The R solution consisted of 0.7M $CaCl_2$, 0.7M $MgCl_2$, 1.5M urea, and 10 mM ammonia buffer.

2.1 Bacteria [4]

The microbes used in this study were first isolated from a Japanese soil and named "*NO-A10*". The strain was recognized as *Sporosarcina. Sp.*. The ureolytic microbes will induce the following reaction [6].

$$CO(NH_2)_2 + 2H_2O \rightarrow 2NH_4^+ + CO_3^{2-} \quad (1)$$

The process is catalytic and very rapid. Under the existence of metal ions, such as Ca and Mg ions, carbonates can be produced [1][2][4].

2.2 Sand Materials

The sand materials used were natural medium sand. The maximum grain size was 0.85 mm and the average size was 0.282 mm. The density of the particles was 2.68 g/cm^3. The embankment was built with dry sand, as shown in Fig.1. The bulk density of the sand layer was 1.6 g/cm^3 in average.

2.3 Injection pipe

The injection pipe with a diameter of 5cm was buried by a depth of 50 cm at the center of the conical embankment. The length of the injection part was 20 cm, as shown in Fig. 2. The mixed

solution was injected with a water head ranging from 1 to 2 m.

2.4 Experimental Procedures

The mixture of B and R solution was injected into the dry sand layer. The solution was injected three times with an interval of one week. After 6 days from the last injection, the cemented sand was excavated. The samples were obtained from various points to measure carbonate content (CC). The CC was measured using a device developed by Kato and Okabe [4].

3. Results and Discussion

The excavated cemented zone is a column, as shown in Fig. 3. The diameter was approximately 80 cm and the height was 100 cm.

The vertical and horizontal distributions of CC are obtained, as shown in Figs. 4. It seems that the nearer the measurement of positions from the injection mouth, the higher the CC. It is considered that the cementation of sand was due to the bacteria adsorbed on the surfaces of sand particles [2][4].

4. Conclusion

A horizontally radial injection of the mixed solutions caused a cemented sand column. The carbonate content in the sand column seemed to be reflected by the distribution of microbes.

Acknowledgements

This study was partially supported by Kakenhi (22560498), Japan Society for the Promotion of Science (JSPS). The authors are grateful to Professors S. Ono and Y. Sato, Tokai University, for their great helps.

References

[1] De Muynck, W., De Belie, N., Verstraete, W., Microbial carbonate precipitation in construction materials: A review, *Ecological Engineering* 36, 2010, pp.118-136.

[2] Fukue, M., Ono, S., Sato, Y., Sakamoto, I. and Iwata, T., A transport technique of microbes for soil improvement using microbial precipitation of carbonates, Proc. 15th International Conf. on Experimental Mechanics, 2012, pp.1-14.

[3] Yee, N., Fein, J. B., Daughney, C. J., Experimental study of the pH, ionic strength, and reversibility behavior of bacteria-mineral adsorption, *Geochemica et Cosmochimica Acta* Vol. 64,4,2000, pp.600-617.

[4] Fukue, M., Ono, S., Sato, Y., Cementation of sands due to Microbiologically-induced Carbonate, *Soils and Foundations*, 2011. 51,1, pp.83-93.

Fig.1 Sand embankment used for injection test.

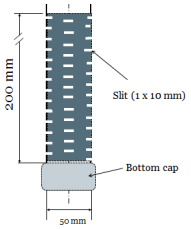

Fig.2 Injection pipe used in the study.

Fig.3 Excavated cemented sand column.

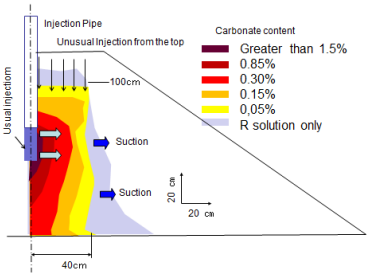

Fig.4 Distribution of carbonate content.

30th DANUBIA-ADRIA
Symposium on Advances in Experimental Mechanics
September 25-28, 2013 - Primošten, Croatia

3A11 109

MORPHOLOGY OF THE ARTICULAR SURFACES OF BIOLOGICAL KNEE JOINTS GIVES ESSENTIAL HINTS TO CONSTRUCT FUNCTIONAL KNEE ENDOPROSTHESES

Hans Nägerl[1)], Henning Dathe[1)], Christoph Fiedler[2)], Luiko Gowers[1)], Stephanie Kirsch[1)], Dietmar Kubein-Meesenburg[1)], Martin Wachowski[3)]

[1)] University of Göttingen, Biomechanical Working Group in Dept. of Orthodontics; [2)]Lima Corporate;
[3)]University of Göttingen, Dept. of Trauma Surgery, Robert-Koch-Straße 40, 37075 Göttingen, Germany.

Corresponding author: hnaeger1@gwdg.de

1. Introduction

Biological knee joints (BKJ) have a medial and a lateral compartment. In each a contact spot between the incongruent articular surfaces is produced when the BKJ are set into function by force closure. The BKJ of man (BKJM) or domestic pigs (BKJP), when stimulated by the skeletal muscles, solely allow almost plane flexion/extension motions. We show that any symmetrical relations do exist neither between the lateral and medial femoral nor between the lateral and medial tibial articular surfaces. A couple of plane tibial/femoral contact curves exists in the lateral as well as in the medial compartment. The lateral and the medial couple of contact curves are linked up to a constrained cam mechanism for flexion/extension.

2. Morphological demonstrations

Fresh or preserved BKJ (with almost natural mobility), still possessing the entire ligament apparatus with the menisci, were moved under force closure into several positions of flexion-/extension. Into each, tibia and femur were locked by metal plates, commonly used for osteosynthesis. After releasing, the respective flexion/extension positions could be exactly located again by means of the plates. After removing all ligaments, menisci and capsule, tibia and femur were again locked by the plates in the selected positions. Now, the respective contacts were marked which finally defined the contact curves on the tibial and femoral articular surfaces. Along each curve a thin lead wire was glued so that it reproduced the plane curve. The planes of the lateral and medial contact curves were parallel. Teleradiographs of the femoral compartments of BKJM, parallel adjusted to the planes, revealed the asymmetry of the femoral contact curves. The center of the medial contact curve (M_{Fm}) was always shifted by some mm to anterior compared to center M_{Fl} in all 20 BKJM investigated (Fig. 1). The tibial contact curve was laterally convex and medially concave. Centres: M_{Tm} and M_{Tl}.

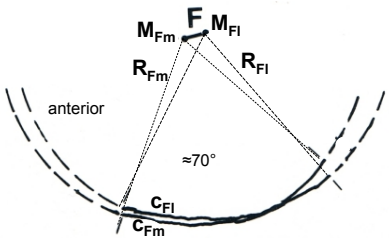

Fig. 1: Center M_{Fm} of the medial contact curve c_{Fm} was always shifted by some mm to anterior compared with M_{Fl} of the lateral contact curve c_{Fl}.

In BKJP both tibial are convex as sagittal cuts demonstrate (Fig. 2).

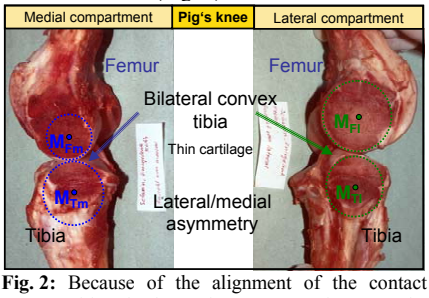

Fig. 2: Because of the alignment of the contact curves neither the femoral axes M_{Fm} and M_{Fl} nor the tibial axes M_{Tm} and M_{Tl} do coincide.

3. Functional meaning of the asymmetry

The four axes, M_{Fm}, M_{Fl} and M_{Tm}, M_{Tl}, defined by curvature centers of the contact curves, link up themselves to a closed four-bar-chain which is kinematically equivalent to the cam

mechanism, given by the four plane contact curves, for not too large degrees of flexion/extension out of home position of the BKJ. In the BKJM the home position is given by full extension. Then the BKJM can only be flexed around an instantaneous rotational axis (IRA) which is geometrically located near the contacts of the articular surfaces (Fig. 3). Hence, in the BKJM the articular surfaces are predominantly rolling during the stance phase of the human gait. The problem of friction is solved kinematically because sliding is transferred to rolling during high compressive loads.

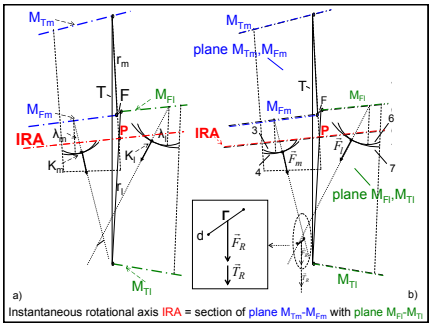

Fig. 3: Initial four-bar-chain of the BKJM, home position. In flexion the articular surfaces are predominantly rolling. The two articular forces $\vec{F}_m$ and $\vec{F}_l$ form a force wrench: torque $\vec{T}_R$. 3, 4, 6, 7: transverse contours produced by intersections of the planes M_{Tm}, M_{Fm} and M_{Tl}, M_{Fl} in the respective compartments. K_m, K_l = contact centres.

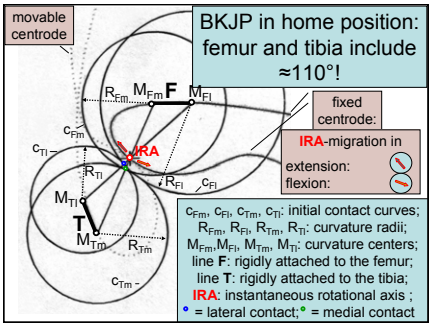

Fig. 4: Out of home position the BKJP can be flexed or extended. The IHA lies near the articular contacts.

Also the BKJP (Fig. 4) is kinematically optimized for controlling friction. In the extending knee, when the jumping pig loads the articular surfaces with high compressive forces, the BKJP is predominantly rolling.

4. Conventional knee endoprostheses

The conventional knee endoprostheses on the market usually show in the lateral compartment, in contrast to the BKJM, a concave "tibia plateau". This geometrical design implies that the IHA run near the centers of the femoral condyles. Thus, they can never show a rolling of the articular surfaces under load in the stance phase of gait: They do not approximate the natural knee kinematics in no way.

5. Total Knee Replacement (TKR) with natural kinematics (AEQUOS).

In the AEQUOS prostheses G1 and G2 as well, the lateral "tibia plateau" is sagittally convex as it is in the natural BKJM. Both TKR approximately show natural kinematics in flexion (Fig. 5).

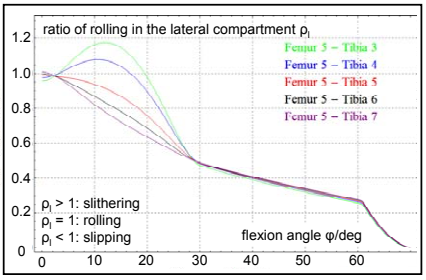

Fig. 5: Aequos G2: the ratio of rolling is close to pure rolling in the range (0 - 25°) of flexion. The different relations $\rho_l(\varphi)$ are given by different sizes of tibia replacement.

6. Conclusion

To achieve approximately natural knee kinematics by artificial knee endoprostheses, the lateral tibial articular surface must be convexly shaped in sagittal direction.

30th DANUBIA-ADRIA
Symposium on Advances in Experimental Mechanics
September 25-28, 2013 - Primošten, Croatia

3A12 067

MODELLING AND SIMULATION OF CORONARY STENTS

Miksa Kovács[1], Dóra Károly[1], Eszter Bognár[1,2]

[1] Budapest University of Technology and Economics, Faculty of Mechanical Engineering, Dept. of Materials Science and Engineering, Bertalan L. u. 7, 1111 Budapest, HUNGARY. E-mail: karoly.dora@gmail.com, miksa.kovacs@gmail.com

[2] MTA–BME Research Group for Composite Science and Technology, Műegyetem rkp. 3, 1111 Budapest, HUNGARY. E-mail: eszter@eik.bme.hu

1. Introduction

In the European Union the most common reason of death is the disease of the cardiovascular system, within that the most significant is the coronary artery disease. Currently the vascular stenting procedure is the most advanced treatment, which can restore the coronary circulation. The stent is a biocompatible mesh, which is inserted into the narrowed section of the artery to dilate and prop it up; hereby it ensures continuous flow of blood [1,2].

Physicians' experience shows that stents after a period of time may undergo undesirable processes that cause the narrowing of the expanded artery (restenosis). If engineers are able to design implants from better material or with a different geometry it may reduce the likelihood of restenosis.

In vivo and in vitro experiments are difficult to implement, therefore the finite element tests can help to evaluate the behaviour of the stent. Stent patterns are comparable by the simulations. The best stent geometry can be chosen, and simulations also help to improve the properties of existing stents, or even the development of new stent patterns [3].

2. Methods

2.1 Models

A total of 7 original and 6 simplified models were designed in SolidWorks software. The original models were based on the stent patterns (Fig. 1/(b)), which we get from the measured and evaluated microscopic images taken of stents on the market. These are the kind of stents doctors use nowadays. After determining the exact dimensions the simplified stent patterns and models were made. The 3×12 mm (A) stent along with the measured stent pattern and the original model can be seen in Fig. 1.

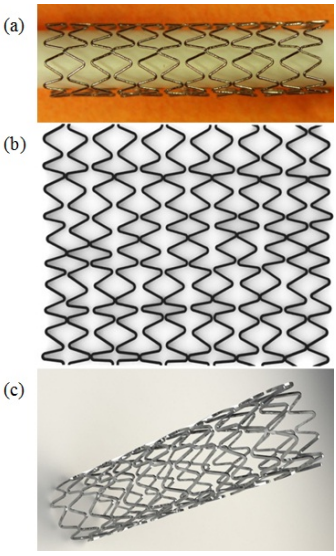

Fig. 1 (a) (A) stent, (b) the stent pattern, (c) the model

2.2 Simulations

We carried out finite element simulations on the designed models using SolidWorks Simulation module. We defined two different materials as input data. A 316L stainless steel integrated in the program, and a L605 CoCr alloy defined manually.

In the simulations the first ring of the stents were considered fixed and a 0.05 N force were applied on a pair of struts in the last ring. We ran the simulations for every pair of struts with both materials.

3. Results

3.1 Location of bridges

In terms of our research the stent geometries can be divided into two groups according to the interchangeability of the fixed and loaded end of stents. This depends on the location of the bridges (struts between rings). In the group that came up with a different result after changing the loaded and the fixed end, we ran the simulation both ways and calculated an average displacement value for both end. Based on this it can be said that the displacement values are clearly separable when applying the load on different end.

The importance of the location of the bridges can also be seen in the case of (A) stent. Fig. 2 shows the difference between the displacements when applying the force on different pairs of struts. A stent bends far less if it has bridges on the compressed side. So it is preferable to use "shifted" arrangement for the bridges, since this way we can prevent high displacement value in a certain direction.

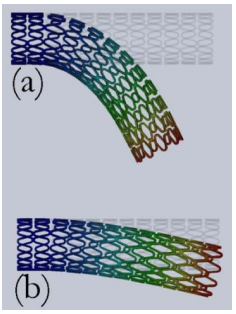

Fig. 2 Displacement of (A) stent with force on the (a) 4th pair of strut (b) 7th pair of strut

3.2 Geometry of bridges

The value of displacement depends largely on the geometry of bridges. In all cases the maximum stress arises in the bridges and at the connection of bridges and struts. Therefore it is worth to model and examine the bridges separetly varying their number and geometry. Preliminarily, we consider

Fig. 3 "S" shaped bridge

that between two rings at least three "S" shaped bridges (Fig. 3) would be appropriate, since this way the stent would not shorten during the expansion.

3.3 Sizes of struts

We investigated the change in strut sizes impact on mechanical properties. In case of smaller strut width and thickness the displacement is larger, so the stent is more flexible. The metallic surface area is also smaller, which decreases the probability of restenosis. Inferring from the above, we can assume that in order to achieve an optimal stent, material with a higher Young modulus and smaller strut sizes are advisable. The excessive reduction of strut width is however not recommended, because the stent could not withstand the pressure of the blood vessel and collapse.

4. Remarks

- Stent patterns greatly influence several functional properties of stents. After examining the stent patterns, we gave a proposal for optimal stent geometry.
- Due to the limitations of the present work, continuing this research is definitely justified. Further step would be designing a new and innovative stent pattern.

Acknowledgements

First we would like to thank the Department of Materials Science and Engineering and colleagues there for providing us with the environment and facilities to complete this project.

This work is connected to the scientific program of the "Development of quality-oriented and harmonized R+D+I strategy and functional model at BME" project. This project is supported by the New Hungary Development Plan (Project ID: TÁMOP-4.2.1/B-09/1/KMR-2010-0002).

References

[1] Topol, E. Coronary and Peripheral Angioplasty: Historic Perspective. Textbook of Interventional Cardiology. 2003.

[2] Bertrand, O.F., et al. Biocompatibility Aspects of New Stent Technology, J Am Coll Cardiol. 1998, 32, pp. 562–571.

[3] Berta, B., et al. Long-Term Clinical Follow-Up after Drug-Eluting Stent Implantation for Bare Metal In-Stent Restenosis. J Interv Cardiol. 2013,10.

[4] Migliavacca, F. et al. Mechanical behavior of coronary stents investigated through the finite element method. Journal of Biomechanics, 2002, 35, pp. 803-811.

30th DANUBIA-ADRIA
Symposium on Advances in Experimental Mechanics
September 25-28, 2013 - Primošten, Croatia

3A13 137

METALLIC BONE SCAFFOLDS - IMPACT ORIENTATION ON THE BONE TISSUE REACTION

Jakub Słowiński[1]

[1] Wroclaw University of Technology, Institute of Materials Science and Applied Mechanics, Smoluchowskiego 25, 50-370 Wroclaw, POLAND. E-mail: jakub.slowinski@pwr.wroc.pl

1. Introduction

Metallic bone scaffold can be use to mimic trabecular bone tissue especially in the place of destruction. According to numerous works as well as long-term clinical studies the most proper material for scaffold is titanium and its alloys.

In the case of metallic scaffolds, which has regular structure, the orientation of the scaffold can have great impact on the surrounding bone tissue. Another major feature of the scaffolds is diameter of pores. According to the literature the most positive effect of implantation was observed in scaffold with pores diameter of 400–600 μm.

Modern orthopedics tends to use implants optimized for the selected patient [1,2]. It is not always possible to carry out accurate optimization, so the solution is to look for other structural possibilities.

2. Methods

A numerical model of bone metallic scaffold was prepared using Ansys software. The geometry of scaffold was generated using a script written in APDL language - Fig. 1. Model of tibia bone, where scaffold was numerically implanted, was prepared according to CT data.

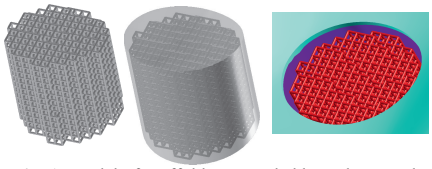

Fig. 1. Model of scaffold surrounded by volume and implanted into the bone

The bone was modeled using solid tetrahedral elements. To build the scaffold model 3d beam elements were used. As an implantation place the area under the articular surface of lateral condyle was chosen due to the boundary conditions, e.g. loads – Fig. 2. Connection between bone and implant was modeled using contact elements.

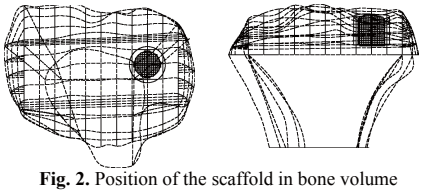

Fig. 2. Position of the scaffold in bone volume

Model was loaded by external forces according to Hurwitz model [3]. Bone was divided into compact and spongy bone. Material properties of scaffold was taken from Matweb site – see Tab.1.

In that paper a numerical simulation of impact structure of scaffold on the stress and strain distribution in the bone was obtained. First structure was the classic metallic scaffold in which beams was parallel to main axis of bone. Second structure has beams not parallel to any axis of the bone. The third implant contained in its structure a volume of solid alloy as a filling inside. This idea was associated with the possibility of penetration of the implant structure by bone cells. It was also associated with the production capacity of the real structures using rapid prototyping techniques.

Material	E [MPa]	v [-]
compact bone	18600	0.3
spongy bone	450	0.42
scaffold	113000	0.34

Tab. 1. Material properties used during simulation

3. Results

Stress distribution obtained for the first structure – Fig.3, was higher than for the second one. This is associated with the beams parallelism to the bone axis and loads directions. Stress distribution in the implant was associated with strain a stress distribution in the bone. This of course has an impact on the tissue remodeling.

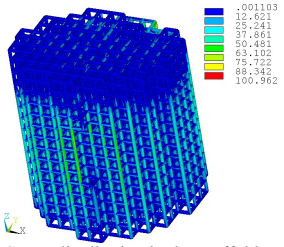

Fig. 3. Stress distribution in the scaffold structure

In close proximity to the model calculated the stress reached a value of up to 30 Mpa – Fig. 4. These values were also associated with the geometry of the slice in which the implant was placed.

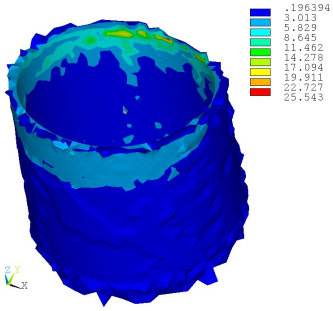

Fig. 4. Stress distribution in the close proximity of the scaffold

One of difficulties in creating models was the ability to generate samples of real scaffolds. For large models the resulting files was enormous, so as a solution models with solid interior was proposed. The next step need to carry out is to check how bone reacts on the shape and structure of scaffold.

Acknowledgements

The project have been funded from *Funds for research for the development of young scientists*. Grant number B20110/I19

References

[1] Hutmacher, D. W., Sittinger, M., Risbud, M. V., Scaffold-based tissue engineering: rationale for computer-aided design and solid free-form fabrication systems. Trends Biotechnol., Vol. 22, 2004. pp. 354–362.

[2] Słowiński J., Procedure of generating the individually matched bone scaffolds, Acta Bioeng Biomech. Vol. 13(3), 2011. pp. 15-25

[3] Hurwitz, D. E., Sumner, D. R., Andriacchi, T. P., Sugar, D. A., Dynamic knee loads during gait predict proximal tibial bone distribution. Journal of Biomechanics, Vol. 27, 1998. pp. 423–430

30th DANUBIA-ADRIA
Symposium on Advances in Experimental Mechanics
September 25-28, 2013 - Primošten, Croatia

3A14 095

EXPERIMENTAL INVESTIGATION OF FLOW THROUGH A CONSTRICTED TUBE

Jan Kolínský[1], Ludmila Nováková[1], Josef Adamec[1], Jaroslav Kudlička[2]

[1] Czech Technical University, Faculty of Mechanical Engineering, Department of fluid dynamics and thermodynamics, Technická 4, Praha 6, 160 07, CZECH REPUBLIC. E-mail: jan.kolinsky@fs.cvut.cz, ludmila.novakova@fs.cvut.cz, josef.adamec@fs.cvut.cz

[2] Charles University in Prague, 1st School of Medicine, Third Department of Internal Medicine, General University Hospital, U Nemocnice 1, 12808 Prague, CZECH REPUBLIC. E-mail: jaroslav.kudlickak@vfn.cz

1. Introduction

The aim of this contribution is to present the results obtained by pressure drop measurement and 2D PIV (Particle Image Velocimetry) flow field measurement in models of constricted pipe. The research was motivated by the study of the flow in an abnormal narrowing in blood vessels - stenosis. This in vitro experiment relates to the clinical examination [1], where the function of maximum velocity is a vascular hemodynamics parameter which is commonly used to determine the degree of stenosis.

2. Methods

2.1 Experimental bench

The experimental bench was designed to measure the flow field in an axial plane by 2D PIV method and pressure loss simultaneously. PIV measurement was made by continuous laser diode and high-speed camera (Olympus DF). Pressure drop was evaluated from two absolute pressure sensors mounted over the models of stenosis.

2.2 Models

The models of axisymmetric stenosis of degree 25%, 50%, 75% used in this research were made from plexiglass. Extra models of axisymmetric 75% area reduction with abrupt contraction and asymmetric (off-centred) 75% area reduction stenoses were made; see Tab. 1.

2.3 Measured flow regimes

The flow was measured during six stationary regimes equal to Reynolds numbers 50, 120, 340, 1000, 2000, and 3000 in the non-constricted diameter (26 mm) of the tube. The lower regimes range physiological flows up to the higher regimes when the flow becomes turbulent.

Stenosis model	**Tube diameter [mm]**	**Neck diameter [mm]**	**Area ratio [%]**	**Pressure loss coefficient [1]**
Straight tube	26	26	0	0
Stenosis 25 gradual contraction	26	22.5	25	0.1697
Stenosis 50 gradual contraction	26	18,4	50	1.0982
Stenosis 75 gradual contraction	26	13	75	10.7280
Stenosis 75 gradual contraction, asymmetric	26	13	75	14.8548
Stenosis 75 sudden contraction	26	13	75	15.2720

Tab. 1. Stenosis models properties.

3. Results

3.1 Pressure loss

Absolute pressure in front of and behind the stenosis was measured for 30 seconds for every model of stenosis and every regime, and mean difference was determined. These differences Δp dependent on flow rate were evaluated for every model in a form which supposes constant pressure loss coefficient ζ.

$$\zeta = \frac{2\Delta p}{\rho v^2}. \qquad (1)$$

Obtained pressure loss coefficients ζ are noted in Tab. 1. and furthermore they are represented in Fig. 1.

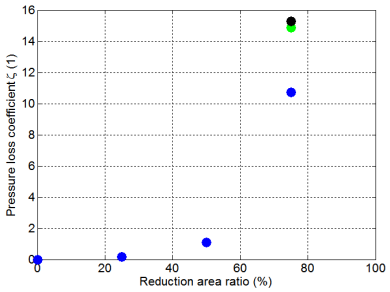

Fig. 1. Pressure loss coefficients: blue – axisymetric, green – asymetrci, black –sudden contraction.

3.2 Velocity field

Velocity field was mapped in 2D axial plane. Sudden contraction of flow cross-section forms a recirculation zone in peripheral area. This zone is driven by the high velocity jet formed in the valve [2]. The flow through stenosis was visualized. The research presents the effect of geometry on the flow field patterns formation.

The issue is the influence of the area reduction ratio on the maximum velocity reached in the jet and on the recirculation zone size.

Fig. 2. shows the maximum velocity in each cross section of the tube divided by the maximum velocity along the whole length coordinate. The scheme of stenosis is indicated at the bottom of the Figure and corresponds to the length coordinate.

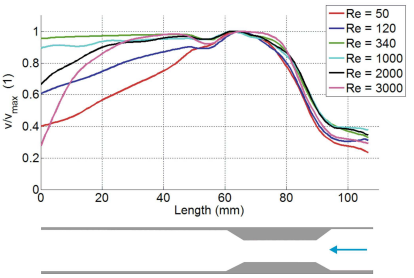

Fig. 2. Dimensionless velocity along the length coordinate.

The Figure of dimensionless maximum velocity shows the acceleration in the neck and the region behind the stenosis, vhere the velocity profile expands gradually downstream of the stenosis. These results for different stenosis geometries and different flow regimes are important in that they can be compared with the results obtained in vivo by ultrasonography.

4. Remarks

- The pressure loss coefficients for different geometries of stenosis were determined. Pressure loss measurements would help determine the energy loss relevance of stenosis in dependence on its degree.
- The flow field was visualized by PIV method and the maximum velocity in cross section was evaluated as a function of length. The size of the recirculation zone as a function of Re number was observed.

References

[1] Malik, J., Slavikova, M., Malikova, H., Maskova, J., Many clinically silent access stenoses can be identified by ultrasonography, Journal of Nephrology. 15. 2002. pp. 661-665.

[2] Netrebska, H., Schmirler, M., Matecha J., Adamec, J.,The Stenosis Shape Influence on the Flow Pattern in Distal End-to-Side Anastomosis, International Journal of Transport Phenomena. vol. 9. No. 4. 2007. pp. 339 - 347.

30th DANUBIA-ADRIA
Symposium on Advances in Experimental Mechanics
September 25-28, 2013 - Primošten, Croatia

3A15 136

FMEA RISK ANALYSIS IN A DIALYSIS UNIT

Manuela Stroili[1], Marco Ianche[2], Andrea Cressi[3], Francesca Cosmi[3]

[1] AO-U Ospedali Riuniti di Trieste, S.S.D. Technology Assessment, Trieste, Italy

[2] AO-U Ospedali Riuniti di Trieste, S.C. Nefrologia e Dialisi, Trieste, Italy

[3] Università degli Studi di Trieste, DIA, Via Valerio 6/4, 34127, Trieste, Italy. E-mail: cosmi@units.it

1. Introduction

Hospitals, thanks to a constant evolution of health technology, have the task to improve reliability of services and to preserve patients and workers from malfunctions, both mechanical and human. To this aim, recently, reliability tools have started to be adopted in the health field, see for example [1], [2] and [3].

In its constant pursuit for a better health service, in 2012 the Technology Assessment structure at the Azienda Ospedaliero-Universitaria of Trieste started an interdisciplinary activity of verification of malfunctions occurring in the dialysis and nephrology unit.

2. Materials

The core of this study consisted in a risk analysis of the possible failures involving all the technical elements of the medical devices used in the dialysis and nephrology unit, namely the artificial kidneys or monitors. An interdisciplinary work group was formed to investigate the failures occurring in one year of bicarbonate-dialysis activity in the 19 monitors of the unit [4].

The examined devices belong to three different models of artificial kidney, from three successive technical generations, and have a working life between 10000 and 28000 hours of service. For each device, the error records and hours of operation data were examined together with the technical and user manuals. As an example, Tab. 1 reports the failures occurred in one of the models.

3. Methods

The data collected were elaborated using the FMEA methodology prescribed in the CEI EN 60812-2006 standard "Analysis techniques for system reliability" [5]. For the three devices examined, 49 different failure modes could be identified. The overall effect on the hemodialysis procedure was evaluated for each of them. Based on this analysis, a risk classification was made by means of three scales, taking into account the probability, severity and detectability factors respectively [5]. By computing the product of these three factors, it was possible to assign a Risk Priority Number (RPN) value to each identified failure mode. The RPN can be regarded as an index of the gravity of the consequences, or the hazard, of the examined fault.

Failure	Frequency
pH sensor anomaly	17
No heater power	14
Power fuse error	4
Conductivity error	4
Calibration param. error	3
Acid concentration not correct	2
Excess pressure in degasser	2
Buzzer error	2
Main flow too low	2
Air sensor failure	1
Heparin pump failure	1
Incorrect conductance	1
Venous flap failure	1
Too long since last calibration	1
Out of range voltage	1
Degasser engine malfunction	1
Air sensor malfunction	1

Tab. 1. Examples of malfunctions in one model.

4. Results

The failure modes were classified based on the hazard linked to their effects. Our ranking starts with a maximum RPN value of 120 down to a minimum value of 4, Fig.1. In particular, 9 failure modes, 19.4% of the total, were found to have RPN values equal to or greater than 60, Table 2. Corrective actions to return these values within the range of acceptable risk are considered a priority.

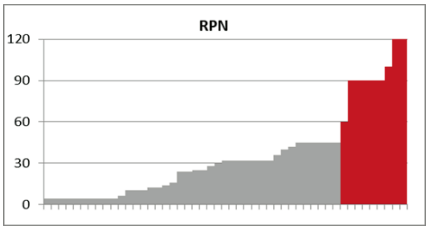

Fig. 1. Ordered PRN values.

5. Remarks

- A very significant outcome of this application of FMEA lies in the fact that, following the risk analysis performed, it is possible to address an optimization of the inventories based on the knowledge of which machine components are at a greater risk of failure, resulting in important savings.
- Moreover, an analysis of the technical reasons that determine the most critical faults also helps in the decision to purchase next generation equipment with modified internal control systems or using more expensive disposable kits. This is already happening in the dialysis and nephrology unit after the first observations offered by the multidisciplinary group activated by the Technology Assessment structure.
- With the aim of choosing the best technique for the patients safety and of improving preventive maintenance, this work will continue and monitor the performances of the other devices operating in the nephrology and dialysis unit.
- Overall, the analysis here discussed constitutes a first step towards a cost/failure analysis for a more reliable, targeted and rational maintenance service.

Acknowledgements

The Authors wish to thank the dialysis technician Giuliano Pacor for his kind assistance during data collection and interpretation.

References

[1] Bonfant, G. et al., Clinical risk analysis with failure mode and effect analysis (FMEA) model in a dialysis unit. J. nephrology, **23**, 2010. pp. 111-118.

[2] Meyrieux, C. et al., FMEA applied to the radiotherapy patient care process. J.Société française de radiothérapie oncologique **16**, 2012. pp. 613-618.

[3] Paolini M. et al., Proactive evaluation of clinical risk: a FMECA analysis in pediatric chemotherapy. Annali di igiene : medicina preventiva e di comunità **25**, 2013. pp. 15-21.

[4] Stroili M. et al. Applicazione della Tecnica FMECA per la valutazione degli interventi di Manutenzione programmata nel Reparto di Emodialisi nell'A.O.-U. "Ospedali Riuniti" di Trieste, Poster, XIII°Congresso Nazionale AIIC, Napoli,11-12 aprile 2013.

[5] CEI IEC 60812:2006-1, second edition.

Component	Failure mode	Effect	Probability	Gravity	Detection	RPN
Air detector	Failure	Presence of air in the fluid	4	10	3	120
Air detector	No signal	Air detection impossible	4	10	3	120
Conductivity sensor	Out of service	Conductivity evaluation impossible	5	5	4	100
Buzzer	Out of service	Lack of audible alarm	3	10	3	90
pH sensor	Damaged	pH evaluation impossible	6	5	3	90
Conductivity sensor	Damaged	Incorrect assessment of flow parameters	6	5	3	90
Blood detector	Out of service	Possible loss of blood from patient	3	10	3	90
Priming detector	Not working	Possible blood in the venous line	3	10	3	90
Battery	Not working	shutdown in case of power failure	2	5	6	60

Tab. 2. FMECA table for RPN≥ 60

30th DANUBIA-ADRIA
Symposium on Advances in Experimental Mechanics
September 25-28, 2013 - Primošten, Croatia

3A16 130

BIOMECHANICAL ANALYSIS OF PROXIMAL HUMERAL FIXATION USING LOCKING PLATES

Fabijan Čukelj [1], Janoš Kodvanj [2], Martin Surjak [2]

[1] Clinical Hospital Center Split Spinčićeva 5, 21000 Split, Croatia

[2] University of Zagreb, Faculty of Mechanical Engineering and Naval Architecture, Ivana Lučića 5, 10 000 Zagreb, Croatia.

Corresponding author: martin.surjak@fsb.hr

1. Introduction

Proximal humerus fractures often occur in elderly population with an osteoporotic bone substance. About 20% of these fractures need surgical treatment, especially comminuted and displaced fractures [1, 2]. A locking plate fixation has become one of the most popular methods for repairing proximal humerus fractures [3]. The goal of this study was to compare the stiffness of anatomically formed novel locking plate with polyaxial screws with a commonly used Philos (Synthes Switzerland) locking plate. Both plates were made of titanium. All tests were conducted on the artificial osteoporotic bone model with an osteotomy gap at the surgical neck and the displacements were determined by digital image correlation.

2. Experimental setup

The bone models were represented by the artificial bone *Synbone* (Malans, Switzerland). The 10 mm thick slice was cut out from bone models to simulate a comminuted fracture (Fig.1).

Fig. 1: Bone model

For proper positioning of the models on the testing machine the distal end of each specimen was potted with PMMA *SCS-Beracryl D-28* (Suter – Kunststoffe AG, Switzerland) in a cylindrical steel tube. Each plate was mounted to the osteoporotic bone with seven 3,5 mm locking screws as shown in Figure 1. The experiments were conducted on the screw-drive Messphysik Beta 50-5 testing machine. For the axial compression test each model was mounted vertically on the support according to Figure 2 and a quasi-static loading was applied.

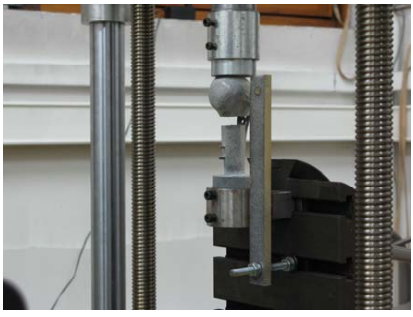

Fig. 2: Compression test

The support has the ability of angle adjustments and thereby allows accurate positioning of the specimen. Abduction test setup is shown in Figure 3.

Fig. 3: Abduction test

All tests were conducted in linear elastic range in displacement control at a rate of 1.2 mm/min and during the abduction test the rate was set to 5 mm/min. Intact healthy and osteoporotic bone models were also tested in order to determine the stiffness of the bone models.

Displacements were measured by using the Aramis 4M optical system (GOM mbH, Germany). On all specimens a random spray pattern was applied, which was necessary for following the deformations of the specimen. The optical system was calibrated prior to the measurement for appropriate measuring volume. The models were first recorded in the unloaded state and then every second during the loading. The resulting images were discretized with square facets (15x15 pixels) representing the measuring points [4].

3. Results and conclusion

Figure 4 shows the displacement field at compression test and the measured distance between two points marked on the opposite sides of the fracture gap during loading.

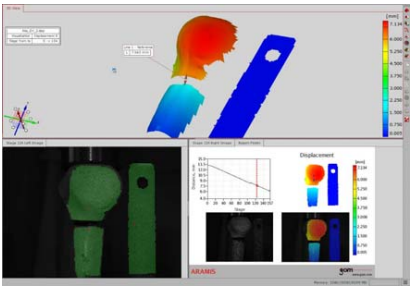

Fig. 4: Displacement field at compression test

Comparison of stiffness for plate constructs and intact bones is shown in Figure 5.

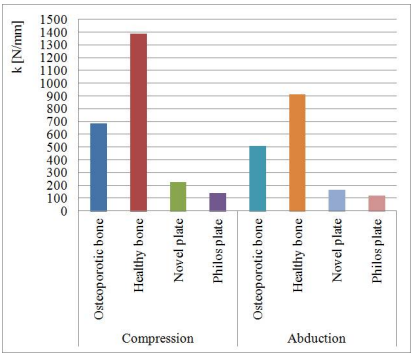

Fig. 5: Stiffness comparison

Obtained results indicate that the newly developed plate has higher stiffness in linear elastic range than commonly used Philos plate.

4. References

[1] Brianza S., Plecko M., Gueorguiev B., Windolf M., Schweiger K., Biomechanical evaluation of a new fixation technique for internal fixation of three-part proximal humerus fractures in a novel cadaveric model, Clinical Bimechanics, 25, 2010, pp. 862-892.

[2] Seide K., Triebe J., Faschingbauer M., Schulz A. P., Püschel K., Mehrtens G., Jürgens Ch., Locked vs. unlocked plate osteosynthesis of the proximal humerus- A biomechanical study, Clinical Biomechanics, 22, 2007, pp. 176-182.

[3] Mathison C., Chaudhary R., Beaupre L., Reynolds M., Adeeb S., Bouliane M., Biomechanical analysis of proximal humeral fixation using locking plate fixation with an intramedullary fibular allograft , Clinical Biomechanics, 25, 2010, pp. 642-646.

[4] Aramis User Manual – Software, GOM mbH, Germany 2009.

30th DANUBIA-ADRIA
Symposium on Advances in Experimental Mechanics
September 25-28, 2013 - Primošten, Croatia

3A17 129

Mechanical analysis of the weakness of cone-coupling used in modular assembled hip-prosthesis

Kodvanj Janos[1], Beer Rudolf J.[2], Huber Wolfgang[3]

[1] University of Zagreb , Faculty of Mechanical Engineering and Naval Architecture, Ivana Lucica 5, HR-10000 Zagreb, CROATIA. E-mail: janos.kodvanj@unizg.hr
[2] Technical University Vienna, Faculty of Civil Engineering, Karlsplatz 13, A-1040 Vienna AUSTRIA. rudolf.beer@tuwien.ac.at
[3] Herz-Jesu Hospital Vienna, Baumgasse 20A, A-1030 Vienna AUSTRIA: dr.wolfgang.huber@aon.at

1 Introduction

Cone-tapers are used in designing modular composed hip-prosthesis. This method offers the surgeons multiple advantages. One of the benefits is given by the fact of allowing a better reconstruction of the individual joint geometry of the patient. Another great advantage is given if it becomes necessary to change parts of the Implant. However it may happen that the lifetime of a modular assembled prosthesis is sometimes strongly reduced by pure mechanical failure, for instance by loosening of the contact between the male and female partner of the cone-tapers; crevice and fretting corrosion can be observed on the original contact surfaces of the partner. The question is, what is the reason for it, what happened first even in cases of an ideal correspondence of the partners from the geometrical point of view and without failure during mounting.

2. Method

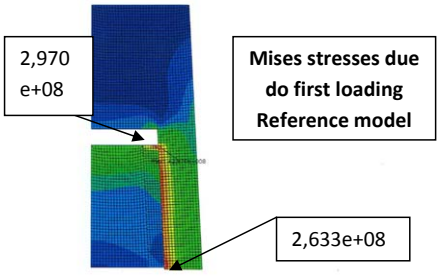

Fig. 1

Fig. 1 shows as an example of preliminary FEM studies [1,2] that the most stressed areas during mounting using an axial effective force are the small contact area concentrated around the contact-points KP0 and KP1 (Fig. 2). The maxima are in KP1 is located at the male-side and in KP0 at the female-side. As it is noted in all other cases observed, the most stressed area due to the mounting procedure is always the top of the male.

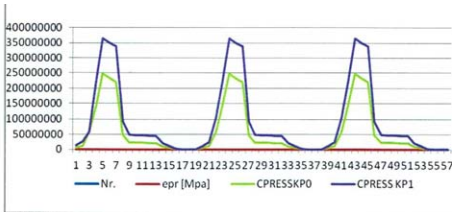

Fig. 2

Fig. 2 shows the normal pressure CPRESS between the male and the female part of the cone taper for the contact-points (s. Fig. 4) KP0 (green) and KP1 (blue) and demonstrates that CPRESS in KP1 is nearly twice in KP0.

If the failure starts already during mounting it occurs in the area of contact-point KP1 (Fig. 2) on the male it may happen due to a local plastic deformation of this area.

This study is concerned on the inherent – primary-weakness of cone-coupling devices from the mechanical point of view. It uses a FE–simulation of trend-studies for cyclic loading of this kind of coupling devices. The

result is that failure may already start during mounting due to overloading the small contact- area on the top of the male partner of the cone-taper causing a small plastic deformation of this area. If this happened the ideal contact between the partners is already disturbed and the area of load transport between becomes smaller. This starts an increasing process, comparable with the well-known process of gradual expansion of crakes. This process is strongly influenced by the parameter by the original cone-taper geometry and by the roughness of the contact surfaces.

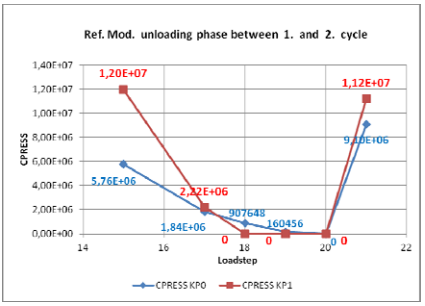

Fig. 3

Fig. 3 shows the corresponding unloading phase between first and second cycle.

It is of course not possible to avoid this failure mechanism but it is possible to choose the parameters of the cone-taper so that the inherent weakness of this mechanical solution becomes negligible within the range of possible loading forces known also from the different gait-analysis.

Fig. 4 shows the contact geometry of the reference model for the FEM analysis, with *x*-axis as axis of rotation.

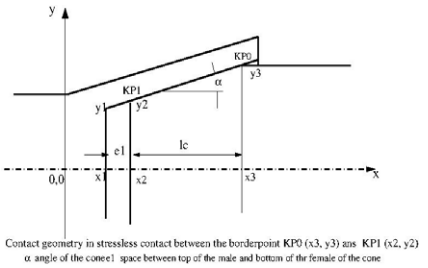

Fig. 4: Reference model for the FE analysis

For calculation the *xy*-plane of the rotational model was kept rigidly.

During this study only the angle of the cone and its length were kept constant, all other parameters of the cone-taper were varied due it special use.

3. Criteria

Within the framework of this study it was not possible to simulate the real mounting-procedure using a hammer stroke. For this reason we tried to determine the combination of the joint-parameters with which the danger of a partial plastification of the contact area, leading to gaps (see Fig. 3) becomes a minimum. This procedure is of course limited by the body-height of the patient and by the function of the prosthesis.

4. Literature

[1] Kodvanj, J., Huber, W., Beer,R.J., Two different sources of failure mechanisms in modular Hipendoprosthesis. Proc. of the 24th Danubia Adria Symposium 2007, pp 203-204

[2] Kodvanj, J., Huber, W., Beer R.J., Failure mechanism in modular total hip arthroplasty. Proc. of the 25th Danubia Adria Symposium 2008, pp 119-120

30th DANUBIA-ADRIA
Symposium on Advances in Experimental Mechanics
September 25-28, 2013 - Primošten, Croatia

3A18 150

GREEN COMPOSITES: A REVIEW OF STATE OF ART

Silvia De Paola[1], Cristiano Fragassa[1], Giangiacomo Minak[1], Ana Pavlovic[1]

[1]University of Bologna, Dept. of Industrial Engineering, viale Risorgimento 2, IT-40136 Bologna, ITALY e-mail: silviadepaola@libero.it

1. Introduction

The rising concern towards environmental issues and the need to find a realistic alternative to glass reinforced composites has led to increase interest about polymer composites filled with natural-organic fillers, that comes from renewable and biodegradable sources. The aim of the project is to raise people awareness regarding the scientific and technological knowledge of green composite materials in order to support a larger application in whole industry sectors. This short review briefly illustrates the main paths and results of research (both academic and industrial) on this topical subject, providing a quick overview.

2. Green Composites' State of Art

Currently numerous research groups are dedicated to minimising the environmental impact of polymer composite production, where the polymer matrices are derived from renewable resources such as polylactide (PLA), thermoplastic starch (TPS) or thermoset matrices. Their high renewable content derives from vegetable oils and, combined with natural reinforced fibers (NF) to form environment-friendly and fully degradable composite laminates, they represent a potential substitute for petroleum based resins.

2.1 Ecobased Matrices

The polymer matrices availability is nowadays poor, but it rapidly grows as more studies are done and more informations are given. The different kinds of bio based polymer matrices used are listed below:

- Thermoset matrices: polyols are compounds with multiple hydroxyl functional groups available for organic reactions, and they react with a large number of chemical species, called curatives or hardeners, to produce cross-linked thermoset matrices. The most important oil used in polyols production is soy bean oil, but also cashew nut oil could give the same results. In order to decrease the impact of its activity on global warming, polyols can be also combined with petroleum based chemicals.

- Thermoplastic matrices: the most commercially available plastic matrix is the cellulose one, which is properly toughened thus it is considered a 100% bio-based matrix. Starch based polymers and Poly (lactic acid) PLA are both available: the employment of the first ones depends on the ability to reduce their moisture absorption, while the second one has similar properties to polystyrene. Summing up, the employment of these bio-based polymers depends on the possibility to modify their properties in order to obtain an easier processing and improve toughness in the final biocomposite.

2.2 Natural Fibers

Natural fibers are compounds combining cellulose, hemicellulose and lignin; they can be derived from leaf (e.g. sisal), bast (e.g. flax, hemp), seed (e.g. cotton) and fruit (e.g. coir). The most important advantages of natural fibers relate to environmental issues: they are biodegradable and carbon positive since they absorb more carbon dioxide than they produce. In addition, they are non-irritating and tend to be non-abrasive, with the latter property resulting in reduced wear on tooling and manufacturing equipment. Other important advantages are shown in term of specific material properties: using natural fibers in substitution of synthetic ones, it's possible to reduce the weight of a composite material by up to 40% and it's also possible to improve flexural strength, stiffness and ductility. However, in terms of overall strength properties, synthetic fibers perform better than natural ones, even if there are some natural fibers that can approach the tensile modulus, E, of glass.

2.3 Hybridization

The hybrid systems for improved material or structural performances is a well-known concept in engineering design. A recent work has shown that the properties of hybrid natural/glass composite loading have been found to be an effective way to improve composite's mechanical properties and dimensional stability (moisture, temperature, etc.). The stiffness of biocomposites can thus be overcome by structural configurations that place material in specific locations for higher structural performances.

3. Tables

In the table below, Tab.1, a physical and mechanical properties comparison between natural and synthetic fibers is shown. As noted, natural fibers have lower density values and they fit perfectly for non structural uses. In these terms, natural fibers can replace synthetic ones obtaining even more efficient results.

Fibers properties	Density (g/cm^3)	Tensile Strength (MPa)	Tensile Modulus (GPa)	Strain (%)
JUTE	1.3-1.45	393-773	13-26.5	1.16-1.5
FLAX	1.50	345-1100	27.6-80.0	2.7-3.2
HEMP	-	690	-	0.6
BASALT	2.65-2.80	4000-4700	84-87	3.15
SISAL	1.45	468-640	9.4-22.0	3-7
E-GLASS	2.5	2000-3500	70	2.5
ARAMID	1.4	3000-3150	63-67	3.3-3.7
CARBON	1.7	4000	230-240	1.4-1.8

Tab. 1. Fibers' mechanical properties

4. Equation

Tensile modulus (Eq.1) of composite materials depends on matrix and fiber volume fraction and it is calculated using the following equations:

$$E_{xx} = V_f E_a + V_m E_m, \qquad (1)$$

$$E_{yy} = \frac{1}{\frac{V_f}{E_t^f} + \frac{V_m}{E_m}}, \qquad (2)$$

5. Processing and processability

Literature data on green composites show a clear prevalence of wood end natural fibers in combination with polyolefins: this influences the information available on processing and processability. Typical processing techniques include extrusion followed by injection or compression molding. During the processing, temperature must not exceed 200°C and the retention time of the material exposed to high temperatures should not be too long in order to avoid fibers' enervation. Very common technologies for NF composite materials are resin transfer molding, vacuum injection molding, structural reacting injection molding, injection molding and compression molding.

6. Future Research Directions

New environmental regulations and changing governmental attitudes have stimulated the research of new products and processes environmental friendly. Natural fiber reinforced biodegradable polymer composites appear to have a bright future for a wide range of applications. These biocomposite materials with various interesting properties may soon be competitive with the existing fossil plastic materials. However, the present low level of production and high cost suggest they may apply to industrial application.

7. Supporting institutions

This research is supported by the „De Urbis Vento“ project financed by Italian Ministry of the Environment.

References

[1] J. Sahari, S.M. Sapuan, Natural fiber reinforced biodegradable polymer composites, Rev.Adv.Mater.Sci. 30 (2011) 166-174.

[2] G. Bogoeva-Gaceva, M. Avella, M.E. Errico, Natural Fiber Eco-Composites, POLYM. COMPOS., 28:98–107, 2007.

[3] D. Bertomeu, D. Garcia-Sanoguera, O. Fenollar, T. Boronat, R. Balart, Use of Eco-Friendly Epoxy Resins From Renewable Resources as Potential Substitutes of Petrochemical Epoxy Resins for Ambient Cured Composites With Flax Reinforcements. POLYM. COMPOS., 33:683–692, 2012.

30th DANUBIA-ADRIA
Symposium on Advances in Experimental Mechanics
September 25-28, 2013 - Primošten, Croatia

3A19 152

RELATIONSHIP AMONG MINERAL CONTENT AND MECHANICAL PROPERTIES FROM COMPRESSION TEST OF HUMAN TRABECULAR BONE

Angela Andrzejewska[1)], Adam Mazurkiewicz[2)], Maciej Topoliński [1)]

[1)] Students Scientific Biomedical Engineering Group 'BioMed', University of Technology and Life Sciences, Mechanical Engineering Faculty, Kaliskiego 7 Street, 85-789 Bydgoszcz, Poland.

[2)] University of Technology and Life Sciences, Mechanical Engineering Faculty, Kaliskiego 7 Street, 85 - 789 Bydgoszcz, Poland.

Corresponding author: adam.mazurkiewicz@utp.edu.pl

1. Introduction

The mineral content of human trabecular bone in one of main pointer which decided about strength of trabecular bone.

Its changes with age. About 20-30 years of age is maximal, next started a gradual process of bone loss and a decrease in bone strength begin to occur.

The aim of the work is to determine relationship among mineral content and mechanical properties from compression test of human trabecular bone.

2. Material and method

Material to the investigation were 42 samples of human trabecular bone. Samples were collected from osteoporotic and coxarthrotic femoral heads gained in result of hip arthroplasty. The samples have diameter 10 mm and 8.5 mm height. Manner of collecting sample is presented in fig. 1.

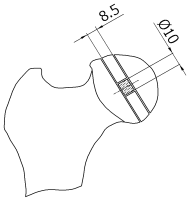

Fig. 1: Manner of collecting sample. Axis the sample coincided with the axis of the head and neck of the femur

The compression test was carried out using the testing machine INSTRON 8874. The initial loading was 5-7 N. Strain rate was $\dot{\varepsilon} = 1\%$. From the test obtained value elastic modulus E from range of strain $\varepsilon = 0{,}6 \div 0{,}8$ %, and value ultimate compression strength бc, eg. values in point first maximum on compression curve.

In scientific investigation trabecular bone mostly for description mineral content of bone is used apparent density App.D [1] or ash density Ash.D [2,3].

In the aim of estimate mineral content of bone we used ash density. In this aim samples were burned in temperature 500 ^{o}C by 15 hours [4]. After burning in sample remains only mineral phase because organic phase was destroyed due to the effect of temperature.

Ash density Ash.D was calculated by divide mass burned sample by its volume before burning.

3. Results

In Tab. 1-2 presented obtained values of ash density Ash.D, elastic modulus E and ultimate compression strength бc for both groups of samples.

In Figs. 2-5 presented relationships among ash density, elastic modulus and compression strength for both groups of samples.

	min	max	mean	SD	RSD
Ash.D, g/cm^3	0,113	0,592	0,251	0,097	39 %
E, MPa	41,091	424,181	244,73	107,636	44 %
бc, MPa	2,329	13,105	6,582	2,946	45 %

Tab. 1: Values of ash density Ash.D, elastic modulus E and ultimate compression strength бc for osteoporotic samples

	min	max	mean	SD	RSD
Ash.D, g/cm^3	0,174	0,513	0,341	0,089	26 %
E, MPa	59	920,172	503,964	261,581	52 %
бс, MPa	1,678	25,288	12,844	6,326	49 %

Tab. 2: Values of ash density Ash.D, elastic modulus E and ultimate compression strength бс for coxarthrotic samples

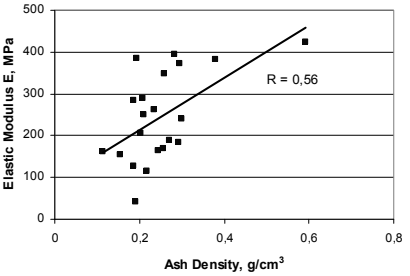

Fig. 2: The graph dependence between Ash.D and elastic modulus E for osteoporotic samples

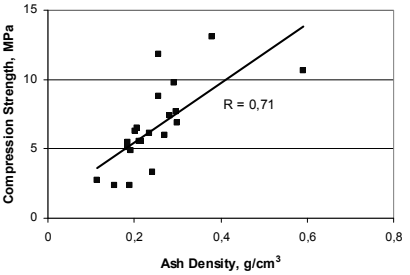

Fig. 3: The graph dependence between Ash.D and compression strength бс for osteoporotic samples

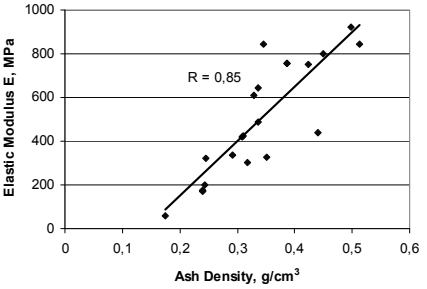

Fig. 4: The graph dependence between Ash.D and elastic modulus E for coxarthrotic samples

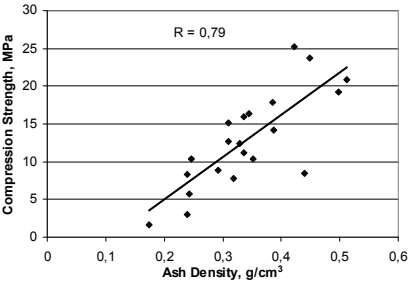

Fig. 5: The graph dependence between Ash.D and compression strength бс for coxarthrotic samples

4. Summary

Results obtained from both groups of samples are clearly different. For Ash.D range of obtained scores is similar but mean value is higher for coxarthrotic samples.

The mean value for E and бс is also different for both groups of samples. For coxarthrotic samples it is about 100 % more related to osteoporotic group.

Exist relationships among results obtained from compression test and Ash. D for both groups of samples. The relationships are stronger for coxarthrotic samples especially for elastic modulus.

5. References

[1] C. Rice, S. Cowin, J. Bowman, On the dependce the elasticity and strength of cancellous bone on apparent density. Journal of Biomechanics, Vol. 21 (1988) 155-168.

[2] L. Mosekilde, C. Danielsen, Biomechanical competence of vertebral trabecular bone in relation to ash density and age in normal individuals. Bone, Vol. 8 (1987) 79-85.

[3] R. W. Goulet, S. A. Goldstein, M. J. Ciarelli, J. L. Kuhn, The relationship between the structural nad orthogonal compressive properties of trabecular bone. Journal of Biomechanics, Vol. 27 (1994) 375-389.

[4] H. Yuehuei, R. Draughn, Mechanical testing of bone and the bone-implant interface. CRC Press, New York 1999.

30th DANUBIA-ADRIA
Symposium on Advances in Experimental Mechanics
September 25-28, 2013 - Primošten, Croatia

3B21 111

NANOINDENTATION OF WOOD CELL WALLS: EFFECTS OF DIFFERENT SAMPLE PREPARATION METHODS

Leopold Wagner[1], Thomas K. Bader[1], Karin de Borst[2]

[1] Vienna University of Technology, Institute for Mechanics of Materials and Structures, Karlsplatz 13/202, 1040 Vienna, Austria, E-mails: leopold.wagner@tuwien.ac.at, thomas.bader@tuwien.ac.at

[2] University of Glasgow, School of Engineering, Glasgow G12 8LT, Scotland, UK. E-mail: karin.deborst@glasgow.ac.uk

1. Introduction

Nanoindentation is frequently used for the investigation of the mechanical properties of wood cell walls [1,2]. It is still not entirely clear how the measurement results may be affected by the way the sample is prepared. Wood is commonly embedded into resin in order to stabilize the cell walls during microtome cutting and indentation [1-3]. It remains uncertain whether the resin penetrates the cell wall and, thus, influences the response of the material during nanoindentation. Herein, indentation properties from samples embedded into two different types of resins, as well as from testing apparently non-embedded wood cell walls, are presented. In addition, the exposure of the samples to heat either during the embedding process itself or prior to the sample preparation e.g. during oven drying, may affect the resulting material properties. While typical resin curing temperatures reach 70 °C, oven drying is carried out at around 100 °C. These temperatures might exceed the glass transition temperatures of the wood polymers [4]. Also cracks in the cell walls may occur upon drying, influencing the measured quantities. Test results are presented for samples having undergone multiple harsh drying cycles from a fully water saturated state, in order to identify potential effects of sample heating on the measured indentation modulus and the hardness of wood cell walls.

2. Materials and Methods

A rod of 15x2x2 cm^3 (LxRxT) of knot-free Norway spruce (*Picea abies* [L.] Karst) wood was cut into five cubes of 2x2x2 cm^3 (LxRxT, Fig. 1a,b). One cube was excluded from further treatments and served as reference material (REF). Four cubes (D1 to D4) were water saturated under vacuum for 48 h and then put into an oven at 103 °C until the mass was constant. The procedure was repeated four times and one cube was removed after each cycle, leading to a series of 1 to 4 drying-wetting cycles for the cubes D1 to D4.

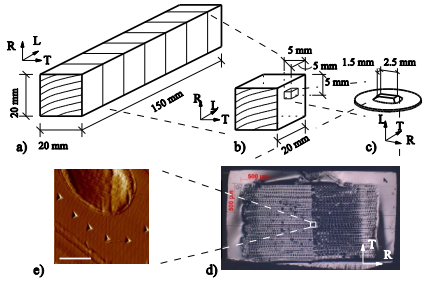

Fig. 1. Sampling procedure: a) initial rod, b) cubes (REF, D1-D4), c) NI-specimen, d) cellular structure of a NI-specimen, e) indents on the S2 cell wall layer (bar = 5 µm)

Small wood specimens (2x2.5x1 mm^3, LxRxT, Fig. 1c) were cut from each of the five cubes to prepare the NI specimens as described in Wagner et al. [3]. The standard embedding resin (Agar Low Viscosity Resin Kit - A-LV) curing at 60°C was used. To study the effects of different embedding materials, two more specimens were cut from the untreated reference cube and prepared slightly differently: One specimen was embedded in the standard resin but not subjected to vacuum during the embedding, leaving non-embedded wood cells in the center of the specimen; another specimen was embedded according to the standard procedure using a different embedding resin (Struers EpoFix - S-EF), which is cured at room temperature. The nanoindentation tests were performed in load

controlled mode, using a 3-step load function, a Berkovich tip and controlled climatic conditions (20 °C/60% relative humidity). Indents were placed in the S2 cell wall layer of selected latewood cells as well as in the cell corner middle lamella (CCML) between them (Fig 1e). The indentation modulus *M* and hardness *H* were calculated according to Oliver and Pharr [5].

3. Results and Discussion

Upon drying, the cubes showed a slight mass loss of up to 0.75%, possibly due to the extraction of soluble agents from the cell walls. A slight increase of both *M* and *H* could be observed in the CCML, which did not become significant ($p>0.01$, paired t-test, Figure 2a,b). In the S2 cell wall layer, *H* also showed a slight increase (n.s. $p>0.01$), while M did not show any trend upon repeated heating and drying (Fig. 2c,d). The slight increase of *H* in the CCML and the S2 layer might be a result of the mass loss during repeated water saturation and drying, suggesting the extracted agents to act as plasticizers in the cell walls.

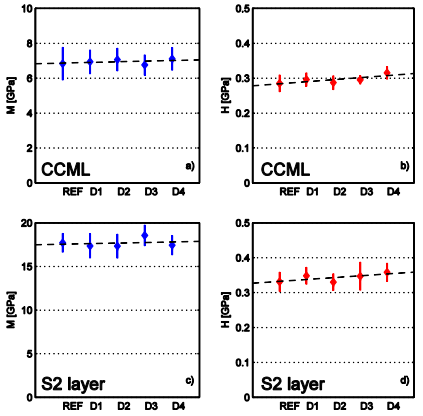

Fig. 2. a) Indentation modulus *M* and b) hardness H of the cell corner middle lamella (CCML), c) *M* and d) *H* of the S2 cell wall layer

Embedding the wood specimens into different resins did not change the measured *M* and *H* significantly ($p>0.01$, Tab. 1). Also testing non-embedded cell walls did not result in significantly different *M* and *H* ($p>0.01$), although the standard deviation increased by a factor of 2 to 3 (Table 1). The higher experimental scatter might be a result of various sources, including damage of the non-embedded cell walls during sample preparation and local variability of the cell wall microstructure, in particular of the cellulose microfibril angle [3].

Sample	A-LV (REF)	S-EF	no vacuum
M [GPa]	17.708 (1.072)	18.225 (1.355)	17.667 (3.055)
H [GPa]	0.331 (0.027)	0.348 (0.032)	0.360 (0.057)

Tab. 1. Mean indentation modulus *M* and hardness *H* of the S2 cell wall layer using different embedding materials/techniques (standard deviation in brackets).

4. Conclusions

In this study, influences of sample preparation for nanoindentation on the measured indentation properties (*M* and *H*) were studied. The measurement results did not vary significantly for all applied sample preparation procedures. Neither did repeated heating nor drying prior to the sample preparatio result in significant changes of the indentation modulus *M* and the hardness *H*.

Acknowledgements

The authors would like to acknowledge the financial support from the Vienna University of Technology via the Innovative Project: "*Microstructural and chemical characterization of softwood degradation by basidiomycetes and its effects on the mechanical behavior*".

References

[1] Wimmer, R., Lucas, B.N. Comparing mechanical properties of secondary wall and cell corner middle lamella in spruce wood. IAWA J, **18**(1), 1997, pp. 77-88.

[2] Wagner, L., Bader, T.K., de Borst, K. Nanoindentation of wood cell walls: Effects of sample preparation and indentation protocol. submitted to J Mater Sci

[3] Wagner, L., Auty, D., Bader, T.K., de Borst, K. Key parameters controlling stiffness variability within trees: a multiscale experimental-numerical approach. Trees, **27**, 2013, pp. 321-336.

[4] Irvine, G.M. The glass transitions of lignin and hemicellulose and their measurement by differential thermal analysis. TAPPI J, **67**, 1984, pp. 118-121.

[5] Oliver, W.C, Pharr, G.M. An improved technique for determining hardness and elastic modulus using load and displacement sensing indentation experiments. J Mat Res, **7**, 1992, pp. 1564-1583.

30th DANUBIA-ADRIA
Symposium on Advances in Experimental Mechanics
September 25-28, 2013 - Primošten, Croatia

3B22 124

THE USE OF COMPUTED TOMOGRAPHY AND ULTRASONIC IMAGING FOR ASSESSMENT OF DEFECTS IN PLATES MADE OF PLASTIC MATERIALS

Daniela Ioana TUDOR, Stefan Dan PASTRAMA, Anton HADAR

[1] University Politehnica, Department of Strength of Materials, Faculty of Engineering and Management of Technological Systems, Splaiul Independentei 313, Sector 6, 060042, Bucharest, ROMANIA. E-mail: stefan.pastrama@upb.ro

1. Introduction

In manufacturing of high performance plastic materials, it is very important to obtain structures without defects that may affect the behaviour in service. In order to respect such a request, one may perform non-destructive evaluation of structures made of plastic materials. These methods provide a quantitative evaluation of possible inner or outer defects in the studied structure. The obtained data about existence, shape and size of flaws can be further used as input data in numerical analyses for assessment of influence of defects on the behaviour in service and lifetime of the structure.

In this paper, the non-destructive evaluation of a stratified plate, made of plastic material is presented [1]. Two methods were used for this purpose: X-ray computed tomography (CT-scan) [2] and ultrasonic imaging [3].

2. Experimental set-up and results

The stratified plate was manufactured by successive casting of two layers of polyesteric resin and has a rectangular shape of 100 x 100 mm. (Fig. 1). The thickness of each layer was 1.3 mm.

The purpose of the non-destructive evaluation was to determine the possible inner defects (lack of adherence between layers, voids, etc.).

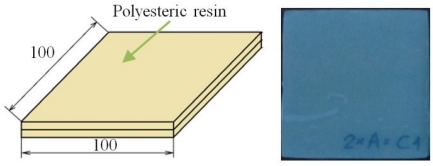

Fig. 1. The studied structure

Using the CT-scan, a 3-D reconstruction of the geometry of the studied structure was obtained.

The results were processed in two stages: the first one when the presence, shape, position and dimensions of defects were established and the second, in which segmentation of planes was realized having as final result the 3-D reconstruction of the plate.

A series of tomographic images was obtained from the CT-scan (Fig. 2), emphasizing a lack of adherence between the layers (the main defect), having a maximum length L_{max} = 37mm and a maximum width W_{max} = 5 mm on a depth h_{max} = 1.1mm. Other defects, whose dimensions are hardly measurable using this technique, were also put in evidence.

In the second stage, the 3-D reconstruction of the plate was achieved (Fig. 3). The obtained model was further used in a numerical analysis in order to establish the influence of the defects on the behaviour in service and on the lifetime of the structure.

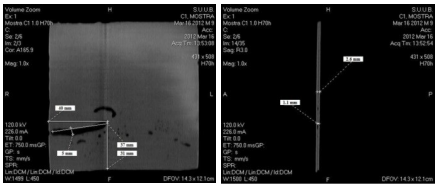

Fig. 2. CT-scans processing

The non-destructive evaluation of the samples was made also using ultrasonic imaging by immersion in mineralized water (as a coupling environment). *Bottom echo* and *defect echo* automatic scanning were performed.

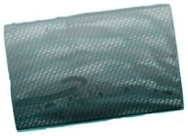

Fig. 3. The reconstructed plate (transparent mode)

The ultrasonic images of the defects detected within the plate are presented in Fig 4 (ultrasonic images in amplitude – used to determine the in-plane dimensions and shape) and in Fig. 5 (ultrasonic images in time of flight (used to obtain the depth of defects).

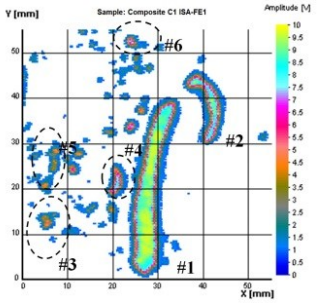

Fig. 4. Ultrasonic image in amplitude [4]

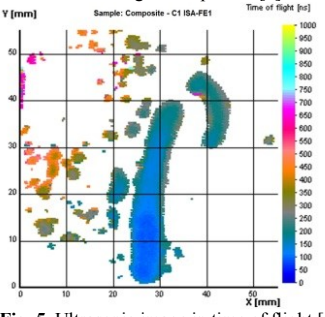

Fig. 5. Ultrasonic image in time of flight [4]

Following the processing of the above mentioned images, the dimensions and positions of defects in the plate were obtained. The results are listed in Table 1.

Nr.	Position X [mm]	Position Y [mm]	Length X [mm]	Length Y [mm]	Depth [mm]
1	24.6÷33.6	1.7÷39.0	9.0	37.3	1.2÷1.5
2	36.6÷43.5	30.6÷45.1	6.9	14.5	1.3÷1.5
3	19.2÷22.2	18.8÷24.5	3.0	5.7	1.3÷1.4
4	23.1÷24.9	33.1÷34.9	1.8	1.8	1.4÷1.5
5	6.0÷8.4	24.0÷29.1	2.4	5.1	1.6÷1.8
6	23.1÷25.2	51.5÷53.3	21.	1.8	1.4÷1.6

Tab. 1. Position and dimensions of defects

3. Conclusions

Using two different non-destructive methods, evaluation of defects in a plate made of plastic material was undertaken. The presence, shape, position and dimensions of defects were obtained, realizing thus a complete image of the structure. The exact characterization of manufacturing defects using X-ray computed tomography is difficult, but one gets a fair approximation of such flaws. Ultrasonic imaging provides detection of interior defects with high precision.

The major advantage of X-ray computed tomography is that it allows a 3D reconstruction of the structure, putting thus in evidence all surface and inner defects that appear during the manufacturing process or in service.

The information obtained following non-destructive evaluation are enough to allow the user to design reliable calculus models for further mechanical characterization of the influence of defects on the lifetime of the structures.

Acknowledgements

The experimental research and processing of the results were undertaken in the Laboratory of Advanced Methods of the Nuclear NDT Research & Services Company, Bucharest, Romania. The help of Dr. Marian Soare is gratefully acknowledged.

References

[1] Tudor, D.I., Contributii privind evaluarea cantitativa a influentei defectelor de material asupa capacitatii portante a unor structuri – (Contributions regarding the quantitative evaluation of the influence of material defects on the carrying capacity of some structures) – PhD Thesis, University Politehnica of Bucharest, 2012.

[2] *** Computed tomography – Physical Principles, Clinical Applications and Quality Control, third edition, British Columbia Institute of Technology Burnaby, British Columbia, Canada, 2009

[3] Deutsch, V., Platte, M., Vogt, M., Ultraschallprufung - Grundlagen und Industrielle Anwendung (Ultrasonic control – principles and Industrial Applications), Springer-Verlag, Berlin, 1997 (in German).

[4] ***S.C. Nuclear NDT Research & Services S.R.L., Raport de imagistica ultrasonica nr. 298 - proba C1 (Ultrasonic imaging report nr. 298 – sample C1) / 03.07.2012 (in Romanian).

30th DANUBIA-ADRIA
Symposium on Advances in Experimental Mechanics
September 25-28, 2013 - Primošten, Croatia

3B23 098

DETECTION OF A CRACK IN CEMENT SPECIMENS

Tomáš Plachý[1], Pavel Tesárek[1], Michal Polák[1], Jakub Okénka[1]

[1] Czech Technical University in Prague, Faculty of Civil Engineering, Thákurova 7, 166 29 Prague 6 – Dejvice, Czech Republic, E-mail: plachy@fsv.cvut.cz, pavel.tesarek@fsv.cvut.cz, polak.michal@fsv.cvut.cz, okenkaj@gmail.com

1. Introduction

This paper is focused on testing of cement specimens by impact excitation non-destructive technique. The objective was to find dynamic properties of the specimens without a crack, with a crack and with a healed crack by cement paste and their comparison. The metrology of impact excitation technique is based on previous researches [1, 2].

2. Experimental methods and specimens

The impulse excitation method was used for measuring of the fundamental resonant frequencies of longitudinal, transversal and torsional vibration of the specimens. Brüel&Kjær equipment was used for testing (Fig. 1.).

Fig. 1. Brüel&Kjær equipment.

The impact hammer Brüel&Kjær 8206 with force transducer inside was used for excitation and the acceleration transducer Brüel&Kjær Type 4519-003 was used for response measurement. Both signals, the excitation force and the acceleration, were recorded and transformed using Fast Fourier Transform (FFT) to the frequency domain, and the Frequency Response Function (FRF) was evaluated from these signals using the vibration control station Brüel&Kjær Front-end 3560-B-120 and program PULSE 13.4. The test was repeated five times for each specimen and resultant readings were averaged. From an averaged FRF, the fundamental resonant frequency was determined for each specimen [1]. For measuring of transversal, longitudinal and torsional vibration, the specimen was set as it is shown in Fig. 2. Specimens were made in standard dimension for laboratory tests – 40×40×160 mm [3]. The specimens were made out of cement CEM I 42.5R (Radotín, CZ) with water/cement ratio 0.4. The crack was made 60 mm from one end of the specimen. The "healing" of the crack was made by means of pushing of the fresh cement paste into the crack.

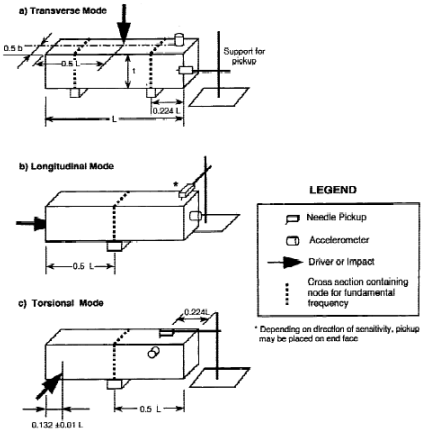

Fig. 2. Location of the accelerometer and position of hammer impact in accordance to [3].

3. Experimental results

Measurements of resonant frequencies was carried out on the reference specimens (without the crack), on the specimens with the open crack, on

the specimens 30 min after healing of the crack and then after 4 days. The measurement after 30 min after healing the crack is not included in the next figures due to non-significant change in resonant frequencies in comparison with cracked specimens.

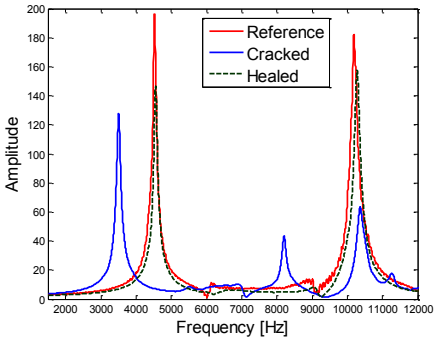

Fig. 3. Transversal frequencies.

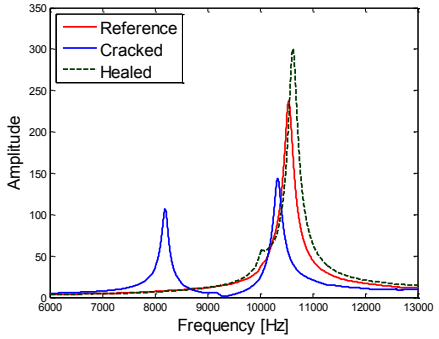

Fig. 4. Longitudinal frequencies.

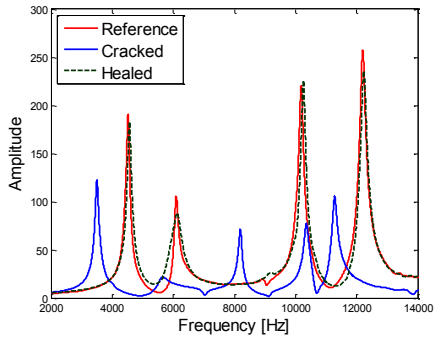

Fig. 5. Torsional frequencies.

In all 3 figures (Fig. 3 to 5), there is visible that the crack has an influence onto the 1st resonance frequencies for all 3 types of vibration. The resonance frequencies decreased significantly for all three basic modes of vibration. Also new resonance frequencies were found. Especially for the transversal vibration, new modes of vibration appeared. The ratio between the 1st and the 2nd resonance transversal frequencies of cracked specimen decreased in comparison with the reference specimen. The same phenomenon was observed for the longitudinal vibration. After healing there was observed, that the new frequencies were vanished, main resonant frequencies were shifted onto reference position and ratios of the 1st and the 2nd frequencies returned to referent values [4].

4. Conclusions

The impact excitation technique was used successfully for detection of a crack in cement specimens and for evaluation of the healing of a crack. This technique will be used in further researches to examine capability of bacteria to heal a crack in cement specimens – bioremediation of cement.

Acknowledgement

The financial support of this experiment by the Czech Technical University in Prague as the SGS project No. 12/117/OHK1/2T/11 and Ministry of Education of the Czech Republic as the project No. MSM 6840770031 is gratefully acknowledged.

References

[1] Plachý, T., Tesárek, P., Wilczynska, A., Padevět, P., Experiment in real conditions: Mechanical properties of gypsum block determined using non-destructive and destructive methods, International Conference on Engineering Mechanics, Structures, Engineering Geology, International Conference on Geography and Geology – Proceedings, 2010. pp. 418-423.

[2] Boukria, Y., Limam, A., Experimental damage analysis of concrete structures using the vibration signature – Part II: Located damage (crack), International Journal of Mechanics, Issue 1, **6**, 2012. pp. 28-34.

[3] ASTM C215-2 – Standard Test Method for Fundamental Transverse, Longitudinal, and Torsion Resonant Frequencies of Concrete Specimens. ASTM International, 2002.

[4] ČSN 73 1372 – Testing of concrete by resonance method (in Czech), ÚNMZ Praha, 1982.

30th DANUBIA-ADRIA
Symposium on Advances in Experimental Mechanics
September 25-28, 2013 - Primošten, Croatia

3B24 085

CASE STUDY ON DAMAGE DETECTION POSSIBILITY IN P91 AND 40HNMA STEELS USING MAGNETIC NDT TECHNIQUES

B. Augustyniak[1], L. Piotrowski[1], M. Chmielewski[1], Z. Kowalewski[2], K. Makowska[3]

[1] Gdansk University of Technology, Faculty of Technical Physics and Applied Mathematics, Narutowicza 11/12, 80-233 Gdansk, POLAND. E-mails: bolek@mif.pg.gda.pl, lesio@mif.pg.gda.pl, bzyk@mif.pg.gda.pl

[2] Institute of Fundamental Technological Research, Swietokrzyska 21, 00-049 Warsaw, POLAND. E-mail: zkowalew@ippt.gov.pl

[3] Motor Transport Institute, Jagiellonska 80, 00-049 Warsaw, POLAND. E-mail: krystyna.makowska@its.waw.pl

1. Introduction

Elaboration of nondestructive technique (NDT) which is useful for damage detection of exploited steel elements of seems to be very actual and open task for scientific society. In the case of ferromagnetic materials one can assume that such a technique is possible because magnetic properties are strictly related to steel microstructure. We present results of research on tests of damage detection of two martensite like steels (grades P91 and 40HNMA) using two complementary magnetic NDT techniques based on classical Barkhausen effect (HBE) and magnetoacoustic emission (MAE), respectively. Microstructure modification of these steels was due to or plastic deformation made by tension (PD) or to creep damage (CD). This work enhances our previous tests with damage steel state detection where mainly results of MAE have been exploited [1,2,3,4].

2. Experimental

The microstructures of 40HNMA and P91 steels consist of the sorbite with remaining needle martensite configuration. They differ, however, in mechanical properties: the yelding point *Rm* and ultimate tensile stress *Re* are about two times higher for 40HNMA in comparison to P91 steel [2]. The plane specimens having rectangular cross section of 5 mm×7 mm dimensions and gauge length of 40 mm. Tensile tests had been performed at room temperature while creep tests were made at T = 773K with stress s = 250 MPa for 40HNMA and s = 290 MPa for P91 steels, respectively. Each process was interrupted for a range of the selected time periods in order to achieve specimens with an increasing level of plastic strain. After each loading process the specimens were tested using magnetic method. Magnetic properties were measured using standard laboratory method of magnetisation, where hysteresis loop $B(H)$ with the HBE and also the MAE can be achieved [5]. An intensity of the HBE is given by the rms (root mean square) voltage *Ub* induced in pick-up coil. We compared here the integrals of those envelopes for one period of magnetisation (*Int Ub*). The MAE voltage signal is detected with resonant acoustic transducer. The rms envelope (*Ua*) is integrated and provides an descriptor of MAE intensity - *Int Ua.*

3. Results

Full paper will present the nuances of the envelopes of HBE and MAE intensity signals. Here we report and compare the integrals *Int Ub* and *Int Ua* which are plotted as a functions of resulting plastic strain *e* in Fig. 1 for MAE and in Fig. 2 for HEB, respectively. These plots reveal that both types of damage lead to specific modifications of intensities of both effects. These features can be summarized as follows. Magnetoacoustic emission intensity, as shows Fig. 1, evidently decreases monotonously in function of plastic strain after tensile test. This decrease is of order -50 % against level for initial stage. Creep damage reduces MAE intensity for P91 steel and increases (in not monotonous way) for 40HNMA steel. One can state that decrease of MAE for P91 steel is more pronounced when tensile test is performed.

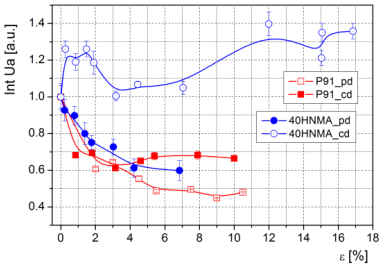

Fig. 1 Relative change of MAE intensity in function of deformation level for P91 steel (squares) and 40HNMA steel (circles) after plastic deformation (full) and creep damage (open)

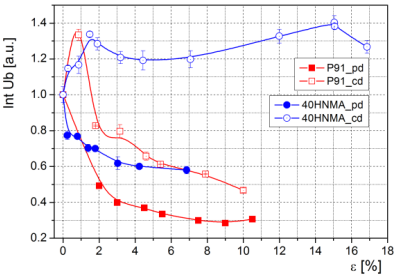

Fig. 3 Relative change of HBE intensity in function of deformation level for P91 steel (squares) and 40HNMA steel (circles) after plastic deformation (full) and creep damage (open)

Plots in Fig. 2 depict also monotonous like decrease of HBE intensity for both steels but only in the case of the tensile test. This decrease (of order of -70%) is higher for P91 steel. Creep test leads to non monotonous variation of HBE intensity. Its intensity (for both steels) peaks for relatively low level of strain (range of 1 – 2 %) and than decreases for P91 steel and again increases for 40HNMA steel. We will discuss qualitatively the as observed relationships linking them with modifications of dislocation densities and creation of voids. The as detected fundamental difference of magnetic properties of 40HNMA and P91 steels when creep test is applied can be attributed mainly to voids creation at 40HNMA steel. This effect was reported recently in [6].

4. Remarks

- All this depicts high capability of the as applied magnetic NDT techniques for detection and assessment of microstructure modification when mechanical damage is in question, mainly when both techniques are used simultaneously.

Acknowledgements

This work was supported partially by grant from NCBR Nr PBS1/A9/14/2012.

References

[1] Kowalewski, Z.L., Szelążek, J., Mackiewicz, S., Pietrzak, K., Augustyniak, B., Evaluation of damage in steels subjected to exploitation loading destructive and non-destructive methods, Int. Journal of Modern Physics B, vol. 22, 2008. pp. 5533-5538.

[2] Kowalewski, Z. L., Szymczak, T., Makowska, K., Augustyniak B., A role of destructive and non-destructive tests in creep damage identification, Key Engineering Materials, vols. 488-489, 2012, pp. 315-318.

[3] Augustyniak, B., Chmielewski, M., Piotrowski L., Kowalewski Z.L., Comparison of properties of magnetoacoustic emission and mechanical Barkhausen effects for P91 steel after plastic flow and creep. IEEE Transaction on Magnetics. Vol. 44, 2008, pp. 3273-3276

[4] Piotrowski L., Augustyniak B., Chmielewski M., Kowalewski Z.L., Possibility of application of magnetocoustic emission for the assessment of plastic deformation level in ferrous materials, IEEE Trans. on Magnetics, vol. 47, no. 8, 2011, pp. 2087-2092.

[5] Augustyniak, B., Chmielewski M., Sablik, M. J.; Multiparameter Magnetomechanical NDE; IEEE- Trans. on Magnetics, vol. 36, 2000, pp. 3624-3626.

[6] Makowska, K., Kowalewski, Z.L., Augustyniak, B., Structural degradation and mechanical properties variations of steels evaluated by means of Barkhausen noise parameter, 25th Symposium on Experimental Mechanics of Solids, Jachranka, Poland, October 17 - 20, 2012.

30th DANUBIA-ADRIA
Symposium on Advances in Experimental Mechanics
September 25-28, 2013 - Primošten, Croatia

3B25 071

EXPERIMENTS ON GUIDED WAVES PROPAGATION IN HOLLOW IMMERSED PIPES

Mihai Valentin PREDOI[1], Cristian Cătălin PETRE[2]

[1] University POLITEHNICA of Bucharest, Faculty of Biotechnical Systems Engineering, Department of Mechanics, Splaiul Independentei 313, Bucharest, ROMAINA. E-mail: mihai.predoi@mail.upb.ro

[2] University POLITEHNICA of Bucharest, Faculty of Engineering and Management of Technological Systems, Dept. of Materials Strength, Splaiul Independentei 313, Bucharest, ROMAINA. E-mail: cristian.petre@promteh.ro

1. Introduction

The modern trend in Nondestructive Testing (NDT) is to use guided waves for their potential of long range inspection. The problem of acoustic wave propagation in infinite homogeneous tubes represents a topic of great interest for the petrochemical and nuclear industries. Gazis [1] investigated the propagation of free harmonic waves for axisymmetric and asymmetric motions in isotropic hollow cylinders. Many researchers have investigated the capability of defect detection and sizing, using guided waves in pipes, e.g. Alleyne et al. [2], Demma et al. [3]. The present paper continues the works [4], [5] by the same authors, presented at previous Danubia Adria Symposiums.

In some cases, pipes are used to convey air or other gases towards submerged facilities. The on-site inspection of these pipes faces a new difficulty represented by the ultrasonic energy radiation in the surrounding fluid. Moreover, the propagating modes are not attenuated all in the same ratio and the attenuation depends on frequency, as shown by Long et al. [6]. The present paper represents a preliminary experimental study intended to assess the detectability of signals in the presence of fluid around a pipe and the fluid influence on the propagation of ultrasonic waves.

2. Experimental setup

The experimental setup (Fig.1) includes a pulser-receiver connected to a Krautkramer B1S (1MHz central frequency longitudinal waves) ultrasonic transducer. The transducer is placed vertically and the pipe is placed on top of the transducer using silicon as acoustic coupling. The amplified signal is displayed and stored on a Tektronix TDS 3000 B Digital phosphor oscilloscope.

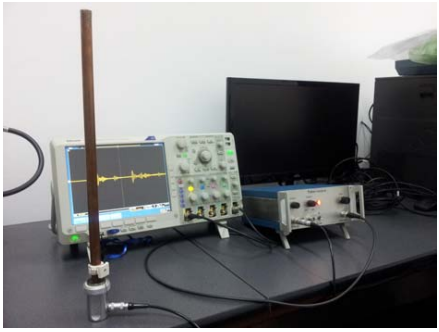

Fig. 1. Experimental setup for the reference signal.

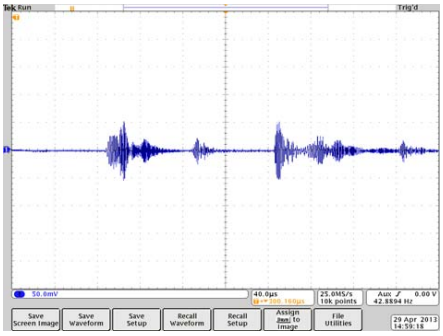

Fig. 2. The reference signal, pipe in air.

The reference signal is thus recorded (Fig.2) for the brass pipe (E=110GPa, ρ=8700 kg/m3, ν=0.35) of outer radius R=7.5mm, wall thickness of 1mm,

and 385 mm long.The pipe with the transducer attached to one end is immersed in a water container. The immersed end of the pipe is sealed and the immersed length is 90 mm.

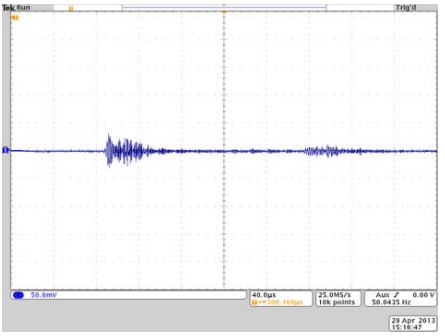

Fig. 3. Reflected signal for the hollow immersed pipe.

The corresponding signal is presented on Fig. 3. It is clearly apparent the attenuation of the first wave packet. Moreover, the second wave signal from Fig. 2 is now completely attenuated. The same high attenuation is remarked for the last signals, but from the third initial wave packet it remains a measurable signal.

3. Remarks

Signal attenuation in pipes represents a major technical difficulty, reducing the inspection range. This preliminary study has revealed however that propagation over 770 mm pipe length, from which propagation along 180 mm of immersed pipe, still offers the possibility to receive measurable ultrasonic longitudinal wave signals. The group velocities will confirm the specific modes propagating in the pipe generated using the piston-like method. A confirmation of mode conversion at the air-water interface remains to be conducted.

Acknowledgements

The research work funding by the Romanian UEFISCDI Exploratory Research Project PN-II-ID-PCE-2011-3-0512 is highly acknowledged.

References

[1] Gazis, D.C., Three-Dimensional Investigation of the Propagation of Waves in Hollow Circular Cylinders, J.Ac.Soc.Am., **31**, 1959, pp. 568-587.

[2] Alleyne, D.N., Pavlakovic, B., Lowe, M.J.S., Cawley, P, Rapid, Long Range Inspection of Chemical Plant Pipework Using Guided Waves, Rev. Prog. Quant. NDE, **20**, 2001, pp. 180-187.

[3] Demma, A., Cawley, P., Lowe, M.J.S., Roosenbrand, A.G., Pavlakovic, B., The reflection of guided waves from notches in pipes: a guide for interpreting corrosion measurements, NDT&E International 37 2004, pp. 167–180

[4] Predoi, M.V., Soare, M., Petre, C. C., Pipes inspection using longitudinal guided waves based on finite elements simulation, DAS2011, Siofok, Hungary, Sept.28-Oct.01, 2011.

[5] Petre, C. C., Predoi, M.V., Soare, M., Multipoint generation of guided waves in pipes. Experimental validation. DAS2012, Belgrade, Serbia, Sept.26-29, 2012.

[6] Long, R. Lowe, M., Cawley, P., Attenuation characteristics of the fundamental modes that propagate in buried iron water pipes, Ultrasonics **41**, 2003, pp. 509–519.

30th DANUBIA-ADRIA
Symposium on Advances in Experimental Mechanics
September 25-28, 2013 - Primošten, Croatia

3B26 019

ULTRASONIC DETECTION OF RAILROAD AXLE CRACKS UNDER WHEEL HUB WITH LONGITUDINAL WAVES

Jacek Szelążek[1], Piotr Gutkiewicz[1], Paweł Grzywna[1]

[1] Institute of Fundamental Technological Research, PAS, Pawińskiego 5B, 02-106 Warsaw, Poland
E-mail: jszela@ippt.gov.pl

1. Introduction

In railroad transport, fatigue cracking of railroad axles are one of the major source of railroad accidents. To detect cracks emerging on surface of an axle ultrasonic technique (UT) is widely used. Axles are usually tested during periodic inspection of wheelsets. Dangerous fatigue cracks often emerge on the axle wheel-seat. These cracks are covered with a wheel hub press fitted on the axle. Schema of UT detection of such cracks with shear and longitudinal waves is shown on Fig. 1. Depending on axle and wheel geometry, specific angle probeheads for ultrasonic shear (SV) and longitudinal (L) waves are used in tests. To detect a crack with shear wave it is necessary to couple the probeheads to the cylindrical part of the axle, between wheel-seats. Such test can be performed on the wheelset dismantled from the bogie. Testing with longitudinal wave requires access to the flat, front axle face what enables inspection of axles in cars, on track (Fig. 1.).

In both cases, ultrasonic pulse reflects on a corner formed by cylindrical surface of the axle and surface of the crack. When detecting crack situated under the wheel hub, echo amplitude can be affected (reduced) by the contact between axle and wheel press fitted on axle. Amplitude of the ultrasonic wave reflection on the axle-seat – wheel hub boundary is lower comparing to reflection on steel – air boundary. Value of reflection coefficient depends on contacting surfaces conditions like roughness, presence (or not) of the grease and pressure. The influence of above factors on UT detection of such cracks with shear waves is described in details in [1]. Paper describes the influence of wheel-axle contact on UT detection of fatigue crack detected with longitudinal wave launched form the axle face.

2. Experiment

Fig. 2 present the experiment setup. Two steel samples, made of carbon steel with surface roughness the same as in axle and wheel bore (Ra =1,6 μm), were pressed with force F. Three angle ultrasonic probes for 3 MHz longitudinal wave, refraction angle 27°, were fixed to the samples.

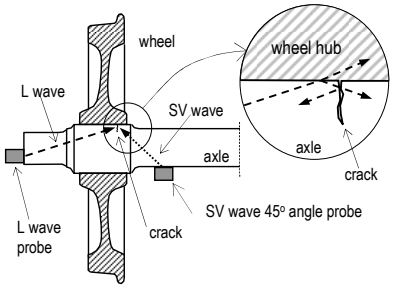

Fig. 1. Methods of ultrasonic crack detection in railroad axle with shear and longitudinal waves.

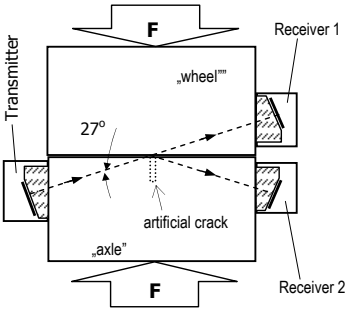

Fig. 2. Setup to evaluate coefficients of reflection and transmission for longitudinal wave and flaw echo amplitude on pressure between contacting surfaces.

The first readings were taken on flat samples. Signals received by two receiving probes allowed to monitor reflection and transmission coefficient changes with contact pressure.

Next measurements were performed with transmitting probe operating in echo mode, on samples with artificial cracks (dotted line on Fig 2) of various depths. These tests allowed to monitor the dependence of flaw echo amplitude changes on pressure between samples. To imitate real conditions, tests were performed for "dry" contacting surfaces and for surfaces covered with grease.

3. Results

Figs. 3 and 4 present dependence of artificial flaw echo amplitude on contact pressure between samples. Fig. 3 for samples with grease between samples, Fig.4 – without any grease (dry contact).

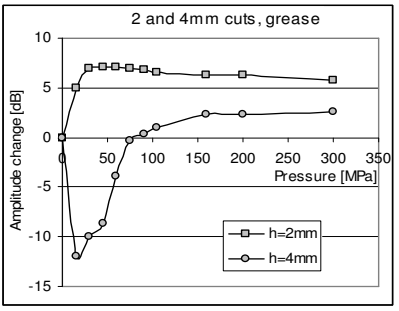

Fig. 3. 2 and 4 mm deep cut echo dependence on contact pressure. Grease between samples.

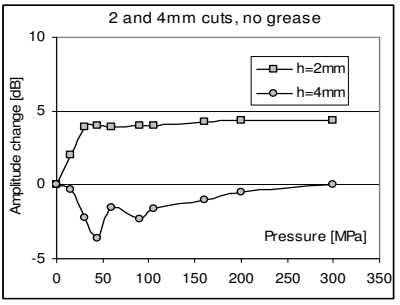

Fig. 4. 2 and 4 mm deep cut echo dependence on contact pressure. No grease between samples

It can be seen that for both, "dry" and "grease" contact, echo amplitude depends on pressure between samples. As expected higher amplitude changes with pressure are observed for samples covered with grease. Amplitude changes also depend on artificial crack depths. For 4 mm cut (cut depth equal to about 2 wavelength) echo amplitude drops for contact pressure up to 75 MPa and 300 MPa for "grease" and "dry" conditions respectively. Significant amplitude drop, equal to about 12dB, was observed for "grease" condition and low pressure. However, for 2 mm cut (depth comparable to the wavelength) echo amplitude rises with contact pressure. For "grease" conditions this amplitude increase reaches 7.5 dB for pressure equal to 25 MPa only.

4. Conclusions

Results of presented experiment show that echo amplitude for crack situated under the wheel hub and detected with longitudinal wave launched form the axle face, depends on numerous factors. They are: pressure between axle seat and wheel-hub (which can vary from point to point [2]), conditions (dry, grease) and also crack depth. Echo amplitude for dangerous cracks, depth higher that a wavelength, can be reduced by factor 4. Results show that calibration of ultrasonic equipment on artificial flaws cut on free axle surface (without contact with wheel hub) can lead to errors. Sensitivity of ultrasonic test determined in such a way will not ensure detection of cracks, of the same depths in a wheelsets.

One more factor reducing fatigue crack echo amplitude is lower than 100% reflection coefficient of longitudinal wave on crack surface. Railroad axle in a car is subjected to bending. Fatigue crack can be opened or closed depending on position of a wheelset in relation to load direction. Measurements performed in the first experiment (on flat samples) showed that, for L wave and 27° incidence angle, echo amplitude drop resulting from contact pressure can reach 10 dB. Both effects, pressure on axle-wheel boundary and compressive stress on crack surfaces, can sum up. In result echo amplitude of a real crack in the axle can be reduced by factor 14 comparing to echo amplitude measured on the same depth reflector, on free axle.

References

[1] Kazunari Makino, Shiro Biwa, Influence of axle–wheel interface on ultrasonic testing of fatigue cracks in wheelset. Ultrasonics, 53, 2013, pp.239-248].

[2] M.B. Marshall, R.Lewis, R.S. Dwyer-Joyce F. Demilly, Y. Flament, Ultrasonic Characterisation of Wheel Hub/Axle Interference Fit Pressures, Journal of Rail and Rapid Transit, Vol. 225, 2011, pp 287-298

30th DANUBIA-ADRIA
Symposium on Advances in Experimental Mechanics
September 25-28, 2013 - Primošten, Croatia

3B27 115

STIFFNESS IMPROVEMENT OF 45S5 BIOGLASS®-BASED SCAFFOLDS THROUGH PCL AND COLLAGEN COATINGS: AN ULTRASONIC STUDY

Jasmin Hum[1], Krzysztof W. Luczynski[2], Patcharakamon Nooeaid[1], Pippa Newby[3], Olaf Lahayne[2], Christian Hellmich[2], Aldo R. Boccaccini[1]

[1] Institute of Biomaterials, University of Erlangen-Nuremberg, 91058 Erlangen, Germany

[2] Institute for Mechanics of Materials and Structures, Vienna University of Technology, Karlsplatz 13, 1040 Vienna, Austria. E-mail: Krzysztof.Luczynski@tuwien.ac.at

[3] Department of Materials, Imperial College London, United Kingdom

1. Introduction

Due to its excellent bioactivity, 45S5 Bioglass® is being highly considered in tissue engineering scaffold development. In order to enhance vascularization promoting tissue growth, these scaffolds typically exhibit a highly interconnected porous structure with a porosity between 80 and 90% (see Fig. 1). Often, Bioglass®-based scaffolds of such a high porosity exhibit insufficient stiffness.

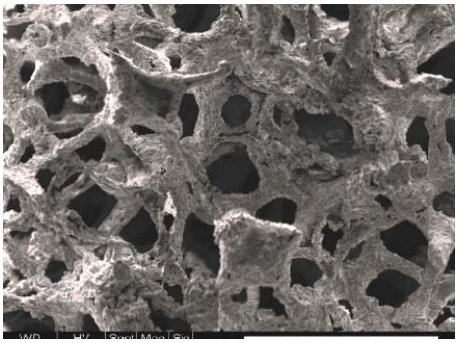

Fig. 1. Scanning Electron Micrograph (SEM) showing the typical highly interconnected macro-porous structure of as-fabricated uncoated Bioglass® scaffold.

2. Materials and methods

In order to increase the stiffness of Bioglass®-based scaffolds fabricated by the foam replica method, the herein investigated scaffolds were coated with collagen, gelatin, polycaprolactone (PCL), alginate, and poly(L-lactic acid) (PLLA) [1, 2]. The resulting stiffness gain was quantified by means of ultrasonic measurements [3, 4, 5, 6].

3. Results

Accordingly, PCL and collagen coatings increase the overall scaffold's stiffness (C_{1111}^{scaff}), as comparing to uncoated scaffolds, by 58% and 38%, respectively; while no remarkable stiffness increase was recorded for the other coatings. To reveal the influence of the coatings' stiffnesses (E_{coat}) on the overall scaffolds' stiffnesses (i.e. the micromechanical interactions patterns between Bioglass® and different coatings) a dimensionless relation between coating volume fraction and the ratio of C_{1111}^{scaff}–over-E_{coat} was investigated. Together with ($C_{1111}^{scaff}/E_{coat}$)-values stemming from ultrasonic experiments, theoretical values predicted applying the classical isotropic self-consistent micromechanics scheme [7, 8, 9, 10, 11] were taken into account (see Fig. 2).

Fig. 2. Dimensionless relation between the coating's volume fraction and the ratio of coated scaffold stiffness to the Young's modulus of respective coating, for PCL- and collagen-coated scaffolds.

The fact that the relation between coating volume fraction and the ($C_{1111}^{scaff}/E_{coat}$)-ratio are significantly different among chosen coatings indicates distinct micromechanical interactions patterns.

Additionally, scanning electron microscopy (SEM), revealed that PCL (unlike collagen) did not clog the micropores of the as-fabricated scaffolds (which supports the thesis of different micromechanical interactions patterns), which are deemed essential for cell seeding and the resulting in-growth of bone tissue (see Fig. 3).

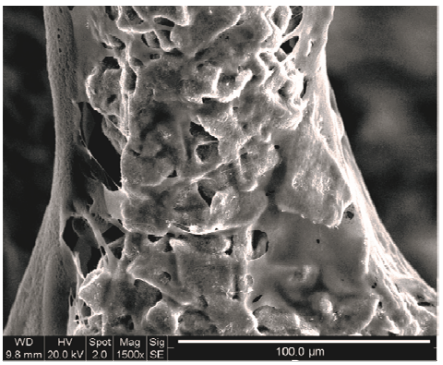

Fig. 3. Proper figure description.

4. Conclusion

Summarizing, ultrasonic tests present an easy-to-perform and non-destructive alternative to traditional mechanical tests. Profound investigation of morphology, together with micromechanical analysis and ultrasonic tests, reveal the manner in which biopolymer coatings affect the stiffness of highly porous scaffolds. In case of the investigated Bioglass®-based scaffolds, PCL as well as collagen infiltrate the cracks present in the struts increasing the stiffness of the overall structure. The PCL coating not only contributed the most among the investigated coatings to the increase of stiffness, but also unlike the other coatings, it did not clog the scaffold pores, whose preservation is mandatory for the biological functioning of the scaffolds. The latter finding, together with the fact that PCL leads to significant increase in stiffness, makes this biopolymer a very promising possibility for coating Bioglass® scaffolds without sacrificing their excellent bioactive properties.

Acknowledgements

Financial support to Jasmin Hum by a research fellowship of KMM-VIN (www.kmm-vin.eu) is gratefully acknowledged. Moreover, Krzysztof Luczynski and Christian Hellmich are grateful for funding within the project MICROBONE (grant number 257023), granted by the European Research Council (ERC).

References

[1] Yunos, D.M., Bretcanu, O. and Boccaccini, A.R., Polymer-bioceramic composites for tissue engineering scaffolds. J. Mater. Sci. **43**, 2008. pp. 4433-4442.

[2] Chen, Q.Z. and Boccaccini, A.R., Poly(D,L-lactic acid) coated 45S5 Bioglass®-based scaffolds: Processing and characterization. J. Biomed. Mater. Res. **77A**, 2006. pp. 445–457.

[3] Kohlhauser, C., Hellmich, C., Vitale-Brovarone, C., Boccaccini, A.R., Rota, A. and Eberhardsteiner, J., Ultrasonic Characterisation of Porous Biomaterials Across Different Frequencies, Strain, **45(1)**, 2009. pp. 34-44.

[4] Kohlhauser, C. and Hellmich, C., Ultrasonic contact pulse transmission for elastic wave velocity and stiffness determination: Influence of specimen geometry and porosity, Eng. Struct, **47**, 2013. pp. 115-133.

[5] Carcione, J.M., Wave Fields in Real Media: Wave Propagation in Anisotropic, Anelastic and Porous Media. Pergamon, Oxford, UK, 2001.

[6] Luczynski, K.W., Brynk, T., Ostrowska, B., Swieszkowski, W., Reihsner, R., Hellmich, C., Consistent quasi-static and acoustic elasticity determination of PLLA-based rapid-prototyped tissue engineering scaffolds, J Biomed Mater Res A, **101(1)**, 2013. pp. 138-144.

[7] Eshelby, J.D., The determination of the elastic field of an ellipsoidal inclusion, and related problems. Proceedings of the Royal Society of London. Series A, Mathematical and Physical Sciences, **241**, 1957. pp. 376-396.

[8] Hill, R., A self-consistent mechanics of composite materials, J. Mech. Phys. Solids, **13(4)**, 1965. pp. 213–222.

[9] Zaoui, A., Continuum Micromechanics: Survey. J. Eng. Mech., **128(8)**, 2002. pp. 808-816.

[10] Mori, T., Tanaka, K., Average stress in matrix and average elastic energy of materials with misfitting inclusions, Acta Metallurgica, **21(5)**, 1973. pp. 571-574.

[11] Benveniste, Y.A., A new approach to the application of Mori-Tanakas theory in composite materials, Mechanics of Materials, **6**, 1987. pp. 147-157.

30th DANUBIA-ADRIA
Symposium on Advances in Experimental Mechanics
September 25-28, 2013 - Primošten, Croatia

3B28 032

ASSESSMENT OF MATERIAL DEGRADATION BY MEANS OF ACOUSTIC BIREFRINGENCE AND ELASTOACOUSTIC COEFFICIENT

K. Makowska[1], Z. L. Kowalewski[1,2], J. Szelążek[2], S. Mackiewicz[2], P. Gutkiewicz[2]

[1] Motor Transport Institute, Centre of Material Testing and Mechatronics, 80 Jagiellońska Street, 03-301 Warsaw, POLAND. E-mail: katarzyna.makowska@its.waw.pl

[2] Institute of Fundamental Technological Research, Polish Academy of Sciences, Department for Strength of Materials, 5B Pawińskiego Street, 02-106 Warsaw, POLAND. E-mail: zkowalew@ippt.pan.pl

1. Introduction

Ultrasonic method, that characterises a fast execusion of measurement and its relatively low cost, is the one of non-destructive techniques most often used for damage assessments. It has to be noticed, however, that the conventional ultrasonic parameters, e.g. ultrasonic wave velocity and attenuation coefficient have some limits in appliacation [1]. The difficulty in measuring of the both parameters appears in the case of material microstructure heterogeneity, surface roughness, and additionally, taking into account the wave velocity – in assessment of a thickness of the elements tested [2]. It hast to be also mentioned that the ultrasonic wave velocity and attenuation coefficient allow to detect material damage in the late stage of material exploitation, when voids are already created [2].

The paper presents an attempt for application of two other ultrasonic parameters such as acoustic birefringence and elastoacoustic coefficient in the early stage of degradation of medium carbon steel after plastic deformation and accelerated creep. The acoustic birefringence is based on a velocity difference between two shear waves polarized in the mutually perpendicular directions [3]. Its variation is attributed to the material texture (grain orientation, oriented voids resulted from creep for example) that changes itself during loading of a material [4]. The measurements are usually carried out using the same ultrasonic probes, rotated about 90º (ultrasonic beam goes through the same thickness of material and reflects from the same area of the opposite surface [2]). In this way the errors related to the construction design and heterogeneity of a material can be eliminated. The elastoacoustic coefficient represents a proportionality factor between stress and relative changes of the wave velocities [2]. In the measurements of elastic coefficient a phenomenon of the elastoacoustic effect is used. This effect is explained on the basis of nonlinear elasticity theory. According to it the wave velocity depends on stress introduced into a material [5].

The results of our investigations gave knowledge whether the changes in microstructure and mechanical properties may be detected in the early stage of material exploitation by ultrasonic technique.

2. Experimental procedure

The specimens of power plant steel were subjected to plastic deformation or accelerated creep. Each process was interrupted for a range of the selected time periods in order to achieve specimens with increasing level of prestrain. After each loading process the specimens were tested using ultrasonic technique.

The acoustic birefringence was calculated according to the following relationship:

$$B = 2\frac{t_{Tl} - t_{Tp}}{t_{Tl} + t_{Tp}} \qquad (1)$$

where:

t_{Tl} – time of flight of the shear wave for longitudinal polarization direction;

t_{Tp} – time of flight of the shear wave for perpendicular polarization direction.

The times of flight of the ultrasonic waves were measured by the echo method. The elastoacoustic coefficient was determined using the following equation:

$$\beta = \frac{t_0 - t_\sigma}{t_\sigma} \cdot \frac{1}{\sigma} \qquad (2)$$

where:

t_0 – time of flight of ultrasonic wave in the unloaded material,

t_σ – time of flight of ultrasonic wave in the uploaded material,

β – elastoacoustic coefficient,

σ – stress within the range of elasticity.

The times of flight of the ultrasonic waves were measured by through-transmission method. Subsequently, static tensile tests and microstructural investigations were carried out. Finally, the relationships between parameters determined by means of the non-destructive and destructive methods were found.

3. Selected results

The experiment was carried out on two series of the 40HNMA steel that consists of sorbite microstructure with remaining the needle martensite configuration. First series came from unexploited material subjected to quenching and tempering, while the second one was cut off from the exploited tube. In both cases the same conditions of creep testing were applied (σ = 250MPa, T = 500ºC).

In the case of 40HNMA steel without prior loading history a decrease of the acoustic birefringence was observed for specimens after plastic deformation and accelerated creep (Fig. 1). Variations of the acoustic birefringence were caused by the rotations of material grains. During this process they try to set themselves parallel to the stress direction enforcing a deformation [4]. The higher values of the coefficient for the steel after creep are explained by annihilation of material defects due to temperature of the process.

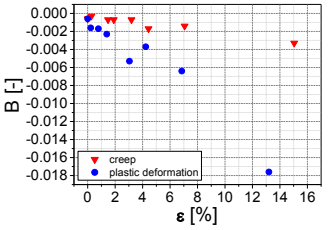

Fig. 1. Variation of the acoustic birefringence for the 40HNMA steel after quenching and tempering versus strain.

In the case of 40HNMA steel cut off from the tube an increase of the acoustic birefringence for specimens after creep was identified (Fig. 2). It is caused by an occurrence of microcracks in the material matrix.

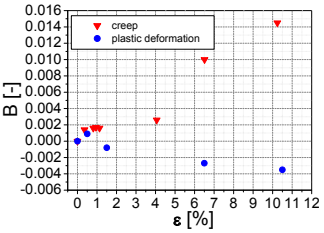

Fig. 2. Variation of the acoustic birefringence for the 40HNMA steel cut off from the exploited tube versus strain [3].

4. Conclusions

- The acoustic birefringence might be useful in assessment of a state of material degradation in the late stage of material exploitation.
- A variation of the elastoacoustic coefficient was observed in the early stage of exploitation for the 40HNMA steel cut off from the tube and subjected to accelerated creep. The parameter was not sensitive on damage development in the advanced stage of material exploitation.

References

[1] Kowalewski, Z.L., Mackiewicz, S., Szelążek, J., Pietrzak, K., Augustyniak B., Evaluation of damage development in steels subjected to prior deformation: destructive and nondestructive techniques, Journal of Multiscale Modelling, **1**, 2009. pp. 479-499.

[2] Mackiewicz, S., Possibilities of ultrasonic evaluation of energetic steels as a result long-term exploitation (in Polish), Conference Book, VII Information and Training Seminar: Diagnostic and Renovations Energetic Devices. New Diagnostic Problems on the Old Power Units, Ustroń, Poland, 2005.

[3] Szelążek, J., Mackiewicz, S., Kowalewski, Z.L., New samples with artificial voids for ultrasonic investigations of material damage due to creep, NDT&E International, **42**, 2009. pp. 150-156.

[4] Mackiewicz, S., Kowalewski, Z.L., Szelążek, J., Deputat, J., Mechanical and ultrasonic research of materials failure condition due to creep process (in Polish), Przegląd Mechaniczny, **7-8**, 2005. pp. 15-24.

[5] Hyghes, D.S., Kelly, J.L., Second-order elastic deformation in solids., Phys. Rev., **92**, 1953. pp. 1145.

30th DANUBIA-ADRIA
Symposium on Advances in Experimental Mechanics
September 25-28, 2013 - Primošten, Croatia

3B29 099

MICRO AND NANOHARDNESS TESTING OF LASER WELDS

Hana Sebestova[1], Radim Ctvrtlik[2], Hana Chmelickova[1], Jan Tomastik[1]

[1] Palacky University in Olomouc, Faculty of Science, RCPTM, Joint Laboratory of Optics of Palacky University and Institute of Physics of the ASCR, 17. listopadu 12, 771 46 Olomouc, CZECH REPUBLIC. E-mails: hana.sebestova@upol.cz, hana.chmelickova@upol.cz, jan.tomastik@upol.cz

[2] Institute of Physics of the Academy of Sciences of the Czech Republic, Joint Laboratory of Optics of Palacky University and Institute of Physics of the ASCR, 17. listopadu 50a, 772 07 Olomouc, CZECH REPUBLIC. E-mail: ctvrtlik@fzu.cz

1. Introduction

Hardness tests are widely used for weld mechanical properties evaluation and thus its quality estimation. Typical increase of weld metal hardness followed by its decrease in heat affected zone can be observed in most of conventionally prepared weld joints [1]. In case of laser welding, much higher cooling rates are present and thus different weld characteristics can be expected. Especially thin sheets (< 1.5 mm) seam welding with a pulsed laser results in very small-sized welds with heat affected zone often unobservable using light microscopic techniques [2]. In such cases utilization of micro- and especially nanoindentation techniques is appropriate for reliable measurement of mechanical properties of the welded material.

Nanoindentation (depth sensing indentation) is a contact based technique widely used for evaluation of mechanical properties at small scales. During a typical test a diamond tip of known geometry is pressed into the sample surface, while the indentation load and depth are continuously recorded. This method can provide us with new information about fine welds properties.

2. Experiment

Pulsed Nd:YAG laser LASAG KLS 246-102 with maximal average power 150 W was used for bead-on-plate welding of 0.6 mm thick AISI 304 stainless steel sheet. Pulse repetition frequency 13 Hz, welding speed 4 mm.s^{-1} and working distance 4 mm under the focal plane were kept constant during all experiments. Protective argon gas (8 l.min^{-1}) was applied coaxially with the laser beam. Other processing parameters are concluded in Tab. 1.

Sample no.	Pulse length [ms]	Pulse energy [J]	Average power [W]	Peak power [kW]
I	2.6	3.5	45.5	1.35
II	3.9	4.7	61.1	1.21
III	3.4	5.9	76.7	1.74
IV	3.4	6.2	80.6	1.82

Tab. 1. Applied processing parameters.

3. Hardness measurement

3.1 Vickers microhardness tests

First, polished sample of basic material mounted in cold casting resin was etched with a mixture of hydrochloric and nitric acid (3:1) to induce its microstructure.

Basic material microhardness was evaluated using automatic hardness tester LECO AMH43 with Vickers indenter at applied load of 500 mN. Fifteen measurements were performed. The average value reached (270 ± 25) HV 0.05.

Second, metallographic specimens of cross sections perpendicular to the welding direction were prepared in the same way as the basic material. Weld microhardness was measured along the centre of the weld cross section from its surface to the root in discrete points spaced by 70 μm or 100 μm, respectively. Supplemental measurements were performed perpendicularly, in the centre of the metal sheet (indexed with "p"). Fig. 2 presents examined weld cross sections with the designation of indents positions.

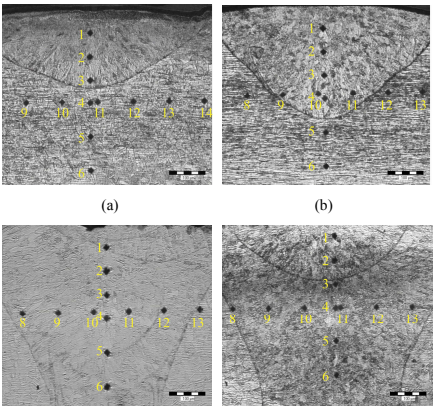

Fig. 2. Weld cross sections after the microindentation test (sample I (a), II (b), III (c) and IV (d)).

Laser power applied in case of sample I and II was insufficient for the full penetration. Thus only few indents lie in the weld metal. Fig. 3 presents results of microhardness measurements that show a noticeable scatter.

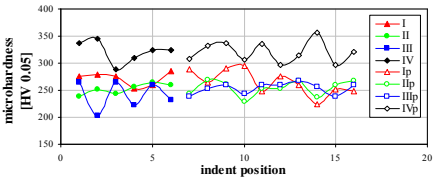

Fig. 3. Results of microhardness measurements.

3.2 Nanoindentation

Selected samples of laser welds were also examined by the nanoindentation to study local weld properties in detail. The measurements were carried out using the fully calibrated NanoTest NTX system (MicroMaterials). Room temperature indentation with Berkovich indenter was performed at load of 50 mN. The position of investigated area of the weld is displayed in Fig. 4 together with measured data of sample II. The spacing of indents was 30 μm.

Comparing nanoindentation data with respect to the indents position, certain hardness decrease on the boarder of the weld metal and basic material can be observed.

Nanoindentation provides us also with reduced elastic modulus data that are also displayed in Fig. 4.

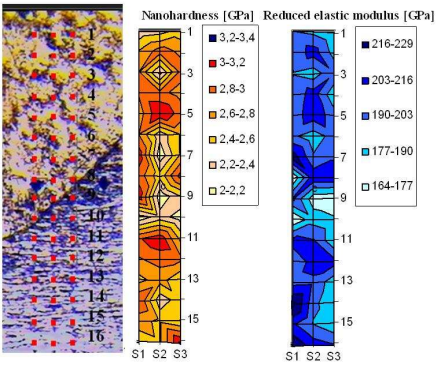

Fig. 4. Position of nanoindents and corresponding nanohardness and reduced elastic modulus results (sample II).

4. Remarks

- Vickers test did not reveal any significant increase in weld metal microhardness. Laser welds performed with similar processing parameters reached very different microhardness values. Measured profiles depend on individual weld cross section structure that seems different for different cut positions. This is caused by the specific orientation of weld metal grains resulting from relatively small 63% pulse overlap.
- Higher spatial resolution of nanoindentation revealed local decrease of hardness and elastic modulus at the boarder of weld metal and basic material.
- More detailed results with adequate comment will be presented at the conference.

Acknowledgements

The authors gratefully acknowledge the support by the Operational Program Education for Competitiveness - ESF (CZ.1.07/2.4.00/17.0084) and by the Technology Agency of the Czech Republic (TA01010517).

References

[1] Jenney, C. L., O'Brien, A., Welding Handbook, Volume 1 – Welding Science and Technology (9th edition). AWS, 2001.

[2] Steen, W. M., Laser Material Processing (3rd edition). Springer, 2003.

30th DANUBIA-ADRIA
Symposium on Advances in Experimental Mechanics
September 25-28, 2013 - Primošten, Croatia

3B30 026

THE INFLUENCE LONG AXIAL COMPRESSION ON MICRO-MECHANICAL PROPERTIES OF LAMELLAR IN ANNULUS FIBROSUS

Małgorzata Żak[1], Celina Pezowicz[1]

[1] Wrocław University of Technology, Faculty of Mechanical Engineering, Division of Biomedical Engineering na Experimental Mechanics, Łukasiewicza 7/9, 50-371 Wrocław, POLAND. E-mail: malgorzata.a.zak@pwr.wroc.pl

1. Introduction

The annulus fibrosus of intervertebral disc is creates an organized network of collagen fibers. Simultaneously orientation of collagen fibers determines the anisotropic mechanical properties in intervertebral disc [2].

The aim of this study was to determine the impact of long axial compression on structural of intervertebral disc. Changes in the structure was characterized on the basis of the mechanical properties of lamellar in annulus fibrosus defined in microscopic level.

2. Material and Methods

The study was conducted on 10 pigs lumbar spines motion segments without neural arch. Segments were divided into 2 groups: with nondegenerate intervertebral disc (physiological) and after long compression test - pathological intervertebral disc.

Long axial compression test was carried out on the testing machine MTS 858 Mini Bionix. The test was performed for 100 000 load cycles at a frequency of 2 Hz. Segments loaded axial force between 150N to 650N, to simulate daily range of loads on the spine.

Micro-mechanical properties of lamellar were carried out on samples obtained from the anterior parts of motion segments. Sections 40–50μm in nominal thickness were cut from multi lamellar blocks Fig.1a. Microtensile samples with dimensions of 1.60±0.46mm length and 2.46±0.47mm width were trimmed from remain mono-aligned area of tissue.

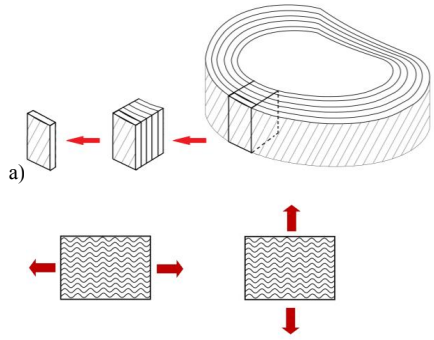

Fig. 1. Preparation of material: a) method of cuting the samples from the multi lamellar blocks of annulus fibrosus. Direction of stretching the micro samples: b) parallel, c) perpendicular.

To maintain comparable test conditions the samples were stored in saline at 4÷7ºC [2]. Samples were stretched in two directions: parallel and perpendicular to collagen fibers alignment direction (Fig.1.b,c). Uniaxial tensile test performed on especially designed system stretching the samples in the microscopic level. The samples were stretched at a constant speed loading 0.06mm/s in both directions.

3. Results and discussion

The basic mechanical properties (σ_{UTS} - ultimate tensile strength, ε_N - strain at failure) were determined from the non-linear stress-strain characteristics. Samples revealed different breaking mechanisms in depending on the direction of tensile [1]. Samples stretched in parallel direction show slight increase in value as opposed to transverse direction.

3.1 Parallel direction of stretching

During tensile specimens in the parallel direction, can be divided into scopes corresponding to the characteristic stage of straighten and move the collagen fibers.

Both mechanical properties (σ_{UTS}, ε_N) of the specimens excised in the parallel direction was higher in physiological by about 24% than pathological Fig.2.

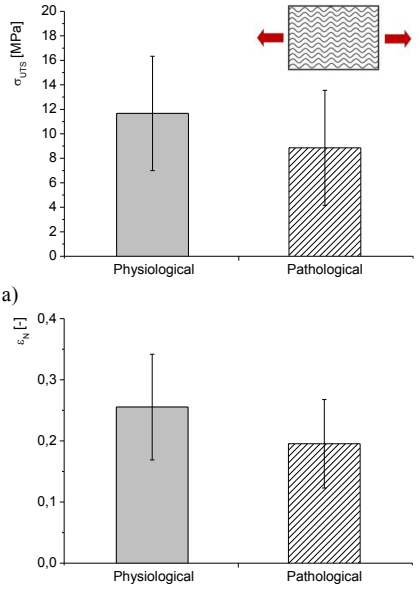

Fig. 2. Mechanical properties of micro samples stretched in parallel to collagen fibers direction: a) ultimate tensile strength (σ_{UTS}) b) strain at failure(ε_N).

3.2 Perpendicular direction of stretching

In the case of samples stretching in perpendicular direction, collagen fibers are separated. In comparison to parallel stretching, transversely stretched samples are characterized by a slight increase in σ_{UTS}, which is maintained at a constant level.

The specimens excised in perpendicular direction from showed σ_{UTS} by about 60% higher in physiological intervertebral disc than in pathological Fig.3.a. However, in both groups, there were no significant differences in strain value Fig.3.b.

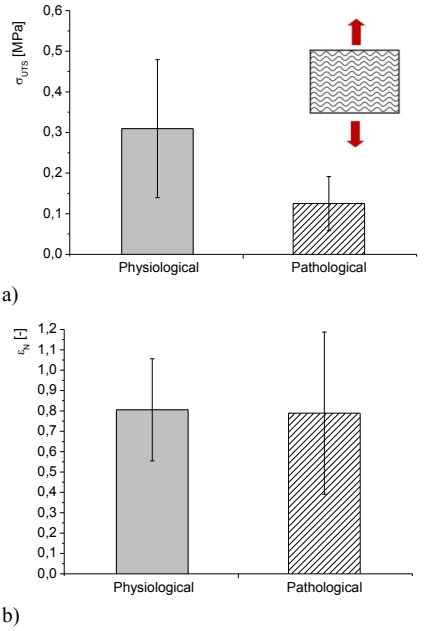

Fig. 3. Mechanical properties of micro samples stretched in perpendicular to collagen fibers direction: a) ultimate tensile strength (σ_{UTS}) b) strain at failure(ε_N).

The results confirm the annulus fibrosus anisotropy and indicate that the orientation of the collagen fibers has an effect on the mechanical properties. The results of the research showed how changes mechanical properties of collagen fibers which induced pathological changes.

Acknowledgements

This research project is supported by grant No. NN518501139.

References

[1] Pezowicz C.A., Robertson P.A., Broom N.D., Intralamellar relationships within the collagenous architecture of the annulus fibrosus imaged in its fully hydrated state, J Anat., 207(4), 2005, pp. 299-312.

[2] Pezowicz C.A., Robertson P.A., Broom N.D., The structural basis of inter-lamellar cohesion in the intervertebral disc wall, J Anat., 208(3), 2006, pp. 317-330.

30th DANUBIA-ADRIA
Symposium on Advances in Experimental Mechanics
September 25-28, 2013 - Primošten, Croatia

3B31 063

EXPERIMENTAL INVESTIGATION OF BARLEY VISIBLE IMPACT DAMAGES ON AEROSPACE COMPOSITE STRUCTURAL PARTS

J. C. GÖSSL[1], Z. RÁCZ[1], M. FLEISCHMANN[1], J. NOISTERNIG[1]

[1] FACC AG, Fischerstrasse 9, A-4910 Ried im Innkreis, Austria. E-mail: j.goessl@facc.com

1. Introduction

Advanced composites have many advantages as aircraft structural materials and for this reason their use is becoming increasingly widespread. Impact damage is a major concern in laminated composite structures and sandwich construction, as accidental impacts frequently cause damage, severely reducing structural strength and stability. Relationships between forces and deformations are much more complicated in composites than in conventional metallic materials due to composites' higher transverse shear and transverse normal stress deformability.

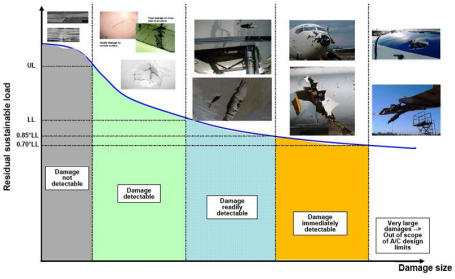

Fig. 1. Damage Size [5]

Fragility of composite materials to impact loading limits their application in aircraft structures. In particular, low velocity impacts – tools dropped during maintenance or foreign object damage during landing and takeoff – can cause a significant amount of delamination, even though the only external indication of damage may be a very small surface indentation. This type of damage is often referred to as barely visible impact damage (BVID), and it can cause significant degradation of structural properties. If the damaged laminate is subjected to high compressive loading, buckling failure may occur.

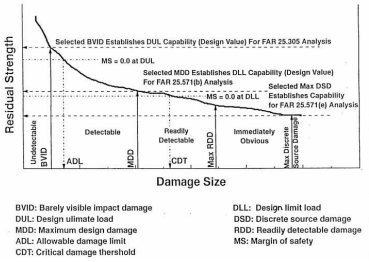

Fig. 2. Residual strength requirements versus damage size [1]

The extent of BVID damage is difficult to measure as it cannot be seen by visual inspection and damage is hidden among the layers that cause inter-laminar strength reduction, inducing secondary invisible effects.

2. Applying BVIDs on structural parts

Barely visible impact damages according to the definition of damage Categories 1 – 5 out of CMH-17 [1] (see Fig. 1) are Category 1 and based on a no-growth concept, meaning that damages up to the boundary of optical detectability. Kassapoglou quantified BVID with his specification as indentions left by impacts and its local damages that are barely visible from a distance of about 120cm [2].

This fact leads directly to the challenge that a specific dent depth is postulated for introducing the damages on structural composite parts. Performing impact calibrations on representative flat panels in order to determine the required energy level for applying the damages on structural parts is recommendable process.

The following details may have an influence, when impacts completed by a drop tower/gas gun

under defined laboratory conditions are allocated on structural parts:

- Detailed design configuration of structural part impact location are not transferable to flat test panels
- Influence of geometries at impact location
- Interaction with hardware in surrounding regions
- Final production processes (primer, painting, coating, …)
- Interaction of configuration (laminate – core – adhesive)

A main deviation of required energy level determined from flat panels to structural parts is directly connected to the finishing works (painting and priming). The main factor that affects the indentation is the underlying honeycomb structure beneath the core. As shown in the Fig. 3 below, if the impact occurs in an intersection region of the honeycomb structure, for thin ply composites, the increased strength will result in a decreased indentation.

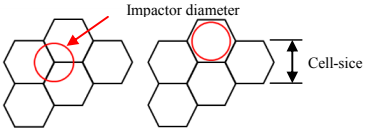

Fig. 3. Honeycomb support behavior

3. Devices

BVID impacts can be simulated on the drop tower and air cannons/gas gun in the test facility under laboratory conditions.

Drop towers have a very good repeatability as well as accuracy. The main field of use is under laboratory conditions (flat panels) and plain structures (coupon test)

Shooting devices like gas guns offer more flexible in regards of shape of the tests parts and introduction direction of impacts. A prerequisite is that the processes are well defined, as such devices have many factors affecting repeatability as well as accuracy.

The gas gun is an impacting device used to cause BVID or VID of a known energy and impact depth as shown in Fig. 4.

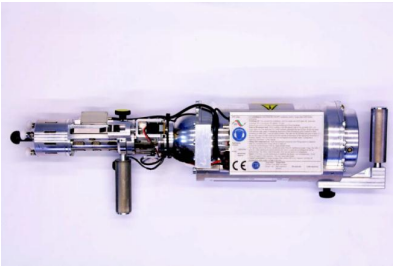

Fig. 4. Gas Gun

The gas gun expels a projectile to impact a target via the use of compressed air. A displacement sensor calculates the velocity of the projectile as it moves through the barrel and from this the impact energy is calculated. The Gas Gun is rated to an accuracy of +/- 5%, however an accuracy of +/- 2.5% is commonly achievable [3], [4].

4. Conclusion

This paper describes a strategy for predicting internal damages in a laminated composite structure as well as sandwich structures when subjected to low-velocity impact. The aim was to obtain a better understanding of and solutions for the notorious reduction in strength of aircraft compression panels when they suffered barely visible impact damage (BVID). Secondly the aim was to transfer this knowledge from laboratory conditions to conditions on structural parts to produce significant and realistic testing results.

Furthermore a strategy of preparing BVIDs with gas guns and reoccurring influences shall be presented by allocating BVIDs from laboratory conditions to conditions on structural parts.

References

[1] CMH-17, Composite Materials Handbook

[2] DOT/FAA/AR-01/124, Test and Analysis of Composite Sandwich Panels with Impact Damage, Office of Aviation Research, Washington, 2002

[3] Airbus “Introduction of impacts with mobile compressed air”, RP1001654

[4] ID, Im Hüttental 10, 85125 Kinding, Germany “Manual Mobile Impactor Manual”

[5] “Damage tolerance of composite structures in aircraft industry” Presentation, Dr. Mircea Calomfirescu and Dr. Holger Hickethier, EADS Defence and Security, Military Air Systems (MAS) Manching, Germany, 2010

30th DANUBIA-ADRIA
Symposium on Advances in Experimental Mechanics
September 25-28, 2013 - Primošten, Croatia

3B32 057

PIEZOELECTRIC STRAIN SENSOR LOCAL AND GLOBAL STIFFNESS INFLUENCE ON GLASS FIBER REINFORCED COMPOSITE

Michał Kowalik[1], Marcin Obszański[1], Witold Rządkowski[1], Karol Suprynowicz[1], Paweł Pyrzanowski[1]

[1] Warsaw University of Technology, Institute of Aeronautics and Applied Mechanics, Faculty of Power and Aeronautical Engineering,; Nowowiejska 24, 00-665 Warsaw, Poland, E-mail: mkowalik@meil.pw.edu.pl,

1. Introduction

In recent years there is a need to increase development of smart and low weight and low energy consumption sensors and actuators for engineering applications. Sensors which are independent from external energy sources, or their energy consumption is negligible are desired. These requirements can be met by piezoelectric materials. When mechanical force is applied to piezo-material, due to the direct piezoelectric effect, an electrical voltage is generated. Although due to inverse piezoelectric effect it can induce force, when electric field is applied. Different application of piezoelectric materials makes them appropriate for the development of systems that such sensor-active vibration damper [1]. Unfortunately, such a sensor has an impact on the local stiffness, due to the high Young's modulus and thickness (compared to the resistive strain gauge).

2. Methods

2.1 Static tensile test

Sensors used in experiments were M2807-P1 (28x7x0.3mm) made by Smart-Material Corp.

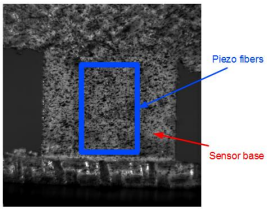

Fig. 1. M2807-P1 piezo sensor clamped in machine.

Piezo material is PZT5AH1 Navy Type II with longitudinal active part, and transverse electrodes [2]. In first step both piezo sensor and GFRP were investigated separately to obtain independent material properties. GFRP specimens were made of two layers of 0/90 glass fabric (total thickness is 0.4 mm). All specimens were also measured using Digital Image Correlation (DIC) for a better accuracy. DIC was used to measure true strain and to obtain real material properties both of sensor and GFRP, which were later used in FE analysis (Tab. 1)

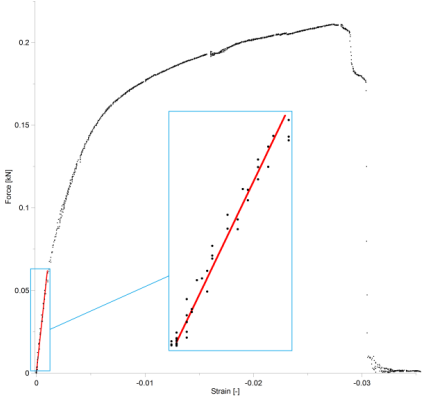

Fig. 2. Tension curve of piezo sensor. Magnified line represents linear Young's Modulus for piezo sensor.

2.2 Finite Element Method

Model was built with c.a. 500 000 20-node elements. All material models were assumed as isotropic and linear elastic.

Material data	GFRP	Piezo sensor
Young Modulus [GPa]	12	10.6
Poisson ratio [-]	0.31	0.13

Tab. 1. Material properties.

3. Results

Results of longitudinal strain obtained after loading the specimen (0.4 mm thick cross-ply GFRP) with 900N force are presented on Fig. 3. Area, where piezo sensor is bonded, is significantly stiffer than rest of the specimen, resulting in non-uniform axial strain distribution.

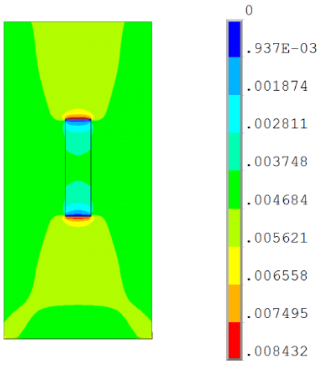

Fig. 3. FE longitudinal strain (specimen and sensor).

Influence of sensor stiffness on GFRP is also presented on Fig. 4., where for clarity piezo element is not shown. Specimen was only 0.4 mm thick, so influence is observed on both sides.

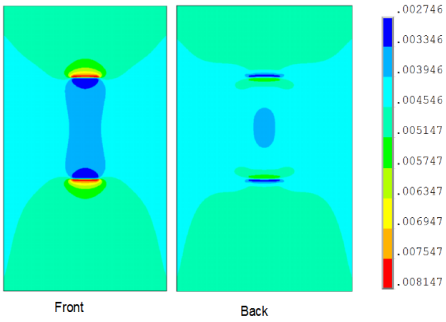

Fig. 4. FE longitudinal strain in GFRP.

Strain measured directly at piezo sensor (centerline of pizeo sensor is located exactly at centerline of GFRP) is about 20% lower than strain measured at other locations (Fig. 5.).

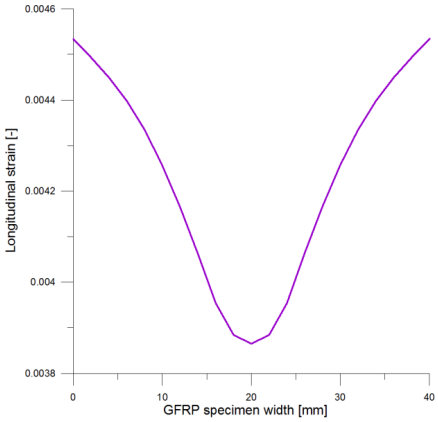

Fig. 5. Longitudinal strain thru width of specimen.

4. Remarks

- Piezoelectric strain sensor has strong influence on local stiffness of observed model, while global stiffness remains unchanged.
- Strain measured with piezo sensor at flexible parts might be underestimated due to relatively high stiffness of sensor.

Acknowledgements

Financial support of Structural Funds in the Operational Programme - Innovative Economy (IE OP) financed from the European Regional Development Fund - Project "Modern material technologies in aerospace industry", Nr POIG.01.01.02-00-015/08-00 is gratefully acknowledged.

References

[1] R. Paradies, P. Ciresa, Active wing design with integrated flight control using piezoelectric macro fiber composites, Smart Materials and Structures 18, 2009.

[2] N. Hagood, R. Kindel, K. Ghandi, P. Gaudenzi, Improving Transverse Actuation of Piezoceramics using Interdigitated Surface Electrodes, Smart Structures and Intelligent Systems, 1993. pp. 341-352

30th DANUBIA-ADRIA
Symposium on Advances in Experimental Mechanics
September 25-28, 2013 - Primošten, Croatia

3B33 060

ESTIMATION OF PIEZOELECTRIC STRAIN SENSOR INFLUENCE ON GLASS FIBER REINFORCED COMPOSITE SAMPLE'S STIFFNESS USING DIGITAL IMAGE CORRELATION

Karol Suprynowicz[1], Michał Kowalik[1], Marcin Obszański[1], Witold Rządkowski[1], Paweł Pyrzanowski[1]

[1] Warsaw University of Technology, Institute of Aeronautics and Applied Mechanics, Faculty of Power and Aeronautical Engineering; Nowowiejska 24, 00-665 Warsaw, Poland, E-mail: ksuprynowicz@meil.pw.edu.pl

1. Introduction

Macro Fiber Composite (MFC) piezoelectric devices have numerous uses ranging from strain gauges, to actuators and energy harvesting devices. As a strain gauge it offers high sensitivity and bandwidth allowing it to measure signals with frequency up to 3MHz. Additional advantages include damage tolerance and reliability. MFC devices can be used as actuators for introducing both static displacement and vibrations. Their structure and dual sensor/actuator nature requires large cross-section area, which in conjunction with high stiffness of piezoelectric ceramic material can influence both local strain distribution in the sample and global sample's stiffness.

2. Methods

A flat sheet of glass fiber reinforced plastic composite was used as a specimen. Reinforcement consisted of two layers of bi-axial (0° - 90°) fabric with 186 g/m^2 weight each. EP52 epoxy resin was used as a matrix. M2807-P1 (28x7x0.1mm) MFC piezoelectric sensor manufactured by Smart Material Corp. was attached to specimen using cyanoacrylate glue. Specimen with attached sensor is visible on Fig. 1. Load was applied in vertical (y) dimension. A uniform paint coating was applied to sample's surface and subsequently covered in black paint spots used as markers for Digital Image Correlation Method.

2.1 Strain measurement

Sub-pixel, two dimensional Digital Image Correlation (DIC) similar to described in [1], was used for determining strain distribution and for attaching four virtual extensometers, two of which are visible on Fig. 1. The other two were attached in analogical location on the reverse side of the specimen. Extensometers were placed parallel to load direction and were used to determine average values of strain across sensor area and reference area undisturbed by sensor.

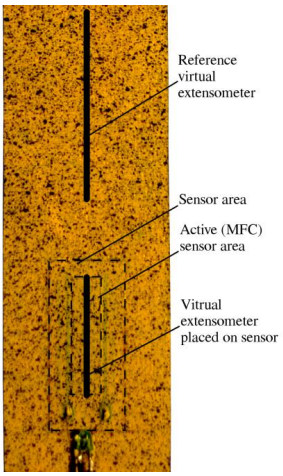

Fig. 1. Piezoelectric sensor attached to CFRP sheet. Extensometers are marked with black lines.

3. Results

Results from the extensometers (Fig. 2) show up to 20% change in stiffness on the sensor side and 10% change on reverse side. Such difference suggests that bending may occur, a notion that was confirmed using Finite Element model. Stress was calculated from load for composite nominal cross section area.

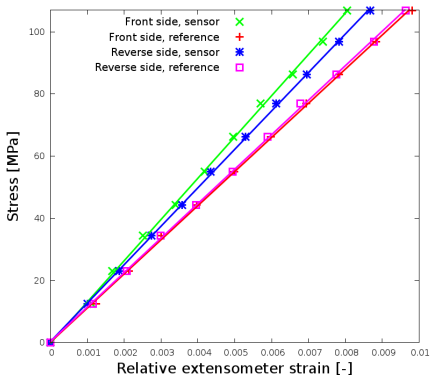

Fig. 2. Strain relative to preload, indicated by optical extensometers placed on sensor and at reference position.

Fig. 3 shows strain distribution for both sides of specimen. Strain in the sensor area is significantly lower than strain on reference area of the sample. Additionally strain concentration can be observed above and below the sensor on the front side. Very low strain values on lower part of the sensor can be attributed to contacts soldered to the sensor surface. An apparent out of scale strain concentration in lower part of the sample's front side was caused by a movement of signal cable attached to sensor, visible on Fig. 1.

4. Remarks

Large differences in stiffness and changes in strain distribution around sensor must be accounted for in numerical models. Numerical model of composite shell structure with MFC actuators is described in [2]. It is also necessary to compensate measurements acquired from the sensor for additional stiffness from sensor's active area, especially in sheet structures similar to shown case. Lack of sensor output correction in shown case could result in indicated values up to 20% lower than those occurring on area undisturbed by sensor.

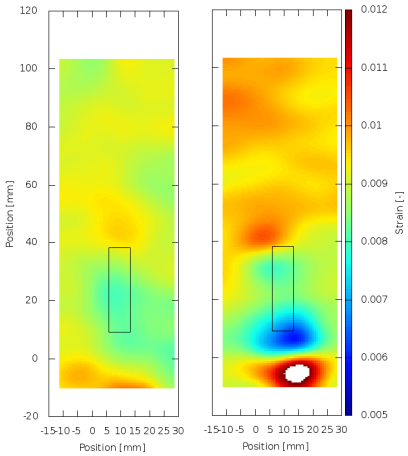

Fig. 3. Distribution of strain in load direction on front (right) and reverse (left) side of the specimen. Sensor was placed on front side. Black rectangle denotes sensor's active area.

Acknowledgements

Financial support of Structural Funds in the Operational Programme - Innovative Economy (IE OP) financed from the European Regional Development Fund - Project "Modern material technologies in aerospace industry", Nr POIG.01.01.02-00-015/08-00 is gratefully acknowledged.

References

1. H. A. Bruck, S. R. McNeill, M. A. Sutton, W. H. Peters III, Digital image correlation using Newton-Raphson method of partial differential correction, Experimental Mechanics Vol. 29 Issue 3, 1989. pp 261-267
2. N. Hagood, R. Kindel, K. Ghandi, P. Gaudenzi, Improving Transverse Actuation of Piezoceramics using Interdigitated Surface Electrodes, Smart Structures and Intelligent Systems, 1993. pp. 341-352

30th DANUBIA-ADRIA
Symposium on Advances in Experimental Mechanics
September 25-28, 2013 - Primošten, Croatia

3B34 132

EXPERIMENTAL AND NUMERICAL ANALYSIS OF SANDWICH BEHAVIOUR UNDER STATIC LOADING

Major Z.[1], Miron M.C.[1], Gerstmayr R.[2], Weitzenböck J.[2]

[1] Johannes Kepler Universität Linz, Institute for Polymer Product Engineering, Altenberger Straße 69, 4040 Linz, AUSTRIA. E-mails: zoltan.major@jku.at, matei.miron@jku.at

[2] TCKT - Transfercenter für Kunstofftechnik, Franz-Fritsch-Straße 11, A-4600 Wels, AUSTRIA, E-mails: r.gerstmayr@gmail.com, joern.weitzenboeck@tckt.at

1. Introduction

Due to their stiff skin and lightweight core structure sandwich materials provide in the same time both high bending stiffness and low weight making them suitable for lightweight application design [1].

The major shortcoming of the sandwich materials comes into play when we are talking about shock loading or localized (point) loading, conditions under which the interfacial damage is the main cause of the material failure [2].

Being the first step in building a complete failure model for the studied sandwich material, the current research is focused on determining the failure modes under static loading of several sandwich configurations.

2. Experimental approach

In order to develop a complete numerical model able to describe the sandwich material failure modes it is necessary to perform tests both on the sandwich material and also separately on the core and skin materials [3]. Also fracture mechanics testing methods must be used in order to build a cohesive zone model for the interface damage characterization [4].

The skin and core materials used for the sandwich structure are presented below (Tab. 1).

Nine different sandwich configurations loaded in 3 and 4 point bending are the subject of the experimental research (see Tab. 2). Laminated composites used for the skin material as well as the sandwich structures were manufactured by TCKT Wels[2].

Ref.	Material name	Description
C1	Airex C 70.75	PVC Foam 80 kg/m^3
C2	Compaqform 100	PS Foam 100 kg/m^3
C3	Compaqform 200	PS Foam 200 kg/m^3
C4	Nomex Honeycomb	Aramid paper honeycomb
GF	Glass Fiber	0/90
CF	Carbon Fiber	0/90

Tab. 1. Materials used for the sandwich composite

Name	Configuration		
M1	2xGF	C1	2xGF
M2	4xGF	C1	4XGF
M3	1xCF	C1	1xCF
M4	2xCF	C1	2XCF
M5	4xCF	C1	4XCF
M6	2XGF	C2	2xGF
M7	3xGF	C3	3xGF
M8	1xGF	C4	1xGF
M9	2xCF	C4	2xCF

Tab. 2. Tested sandwich configurations

The experimental results provided information concerning the maximum loading capability with respect to the sandwich composition (density) and helped identifying the main failure mechanisms for the studied materials: skin failure occurs under local compression, core failure occurs under shear loading and in the case of the honeycomb core local buckling of the honeycomb cells.

3. Numerical approach

Numerical modelling of damage evolution in composite materials has known a continuously growing development in both macro structural damage modelling (cohesive zone model [5]) and also in the microstructural damage modelling (micro cellular modelling). These models can be successfully employed to describe the failure phenomena occurring inside the sandwich material.

Micross is a tool developed by e-Xtream engineering which uses the homogenization method and has implemented damage prediction models for laminate composites and foams [6]. Industry-oriented and aimed at determining the stiffness and the maximum loading capability of a sandwich material loaded in 3 or 4 point bending, Micross is the perfect tool when in need of a quick assessment of the material's mechanical properties (see Fig. 1).

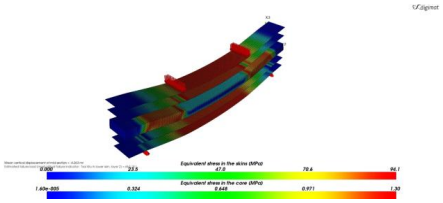

Fig. 1. Results for M1 (max. force 665 N)

In order to assess the validity of the numerical results two comparisons were made: firstly the capability of the software to predict the global force-displacement response of the material (see Tab. 3) and secondly accuracy of determining the maximum loading capability (see Tab. 4).

Material	Experimental displacement at 400 N loading [mm]	Numerical displacement at 400 N loading [mm]
M1	4.4	4.26
M2	2.7	2.74
M4	2.7	2.74
M9	3.8	4.13

Tab. 3. Numerical results – stiffness prediction

Material	Maximum force experimental [N]	Maximum force numerical [N]
M1	640	665
M2	1020	1006
M4	1000	971
M9	450	352

Tab. 4. Numerical results – maximum load

4. Conclusions

Micross shows high potential in optimizing the sandwich structures, providing a fast solution in assessing the influence of material design parameters in the overall sandwich behaviour. Good agreement was obtained for the foam-cored sandwich materials. Further investigations are required concerning the honeycomb accuracy.

5. Further research

Our future research is focused on two main directions:

- Further experimental study of the failure behaviour of the skins, core, interface, and sandwich assembly under both static and impact loading.
- Numerical development of a complete failure model consisting of skin damage modelling for intra and inter laminar failure, core damage modelling, micro buckling damage for the honeycomb core and interface damage modelling.

References

[1] Bitzer, T., Honeycomb technology. Chapman & Hall, 1997.

[2] Xu, L.R., Rosakis, A.J., Impact failure characteristics in sandwich structures, Int. J. Solids Struct., **39**, 2002. pp. 4125-4235.

[3] Miron, M.C., Constantinescu, D.M., U.P.B. Sci. Bull., **73**, 2011. pp. 125-140.

[4] Fuchs, P.F., Major, Z., Experimental determination of cohesive zone models for epoxy composites, Exp. Mech., **51**, 2011. pp. 779-786.

[5] Camanho, P.P., Davila, C.G., Mixed-mode decohesion finite elements for the simulation of delamination in composite materials, NASA/TM-2002-211737, 2002. pp. 1-37.

[6] e-Xtream Engineering, Digimat® help manual, Release 4.2.1, January 2012.

30th DANUBIA-ADRIA
Symposium on Advances in Experimental Mechanics
September 25-28, 2013 - Primošten, Croatia

3B35 112

IMAGING THE MICROMECHANICAL RESPONSE OF WOOD IN STEEL-DOWEL CONNECTIONS

Thomas K. Bader[1], Lech Muszynski[2], Wolfgang Lederer[1], Josef Eberhardsteiner[1]

[1] Institute for Mechanics of Materials and Structures, Vienna University of Technology, Karlsplatz 13/202, A-1040 Vienna, Austria, E-mails: thomas.bader@tuwien.ac.at, wolfgang.lederer@tuwien.ac.at, josef.eberhardsteiner@tuwien.ac.at

[2] Department of Wood Science and Engineering, Oregon State University, Corvallis, OR 97331, US, E-mail: lech.muszynski@oregonstate.edu

1. Introduction

Dowel-type timber connections are widely used in timber engineering structures, due to their ease of application and their ability to transfer high loads. These types of connections act as compliant joints, allowing additional deformations between the structural elements when the joint is loaded. Current design standards require that this compliant characteristic of the joint is taken into account in the design of timber structures [1]. However, the very nature of the joint assembly makes it extremely difficult to directly observe the micromechanical interaction of its component elements. Consequently, current design rules based on external performance observations of the joints do not fully account for the effects of the joint geometry or the loading direction with respect to the fiber direction of the wood on the overall compliance characteristic of the joint.

The aim of this study is to develop an integrated experimental procedure allowing an enhanced *in-situ* insight into the micromechanical interactions governing the global behavior of dowel connections during loading. The approach is to combine traditional embedment tests of steel-dowels in wood with innovative material micro-characterization and measurements based on advanced imaging technologies. The combination of these methods with numerical modeling is expected to bring the testing of complex assemblies to a new level of efficiency and knowledge by removing many limitations of the traditional experimental methods [2].

2. Embedment tests and integrative imaging techniques

Embedment tests were performed on spruce wood specimens with dimensions according to EN383 [3] with 12 mm boreholes and steel dowels (Figure 1). Assemblies were loaded in displacement control using a servo-hydraulic testing machine. The test configuration is illustrated in Figure 1.

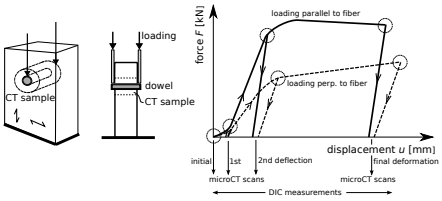

Fig. 1. Test setup and load deformation curves for single dowel connections loaded parallel and perpendicular to fiber direction.

The experimental procedure consisted of step loading of the joint assembly, in which the specimen was unloaded at the first and the second inflection points of the load-displacement curves (Figure 1). Before the test and at each break between loading steps, the 35 mm core of the wood specimen with the borehole was physically extracted from the block specimen to allow for X-ray computed tomography scans revealing the permanent deformation of the internal contact areas. Following the scanning, the core was planted and glued in a matched solid wood material for another loading stage. The procedure continued until 5 mm global joint deformation was achieved. During the loading stages, the surface

deformation maps in the connection have been recorded by means of an optical measurement system based on the digital image correlation (DIC) principle. The surface deformation maps complemented the snapshot volumetric CT data on the permanent deformation inside the wood sample between the loading stages (marked with circles in Figure 1). This procedure was applied to two joint configurations: one loaded along and the other perpendicular to the fiber direction.

3. Results and discussion

The load-deformation characteristics of the investigated samples corresponded well to the typical trends (Figure 1): the initial compliant loading path in specimens is followed by a linear quasi-elastic section until the joint softens and turns into a ductile mode. Further loading would finally lead to brittle failure of the wood.

The optical DIC technique returned (full-field) displacement and strain fields in the wood directly under the dowel. The strain maps reveal a narrow region around the dowel where the material is crushed (seen as high compressive strain), while the deformations further away from the immediate contact zone are considerably smaller (in the elastic range) (Figure 2). This area of large deformations increases slowly but steadily with softening of the load-deformation curve and, further, during the ductile plateau. Deformations perpendicular to grain reveal strain concentrations leading to vertical split running parallel to the fiber direction (Figure 2).

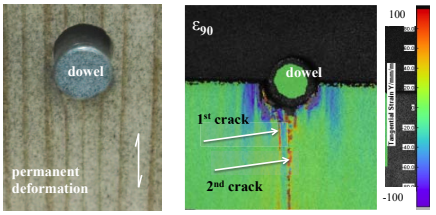

Fig. 2. left: maximum deformation of steel dowel in wood loaded parallel to the grain; right: strains perpendicular to grain illustrating cracking of wood.

Comparing volumetric CT scans of the core material taken after each of the loading stages with the reference scan of the un-deformed specimen taken before the loading procedure allows observation of the gradual densification of wood due to the local collapse of the cellular structure and the increase of the borehole resulting in irreversible deformations of the joint (Figure 2). Both can be readily quantified on the global specimen level (Figure 3). It should be stressed that models employing continuum solid mechanics could not predict such deformation.

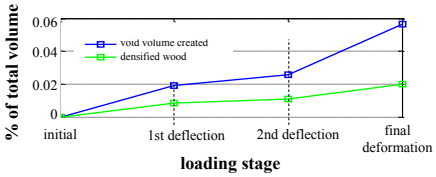

Fig. 3. Change of the void volume and in wood as indicator for irreversible deformations in embedment samples loaded parallel to grain.

4. Conclusions

In this study, traditional embedment tests of steel-dowels in wood were combined with advanced imaging techniques in order to visualize the micromechanical response of wood. Digital image correlation measurements highlighted the strain concentrations in the contact region directly under the dowel. Particularly, the location of strains perpendicular to grain and shear strains as precursors for development of cracks could be visualized. Complementary CT data was found to be consistent with DIC results and reveals buckling and tearing of the cellular structure. These observations explain the challenges faced by the simulation attempts using conventional continuum mechanics models.

Acknowledgements

The authors gratefully acknowledge the financial support of the Austrian Research Promotion Agency (FFG, project number 832803 and 839858) and of CEI-Bois (through the platform “Building with Wood”) for funding the research work within project “MechWood 2”.

References

[1] EN 1995-1-1:2006: Design of Timber Structures – Common rules for buildings.

[2] L. Muszyński, M.E. Launey: Advanced imaging techniques in wood-based panels research. in: Wood-Based Panels - An Introduction for Specialists. State-of-the-Art in Wood-Based Panels Research. COST Action E49 (2010), 177-201.

[3] EN 383:2007: Timber Structures – Test Methods – Determination of embedment strength and foundation modulus for dowel-type fasteners.

30th DANUBIA-ADRIA
Symposium on Advances in Experimental Mechanics
September 25-28, 2013 - Primošten, Croatia

3B36 123

A MODEL OF CALCULUS FOR LOW ENERGY IMPACT ON STRATIFIED HONEYCOMB CORE MATERIAL

Horia Alexandru PETRESCU[1], Stefan Dan PASTRAMA[2], Anton HADAR[3]

[1] University "Politehnica" of Bucharest, Faculty of Engineering and Management of Technological Systems, Bucharest, Splaiul Independentei 313 E-mail: petrescu_horia@yahoo.com

[2] University "Politehnica" of Bucharest, Faculty of Engineering and Management of Technological Systems, Bucharest, Sp. Independentei 313 E-mail: stefan.pastrama@upb.ro

[3] University "Politehnica" of Bucharest, Faculty of Engineering and Management of Technological Systems, Bucharest, Sp. Independentei 313 E-mail: antonhadar@yahoo.com

1. Introduction

In mechanics, an impact is a high force or shock applied over a short time period when two or more bodies collide.

Many types of structures and materials have been tested for impact and impact response, with different results from material to material, but one of the less tested was the stratified honeycomb core material. Regarding this fact, this paper presents a model of calculus for low energy impact on stratified honeycomb core material.

2. Specimens

A stratified honeycomb core material (Figure 1) is a special class of composite materials that is fabricated by attaching two thin but stiff skins to a lightweight but thick core. The core material is normally a low strength material, but its higher thickness provides the sandwich composite with high bending stiffness with overall low density [1].

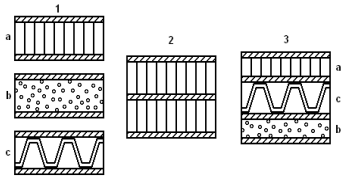

Fig. 1. Sandwich structured composite with simple core (1), double core (2), triple hybrid core (3) a-honeycomb structure, b-rigid foam, c-aluminium sheets**.**

Figure 2 presents a specimen of the sandwich used for impact, with a core thickness of 26 mm and outer shells made of two layered epoxy resin–glass fibre fabric. For each core, there were used two types of outer shells: one made of two layered epoxy resin – glass fibre fabric and one made of one layered epoxy resin – glass fibre fabric.

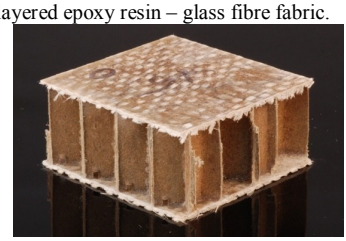

Fig.3. Sandwich specimen

3. Impact analyses

An experimental program consisting of three impact tests in sets of five specimens was performed [2]. The energy of the impact was set to values starting from 5 Joules up to 10 Joules. Figure 3 presents an impacted specimen with an energy of 10 Joules.

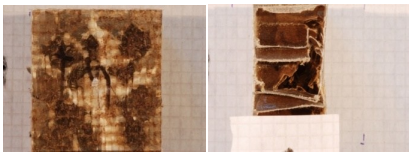

Fig. 3. 10 Joules impacted specimen [1].

For each energy (5, 7.5 and 10 Joules) five tests were performed. The averaged results are presented in Figure 4. We can observe that the force generated during the impact has a peak value of 1100 N for the 5 Joules energy and for the other

energies the force reaches up to 1000 N. The impact took place over a 3.5 ms time interval for the 5 Joules energy and over a 2 ms time interval for the other two energies. After the 3.5 ms mark and the 2 ms mark, the energy-time curve decreases from the maximum value to its minimum.

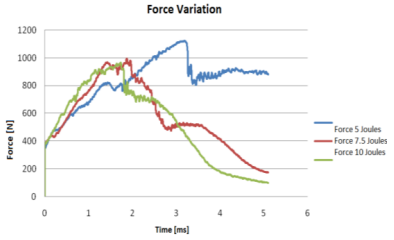

Fig. 5. Force variation over time.

We can conclude that higher impact energy does not actually mean a higher impact force.

4. Numerical analyses

A set of numerical analyses were made in order to fully understand the impact process. For this, a virtual 3D model of the specimen was created following the designs shown in figure 6.

Four points of impact were defined (shown by red dots), one over the centre of a honeycomb cell, one over the middle of a thin wall of the honeycomb core, one over the middle of a thick wall of the honeycomb core and the last one at the top of the junction of three walls.

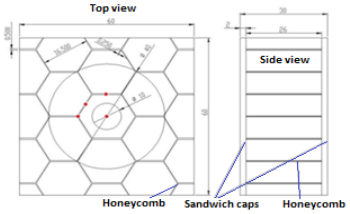

Fig. 6. Specimen dimensions and impact points.

Several parameters were selected considering the results from the experimental tests [3]. A 4.5 ms time interval was set for the program to complete the numerical calculus and also a 10^{-7} s increment was set. The speed applied to the impact hammer was set at v = 4.125 m/s and its mass to a value of 150 g. The resulting impact energy was 5 Joules. Figure 7 presents the numerical model and Figure 8 depicts the numerical results.

These numerical results highlight the importance of impact position over a stratified honeycomb core material regarding maximum stress over time allowing a classification on the ability the structure to absorb kinetic energy, depending on the required shock area**.**

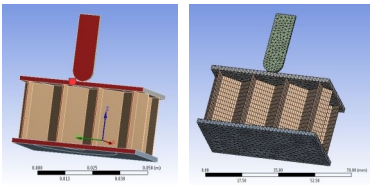

Fig. 7. The numerical model.

Higher stress values represent lower energy absorption potential. We can state that the numerical model was validated because the difference between the numerical results and the experimental results was only 0.45%. In Figure 8 the numerical results are plotted.

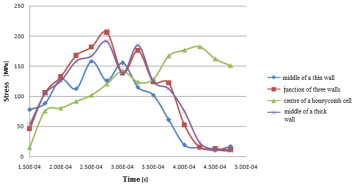

Fig. 8. Numerical results.

5. Conclusions

The numerical model developed for this impact calculus allows a detailed analysis of sandwich plates with honeycomb core.

The four cases of impact created using the finite element numerical analysis, allow a classification on the ability of the structure to absorb kinetic energy, depending on the required shock area. Thus, we can determine the best case in terms of energy absorption.

References

[1]] H.A. Petrescu, "*Contributions to the Study of Behavior of Honeycomb Core Stratified Plates, Subjected to Static and Dynamic Loads",* PhD Thesis, Univ. Politehnica of Bucharest, 2011.

[2] S.T. Hong, J. Pan, T. Tyan, P. Prasad, *"Effects of Impact Velocity on Crush Behaviour of Honeycomb Specimens"*. SAE International, 2004-01-024;

[3] M.A. Crisfield, *"Non-linear Finite Element Analysis of Solids and Structures"* Essentials, vol.1, J. Wiley & Sons, England, 2000.

30th DANUBIA-ADRIA
Symposium on Advances in Experimental Mechanics
September 25-28, 2013 - Primošten, Croatia

3B37 025

FATIGUE INVESTIGATIONS OF MAGNETORHEOLOGICAL COMPOSITES

Michał Królewicz[1]

[1] Wrocław University of Technology, Institute of Materials Science and Applied Mechanics, ul. Smoluchowskiego 25, 50-370 Wrocław, POLAND. E-mail: michal.krolewicz@pwr.wroc.pl

1. Introduction

Magnetorheological elastomers (MRE) are Smart materials which change their mechanical and rheological properties under the application of external magnetic field. This behaviour is known as the magnetorheological effect. MREs can be used in numerous applications, particularly in the areas connected with energy dissipation. For example, these materials may be applied in the automotive industry as elements of shock absorbers, vibration dampers or suspension systems [1,2]. In all these applications the materials have to withstand a large number of working cycles. There is, however, not much literature describing the problem of fatigue in MREs [3].

In this paper the manufactured isotropic magnetorheological elastomers were subjected to preliminary fatigue tests (based on over 1 million cycles of load) and the stability of their mechanical and magnetic properties was investigated.

2. Material

Magnetorheological elastomers are based on two primary components: non-magnetic elastomer matrix and magnetically active filler. In the investigations described in this paper, a thermoplastic elastomer was selected as the matrix material. This polymer was filled with ferromagnetic iron powder with particle size of about 60 µm. Additionally, a plasticizer was used to decrease the stiffness of the matrix. Composition of the samples is shown in Tab. 1.

Iron particles [vol%]	Thermoplastic elastomer [vol%]	Additional plasticizer [vol%]
35	52	13

Tab. 1. Components of MRE specimens.

The materials were manufactured in two stages. Initially, all of the components were mixed at high temperature, using the Plasti-Corder mixer from the Brabender company. After that, the raw isotropic material was shaped under pressure inside a hot hydraulic press. As a result, MREs in the form of 4-mm-thick plates were obtained. A typical sample prepared for cyclic shear testing is shown in Fig. 1. In total, four isotropic specimens were prepared. The manufacturing technology was described in greater detail in [4].

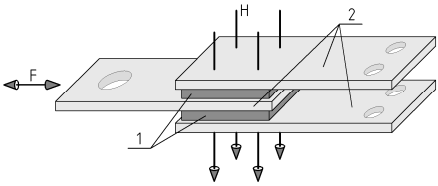

Fig. 1. Test sample: 1 – MRE plates, 2 – non-magnetic clamping plates, H – direction of the magnetic field during experiments, F – direction of the loading force.

3. Experiment

The manufactured samples were subjected to cyclic shearing on a dedicated test stand [4]. The loading was sinusoidal and comprised more than one million (1 296 000) cycles, with a frequency of 5 Hz. The direction of the loading force is shown in Fig. 1. The strain amplitude was equal to 5%. To study how magnetic field influences the mechanical properties of MRE, every 18 000 cycles a magnetic field H=100 kA/m was applied in the direction perpendicular to the sample thickness, as indicated in Fig. 1.

The results are shown in Fig. 2 (magnetic field off) and Fig. 3 (magnetic field on). The maximum registered stress values (τ) tend to decrease only during the first several hundred thousand cycles and then they become stable in time. When the

magnetic field is applied (Fig. 3) the stress values are higher compared to the zero field measurements (please compare Fig. 2 and Fig. 3), but their tendency to decrease and then to stabilise is also observed. This increase in the stress amplitude values in response to the magnetic field is the evidence of the magnetorheological effect occurring in the MRE material.

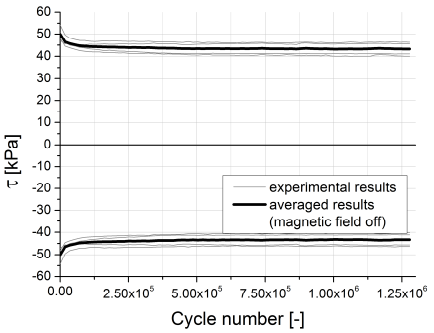

Fig. 2. Stress amplitude values vs. number of load cycles, without external magnetic field.

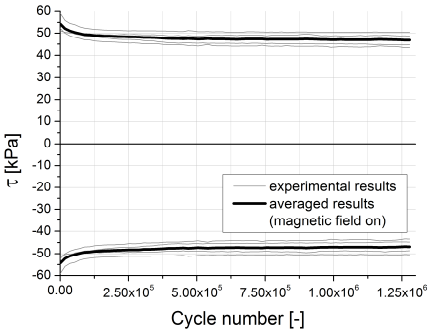

Fig. 3. Stress amplitude values vs. number of load cycles, with external magnetic field acting on MRE.

Another way to express the magnetorheological effect in MRE is to examine how the energy dissipated by the material is changed by magnetic field. This energy is equal to the area of a hysteresis loop in the stress-strain (τ-γ) system. Hysteresis loops, measured at the beginning of the fatigue test, are shown in Fig. 4. It is visible that the application of external magnetic field (0→100 kA/m) increases the area of the loop, so the energy dissipated by the material is also increased. Percentage values of hysteresis loop area change were measured. On average, the loops increased by 46.5% at the beginning of the fatigue test and by 43.5% after stabilisation.

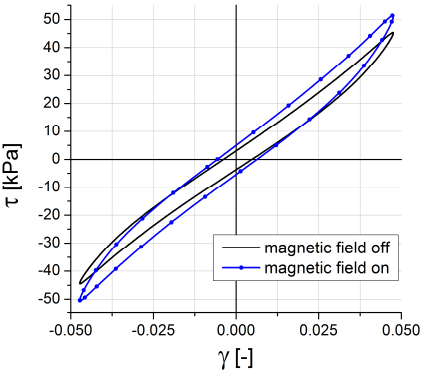

Fig. 4. Exemplary hysteresis loops for isotropic MRE.

4. Results and conclusions

- Fabricated MRE subjected to fatigue tests can easily withstand over 1.2×10^6 cycles of load – their mechanical properties stabilise in time.
- The energy dissipated by these materials can be increased by magnetic field up to 46.5%.
- The manufactured MRE show great potential for applications such as damping of vibrations.

References

[1] Stewart, W.M., Ginder, J.M., Elie, L.D., Nichols, M.E., Method and apparatus for reducing brake shudder, US Patent No. 5816587, 1998.

[2] Barvosa-Carter, W., Johnson, N.L., Browne, A.L., Reversibly expandable energy absorbing assembly utilizing actively controlled and engineered materials for impact management and methods for operating the same, US Patent No. 7140478 B2, 2006.

[3] Zhang, W., Gong, X.L., Jiang, W.Q., Fan, Y.C., Investigation of the durability of anisotropic magnetorheological elastomers based on mixed rubber, Smart Mater. Struct., **19** 085008, 2010.

[4] Kaleta, J., Królewicz, M., Lewandowski, D., Magnetomechanical properties of anisotropic and isotropic magnetorheological composites with thermoplastic elastomer matrices, Smart Mater. Struct., **20** 085006, 2011.

30th DANUBIA-ADRIA
Symposium on Advances in Experimental Mechanics
September 25-28, 2013 - Primošten, Croatia

3B38 028

CORRELATION OF RHEOLOGICAL AND MECHANICAL PROPERTIES OF THERMOPLASTIC AFTER DEGRADATION

Tatiana Liptáková[1], Ján Greguš[2], Monika Halamová[3], Anna Tomiczek[4]

[1-3] University of Žilina, Faculty of Material Engineering, Univerzitná1, 010 26 Žilina, Slovakia
E-mail: tatiana.liptakova@fstroj.uniza.sk, jan.gregus1@gmail.com, halamovam@fstroj.utc.sk

[4]Eng. Faculty of Mechanical Engineering of the Silesian University of Technology, Gliwice, Poland,. E-mail: (Anna.Tomiczek@polsl.pl

1. Introduction

The plastics versatility makes them suitable for a whole range of construction applications especially the most common thermoplastics polyethylene (PE) and polypropylene (PP) [1]. Many of plastic devices and components are expected long durability and high reliability. Degradation processes in polymers can evoke macromolecular splitting, crosslinking, monomer production, low molecular weight substances, change of substituents etc. and thus change their utilize properties [2,3]. The suggested method of studying changes in material by measurement of chosen rheological parameters takes easy specimen preparation and the measurement conditions can be exactly repeated. The changes can be measured as the response of the material to deformation by periodic forces (during forced vibration or small-amplitude oscillatory shear) [4,5,6].

It is very important to search correlation between rheological and mechanical properties because they are important for definition of utilize properties of products and measurements of mechanical properties require difficult sample preparation and adequate quantity of material.

2. Experiments

Rheological and mechanical properties of thermoplastic polypropylene, before and after exposure in chemical environment and UV box, were measured. Using the Frequency sweep test, changes of viscoelastic properties of polymer were determined with respect to their molecular structure, average molar mass and their behavior in thermoplastic processes. As experimental material polypropylene samples were used and subjected to influence of n-hexane solution for period of 3 months. Exposure in the UV box lasts for 500 and 1000 hours. Measurements were performed using oscillating Physica Rheometer MCR 301 and carried out at the temperature of 160 °. Tensile test (LabTest 5.20 ST) and hardness measurement (Shore D) were used for mechanical properties evaluation.

3. Experimental results

Degradation process resulted in changes of complex dynamic viscosity, storage and loss modulus, changes in molar mass and its distribution. During the test stress and strain are not in phase, the strain delays behind the stress by a phase angle. If the oscillatory shear is sinusoidal, then ***shear stress*** is equal to

$$\tau(t) = \tau_0 \cdot e^{i\omega t} = \tau_0(\cos \omega t + i \cdot \sin \omega t) \qquad (1)$$

τ_0 - stress amplitude, ω - angular frequency, t - time and $i = \sqrt{-1}$.

The first G′ is in phase with strain, and the second G″ is out of phase with strain with angle δ. Therefore, two dynamic moduli can be defined as

$$G' = \frac{\tau_0}{\gamma_0}\cos\delta \quad (2) \quad \text{and} \quad G'' = \frac{\tau_0}{\gamma_0}\sin\delta \quad (3)$$

G′ is called ***storage modulus (***represents the elastic behavior) and G″ is called ***loss modulus*** represents the viscous behavior. tg δ - ***damping factor*** reveals the ratio of the viscous and the elastic portion of the viscoelastic deformation behavior. Idealelastic behavior is specified in term of δ = 0 ° as tg δ = 0 and the idealviscous behavior can be expressed by δ = 90 ° as tg δ = ∞. Changes of the measured mechanical properties were determined too.

The values of complex viscosity η^* at the angular frequency 0.05 rad.s^{-1}, modulus in the cross point ***G,*** hardness and tensile strength R_m after different time of polypropylene exposure in hexane and UV box are shown in Tab. 1.

Environment and time	G [MPa]	η [Pa.s]	Hardn. [HD]	R_m [MPa]
No exposure	$2.34.10^4$	$1.1.10^5$	73,9	32,57
Hexane 3 month	$3,45.10^4$	$9,6.10^3$	69	28,92
UV box 500 hours	$2,32.10^4$	$1.0.10^5$	73,3	37,32
UV box 1000 hours	$2,3.10^4$	$8.6.10^4$	75,2	35,56

Tab. 1 Changes of the measured parameters after degradation

Fig. 1. shows course of the internal damping and complex viscosity of PP after 0, 500 and 1000 hours in the UV box. In Fig. 2. there are the same parameters but measured after 3 month in hexane.

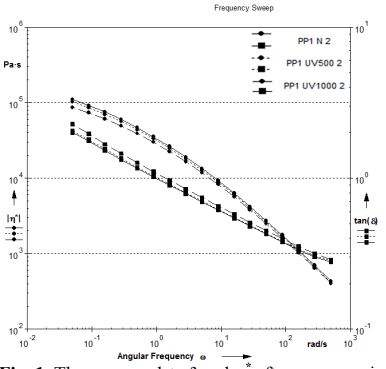

Fig. 1. The measured ***tg δ*** and η^* after exposure in UV box.

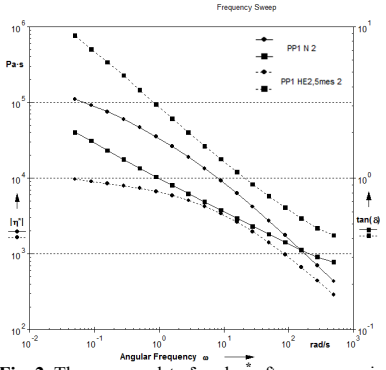

Fig. 2. The measured ***tg δ*** and η^* after exposure in hexane.

4. Conclusions

- Degradation of thermoplastic polymer PP changes after exposure in hexane and UV box rheological properties and mechanical properties in a different way.
- The value for moduli in cross point after exposure in hexane increases (PP is more plastic), complex viscosity decreases as well as hardness and tensile stress. It means the polymer chains are broken, average molar mass drops.
- Degradation of PP in UV box is more complicated. Values of moduli are changed very little and viscosity dropped after 1000 hours exposition and in opposite, hardness increased. It means that degradation in UV box causes crosslinking in surface layers and under the surface the PP chains are broken. It explains discrepancy between viscosity and mechanical properties.
- It is supposed, that the next investigation in this area will confirm that rheological measurements are a very good resource for determining of thermoplastics degradation measure.

Acknowledgements

The research was supported partially by Scientific Grant Agency of Ministry of Education, Science and Sport of Slovak Republic and Slovak Academy of Science grant VEGA No. 1/0066/11

References

[1] Liptáková T., Alexy P., Gondár, E., Khunová V.: *Polymer construction materials (in. Slovak)*, EDIS University of Žilina, 2012.
[2] Ravva A.: *Principles of Polymer Chemistry*, 2nd edition, Plenum Publishers, USA, 2000.
[3] Woishnis W., Ebnesajjad S.: *Chemical Resistance of Polymers*, Elsevier, 2012.
[4] Mezger, T.G. *The rheology handbook*. 2nd ed. Hannover: Vincentz Network, 2006.
[5] Kohavec J.: *Rheology of Polymer Systems*, Wiley-VCH, Praha, 2000.
[6] Farrar D.F., Rose J. *Rheological properties of PMMA bone cements during curing*. In Biomaterials, vol. 22, no. 22, 2001.

30th DANUBIA-ADRIA
Symposium on Advances in Experimental Mechanics
September 25-28, 2013 - Primošten, Croatia

3B39 138

DRAPING SIMULATION OF WOVEN FABRICS FOR A FIRE BOTTLE KEEL

Schimmel C.M., Cakmak U.D., Major Z.

Institute for Polymer Product Engineering, Johannes Kepler University Linz, Altenberger Str. 69, 4040 Linz, AUSTRIA.

E-mails: christoph.schimmel@jku.at, umut.cakmak@jku.at, zoltan.major@jku.at,

1. Introduction

One crucial step of designing woven reinforced plastics is the unknown actual fibre orientation after draping (forming) them into a mould. Hence, mechanical analyses are based on the idealized theoretical fibre orientation. For 3D-curved parts this issue is even more prone. The objective of this work is to simulate the draping process of carbon woven fabrics on 3D-curved tools for efficient and mechanically reliable designed products. A methodology, which combines numerical and experimental procedures, is introduced to shorten the product's time to market. The study was based on the simulation of a Fire Bottle Keel for a Formula 1 car. This part was already produced and used, and so a huge experience in both the mechanical performance and the optimized manufacturing was available. However, numerical simulation had not been considered.

2. Draping Simulation

A kinematic simulation tool (FiberSIM, Siemens PLM, Linz, A) was utilized to simulate the draping process. From that the fibre orientation dependent (0°/90° and +/-45°) flat patterns, which are necessary to manufacture the part, have been determined. In addition the real fibre orientation could be further transferred to the numerical structural analyses (e.g., FEM) in order to consider the actual orientation dependent mechanical behaviour. One major simulation step involves the definition of the region on the curved part for the patches of woven fabrics (i.e., the woven fabric's material width exceeded and so the part had to be build up in patches). Different variations were considered and simulated for these patches.

To determine the optimal drapeability of the patches, the following procedure was implemented in the design process:

- **Geometry:** create the geometry and net-boundaries (if necessary an extended boundary can also be defined)
- **Start-point of draping:** create the origins, zero directions and define the fibre orientation
- **Simulation:** iterative variation of the above mentioned in order to get the optimized draping process
- **Darts for lifted regions:** create darts (slit and V-shape) and change the origin for further optimization
- **Flat pattern:** create the flat patterns and check the producibility.

Using this procedure the whole layup of the Fire Bottle Keel was simulated and the optimized draping strategy (start-points, patches, etc.) was determined including the flat patterns for manufacturing the part.

3. Experimental approach

The flat patterns were used to produce the numerical optimized part and the simulated fibre orientations were compared to the actual orientations. The prepreg flat patterns were cut out of two different thick materials (see Tab 1) by a Cutter (LR-1600, Zünd, Altstätten, CH).The part was laminated with this two materials symmetrically. Moreover two thicknesses of the material were used, since the thin material's mesh was smaller and therefore required to seal the part. Seven encapsulating plies (four of the thick material, three of the thin material) with several reinforcement plies were used for hand laminating. The plies were laminated on a core.

Tab. 1. Materials used for laminating

Material	Name	Description	Manufactured
M1	MTM49-3/CF5700-42% RW	Atlas woven	CYTEC Industries, NJ, USA
M2	MTM49-3/CF4534-40% RW	Twill woven	CYTEC Industries, NJ, USA

Finally the part was wrapped in a silicon hull to enhance the surface quality of the finished part and then put in to a vacuum bag. After baking in an autoclave at 120°C for four hours the core was removed.

4. Exemplary Results

Here only the results of two regions of the part will be presented. Based on the bottom ply a case study to optimize the origin and the start-point of the draping process were done (see Fig 1). Three origins, one on the top of the ply, one in the middle and one at the end were simulated

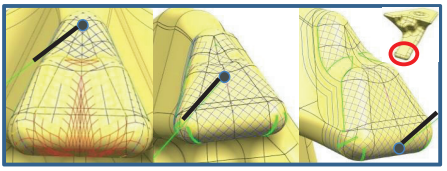

Fig. 1. Bottom ply case study; *origin* (point) and *zero direction* (line) at *top*, *middle* and *end* position (from left to right).

In Fig.1 the red area shows the lifting of the woven, the yellow area indicates a warning and the blue area represents an ideal draped woven fabric. Darts (green lines in Fig. 1) are also necessary in order to reduce lifting and fibre orientation deviation. The simulation showed that the optimal location for the start-point of draping is the end of the bottom region. The next step was to optimize the origins for 0°/90° and +/-45° fibre orientations (see Fig 2).

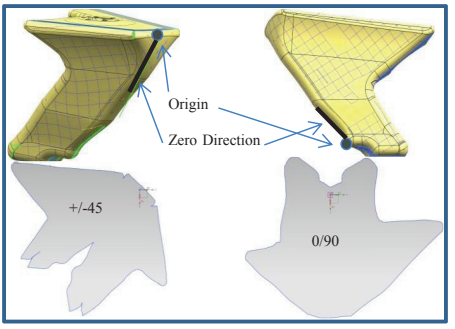

Fig. 2. Front Ply 0°/90° vs. +/- 45°

It was observed that for the same region different fibre orientated fabrics have a different optimal origin and therefore different flat pattern geometries. In this context optimal means no lifting of the fabric after draping and low fibre orientation deviation. According to the performed draping simulation the flat pattern were generated and produced (see Fig 3) with a Cutter.

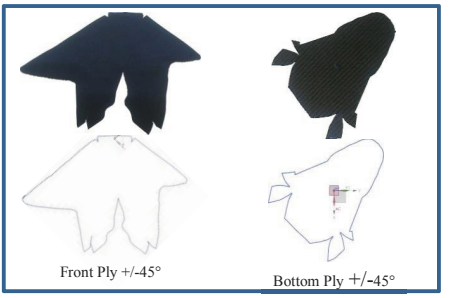

Fig. 3. Simulated flat pattern compared to real flat pattern

Figure 4 shows the hand laminated part and it can be concluded that the simulated draping process works good in manufacturing.

Fig. 4. The finished hand laminated Fire Bottle Keel

5. Conclusions

Kinematic simulation of the draping process reduces time and cost to get the optimal strategy (start point, patch geometries, etc.) in manufacturing the part. This study showed that the more the geometry is curved the higher will be the experimental effort to define the draping process. Simulation helps to analyse different variation virtually and the results of this work indicates that a good agreement to the reality can be achieved.

Acknowledgements

This project was supported by Peak Technology (Holzhausen, A). The authors greatly appreciate the cooperation with Peak Technology in the framework of a "FFG-Innovationsscheck".

References

C. Cherif, Textile Werkstoffe für den Leichtbau, Chapter 15: Modellierung und Simulation, Springer, 2011

T. May-Plumlee, J Eischen, N. Kenkare, and P. Pandurangan, Evaluating 3D Drape Simulations: Methods and Metrics, College of Textiles, North Carolina State University, 2003

30th DANUBIA-ADRIA
Symposium on Advances in Experimental Mechanics
September 25-28, 2013 - Primošten, Croatia

4A01 119

ADVANCES IN EXPERIMENTAL MECHANICS BY THE SYNERGETIC COMBINATION OF FULL–FIELD MEASUREMENT TECHNIQUES AND COMPUTATIONAL TOOLS

Gabriella Bolzon

Politecnico di Milano, Department of Civil and Environmental Engineering, Piazza Leonardo da Vinci 32, 20133 Milano, ITALIA. E-mail: gabriella.bolzon@polimi.it

1. Introduction

The continuous improvement of full–field measurement techniques has fostered the development of mechanical testing procedures of increasing complexity, which can be performed at smaller and smaller scales, in non–destructive manner even on final components [1] and on heterogeneous material samples [2].

Contemporarily, the design of the experiments and the interpretation of the acquired data benefit of the realism of available numerical models and of the enhanced effectiveness of several computing tools [3].

This contribution summarizes recent experiences relevant to the synergetic coupling of experimental and computational mechanics.

2. Methods

Different techniques based e.g. on microscopy (Fig. 1), digital image correlation (Fig. 2), laser profilometry (Fig. 3) can be exploited to recover the geometry of the imprint left on the material surface by hardness or instrumented indentation tests [1], the whole displacement field over the surface of heterogeneous material specimens [2], the out–of–plane components of inflated membranes [4].

These pieces of information constitute the input data of inverse analysis procedures exploited to diagnostic purposes, to recover the parameters governing the mechanical response of material samples as the result of the minimization of the discrepancy between the available measurements and the output of the simulated experiments, often involving non-linear phenomena like large inelastic deformation and fracture.

The related large computational burden, otherwise usually prohibitive for repetitive use in industrial environment, can be alleviated by proper model reduction techniques [3].

3. Results

The graphs in Fig. 1 reproduce the profile of the residual deformation left on the surface of pipeline steel by Rockwell indentation performed at 2 kN maximum force. The topography is obtained by a portable microscope with variable focal distance, which can be exploited also for in–situ diagnostic analyses.

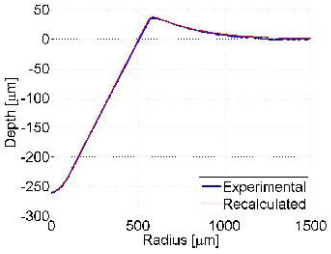

Fig. 1. Experimental and numerical profile of the imprint left on steel by Rockwell indentation [1].

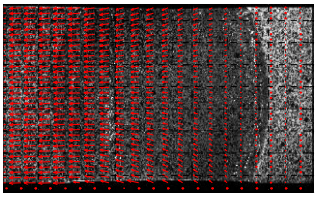

Fig. 2. The displacement field in an heterogeneous material specimen subjected to tensile test [2].

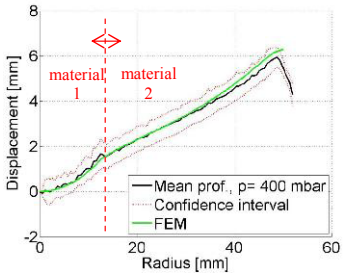

Fig. 3. Mean profile of an inflated heterogeneous membrane: experimental and numerical results.

The experiment is simulated by a FE model, which accounts for the large displacements and strains that develop under the indenter tip. The elastic–plastic constitutive parameters recovered by the comparison of numerical and experimental results permit to reproduce the imprint mapping with the accuracy shown in Fig. 1.

The nominal values of the identified material properties, listed in Table 1, correspond to those resulting from classical uniaxial tensile test; see [1] for details.

Full–field measurements can be exploited for the mechanical characterization of heterogeneous specimens, shown for instance in Fig. 2. The picture visualizes the aluminum laminate inclusion, which is embedded in a paperboard composite in the cap opening area of beverage packaging. The represented displacement distribution, obtained by digital image correlation, is exploited for the identification of the material properties, inferred from the numerical simulation of the test [2].

The calibrated mechanical model of the heterogeneous material system is validated on the basis of independent measurements, concerning inflation test performed according to [4]: a flat sample of the paperboard composite is placed over the circular hole (10 cm diameter) of a pressure vessel and fixed by an air proof flange; the change of geometry of the inflated membrane is monitored by a rotating laser blade, which returns quantitative information on the out–of–plane displacements.

The mean profile of one specimen tested at 400 mbar (40 kPa) pressure is shown in Fig. 3 with the corresponding confidence interval. Data are noisy due to the reflective properties of the surface of the packaging material but the presence of the aluminum laminate inclusion is clearly evidenced. The average measurements compare well with the output of the numerical simulation of the experiment.

	Elastic modulus (GPa)	Yield limit (MPa)	Tensile strength (MPa)
Indentation	193 (±34)	444 (±34)	569 (±1)
Tensile test	191 (±32)	431 (±20)	541 (±9)

Tab. 1. Mechanical parameters (nominal values) recovered by indentation and tensile test [1].

4. Remarks

The coupling of complementary investigation tools in experimental and computational mechanics has twofold implications:

- the design and the interpretation of the results of sophisticated testing procedures can be supported by appropriate simulation models;
- modeling techniques can be validated on the basis of their capability of reproducing full–field measurements.

These circumstances foster the continuous improvement of both experimental and numerical methodologies supporting the diagnostic analysis of materials and structures.

Acknowledgements

The research activities summarized in the present contribution have been carried out with the collaboration and the financial support of the companies Venezia Tecnologie (Venezia, Italy) and Tetra Pak Carton Ambient (Modena, Italy).

References

[1] Bolzon, G., Molinas, B., Talassi, M., Mechanical characterisation of metals by indentation tests: an experimental verification study for on-site applications, Strain, 48, 2012, pp. 517–527.

[2] Bolzon, G., Buljak, V., Zappa, E., Characterization of fracture properties of thin aluminum inclusions embedded in anisotropic laminate composites, Fratt. Integr. Strutt., **19**, 2012, pp. 20–28.

[3] Bolzon, G., Buljak, V., An effective computational tool for parametric studies and identification problems in materials mechanics, Comput. Mech., **48**, 2011, pp. 675–687.

[4] Ageno, M., Bolzon, G., Maier, G., An inverse analysis procedure for the material parameter identification of elastic–plastic free–standing foils. Struct. Multidisc. Optim., **38**, 2009, 229–243.

30th DANUBIA-ADRIA
Symposium on Advances in Experimental Mechanics
September 25-28, 2013 - Primošten, Croatia

4A02 093

POSSIBILITY OF APPLICATION OF THE SIMULATION BASED RELIABILITY ASSESSMENT METHOD IN MODELING OF STRUCTURES

Petr Kesl[1], FrantišekPlánička[1]

[1] University of West Bohemia in Pilsen, Faculty od Applied Sciences, Department of Mechanics, Univerzitní 8, 306 14 Plzeň, CZECH REPUBLIC. E-mail: pkesl@kme.zcu.cz, planicka@kme.zcu.cz

1. Introduction

The Simulation Based Reliability Assessment SBRA Method is a probabilistic method using the Monte Carlo simulation. Substance of that method consists in repeated calculations of relatively simple equations, where entering variables (dimensions of the body, mechanical properties, loads, etc.) can be constant or defined by histograms, respectively. Mentioned ahead SBRA Method using Monte Carlo Simulation is a significant tool for probability of failure of components or structures determination. Used relationships are simple, very often known from Mechanics of Materials, but a clearly defined set of variable quantities is necessary.

Loads are determined by so called Load Duration Curves which quantify the concrete loads in time. For the increasing of the simulation speed, the incoming variable quantities are converted into histograms which can be easily stored in databases. There is a sure possibility for the designer to assume some degree of randomness and to choose causes when the random behaviour of incoming quantities are of a great importance or when they can be neglected from point of view structure behaviour.

Modeling of engineering problems can be very often a way to solve them. It is generally based on the conditions

$$(\pi_i)_S = (\pi_i)_M , \quad i = 1, 2, ..., m \ (1)$$

where π_i are so called dimensionless parameters for structure (subscript S) and model (sub. M)

$$\pi = x_1^{e_1} \ x_2^{e_2} \ .....x_n^e \qquad (2)$$

if the solved problem depends on n variables x_i (expressing physical, geometrical etc. quantities).

$m = n - r$ represents number of independent π term, r is rank of so called dimensional matrix, see [2]. There is assumed that solved problem is described by n physical quantities x_i, $i = 1, 2, .., n$ containing k so called primary quantities with primary units $\lfloor L_j \rfloor$, $j = 1, 2, .., k$. The necessary procedure in described in [2].

2. Experimental results

Composite material was used to simulate deflection w_S of the steel beam Fig. 1 of dimensions stated in Tab. 1.

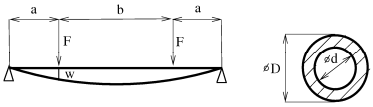

Fig. 1. Simply supported beam.

	l	*a*	*b*	*d*	*D*
Beam	1000	375	250	22,08	37,9
Model	800	300	200	17,664	30,32

Tab. 1. Dimensions of the steel beam and of the composite model in *mm*

Young modulus of steel was $E_S = 2 \cdot 10^5 \ MPa$ and of composite material $E_M = 5{,}61 \cdot 10^4 \ MPa$. To solve the problem the deflection w is a function of following variables: $l = 2a + b, a, b, D, d$ (geometry quantities), loading force F, property of material E. Dimensions of the model (Tab. 1) were determined using modelling rules (1).

The load of the model $F_M = 2kN$ and corresponding experimentally determined deflection was $w_M = 17{,}5\,mm$. Using rules of the model simulation the loading force of steel beam was determined as $F_S = 1{,}12 \cdot 10^7\ kN$ and the corresponding defection was $w_S = w_M\, l_S = 21{,}87\,mm$.

3. SBRA method application

Deflections of steel beam and composite model were determined using SBRA Method. As an input were taken into account following random variable quantities: dimensions of the body and corresponding geometry quantities, Young´s modulus of elasticity, and loading. Gauss´s distributive functions for mentioned above quantities were used.

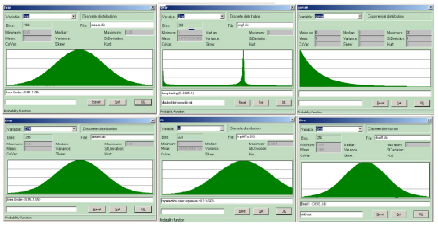

Fig. 2. General distribution functions used for calculations.

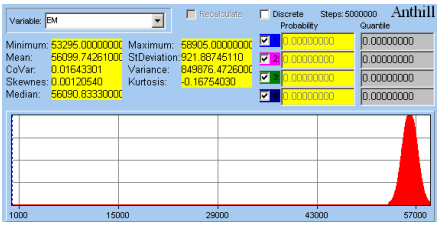

Fig. 3. Gauss´s limited distribution function of Young´s modulus of elasticity E_M of composite.

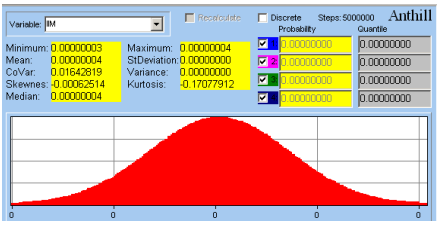

Fig. 4. The distribution function of second moment of area I_M of the model.

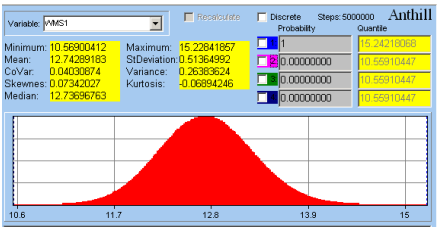

Fig. 5. The distribution function of deflection w_M of the model.

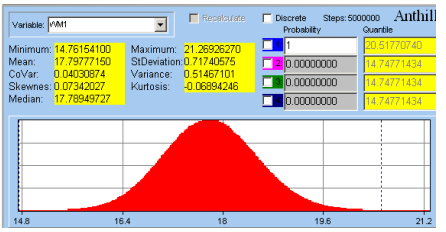

Fig. 6. The distribution function of deflection w_S of the steel beam.

4. Conclusion

Obtained results show very good correspondence between deflections w_S of the steel beam and its model w_M. It gives a sure possibility of application of the SBRA Method in the case of modelling of technical problems, but there is necessary more verification for generalization of that conclusion.

Acknowledgements

The research work was supported by the Project SGS-2013-036.

References

[1] Plánička, F., Šolc, M., Marek, P. From Partial Factors Design to the SBRA Probabilistic Method, Acta Mechanica Slovaca Vol. 15, No 2/2011. pPp. 22-27

[2] Plánička, F., Krystek, J. Dimensional Analysis and Modelling in Mechanics of Materials, Proceedings of 28th Danubia-Adria Symposium on Advances in Experimental Mechanics 2011, Siófok, Hungary. Pp. 229-230.

[3] http://www.sbra.anthil.com/lit/publications.html

30th DANUBIA-ADRIA
Symposium on Advances in Experimental Mechanics
September 25-28, 2013 - Primošten, Croatia

4A03 014

THE MECHANICAL RESPONSE OF MARBLE EPISTYLES STUDIED WITH THE AID OF INNOVATIVE EXPERIMENTAL TECHNIQUES

Stavros K. Kourkoulis[1], Ermioni D. Pasiou[1], Ilias Stavrakas[2], George Hloupis[2], Dimos Triantis[2]

[1] National Technical University of Athens, Dept. of Mechanics, Laboratory of Testing and Materials, Theocaris Building, Zografou Campus, 157 73, Athens, GREECE. E-mail: stakkour@central.ntua.gr

[2] Technological Educational Institution of Athens, Dept. of Electronics, Laboratory of Electrical Characterization of Materials and Electronic Devices, 122 10, Athens, GREECE. E-mail: triantis@teiath.gr

1. Introduction

The mechanical response of stone-mortar-metal complexes concerns engineers working for restoration projects of ancient monuments. In case of excessive loading fractures are expected to start from the interior of the stone volume around the corners of the grooves accommodating the metallic element. Obtaining data from these regions is imperative, in order to gain overview of the mechanisms leading to premature fracture of the stone body rather than of the metallic reinforcing elements.

Traditional experimental techniques (like strain gauges) or even some modern ones (like the Digital Image Correlation - DIC) provide data pumped from the outer surface of the specimens while the internal fracture mechanisms, are activated well before any visible phenomena appear on the surface. It is thus necessary to devise experimental systems which provide data directly from the interior of the specimens. Such systems are mainly based on detection of elastic waves (Acoustic Emissions), the electrical resistance variation of the specimen etc. The main limitation is that their data are rather quantitative while a direct correlation with the respective data of traditional techniques is not as yet available.

In this study a combined experimental arrangement is described providing data from the interior of a marble-cement-titanium complex. The adopted techniques involve the detection of weak electrical current emissions (Pressure Stimulated Currents-PSC) [1] (a) and Acoustic Emission (AE) events (b), modern Digital Image Correlation (DIC) (c) and traditional clip-gauge extensometers (d).

2. Experimental study

2.1 The materials and the specimens

The specimens were constructed from Dionysos marble due to the similarity of its properties with the respective ones of the authentic material of the Parthenon Temple [2]. The specimens simulated epistyles of ancient stone monuments mutually connected using a metallic "I-shaped" connector and suitable mortar. They were prepared by experienced technicians of the Parthenon work-site: A groove of depth equal to 7 cm was sculptured in two marble blocks (Fig.1a) and a titanium connector was placed in the groove which was then filled with liquid mortar (Fig.1b). The mortar consisted of one part of white cement and three parts of silica sand. Before tested the specimens were cured for at least 28 days.

2.2 Experimental procedure and results

The specimens were subjected to shear with the aid of a very stiff 250 kN INSTRON servohydraulic frame. Suitable gripping devices were prepared to limit, to the minimum possible, any parasitic effects, in the form of bending or torsional moments (due to inherent asymmetries of the specimens) (Fig.1c).

To apply the PSC technique a pair of electrodes were attached on the front surface of the specimens close to the area where marble's fracture is expected. To measure the electrical current the Keithley 6517A electrometer was used resolving currents as low as 0.1 fA. In addition, an 8-channel AE acquisition system (Physical Acoustics) was used to detect the AE events. For the DIC technique a novel 3D-system by LIMESS was used. Finally the relative displacement of the two blocks was measured using two clip-gauge extensometers.

The time variation of the PSC and the load induced are shown in Fig.1d. An abrupt load drop was recorded at time t_f=1000s approximately implying a change on the mechanical behavior of the system. The study of the temporal behavior of the PSC shows that a gradual reduction of the PSC is recorded before the load drop marking the onset of significant damages in the bulk of the specimen [1].

After performing 3D-location analysis of the AE data, it was seen that, until the instance of the load drop, the AE events recorded were limited. A few seconds before the load drop occurred, a rapid increase of the AE events from the interface of the two blocks was recorded (Fig.1d). Along the same line the horizontal displacement of the mortar, in the immediate vicinity of the same interface, recorded by the DIC system is plotted in Fig.1e. It is seen that, while the two blocks are initially moving as a rigid body, at the critical instance, detected by the PSC/AE systems, they start moving almost independently. The above, support the opinion that the load drop is related to the failure of the mortar, in the region of the specimens' blocks interface.

3. Discussion and conclusions

Detailed analysis of all the data gathered from this combined "attack" indicates that not only the mortar's failure but also the fracture of the marble volume itself follows after similar characteristics of the PSC and AE records well before anything is detected by either the clip-gauges or the DIC system. Fig.1f shows the temporal development of the AE events around the groove's corners. The events that originated from the critical location (pink line), where fracture occurred, start exceeding the ones from other regions exactly when a slope change of the load-time curve appears, indicating fracture initiation. In addition a clear increase of the AE rate is observed at the loads' peak value.

Although the laboratory reproduction of shear is a difficult task, the present protocol provided some rather interesting conclusions. Specifically, the fracture onset was found to be directly related to a PSC drop while both the PSC and the AE records are in excellent mutual agreement and also to the DIC data. It is thus indicated that the techniques adopted can be used as flexible tools for spatially monitoring the evolution of mechanical damage.

Acknowledgements

This research has been co-financed by the European Social Fund (ESF) and Greek national funds through the Operational Program "Education and Lifelong Learning" of the National Strategic Reference Framework - Research Funding Program: Heracleitus II. Investing in knowledge society through the ESF.

References

[1] Stavrakas, I., Anastasiadis, C., Triantis, D., Vallianatos, F., Natural Hazards and Earth System Sciences, **3**, 2003, pp. 243-247.

[2] Exadaktylos, G.E., Vardoulakis, I., Kourkoulis, S.K., Int. J. Solids & Structures, **38**, 2001, pp. 4119-4145.

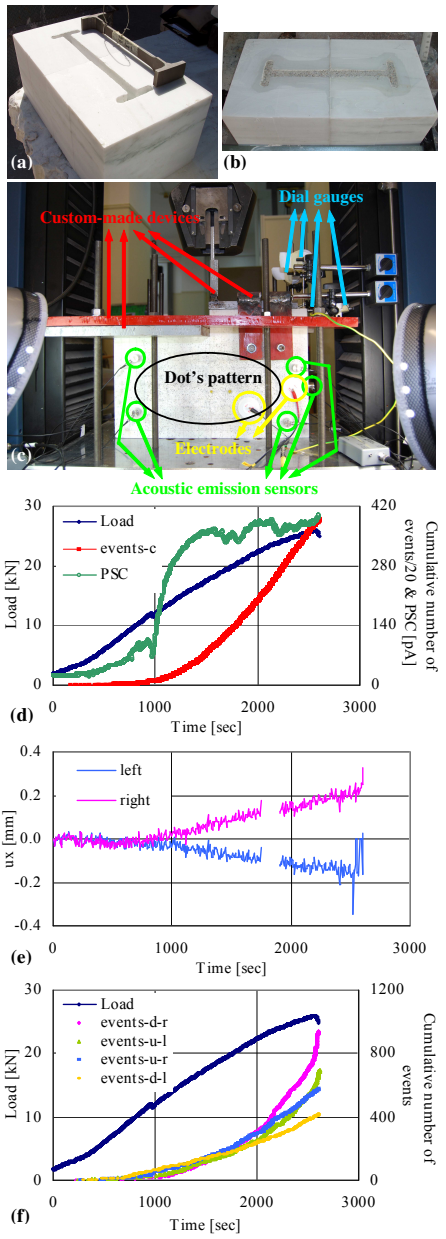

Fig. 1. (a) A typical specimen during the construction and (b) after the groove was filled. (c) An overview of the experimental set-up. (d) The variation of the load, PSC and acoustic events versus time. (e) The horizontal displacements of the mortar's central portion versus time. (f) Load and acoustic events from the regions around the groove's corners versus time.

30th DANUBIA-ADRIA
Symposium on Advances in Experimental Mechanics
September 25-28, 2013 - Primošten, Croatia

4A04 044

PRACTICAL FIRE DESIGN OF PARTIALLY ENCASED COMPOSITE STEEL-CONCRETE COLUMNS

Sadaoui[1], S. Illouli[2]

University of Tizi-ouzou, Faculty of Construction Engineering, Tizi-ouzou, 15000, Algeria. E-mails: a_sadaoui@yahoo.com[1] , saidillouli@yahoo.fr[2]

1. Introduction

The use of partially encased composite steel-concrete structural elements has many advantages such as; reduced overall dimensions, ease of prefabrication and erection, increased fire resistance, good energy dissipation and higher rigidity for use in lateral-load resisting systems. Due to the existence of substantial temperature gradients, the theoretical evaluation of the fire resistance of such sections is very complex, and is not practical for everyday design. To this end, the Eurocode 4 in its part 1-2 [1] proposes two methods to determine the fire resistance of composites columns subject to a standard ISO fire. The first uses tabulated values previously established for the most common cross-sections based on experimental and empirical results. Often of a quick and easy application, its results are generally very conservative as it predicts very high values for the required reinforcement.

The second method which had been at the origin developed by Jungbluth [2], is based on simplified analytical formulas for individual structural elements. Its principle is to calculate the ultimate load carrying capacity of the element by dividing the section into different zones. The material properties for each zone are modified using reduction factors, which depend on the average temperature in the zone. These temperatures are determined by considering the section to be exposed to an ISO fire for the required fire resistance period. For partially encased profiles, this method is detailed in EC4 1-2 Appendix G. The apparent simplicity of this method is indeed relatively superficial because of more tasks which are involved by handle calculation when especially the compression load applied to the column is eccentric. In fact, The Eurocode 4 unfactored eccentric load strength was based on the cross-section and column axial load bending moment strength interaction diagrams, which needs in the first step to be calculated. An approximate five-points M-N diagram is usually considered for bending applied about the minor axis of the partially encased steel-section. In the second step, the approximated interaction curve is used in the design procedure using a step-by-step to determine finally by doing some iterations the ultimate eccentric resistance for the whole column.

The aim of the present investigation is to present an efficient simple and practical method for the calculation of the fire resistance of an encased eccentric composite steel-concrete subjected to an eccentric loading.

2. Proposed practical design method

A practical approach based on the Campus Massonnet formula [3] initially elaborated for steel columns can be adapted for partially encased composite steel-concrete columns. The buckling strength of a composite steel concrete column eccentrically loaded can be solely formulated as:

$$N_{f_i,Rd,e} = \chi_e . N_{fi,Rd} \qquad (1)$$

where $N_{fi,Rd}$ is the buckling resistance or the resistance in axial compression of the column in reference to the eccentricity e = 0 of the applied load and χ_e is an equivalent correction buckling coefficient depending on the eccentricity, and given as:

$$\chi_e = \frac{\chi_0(\bar{\lambda})}{1 + \dfrac{k_1 . e}{h\left(\dfrac{1}{\chi_0(\bar{\lambda})} - 0.3\bar{\lambda}^2\right)}} \qquad (2)$$

where χ_0 and $\bar{\lambda}$ are respectively the reduction coefficient and the slenderness ratio of the column at ambiant temperture as defined in in EC4-1-1.

The parameter k_1 is related to the plastic eccentricity and taken equal to with $k_1 = 4$. However, the application point of the eccentric load should remain inside the composite cross-section of the column accordingly to the strong or weak axis which is considered in the calculation.

3. Application

Figure 1 shows an eccentric pin-ended column with a partially encased composite cross-section made of an HD 400x400x187 steel profile [2,4]. It is an interior column on the ground floor of a five storey office building. The column is heated on all four sides and subjected to a standard fire type ISO834.The storey height is 3.75 meters, and the applied load is assumed to act at 98 mm from the weak axis (z).

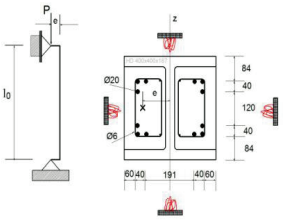

Fig. 1 Geometric details of an eccentric loaded column

The results for a class of resistance time R60 (t=60 min) give: $\overline{\lambda} = 0.382 \rightarrow \chi_0 = 0.9066$, $\chi_e = 0.4658 \rightarrow N_{fi,Rd,e} = 2619.5$ kN. The EC4 gives a value of 2992 kN which is 15% higher. It is apparent clearly that the present method yields good results and involves less steps than the EC4 method, and hence much easier to use in a computer code. In addition, the effects of some of the most influential parameters on the behaviour of the column; such as the applied load, the reinforcement cover, the slenderness ratio and eccentricity, are investigated. Assuming that the fire resistance is a linear function of the level of load, some partial obtained results are shown on the following figures.

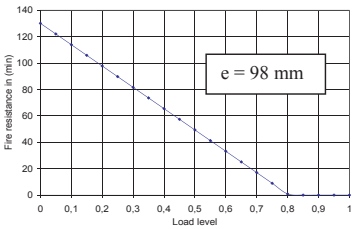

Fig.2 Effect of load level on fire resistance

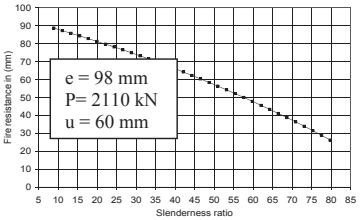

Fig. 3 Effect of slenderness on fire resistance

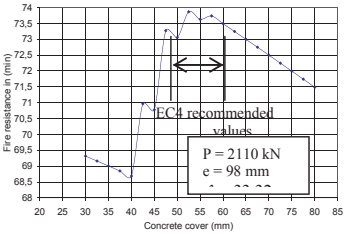

Fig. 4: Effect of concrete cover on fire resistance

4. Conclusion

A practical method for the design for fire resistance of a partially encased composite steel-concrete column was proposed. The method is based on the Campus-Massonet criteria, which was developed initially for steel columns with combined compression and bending. The buckling resistance of eccentrically loaded columns is expressed by a simple formula as a function of an equivalent buckling coefficient taking into account the amount eccentricity. The method combines accuracy, efficiency and convenience obviating the need of M-N interaction diagrams and long iteration process necessary in the EC4 procedure.

References

[1] Eurocode 4: Design of composite steel and concrete structures- Part 1-2, general rules Structural fire design, BS EN 1994-1-2, 2005.

[2] Jungbluth O., Optimierte Verbundbauteile, Stahlbau Handbuch 1, Stahlbeau-Verlags-Gmbh, Köeln, 1982.

[3] Dotreppe J.C., Franssen J.M., Vanderzeypen Y., Dimensionnement des colonnes en béton armé en considérant le problème de la résistance au feu, Rapport de recherche, Univ. Liege, 1995.

[4] Mathieu J., Application de l'EC4, poteau mixte partiellement enrobé sous charge axiale centrée. Revue CM, EC4-MIX 1-01, N1, 2001.

30th DANUBIA-ADRIA
Symposium on Advances in Experimental Mechanics
September 25-28, 2013 - Primošten, Croatia

4A05 002

AN INNOVATIVE EXPERIMENTAL METHOD FOR MEASURING YOUNG'S MODULUS OF THIN FLEXIBLE MULTI-LAYERED MATERIALS (OWN-WEIGHT LARGE DEFORMATION CANTILEVER METHOD)

A.Ohtsuki [1]

[1] Meijo University, Faculty of Science and Technology, Dept. of Mechanical Engineering, 1-501 Shiogamaguchi, Tempaku-ku, Nogoya, Aichi, 468-8502, JAPAN. E-mail: ohtsuki@meijo-u.ac.jp

1. Introduction

In recent years, flexible multi-layered materials with very high performance are widely used to establish cost-effective processing with regard to long-term performance. Therefore, Young's modulus of these flexible materials is very important to predict large deformation. This paper describes a new testing method (*Own-Weight Cantilever Method*) based on a nonlinear large deformation theory. Analytical solutions are derived by using Bessel Functions. By using this method, Young's modulus of each layer in a thin and long flexible multi-layered material can be easily obtained by just measuring the horizontal displacement or the vertical displacement at the free end of the cantilever.

Besides the "*Own-Weight Large Deformation Multi-layered Cantilever Method*" studied here, the "*Single-layered Cantilever Method*" [1], the "*Axial Compression Method*" [2], the "*Circular Ring Method*" [3] have already been developed and reported, based on the nonlinear large deformation theory.

2. Theory

A typical illustration of a load-deflection shape is given in Fig.1 for a multi-layered cantilever (length L) subjected to the total own-weight w ($=\sum_{i=1}^{n} w_i$) consisted of n layers where w_i is the distributed load per unit length of each layer in a multi-layered material with a supporting angle θ_0. The basic equation is derived in the form of:

$$\sum_{i=1}^{n}(E_i I_i)\frac{d^2\theta}{ds^2}+\sum_{i=1}^{n} w_i(L-s)\cos\theta=0 \qquad (1)$$

Introducing the following non-dimensional variables,

$$\left.\begin{aligned}\xi=\frac{x}{L},\eta=\frac{y}{L},\zeta=\frac{s}{L}\\ \gamma=\frac{\sum_{i=1}^{n} w_i L^3}{\sum_{i=1}^{n}(E_i I_i)},\beta=\frac{ML}{\sum_{i=1}^{n}(E_i I_i)}\end{aligned}\right\} \qquad (2)$$

and transforming the variables ($s\rightarrow\zeta$), Equation (1) reduces to Eq.(3).

$$\frac{d^2\theta}{d\zeta^2}+\gamma(1-\zeta)\cos\theta=0 \qquad (3)$$

Finally, the non-dimensional maximum horizontal displacement ξ_A ($=\xi_{max}=x_A/L$) (x_A: horizontal displacement at the free end A) and the non-dimensional maximum vertical displacement $\eta_A(=\eta_{max}=y_A/L)$ (y_A: vertical displacement at the free end A) are obtained as follows.

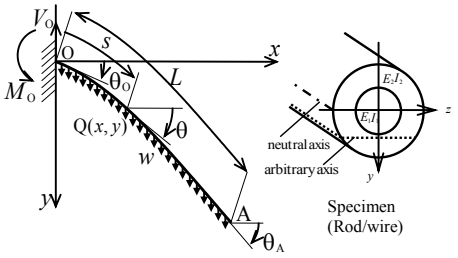

Fig.1 Large deflections of a multi-layered cantilever subjected to own-weight.

$$\xi_A = \int_0^{\zeta_A} \cos\theta d\zeta = \int_0^{\zeta_A} \cos\left[\left(\frac{\theta_A - \theta_O}{2} - q \right) \times \left\{ 1 + \frac{m^2 \cdot \delta^3}{2 \cdot (4/3)} + \frac{m^4 \cdot \delta^6}{2 \cdot 4 \cdot (8/3) \cdot (10/3)} + \cdots \right\} + q + \frac{\theta_A + \theta_O}{2} \right] d\zeta \quad (4)$$

$$\eta_A = \int_0^{\zeta_A} \sin\theta d\zeta = \int_0^{\zeta_A} \sin\left[\left(\frac{\theta_A - \theta_O}{2} - q \right) \times \left\{ 1 + \frac{m^2 \cdot \delta^3}{2 \cdot (4/3)} + \frac{m^4 \cdot \delta^6}{2 \cdot 4 \cdot (8/3) \cdot (10/3)} + \cdots \right\} + q + \frac{\theta_A + \theta_O}{2} \right] d\zeta \quad (5)$$

The following formula based on Eq.(2) is useful in calculating each Young's modulus E_i.

$$\sum_{i=1}^{n} (E_i I_i) - \frac{\sum_{i=1}^{n} w_i L^3}{\gamma} = 0 \quad (6)$$

In order to calculate each Young's modulus E_i from Eq. (6), One quantity γ (: the non-dimensional load) is required. The value of γ is obtained from a chart (: Nomograph, omitted here) of γ-x_A relation (x_A: the horizontal displacement) [Method 1] or γ-y_A relation (y_A: the vertical displacement) [Method 2].

3. Exerimental Investigation

Several experiments were carried out using a two-layered wire [SWPA: a spring steel wire, length: L_1=800.0 mm, diameter: d_1=0.5mm, distributed load per unit length w_1=15.213×10^{-3} N/m + Cu: an electrodeposited Copper layer, thickness: (d_2–d_1)/2= 0.02 mm (i.e., d_2: 0.54 mm), distributed load per unit length w_2=2.862×10^{-3} N/m]. Young's moduli of Cu obtained by applying Method 1 and Method 2 [Note: examples of SWPA were omitted here.] are shown in Fig.2. The measured values of Method 1 and Method 2 remain nearly constant for various lengths L and

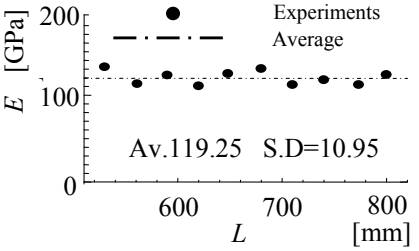

(a) Method 1(Data: x_A)

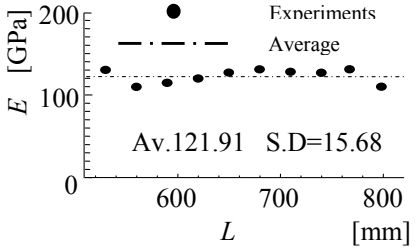

(b) Method 2(Data: y_A)

Fig.2 Comparison of Young's moduli of an electro-deposited copper (Cu: E_2) between the twomeasuring methods for various values of the specimen length L.

the standard deviation (S.D.) is small although every method has a little scattered values.

Acknowledgements

The author thanks to Mr. Noma. A., Meijo University, Japan, for assistance in this work.

References

[1] Ohtsuki, A., A New Method for Measuring Young's Modulus of Flexible Thin Materials Using a Cantilever. Proceedings of the 4th International Conference on Advances in Experimental Mechanics, Southampton, Vol.3-4, 2005, pp. 53-58.

[2] Ohtsuki, A., A New Method of Measuring Young's Modulus Using Postbuckling Behaviours. Proceedings of the 2006 SEM Annual Conference & Exposition on Experimental and Applied Mechanics, St.Louis, Section 78, pp. 78(1)-78(8)[CD-ROM], 2006.

[3] Ohtsuki, A. and Takada, H., A New Measuring Method of Young's Modulus for a Thin Plate/ Thin Rod. Transactions of Japan Society for Spring Research, No.47, 2002, pp. 27-31.

30th DANUBIA-ADRIA
Symposium on Advances in Experimental Mechanics
September 25-28, 2013 - Primošten, Croatia

4B01 097

CREEP OF THE CEMENT PASTE WITH ADDITION OF 40 % FLY ASH IN ADVANCED AGE

Pavel Padevět[1], Petr Bittnar[1]

[1] Czech Technical University in Prague, Faculty of Civil Engineering, Department of Mechanics. Thákurova 7, 166 29 Prague 6, Czech Republic. E-mails: pavel.padevet@fsv.cvut.cz, petr.bittnar@fsv.cvut.cz

1. Introduction

Knowledge of the properties of cement pastes with addition of fly ash is an important piece of knowledge for the design of structures, in which the ash is used. The amount of fly ash in cement affects the rate of hydration of the cement components. The changing the amount of fly ash in cement also causes positives like a lower production the cement in achieving similar final properties, a lower rate of rice the strength and lower heat of hydration.

The compression strength, tension strength in bending, modulus of elasticity, creep coefficient, volume weight is material properties important for design of the building constructions [1]. This work presents results of measurements and mathematical modeling of the creep evolution.

2. Tested material

The cement paste is fine grain and homogeneous material. The homogeneity of material is suitable for measurement the creep on the small specimens. The material that retains their hydration properties can occur by adding of the fly ash in the Portland cement.

Portland cement CEM I 42.5R was used for the preparation of the cement paste in this work. The classical fly ash was used as an additive to the cement paste. Usual amount of the fly ash added to the cement paste is between 20 – 30 % of the cement weight. In this case the ratio c/fa (cement/fly ash) was higher, namely 60/40. The 40 % of the cement weight was used to the replacing by classical fly ash. Water cement ratio 0.4was used, for its tried and suitable consistency.

The specimens were prepared in the plastic moulds. The specimens were placed in the water for one month and then were left on air.

3. Testing of cement paste

The most important change of compressive strength is in the first three months after production. At the age of 10 months, the material is stable from the viewpoint of strength. The testing equipment allowed the using specimens with length maximally 70 mm. The diameter of

Fig. 1. Instrumentation of testing.

tested specimens was 10mm. These dimensions of the specimens allow testing in the lever mechanism, as shown in Fig. 1. The specimens tested for creep are loaded with weight that is placed on the lever apparatus. The specimens tested on shrinkage are not contrary loaded with weights. Creep was measured at the 4 specimens and shrinkage at the 2 specimens. Two specimens were dried before start of testing and two specimens were saturated in the water for measurement of the creep. Similarly, for the shrinkage, one specimen was dried and second specimen was saturated in the water.

The deformations of the specimens were measured during the whole time of testing. The specimens were loaded with weights at the beginning of the test. Specimens were unloaded after 30 days of measurement, as it sees in Fig. 4 and 5. The temperature was constant during the test [2]. Also, the moisture conditions of specimens were maintained in the steady state.

4. Results and simulation of creep

The results of measurement are displayed in Fig. 2 and 3. Firstly, in Fig. 2 is curve of the basic creep in 30 days measurement. Basic creep is calculated like the difference between creep of dried specimen and shrinkage of the dried specimen, too. Similarly, result of the creep of water saturated specimen is displayed in Fig. 3. In both cases is significant rapid increase of the creep in the first 12 days, due to the load.

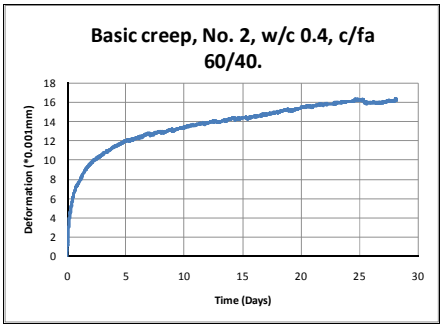

Fig. 2. Basic creep of cement paste with fly ash.

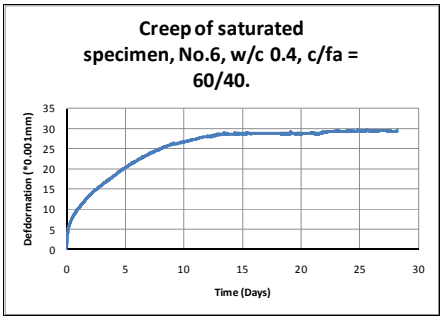

Fig. 3. Creep of cement paste with fly ash (saturated).

Creep was mathematically simulated by B3 model, which is compounded in environment OOFEM [3]. Results of model depending on the material properties of the cement paste, the age of material and humidity conditions.

The results are the creep coefficients q_1 to q_4, with which it works B3 model of creep of concrete.

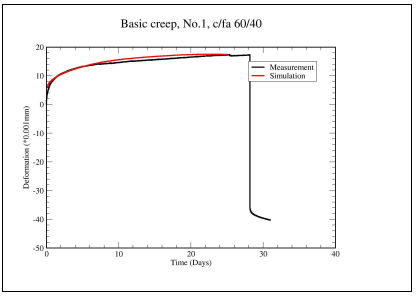

Fig. 4. Simulation of basic creep of the specimen No.1.

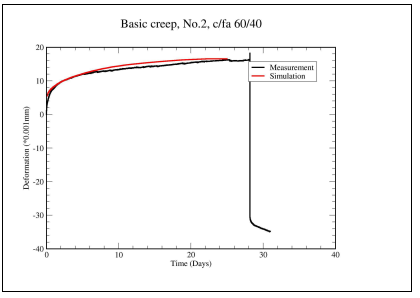

Fig. 5. Simulation of basic creep of the specimen No.2.

5. Summary

The results of experiments correspond with simulation very good, see Fig. 4 and 5. The model B3 is suitable for simulation of the cement paste creep. The size difference of creep saturated and dried material is doubled after 30 days.

Acknowledgements

This work has been supported by project GACR under No. 104/11/2285.

References

[1] Padevět, P., Zobal O., Change of Material Properties of the Cement Paste CEM I, in Proceedings of the 48th International Scientific Conference on Experimental Stress Analysis, Velké Losiny, May – June 2010, pp. 307-310.

[2] Polák, M., Plachý, T., Long-Time Monitoring of Thermal Action on a Prestressed Concrete Bridge Structure, in Proceedings of the 48th International Scientific Conference on Experimental Stress Analysis ,Velké Losiny, May – June 2010, pp. 369-376.

[3] Patzák, B., OOFEM project home page, http://www.oofem.org, 2000.

30th DANUBIA-ADRIA
Symposium on Advances in Experimental Mechanics
September 25-28, 2013 - Primošten, Croatia

4B02 035

ULTRA LONG FATIGUE LIFE OF 50CrMo4 STEEL WITH STRENGTHENED SURFACE BY HIGH ENERGY SHOT PEENING

Libor Trško[1], Otakar Bokůvka[1], Mario Guagliano[2], František Nový[1], Marián Hazlinger[3]

[1] University of Žilina, Faculty of Mechanical Engineering, Department of Materials Engineering, Univerzitná 1, 010 26 Žilina, SLOVAK REPUBLIC. E-mails: libor.trsko; otakar.bokuvka; frantisek.novy@fstroj.uniza.sk

[2] Politecnico di Milano, Department of Mechanics, Via La Masa 34, 201 58 Milano, ITALY. E-mail: mario.guagliano@polimi.it

[3] University of Technology, Bratislava, Faculty of Materials Science and Technology in Trnava, Bottova 23, 917 24 Trnava, SLOVAK REPUBLIC. E-mail: hazlinger@stuba.sk

1. Introduction

At the actual operation, the components and constructions are loaded mainly by repeating loading that could lead to the ultimate state, fatigue fracture in the final consequences. With regard on this fact the fatigue degradation mechanisms are studied for more than 170 years. The strain or stress vs. number of cycles plot (S-N dependence) incl. conventional fatigue limit usually referred to $N = 2\times10^6 - 10^7$ cycles (steels and cast irons) were till now the main dependences used at evaluation of fatigue properties of structural materials [1]. With the aim to prolong the fatigue lifetime of components and equipments (reliability and safety demands) it is necessary to study except low-cycle fatigue and the high-cycle fatigue also the ultra-high cycle fatigue life ($10^8 < N < 10^{10}$ cycles) [2]. Special testing equipments with the working frequencies about 20 kHz are used for fatigue testing in region of ultra-long fatigue life with regard on the economy and effectiveness [1]. In the ultra-high cycle region fatigue cracks usually initiate on an free surface but sometimes subsurface fatigue crack initiation can be observed. From this point of view are efforts to eliminate or decrease the place of maximal stress and cyclic loading concentration, to increase the time for initiation of fatigue cracks. The different technologies of surface treatments are used with contrary results [3]. The shot peening is one of the effective methods for the surface treatment of structural materials. In this process the surface of a component is bombarded with a multitude of small hard spherical shots moving at high velocity. As a result of the collision of the shots with the surface of the component are small dimples created by plastic deformation of the surface. After impact of multiple shots these parameters of free surface and subsurface layers are affected – surface texture and surface topography, surface hardness and sub-surface dislocation density which results in changes of intensity and distribution of sub-surface residual stresses. Modification of primary surface and sub-surface parameters can increase the fatigue lifetime of components [4, 5].

In this paper authors publish their own partial results of experimental examination of ultra-long fatigue life of 50CrMo4 steel after surface strengthening by high energy shot peening.

2. Experiments and Results

The experimental works, metallography analysis, microhardness tests, shot peening and fatigue tests were carried out on the low-alloyed 50CrMo4 steel which chemical composition and mechanical properties are stated in Tab. 1.

C	Mn	P	S	Si	Cr	Mo
0.46 0.54	0.50 0.80	max. 0.025	max. 0.035	max. 0.40	0.90 1.29	0.15 0.30
R_e [MPa]		R_m [MPa]		A_5 [%]		
702		929		15.0		

Tab. 1. Chemical composition (in weight %) and mechanical properties of tested steel 50CrMo4.

Microstructure created by mixture of bainite, sorbite and perlite is shown in Fig. 1. The fatigue tests were performed with using methods by authors [1] at high-frequency sinusoidal cyclic

tension-compression loading (testing frequency f ≈ 20 kHz, T = 20 ± 10 ˚C, water cooling of specimens with anticorrosive inhibitors, parameter of cycle asymmetry R = -1) with use of high-frequency

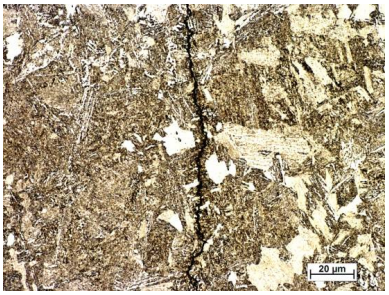

Fig. 1. Microstructure of 50CrMo4 low-alloyed steel in the place of fatigue crack, etch. Nital.

testing equipment KAUP-ZU Zilina, SK. The round bar specimens (11 specimens with machined and polished surface – marked NP and 11 specimens with shot peened surface – marked SSP) with 4 mm in diameter in the central part were used during the fatigue tests. The investigated number of cycles was in the region from $N \approx 4.87 \times 10^6$ to $N = 1.55 \times 10^9$ cycles. The high energy shot peening treatment of specimens [6] was

Shot type	Almen intensity	Coverage [%]
S170 (steel shots, ø = 425 μm)	15.6	1000

Tab. 2. Parameters of performed high energy shot peening.

realized with the use of parameters including Almen intensity presented in Tab. 2. Microhardness measurement on the cross section of specimens was carried out by Vickers method at a loading 50 gf (HV 0.05). The results of microhardness tests and fatigue tests for specimens before and after high energy shot peening are shown in Figs. 2 and 3 respectively.

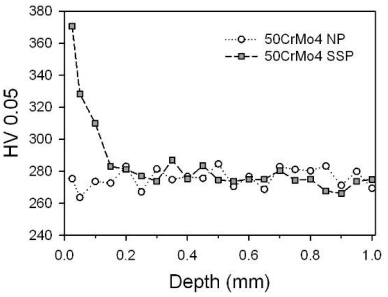

Fig. 2. Surface layers microhardness values of 50CrMo4 low-alloyed steel before (NP) and after high energy shot peening (SSP).

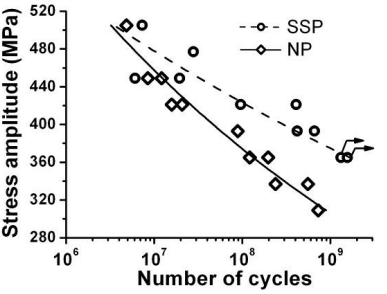

Fig. 3. S-N curves of 50CrMo4 low-alloyed steel before (NP) and after high energy shot peening (SSP).

3. Conclusions

With regard on the carried out of experimental works it can be stated that application of high energy shot peening had a major positive influence on the fatigue life in the ultra-high cycle region, represented by S-N curves. Surface strengthened layer with compression residual stresses increased the number of cycles necessary for fatigue crack initiation. Increase of fatigue strength is more significant with increasing number of cycles. Despite these facts, according to the regression curves of S-N diagrams, in this case shot peening would have negative influence on fatigue life in regions of lower number of cycles.

Acknowledgements

The research was supported by the Scientific Grant Agency of the Ministry of Education, Science and Sports of the Slovak Republic and Slovak Academy of Sciences, grant No. 1/0743/12 and by European regional development fund and Slovak state budget by the project ITMS 26220220048.

References

[1] Bokůvka, O. et al., Low and High Frequency Fatigue Testing. EDIS ŽU Žilina, 2000.

[2] Bathias, C., Paris, D. C., Gigacycle Fatigue in Mechanical Practice. M. Dekker, New York, 2005.

[3] Klesnil, M., Lukáš, P., Únava kovových materiálů při mechanickém namáhání. Academia Praha, 1975. (in Czech)

[4] Abadie, F. et al., Shot peening: A Dynamic Application and its Future. Zürich MFN, 2006.

[5] Bagherifard, S., Guagliano, M., Fatigue Behavior of a Low Alloy Steel with Nanostructured Surface Obtained by Severe Shot Peening. In. *Eng. Frac. Mech*., 2012, p. 56-58.

[6] PEEN SERVICE – NORBLAST GROUP s.r.l., Prop. Handbook – Surfaces Eng., Bologna, 2011.

30th DANUBIA-ADRIA
Symposium on Advances in Experimental Mechanics
September 25-28, 2013 - Primošten, Croatia

4B03 052

FATIGUE STRENGTH/LIFE ESTIMATIONS BASED ON THE CRITICAL DISTANCE STRESS THEORY

Toshio Hattori[1], Muhammad Amiruddin Bin Ab Wahab[2] and Minoru Yamashita[3]

[1] Gifu University, Faculty of Mechanical Engineering, 1-1 Yanagido, Gifu, JAPAN. E-mail: hattori@gifu-u.ac.jp

[2] Graduate School Student, Gifu University, 1-1 Yanagido, Gifu, JAPAN.

[3] Gifu University, Faculty of Mechanical Engineering, 1-1 Yanagido, Gifu, JAPAN.

1. Introduction

In general the critical distance stress theory (point method and line method) were used for estimation of fatigue limit with any shape structures. In this method the fatigue limit can be obtained using typical material strength parameters such as the fatigue limit of smooth specimens σ_{w0} and the threshold stress intensity factor range ΔK_{th} of the cracked specimens. In the case of point method, the fatigue failure supposed to occur when the stress range at specific length r_c from maximum stress point reach $\Delta\sigma_{w0}$. This r_c can be derived as follows.

$$r_c=(\Delta K_{th}/\Delta\sigma_{wo})^2/2\pi \qquad (1)$$

In this paper we extended this method to the low cycle fatigue regions. Then I will explain this development in detail. Firstly the critical distance in low cycle fatigue region is derived by interpolating between critical distance in fatigue limit as shown in above and critical distance in static strength. This static strength critical distance can be derived using ultimate strength of smooth specimen σB and the fracture toughness K_{IC} of the cracked specimen as follows.

$$r_c'=(K_{IC}/\sigma_B)^2/2\pi \qquad (2)$$

The critical distance in each stress level is calculated by interpolation of critical distance on fatigue limit (r_c) with critical distance on static strength (r_c') as shown by chain line in Fig. 1(right). The critical distance on objective conditions (structure, load) can be estimated by reflecting the stress distributions of objective structure as shown by dotted line in Fig. 1(right). The low cycle fatigue life in this objective condition can be estimated by applying this reference stress σ at critical distance r on S-N curve of smooth specimens as shown in Fig. 1(left upper).

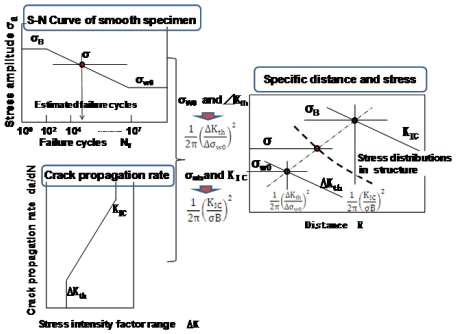

Fig.1 Derivation of specific distance in low cycle fatigue region and estimation of low cycle fatigue life

2. Applications and results

To confirm the validity of this critical distance approach we applied this method on low cycle fatigue life estimation of circle hole specimens and fretting fatigue specimens.

2.1 Application on hole specimens

Circle hole specimen used on this test are shown in Fig. 2, and material properties of SS400 steel are shown in Table 1. Critical distance on fatigue limit r_c and on static strength r_c' are estimated using Eq.(1),(2) as 0.077mm and 1.24mm respectively, and shown in Fig.3 by ● points. By interpolating these two points the

critical distances on arbitrary conditions are estimated as solid line(predict line) in Fig. 3.

$$r_c = \frac{1}{2\pi}\left(\frac{\Delta K_{th}}{\Delta\sigma_{wo}}\right)^2 = \frac{1}{2\pi}\left(\frac{6.7\times10^6}{305\times10^6}\right)^2 = 0.077 \quad \text{(mm)}$$

$$r'_c = \frac{1}{2\pi}\left(\frac{\Delta K_c}{\Delta\sigma_b}\right)^2 = \frac{1}{2\pi}\left(\frac{39.5\times10^6}{448\times10^6}\right)^2 = 1.24 \quad \text{(mm)}$$

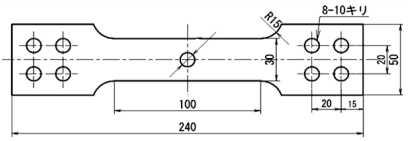

Fig.2 Dimensions of circle hole specimens with circle diameter 4mm

Table 1 Mechanical properties of SS400 steel

$\triangle\sigma_{w0}$ [MPa]	$\triangle K_{th}$ [MPa·m$^{1/2}$]	σ_B [MPa]	K_{IC} [MPa·m$^{1/2}$]
305	6.7	448	39.5

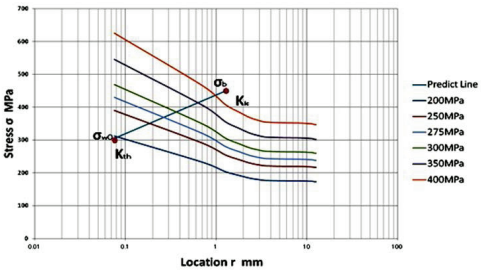

Fig.3 Stress distributions in circle hole specimen with circle diameter 4mm

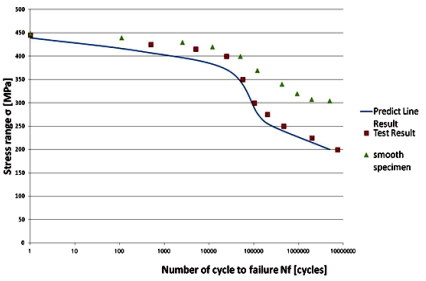

Fig.4 Estimated and experimental S-N curves of circle 4mm specimens

These estimated full range S-N curves coincided well with the experimental results as shown in Fig.4 for circle hole specimens.

2.2 Application on fretting fatigue specimens

Then we will apply this extended critical distance theory on the fretting fatigue life prediction. In Fig.5(left upper) the S-N curve of Ni-Mo-V steel smooth specimen in complete reversed loading conditions (R=-1), and in Fig.5 (left under) the crack propagation characteristic of cracked specimen is shown. From these material characteristics we can obtain the critical distance r_c as 0.011mm and r_c' as 2.13mm as shown in Fig. 5 (right).

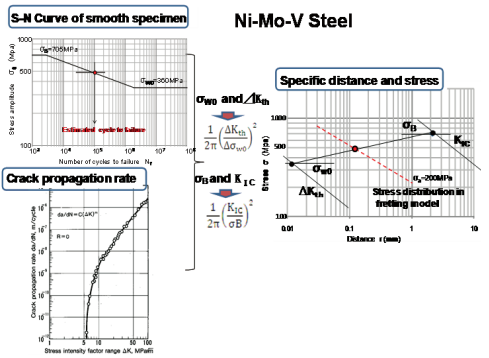

Fig.5 Derivation of specific distance in low cycle fatigue region and estimation of low cycle fretting fatigue life

The critical distance on each loading conditions can be estimated by reflecting fretting stress distributions on Fig.5 (right) as shown by dotted line. The low cycle fretting fatigue life can be estimated by applying this stress level at critical distance on S-N curve of smooth specimens as shown in Fig. 5 (left upper). By connecting these fretting fatigue life on each stress level we can estimate the fretting fatigue S-N curve as shown in solid line in Fig.6.

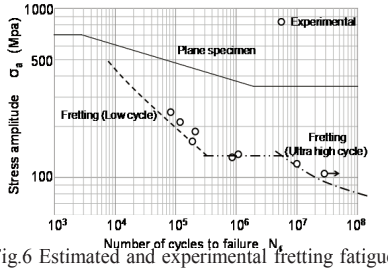

Fig.6 Estimated and experimental fretting fatigue S-N curves

30th DANUBIA-ADRIA
Symposium on Advances in Experimental Mechanics
September 25-28, 2013 - Primošten, Croatia

4B04 003

LOW-CYCLE FATIGUE BEHAVIOR OF 6061 ALUMINUM ALLOY PLATED WITH MULTI-LAYERED COATINGS

Ya. B. Unigovski[1], E.M. Gutman[2], E. Gerafi[3], A.Grinberg[4]

[1] Ben-Gurion University of the Negev, Department of Materials Engineering, Beer-Sheva 84105, Israel. E-mail: yakovun@bgu.ac.il.
[2] Ibid., E-mail: gutman@bgu.ac.il.
[3] Ibid., E-mail: eliorg@bgu.ac.il.
[4] Ibid., E-mail: argrinberg@elta.co.il.

1. Introduction

Electroless nickel (EN) is an engineering coating, normally used because of its excellent corrosion and wear resistance. The results obtained for 7075-T6 [1] and 2618-T61 [2] aluminium alloys coated with an EN deposit show that the coating can give rise to a significant improvement in the high-cycle fatigue performance of the substrate at medium and low stresses. However, in engineering applications, relatively low-frequency strain cycling as a consequence, e.g., of start and stop operations, generates low-cycle fatigue (LCF) failure if various stress concentrators, such as microcracks, notches, welds, etc., result in local cyclic plastic deformation in the component.

In the literature, there are no reported studies with respect to the LCF behavior of Al alloys plated with multi-layered deposits. Therefore, an investigation of low-cycle fatigue of a multi-layered Al alloy is of vital importance for the design of structural components.

2. Experimental

Solutionized and artificially aged 6061-T6 aluminum alloy consists of, wt.%: 0.4 - 0.8 Si, ≤0.7 Fe, 0.15 - 0.40 Cu, ≤0.15 Mn, 0.8 - 1.2 Mg, 0.04 - 0.35 Cr, ≤0.15 Ti, ≤0.25 Zn, other elements ≤0.05% each, 0.15% total, 95.85 – 98.56 Al. The alloy was coated with a single 12- μm or 26- μm - thick layer of electroless nickel (sets 2 and 3, respectively). These layers were deposited on the alloy surface in accordance with ASTM B733 Type V, SC2/SC3. To increase the adhesion of electroless nickel (EN) to the aluminum alloy surface, heat treatment at 180°C during one hour was performed after the coupon plating process. Two-layered deposits include an inner 12-μm-thick or 26-μm-thick EN and an outer 3-4-μm-thick electrodeposited Ni (EDN) layers performed in accordance with the standard SAE AMS 2424F-2010 in a nickel sulfamate bath. Three-layered coatings have an 3-μm outer layer of silver (set 6) or 0.2-μm gold (set 7) deposited in accordance with ASTM B700 Type 1 Grade A Class N (thickness class 10μm) or ASTM B488 Type 1 Grade C Class 0.1μm, respectively. The samples had the gauge width and length of 10 and 32 mm, respectively.

The specimens were tested on a Model IP-2 pure bending fatigue machine with the capacity of around 50 Nm in a strain-controlled loading mode at the strain ratio $R = \varepsilon_{min}/\varepsilon_{max}$ amounted to 0.1. The scheme of the LCF test and a view of the sample deflection measurement are given in Ref. [3]. The sine-wave input form with the frequency of 0.4 Hz was used. The plastic strain amplitudes $\Delta\varepsilon_{pl}$ varied from about 0.002 to 0.0010.

3. Results and discussion

The $\Delta\varepsilon_{pl}$ – N diagrams for the substrate 6061 and coated alloy are presented in Fig. 1 where the curve numbers are the set numbers. The fatigue life of 6061 substrate dramatically decreases with an increase in the plastic strain amplitude $\Delta\varepsilon_{pl}$ from 0.003 to 0.010.

The mean lifetime of the alloy plated with 12-μm and 26-μm-thick EN layers amounted to 13,008 and 5.535 cycles, respectively, as compared to 45,849 cycles for the substrate at the smallest plastic strain amplitude of 0.003 (Fig. 1). Therefore, the relative lifetime N_{fc}/N_{fs} of these coated systems (sets 2 and 3) amounted only to

0.28 and 0.12 as compared to the substrate, where N_{fc} and N_{fs} are the numbers of cycles to failure for the coated alloy and the substrate, respectively. An increase in the plastic strain up to 0.005 and 0.010 leads to an additional degradation of fatigue properties both for 12-μm- and 26-μm-thick EN deposits.

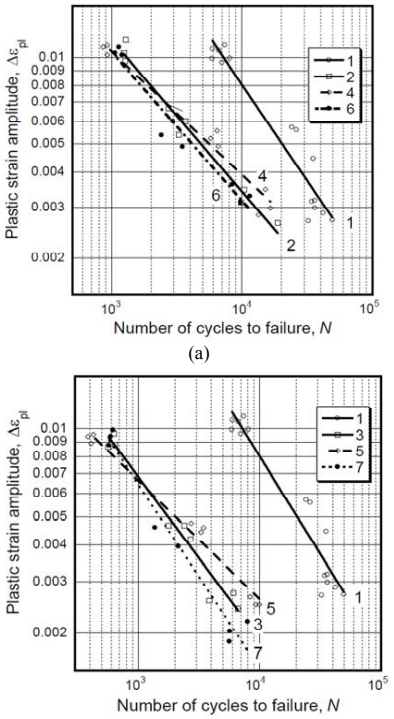

Fig. 1. Fatigue life of Al 6061-T6 substrate (1) as compared to that for the 6061-T6 alloy coated with a single layer (2, 3); two-layer (4, 5) and three-layer (6, 7) coatings depending on plastic strain amplitude.

The second 4 μm-thick EDN-layer electroplated on the electroless Ni layer (sets 4 and 5) insignificantly reduced the fatigue life of the coated alloy at a relatively high plastic strain of 0.010, probably, due to the 'thickness effect': the thicker the coating, the greater lifetime reduction (Fig. 1). However, at medium and low strain levels corresponding to the number of cycles more than 10^3, a marked improvement of fatigue properties was found. For example, at $\Delta\varepsilon pl = 0.003$, lifetime of sets 4 and 5 amounted to 15,014 and 9,197 cycles, respectively, as compared to 13,008 and 5.535 cycles for sets 2 and 3, which were not electroplated with EDN.

In accordance to our data, the hardness value of electroplated nickel is about 1.9 GPa vs. 5.1 GPa for electroless nickel. It seems that at relatively minor plastic strain amplitudes, a much more ductile electroplated Ni-layer prevents crack formation on the outer surface of the coated alloy and, probably, in the interface between Ni layers. At high strains, EDN layer does not prevent the intensive cracking observed already after the first cycle contrary to that for a lower plastic strain. Cracking after the 1st cycle was found at $\Delta\varepsilon_{pl}$ = 0.010 both in the outer EDN layer and in the inner 12-μm-thick EN deposit

It was found that cracking occurs, mainly, at the interface between the inner electroless nickel layer and the Al substrate. As expected, the cracks nucleated near various heterogeneities of the surface. In contrast to high-cycle fatigue fracture patterns, the LCF fracture surface includes the striations in the area of an initial rupture close to the sample surface both in the substrate and in EN deposit.

4. Remarks

- Electroless Ni (EN) deposit worsens low-cycle fatigue properties of 6061 Al alloy. Incipient cracks in a multi-layered alloy origin, mainly, in the EN layer.
- The second electroplated Ni layer improves the fatigue properties of coated alloy.
- The third silver or gold layer worsens fatigue properties of the system.

Acknowledgements

We would like to thank Dr. E. Kolmakov, D. Hen, M. Shitrit, A. Levin, H. Didi, and A. Jarashneli (Ben-Gurion University of the Negev) for kind assistance in fatigue tests, SEM and XRD.

References

[1] E.S. Puchi-Cabrera, C. Villalobos-Gutierrez, I. Irausquın, J. La Barbera-Sosa, G. Mesmacque, Int J Fatig 28, 2006, 1854–1866.

[2] B. Lonyuk, I. Apachitei and J. Duszczyk, Scripta Materialia 57, 2007, 783-786.

[3] Ya.B. Unigovski, G. Lothongkum, E.M. Gutman, D. Alush, R. Cohen, Corros Sci 51 (12), 2009, 3014-3020.

30th DANUBIA-ADRIA
Symposium on Advances in Experimental Mechanics
September 25-28, 2013 - Primošten, Croatia

4B05 005

INFLUENCE OF RIPENING ON THE EVOLUTION OF THE MAIN MECHANICAL AND STRUCTURAL PROPERTIES OF THE POLYCRISTALLINE ALLOY 42000.

Ahmed HAKEM*[1], Youcef BOUAFIA[1].

[1]Laboratory LaMoMS, Mouloud MAMMERI university of Tizi-Ouzou, 15000 Algeria.
* Corresponding Author E-mail: a_hakem1951@yahoo.fr

Key words: *Al - Si, sand, shell, ripening, income, mechanical properties.*

1. Abstract

This study aims to determine the influence of the chemical composition of industrial sand casting and metal shell cast by gravity at room temperature or under pressure both mechanical and manual metal parts for the various achievements SNVI (Aluminum Foundry Unit Rouiba) and ENEL (Unit engine Freha in Tizi-Ouzou) Algeria and heat treatments on mechanical behavior of fracture, quasi-static axial tensile united, Brinell hardness, almost dynamic resilience and microstructure of the alloy foundry chemical designation AlSi7Mg and digital 42000, The addition of 7% silicon and magnesium percentage (≤ 1% Mg) in aluminum are the principal agents of the improvement of mechanical properties in addition to specific heat treatments which show different types of precipitates that hinder the movement of dislocations.

The physical characterization, chemical and general engineering in particular is crucial for the design of various metal parts subject to external forces varied constituents various mechanisms in motion a mechanical component. The designer can neither calculate nor resize these parts without identifying and quantifying their characteristics. To determine them, we reproduce these solicitations using static and dynamic tests, usually conducted on standard specimens.

The alloy AlSi7Mg, which governs our study, is a shade containing some magnesium added in small amounts (0,20 to 0,40) % Mg alloy to allow hardening and efficient use in applications with high mechanical properties in T46 condition. This alloy contains 7% of silicon, which gives very good properties implementation in foundry (average flow ability, low volumetric contraction during solidification, reduction of withdrawal to the solid state and the expansion coefficient.). It is used for complex shapes, to requirements of mechanical strength and maximum thicknesses which are very low (~ 8 mm).

The unalloyed aluminum with mechanical properties very reduced, leading to add two items of very low density with 7% silicon and traces of magnesium less than 1% (≤ 1% Mg) which is the lightest of all metals capable of stable industrial employment to improve their properties and obtain an alloy AlSi7Mg super lightweight. The alloy foundry ultimate AlSi7Mg governing our study is an alloy with a set of properties that in many circumstances make it an irreplaceable material. Among these include the addition of a high percentage of silicon and a low percentage of magnesium to aluminum as the main potential agents of improvement largely mechanical properties, low density (~2,6) results in equal volumes of documents about three times less severe than if they were made of steel or copper, combined with very good corrosion resistance and low melting temperature (660°C) facilitating its development in all casting processes. These alloying elements come into solution and may also be present as intermetallic phases. The composition of these phases, but above all their delicacy, their distribution, their consistency vis-à-vis the aluminum matrix, their frailties, their stability as a function of heat treatments are also decisive for the properties of the alloy.

2. Problem

Non-alloy aluminum with mechanical properties very reduced, leading to add two items of very low density with 7% silicon and traces of magnesium less than 1% (≤ 1% mg) which is the lightest of all stable metals susceptible of industrial employment to improve their properties and obtain a super light alloy AlSi7Mg. The addition of a high percentage of silicon and a low percentage of magnesium to aluminum are the main vectors and improving agents largely mechanical.

Our goal is to make a direct contribution for the study of mechanical strength, hardness, resilience and structural properties of the alloy foundry AlSi7Mg used in sand casting and metal shell both mechanical and manual.

The reference state is designated as cast, noted: F. to try to increase over the strength characteristics of the state F and obtain substantially high stress elasticity, rigidity of large modules with small deformations, the material of 42000 numerical designation is subject to specific treatments T46.

3. Experimental procedure

To determine the behavior of the material deal with various stresses it may encounter during use, these solicitations are reproduced using static or dynamic tests, usually conducted on standard specimens in order to know the characteristics figures of the material. Four techniques are used, namely traction to identify the various constraints, the brinell hardness HB for the stress field, resilience Kcv us about the mode of fracture, fragility and resistance to shock and metallographic to identify structures.

We will describe in more detail and present in the main mechanical characteristics of the material obtained from chemical composition by AlSi7Mg purpose of this study.

References

[1] Ahmed Hakem, Y. Bouafia, Influence of User Development and Aging on Mechanical Characteristics and microstructure of the alloy foundry AlSi10Mg, ACMA, 2010, 12-14 May 2010, Marrakech, Marocco.

[2] Ahmed Hakem, Y. Bouafia, S. Naïli, A. Bouhaci, Development of industrial aluminum alloys foundry AlSi7Mg, AlSi10Mg and AlSi13Mg, International Symposium - Characterization and Modeling of Materials and Structures 16, 17 and18 November, 2008 - University Mouloud Mammeri Tizi-Ouzou, Algeria.

[3] Ahmed Hakem, memory magister, Microstructure and Mechanical Properties of Alloy hypoeutectic AlSi7Mg, 2005, Department of Engineering - Mechanical Engineering, Faculty of Engineering Building, University Mouloud Mammeri Tizi – Ouzou . Algeria.

[4] M. Colombia and Coll, Industrial Materials: Metal Materials, p.867, Dunod, Paris (2000).

[5] Jean-Paul Baillon, Jean-Marie Dorlot, Materials, p.729, 3rd edition, Ecole Polytechnique de Montreal, Montreal (2000).

[6] Jean Baralis Gerard Maeder, Handbook of Metallurgy: (Preparation, structure, properties, normalization), p.232, 1ereédition, AFNOR-Nathan, Paris (1997).

[7] Bruno Barlas, study of behavior and fatigue damage in aluminum alloy casting, thesis submitted and publicly defended the 5 'in February 2004, Ecole des Mines de Paris, p228.

[8] Asserin-Lebert Experimental study and prediction of failure mechanisms of plates and joints butt welded aluminum alloy 6056, and presented publicly defended February 18, 2005, Ecole des Mines de Paris, p190.

[9]Lakhtine. Metallography and heat treatment of metals, Third Edition Mir, 1982.

[10]Solidifications characteristics of aluminum alloys: Volume 2: Foundry alloys, Amer Foundry society, 1993.

[11] L. Bäckerud, Solidification characteristics of aluminum alloy, Oslo, Norway: Skanaluminium,Universitetsforlaget AS, 1986-1996

30th DANUBIA-ADRIA
Symposium on Advances in Experimental Mechanics
September 25-28, 2013 - Primošten, Croatia

5A01 116

MEASUREMENTS OF HYDRODYNAMIC FORCES AT A PRESSURE SEGMENT OF THE BOTTOM OUTLET OF A GRAVITY DAM

Boris Huber [1], Norbert Krouzecky [1]

[1] Institute of Hydraulic Engineering, Vienna University of Technology, Karlsplatz 13/222, 1040 Vienna, Austria

Corresponding author: norbert.krouzecky@tuwien.ac.at

1. Introduction

As part of a planned development of a gravity dam, built in the 1920s, its spillway will be expanded from the current 60 m³/s to 355 m³/s in the future. To do this, a flap will be installed on the crest of the spillway. The Institute of Hydraulic Engineering of the Vienna University of Technology was entrusted with the implementation of hydraulic model tests.

Fig. 1: Dam and bottom outlet, full model, downstream view

Additional to questions of the maximum possible discharge over the flap, scour protection and bank stability, the plunge pool and the possible danger of a driftwood jam, the hydrodynamic forces on the pressure segment of the bottom outlet in the cases of opening and closing the roller gate and also in a stationary position were to be investigated and the pressures measured.

2. Experimental Investigations

2.1 Model stand

The measurements of the hydrodynamic forces were carried out in a 50 cm wide flume as a section model in a scale 1:16.

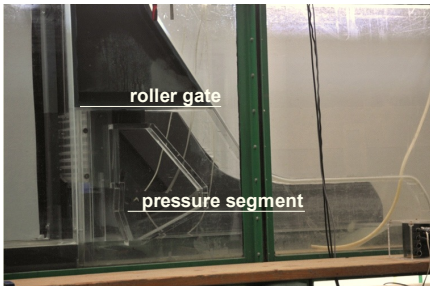

Fig. 2: Section model, M 1:16

The measurements were performed at fixed segment-opening heights of 16, 32, 48 and 80 cm (prototype values) with a constant upstream water level. To avoid friction the pivot was fitted with special ball bearings and the hydraulic cylinders were replaced by rods with load cells (HBM Type: S2 100 N)

2.2 Force measurements

During the experiments with the moving roller gate the force on the rods, the opening height of the gate and the pressures on the pressure segment were recorded. The space between the gate and the segment was filled with water almost all the time. The water flow took place over, under and beside the segment. Only in the case where the opening gap of the gate became smaller than the opening of the segment, was it no longer overflowed.

The force curve for different opening and closing operations, depending on the opening of the roller gate, showed that in the case of larger opening heights the force measured corresponds approximately to the force of gravity.

With small opening heights of the gate in the range of the segment opening, there was an increase in the downward force of about 8.2 to

24.6 kN (prototype). The dynamic load during the opening process was largest if the gap below the segment had a height of 0.48 m. This additional suction effect amounted to a maximum value of about 20% of its own weight.

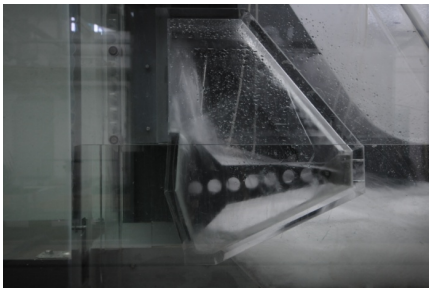

Fig. 3: Flow conditions with a segment opening of 16 cm, contactor opening 3.20 m (prototype values)

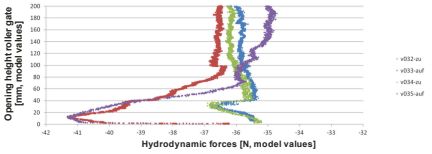

Fig. 4: Hydrodynamic forces (model values) as a function of the opening height of the roller gate, segment opening 0.48 m

In addition, measurements made on the stationary gate showed, that the forces on the moving gate, especially in the initial phase of the opening process, were much higher than the forces on the stationary gate.

2.3 Pressure measurements

The pressure measurements at four points along the surface of the gate used a capacitive pressure transmitter Keller series 41, with a measuring range 0 to 0.1 bar.

The highest pressures occurred in the case of an opening height of the roller gate of 3.2 m. On average they were slightly below the storage target. The maximum value was measured at the second measuring point from above during a segment opening height of 0.16 m. The biggest pressure fluctuations occurred at a segment opening height of 0.16 m in the upper area as well as at the segment opening height of 0.80 m in the lower area of the segment.

2.4 Frequency analysis

The auto power spectrum of the response showed that fluctuations occurring in either the force or the pressures cause a particular excitation frequency.

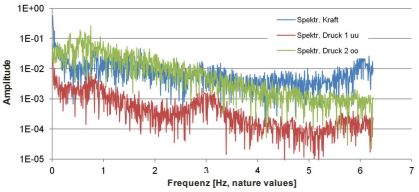

Fig. 5: Power spectra, segment opening 0.48 m, gate opening 0.32 m (prototype values)

3. Conclusions

The investigations showed the largest hydrodynamic force was approximately 24.6 kN greater than the weight of the pressure segment and acted downwards. This additional pull was equivalent to c. 20% of its own weight. It occurred at a segment opening of 0.48 m during the opening process. The greatest pressure on the segment was measured at the uppermost measuring point. It was about 17.50 m head above the contact point of the segment.

30th DANUBIA-ADRIA
Symposium on Advances in Experimental Mechanics
September 25-28, 2013 - Primošten, Croatia

5A02 050

DETERMINATION OF SIMULATION PARAMETERS FOR SPACE-HARMONIC ANALYSIS OF PERIODICALLY STIFFENED PANEL

Ante Skoblar[1], Roberto Žigulić[1], Sanjin Braut[1], Goranka Štimac[1]

[1] University of Rijeka, Faculty of Engineering, Vukovarska 58, HR-51000 Rijeka, CROATIA.
E-mails: askoblar@riteh.hr, zigulic@riteh.hr, sbraut@riteh.hr, gstimac@riteh.hr

1. Introduction

Space-harmonic analysis is used to determine sound transmission through periodically supported panel and includes a definition of the panel vibrations and acoustic fields on both sides of the panel. Periodically stiffened panel, with the aspect ratio of panel elements (bounded by stiffeners) greater than three or so, can be represented approximately by a one dimensional periodically supported beam for the case when the acoustic field intensity vectors are in a plane perpendicular to the panel and the supports (Fig. 1), [1-2].

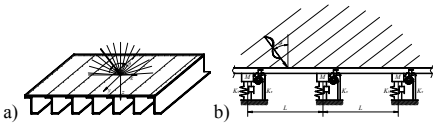

Fig. 1. Schematic representation of a) finite stiffened panel and b) the corresponding infinite beam

In this extended abstract the determination of equivalent simulation parameters of space-harmonic analysis (elastic modulus and stiffness) for the experimental model on Figure 2 is described.

Fig. 2. Experimental model of periodically supported panel with an axial exciter Schenck VibroPower 41

2. Determination of simulation parameters

Experimental model consists of a steel plate on which the elastic elements (homogeneous rubber seals with rectangular cross-section) are periodically glued and are supported with a steel frame. Steel plate modulus of elasticity is determined by measuring the transient response first eigenvalue for the steel strip (Fig. 3a) clamped on one side using Euler-Bernoulli beam theory for clamped-free boundary condition. Accuracy of results is confirmed by the finite element model.

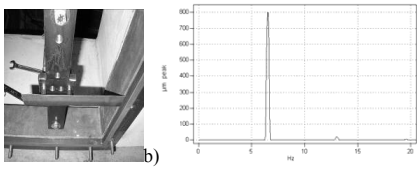

Fig. 3. a) Experimental model of steel strip clamped on one side and b) free vibration frequency spectrum

Steel plate structural damping is determined from the transient response of steel strip (Fig. 4) by calculating the logarithmic decrement for lightly damped structures (ζ<0.1).

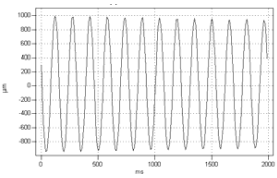

Fig. 4. Steel strip transient response

Panel overall structural damping is determined from the transient response of the whole panel (Fig. 5) by calculating the logarithmic decrement

for lightly damped structures noting that the obtained damping is $\zeta = 0.12$. Damping value is confirmed with the half-power bandwidth method for the first eigenvalue on the panel frequency response diagram (Fig. 6).

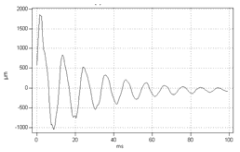

Fig. 5. Panel transient response

Elastic supports modulus of elasticity is determined from matching of measured and calculated first eigenvalue which is calculated with the finite element model into which all known parameters, together with the panel overall damping coefficient, is included (Fig. 6). Elastic supports damping is calculated in the same way except steel plate damping is used instead of panel overall damping coefficient. Now, all the parameters for the panel finite element model is defined and appropriate direct frequency response is given on Fig. 7.

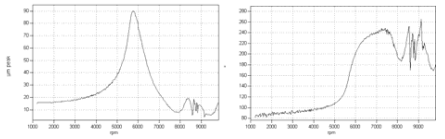

Fig. 6. Panel frequency response for the excitation and sensor in the panel 4th period (see Fig. 2)

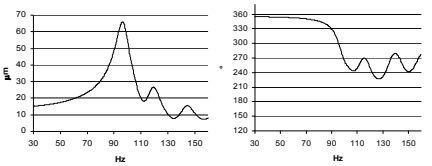

Fig. 7. Simulation result of panel direct frequency response using finite element method

The first (97.3Hz) and the fourth eigenvalue (143.9Hz) of flexural vibration on x-axis (Fig. 1) are visible on measurements and simulations while the second (103.6Hz) eigenvalue is not visible at all and the third (118.9Hz) eigenvalue is visible just on simulation even though at position of axial exciter and sensor there are amplitudes of all mentioned modes. That is caused by structure damping and vicinity of the first three eigenvalues.

Determination of equivalent simulation parameters for space-harmonic method from simulation parameters for finite element method is done because the beam model in space-harmonic method is infinite. Equivalent steel plate modulus of elasticity is determined from matching of the first eigenvalue of steel plate (Fig. 8a) and infinite periodically simply supported beam. This eigenvalue is the reference because its value do not change with the number of equal panel periods. Specified eigenvalue is also the same for finite beam so the steel plate equivalent modulus of elasticity is determined using Euler-Bernoulli beam theory with the pinned-pinned boundary condition.

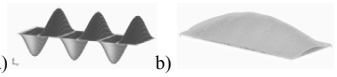

Fig. 8. Reference mode for a) calculation of the equivalent steel plate elastic modulus and b) calculation of equivalent supports stiffness

Equivalent supports stiffness is determined from matching of the first eigenvalue of the panel and infinite periodically supported beam (Fig. 8b) at which the minimum sound transmission loss appears (Fig. 9).

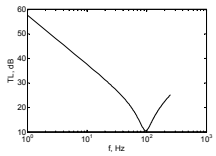

Fig. 9. Sound transmission loss diagram

3. Remarks

- Equivalent values of the steel plate modulus of elasticity and the support stiffness are determined from the reference eigenvalues and modes of vibration.
- The panel damping value is at upper limit of lightly damped structures.

Acknowledgements

This work was supported by project IPA CBC /2nd/0127/AdriaHUB.

References

[1] Mead, D. J., Wave propagation in continuous periodic structures, Journal of Sound and Vibration, 190(3), 1996. pp. 495-524.

[2] Lee, J.-H., Kim, J., Analysis of sound transmission through periodically stiffened panels by space-harmonic expansion method, Journal of Sound and Vibration, (2002) 251(2), pp. 349-366.

30th DANUBIA-ADRIA
Symposium on Advances in Experimental Mechanics
September 25-28, 2013 - Primošten, Croatia

5A03 020

FALLING CHAIN – EXPERIMENTAL VALIDATION OF NUMERICAL SIMULATIONS

Pawel Fritzkowski[1], Henryk Kaminski[1]

[1] Poznan University of Technology, Faculty of Mechanical Engineering and Management, Institute of Applied Mechanics, 24 Jana Pawła II St., 60-965 Poznan, POLAND. E-mails: pawel.fritzkowski@gmail.com, henryk.kaminski@put.poznan.pl

1. Introduction

Many problems considered by the pioneers of mathematical physics were devoted to one-dimensional continua including flexible slender bodies like ropes and chains. For centuries many types of models, both continuous and discrete, have been developed to describe dynamics of such systems. Nowadays, results of theoretical and numerical studies can be easily verified by experiments. For instance, motion of string pendula was investigated by Kuhn et al. [2] and Takehara et al. [4] whereas Schagerl et al. [3] and Tomaszewski et al. [5] analyzed fall of a folded chain.

However, the reported studies usually focus on a short time interval – initial phase of motion which relates to a sharp peak in the velocity of the chain tip. Moreover, most authors have neglected air resistance. In this paper results of numerical and laboratory experiments are confronted. The analyses are performed for motion lasting several seconds. In the simulations the air drag is taken into account.

2. Methods

In the laboratory experiments we used a steel chain consisting of $n = 34$ links (see Fig. 1). Each segment has length $l = (16 \pm 0.1)$ mm and width $b = (5 \pm 0.1)$ mm. Total length of the system $L = (446 \pm 1) \cdot 10^{-3}$ m and mass $M = (17 \pm 1) \cdot 10^{-3}$ kg. as can be seen in Fig. 1, every second link is marked with a coloured stripe.

The chain is suspended against a background of a firm whiteboard (see Fig. 2). As a support we use an additional link, fixed in the vertical plane, perpendicular to the board. It enables free swinging of the system. The other end of the chain, B, is attached with a bolt and is released manually.

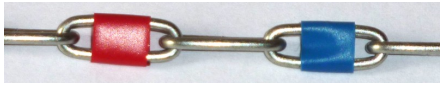

Fig. 1. Chain used in the laboratory experiments

Motion of the system is recorded on a high speed camera (Photron 1024 PCI) at 1024×1024 pixel resolution, at frame rate of 500 fps. Controlling the camera settings as well as data acquisition are done via a computer with an appropriate software. For motion analysis, i.e. tracking of points and determining their positions in particular frames, the Photron Motion Tools application is used.

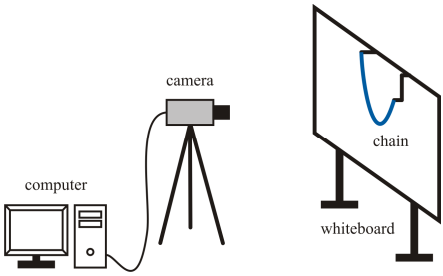

Fig. 2. Schematic model of the experimental setup

Numerical simulations of the chain motion are based on the two-dimensional discrete model discussed in Ref. [1]. The links are treated as cylindrical rigid rods of length $l = L/n$, mass $m = M/n$ and diameter d; the elements are connected by dissipative joints. Equations of motion of the system can be written as:

$$\mathbf{M}(\mathbf{q})\,\ddot{\mathbf{q}} = \mathbf{f}(t, \mathbf{q}, \dot{\mathbf{q}}), \qquad (1)$$

where **q** is the vector of angular generalized coordinates (see Fig. 3). The term **f** includes the generalized forces Q_i of different nature. The ones related to air resistance results from the classical approach: the drag force proportional to the velocity squared. Empirical formula of the drag coefficient is assumed for a cylinder of diameter $d = b$. In turn, the viscoelastic damping in the joints is described by a uniform coefficient c_φ. The equations (1) are solved with a use of the MEBDFV solver [1].

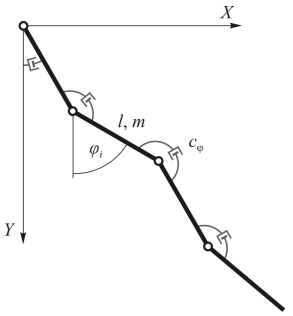

Fig. 3. Multibody model of a chain

3. Results

Experiments have been conducted for two initial configurations of the chain, i.e. different position of the end *B* (see Tab. 1). The damping coefficient was estimated by trial and error. The distance between the numerical and experimental data was calculated by taking positions of the last link only. The optimal value of the parameter was found to be $c_\varphi = 6.2 \cdot 10^{-6}$ Nm·s.

Experiment designation	x_B [m]	y_B [m]	d_{RMS} [m]
I.	0.279	0.087	0.0118
II.	0.390	0.087	0.0113

Tab. 1. Initial position of the chain tip and the RMS distance between the numerical and experimental data

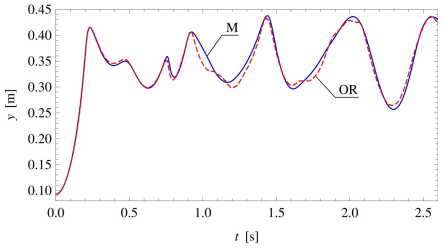

Fig. 4. The *y*-coordinate of the last link

Figure 4 presents the *y*-coordinate of the *n*th link of the model (M) and the real object (OR). Values of the RMS distance, d_{RMS}, calculated over time interval $t \in \langle 0, 2.6 \rangle$ s are given in Tab. 1. As it can be seen, there is a high agreement between M and OR. The function $d_{RMS}(t)$ does not exceed $0.08L$ in both cases. The maximal differences are connected to violent motion which is typical for the classical case of the folded chain [5].

4. Remarks

- The model used in the simulations is based on restrictive assumptions: planar motion of the chain; viscoelastic damping approximates friction between links; same coefficient c_φ for all the joints; drag coefficient for a simplified element shape.
- However, there is a good agreement between the numerical results and the experimental data. It seems that the applied model allows us to faithfully simulate global dynamics of the analyzed real system.

Acknowledgements

This work has been supported by 21-407/2012 DS-MK grant.

References

[1] Fritzkowski, P., Kaminski, H., A discrete model of a rope with bending stiffness or viscous damping. Acta Mech. Sin., **27**, 2011. pp. 108-113.

[2] Kuhn, A., Steiner, W., Zemann, J., Dinevski, D., Troger, H., A comparison of various mathematical formulations and numerical solution methods for the large amplitude oscillations of a string pendulum, Appl. Math. Comput., **67**, 1955. pp. 227-264.

[3] Schagerl, M., Steindl, A., Steiner, W., Troger, H., On the paradox of the free falling folded chain. Acta Mech., **125**, 1997. pp. 155-168.

[4] Takehara, S., Terumichi, Y., Nohmi, M., Sogabe, K., Numerical and experimental approaches on the motion of a tethered system. J. Sys. Des. Dyn., **2**, 2008. pp. 1106-1117.

[5] Tomaszewski, W., Pieranski, P., Geminard, J.C., The motion of the freely falling chain tip. Am. J. Phys., **74**, 2006. pp. 776–783.

30th DANUBIA-ADRIA
Symposium on Advances in Experimental Mechanics
September 25-28, 2013 - Primošten, Croatia

5A04 015

EXPERIMENTAL AND NUMERICAL STUDY REGARDING THE PARALEL PLANE TEST FOR POLYETHYLENE PIPE STIFFNESS

Adrian Pascu[1], Valentin Oleksik[1], Ionel Ciupe[1]

[1] "Lucian Blaga" University of Sibiu, Faculty of Engineering, Emil Cioran street, no. 4, 550024, Sibiu, ROMANIA. E-mail: adrian.pascu@ulbsibiu.ro, valentin.oleksik@ulbsibiu.ro, ion.ciupe@ulbsibiu.ro

1. Introduction

Stiffness can be define like a as resistance to deflection. Ring stiffness is similar in form to the leaf spring stiffness and it contains the term, EI/D^3, which shows up in every analysis of ring deformation and deflection. For a pipe with a rectangular wall cross section, $I = t^3/12$ centroidal moment of inertia of the cross sectional area (of the wall per unit length in the case of a pipe), the bending stiffness of a pipe according to ASTM D2412 – 11 [3] becomes:

$$SN = 0.083 \frac{E}{(D/t)^3} \left[\frac{N}{mm^2} \right], \quad (1)$$

Term D/t is another form of ring stiffness. Stiffness can be expressed in a variety of ways, but for pipe stiffness, is preferred by plastic pipe industries because it can be measured by a parallel plate test (PPT). To perform this test, a length of pipe, usually longer than one diameter, on a flat surface is F-loaded as shown in Fig. 1. As load F is applied in increments, corresponding deflections (δ) are measured [1].

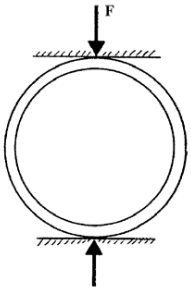

Fig. 1. Parallel plate test for pipe

2. Tests and acquisition of experimental results

For determining the deformation of polyethylene pipes used for the transport of natural gas, experimental tests were performed using a universal testing machine, Instron 5587. The samples were cut in the form of rings from pipe (made from PE80 and PE 100) with 90 mm external diameter and 8.2 mm thickness [4]. For this pipes, the ring stiffness calculated with equation (1) are SN_{PE80} = 0.076 and SN_{PE100} = 0.101 (E_{PE80} = 0.9 GPa, E_{PE100} = 1.2 GPa).

All the tests were conducted in order to determine the mode of deformation of such specimens to determine the elastic recovery and to determine the strains and tensions that arise in such structures. For these experimental measurements, in addition to Instron machine software it was also used an optical method that uses equipment of the type Aramis 2M.

For the pipe studied they were cut in pieces of about 50 mm long, which were requested by radial compression. For the data optical acquisition using Aramis 2M system, before being required to compression, the pipe pieces were coated with quick-drying slip matt white paint and after that, it was sprayed with graphite spray on exposed areas of the imaging system (Fig. 2). Polyethylene pipes were requested to a maximum compression force of 2 kN, the loading speed being of 10 mm / min, achieving at the same time as the data acquisition deformation of the pipe by the Aramis 2M system and the behavior data from their compression using Instron machine software, BlueHill.

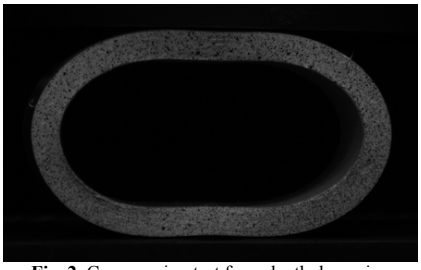

Fig. 2. Compression test for polyethylene pipe

Using the software equipment Aramis 2M there were determined the following: deformations (displacements of points on the pipe contour) in the three directions (Δx, Δy (Fig.3), Δz), total deformation (Δe), the main specific deformation (ε_1), the Tresca equivalent specific deformation (ε_T), the VonMises equivalent specific deformation (ε_{VM}), relative thinning (δ).

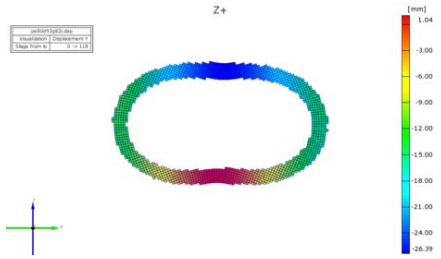

Fig. 3. Pipe displacement on vertical direction (Oy)

Using the BlueHill software from Instron machine, we determined the load - deformation characteristic curves for pipes studied (Fig. 4).

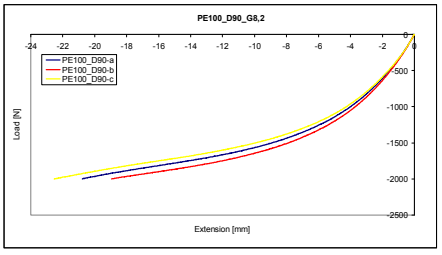

Fig. 4. Experimental load - extension curves

3. Numerical simulation

For a dynamical analysis of pipe compression was used Ls-Dyna software, and for visualization of results was used Lsprepostd software. For this analysis we create three differed parts: the pipe (deformable body) and two compression plate (rigid body) one superior (this have a displacement on vertical direction) and one inferior (fixed).

In this analysis we focus on the same results like for the experimental tests. In fig. 5 is show the displacement of pipe on vertical direction (Oy), obtained for the last increment of this numerical analysis.

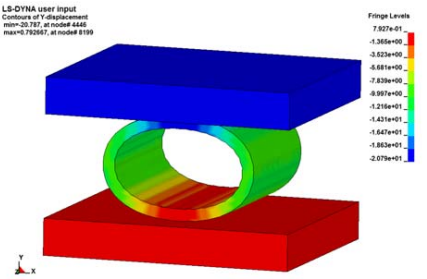

Fig. 4. Numerical

4. Remarks

- Using the Instron and Aramis equipments is possible to determinate pipe deformation in all three directions, and also the stress and strain state of pipe specimen. Using material data obtained after the experimental testing (characteristic curves) is possible to make, using Ls-Dyna software, a dynamic simulation.
- If we compare the experimental results with the numerical results (obtained using the finite element method), we observe the maximum value of pipe displacement on vertical direction is δ_y=26.39 mm in case of experimental test, and δ_y=20.79 mm, in case of numerical analysis, difference between this two is ε=21.20%.

References

[1] Watkins, R.K., Anderson, L.R., Structural Mechanics of Buried Pipes, CRC Pres LLC, 2000.

[2] Lari, L., Lifchtz, E. – Promote Understanding the Performance of Gas Pipeline Systems, New York, Manneglif, 2003.

[3] *** - ASTM D2412 – 11 - Standard Test Method for Determination of External Loading Characteristics of Plastic Pipe by Parallel-Plate Loading.

[4] *** SR ISO 4065:1995, Țevi de materiale termoplastice. Tablou universal al grosimilor de perete.

[5] * * * SR – ISO 1872-1, Materiale plastice.

30th DANUBIA-ADRIA
Symposium on Advances in Experimental Mechanics
September 25-28, 2013 - Primošten, Croatia

5A05 007

INFLUENCE OF BOUNDARY CONDITIONS ON THE STATE OF STRESS AND STRAIN IN DEEP GIRDER

Diana Šimić[1], Katina Miović[2]

[1] University of Zagreb, Faculty of Civil Engineering, Kačićeva 26, HR-10000 Zagreb, CROATIA. E-mail: dianas@grad.hr

[2] Tehnoekspert d.o.o., Vladimira Ruždjaka 9B, HR-10000 Zagreb, CROATIA. E-mail: katinamiovic@yahoo.com

1. Introduction

The analysis of stresses and strains in two reinforced concrete deep girders was performed theoretically, applying the finite element method, whereas the experimental part, i.e. the structures' models testing were undertaken in the laboratory. Reinforced concrete deep girder M1 38 cm thick, is relied on reinforced concrete pillars which are fixed into the base, Fig.1. Another reinforced concrete deep girder M2 38 cm thick, is rigidly fixed into the base, Fig.2.

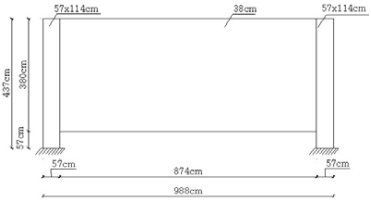

Fig. 1. Reinforced concrete deep girder M1.

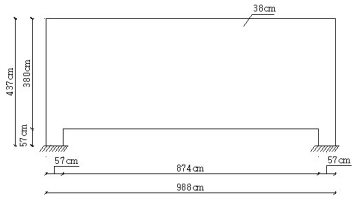

Fig. 2. Reinforced concrete deep girder M2.

The models for laboratory testing were developed in 1:10 scale, manufactured from medium density fibreboard plate 38 mm in thickness. Model 1 is a deep girder which is relied on pillars that are fixed into the base. The pillars were glued and fastened with screws to the girder of MDF. A disposition of measuring spots and load scheme for model 1 is shown in Fig. 3.

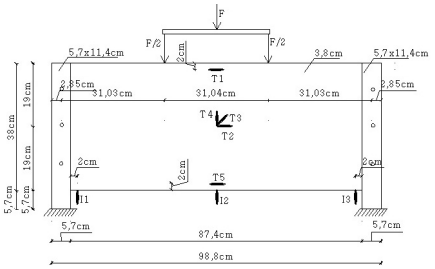

Fig.3. Disposition of resistance strain gauges "T", inductive strain gauges "I" and load scheme on model 1.

Model 2 is a deep girder which is rigidly fixed into the base and its load scheme and disposition of measuring spots is shown in Fig. 4. Measuring of strains was conducted with resistance strain gauges, and displacements were measured with inductive strain gauges [1].

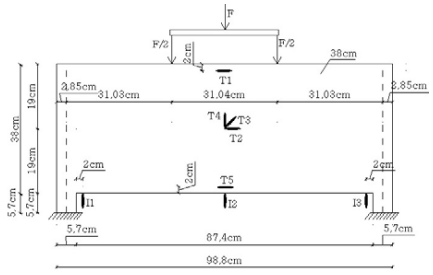

Fig.4. Disposition of resistance strain gauges "T", inductive strain gauges "I" and load scheme on model 2.

Mechanical characteristics of material (medium-density fibreboard or MDF) were determined prior to models testing. Material's

tensile strength was determined on the specimens *l/b/h=38/3.8/3.8cm* via bend testing and amounts σ_M*=26.48 MPa*. Compressive strength was tested on specimen *d/b/h=7.6/3.8/7.6cm* and amounts σ_M*=139.3 MPa*. Elastic constants of MDF: elasticity module *E=3235MPa* and Poisson's ratio *v=0,3* were determined on prismatic specimens *d/b/h=7.6/3.8/22.8cm*.

2. Experimental Results

The testing of model 1 was conducted in fifteen phases, and model 2 in eleven phases through gradual growth of loading. Maximum loading for model 1 amounted F=53.5 kN, and for model 2 was F=50 kN. The testing model 2 is shown in Fig. 5, and the detail of deep girder reliance of model 1 is shown in Fig. 6.

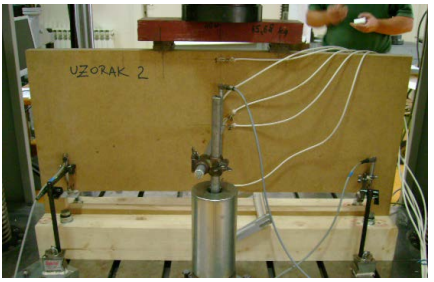

Fig. 5. Model 2, ready for testing.

Fig. 6. The detail of deep girder reliance of model 1.

During the models testing, strains and displacements were measured. To obtain equal stress condition on the reinforced concrete deep girder's prototype and on the belonging model in the laboratory, a dimensional analysis implies that the structure's prototype should be loaded with 100 times bigger load than the load model. E_b=25000 MPa elasticity module was taken for concrete. Deflections on the model and on the deep girder's prototype are in the ratio 125/160.

The investigation results for the load F=15 kN model1 and model 2 were taken for the sake of comparison, and they are corresponding with the load of the deep girder prototype F=1500 kN. The reinforced concrete deep girder models were analyzed using the software program package SAP 2000 [2]. Deep girders were modelled using plate elements, while the columns were modelled by bar elements [3]. Fig 7 shows diagrams of normal stresses in the middle of the span for reinforced concrete deep girders M1 and M2 obtained by FEM computation on the prototype and experimentally, by model investigation (10 times minimized) at the loading F=1500 kN.

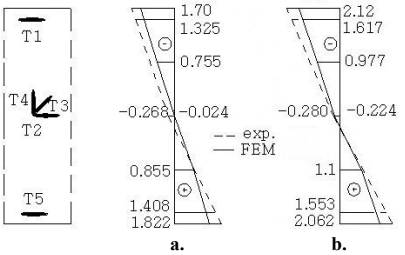

Fig. 7. Stress diagrams σ [MPa]: a) deep girder M1, b) deep girder M2.

Displacement results of reinforced concrete deep girders M1 i M2 at load F=1500 kN are given in Tab.1.

Tab. 1. Displacement results of deep girders M1 i M2 at load F=1500 kN.

Deep girder		Displacement [mm]		
		I1	I2	I3
M1	Testing	0.110	0.623	0.120
	Computation	0.0595	0.390	0.0595
M2	Testing	0.489	0.897	0.402
	Computation	0.156	0.468	0.156

3. Conclusion

The results analysis of conducted investigations for two reinforced concrete deep girders (M1 and M2) indicated that the differences in stresses amounted even up to 18%, and in displacements up to 16, 7%. A deep girder with the columns (M1) is a better solution for the construction than the deep girder (M2) rigidly fixed into the base.

References

[1] Dally J. W., Riley W. F, Experimental Stress Analysis, Mc.Graw-Hill, Inc. New York, London, Tokyo, 1991.
[2] Sap 2000 Analysis Reference Manual, Computers and Structures, Inc., Berkeley, California, 2002.
[3] Sorić, J.: Metoda konačnih elemenata, Biblioteka tehnička mehanika, Zagreb, 2004.

30th DANUBIA-ADRIA
Symposium on Advances in Experimental Mechanics
September 25-28, 2013 - Primošten, Croatia

5A06 110

EXPERIMENTAL INVESTIGATION OF REHABILITATING A RC BRIDGE BY ADDING A CONCRETE OVERLAY

Yvonne Theiner, Martin Drexel and Günter Hofstetter

University of Innsbruck, Institute of Basic Sciences in Engineering Science, Technikerstr. 13, 6020 Innsbruck, Austria.

Corresponding author: yvonne.theiner@uibk.ac.at

1. Introduction

Most of the literature on strengthening of existing reinforced concrete structures by adding a concrete overlay is based on lab tests [1], [2]. Contrary to the latter, in the present contribution an experimental study of strengthening a reinforced concrete bridge by a concrete overlay is presented. The RC plate girder bridge to be strengthened was built in 1970 as part of the Austrian road network and is characterized by a width of 15 m and four webs and three spans in longitudinal direction (Fig. 1). For restoring the load bearing capacity of the aged bridge and for improving its structural capacity, a 90 mm thick reinforced concrete overlay is added.

Fig. 1: View of the reinforced concrete bridge to be strengthened.

2. Experimental Program

In the framework of the experimental investigation depth dependent and time dependent moisture distribution profiles of the existing bridge deck and the added concrete overlay were determined by means of a non-destructive system. The measurements of mass water contents were started before the beginning and continued during rehabilitation work and are still going on. Furthermore, deformations of the strengthened concrete bridge, ambient temperature, relative ambient humidity and wind speed were monitored by means of respective sensors.

For investigation of the restraint effects exerted from the substrate to the overlay, the in-situ measurements were accompanied by a comprehensive laboratory test program concerning the evolution of shrinkage strains. Hence, water desorption isotherms and the ultimate drying shrinkage strains were determined for both, the substrate and overlay concrete. Additionally, time dependent moisture distribution profiles and combined autogenous and drying shrinkage strains were determined on prismatic lab test specimens.

3. Experimental results

3.1 In-situ measurements

Multi-Ring Sensors (MRS) for measuring electrolytic resistances were placed in the existing bridge deck as well as in the concrete overlay.

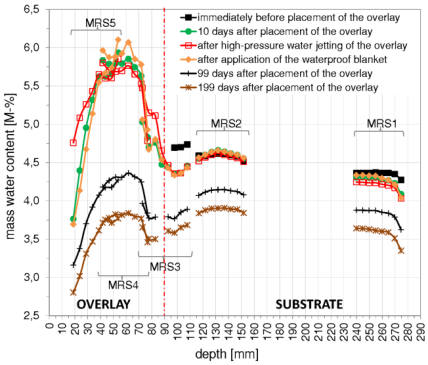

Fig. 2: Mass water content distributions in the existing bridge deck for different steps during the rehabilitation work.

By means of calibration curves the electrolytic resistances, measured at the 8 measuring points of each MRS, were converted to the respective mass water contents. Fig. 2 exemplarily from left to right shows the moisture distribution profiles from the top surface of the overlay to the lower surface of the existing bridge deck during the rehabilitation work.

3.2 Laboratory measurements

The water desorption isotherms and the ultimate drying shrinkage strains of substrate and overlay concrete were determined on thin lab test specimens. After moisture equilibrium during moist curing was achieved, the thin specimens were stored in 5 desiccators until constant values of relative ambient humidity (RH) of 97%, 85%, 75% 59% and 43% were achieved, respectively. Fig. 3 shows the mean values of the equilibrium mass water content for the mentioned five values of ambient relative humidity for both, the substrate concrete and the overlay concrete.

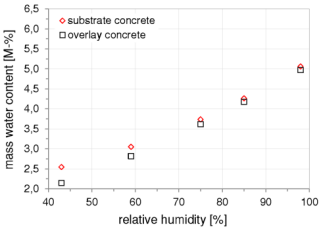

Fig. 3: Water desorption isotherms (mean values) for substrate concrete and overlay concrete.

3.3 Comparison of lab test results and in-situ measurements

In addition to the lab tests mentioned so far, further lab tests were carried out on 3 concrete prisms with dimensions of 300 x 300 x 90 mm. The prisms were casted at the construction site during strengthening of the RC bridge. They were equipped with Multi-Ring Sensors (MRS). The lateral surfaces of 2 prisms were sealed immediately after casting for achieving one-dimensional moisture migration. One prism was additionally sealed at the top surface for considering the effects of primer and waterproof blanket, which were applied on the overlay surface of the RC bridge. Comparison of the mass water content distributions of the latter with the respective distributions of the concrete overlay is shown in Fig. 4. The comparison clearly shows the effects of convective surface moisture transfer due to wind at the construction site.

Due to a pronounced surface moisture transfer between RC member and environment compared to the one occurring between lab test specimen and uniform climatic conditions, moisture equilibrium between existing bridge deck and overlay concrete will be achieved long before the composite specimen shows a uniform distribution of mass water content along the interface.

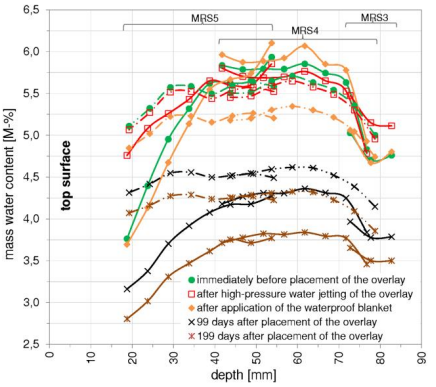

Fig. 4: Comparison of the mass water content distributions measured in the concrete overlay (continuous lines) and in a lab test specimen (dashed lines) for selected time instants.

Comparison of the in-situ measurements with previous lab test results [2] will allow the assessment of surface preparation on the bonded overlay behaviour and, hence, the examination of the significance of results from lab tests for real bridge decks strengthened by overlays.

4. Acknowledgements

Financial support for this research project by the Austrian Federal Provinces is gratefully acknowledged.

5. References

[1] J. M. Calixto, E. F. Pires, S.A. Lima, E. M. Piancastelli, Behavior of Reinforced Concrete Slabs Strengthened in Flexure by Concrete Overlays. ACI - Special Publication, Vol. 229 (2005), 389-406.

[2] Y. Theiner, G. Hofstetter, Evaluation of the effects of drying shrinkage on the behavior of concrete structures strengthened by overlays. Cement and Concrete Research, Vol. 42 (2012), 1286-1297.

30th DANUBIA-ADRIA
Symposium on Advances in Experimental Mechanics
September 25-28, 2013 - Primošten, Croatia

5A07 103

TESTING OF CRACKED CONCRETE SLABS

Marko Bartolac, Mladenko Rak, Marina Frančić

University of Zagreb, Faculty of Civil Engineering, Fra Andrije Kačića Miošića 26, HR-10000 Zagreb, CROATIA. E-mails: mbartolac@grad.hr, rak@grad.hr, mfrancic@grad.hr

1. Introduction

This paper presents testing of cracked concrete slabs in a three-storage underground garage in one shopping center in Zagreb. Axial dimensions of the slabs supported by rectangular columns (1,2 m x 0,6 m) are 8 m x 8 m and their thickness is from 28 cm to 32 cm, depending on the slab's position. Most of the cracks appeared soon after the center was built, in 2007. These cracks present a constant problem for durability of slabs because water (comes into garage by cars during rain or snow) that leaks through them causes corrosion of reinforcement bars and, subsequently, deterioration of concrete protection layer. Some of the cracks spreaded through whole height of the slabs and, therefore, testing of the slabs was needed in order to check their load bearing capability before making decisions about their sanation. Although four cracked slabs were tested, we will here show brief results for one characteristic slab.

2. Testing description

Slabs were tested both statically and dynamically. For static load, four forklifts were used that approximately matched the design load (Fig. 1). During static testing, displacement was measured in the center of the slab and strain were measured in total of 10 positions, in upper (compression) and lower (tension) zone of the slab (Fig. 2). Both parameters were measured with inductive sensors. Strain measurement positions were determined, among standard criteria, by taking crack position into consideration.

Fig. 2. Slab loaded with forklifts.

During dynamic testing, modal parametrs (modal shapes, frequencies and damping ratios) of the slabs were determined by means of operational modal analysis (OMA) using piezoelectric accelerometers (9 measuring positions, Fig. 3) and associated analyzer. Excitation was induced by jumping on the slab.

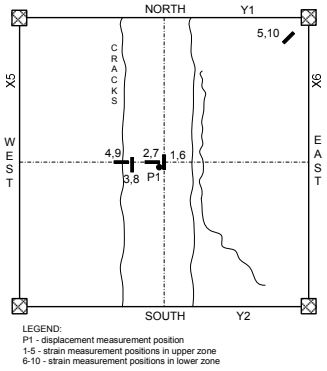

Fig. 2. Measurement positions for static testing.

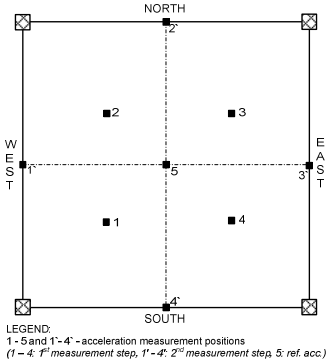

Fig. 3. Measurement positions for dynamic testing.

3. Testing results

Following tables (Tab. 1 and Tab. 2) and figures (Fig. 4 and Fig. 5) are showing results of static testing. Tables show maximum measured values and values remained after unloading the slab.

Measurement position	$\varepsilon_{maximum}$ [μm/m]	$\varepsilon_{remained}$ [μm/m]
1 (up)	-27,0	-0,8
6 (down)	15,4	1,2
2 (up)	-16,4	-0,7
7 (down)	9,7	0,5
3 (up)	-18,9	-0,5
8 (down)	35,6	2,2
4 (up)	-82,4	3,9
9 (down)	77,1	6,9
5 (up)	22,3	1,2
10 (down)	-36,2	0,8

Tab. 1. Strain measurement results.

Displacement in center of the slab	$w_{maximum}$ [mm]	$w_{remained}$ [mm]
	1,92	0,07

Tab. 2. Displacement measurement results.

Fig. 4 shows time record of strain in measurement positions in lower zone of the slab. The slab was loaded twice to investigate (proove) its elastic behavior.

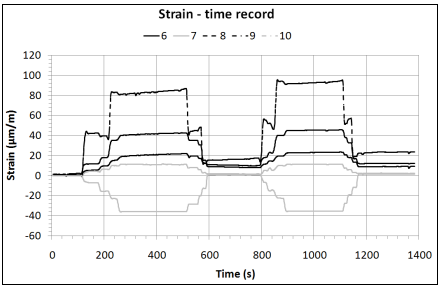

Fig. 4. Strain record.

Modal frequencies and damping ratios (Tab. 3) are determined from analysis of records of singular values of autospectral densities. Fig 5. shows experimentally determined first and second modal shape.

Mode	Frequency [Hz]	Damping ratio [%]
1	10,94	3,07
2	18,52	1,12
3	21,33	0,78
4	28,57	0,50
5	35,91	0,51

Tab. 3. Modal frequencies and damping ratios.

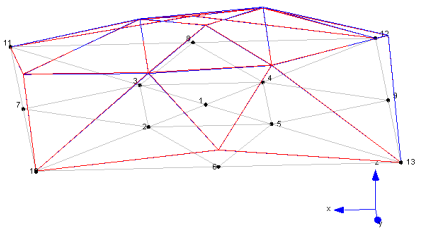

Fig. 5. First modal shape (10,94 Hz).

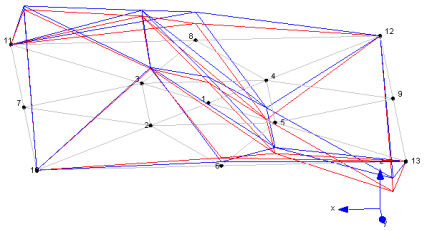

Fig. 6. Second modal shape (18,52 Hz).

4. Conclusion

Behavior of cracked slabs under load was elastic what is proven with negligible remained values of strain and displacement. Results of dynamic testing show that global stiffness of the slabs is preserved. Therefore, load bearing capability of the slabs is insured and sanation is needed only for durability reasons.

References

[1] Rak, M., Damjanović, D., Duvnjak, I., Bartolac, M., Čalogović: Report on static and dynamic testing of slabs POZ 100 and POZ 200, University of Zagreb, Faculty of Civil Engineering, Department of Engineering Mechanics, 2013.

[2] Zihai, S: Crack analysis in structural concrete, Theory and Applications., Elsevier, 2009.

[3] Nilson, A. H., Darwin, D., Dolan, C.: Design of concrete structures, McGraw-Hill, 2004.

30th DANUBIA-ADRIA
Symposium on Advances in Experimental Mechanics
September 25-28, 2013 - Primošten, Croatia

5A08 091

A DESIGN OF A NEW MAGNETIC REFRIGERATOR BASED ON THE MAGNETO-BAROCALORIC EFFECT

Agata Czernuszewicz, Jerzy Kaleta, Daniel Lewandowski

Wroclaw University of Technology, Institute of Materials Science and Applied Mechanics, Mariana Smoluchowskiego 25, 50-370 Wroclaw, Poland. E-mail: agata.czernuszewicz@pwr.wroc.pl

1. Introduction

The magneto-barocaloric effect is a combination of the magnetocaloric effect and the barocaloric effect. It is a physical phenomenon that causes temperature changes in selected materials. This effect can be applied in various cooling devices. A refrigeration method based on the magneto-barocaloric effect is the so-called magnetic cooling. The magnetic refrigerator utilises solid-state refrigerant. It is environmentally-friendly alternative to the most commonly used vapour-compression technology. Conventional refrigerators employ gases which contribute to global warming and ozone layer depletion. Moreover, they are less energy-efficient compared with magnetic cooling devices.

The magneto-barocaloric effect is exhibited by first-order magnetic materials. Magnetisation and application of the pressure cause an increase in their temperature as well as a decrease in magnetic entropy. Demagnetisation and pressure release result in temperature drop and magnetic entropy rise.

The paper presents a design of a test stand for studies of materials that exhibit the magneto-barocaloric effect. The test stand is at present under construction.

2. Structure of the test stand

A device to study the magnetocaloric effect was presented by the authors in [1]. This test stand will be developed in order to enable introduction of stresses in tested materials (to cause the barocaloric effect). The general scheme of the new device is shown in Fig. 1.

The stand is composed of 6 main parts: a magnetic bed, a magnet, a pump, a force transmitting system and two heat exchangers (cold and hot).

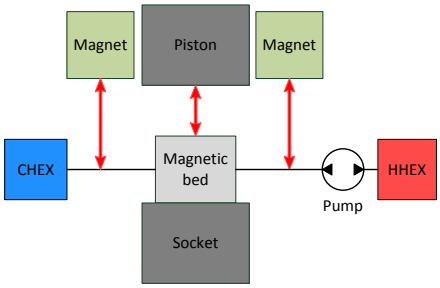

Fig. 1. General scheme of the test stand.

The magnetic bed is a main part of the device. Fig. 2 presents a model of the magnetic bed. The bed has two inlets/outlets for a fluid flow. One is connected with a cold heat exchanger and the other is connected with a pump. The magnetic bed is filled with a tested material. The magneto-barocaloric material has a form of pipes. The thickness of their wall amounted to 1 mm. These pipes are connected in parallel with the aid of flexible pipes (made of plastic). Furthermore, flexible pipes separate tested pipes from one another. Each magneto-barocaloric pipe has two inlets/outlets for a heat transfer medium flow. Inlets/outlets are located on opposite sides of pipes in order to force fluid to flow along their entire length. The magneto-barocaloric pipes are fasten to two composite plates that fulfil functions of a bottom and a top. Moreover, the plates isolate the magneto-barocaloric material from a socket and a piston in order to prevent heat exchange.

The magnetic bed is placed in the socket. The force is transmitted to the magneto-barocaloric material by a piston (it causes introduction of stresses in the tested material). In the same time the

material is magnetised by a 1 T magnet assembly. This assembly is built out several permanent magnets that concentrate and homogenise the magnetic field on the one side and reduces on the other side. This arrangement is the so-called Halbach array [2]. The piston and the Halbach array are moveable in order to cyclically magnetised/demagnetised and applied/released pressure in the magneto-barocaloric material therefore its temperature is changing.

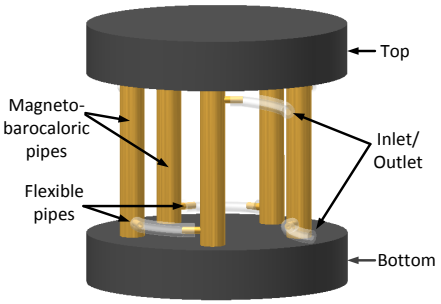

Fig. 2. Model of the magnetic bed.

To exchange a heat in the system a two-directional pump, a heat transfer medium and two heat exchangers are employed. The medium is in liquid form. It is transferred with the aid of the peristaltic pump. The heat generated by the magneto-barocaloric material is transported to the hot heat exchanger which expels it to the environment. The heat from the cold heat exchanger is absorbed by the fluid after the demagnetisation process. This heat exchanger is insulated.

3. Work cycle

The device works in AMR (Active Magnetic Regenerator) work cycle [3]. In this cycle material fulfils the function of refrigerant as well as regenerator. The AMR work cycle consists in four steps. In the first step magneto-barocaloric material is magnetised and uniaxial pressure is applied in adiabatic conditions. This process causes increase in material's temperature. The second step is a process in the constant magnetic field and at constant pressure. In this stage the medium flows from the cold heat exchanger, absorbs heat from the material and removes it to the hot heat exchanger. As a result temperature of the material decreases. The third step is adiabatic demagnetisation and pressure release. After this process temperature of the magneto-barocaloric material decreases. The last step is a process without either magnetic field or uniaxial pressure. In the process the medium flows from the hot heat exchanger, expels heat to the material and absorbs heat from the cold heat exchanger.

4. Conclusion

In the paper a concept of the magnetic refrigerator based on the magneto-barocaloric effect was presented. The device will generate cooling power thanks to magnetisation/ demagnetisation process and pressure apply/release process.

The employed refrigerant will be a solid material, hence the device will be more environmentally-friendly compared with conventional refrigerators. The prototype is currently under construction.

Acknowledgements

The research was done partially under the project: Seventh Framework Programme of the European Community (2007-2013), GREEN KITCHEN - Energy efficiency, optimised resources use and process innovation of home appliances and their domotic integration N° 251600 "Marie Curie Action: IAPP".

References

[1] Czernuszewicz, A., Kaleta, J., Królewicz, M., Lewandowski, D., Mech, R., Wiewiórski, P., A test stand to study the possibility of using magnetocaloric materials for refrigerators. In Proceedings of 5th International Conference on Magnetic Refrigeration at Room Temperature (Thermag V), editors C. Vasile-Muller and P. Egolf, International Institute of Refrigeration, 2012, pp. 517–524.

[2] Raich, H., Blümler, P., Design and Construction of a Dipolar Halbach Array with a Homogeneous Field from Identical Bar Magnets: NMR Mandhalas, Concepts in Magnetic Resonance Part B: Magnetic Resonance Engineering 23B (1), 2004. pp. 16–25.

[3] Steyert, W. A., Stirling-cycle rotating magnetic refrigerators and heat engines for use near room temperature, J. Appl. Phys. 49, 1978. pp. 1216–1226.

30th DANUBIA-ADRIA
Symposium on Advances in Experimental Mechanics
September 25-28, 2013 - Primošten, Croatia

5A09 055

BEARING CAPACITY OF A LAMINATED GLASS BEAM

Domagoj Damjanović[1], Joško Krolo[1], Ana Skender[1], Zrinka Brkić[1], Stjepan Pavlinić[1]

[1] University of Zagreb, Faculty of Civil Engineering, Fra Andrije Kačića. Miošića 26, 10 000 Zagreb, CROATIA. E-mail: ddomagoj@grad.hr

1. Introduction

Glass beam which is the subject of this research is the main load bearing element of the new entrance canopy of hotel Dubrovnik located in the centre of Zagreb. Structure of the canopy is designed entirely from glass. This paper presents experimental testing of laminated glass beam and determination of elasticity modulus and bending tensile strength. Laminated glass refers to two or more glass panes bonded together with an elastomeric interlayer such as polyvinyl butyral (PYB) to improve the post-breakage characteristics of the glass [1]. The concerned laminated glass beam consist of three 15 mm thick tempered glass panes bonded by interlayer and the glass cover plates consist of two 10 mm tempered glass panes. Static system of the glass beam is a simple beam with overhanging (2,0 m + 3,0 m). Beams are placed at 0,8 distance and covered by cover plates.

2. Mechanical parameters of the laminated glass

In order to determine the mechanical parameters of the basic material (laminated glass) bending tests were performed on small specimens.

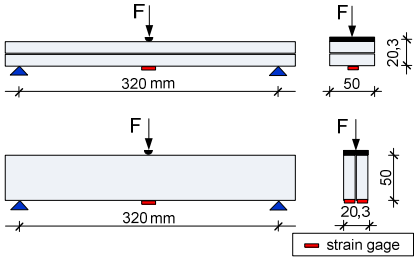

Fig. 1. Testing of the basic material

6 specimens were subjected to three point bending test, 3 were tested perpendicularly to the direction of glass layers and the other 3 parallel to the glass layers, as shown in Fig. 1.

Values of experimentally determined elasticity modulus and bending tensile strength in two directions are shown in table 1 [2].

Bending direction	Spec.	Elasticity modulus [GPa]	Bending tensile strength [MPa]
Perpendicular to layers	1	39,1	96,5
	2	37,7	90,6
	3	38,6	99,0
	$\bar{x} \pm s$	38,5±0,7	95,3±4,3
Parallel to layers	4	66,8	200,2
	5	67,1	174,4
	6	67,0	190,7
	$\bar{x} \pm s$	67,0±0,1	188,4±13,1

Tab. 1. Elasticity modulus and bending tensile strength

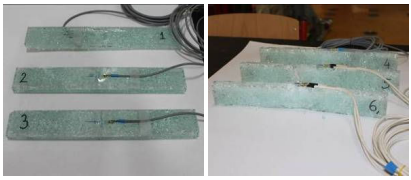

Fig. 2. Specimens of basic material

3. Experimental testing of glass beam

Total value of unfactored load (structure weight + snow load) is 3,625 kN/m along the glass beam, and resulting bending moment at the support is 16,31 kNm. Test loading was applied at the distance of 2,7 m from the support [2]. The resulting bending moments were compared to the design values caused by unfactored load in order to determine the safety coefficient. Test arrangement and measuring points are shown in figure 3.

Glass beam was tested to the level of test load ($F_{exp.}$ = 20 kN) that is equivalent to unfactored

design load with safety coefficient k = 3.31 [2]. Up to that level of load, beam acted completely elastic and no damages were observed.

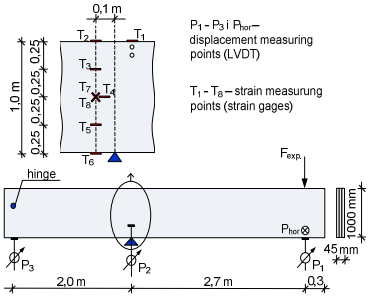

Fig. 3. Glass beam test arrangement

Testing of the glass beam was carried out using universal testing machine Zwick Z600, pictures of test arrangement and measuring points are shown in figure 4. and figure 5.

Fig. 4. Testing of the glass beam

Fig. 5. Strain measuring points

Figure 6. shows force – strain diagrams during the testing and in figure 7. stress distribution in the cross section above the support is shown. The maximum stress of +5,6 MPa was recorded at the top of the support cross section. The maximum tensile stress recorded during testing corresponds to 3% of the bending tensile strength.

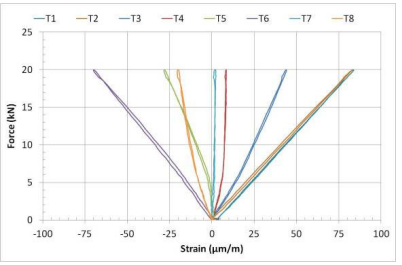

Fig. 6. Force – strain

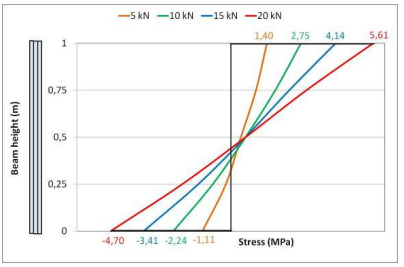

Fig. 7. Stress in the cross section above the support

4. Conclusions

During the experimental testing beam acted completely elastic without any damages, reaching the safety coefficient of k = 3,31. If the stress level reached during experimental testing (5,61 MPa) is compared to the stress reached in 3-point bending test of basic material (188,4 MPa), we can conclude that there are extremely high reserves in the bearing capacity of tested glass beam beyond the reached level of test load. Even if for some reason one of the glass panes breaks the scattered glass pieces would stick to the interlayer and in that way prevent people from getting injured and the other panes could continue to carry the loads [3]. Taking into account the behavior of laminated glass and results of experimental testing glass beam can be regarded as safe.

References

[1] Fam, A., Rizkalla, S., Structural performance of laminated and unlaminated tempered glass under monotonic transverse loading, Construction and Building Materials, 20, 2005. pp. 761-768.

[2] Rak M., Damjanović, D., Krolo, J., Report on testing of glass beam. 64-180-75/2013. Universitiy of Zagreb, Faculty of CE.

[3] Froling, M., Strength design methods for laminated glass, Division of structural mechanics, Lund University, Sweden, 2011.

30th DANUBIA-ADRIA
Symposium on Advances in Experimental Mechanics
September 25-28, 2013 - Primošten, Croatia

5A10 090

SYSTEM OF MAGNETOSTRICTIVE ACTUATOR FOR ENERGY HARVESTING FROM ULTRASONIC WAVE

Jerzy Kaleta[1], Rafał Mech[1], Przemysław Wiewiórski[1]

[1] Wrocław University of Technology, Institute of Materials Science and Applied Mechanics, Mariana Smoluchowskiego 25, Wrocław, POLAND. E-mail: rafal.mech@pwr.wroc.pl

1. Introduction

The subject of this paper was to explain the power transmission process through ultrasonic mechanical vibration using SMART materials, as a new idea for Energy Harvesting (EH) method [1]. Using magnetostrictive and electrostrictive materials that under the influence of adequately strong magnetic and electric fields change their size and which are characterized by the fact that under load produce a magnetic or electrical field, energy harvesting process is very practical [2, 3].

The aim of this work is to provide electrical power, by use of mechanical energy, for small electronic devices with one low power microcontroller. That makes this type of powering method self-sufficient, very often for decades or even for life time.

The main goal was to find the mechanical application for the chosen types of devices. In order to perform this task it was necessary to define whether all the types of harvesters are suitable for using them in mechanical environment.

In order to perform the researches of the chosen different magnetic composition device types, the actual object for testing was specified. After the objects were chosen, the preliminary test stands was made to allow proper performance check of the ultrasonic power stability. During the testing process, great attention was dedicated to the harvesting devices based on magnetostrictive materials. The new idea of harvesting device's type with dual magnetostrictive rods was presented and tested for the better operational understanding.

2. Magnetostrictive actuator

Presented in this paper energy harvesting system consists of the actuators which are processing electrical energy into mechanical vibrations and harvesters which are responsible for the reverse process. Transfer of mechanical energy takes place by the generation of ultrasonic waves by the actuator and collection of this wave by the stimulated magnetostrictive material inside the harvester device.

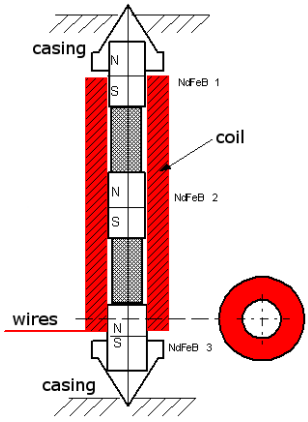

Fig. 1. Scheme of the actuator's and harvester's magnetostrictive cores.

Actuators and harvesters used in this studies, are based on the Terfenol-D (GMM, Giant Magnetostrictive Material) and its composites. GMM materials change their dimensions under the influence of a magnetic field, while under the influence of mechanical stress (deformation) they generate a strong magnetic flux. Magnetic field changes caused by the mechanical stress may be used to generate electricity. It can be done by placing the Terfenol-D core inside the induction coil. The aforementioned solution was applied to the construction of the resonant power test stand. Construction of active element is shown in Fig.1.

Two cores made of solid Terfenol-D, or in a form of composite, were placed between three neodymium NdFeB magnets and then placed inside the coil.

3. Test stand

The idea of supplying the harvesters nodes with use of ultra-sonic vibration of the construction was shown in Fig.2. One should notice that, such solution might have variety of different configuration. This is related to the fact, that as a transmitting devices, one can use actuators based on different materials, such as piezoelectric or magnetostrictive. The same situation is possible with the harvester devices.

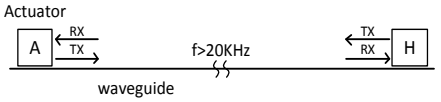

Fig. 2. Scheme of powering of the final harvester nodes, through mechanical vibrations in the ultrasonic range.

The possibility of transmission of energy over long distances, with the use of magnetostrictive harvesters system, was studied on the example of the steel rail (DIN-3). The element of this type has been selected mainly due to the cross-sectional profile in the shape of letter C. Rail of such a profile is characterized by a high resistance to: bending, buckling and twisting.

4. Results

Construction of the test rig was based on two DIN beams, between which magnetostrictive modules were placed as it was shown in Fig.3. DIN beams were pressed against each other by the elastic bands placed at a distance of 10 mm from the axis of the hole.

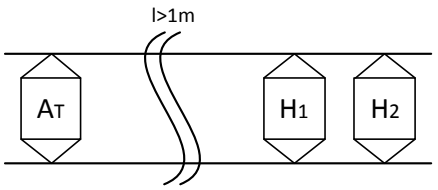

Fig. 3. Scheme of the resonator with a chosen actuator/harvester configuration.

Following the assembling of each version of ultrasonic power supply, signal was scanned with frequency spectrum analyser. On the input of the resonant power supply, a signal with continuously changing frequency was applied. At the same time, the signal of received power, was recorded on the one of harvesters. After completion of the experiment based on the time course from harvester, a spectral analysis with the usage of Fourier transform was done - sample of the frequency response is shown in Fig.4. Based on this solution, the frequency of the power supply, at which harvester has its highest output voltage, was chosen. The highest amplitudes were usually in ultrasonic band. Useful band begins above 22 kHz.

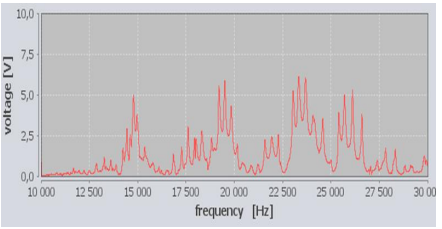

Fig. 4. The frequency spectrum of construction, based on 1 actuator and 2 harvesters mechanically coupled through the two DIN-3 beams.

5. Remarks

In order to allow free propagation of acoustic wave from the active elements to the construction, an appropriate contact between magnetostrictive elements and construction must be provided.

The highest voltage values have been obtained for the ultrasonic frequencies. Analysing the results obtained for different resonant power supplies, it can be stated that it is possible to transfer the energy on a distance without the use of electrical wires.

References

[1] Kaleta J., Lewandowski D., Wiewiorski P., Mech R., Liberda M. (2010), Power generating by high pulse mechanical stimulation of magnetic coupled NdFeB and Terfenol-D, SPIE San Diego.

[2] Wang L., Yuan F. G. (2008),Vibration energy harvesting by magnetostrictive material, Smart Material Structure, IOP Pub-lishing.

[3] Torah R., Glynne-Johns P., Tuodor M., O'Donnell T., Roy S., Beeby S. (2008) Self-powered autonomous wireless sensor node using vibration energy harvesting, Measurement Science and Technology, IOP Publishing.

30th DANUBIA-ADRIA
Symposium on Advances in Experimental Mechanics
September 25-28, 2013 - Primošten, Croatia

5A11 054

MEASURING FORCES IN TENSIONING BOLTS ON THE ANTENNA TOWER

Tomislav Baškarić[1], Todor Ergić[1], Darko Damjanović[1], Pejo Konjatić[1]

[1] J. J. Strossmayer University of Osijek, Mechanical Engineering Faculty in Slavonski Brod, Trg I. B. Mazuranic 2, HR-35000 Slavonski Brod, CROATIA. E-mail: tomislav.baskaric@gmail.com

1. Introduction

Since telecommunication services continue to expand, wireless providers are deploying more and more base station antennas in order to meet the growing demand. As a result, antenna towers and support structures are being pushed to the limits of their load capacity. It is therefore important to understand the impact that each base station antenna has on the overall tower load. Base station antennas not only add load to the towers due to their mass, but also in the form of additional dynamic loading caused by the wind [1]. Therefore after adding additional antennas to the tower a repair of one tower antenna and tensioning bolts was caried out.

Fig. 1. TV Tower at the top of Biokovo Mountain

This antenna was antenna tower Sveti Juraj on mountain Biokovo, Figure 1. During the year 2011 a measurement of forces in a tensioning bolts was carried out in order to control projected forces after the completion of repairs.

2. Reconstruction of the tower

Antenna tower was originally designed and constructed without tensioning bolts. During the operation there was a need for adding a new load on the tower and it was necessary to reconstruct the tower. The first reconstruction was provided by adding 24 vertical bolts in the lower section of the tower and 18 bolts in the upper section, needed to carry dynamic loads due to wind. Because of the geometry of the tower it was not been possible to set up all 18 bolts in the upper section. In the last reconstruction on the tower, a new tensioning bolts and screws were placed. Demanded forces of 60 kN per bolt are required in the lower tensioning bolts and forces of 90 kN are required in the upper tensioning bolts. This force distribution is achieved in three steps. After further analysis of the construction, requirements are changed and it was necessary to achieve a forces of 110 kN in lower and 60 kN in the upper bolts.

3. Methods of measurement

Measuring forces in tensioning bolts was done by measuring the deformation of tensioning bolts using strain gauges. Control measurements were performed in two ways, by measuring the displacement of tensioning bolts and by method of measurement natural frequencies of tensioning rods (strings) [2,3]. Force is calculated from the frequency using the expression:

$$F = 4 \cdot q \cdot l^2 \cdot f^2 , \qquad (1)$$

where:

l – lenght of the tensioning screw, m

f – natural frequency, Hz

q – mass per length unit, kg/m

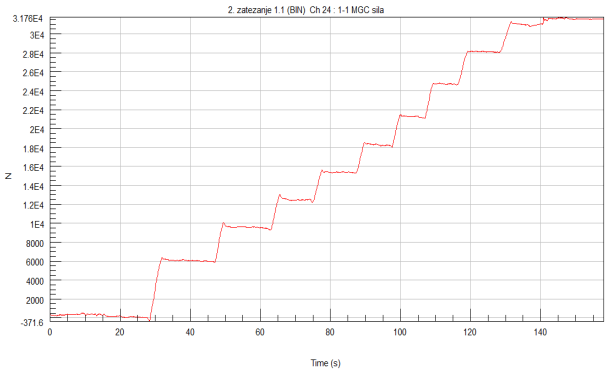

Fig. 2. The force vs. time diagram during tightening one of the bolts

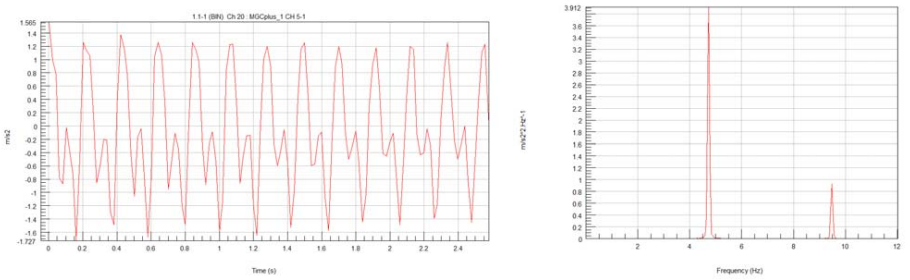

Fig. 3. Diagram of measured acceleration during measuring natural frequency of tensioning bolt (left hand side) and amplitude - frequency characteristics of bolt (right hand side)

Figure 2 shows the amount of force in time at tightening of one of the tensioning bolts.

Figure 3 Shows the graph of the measured acceleration on the tensioning bolt to determine the natural frequencies and frequency-amplitude characteristics of the bolt.

Difficulties in the measurement were created by unfavorable weather conditions (rain, wind), difficult access to the location of measurement and hardly achiveable required torque for tightening bolts. Wind influence on the results can be seen in the graphical results.

4. Results

Results obtained by measuring with strain gauges were confirmed by method of measuring natural frequency of tensioning bolts. This method is approximate and can be used as a control only. For accurate measurements it is necessary to apply methods that can accurately determine the natural frequencies such as the method of excitation and response by measuring the phase angle between them.

The distribution of forces in upper tensioning bolts deviates less than 4% from mean value force, and the same situation is in the lower section bolts.

References

[1] M. Ferris, Wind Loading On Base Station Antennas, Commscope, 2009

[2] T. Ergić, Izvještaj o mjerenju sila u zategama na tornju Sveti Juraj na Biokovu, Strojarski fakultet u Slavonskom Brodu, 10.08.2011

[3] User manual Catman AP, Hottinger Baldwin Messtechnik, 2011

30th DANUBIA-ADRIA
Symposium on Advances in Experimental Mechanics
September 25-28, 2013 - Primošten, Croatia

5A12 089

DISSIPATION OF IMPACT ENERGY BY CELLULAR COMPOSITES FILLED WITH MAGNETORHEOLOGICAL FLUIDS

Damian Bodniewicz[1], Daniel Lewandowski[1], Jerzy Kaleta[1]

[1] Wrocław University of Technology, Institute of Materials Science and Applied Mechanics, Mariana Smoluchowskiego 25, Wrocław, POLAND. E-mail: damian.bodniewicz@pwr.wroc.pl

1. Introduction

At present, in the field of protection against impact effects, high hopes are located in semi-active or active methods of energy dissipation. They are based on an adaptive reaction of absorbing element to impact conditions (Adaptive Impact Absorption, AIA) [1]. However, they require the final control element of variable rigidity. The example which fulfill the requirement are MagnetoRheological Composites, MRC.

The work presents impact tests performed on magnetorheological composites with the matrix made of an elastic porous material.

2. Magnetorheological composites

Magnetorheological composites belong to the SMART materials group, properties of which change as a result of external stimulus. They are composed of magnetorheological fluid, MRF, and a carrier structure in the form of elastic, porous matrix (Fig. 1).

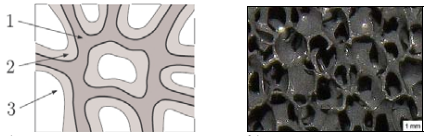

a) b)

Fig. 1. Magnetorheological composite: a) internal structure diagram: 1 – porous matrix, 2 – thin layer of MRF, 3 – free space [2]; b) real view of composite.

Unique properties of the discussed composites are related to a change in the MRF yield point as the result of magnetic field stimulation. It has to be stressed that by controlling the MRF share in the matrix, the initial "programming" of material damping properties is possible.

3. Impact tests

The main purpose of work was to determine energy damping capacities of MRC.

3.1 Test stand

The tests needed to be performed on an experimental stand (Fig. 2), which in the controlled way simulated conditions of impact into manufactured specimens. At the same time it allowed for stimulation of composite with a magnetic field of various intensities.

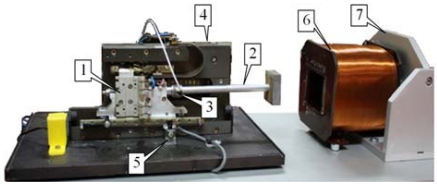

Fig. 2. Impact test stand: 1 – slidable element with a constant mass; 2 – bar ended with a piston; 3 – piezoelectric force sensor; 4 – housing; 5 – displacement measurement system; 6 – magnetic system with an assembled material specimen; 7 – fixed partition.

3.2 Composite specimens

For tests of the impact energy damping capacities, three composite specimens were manufactured with different contents of the MRF, and one specimen (U0) free of the magnetically active fluid (see Tab. 1).

Specimen	MRF volume fraction [%]
U0	0
U1	10
U2	15
U3	25

Tab. 1. Specimens for impact tests.

3.3 Results

The following parameters were considered as significant in evaluating the MRC damping capacities:

- exit velocity (V_w) - the direct correlation with the kinetic energy of hitting element (Fig. 3);
- total work (W) performed by composite during impact – Fig. 4;
- strain size of composite specimens (Δl).

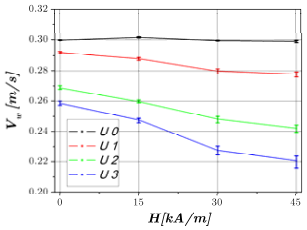

Fig. 3. Dependence of the exit velocity (V_w) of impacting part upon the magnetic field intensity value (H).

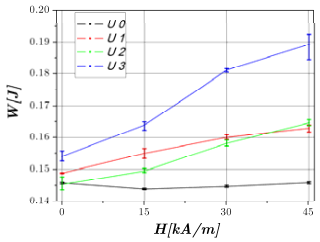

Fig. 4. Value of the total work (W) performed by the damping material as a function of the magnetic field intensity.

4. Remarks

- All considered damping quantities for the specimen without MRF were identical, regardless of the magnetic field value. This indicated that, according to expectations, no magnetorheological damping effect was observed for that specimen.
- The lowest value of the exit velocity V_w was registered for the U3 specimen when it was exposed to the strongest magnetic field (H=45 kA/m). The work performed by composites increases in two cases: when the magnetorheological fluid share in the MRC rises and when MRC was stimulated with higher values of H. In the extreme case the growth in total work (W) of 25% was achieved. Stimulation of the U3 specimen with the maximum field intensity caused the highest reduction in the porous material deformation size Δl.
- It was shown that damping properties of magnetorheological composites may be controlled by stimulation with magnetic field of various intensities and content change of the magnetorheological fluid in MRC.

Acknowledgements

The research was supported by Wrocław Research Centre EIT+ within the project "The Application of Nanotechnology in Advanced Materials" – NanoMat (POIG.01.01.02-02-002/08) financed by the European Regional Development Fund (Innovative Economy Operational Programme, 1.1.2).

References

[1] Graczykowski, C., Holnicki-Szulc, J., Jankowski, Ł., Mikułowski, G., Ostrowski, M., Pawłowski, P. K., Adaptive Impact Absorption. Smart Technologies for Safety Engineering. John Wiley & Sons, Great Britain, 2008. pp. 153-213.

[2] Kaleta, J., Lewandowski, D., Inelastic properties of magnetorheological composites: I. fabrication, experimental tests, cyclic shear properties. Smart Materials And Structures, 16, 2007. pp. 1948-1953.

30th DANUBIA-ADRIA
Symposium on Advances in Experimental Mechanics
September 25-28, 2013 - Primošten, Croatia

5A13 074

EXPERIMENTAL STRESS-STRAIN ANALYSIS OF COMPOSITE BEAMS

Petar Smiljanic[1], Aleksandar Sedmak[2], Emina Dzindo[3]

[1]Company 'Problem' Belgrade

[2]Faculty of Mechanical Engineering, University of Belgrade, Kraljice Marije 16, Belgrade, Serbia E-mail: asedmak@mas.bg.ac.rs

[3]Innovation Center of Faculty of Mechanical Engineering Belgrade, Kraljice Marije 16, Belgrade, Serbia

E-mail: edzindo@mas.bg.ac.rs

1. Introduction

The experimental part includes the following: composite wooden beams reinforced with steel bands. Two sets were done with three identical pieces of different composite beams:Carbon steel strips reinforced, boxed fir beam. Carbon steel strips reinforced fir solid beam. Analyses were performed with at the maximum loaded beams. Value of the force at which the fracture zone was created has caused greater deformation than the calculated one. The study confirms the characteristics of calculation capacity. Increase of the beam deflection is proportional to the increase in bending force. The values for the corresponding deflection of force are different from the numerically obtained due to higher stiffness of the used wooden beams. We can notice that the distributions of stresses due to the different elasticity modulus are not equal. This is a basic idea for usage of composite beams. This allows us beam calculation the to maximize potential of used materials.

2. Experiments

Data were obtained for samples of materials, which may not fully correspond to those included in testing.

Dynamic properties of bonded joints were tested during two years totally, up to six months by specimen. For that purpose, was built dynamic testing machine with constant amplitude, Fig. 1.

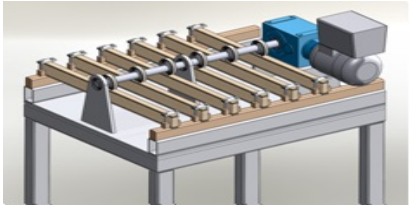

Fig. 1. Specimen dynamic testing machine

Specimens are made from Fir, Plane Carbon Steel and SIKAFLEX 221 (Fig. 7). Characteristics of used materials are in Table 2. The goal is to notice weaknesses in dynamic loads on this bonded beam system. Six specimen were tested simultaneously in external weather conditions.

Differences are in bonded surface pretreatment. There are two different types of pretreatment:

1. Direct SIKAFLEX 221 application on wood and metal surfaces
2. Two component epoxy pretreatment before SIKAFLEX 221 application.

Material:	**SIKAFLEX 221**
Name	Polyurethane adhesive
Produced by:	SIKA
Material type:	Linear-Elastic Isotropic
Brake criteria:	Max von Misess stress
Note:	Tensile strength and yield strength are taken as equal.

Tab 1. Sikaflex 221

Specimens were tested in two periods. After one year and after 18 months in duration of 4300

hours. Totally three specimens of each surface pretreatment were tested simultaneously. Dynamic load was applied with:

- Amplitude: A=10mm;
- Maximum stress in metal strip (calculated): 21.7 (MPa)
- Duration of dynamic load: 4300 hours
- Frequency: 1

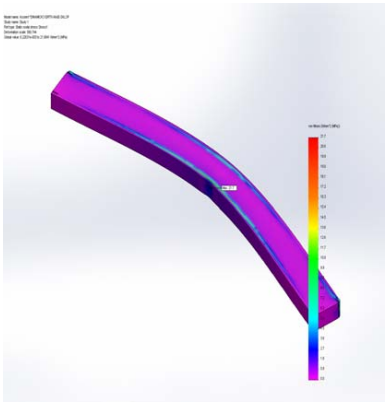

Fig. 2. Specimen maximum stresses during dynamic testing

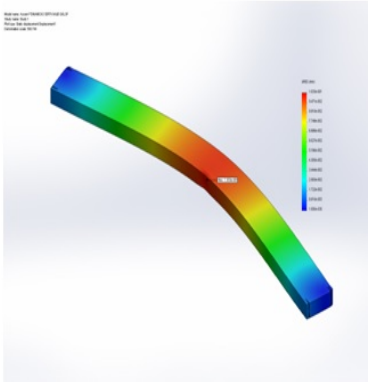

Fig. 3: Specimen deformation

3. Results

Specimen with no pretreatment were sensitive on metal surface rust formation in contact with SIKAFLEX 221. Rust was formed on 31,5% of metal strip surfaces. That produce delaminating of trusses bonded layers caused by dynamic load. Epoxy pretreated surfaces are not damaged and bonded trusses had measured capacity reduction lower than measurement error (<5%).

4. Discussion

Influence of Urethane, Polyurethane and Epoxy metal coatings are well known, but there are no information about influence of SIKAFLEX 221 or similar material applied on carbon steel surfaces directly. Epoxy surface treatment was uses for comparison.

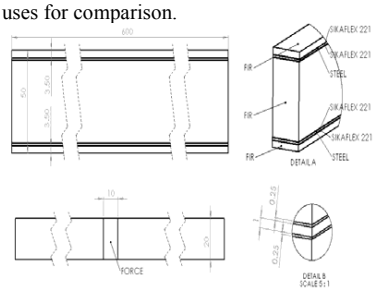

Fig. 4. Specimen details.

5. Conclusion

It is necessary to use corrosion pretreatment of carbon steel surfaces bonded with Polyurethane. Using low quality wood material as bearer filling, gives significant advantage in comparison to laminated wood bearings in terms of price, producing simplicity, material acquisition and production time.

References

[1] P. Smiljanic, A Sedmak, E Dzindo 'Experimental and Numerical Stress-strain Analysis of Composite Beams", ICMEM 2012 , Presov, Slowakia, 2012.

30th DANUBIA-ADRIA
Symposium on Advances in Experimental Mechanics
September 25-28, 2013 - Primošten, Croatia

5A14 088

A STUDIES OF MECHANICAL AND STRUCTURAL PROPERTIES ON SOL-GEL DERIVED COATINGS FOR METALLIC IMPLANTS

Anna Donesz-Sikorska[1], Justyna Krzak-Roś[1], Agnieszka Śmieszek[2], Jakub Grzesiak[2], Krzysztof Marycz[2], Jerzy Kaleta[1]

[1] Institute of Materials Science and Applied Mechanics, Wroclaw University of Technology, Wroclaw, POLAND. E-mails: anna.donesz-sikorska@pwr.wroc.pl, justyna.krzak-ros@pwr.wroc.pl, jerzy.kaleta@pwr.wroc.pl

[2] Electron Microscopy Laboratory, University of Environmental and Life Sciences Wroclaw, POLAND. E-mails: adziewicka@gmail.com, grzesiak.kuba@gmail.com, krzysztofmarycz@interia.pl

1. Introduction

Coatings and surface modification of materials are of considerable interest, because they can be used to tune their physical, chemical and even biological properties [1-3]. The ability to improve the surface properties enables designing of a material with controlled features.

A good example is sol-gel process which allows to obtain, in a relatively low temperature multi-component material with properties controlled at the molecular level [4]. Compared to conventional thin film processes this technique allows for better control of the chemical composition and microstructure of the coating, preparation of homogeneous films, reduction of the densification temperature, and last but not least, simpler equipment and lower cost [5].

2. Materials and Methods

Silica, titania and silica/titania sol-gel derived coatings were synthesis using following precursors: tetraethyl orthosilicate (TEOS), tetramethyl orthosilicate (TMOS), titanium n-butoxide (Ti-nBO), titanium izopropoxide (TIPO), titanium(IV)ethoxide (TiEO), isobutyl trimethoxysilan (iBtMOS). Butanol (BuOH), etanol (EtOH) or propanol (PrOH) were used as solvent, and acetylacetone (AcAc) as a comlexing agent of titanium precursor. Mentioned above substrates were homogenized in an acidic medium (HCl) on a magnetic stirrer at room temperature. Received hydrolyzates were applied on stainless steel 316L probes using dip-coating technique with controlled parameters, and annealed at 250^{0}C for 12hrs.

2.1 Surface morphology and topography

The surface morphology and topography of the coatings were investigated using a scanning electron microscope (SEM) Evo LS 15 Zeiss and Atomic Force Microscope (AFM) XE-100 Park Systems. For each coating, images were made using SE1 and CZ BSD detectors at following magnifications: 50, 100, 500, 1000 and 5000x. Elemental analysis and distributions of elements were performed at magnifications of 500x using Bruker detector in SEM microscope. Atomic force microscopy images of silica, titania and silica/titania coatings were obtained using contact mode in AFM XE-100 Park Systems.

2.2 Raman spectroscopy

The chemical structures of synthesized coatings was performed using Raman spectroscopy. The Raman spectra were measured on a dispersive Raman Spectrometer LabRAM HR800 Horiba Jobin Yvon. The incident laser excitation was provided by a water-cooled argon laser source operating at 514,5 nm.

2.3 Uniaxial tension

The mechanical strength of coatings deposited on 316L stainless steel foil were examined during tensile strength testing by an auto-controlled Tensile Tester (Fig. 1) combine with Scanning Electron Microscope Evo LS15 at a loading speed of 0,2 mm/min. The load and displacement were automatically recorded for every moment during whole test.

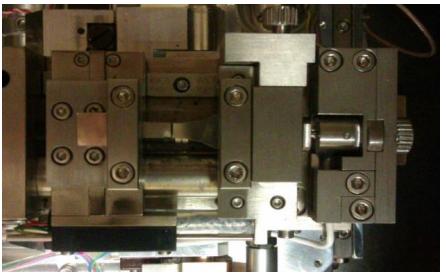

Fig. 1. Tensile tester- X MT 10222.

2.4 In vitro test

Effect of the coatings on the viability and proliferation of the ADMSC cell culture was tested in the colorimetric assay using Alamar Blue. Analysis of the morphology of cells cultured in the presence of tested materials was performed using fluorescence microscopy. The preparations were labeled with a fluorescent dye DAPI staining nuclei. evaluation of distribution of cells on the material was performed using a scanning electron microscope.

3. Results

Our research showed that silica and silica/titania layers were transparent, homogeneous, smooth and covered the 316L substrate , uniformly. In turn, TiO_2 coatings had characteristic robust topography. These observations were confirmed by results obtained from atomic force microscopy (AFM) experiments which demonstrated significant differences in roughness parameters (e.g. R_a, R_q) of obtained surfaces.

In all samples after tensile testing observed uniform coverage of the substrate by each of coating, and high adhesion to the metallic substrate. Even after breaking the substrate, obtained coatings did not undergo delamination and peeling off coatings.

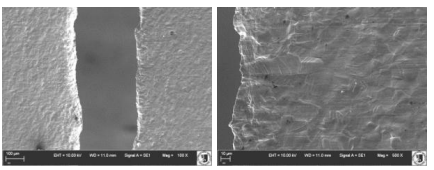

Fig. 2. SEM images of pure foil 316L after tensile testing.

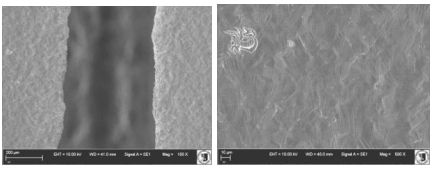

Fig. 3. SEM images of SiO_2/TiO_2 coating after tensile testing.

The Raman spectra of SiO_2,TiO_2 and SiO_2/TiO_2 hibrid oxides deposited on stainless steel 316L confirms the presence of silica (Si-O-Si), titania (anatase) and silica/titania (Si-O-Ti) network. It proves that these networks were created during the condensation.

Obtained *in vitro* results indicate a stimulating effect of all coatings onto ADMSC cells. The higher proliferation factor values were noticed for titania and silica/titania materials, especially after 24h and 168h cell culture. Moreover cells showed variable morphology and adhesion to the substrate, depending on type of sol-gel derived coating. Morphologically normal cells which adhered properly to every type of material were observed, however distribution and number of cells were different onto obtained biomaterials.

References

[1] Arcos, D., Vallet-Regí, M., Sol–gel silica-based biomaterials and bone tissue regeneration, Acta Biomaterialia **6**, 2010, pp. 2874–2888.

[2] Kumar, N., Jyothirmayi, A., Soma Raju, K.R.C., Subasrin, R., Effect of functional groups (methyl, phenyl) onorganic–inorganic hybrid sol–gel silica coatings on surface modified SS 316, Ceramics International **38** (8), 2012. Pp. 6565–6572.

[3] Shi, Z., Neoh, K.G., Kang, E.T. , Poh, C.K., Wang, W., Surface Functionalization of titanium with carboxymethyl chitosan and immobilized bone morphogenetic protein-2 for enhanced osseointegration, Biomacromolecules ,**10**, 2009, pp. 1603–1611.

[4] Brinker, C.J., Hurd, A.J., Schunk, P.R., Frye G.C., Ashley, C.S., Review of sol-gel thin film formation, J. Non-Cryst. Solids, **147**, 1992. pp. 424–436.

[5] Brinker, C.J., Raman, N.K., Logan, M.M., Seghal, R., Assink, R.A., Hua, D.W., Ward, T.L., J. Sol–Gel Sci. Technol., **4**, 1995. pp. 117-123.

30th DANUBIA-ADRIA
Symposium on Advances in Experimental Mechanics
September 25-28, 2013 - Primošten, Croatia

5A15 125

MEASUREMENT OF ELASTICITY OF EXPANSION RADIATORS FOR POWER TRANSFORMERS

Mislav Ilijašević, Stjepan Baršun[1]

[1] Koncar Distribution and Special Transformers Inc., Josipa Mokrovica 8, HR-10090 Zagreb, Croatia
E-mail: mislav.ilijasevic@koncar-dst.hr

1. Introduction

Power transformers are filled with oil. Function of oil is to serve as electrical insulator, and for cooling purposes. Temperature of oil in transformer varies between -25 and 90 °C, depending on load conditions. Transformer oil change its volume depending on temperature, and for that range oil will change its volume for roughly 8%. Transformer design incorporate conservator, a tank at the top of the transformer, whose function is to allow oil to change volume.

Transformer design without conservator will greatly simplify maintenance of the transformer. To achive that, some elastic element have to be introduced in transformer, to allow the oil to change volume. Idea is to use radiator for that purpose. Radiators are made of 1 mm thick steel plates, imprinted and welded to increase their rigidity. If radiators are made more elastic, they may be used for sealed type transformers (without conservator). Based on the experience with selad type distribution transformers, expected workig pressure should be around 0.25 bar.

2. Method of masurements of elasticity

Principle of measurement is to measure volume of oil pumped into radiator, and to measure pressure in the radiator. That way correlation between volume and pressure is established. Working pressure is the maximum pressure radiator may withstand with no permanent deformation of the radiator.

Several designs of expansions radiators were made, and tested. Machine designed to test endurance of corrugated tanks for distribution transformers was used, as shown in Fig. 1.

Fig. 1. Testing equipment

4 different designs of expansion radiators were made. Some of them were too elastic (plastic deformation occured at very low pressure leves), and some of them were too rigid (change of volume was too small). One design showed preferred characteristics - desirable elasticity and pressure levels. Test resuts of that design are shown in this paper.

3. Results of experimental testing

3 different heights of radiators were tested - 1100, 1300 and 1800 mm. Fig. 2 show results of measurements of radiator elasticity.

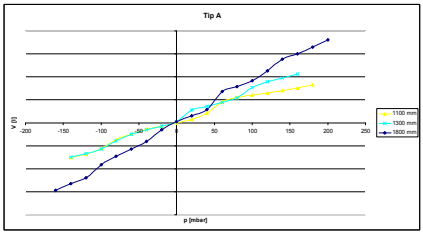

Fig. 2. Elasticity of expansion radiators

Slope of the elasticity curve shows radiator elasticity - 1100 mm radiator curve is more laid than 1800 mm radiator curve, therefore it has higher pressure for the same amount of volume change, meaning it has less elasticity.

During manufacturing, radiator is subjected to large amount of heat stress (welding, hot dip galvanizing). Result of that is residual stress, and it is clearly visible during testing. Radiator is tested first time right after is delivered from workshop, and second time after is subjected to cyclic load (10 cycles, working pressure level). Cyclic load allows residual stresses to relax. Fig. 3 show results of such measurement. It is clearly visible that after 10 cycles elasticity of radiator increased.

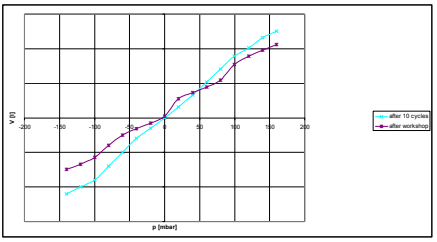

Fig. 3. Elasticity of radiator as a function of cyclic load applied

Type of anticorrosion protection have impact on elasticity of radiator. Hot dip galvanizing add layer of metal film (80 μm) on the steel plate, and increase its rigidity. That impact clearly showed up during testing. Same type of radiator was manufactured with 2 different protection layers, hot dip galvanazing and solvent paint. Results are shown if Fig. 4. Painted radiator has greater elasticity, that is expected result because hot dip galvanized radiator has thickness of 1.08 mm, if galvanized layer is added to plate thickness.

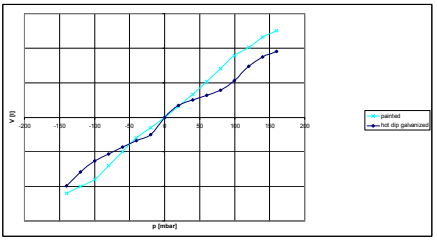

Fig. 4. Elasticity of radiator as a function of anticorrosive protection

Final test was made on a complete transformer. Goal of that test was to determine if there is any other elastic element on the transformer (transformer tank for example), or expansion radiator is the only element that allows oil to expand and contract. Results are shown in Fig. 5. and they shows that transformer has greater elasticity than set of transformer radiators (for around 8%). That means transformer tank has 8% of elasticity of expansion radiators. That impact do not have to be taken into account for design purposes, because it is small in value, and increase safety of the system.

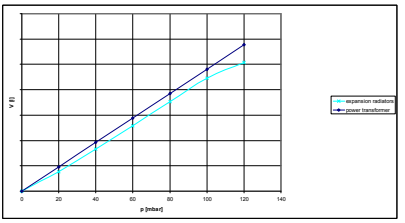

Fig. 5. Comparison of measured elasticity of radiators and transformer

References

[1] EN 10130:2006 Cold Rolled Low Carbon Steel Flat Products For Cold Forming

30th DANUBIA-ADRIA
Symposium on Advances in Experimental Mechanics
September 25-28, 2013 - Primošten, Croatia

5A16 139

ELECTRICAL CURRENT AND ACOUSTIC EMISSIONS WHEN MARBLE SPECIMENS ARE SUBJECTED TO COMPRESSIVE MECHANICAL LOADING

George Hloupis, Ilias Stavrakas, Dimos Triantis, Konstantinos Moutzouris

Laboratory of Electrical Characterization of Materials and Electronic Devices, Dept. of Electronics, Technological Educational Institute of Athens, 122 10, Athens, GREECE. E-mail: triantis@teiath.gr

1. Introduction

The investigation of material pre-failure indications has attracted a wide scientific interest ranging from civil engineering applications to natural hazard precursors. Traditional experimental techniques deal mainly with destructive testing and statistical analysis regarding the determination of the ultimate strength of a material. Various experimental techniques have been developed in order to study the structural changes that take place within the bulk of a material when micro-fracture processes take place. Such techniques include detection of weak electrical current emissions (Pressure Stimulated Currents - PSC) as well as detection of mechanical elastic waves (Acoustic Emission - AE) propagating in the bulk of a specimen when micro-fracture phenomena take place [1].

In this work prismatic marble specimens were subjected to successive loading-unloading-reloading compressive loops, up to loads closely approaching the fracture stress of the material. The PSC technique was applied and the background level of the PSC emission after each loading was studied while approaching the specimen's failure. In parallel the characteristics of the AE recordings, as collected from two AE sensors, are studied and evaluated using the b-value analysis according to the Aki's model and the Guttenberg-Richter relation [2].

2. Experimental Details and Materials

The mechanical load was applied parallelly to the long edge of the prismatic specimens. The experiments were quasi-static under loading control mode and were carried out using an ENERPAC actuator of capacity 100kN. The loading procedure consisted of 9 successive loading-unloading cycles. During each cycle the stress rate was kept constant, equal to 1MPa/s, while the maximum stress value of each cycle was equal to approximately 60MPa, some 15% lower from Dionysos marble compressive strength [3]. At each loading cycle the maximum stress level was kept constant for 200s. During the ninth loading cycle the specimens failed about 15s after reaching the maximum stress.

2.1 Experimental set-up and Materials

The measuring system consisted of an ultrasensitive programmable electrometer (Keithley, 6517A). The sensor was a pair of gold plated electrodes that were installed in parallel to the direction of the mechanical load. In the present experimental protocol, the AE were collected with the aid of an 8-channel PCI-2 AE detection system (Physical Acoustics Corp). The complete experimental set-up is described in previous works of the authors [1].

The specimens were made of Dionysos marble, the material used extensively and almost exclusively for the restoration project of the Parthenon temple on the Acropolis of Athens [3, 4]. The mechanical and physicochemical properties of Dionysos marble were obtained from literature [5, 6]. The dimensions of the specimens were equal to 40 x40x100 mm^3 while the fracture limit, during the specific loading protocol, was found to 64±3MPa.

3. Results and Discussion

The PSC and AE were analyzed for each loading cycle while attention was paid to the 200s time interval where the applied stress was kept constant, equal to about 60MPa. It is known that when an abrupt change of the mechanical load is applied on a specimen a PSC excitation is observed followed by a relaxation at a PSC background level. At this work this PSC background level was studied for the 8 loading loops, since during the ninth loop the PSC never restored due to fracture of the specimens.

Fig. 1 shows the background level of the PSC after the relaxation. It becomes obvious that during

the first six loading cycles (reaching approximately the same mechanical load level) the PSC background level tends to stabilize. During the subsequent loading cycles (#7, #8 and #9) the PSC background level tends to increase.

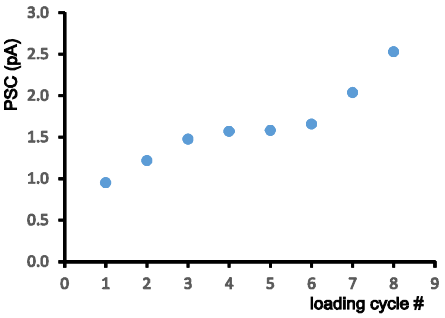

Fig. 1. The background level of the PSC after the relaxation process for each one of the loading cycles.

Analyzing the characteristics of the AE recordings, it was observed that the cumulative number (N) of the AE hits as well as the cumulative energy of the AE emissions during the first six loading cycles become gradually lower, reaching a minimum value during cycles #3, #4, #5 and #6 clearly implying the existence of the Kaiser effect (as it is seen in Fig.2) During the remaining three loading cycles before failure both quantities increase significantly reaching a maximum at the #9 loading path where the specimen fractured.

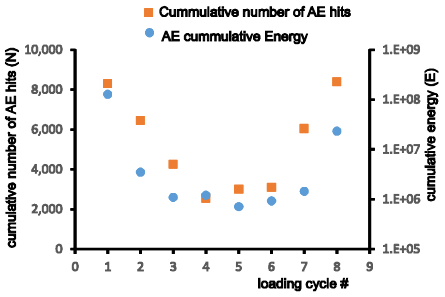

Fig. 2. The behavior of the cumulative number of the AE hits (orange square markers) during each loading increase for the nine cycles and the corresponding cumulative energy of the AE events (blue circle markers).

The results, after performing the b-value analysis according to Aki's model and the Guttenberg-Richter relation [2], are shown in Fig. 3. It becomes clear that the b-value tends to stabilize after the third loading cycle but this behavior is distorted after the sixth loading since after three additional loading cycles the specimens failed.

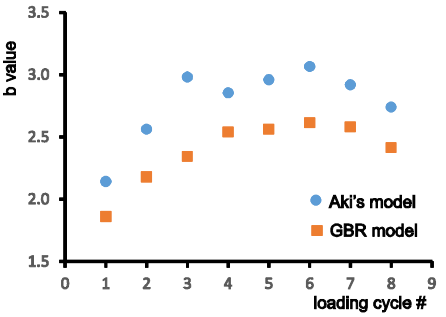

Fig. 3. The b-values after fitting the experimental data using Aki's model (blue circle markers) and GBR relation (orange square markers) during each loading increase for the nine cycles.

Acknowledgements

This research has been co-financed by the European Union (European Social Fund-ESF) and Greek national funds through the Operational Program "Education and Lifelong Learning" of the National Strategic Reference Framework (NSRF) - Research Funding Program: THALES: Reinforcement of the interdisciplinary and/or inter-institutional research and innovations.

References

[1] Stergiopoulos, C., Stavrakas, I., Hloupis, G., Triantis, D., Vallianatos, F., Engineering Failure Analysis, 2013, doi: http://dx.doi.org/10.1016/j.engfailanal.2013.04.015.

[2] Vidya Sagar, R., Raghu Prasad, B.K., Shantha Kumar S., Cement Concrete Res., **42**, 2012, pp. 1094-1104.

[3] Kourkoulis, S.K., Ganniari-Papageorgiou, E., Mentzini, M., Engineering Geology, **115(3-4)**, 2010, pp. 246-256.

[4] Vardoulakis, I., Exadaktylos, G., Kourkoulis S. K., Journal de Physique IV, **8**, 1998, pp. 399- 406.

[5] Exadaktylos, G.E., Vardoulakis, I., Kourkoulis S.K., Int. J. of Solids and Structures, **38(22 -23)**, 2001, pp. 4119-4145.

[6] Kourkoulis, S.K., Prassianakis, I., Agioutantis, Z., Exadaktylos, G.E., Int. J. of Materials and Product Technology, **26(1/2)**, 2006, pp. 35-56.

30th DANUBIA-ADRIA
Symposium on Advances in Experimental Mechanics
September 25-28, 2013 - Primošten, Croatia

5A17 143

EXPERIMENTAL AND ANALYTICAL STUDY ON THE STRENGTH AND STIFFNESS PROPERTIES OF FUSED DEPOSITION MODELED PARTS

Dario Croccolo[1], Massimiliano De Agostinis[1], Giorgio Olmi[1]

[1] University of Bologna, Department of Industrial Engineering (DIN), Viale Risorgimento 2, 40136 Bologna, ITALY. E-mail: dario.croccolo@unibo.it, m.deagostinis@unibo.it, giorgio.olmi@unibo.it

1. Introduction

The Fused Deposition Modeling (FDM) from Stratasys is a typical example of a RP process [1-3]. The part manufacturing consists in the deposition of filaments of a plastic material, such as ABS or ULTEM, onto the partially constructed part. The mechanical properties of FDM processed parts, in particular strength and stiffness, are influenced by a large amount of production parameters [1]. The involved factors are: the build direction (depending whether the specimen is sitting down flat or is lying on one side as it is being generated), the bead width and thickness, the air gap, the raster angle and the number of contours around the component edge. The building procedure is usually arranged, so that the filament is initially deposited all around the component edge. Afterwards, other filaments are deposited at the inner sides of the previously deposited contours, until the stated number of contours has been deposited. The inner part of the component is finally filled by inclined rasters.

The raster orientation and the air gap have a significant impact on the part tensile strength [1, 3]. The build direction also has an influence on compressive strength [2] and on the efficiency of the process [4]. Studies dealing with the effect of contouring are currently missing. The available predictive models are empirically developed and do not account for the aforementioned effect [5]. The influence of contouring is here investigated experimentally, by running tensile tests on different sample types. An analytical predictive model for strength and stiffness is then developed. It is not empirical, but is based on principles of mechanics and accounts for the previously mentioned process parameters and for contouring.

2. Experimental

Twenty five specimens were manufactured in ABS-M30: the geometry was chosen according to the type I in Standard [6]. Five specimen types were considered: four of them were built while sitting down flat, respectively with 1 (Type 1), 4 (T. 2, see Fig. 1), 7 (T. 3), 10 contours (T. 4), and the last one (T. 5, see Fig. 2) was modeled while lying on its side with 1 contour. Five samples were tested per each type. The experimentation was carried out in the displacement controlled mode at the actuator velocity of 20μm/s, with strain measurement by an extensometer at specimen gage and force monitoring by a 25KN load cell.

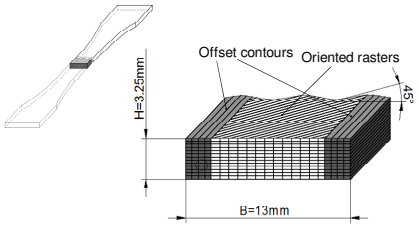

Fig. 1. Type 2 sample: overall view and cross section.

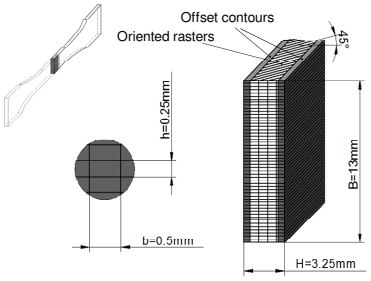

Fig. 2. Type 5 sample: overall view and cross section.

3. Analytical prediction

The application of the developed analytical model is like the simulation of an experimental test: the forces transmitted by the longitudinal (contours) and the inclined rasters, and, consequently, the total force, are determined, based on the applied displacement v.

The force transmitted by the longitudinal contours in one layer is reported in Eq. (1), where k_l is the stiffness of each single bead and n_c is the number of contours. The force transmitted by the (i-th) inclined raster can be computed as in Eq. (2), where α stands for the raster angle, E_b is the Young's modulus of ABS-M30 (in isotropic conditions), b and h are filament dimensions (see Fig. 2) and $l_{(i)}$ is the raster length. $v_{(i)}$ is finally a term being proportional to the applied displacement v. The total force per layer is computed by Eq. (3), where n_l is the number of layers, n_α is the number of inclined rasters, while the $F_{ad.}$ terms account for the adhesive forces between adjacent beads. These forces arise from adjacent rasters being partially fused each other and by different dilatations of inclined beads. The proposed model makes it possible to predict the part strength. The rupture event of every single bead is simulated by automatically setting the transmitted load to zero, as the ultimate strength of the single raster is overcome.

$$F_l = k_l \cdot v \cdot 2 \cdot n_c \tag{1}$$

$$F_{a(i)} = \left[\sqrt{\left(\frac{v_{(i)}}{l_{(i)}} + \sin(\alpha) \right)^2 + \cos^2(\alpha)} - 1 \right] \cdot E_b \cdot b \cdot h \cdot \sin(\alpha) \tag{2}$$

$$F_a = n_l \cdot \left[F_l + (n_\alpha + 1) \cdot F_{\alpha(0)} + \sum_{i=1}^{n_\alpha} F_{Ad.(i)} \right] \tag{3}$$

4. Results

The experimentally determined stress-strain curves for Types 1 to 4 are shown in Fig. 3. Regarding model validation, the experimental and analytical values for the Young's moduli and the strengths are compared in histograms in Fig. 4.

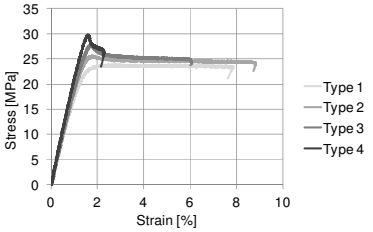

Fig. 3. Exp. stress-strain curves for Types 1 to 4.

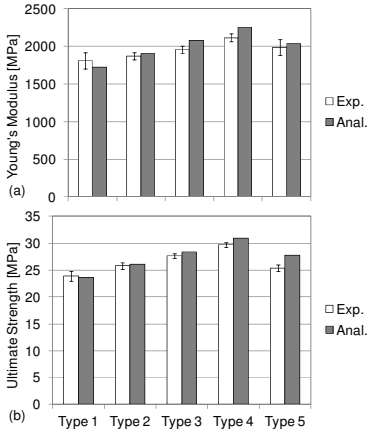

Fig. 4. Analytically determined elastic moduli (a) and strengths (b) compared to experimental values.

5. Remarks and conclusions

- The number of contours indeed affect the mechanical properties: the strength of Type 4 specimen is 24% incremented with respect to that of Type 1, whereas the elastic modulus is increased by 17%. Conversely, the strengths for types 2 and 5, having the same number of contours differ by less than 1MPa.
- The comparison between the experimental and the predicted values of the elastic moduli shows a very good agreement, with errors never exceeding 6.6%. The results concerned with strengths are also very consistent, with errors between 3% and 4% as an average.

Acknowledgements

The present research was supported by the CIRI-MAM Interdep. Center of Bologna Univ..

References

[1] Ahn, S.H., *et al.*, Rapid Prototyping J., **8**, 2002, pp. 248-257.

[2] Lee, C.S., *et al.*, J. Mater. Process. Tech., **187-188**, 2007, pp. 627-630.

[3] Lee, B.H., *et al.*, J. Mater. Process. Tech., **169**, 2005, pp. 54-61.

[4] Thrimurthulu, K, *et al.*, Int. J. Mach. Tool Manu., **44**, 2004, pp. 585-594.

[5] Sood, A.K., *et al.*, Mater. Des., **31**, 2010, pp. 287-295.

[6] ASTM D638 – 10. Standard Test Method for Tensile Properties of Plastics, 2010.

30th DANUBIA-ADRIA
Symposium on Advances in Experimental Mechanics
September 25-28, 2013 - Primošten, Croatia

5A18 146

APPLICATION OF MONOFRACTAL APPROACH TO DESCRIBE SIZE EFFECT IN FATIGUE LIFE PREDICTION FOR ALUMINUM ALLOYS

Tomasz Tomaszewski[1], Janusz Sempruch[1]

[1] University of Technology and Live Sciences in Bydgoszcz, Faculty of Mechanical Engineering, Kaliskiego 7, 85-796 Bydgoszcz, POLAND. E-mail: tomaszewski@utp.edu.pl

1. Introduction

Designing machinery components has been more and more often dimensioning-oriented due to rigidity (thin, geometrically-developed walls) and not strength-oriented; an example can be provided here by extruded sections produced from aluminum alloy. Identifying their strength properties, it is possible to take only the specimens (the so-called mini specimens) [4] which are smaller from those described as normative. To refer the results recorded applying that mini specimens methodology of own fatigue tests to the objects with a different geometry (a different cross-section), the size effect models are applied.

The paper describes the monofractal approach [2]. It is used for the description of the size effect for the range of material strength (tensile strength, fatigue limit, high-cycle fatigue).

The aim of the paper is to determine the parameters of the model for a given group of construction materials. Applying the analysis of the results for various aluminum alloys, it was possible to determine the mean value of the fractal dimension.

2. Size effect

Metal construction materials demonstrate a change in the strength properties together with a change in the cross-sectional area (the so-called size effect). The size of that change depends on the kind and the local features of the material structure (defects, grain size). The size effect is defined based on coefficient K_d, (the quotient of specimen strength with any cross-section to the strength of normative specimen, determined for the same fatigue life). The value of coefficient K_d to cross-sectional area for selected aluminum alloys is given in Fig. 1.

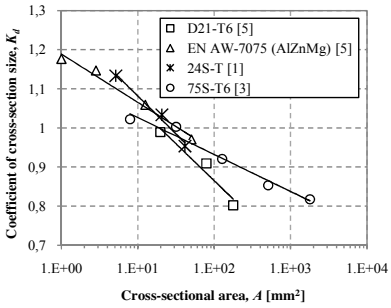

Fig. 1. Dependence of the coefficient of the cross-section size (K_d) to cross-sectional area of the rounded bended specimens – own study based on [1, 3, 5]

3. Monofractal approach [2]

The results of high-cycle fatigue tests are described with the Basquin equation expressed with the following dependence:

$$C = N(\sigma_a)^k \tag{1}$$

where k stands for the slope of line σ_a-N, C is constant of curve σ_a-N. The monofractal approach applied in the paper is based on dependence (1) in which the main assumption is the parallelity of fatigue characteristics σ_a-N (k = const) experimentally determined for the specimens geometrically similar with a different cross-sectional area. For the relationship of constant C, cross-sectional area A can be used to derive the following equation:

$$C_B = C_A \left(\frac{A_A}{A_B} \right)^{-d \, x \, \beta} \tag{2}$$

where A_A, A_B is cross-sectional area of specimens (assuming that $A_B > A_A$), C_A, C_B constants of curve

σ_a-N, $d \times \beta$ is the slope of the line. The graphic representation of dependence (2) is given in Fig. 2.

The monofractal approach uses the fractal dimension ($\alpha = 2 - d$ assuming that $0 \le d \le 0.5$) which defines the relationship of the cross-sectional area to material structure. For the materials with disordered structure, non-homogenous, with a considerable number of defects, the size of that dimension is much lower than 2. The material properties, considering the size effect, can be described with the equation in a general form (3) assuming that $A_A = 1$, $A_B = A$, $C_A = C_1$ (for $A = 1$).

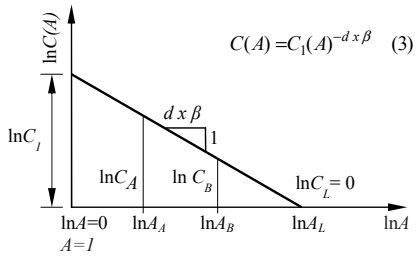

Fig. 2. Dependence of parameter *C(A)* of curve A_n to cross-sectional area *A* in bilogarithmic scale

Based on the parameters of *C* constants for characteristics A_n (determined for the specimens with a different cross-sectional area *A*), there was plotted line *C(A)-A* with slope $d \times \beta$. Parameter *C(A)* and the amplitude of stress σa approaches zero for each value *N*. It leads to receiving non-realistic results for large-size objects (cross-sectional areas), thus limiting the range of the applicability of the approach for the range of large-size specimens.

4. Applying the monofractal approach for aluminum alloys

The monofractal approach was applied for the fatigue tests results for aluminum alloy D21-T6 [5], EN AW-7075 (AlZnMg) [5], 24S-T [1], 75S-T6 [3]. The results were used to determine the plots of the dependence of constant *C* from the cross-sectional area of specimen *A* in the scale of natural logarithm described with function *C(A)*.

Aluminum alloy	*d*	*α*	C_1
D21-T6	0,091	1,909	71,17
EN AW-7075 (AlZnMg)	0,047	1,953	69,15
24S-T	0,081	1,919	66,55
75S-T6	0,045	1,955	71,38

Tab. 1. Parameters of the model of fractal approach to the aluminum alloys analysed

An example of the plot for aluminum alloy 75S-T6 is given in Fig. 3. Detailed parameters from dependence (3) for the alloys analysed are given in Table 1.

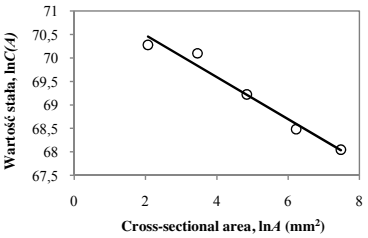

Fig. 3. Example of the plot of the dependence of parameter *C(A)* for the size of cross-section *A* for aluminum alloy 75S-T6

5. Conclusions

The monofractal approach provides a linear description of the sensitivity of the material to a change in the size of the cross-section by applying material constant (fractal dimension). In the dimension range tested it is justifiable due to the linearity of the change of parameter ln *C(A)* and coefficient K_d received.

The model applied for four aluminum alloys has made it possible to determine the mean value of the fractal dimension at the level of $\alpha_{śr} = 1.934$. The knowledge of the values for a given group of construction materials can be used to predict the fatigue life for the range of high-cycle fatigue for the specimens with a different cross-sectional area than the one experimentally tested.

References

[1] Brueggeman W.C. et al., Axial fatigue tests at zero mean stress of 24S-T and 75S-T aluminum-alloy strips with a central circular hole, NACA, 1611, 1948.
[2] Carpinteri A. et al., Size effect in S-N curves: A fractal approach to finite-life fatigue strength, International Journal of Fatigue, 31, 2009, pp. 927-933.
[3] Hyler W.S. et al., Experimental investigation of notch-size effects on rotating-beam fatigue behaviour of 75S-T6 aluminum alloy, NACA, 3291, 1954.
[4] Tomaszewski T., Sempruch J., Determination of the fatigue properties of aluminum alloy using mini specimen, Materials Science Forum, 726, 2012, pp. 63-68.
[5] Troshchenko V.T. et al., Fatigue resistance of metals and alloys, Academy of Sciences of the Ukrainian SSR [in Russian], 1987.

30th DANUBIA-ADRIA
Symposium on Advances in Experimental Mechanics
September 25-28, 2013 - Primošten, Croatia

5A19 151

MECHANICAL CHARACTERIZATION OF ECOCOMPOSITES

Aniona Hyseni[1], Silvia De Paola[1], Giangiacomo Minak[1], Cristiano Fragassa[1]

[1]University of Bologna, Dept. of Industrial Engineering, Viale Risorgimento 2, IT-40136 Bologna, ITALY. E-mail: aniona.hyseni@gmail.com

1. Introduction

The study of materials' mechanical properties is very important for their characterization, specially for the structural parameters which describes their elastic behavior. In order to develop this research topic, the mechanical properties of five kinds of biocomposites, reinforced with natural fibers molded with green matrix, have been tested. Then, the experimental results have been compared with those of carbon and glass composites.

2. Experiments

The five kinds of ecolaminates are produced by resin infusion and hand-up molding. Three of them are composed by a natural fiber combined with an ecofriendly matrix. The other two are hybrids, combined with two different kinds of fibers, both mixed up with a green thermoset resin: the first one is compound with both synthetic and natural fibers, and the last one is compound with two different natural fibers. The comparison composites are made of glass fiber combined with polyester resin. Following the ASTM standards, specimens for each test have been carved appropriately from each laminate.

2.1 Materials

A short description of bio-based materials used for this research is shown below:

Fibers

- Flax fibers: used for NF reinforced composites, flax fibers are considered to be complementary to glass ones. In terms of comparison, flax fibers' tensile modulus is very close to glass fibers' one and their lower density makes them lighter. They can also be matched to the most important thermoset resins. Specimens are made with LINEO FLAXPLY, 300 g/m^2 Balanced Fabrics 0/90.

- Basalt fibers: similar to carbon and glass fibers, they are cheaper than the first ones and have better mechanical properties than the second ones. Basalt fibers are also ecologically clean and non-toxic for the end user. Specimens are made with BASALTEX Fabric Type BAS 350.1500.A 350 g/m^2.

- Carbon fibers: synthetic fibers, readily available on the market, have been used. Specimens are made with G.ANGELONI balanced woven fabric GG201, 200 g/m^2.

- Glass fibers: traditional glass fibers have been used. Specimens are made with G.ANGELONI plain woven fabric VV45, 200 g/m^2.

Matrices

- Epoxy system used for the tests is formulated with a high percentage of carbon biomass in which 56% of the molecule is bio-renewable because of its plant origin. SICOMIN, GREENPOXY 56/GP505 has been used for the specimens.

- Vinylester matrices have been patented as a revolutionary resin technology with low content and emission of styrene. This low-VOC and low-HAP resin formulation minimizes emissions thereby reducing workplace exposure and environmental impact. DISTITRON VE*ef* 220 STZ has been used for the specimens.

- Orthophthalic polyester resin is used as a standard laminating system in the composites industry. For the specimens DISTITRON 105 SXQ has been used.

Composition of the laminates used during the tests is shown in Tab.1. For each laminate five specimens have been produced.

Type specimens	FIBER	MATRIX
I.	FLAX	EPOXY (green)
II.	FLAX	VINYLESTER (low styrene)
III.	BASALT	VINYLESTER (low styrene)
IV.	FLAX-CARBON	EPOXY (green)
V.	FLAX-BASALT	VINYLESTER (low styrene)
VI.	GLASS	POLYESTER

Tab. 1. Kind of laminates

3. Methods

In order to determine all mechanical properties of the laminates considered, the four tests below were done according to proper standards:

- Tensile test is performed according to ASTM D 3039 standard: a thin flat strip of material having a constant rectangular cross section is mounted in the grips of a mechanical testing machine (Instron universal tester, model 8033, has been used) and monotonically loaded in tension while recording load. The ultimate strength of the material can be determined from the maximum load carried before failure.

- Flexural test is performed according to ASTM D 730 standard: a bar of rectangular cross section rests on two supports and is loaded by means of a loading nose midway between the supports (Fig. 1).

Fig.1. Flexural testing machine

- The drop-weight impact test is performed, according to ASTM D-7136 standard, using a balanced, symmetric laminated plate. Damage is imparted through out-of-plane, concentrated impact (perpendicular to the plane of the laminated plate) using a drop weight with a hemispherical striker tip. The damage resistance is quantified in terms of the resulting size and type of damage in the specimen.

- Accelerated aging test uses aggravated conditions of heat and saline solution to speed up the normal aging processes of materials. It is used to determine the long term effects of expected levels of stress within a shorter time, usually in a laboratory by controlled standard test methods.

4. Equations

The Young modulus E has been calculated according to Hooke's law:

$$E = \frac{\sigma}{\varepsilon}, \tag{1}$$

Calculation formulas for each test are listed below:

- Tensile test

$$\sigma_t = \frac{P}{A}, \tag{2}$$

$$\varepsilon_t = \frac{\Delta L}{L}, \tag{3}$$

- Flexural test

$$\sigma_f = \frac{3PL}{2bd^2}, \tag{4}$$

$$\varepsilon_f = \frac{6Dd}{L^2}, \tag{5}$$

- Impact test

$$E_a(t) = \frac{m(v_i^2 - v(t)^2)}{2} + mg\delta(t). \tag{6}$$

Supporting institutions

This research is supported by the „De Urbis Vento“ project financed by Italian Ministry of the Environment.

References

[1] A.P. Caruso, E. Nisini , D. Ghelli , C.Santulli , F.Sarasini , G. Minak, Falling Weight Impact Characterisation of Jute Cloth/Wool Felts Hybrid Laminates. Materials and Design, 2013. A. P.

30th DANUBIA-ADRIA
Symposium on Advances in Experimental Mechanics
September 25-28, 2013 - Primošten, Croatia

5B21 078

FRACTURE MECHANICS BY SELECTIVE LASER SINTERING

Tommaso Maria Brugo[1], Snežana Ćirić-Kostić [3], Ezequiel Poodts[2], Giangiacomo Minak[1,2]

[1] Alma Mater Studiorum – Università di Bologna DIN, viale del Risorgimento 2,40136, Bologna, ITALIA. E-mail: tommasomaria.brugo@unibo.it , giangiacomo.minak@unibo.it

[2] Alma Mater Studiorum – Università di Bologna CIRI MAM Via Terracini 24, 40131 Bologna, ITALIA. E-mail: ezequiel.poodts4@unibo.it

[3] Faculty of Mechanical and Civil Engineering in Kraljevo, University of Kragujevac, Dositejeva 19, Kraljevo, 36000, SERBIA. E-mail: cirickostic.s@mfkv.kg.ac.rs

1. Introduction

Aim of the work is to determine the feasibility of fracture mechanics studies on Selective Laser Sintering Materials (plastics, metals and composites) based on the additive production of specimens containing an artificial crack-like notch.

Specimens produced with different growing direction were tested with or without cracks and their behavior has been compared.

2. Materials and Methods

Fifteen CT specimens were produced in three the directions (Parallel, Transversal and Longitudinal) showed in fig. 1 in Polyammide. They were then mechanically tested and the displacements in all directions were measured by means of Digital image correlation.

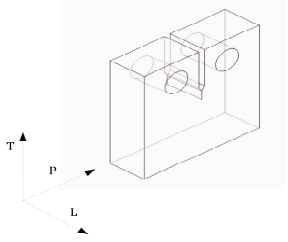

Fig. 1. Growth directions

2.1 Selective laser sintering

Selective Laser Sintering (SLS) was developed at the University of Texas in Austin, by Carl Deckard and colleagues. The basic concept of SLS uses a moving laser beam to trace and selectively sinter powdered polymer materials into successive cross-sections of a three-dimensional part. Additional powder is deposited on top of each solidified layer and sintered.

CT specimens were produced in the „3D Impuls“ laboratory by mean of an EOS Formiga P100 machine using fine Polyammide PA 2200 powder.

2.2 Mechanical Testing

Mechanical test to determine Fracture toughness were performed on a servohydraulic Instron machine equipped with a 25 kN load cell, acording to ASTM D5045 [1].

2.3 Digital Image correlation

Among different techniques of full-field displacement measurement, digital image correlation (DIC) has gained considerable attention during recent years because of its simplicity [3]. This method has become widely used mainly because it does not require complicated optical equipment and, in contrast to most other optical methods, it is applicable to both opaque and transparent materials. DIC has also been used for determination of fracture parameters in various loading modes [4].

Comparison of digital images captured before and after deformation is the basis of the DIC method for determination of displacement field data. The sample is prepared by creating a random speckle of black and white dot patterns. Then, digital images of the specimen surface before and after loading are taken, recorded and ther analyzed by computer to obtain displacement and strain field information. This is performed by matching subsets of pixels between two images. Location of a point in an undeformed subset is found in the

deformed image, and thus its displacements are determined.

For this study a 3D Dantec Dynamics System was utilized.

3. Results

The results obtained in terms of K_{IC} considering valid all the limitation of the normative [1] and the artificial crack as a real one, are shown in table 1.

Direction	mean K_{IC} [MPa m^.5]	*Sd* K_{IC} [MPa m^.5]
L	3.34	0.2
P	3.15	0.02
T	4.52	0.2

Tab. 1. Fracture toughness

The Fracture toughness derived from the experiments is strongly dependent on the orientation and the crack appearance as well. In fig 2 it is possible to se that in the P direction the crack is not well formed, while in the T (and L) directions it is completely smooth.

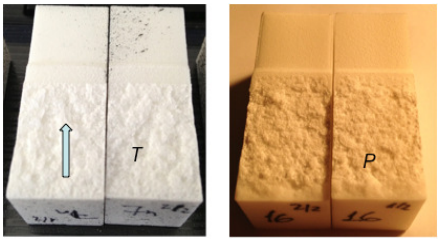

Fig. 2. Crack appearance

Two kinds of load-displacement curves were found as shown in Fig. 3

Some of the specimens, even showing the same maximum load of the others, had a first crack opening phase as shown by the DIC. It means that in some case the artificial crack was not well formed, as shown also in the previous Fig.2.

Due to this it is not possible to use the ASTM normative [1] to determine fracture toughness in these case. Nevertheless it the procedure shown in [4] is feasible by DIC. In fig. 4 shear stresses are shown. It is possible to see that the two peak zones are in correspondence of the corners of the artificial crack, well separated one from the other, while in the case of a real crack they should be contiguous.

4. Remarks

- CT specimens with artificial cracks have been produced by SLS and analyzed under load by DIC.
- The analogies and differences with real crack have been investigated and some critical issues were singled out

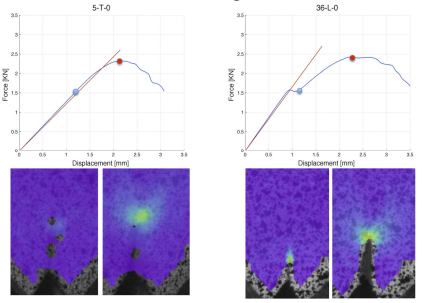

Fig. 3. Load displacement curves.

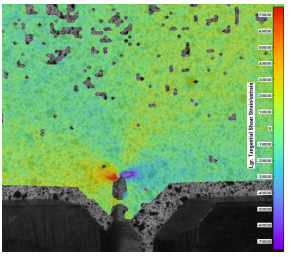

Fig. 4. Shear strain map

Acknowledgements

The author kindly thank Vladimir Stolic.

The work was done under the framework of projects TR35006, TR37020 and POR FESR Emilia-Romagna 2007-2013.

References

[1] ASTM Standard D5045 1999 (2007) Standard Test Methods for Plane-Strain Fracture Toughness and Strain Energy Release Rate of Plastic Materials, ASTM International, West Conshohocken, PA, 2006 DOI: 10.1520/D5045-99R07E01

[2] Yadegari Dehnavi M.R., Eshraghi I, Soltani N, Investigation of Fracture Parameters of Edge V-Notches in a Polymer Material using Digital Image Correlation, Polymer Testing, 10.1016/j.polymertesting.2013.03.012.

[3] Peters W.H., Ranson W.F. Digital imaging techniques in experimental stress analysis. Opt Eng 1982;21(3):427.

[4] McNeill S.R, Peters W.H, Sutton M.A. Estimation of stress intensity factor by digital image correlation. Eng Fract Mech, 1987;28(1):101.

30th DANUBIA-ADRIA
Symposium on Advances in Experimental Mechanics
September 25-28, 2013 - Primošten, Croatia

5B22 092

VARIATION OF MICROPLASTIC LIMIT DURING CYCLIC LOADING

Ľubomír Gajdoš[1], Martin Šperl[1], Jaroslav Kaiser[2], Václav Mentl[2]

[1] Institute of Theoretical & Applied Mechanics v.v.i., Academy of Sciences of the Czech Republic, Prosecká 76, 190 00 Prague 9, Czech Republic. E-mail: gajdos@itam.cas.cz; sperl@itam.cas.cz

[2] University of West Bohemia, Faculty of Mechanical Engineering, Univerzitní 22, 306 14 Pilsen, Czech Republic. E-mail: mentl@kmm.zcu.cz; kaiser@kmm.zcu.cz

1. Introduction

The microplastic limit (MPL) can be considered to be a stress (strain) at which plastic strains begin to occur in some micro-volumes of metal. The occurrence of these strains can not be determined by common methods but they can be detected by means of monitoring changes in magnetic permeability of a ferromagnetic material during application of mechanical load to a specimen [1]. Microplastic strains occur below the fatigue limit, namely as a result of dislocation movement in favourably oriented microregions in the metal lattice. With increasing load the dislocations are gradually piling-up at obstacles, firstly at grain boundaries, and due to that they form short-distance stress fields which obstruct magnetic domains to rotate to the direction of the acting load (strain).

2. Measurement of electrical impedance

The direct measurement of changes in magnetic permeability of a ferromagnetic specimen during straining is difficult but, however it can be substituted by the measurement of changes in either the a.c. resistance of a bare specimen or the inductance of a specimen furnished with a coil wound up on it.

A typical character of these changes is shown on Fig.1 and Fig.2. It can be seen here that the ideal mean curve of the inductance vs. stress hysteresis loop is an increasing function of stress whilst that of the a.c. resistance vs. stress hysteresis loop is a decreasing function of stress. This is due to a concurrence of the direction of tensile strain and magnetic flux lines when measuring inductance and a perpendicularity between tensile strain and magnetic flux lines when measuring a.c. resistance.

A point of deviation from linearity on the increasing branch of either hysteresis loop can be considered to be the microplastic limit [2].

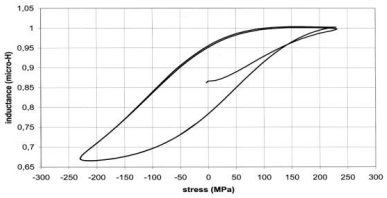

Fig. 1 Inductance vs. stress.

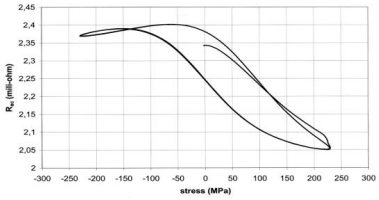

Fig. 2 A.C. resistance vs. stress

3. Results of evaluation of MPL during fatigue

Evaluation of the measured hysteresis loops made it possible to determine magnitudes of MPL for selected numbers of cycles throughout the life. For specimens from low-C steel CSN 411375 they are plotted on Fig.3 together with zero stress inductance L_0 in relation to a relative number of cycles n/N loaded at σ_a = 230 MPa. It can be seen that MPL varied during cycling between 70 MPa and 115 MPa, which is in contrast to the fatigue

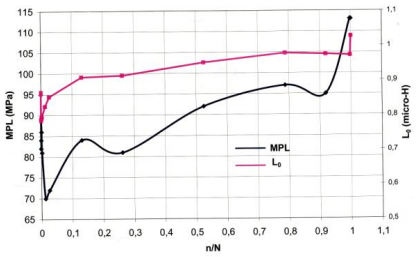

Fig.3 Variation of MPL and L_0 with n/N

limit (FL) σ_f = 170 MPa. Because MPL separates damaging and non-damaging stresses below FL when they interact with stresses above the fatigue limit verifying fatigue tests were made in two-level block cycling.

4. Verifying fatigue tests

Cycling at the reference level σ_{ref} = 242 MPa to fracture was designated as tests A. The mean life, calculated from the mean of the logarithm of the lives, was N_f^* = 17 688 cycles. Two-level block steps with the upper stress level equal to the reference stress and the lower stress lying below the fatigue limit FL were designated as tests B and tests C in relation to that whether the lower stress in the block was higher or lower than the MPL. Characteristics of these tests are summarized in Tab.1.

Tests / para-s	A	B	C
σ_{a1} (MPa)	242	242	242
n_1 (cycles)	17688	5896	5896
σ_{a2} (MPa)	-	150	70
n_2 (cycles)	-	10^6	10^6
σ_{a3} (MPa)	-	242	242
n_3 (cycles)	-	6698	16254
$N_f = n_1 + n_3$	17688	12594	22150

Tab. 1.Stress levels and mean values of the life

It can be noticed from Tab.1 that for tests B and C the number of cycles n_1 realized at the stress level $\sigma_{a1} = \sigma_{ref}$ was one third of the mean life at the reference stress level. If there is any influence of fatiguing below FL, then the total life $N_f = n_1 + n_3$ at the reference stress should differ significantly from the mean life N_f^*. The results in Tab.1 show that this is the case for the tests B with the stress level σ_{a2} laying above MPL. In the tests C a deteriorating effect of fatiguing below MPL was not observed; the effect was rather slightly beneficial. The results of these tests are illustrated in Fig.4.

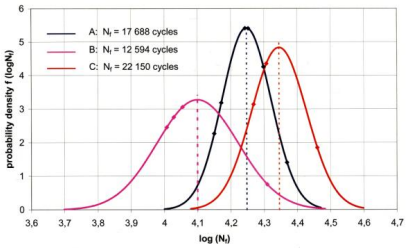

Fig.4 Probability density diagrams for cyclic tests

The probability density curves on Fig.4 illustrate that fatiguing of specimens below FL and above MPL for 10^6 cycles reduced the total life at the reference stress and fatiguing below MPL improved it slightly.

5. Conclusions

Block test – based informative results showed that the MPL divides damaging and non-damaging stresses below FL. The MPL itself is not constant during cycling but it varies: it decreases in the beginning of cycling, reaches its minimum of ~ 70 MPa and then it gradually increases with number of cycles up to about 115 MPa just before fracture.

Acknowledgements

This work was supported by RVO: 68378297 and by the grant project P105/10/2052 of the Grant Agency of the Czech Republic.

References

[1] Gajdoš, Ľ. and Šperl, M., "Microplastic Limit as Determined by the Inductance and Resistance Method", *Proceedings of 29th Danubia-Adria Symposium in Experimental Mechanics*, Belgrade, Serbia, 2012, pp. 44-45.

[2] Gajdoš, Ľ., Šperl, M., Kaiser, J. and Mentl, V., "A Comparison of Probable Magnitudes of the Microplastic Limit of CSN 411375 Steel Determined by the Inductance and Resistance Method", *Proceedings of International Conference "Experimental Stress Analysis"*, Tábor, Czech Republic, 2012, pp. 103-110

30th DANUBIA-ADRIA
Symposium on Advances in Experimental Mechanics
September 25-28, 2013 - Primošten, Croatia

5B23 087

STRESS AND DEFORMATION ANALYSIS OF COMPOUND CYLINDERS IN ELASTIC AND PLASTIC RANGE

Tajana Vaško[1], Franjo Matejiček[2]

[1] Technical College in Bjelovar, Trg Eugena Kvaternika 4, HR-43000 Bjelovar, CROATIA. E-mail: tvasko@vtsbj.hr

[2] Josip Juraj Strossmayer University of Osijek, Mechanical Engineering Faculty in Slavonski Brod, Trg Ivane Brlić Mažuranić 2, HR-35000 Slavonski Brod, CROATIA. E-mail: fmatej@sfsb.hr

1. Introduction

Thick-walled vessels and pipes have found their use in systems with extreme loads and aggressiveness of the surrounding media. Thick-walled cylinders can be loaded with internal overpressure, external overpressure, heat, bending, twisting, and combinations of these load features [1].

In this paper, the analytical and numerical analysis of a compound thick walled cylinder in elastic and plastic range is given. In addition, the condition after completely unloading the cylinder is analysed and the analytical and numerical results are compared.

2. Analytical analysis of the compound cylinder

The analytical analysis is performed on a compound cylinder with rising inner pressure until the complete plastification of the inner tube, see Fig. 1. The presumption for this analysis is that there is no overlap in the initial position of the inner and outer cylinder. For the analytical and numerical analysis of this problem a linear elastic-ideal plastic material model is used. The following were the values of material properties (TStE500): $E = 206855$ MPa and $\sigma_T = 575$ MPa [2].

According to [3] and [4] equations for circular and radial stress for a thick-walled cylinder with internal load in elastic range are given:

$$\sigma_\varphi = \frac{\sigma_T}{\sqrt{3}}\left(\frac{r_T}{r_2}\right)^2\left[1+\left(\frac{r_2}{r}\right)^2\right], \qquad (1)$$

$$\sigma_r = \frac{\sigma_T}{\sqrt{3}}\left(\frac{r_T}{r_2}\right)^2\left[1-\left(\frac{r_2}{r}\right)^2\right]. \qquad (2)$$

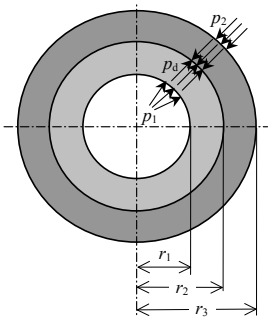

Fig. 1. Symbolic representation of compound tube dimensions and loads

With rising inner pressure, plastification slowly progresses through the inner cylinder, so for further analysis the equations describing the radial and circular stress in the plastic range with considering the von Mieses yield criterion are needed [3, 4]:

$$\sigma_r = \frac{\sigma_T}{\sqrt{3}}\left[2\ln\frac{r}{r_T}+\left(\frac{r_T}{r_2}\right)^2-1\right], \qquad (3)$$

$$\sigma_\varphi = \frac{\sigma_T}{\sqrt{3}}\left[2\ln\frac{r}{r_T}+\left(\frac{r_T}{r_2}\right)^2+1\right]. \qquad (4)$$

Additionally, the condition after unloading the compound cylinder after the complete plastification of the inner cylinder is also described and analysed analytically.

3. Finite Element Method analysis

For the given compound cylinder, see Fig. 1., the numerical analysis using FEM is also performed with additional attention directed to modelling the contact problem [5]. The numerical analysis is performed as an axis-symmetric problem [6] where the schematic of the finite element mesh used is shown, see Fig. 2.

In addition, the state after unloading the cylinder is analysed numerically and compared to the analytical results.

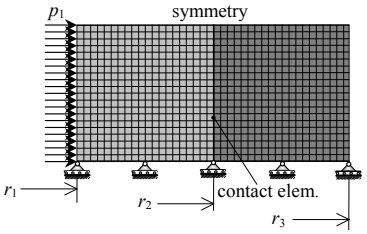

Fig. 2. Axis-symmetric computational domain and the schematic of the finite element mesh for the FEM analysis

4. Elaboration of obtained results

The obtained numerical and analytical results, for the compound cylinder loaded with gradually rising inner pressure, are given in this chapter of the paper.

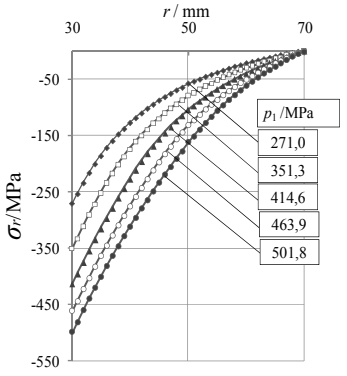

Fig. 3. Comparison of analytical and FEM results of radial stress distribution

Radial and circular stress distributions are compared, see Fig. 3. and Fig. 4., additionally to the comparison of the analytical and numerical results for the condition after completely unloading the compound cylinder after the complete plastification of the inner tube.

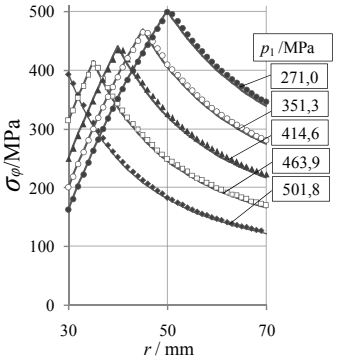

Fig. 4. Comparison of analytical and FEM results of circular stress distribution

5. Conclusion

The aim of this paper was to compare the analytical and numerical results in elastic and plastic range for a compound thick-walled cylinder exposed to rising inner pressure until the complete plastification of the inner tube. Besides that, the results for the state after completely unloading the cylinder are also compared.

References

[1] Darijani, H., Kargarnovin, M.H., Naghdabadi, R., Design of thick-walled cylindrical vessels under internal pressure based on elasto-plastic approach, Materials and Design, **30**, 2009. pp. 3537–3544.

[2] Matejiček, F.: Experimental and numerical Determination of the Parameter of Creep, Österreichische Ingenieur- und Architekten-Zeitschrift, 5, 1999. pp. 211-214.

[3] Alfirević, I., *Uvod u tenzore i mehaniku kontinuuma*, Zagreb; Golden marketing, 2003., pp 408-413, ISBN: 953-212-130-7 http://bib.irb.hr/prikazi-rad?&rad=136063

[4] Gao, X.-L., Elasto-plastic analysis of an internally pressurized thick-walled cylinder using a strain gradient plasticity theory, International Journal of Solids and Structures, **40**, 2003. pp. 6445–6455.

[5] Vaško T., *Elasto-plastična analiza sastavljenih cijevi*, Graduation paper, 2012, http://bib.irb.hr/prikazi-rad?&rad=628587

[6] Bhatnagar, R. M., Modelling, validation and design of autofrettage and compound cylinder, European Journal of Mechanics A/Solids, **39**, 2013 pp. 17-25.

30th DANUBIA-ADRIA
Symposium on Advances in Experimental Mechanics
September 25-28, 2013 - Primošten, Croatia

5B24 040

INCONEL ALLOY'S 718 METALLOGRAPHY EVALUATION AS A PREPARATION FOR FATIGUE TEST

Juraj Belan[1]

[1] University of Žilina, Faculty of Mechanical Engineering, Department of Materials Science, Univerzitná 8215/1, 010 26 Žilina, SLOVAKIA. E-mail: juraj.belan@fstroj.uniza.sk

1. Introduction

INCONEL alloy 718 is a high-strength, corrosion-resistant nickel chromium material used at -253°C to 705°C. The ease and economy with which INCONEL alloy 718 can be fabricated, combined with good tensile, fatigue, creep, and rupture strength, have resulted in its use in a wide range of applications. Examples of these are components for liquid fuelled rockets, rings, casings and various formed sheet metal parts for aircraft and land-based gas turbine engines, and cryogenic tankage [1]. For the past several decades, alloy 718 continues to be used in gas turbines in greater volume and for many applications. High performance demands and high quality requirements especially in disk application have required material homogeneity, grain size control, and high mechanical properties (such as LCF or cyclic stress rupture) at operating conditions.

To summarize the selection process, an alloy with maximum designer confidence in homogeneity and ductility was desired, and wrought alloys fit the bill; forgeability of IN-718 is good. Yield and ultimate strengths plus LCF resistance are quite satisfactory; creep resistance is adequate to the desired maximum application temperature. The alloy is available, has fewer strategic elements, and cost less than competitor alloys. Consequently, IN-718 is the alloy of choice for a majority of gas turbine disks.

2. Experimental material

Chemical composition of INCONEL alloy 718 according to BIBUS Ltd. (CZ) is as follows (all elements in wt %): *C – 0.026; Si – 0.09; Mn – 0.07; P – 0.008; S <0.001; Al – 0.57; B – 0.004; Bi (ppm) <0.1; Co – 0.14; Cr – 19.31; Cu – 0.03; Mo – 2.99; Nb – 5.30; Ni – 53.32; Pb (ppm) – 0.1; Se (ppm) < 3; Ta <0.01; Ti – 0.96; Ni + Co – 53.46; Nb + Ta – 5.31; and Fe – balance*. Some mechanical properties are in Tab. 1.

The bar was heat treated 980°C/1 hrs. AC + heating at 720°C/8 hrs. followed FC (50°C per hour) to temp. 620°C holding time 8 hrs. and air cooled.

	Temperature [°C]	
	20	**649**
Rp 0.2 [MPa]	1213	986
Rm [MPa]	1549	1123
A [%]	21.3	22.6
Z [%]	33.3	68.0
HBW 10/3000	429	-
$\sigma_{T/649}$ [MPa]	-	689
Rupture life hrs.]	-	26.8
A [%] creep	-	45.7

Tab. 1 Mechanical properties of IN 718

3. Experimental results

3.1 Hardness measurements

Hardness measurements were provides by Rockwell (STN EN ISO 6508) and Brinell (STN EN ISO 6506) methods on bar with diameter ϕ 12 mm as supplied by BIBUS company. Results of hardness measurements are in Tab. 2.

Method	
HBW5/750	395.25
HRC	45
HV(*)	452
HBS10/3000(*)	425

Tab. 2. Hardness measurements, (*) according to ASTM E 140-02.

3.2 Microstructure

Bar were cut and moulded into bakelite sample, which have been grinded and polished via regular metallography preparation steps. The samples were observed as none etched for carbide particles identification, Fig. 1, then etched by Kallings for microstructure observing, Fig. 2.

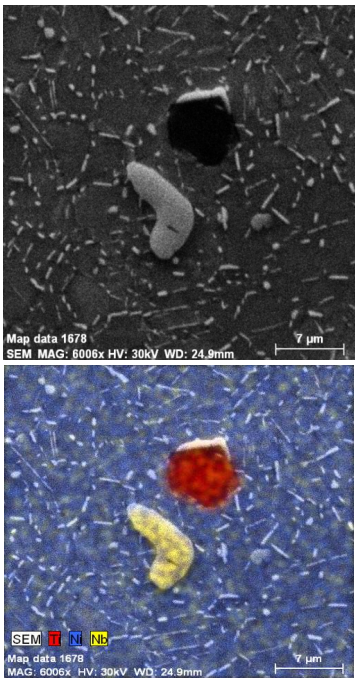

Fig. 1 Identification of carbide particles rich for Ti and Nb content in IN 718 alloy + SEM elements mapping, etch. Kallings, SEM.

Superalloy consists of the austenitic fcc matrix phase γ plus a variety of secondary phases. Secondary phases of value in controlling properties are the fcc carbides MC, $M_{23}C_6$, M_6C, and M_7C_3 (rare) in virtually all superalloy types; gamma prime (γ′) fcc ordered $Ni_3(Al,Ti)$; gamma double prime (γ′′) bct ordered Ni_3Nb; and the delta (δ) orthorhombic Ni_3Nb intermetallic compounds in iron-nickel-base superalloys. The γ′, γ′′, and η phases also are known as geometrically close-packed (gcp) phases.

The superalloy derives its strength mostly from solid-solution hardeners and precipitated phases. Principal strengthening precipitate phases are γ′ and γ′′, which are found in iron-nickel- and nickel-base superalloys.

The δ and η phases are useful (along with γ′) in control of structure of wrought iron-nickel- and nickel-base superalloys during processing [2].

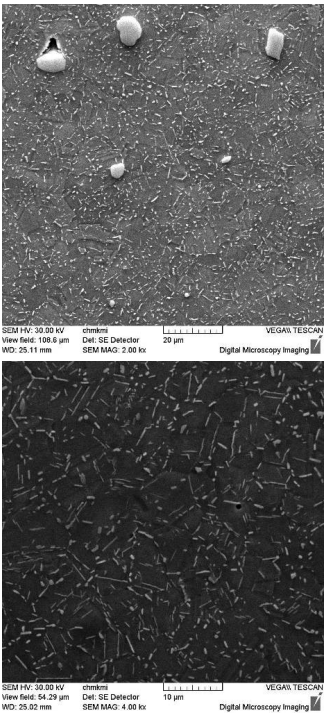

Fig. 2 Microstructure of IN 718 alloy with Ti, Nb carbides and γ´ (small rectangle particles), γ´´ (plate like particles), and rare deformations twins, etch Kallings, SEM.

4. Conclusion

This is a brief description of metallography evaluation of IN 718 alloy, which will be used as an experimental material for further fatigue testing.

Acknowledgements

The authors acknowledge VEGA No. 1/0841/11 and No. 1/0460/11, and European Union - the Project ITMS 26110230004.

References

[1] Available at http://www.specialmetals.com/documents/Inconel%20alloy%20718.pdf

[2] Donachie, M., J., Donachie, S., J., Superalloys: A Technical Guide, 2nd Edition, ASM International, 2002.

30th DANUBIA-ADRIA
Symposium on Advances in Experimental Mechanics
September 25-28, 2013 - Primošten, Croatia

5B25 113

IDENTIFICATION OF FAILURE MODES OF CLT-PLATES BY MEANS OF DIC MEASUREMENTS

G. Hochreiner[1], J. Füssl[1], J. Eberhardsteiner[1]

[1] Institute for Mechanics of Materials and Structures, Vienna University of Technology
Karlsplatz 13/202, 1040 Vienna, Austria. E-mail: georg.hochreiner@tuwien.ac.at

1. Introduction

Cross laminated timber (CLT) has become a favorite structural element especially in the context with concentrated loads and 2D-span structures. Such loads may either be induced from single supports on the borderline or in the interior of the plate or from high wheel-pressure typical for road bridges.

This topic has intensely been investigated for concrete slabs [1] long ago including nonlinear load-carrying behavior due to crack formation but not yet for CLT-elements. At the moment structural modeling [2] is quite restricted to local elastic failure, not taking into account possible post-elastic failure modes leading to even higher ultimate loads than the first elastic peak.

That is why test series with three layered quadratic circumferentially supported CLT-plates were recently performed at Linnaeus University, Växjö. The load carrying behavior due to a concentrated load at mid-span was mainly recorded by means of a digital image correlation (DIC) system, facing the unloaded plate surface (tension side), to make the results more comparable with those from structural modeling by FEM.

2. Experiments

2.1 CLT test specimens

The boards for the production of the CLT-plates were machine-graded according to the profiles C18, C24, and C35. Due to the small size of the plates (3 x 19/1500/1500 mm) finger-jointing of the lamellas was not necessary.

2.2 Test set-up and measuring devices

In order to enable comfortable measuring and protection of the cameras against damage from splitting boards a vertical rig in combination with horizontal application of the concentrated load was selected (see Fig. 1). The test set-up was identical for all test samples (8 plates per grading-class). The direction of the main load carrying capacity was vertical, corresponding to the Y-axis of the coordinate system of the DIC measurement system ARAMIS.

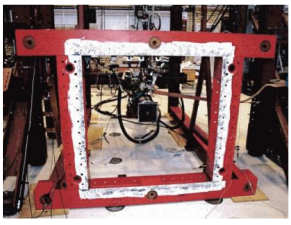

Fig. 1. Vertical test set-up

The 3D full-field displacement measurements were performed with two 4-MPix-cameras. The resolution of the displacement field can be estimated with about 12 mm taking into account a facet-size of 15 pixels and overlapping of 3 pixels. An appropriate speckle pattern was applied manually with a pattern-brush.

3. Results and discussion

It was agreed to perform the tests up to the ultimate load carrying capacity, but several tests were stopped prematurely based on the traditional assumption, that after the first elastic failure no recovery due to a change of the corresponding structural system would be possible. However the benefit of this fact could be used to assess intermediate fracture formations.

3.1 System response

Although it was expected, that the failure modes would follow the classification of the three

grading profiles, only two significant different structural systems could be identified: the one being based on tensile failure of single boards (usually no recovery of the system after the first drop of load) and the other one only exhibiting rolling-shear failure in between the different layers (typical for boards with higher performance of tensile strength, see Fig. 2).

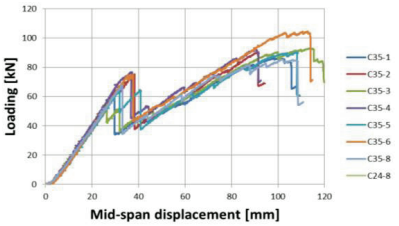

Fig. 2. System recovery (hardening)

3.2 Failure modes

The following evaluation modes supported by the ARAMIS-system could be used for assessment of different aspects:

- *Displacement field with contour lines:* Crack formation is reflected by asymmetry of the field respectively staggered contour lines. The two dominating failure modes are highlighted in Fig. 3.

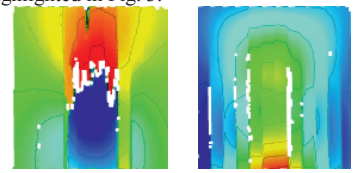

Fig. 3. Y-displacement field:
left: bending failure; right: rolling-shear failure

- *Multi-stage sections for displacements* in the main and transverse load carrying direction: Significant gaps between singles stages reflect the start of crack formation (usually separation of singles layers).
- *Strain field parallel to the grain* of the surface-lamellas: Growth irregularities, discontinuities (tensile failure parallel to the grain) as well as lateral load redistribution (see Fig. 4) can be identified.

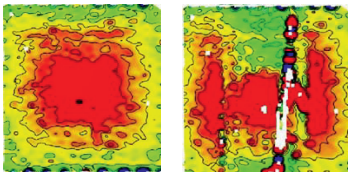

Fig. 4. Tension strains and lateral load redistribution
left: before first failure; right: post-elastic system

- *Strain field perpendicular to the grain* of the surface-lamellas: Reflects discontinuities by opening of probably side-glued edges between single boards perpendicular to the grain.
- *Shear strain field:* Reflects delamination, respectively interface failure between single layers.

Sometimes interpretation of the results becomes more concise if rigid body movement is excluded.

4. Conclusions

- A DIC system is a perfect tool for tracking failure modes of CLT-plates during testing even up to the ultimate load. Different options for the evaluation focusing only single components of the whole field of displacements or strains enable identification of load redistribution as well as typical plate failure modes.
- Although only the surface can be assessed, many conclusions can be extracted also for the load carrying behavior of the interior layer. Nevertheless, the type and location of distinct failure modes may finally only assessed by slicing the test specimens into strips or cubes for visual inspection.
- Failure modes are strongly depending on the strength specifications of the boards. If premature classical bending-tension failure of single boards can be excluded, rolling-shear failure becomes the dominant failure mode. The increase of the plate deformations due to reduced shear stiffness in high stressed areas may change the structural behavior from a first mode (plate bending) to a second mode (membrane system). The size of the structural element and the location of the concentrated loading may be decisive for the final failure mode.

References

[1] Leonhardt, F., Vorlesungen über Massivbau. Vierter Teil: Nachweis der Gebrauchsfähigkeit, Rissebeschränkung, Formänderungen, Momentenumlagerung und Bruchlinientheorie im Stahlbetonbau. Springer-Verlag, Berlin-Heidelberg-New York (1976 + 1978)

[2] Mestek, P., Punktgestützte Flächentragwerke aus Brettsperrholz (BSP) – Schubbemessung unter Berücksichtigung von Schubverstärkungen; Dissertation Technische Universität München (2011)

30th DANUBIA-ADRIA
Symposium on Advances in Experimental Mechanics
September 25-28, 2013 - Primošten, Croatia

5B26 072

IDENTIFICATION OF FAILURE MODES OF CLT-PLATES BY MEANS OF DIC MEASUREMENTS

G. Hochreiner[1], J. Füssl[1], J. Eberhardsteiner[1]

[1] Institute for Mechanics of Materials and Structures, Vienna University of Technology
Karlsplatz 13/202, 1040 Vienna, Austria. E-mail: georg.hochreiner@tuwien.ac.at

1. Introduction

Cross laminated timber (CLT) has become a favorite structural element especially in the context with concentrated loads and 2D-span structures. Such loads may either be induced from single supports on the borderline or in the interior of the plate or from high wheel-pressure typical for road bridges.

This topic has intensely been investigated for concrete slabs [1] long ago including nonlinear load-carrying behavior due to crack formation but not yet for CLT-elements. At the moment structural modeling [2] is quite restricted to local elastic failure, not taking into account possible post-elastic failure modes leading to even higher ultimate loads than the first elastic peak.

That is why test series with three layered quadratic circumferentially supported CLT-plates were recently performed at Linnaeus University, Växjö. The load carrying behavior due to a concentrated load at mid-span was mainly recorded by means of a digital image correlation (DIC) system, facing the unloaded plate surface (tension side), to make the results more comparable with those from structural modeling by FEM.

2. Experiments

2.1 CLT test specimens

The boards for the production of the CLT-plates were machine-graded according to the profiles C18, C24, and C35. Due to the small size of the plates (3 x 19/1500/1500 mm) finger-jointing of the lamellas was not necessary.

2.2 Test set-up and measuring devices

In order to enable comfortable measuring and protection of the cameras against damage from splitting boards a vertical rig in combination with horizontal application of the concentrated load was selected (see Fig. 1). The test set-up was identical for all test samples (8 plates per grading-class). The direction of the main load carrying capacity was vertical, corresponding to the Y-axis of the coordinate system of the DIC measurement system ARAMIS.

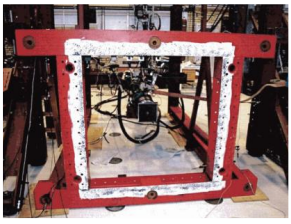

Fig. 1. Vertical test set-up

The 3D full-field displacement measurements were performed with two 4-MPix-cameras. The resolution of the displacement field can be estimated with about 12 mm taking into account a facet-size of 15 pixels and overlapping of 3 pixels. An appropriate speckle pattern was applied manually with a pattern-brush.

3. Results and discussion

It was agreed to perform the tests up to the ultimate load carrying capacity, but several tests were stopped prematurely based on the traditional assumption, that after the first elastic failure no recovery due to a change of the corresponding structural system would be possible. However the benefit of this fact could be used to assess intermediate fracture formations.

3.1 System response

Although it was expected, that the failure modes would follow the classification of the three

grading profiles, only two significant different structural systems could be identified: the one being based on tensile failure of single boards (usually no recovery of the system after the first drop of load) and the other one only exhibiting rolling-shear failure in between the different layers (typical for boards with higher performance of tensile strength, see Fig. 2).

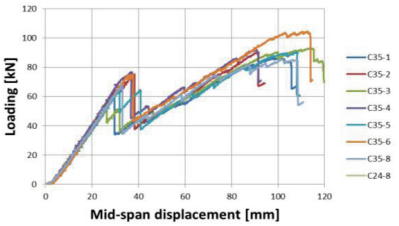

Fig. 2. System recovery (hardening)

3.2 Failure modes

The following evaluation modes supported by the ARAMIS-system could be used for assessment of different aspects:

- *Displacement field with contour lines:* Crack formation is reflected by asymmetry of the field respectively staggered contour lines. The two dominating failure modes are highlighted in Fig. 3.

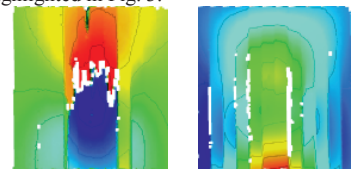

Fig. 3. Y-displacement field:
left: bending failure; right: rolling-shear failure

- *Multi-stage sections for displacements* in the main and transverse load carrying direction: Significant gaps between singles stages reflect the start of crack formation (usually separation of singles layers).
- *Strain field parallel to the grain* of the surface-lamellas: Growth irregularities, discontinuities (tensile failure parallel to the grain) as well as lateral load redistribution (see Fig. 4) can be identified.

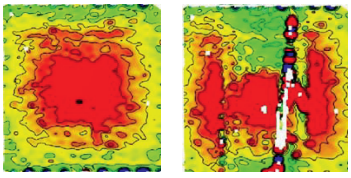

Fig. 4. Tension strains and lateral load redistribution
left: before first failure; right: post-elastic system

- *Strain field perpendicular to the grain* of the surface-lamellas: Reflects discontinuities by opening of probably side-glued edges between single boards perpendicular to the grain.
- *Shear strain field:* Reflects delamination, respectively interface failure between single layers.

Sometimes interpretation of the results becomes more concise if rigid body movement is excluded.

4. Conclusions

- A DIC system is a perfect tool for tracking failure modes of CLT-plates during testing even up to the ultimate load. Different options for the evaluation focusing only single components of the whole field of displacements or strains enable identification of load redistribution as well as typical plate failure modes.
- Although only the surface can be assessed, many conclusions can be extracted also for the load carrying behavior of the interior layer. Nevertheless, the type and location of distinct failure modes may finally only assessed by slicing the test specimens into strips or cubes for visual inspection.
- Failure modes are strongly depending on the strength specifications of the boards. If premature classical bending-tension failure of single boards can be excluded, rolling-shear failure becomes the dominant failure mode. The increase of the plate deformations due to reduced shear stiffness in high stressed areas may change the structural behavior from a first mode (plate bending) to a second mode (membrane system). The size of the structural element and the location of the concentrated loading may be decisive for the final failure mode.

References

[1] Leonhardt, F., Vorlesungen über Massivbau. Vierter Teil: Nachweis der Gebrauchsfähigkeit, Rissebeschränkung, Formänderungen, Momentenumlagerung und Bruchlinientheorie im Stahlbetonbau. Springer-Verlag, Berlin-Heidelberg-New York (1976 + 1978)

[2] Mestek, P., Punktgestützte Flächentragwerke aus Brettsperrholz (BSP) – Schubbemessung unter Berücksichtigung von Schubverstärkungen; Dissertation Technische Universität München (2011)

30th DANUBIA-ADRIA
Symposium on Advances in Experimental Mechanics
September 25-28, 2013 - Primošten, Croatia

5B27 102

EXPERIMENTAL ANALYSIS OF MECHANICAL AND MATERIAL PROPERTIES OF CONCRETE ORLIK DAM AFTER 50 YEARS

Ondřej Zobal[1], Pavel Padevět[1], Vít Šmilauer[1], Lubomír Kopecký[1], Zdeněk Bittnar[1]

[1] Department of Mechanics in Faculty of Civil Engineering, CTU in Prague, Thakurova 7/2077, 166 29 Prague 6 – Dejvice, CZECH REPUBLIC. E-mail: ondrej.zobal@fsv.cvut.cz

1. Introduction

Orlik Dam is one of the most important construction work Czech Republic. Construction of the dam began in 1956 and was completed in 1961. Orlik Dam is the largest water work in the Czech Republic and is part of the Vltava Cascade. Concrete dam is straight, gravity and is high 81,5 m and long 450 m [1]. The volume of material to produce the dam was huge, it was about 923,000 cubic meters of concrete. Great work schedule and sophisticated technological solutions, however, allowed to handle 83% displacement produced as early as 32 months [2].

For the construction of the dam to be used two mixtures - wrapping concrete B170, where was 200 kg/m^3 of cement and fly ash 50 kg/m^3 (replaced by 20 %) and the core concrete B80, where was 130 kg/m^3 of cement and 50 kg/m^3 fly ash (replaced by 27.8 %) [3]. Fly ash was used due to problems with the increase in heat of hydration. The following concrete composition was analyzed material and mechanical properties.

2. Experimental results

The analysis and tests were performed on specimens obtained from bores with a diameter of 80 mm and a bore diameter of 300 mm. Smaller specimens were used for microscopic analysis and moisture analysis, bigger then test the compressive strength and tensile strength.

2.1 Microscopic analysis

Microscopic analysis was performed on a scanning electron microscope XL30 ESEM-TMP with EDAX microanalyzer.

It was found that, thanks to the gravel is minimal space between the grains and so the consumption of cement minimized. The cement paste includes: unhydrated clinkers, mostly belit, remnants of fly ash particles and as mentioned above, there are also very few hollows and pores. Fly ash has pozzolanic activity, and therefore is not in the cement paste almost portlandit.

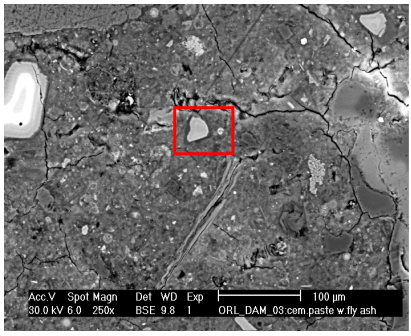

Fig. 1. Microscopic image of concrete from Orlik dam.

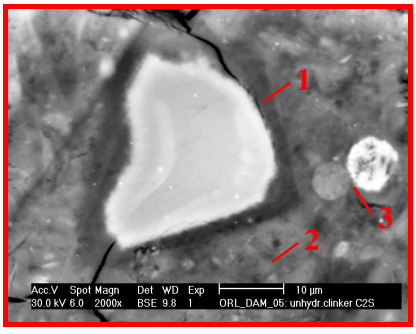

Fig. 2. 1) CSH-HD surroundings the clinker, appears by compact and homogeneous structure; 2) CSH-LD in the hydrated cement matrix, is more heterogeneous; 3) the grains of non-activated fly ash.

2.2 *Determination of volume density and moisture analysis*

The measured volume density is shown graphically in Fig. 3. It can be seen that the difference between the volume density of wrapping concrete B170 and core concrete B80 is minimal, the value is around 2400 kg/m^3.

Core bores diameter 80 mm were cut diamond saw into slices with a thickness of 3-5 mm and split into three groups of ten specimens. Prepared in this way specimens were placed for 10 months at a constant temperature of 20°C water until there was no stabilizing weight. Then were specimens placed for 2 months in the drying oven at 105°C and will be dried to constant weight. The resulting loss of weight is shown in Tab. 1.

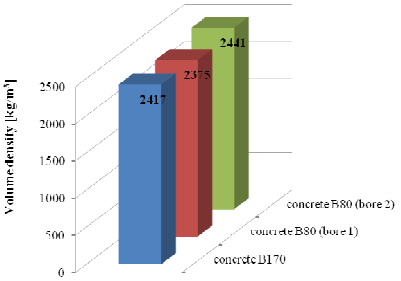

Fig. 3. Volume density of concrete from Orlik dam measured after more than 50 years of operation of the waterworks.

Type of concrete	Type of bore	Average saturate weight	Average dried weight	Loss of weight
	[-]	[g]	[g]	[%]
B170	VO1	58,6	55,5	5,3
B80	VJ1	53,4	50,4	5,6
	VJ2	51,1	48,7	4,7

Tab. 1. Loss of weight completely saturated concrete specimens of Orlik dam after dried completely.

2.3 *Splitting test*

Splitting test was performed on cylinders with a diameter of 300 mm and a height of 220 mm and was found in the transverse tensile strength. The test was performed on six specimens and value was between 3 and 4.5 MPa, which corresponds to about 10% of the compressive strength.

2.4 *Compressive strength test*

Of a cylinder with a diameter of 300 mm were cut with a diamond saw a cube with 200 mm and were tested for compressive strength. The test was performed on four cubes and value of compressive strength ranged from 42 to 51 MPa. From the extant literature, where are presented the results of measurements, was chosen measuring the compressive strength of the cubes 200 mm taken from the finished work and was created Tab. 2. The table shows the development of compressive strength of concrete B170 and B80 during the first year, which is complemented by actual measurement.

Type of concrete	The development of compressive strength [days; MPa]		
	28	365	18615
B170	14,4	33,4	-
B80	10,1	23,4	47,3

Tab. 2. The average compressive strength of concrete from Orlik dam in time, from [4].

3. Remarks

- Comprehensive analysis of the material and mechanical properties of the concrete is performed because it is a unique opportunity to determine the properties of such material after several decades in operation.
- The final concrete is very compact material with little hollows and pores with a high strength, which in the time continues to increase.
- This analysis demonstrated that almost 30% replacement of cement with fly ash had no negative effect on the long-term properties of final concrete.

Acknowledgements

The financial support of this experiment by Project MPO ČR FR-TI3/757 is gratefully acknowledged

References

[1] Povodí Vltavy s. p., informační materiály, (in Czech)

[2] Hydroprojekt Praha (1956). Vodní dílo Orlík soohrnný elaborát – svazek ¼ - textová část, (in Czech)

[3] Keil, J. (1966). Výstavba vodního díla Orlík – sborník statí, Národní podnik vodní stavby, (in Czech)

[4] Vodní dílo Orlík soohrnný elaborát – svazek 2/4 – výkresová část, (in Czech)

30th DANUBIA-ADRIA
Symposium on Advances in Experimental Mechanics
September 25-28, 2013 - Primošten, Croatia

5B28 038

FATIGUE PROPERTIES OF NODULAR CAST IRONS

Alan VAŠKO[1], Libor TRŠKO[2]

[1] University of Žilina, Faculty of Mechanical Engineering, Department of Materials Engineering, Univerzitná 8215/1, 010 26 Žilina, SLOVAKIA. E-mail: alan.vasko@fstroj.uniza.sk

[2] University of Žilina, Faculty of Mechanical Engineering, Department of Materials Engineering, Univerzitná 8215/1, 010 26 Žilina, SLOVAKIA. E-mail: libor.trsko@fstroj.uniza.sk

1. Introduction

Nodular cast iron is a group of cast construction materials with a wide application in engineering practice. It combines high tensile strength and plasticity with high fatigue strength. The contribution deals with the influence of charge composition (different ratio of steel scrap in a charge and different additive for the regulation of chemical composition) on the microstructure and fatigue properties of nodular cast irons.

2. Methods

The specimens from four meltages of nodular cast iron were used for experiments. The meltages were different by charge composition (Tab. 1). The basic charge of individual meltages was formed by different ratio of pig iron and steel scrap and by different additive for the regulation of chemical composition (metallurgical silicon carbide or ferrosilicon). The content of these additives was chosen to achieve approximately the same resultant chemical composition of the meltages. For modification the FeSiMg7 modifier was used and for inoculation the FeSi75 inoculant was used [1].

Meltage number	pig iron [%]	steel scrap [%]	additive
3	40	60	SiC
5	0	100	
8	40	60	FeSi
10	0	100	

Tab. 1. Charge composition of experimental meltages.

The fatigue tests were made at high-frequency sinusoidal cyclic push-pull loading (frequency f ≈ 20 kHz, stress ratio R = –1, temperature T = 20 ± 5 °C) using the ultrasonic testing equipment KAUP-ZU [2].

3. Results

From a microstructural point of view, the specimens from all the meltages are ferrite-pearlitic nodular cast irons with different content of ferrite and pearlite in a matrix, different size of graphite and count of graphitic nodules (Fig. 1).

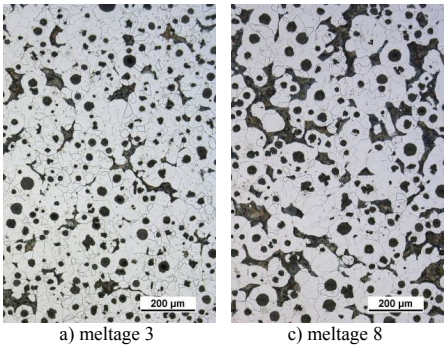

a) meltage 3 (with SiC additive)

c) meltage 8 (with FeSi additive)

Fig. 1. Microstructure of the specimens from cast bars, etched 1% Nital.

The mechanical tests were realized on the specimens made from cast bars. The results of mechanical tests, i.e. tensile strength R_m, elongation A, absorbed energy K and Brinell hardness HB, are given in Tab. 2.

Meltage number	R_m [MPa]	A [%]	K [J]	HBW 10/3000
3	539.0	4.0	30.6	192.3
5	515.7	3.7	17.2	182.3
8	462.6	2.7	24.0	181.3
10	462.6	2.7	19.2	183.0

Tab. 2. Mechanical properties.

For the fatigue tests, ten specimens from each meltage were used to obtain Wöhler fatigue curves $\sigma_a = f(N)$ and determine fatigue strength σ_c for $N = 10^8$ cycles. The results of fatigue tests (relationship between stress amplitude σ_a and number of cycles to failure N_f) are shown in Fig. 2. The values of fatigue strength σ_c are given in Tab. 3.

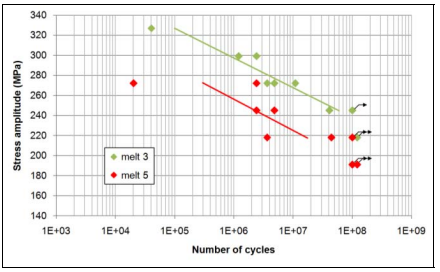

a) meltages 3 and 5 (with SiC additive)

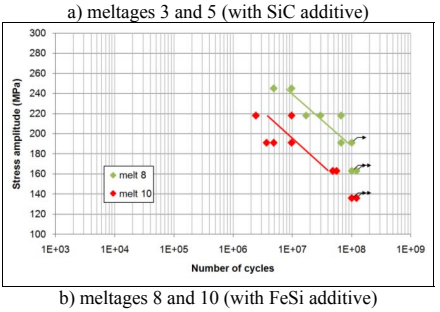

b) meltages 8 and 10 (with FeSi additive)

Fig. 2. Wöhler curves $\sigma_a = f(N)$.

The fatigue strength in the specimens from the meltages with SiC additive is higher than in the specimens from the meltages with FeSi additive. The highest fatigue strength (218 MPa) was reached in the meltage 3 created by 60 % of steel scrap and SiC additive, which has the best mechanical properties.

Meltage number	σ_c [MPa]
3	218
5	191
8	163
10	136

Tab. 3. Fatigue strength.

The fracture surfaces of analysed specimens do not show any remarkable differences; they are characteristic of mixed mode of fracture (Fig. 3).

The fatigue fracture was initiated by casting defect (Fig. 3a). The fatigue fracture is characteristic of intercrystalline fatigue failure of ferrite around graphitic nodules and transcrystalline fatigue failure of ferrite and pearlite in the rest of the area (Fig. 3b). The final rupture is characteristic of transcrystalline ductile failure of ferrite with dimple morphology (Fig. 3c) and transcrystalline cleavage of ferrite and pearlite with river drawing on facets (Fig. 3d).

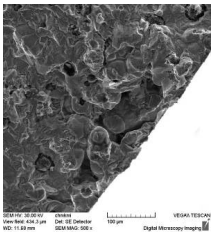

a) initiation of fatigue failure

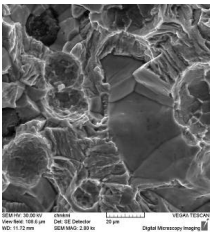

b) fatigue fracture

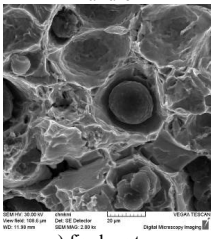

c) final rupture

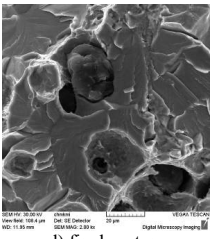

d) final rupture

Fig. 3. Fracture surface of the specimen from the meltage 3 (with SiC additive), $\sigma_a = 272$ MPa, $N_f = 1.1 \times 10^7$ cycles, SEM.

4. Remarks

The results of the experiments show that:

- SiC additive positively influences the microstructure as well as the mechanical and fatigue properties of nodular cast iron,
- the best fatigue properties has the meltage 3 created by 60 % of steel scrap and 40 % of pig iron in the basic charge with SiC additive.

Acknowledgements

This work has been supported by the Scientific Grant Agency of the Ministry of Education of Slovak Republic, grants No. 1/0460/11 and 1/0841/11.

References

[1] Vaško, A., Microstructure and Mechanical Properties of Synthetic Nodular Cast Iron, Arch. of Foundry Eng., 1, 2010, pp. 93-98.

[2] Bokůvka, O., Nicoletto, G., Kunz, L., Palček, P., Chalupová, M., Low & High Frequency Fatigue Testing. EDIS Žilina, 2002.

30th DANUBIA-ADRIA
Symposium on Advances in Experimental Mechanics
September 25-28, 2013 - Primošten, Croatia

5B29 031

NUMERICAL ANALYSIS OF SOME MODIFICATION VARIANTS OF THE SELECTED CRASH CUSHION

Andrzej Kiczko[1], Tadeusz Niezgoda[1], Wiesław Barnat[1], Paweł Dziewulski[1], Tomasz Kula,[2] Sławomir Dzienis[2], Michał Karkowski[2], Dawid Kucharski[2]

[1] Military Academy of Technology, Department of Mechanics and Applied Computer Science, 2 Kaliskiego Street, 00-908 Warsaw, POLAND. E-mail: akiczko@wat.edu.pl, tniezgoda@wat.edu.pl, wbarnat@wat.edu.pl, pdziewulski@wat.edu.pl

[2] Road and Bridge Research Institute, 1 Instytutowa Street, 03-302 Warsaw, POLAND. E-mails: tkula@ibdim.edu.pl, sdzienis@ibdim.edu.pl, michal@ibdim.edu.pl, dawid@ibdim.edu.pl

1. Introduction

The crash cushion is an active device serving for road safety, with which a car has a contact during unintended occurrences in road traffic, special attention is paid to the minimization of direct impacts and their consequences for people in a vehicle. Numerical investigation of energy absorbing shields can help not only at the design stage (because of a speed, easiness of introducing changes, costs of tests, possibilities of simultaneous testing many variants or testing not-yet- existing solutions) but also can serve to conduct reliable, numerical impact tests. In this work the numerical test results are presented. They deal with some modification variants of the selected crash cushion whose numerical model has been subjected to validation by comparison with experimental results which were carried out at the stand for impact tests in Inowrocław.

2. The real stand and the numerical model of a stand

The crush cushion is a thin-walled steel construction resting on 3 posts rammed into earth. Each of construction elements is joined itself by screw joints, as depicted in Fig. 1.

The 3 D model, in the STP universal format, has been made available by the Intermetal firm. It has implemented the geometry to the HyperMesh processor. The next stage is to create a numerical model. An average size of a finite element of a steel construction of a crash cushion is approximately 20 mm. The total quantity of finite elements is about 23000.

Fig. 1. The crush cushion

Experimental boundary conditions are taken into account at numerical tests (Fig. 2).

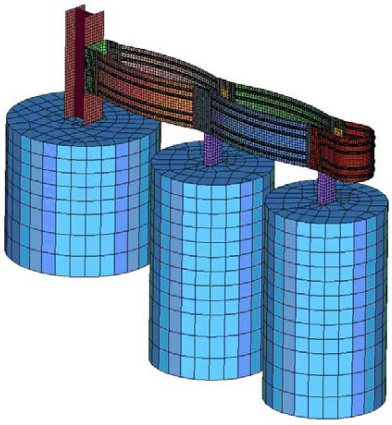

Fig. 2. The numerical model of a crash cushion with a ground model

A numerical model consists of a crash cushion and an undeformed plate with a mass corresponding to a vehicle used in an experimental test. In an experimental test a stiff vehicle of 2700kg driving down from a steel ramp hit into a crash cushion with the initial speed equal to 24 km/h. To transform correctly a real behaviour of a construction during an impact it was necessary to take into account the susceptibility of ground and simplified screw joints, constants for a model of the ground material have been taken from literature [1].

The results of the numerical analysis have been compared with the results of experimental tests. The run of the ASI index at the individual time moments are presented in Fig. 3

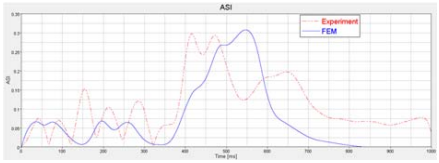

Fig. 3. Comparison of ASI indexes for experimental and numerical tests

3. Numerical model of the modified crash cushion

Modification consists in filling with rigid foams the inner space of a crash cushion (Fig. 4). Additionally, metal joints limiting foam movement during crash tests have been mounted, Fig. 5.

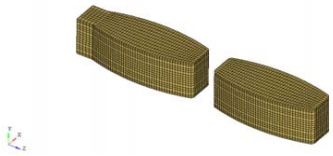

Fig. 4. The numerical model of a rigid foam

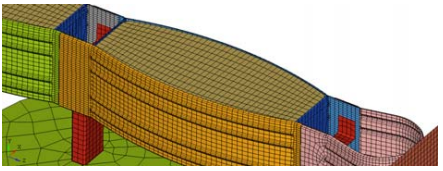

Fig. 5. The numerical model of a modified crash cushion with the rigid foam

4. Results of the numerical analysis of the modified crash cushion

Computations have been carried out for foams with ultimate compressive strength values which are equal to: 0.15 MPa, 0.20 MPa and 0.25 MPa, respectively to the EPS strength (Expanded PolyStyrene).

Diagrams depicting the ASI index time variation are presented in Fig. 6.

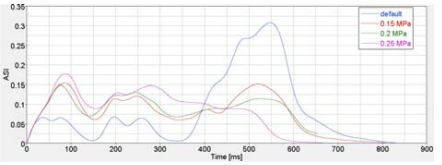

Fig. 6. Comparison of ASI indexes for numerical tests of the original crash cushion (marked as "default") and filled with foams of ultimate compressive strength.

The goal of these experiments is to work out innovative crash cushions with progressive energy consumption, leading to improvements in safety of participants in road traffic. The multi stage, thus universal, character of a shield work allows to protect all road participants (motorcyclists, car and lorry passengers) [2].

Acknowledgements

This study has been supported by the National Centre for Research and Development as a part of the Research & Development Project, No PBS1/B9/3/2012. This support is gratefully acknowledged.

References

[1] Fasanella E. L.; Jackson K. E.; Kellas, S., Soft soil impact testing and simulation of aerospace structures, 10th International LS-DYNA User's Conference; 8-10 Jun. 2008; Dearborn, MI; United States

[2] Barnat W., Dziewulski P., Niezgoda T., Panowicz R., Application of composites to impact energy absorption, Computational Materials Science, 2011, **50**, pp. 1233-1237.

30th DANUBIA-ADRIA
Symposium on Advances in Experimental Mechanics
September 25-28, 2013 - Primošten, Croatia

5B30 101

EFFECT OF INTRINSIC PARAMETERS ON EVALUATION OF CRITICAL LOADS IN NANOSCRATCH TEST

J. Tomáštík[1], R. Čtvrtlík[1]

[1] Regional Centre of Advanced Technologies and Materials, Joint Laboratory of Optics of Palacky University and Institute of Physics of Academy of Sciences of the Czech Republic, Faculty of Science, Palacky University, 17. listopadu 12, 77146 Olomouc, Czech Republic.
E-mails: tomastik@jointlab.upol.cz, ctvrtlik@fzu.cz

1. Introduction

Implementation of thin films has brought specific demands on measurement techniques for assessment of their mechanical properties. In the early 80´s of 20th century scratch test came to use as a primary method for measurement of coatings-substrate adhesion [1-3]. Test consists of pulling the diamond indenter over the sample surface by precisely defined force, while the displacement is continuously measured. Scratching of coating leads to formation of various types of damage (see Fig. 1.). The evaluation of the test is based on microscopic analysis of residual scratch and record of load, distance and time. Onsets of certain types of failure are assigned to the corresponding force load, which determines the so called critical loads (Lc).

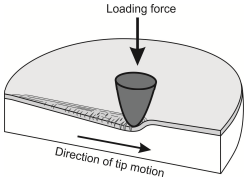

Fig. 1. Scratch test scheme.

Despite the principal experimental simplicity of the test, several specific features have to be recognized. Firstly, disturbance and damage of coating during scratch test can be caused by failure of adhesion as well as cohesion. Therefore, it is necessary to perform thorough microscopic observation to resolve specific failure mechanisms. Influencing parameters are another issue of the scratch test. They can be divided into extrinsic and intrinsic parameters (see Tab. 1.). Extrinsic parameters are attributes of the sample itself; their influence on mechanical stability of the sample is essentially the purpose of scratch test measurement. On the contrary, the influence of intrinsic parameters on scratch test should be avoided. These parameters must be constant during measurement of set of samples.

Intrinsic	Extrinsic
- Loading rate - Scratching speed - Indenter tip radius - Indenter wear - Machine compliance - External test conditions (temperature, humidity)	- Substrate properties (hardness, elastic modulus, coef. of thermal expansion) - Coating properties (thickness, hardness, modulus, residual stress) - Friction coefficient - Surface roughness

Tab. 1. Parameters that affect the scratch test results.

Increase in scratching speed ($\mathrm{d}x/\mathrm{d}t$) results in a decrease of critical load. Increase in loading rate ($\mathrm{d}L/\mathrm{d}t$) increase the critical load. Nevertheless, critical load does not change if the variation of both parameters is proportional, e.g. the ratio $\mathrm{d}L/\mathrm{d}x$ remains constant. However, the change in the value of the ratio $\mathrm{d}L/\mathrm{d}x$ itself results in the change of the critical load. Steimnann et al. [6] have found that tenfold increase in the value of $\mathrm{d}L/\mathrm{d}x$ ratio results in a 20% increase in critical load. Research was primarily focused on values of ratio $\mathrm{d}L/\mathrm{d}x$ = 10–100 N/mm.

Contemporary nanoscratch test uses all attributes in miniaturized scale. Indenters have radii from one to tens microns, which is about ten times smaller than in the classical scratch test. Beake et al. [7] have found, that in the case of thin films even the disproportionate change of scratching speed and loading rate has no effect on critical loads, if the value of $\mathrm{d}L/\mathrm{d}x$ ratio is held below 1 mN/μm.

2. Experiment

The aim of this work is to investigate the effect of dL/dx ratio on critical loads in the case of thicker and more complex multilayer coatings.

Measurements were performed by using the NanoTest apparatus (Micromaterials). Indenter with nominal radius of 10 μm was used. Thorough measurement with laser confocal microscope OLS LEXT 3100 showed that radius is rather 9.2 ± 0.2 μm. The same microscope was used for residual scratch investigation in high magnification. Scratch test procedure consists of at least three scratches for each of the 6 values of dL/dx ratio in the range of 0.17–1.04 mN/μm. This corresponds to scratching speeds in the range of 2.6–10.4 μm/s and loading rates in the range of 5–20 mN/s. In the most cases the scratch length was 450 μm, but for certain measured values it was reduced to 200 μm or prolonged to 1200 μm.

Samples were deliberately chosen on the basis of recognizable and highly reproducible coating failures. Sample A was a two-layer coating consisting of Al and SiO_2 type layers. Sample B was a dielectric multi-layered system based on SiO_2 and Ta_2O_5 layers.

3. Results

Sample A exhibited a sharp brittle adhesive failure which was constrained inside area of residual scratch (see Fig. 2.). Corresponding load is labeled as Lc_3. Sample B exhibited two different failures (see Fig. 2.). Lc_1 is the faint cracking constrained inside residual scratch. Lc_3 is the large area spallation which is of the same size in all tests.

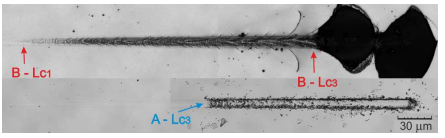

Fig. 2. Residual scratches on the two samples with highlighted failure modes.

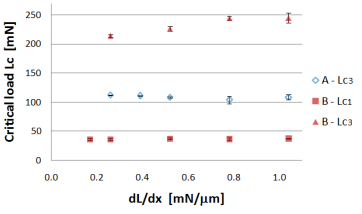

Fig. 3. Variation in three critical loads of two multilayered samples with the dL/dx ratio.

Variation in the critical loads of both multi-layered samples with different values of dL/dx ratio is depicted in Fig. 3.

4. Conclusions

The effect of intrinsic parameters on scratch test results was investigated. Variation of scratching speed, loading rate and consequently the value of ratio dL/dx has no effect on critical loads, corresponding to the small constrained coating failures of the samples, if the ratio dL/dx is smaller than 1 mN/μm.

Acknowledgements

This work has been supported by the Operational Program Research and Development for Innovations - European Regional Development Fund (CZ.1.05/2.1.00/03.0058) and co-financed from European Social Fund and State financial resources (CZ.1.07/2.3.00/20.0017), by Palacky University (internal grant no. PrF_2013_006) and by the Technology Agency of the Czech Republic (TA03010743).

References

[1] Perry, A.J., A review of the methods for the measurement of coating-substrate adhesion, Surf. Coat. Tech., **107**, 1983. pp. 167-180.

[2] Valli, J., TiN coating adhesion studies using the scratch test method, J. Vac. Sci. Tech. A, **3**, 1985, pp. 2411–2414.

[3] Steinmann, P., Hintermann, H.E., Adhesion of TiC and Ti(C, N) coatings on steel, J. Vac. Sci. Tech. A, **3**, 1985, pp. 2394–2400.

[4] von Stebut, J., Rezakhanlou, R., Anoun, K., Michel, H., Gantois, M., Major damage mechanisms during scratch and wear testing of hard coatings on hard substrates, Th. Sol. Films, **181**, 1989, pp. 555–564.

[5] Valli, J., A review of adhesion test methods for thin hard coatings, J. Vac. Sci. Tech. A, **4**, 1986, pp. 3007–3014.

[6] Steinmann, P., Tardy, Y., Hintermann, H.E., Adhesion testing by the scratch test method: The influence of intrinsic and extrinsic parameters on the critical load, Th. Sol. Films, **154**, 1987, pp. 333–349.

[7] Beake, B.D., Ogwu, A.A., Wagner, T., Influence of experimental factors and film thickness on the measured critical load in the nanoscratch test, Mat. Sci. Eng. A, **423**, 2006, 70-73.

30th DANUBIA-ADRIA
Symposium on Advances in Experimental Mechanics
September 25-28, 2013 - Primošten, Croatia

5B31 023

LOW CYCLE FATIGUE PROPERTIES OF PUDDLED STEEL AFTER 100 YEARS OPERATING TIME

Mieczysław Szata[1], Grzegorz Lesiuk[1], Józef Rabiega[2]

[1] Wroclaw University of Technology, Faculty of Mechanical Engineering, Institute of Materials Science and Applied Mechanics, Smoluchowskiego 25, PL-50370 Wrocław, POLAND. E-mail: Mieczyslaw.Szata@pwr.wroc.pl, Grzegorz.Lesiuk@pwr.wroc.pl

[2] Wroclaw University of Technology, Faculty of Civil Engineering, Institute of Civil Engineering, Wyspiańskiego 27, PL-50370 Wrocław, POLAND. E-mail: Jozef.Rabiega@pwr.wroc.pl

1. Introduction

In 19th century, two types of steel were commonly used as a construction material; the puddled steel and the cast one. As it is estimated in [1], that the age of 75% of operating steel railway bridges in Poland exceeds 50 years and more than 43% of them, are the constructions from the 19th century. In Europe, the tendency is similar. The age of 68% of railway bridges is estimated over 50 years and 28% of them are the objects operating more than 100 years. The material investigations and the results of mechanical low-cycle fatigue tests have been described and discussed. The object of our investigations was the I-100 steel profile from the railway station (1850-1900) renovated in (2011-12), called "Dworzec Główny".

2. Material and method

The investigated ancient beam were cut from the floors of the main hall of the "Dworzec Główny" station.

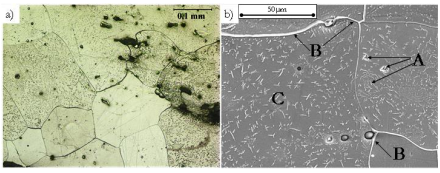

Fig. 1. Microstructure of puddled steel, a) ferrite grains with nonmetal inclusions, light microscopy, b) ferritic structure with brittle, degrading preparations inside (A, C) ferrite grains and thick envelope of Fe_3C on the border of ferrite grains, B – nonmetal inclusion on the border of ferrite grains SEM, etched 3% HNO_3, [2]

After mechanical preparation, the metallographic observations were performed. For a puddled steel, the typical ferrite microstructure with a number of nonmetal inclusions has been shown in Fig.1. A chemical composition was obtained using a gravimetric method (0.06%C, 0.1%Mn, 0.17%Si, 0.198%P, 0.025%). Metallographic observations with SEM have shown typical symptoms for a degraded ferrite microstructure of the old puddled steel from Wroclaw's bridges [3].

3. Low cycle fatigue behaviour of tested puddled steel

Basic mechanical properties were determined during a static tensile test: UTS=376 MPa, YTS=256 MPa, elongation A_5=21.7%, reduction in area Z=34.7%. Low cycle fatigue tests were performed for the described puddled steel according to American Standard ASTM E606 [4]. The measurement stand is shown in Fig. 2. For the investigation, round specimens (diameter 12 mm, gage length l=30mm) were used. A total strain was controlled during the experiment; $\Delta\varepsilon_t$=0.8%, 0.7%, 0.6%, 0.5% 0.4% in tension-compression test (R=-1). A loading frequency was kept on the level of f=0.2Hz. During the test, the temperature was monitored with a thermo-vision camera. The Coffin-Manson equation has been calculated. The total strain amplitude (blue), elastic strain amplitude (red) and plastic strain amplitude (green) have been presented in Fig. 3.

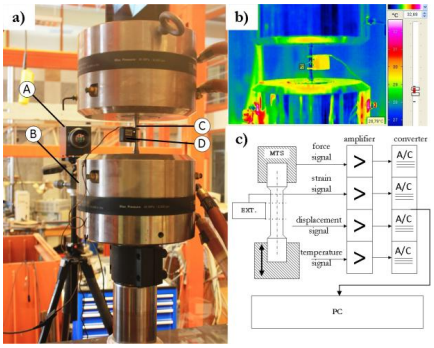

Fig. 2. Measurement stand of low cycle fatigue experiment a) specimen during test (A – thermovison camera, B – hydraulic pulsator MTS 809, C – specimen, D – extensometer), b) the temperature distribution in the sample during test, c) general scheme of measurement stand, [2]

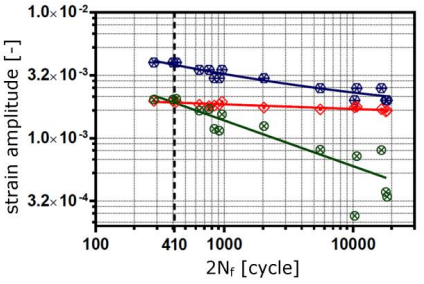

Fig. 3. Coffin-Manson diagram for a puddled steel from the Dworzec Główny construction in Wrocław, after 100 years operating time, [2]

The curves were described in the literature [4]:

$$\frac{\Delta\varepsilon_{pl}}{2} = \varepsilon_f^{'}(2N_f)^c, \qquad (1)$$

$$\frac{\Delta\varepsilon_e}{2} = \frac{\sigma_f^{'}}{E}(2N_f)^b, \qquad (2)$$

where $\Delta\varepsilon_{pl}$ and $\Delta\varepsilon_e$ mark plastic and elastic parts of total strain amplitude, respectively, the $\varepsilon_f^{'}$ and $\sigma_f^{'}$ are cyclic strain and stress parameters. $2N_f$ means a number of reversals to failure, b and c are the exponents of mentioned number of cycles. For a tested steel the cyclic stress-strain and low cycle fatigue parameters are collected in Tab. 1.

	σ_f' [MPa]	ε_f' [-]	b [-]	c [-]
Parameter	442	0.01699	-0.03651	-0.3632

Tab. 1. Cyclic properties of tested puddled steel

4. Conclusions

More than 100 years of operation of the tested puddled steel caused significant changes in the microstructure. These changes consist mainly in separations of brittle phases within the ferrite grains and on their boundaries. It is not indifferent to fatigue properties of investigated objects. The results of low cycle fatigue test show a significant decrease of plastic properties. The $2N_t$ transitional stability was established at 410 cycles. The obtained value ascribes this ancient steel to the group of brittle materials. This situation, combined with a significant number of non-metallic inclusions, can be particularly dangerous during a further exploitation of the object. In the context of safety, the assessment and evaluation of sustainability of components and the influence of intensification of microstructural degradation processes should be taken into account.

References

[1] Bień J., Uszkodzenia i diagnostyka obiektów mostowych, WKiŁ, Warszawa 2010

[2] Lesiuk G., Microstructural and mechanical degradation of 19th puddled steel, PhD Thesis, Institute of Materials Science and Applied Mechanics, Wroclaw University of Technology, 2013 (in Polish).

[3] Lesiuk G., Szata M., "Aspects of structural degradation in old bridge steels by means of fatigue crack propagation", Physicochemical Mechanics of Materials, issue 1/ 2011.

[4] ASTM E606 Standard test method for Strain-Controlled Fatigue Testing.

30th DANUBIA-ADRIA
Symposium on Advances in Experimental Mechanics
September 25-28, 2013 - Primošten, Croatia

5B32 120

FATIGUE PROPERTIES AND THERMAL ANALYSIS OF SHORT GLASS FIBRE REINFORCED POLYAMIDE 6.6

Matteo Mori[1], Andrea Bernasconi[2], David Taylor[3] , Francesca Cosmi[1]

[1] Università degli Studi di Trieste, Dipartimento di Ingegneria ed Architettura, Via Valerio 6/4, 34127, Trieste, Italy

[2] Politecnico di Milano, Dipartimento di Meccanica, Via La Masa 34, 20156, Milan, Italy

[3] Trinity College Dublin, Department of Mechanical and Manufacturing Engineering, College Green, Dublin 2, Ireland

1. Introduction

In recent years, micro-CT has proved to be a very effective and reliable method for assessing the fibre structure in SFRP [1-8]. More recently, efforts have been made in order to apply the technique for studying the damage accumulation processes in these materials [9]. Among other issues, the micro-CT set-up requires samples of narrow gauge section allowing to concentrate damage [9]. The aim of the experimental characterization presented below is threefold:

- a comparison of the mechanical properties of two standard geometries of PA6.6GF10, the smaller ASTM D1822 (9.6 mm^2 section, constant curvature) and the ISO 527-1A (40 mm^2 constant section), used in the previous works;
- a collection of data during interrupted fatigue tests on the ASTM samples, for later use in the damage accumulation investigation;
- a fatigue thermal analysis, possible only on ISO samples due to their larger dimensions.

2. Specimens

The sample geometries are depicted in Fig.1. A total of 25 ISO samples and 30 ASTM samples were used. All specimens were obtained by injection moulding and conditioned at 23°C and 50% relative humidity.

3. Experimental

A servo-hydraulic Instron 8801-A2 machine with a 100kN load cell was employed for tensile and fatigue tests. The ISO samples' strains were recorded by means of an extensometer with 50mm base length, while for the ASTM specimens the movements of the mobile traverse were directly recorded. Four tensile tests and 12 fatigue tests at different stress levels (R=0.1, 2Hz frequency) were performed for each type of geometry. Further fatigue tests on ASTM samples were performed at σ_{max}=52MPa and interrupted at different stages (20%, 40%, 60%, 70%, 80%, 90% respectively) of the corresponding fatigue life (10^5 cycles).

Surface temperatures were acquired along the longitudinal centerline of four ISO samples under fatigue loading in the range between 10000 and 200000 cycles using an infrared thermaCAM P25. Temperatures were recorded every 3 minutes for the first 45 minutes and successively every 30 minutes.

4. Results

The stress-strain and the Wöhler's curves for each geometry, the accumulated damage and hysteresis loops of ASTM samples and the surface temperature recorded at different stress levels for the ISO samples are shown in Fig. 2-6.

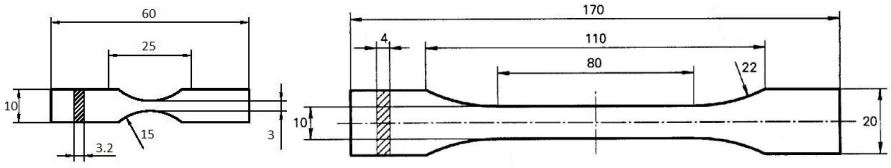

(a) (b)

Fig. 1. (a) ASTM D1822 and (b) ISO 527-1A geometries

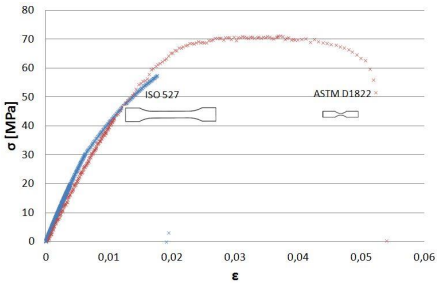

Fig. 2. Stress-strain curves for ISO and ASTM samples

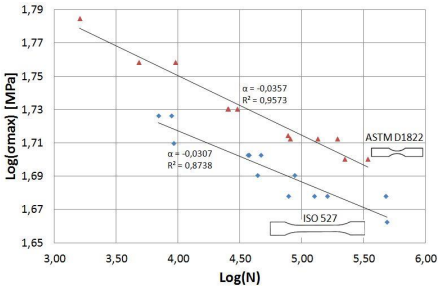

Fig. 3. Wöhler's curve for ISO and ASTM samples

5. Remarks

- The ASTM and ISO samples exhibit very different static and dynamic properties. This result was expected, since different geometries lead to different distributions of the reinforcing fibres which in turn influence the final mechanical behavior [2-8].
- The trend of the maximum and minimum strains and the shifts in hysteresis loops along the strain axis in the interrupted fatigue tests of the ASTM samples are similar. With each 20% increase in life cycles, the area enclosed by the hysteresis loops grows by about 10%.
- The thermal behavior of the ISO samples is characterized by a rapid rise in the surface temperature at the beginning and at the end of the tests. A lower increase (7°C for high stress tests and 3°C for low stress tests) was found in the remaining fatigue life, confirming the trend found in [10] for a PA6GF30.
- The ASTM samples subjected to the interrupted fatigue tests will be further analyzed by means of micro-CT for investigating damage nucleation and progression phenomena, a necessary step for the development of predictive models for fatigue behavior of in SFRP materials.

6. Acknowledgements

Specimens were kindly provided by Radici Plastics.

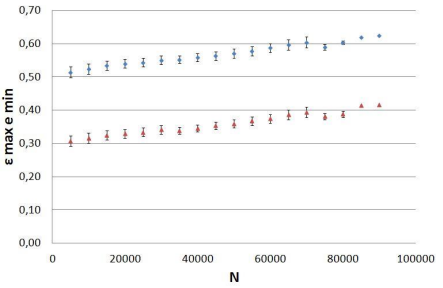

Fig. 4. Accumulated damage for ASTM samples

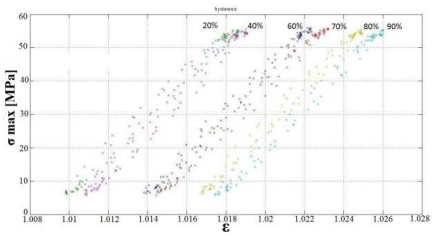

Fig. 5. Hysteresis loops for ASTM samples

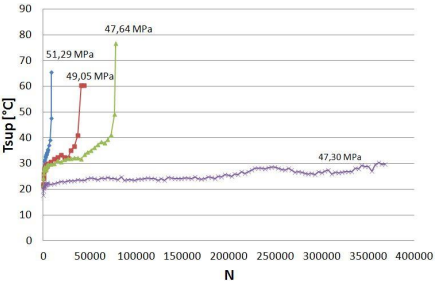

Fig. 6. Surface temperature for ISO samples

7. References

[1] Bernasconi A., Cosmi F., Dreossi D. (2008) Comp. Scie. Tech.,68, 2574-2781
[2] Cosmi F., Bernasconi A. (2010) Materials Engineering, 17, 2, 6-10
[3] Bernasconi A., Cosmi F., Zappa E., (2010) Strain, 46, 435–445
[4] Cosmi F. (2011) Strain, 47, 215–221
[5] Cosmi F. (2011) Procedia eng., 10, 2135-2140
[6] Bernasconi A., Cosmi F. (2011) Procedia eng., 10, 2129-2134
[7] Cosmi F., Bernasconi A., Sodini N. (2011) Comp. Scie. Tech.,71, 23-30,
[8] Bernasconi A., Cosmi F., Hine P.J. (2012) Comp. Scie. Tech., 72, 2002-2008
[9] Cosmi F., Bernasconi A. (2013) Comp. Science and Technology,79, 70-76
[10] Bernasconi A., Kulin M. R. (2009) Polymer Composites, 30, 154 - 161

30th DANUBIA-ADRIA
Symposium on Advances in Experimental Mechanics
September 25-28, 2013 - Primošten, Croatia

5B33 022

FRACTURE TOUGHNESS INVESTIGATIONS OF METAL MATRIX COMPOSITES REINFORCED BY CERAMIC FIBRES

Tadeusz Szymczak[1], Zbigniew L. Kowalewski[1, 2]

[1] Motor Transport Institute, Centre for Material Testing and Mechatronics, ul. Jagiellońska 80, 03-301 Warsaw, POLAND. E-mail: tadeusz.szymczak@its.waw.pl

[2] Institute of Fundamental Technological Research of PAS, Department for Strength of Materials, ul. Pawińskiego 5B, 02-106 Warsaw, POLAND. E-mail: zkowalew@ippt.pan.pl

1. Introduction

Characterisation of modern materials for engineering applications requires data from standard tensile or compressive tests in order to determine basic mechanical parameters. Besides of such parameters as: Young's modulus, proportional limit, yield point, ultimate tensile strength a knowledge concerning the stress intensity factor (SIF or K_I) is necessary. It is known that SIF describes material resistance to brittle cracking. The stress intensity factor is investigated using specimens having a notch containing a fatigue crack at its tip and by applying the following stages of the experimental procedure: (a) pre-cracking of fatigue zone, (b) testing under monotonic tension [1]. Several types of specimens are used, e.g. compact tension (CT); disk-shaped; single edge [2]. In many experimental cases, dimensions of specimens are limited by a material volume. Therefore, different sizes of specimens can be applied, i.e. standard [2] or miniature [3].

The objective of this paper is to determine the critical value of stress intensity factor of a metal matrix composite (MMC) reinforced by the Saffil ceramic fibres.

2. Details of experimental procedure

The 44200 aluminium alloy reinforced by a different percentage content of Al_2O_3 Saffil ceramic fibres, 10%, 15% and 20%, was selected for investigation. As reported in [4] the ultimate tensile strength and the Young's modulus of this type of reinforcement are equal to 1800 MPa and 300 GPa, respectively. All tests were performed using compact tension specimens (CT). With respect to a limited volume of the composite, the applied specimen was four times smaller than the typical one.

2.1 Specimen and validation process

The compact tension specimen, shown in Fig. 1, was designed on the basis of guidelines contained in the ASTM [2] and PN-EN standards [5].

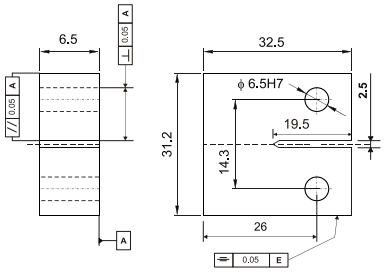

Fig. 1. Compact tension specimen (CT).

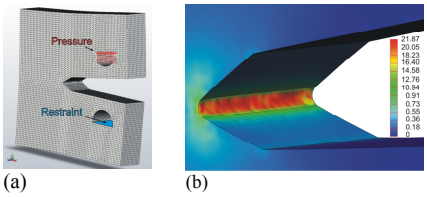

(a) (b)

Fig. 2. Boundary conditions (a); the Huber-Mises-Hencky's effective stress at the tip of notch (b).

The specimen geometry was validated using finite element analysis (FEA). The loading and boundary conditions (Fig. 2a) were similar to those applied in the servo-hydraulic testing machine. The

specimen was modelled using 3D solid body divided into 374088 3D elements and 528467 nodes, Fig. 2a. Selected results, e.g. Huber-Mises-Hencky's effective stress at the tip of notch, are illustrated in Fig. 2b. They show a typical concentration of the effective stress in a field close to the tip of notch.

2.2 Investigation of fracture toughness

All fracture toughness tests were conducted using the 8802 Instron servo-hydraulic testing machine at room temperature. The specimens were mounted in the loading system by applying special grips. Crack tip opening displacement was measured by means of the clip on knife edge extensometer of 10 mm gauge length.

The crack propagated in perpendicular direction with respect to the opposite side of the specimen, independently on the content of Al_2O_3 Saffil fibres. Each specimen was observed at different magnification, i.e. macro- and micro-scales to distinguish features of the fracture surface. The results of macro-scale observations obtained at small magnification indicated several geometrical sections in the decohesion surface, i.e. plane of fatigue pre-cracking, and tension zone having two sloping fracture areas and tearing section.

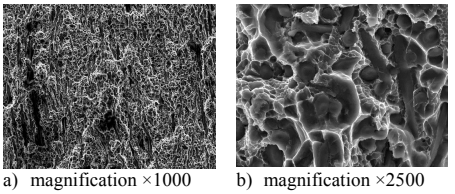

a) magnification ×1000 b) magnification ×2500

Fig. 3. Microscope images of fatigue fracture surface of the 44200+20% Saffil fibres composite.

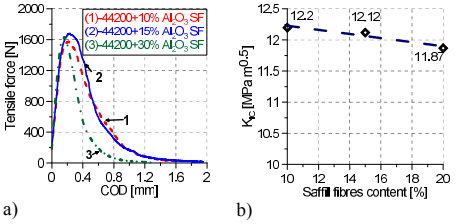

a) b)

Fig. 4. Tensile force versus COD (a), variations of K_{IC} as a function of Saffil fibres content (b).

The microscopic analysis of the fatigue fracture surface was performed at magnification equal to 18, 100, 1000 (Fig. 3a), 2500 (Fig. 3b). The results did not exhibit any typical features observed on the specimen surface after fatigue testing. Instead of them, a local delamination of the structure was observed in the case of composite with 20% Al_2O_3 Saffil fibre content, Fig. 3b. It occurred in the form of voids between the base material and fibres.

Variations of the tensile force versus crack tip opening displacement, exhibited the I-st mode fracture, Fig. 4a. The critical values of the stress intensity factor of the 44200 aluminium alloy reinforced by 10%, 15% and 20% of the Saffil fibres reached the following levels: 12.20, 12.12 and 11.87 [MPa×m$^{1/2}$], respectively, Fig. 4b. Values of the K_{IC} decreased slightly with an increase of the Saffil fibre content.

3. Remarks

- A miniaturized compact specimen can be successfully applied to determine the K_{IC}.
- A pre-cracked zone in the composite did not has typical features usually observed on the specimen surface after fatigue.
- An influence of the Al_2O_3 Saffil fibres of the content within the range from 10% to 20% on the critical stress intensity factor was negligible small.

Acknowledgements

This paper was supported by the KomCerMet project (No. POIG. 01.03.01-14-013/08-00 founded by the Polish Ministry of Science and Higher Education) on the years 2007÷2013.

References

[1] Dobrzański L., Nowosielski R., Testing of metals and alloys, vol. I, „Investigations of mechanical and physical properties", Silesia University of Technology, Gliwice 1986.

[2] Standard Test Method for Plane-Strain Fracture Toughness of Metallic Materials, Annual Book of ASTM Standards, Metals Test Methods and Analytical Procedures, Metals-Mechanical Testing: Elevated and Low-Temperature Tests; Metallography, **03.01**, 1993, pp. 509-539.

[3] Golerthan S., Herberg D., Baruj A., Eggeler G., Compact tension testing of martensitic/ pseudoplastic NiTi shape memory alloys, Mater. Sci. Eng., **481-482**, 2008, pp. 156-159.

[4] Naplocha K., Kaczmar J.W., Tribological properties of Al 7075 alloy based composites strengthened with Al_2O_3 fibres, Archives of Foundry Engineering, **11**, Special Issue 2, 30/2, 2011, pp. 153-158.

[5] PN-EN ISO 12737:2011, Metals-Fracture toughness at biaxial strain state, 2011.

30th DANUBIA-ADRIA
Symposium on Advances in Experimental Mechanics
September 25-28, 2013 - Primošten, Croatia

5B34 117

TMF ON TUBE SPECIMEN AND MATERIAL PARAMETER APPROXIMATION

Michael Spary[1], Aleksandar Stanojevic[1], Gerhard Winter[1], Florian Grün[1]

[1] Montanuniversität Leoben, Chair of Mechanical Engineering, Franz-Josef Str. 18, 8700 Leoben, AUSTRIA. E-mail: michael.spary@stud.unileoben.ac.at

1. Introduction

The reaction of the hollow cylindrical specimen under Thermo- Mechanical- Fatigue (TMF) comparing to the standard solid cylindrical specimens, declared by the Code of Practice (COP) [3] will be investigated. This try will be a step to test specimens which are close to components. The TMF-test rig is prepared to specimens which are greater than the standard test specimen. After the required modifications the tube results are compared to the results from the standard specimen by equal test conditions. The test schedule comprised the influence of the maximum temperature and of the strain constraint factor to the lifetime behavior for both types of specimens. Furthermore a routine was developed, that allows the calculation of parameters for material models. FE-simulation software use this models for modeling plastic material behavior. The routine delivers a rather accurate and quick approximation of parameters simplifying all following evaluation processes.

2. Approach and Results

The standard specimen and the tube are mado of the same material, austenitic steel X6CrNiMoTi17-12-2. Fig. 1 shows the mounted tube test specimen installed in the TMF-machine with applied thermocouples and extensometer.

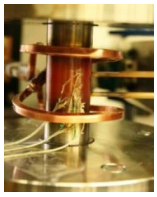

Fig. 1. Fitted tube test specimen at the TMF-machine

The tube requires special terms to measure the temperature. The only potential to measure the temperature without an affect coming from the heating coil, is to weld on the thermocouples.

2.1 Tube test specimen geometry

Two different types are investigated. The difference between both types describes the factor from outer diameter *D* to the wall thickness *t*. According to the COP the D/t-factor should be small. As seen by the first test's the tube with the highest *D/t*- factor is not practicable for the TMF-testing method. The tube used for investigations offers an outer diameter from 23 [mm] and a wall thickness of 1 [mm], *D/t*=23. The standard specimen is solid and has a diameter of 7 [mm]. Fig. 2 shows the geometry of the tube specimen.

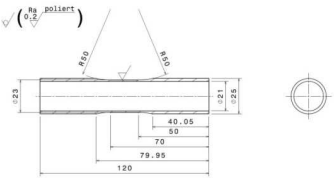

Fig. 2. Tube specimen geometry, factor *D/t*=23

2.2 Testing results

The characteristic hysteresis are shown in Fig.3, left the tube and right the standard specimen.

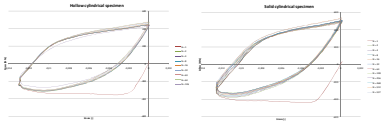

Fig. 3. Stress-strain hysteresis at same conditions, left tube, right standard specimen

Comparing the lifetime behavior from both specimen types addicts a longer lifetime for standard specimens. Fig. 4 shows the influence from the maximum temperature to the tube test specimen and the standard test specimen. The comparative lifetimes from different maximal temperatures are similar. Testing mode is out of phase (OP, compressive stress by maximum temperature), strain constraint ratio is one.

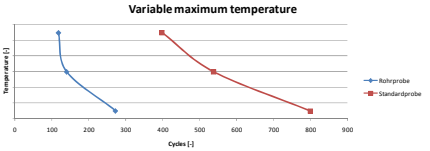

Fig. 4. Lifetime influenced by the maximum temperature

2.3 *Parameter approximation*

Based on the data of the TMF test results a material model can be created. By using this model the material behavior can be foreseen for various testing conditions (temperature, mechanical load, etc.). As the process of obtaining a material model is relatively complicated and time-consuming, a first approximation of the required parameters for the material model is aspired. The developed routine uses the stress-strain loop at the half number of cycles and considers only the plastic part of the hysteresis. The plastic part is defined by the yield stress σ_0.

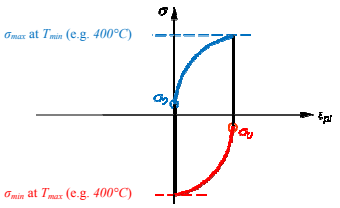

Fig. 5. Plastic stress-strain loop with yield stress σ_0 for tension and compression.

Fig. shows a typical OP-TMF test. The section above σ_0 on the tension side and beneath σ_0 on the compression side will be considered for the calculation. The used equation for the parameter fit (1) describes the kinematic part of the combined hardening model for the first cycle. This model delivers a satisfying approximation described by the following three equations:

$$\alpha_k = \frac{C_k}{\gamma_k}\left(1 - e^{-\gamma_k \varepsilon_{pl}}\right), \qquad (1)$$

$$\alpha = \sum_k \alpha_k , \qquad (2)$$

$$\sigma = \sigma_0 + \alpha . \qquad (3)$$

For the better quality of the approximation three temperature-dependent parameters have been used, *k=3* in equation (2) and used in (3) to calculate the stress. The fit is carried out using the last mean square method on the tension and compression curve separately (tension and compression curve of the loop). The results of the approximation are the temperature-dependent yield strength σ_0 and all plastic parameters $C(T)$ and $\gamma(T)$, see Fig. 6.

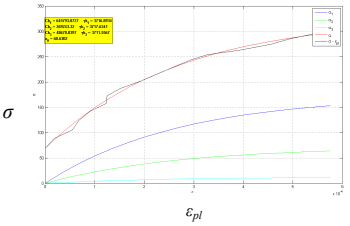

Fig. 6. Fit of the plastic section of the hysteresis with σ1, σ2 and σ3

3. Outlook

Tubes with other D/t- factor and machined inner sides will be investigated in further tests. The developed routine for describing the material behavior will be implemented for a first approximation at the beginning of every material model creation process.

References

[1] Spary M., Tube test specimen deployed for Thermo-mechanical Fatigue, Diploma Thesis, Montanuniversität Leoben, Leoben, (2013).

[2] Stanojevic A., Automatic Determination of Parameters for Thermo-Mechanical Loaded Specimen, Diploma Thesis, Montanuniversität Leoben, Leoben, (2012), 115.

[3] Validated Code-of-Practice for Strain-Controlled Thermo-Mechanical Fatigue Testing Peter Hähner, Ernst Affeldt, Tilmann Beck, Hellmuth Klingelhöffer, Malcolm Loveday, Claudia Rinaldi Report 2005

30th DANUBIA-ADRIA
Symposium on Advances in Experimental Mechanics
September 25-28, 2013 - Primošten, Croatia

5B35 118

FATIGUE BEHAVIOR OF THREADED CAST A356/STEEL CONNECTIONS

G. Nicoletto, E. Riva

^ Dept. of Industrial Engineering – University of Parma – Parma – Italy
gianni.nicoletto@unipr.it

Threaded connections subjected to fatigue loading are found in many applications, [1]. The notched geometry associated to the threads and the local contact stresses require careful evaluation of factors such as part stiffness, preload, thread forming method, etc.. The most critical location in fatigue is the first engaged thread of the screw with up to 70 % of failures, [1]. The fatigue notch factor and the nominal stress approach are used to assess steel bolts and bolted joints in fatigue. However, such approach is always not applicable.

In internal combustion engines, a critical threaded connection, i.e. the bulkhead/bearing cap connection, is a fatigue concern as cracking may be experienced on dynamometer tests. Fig. 1, taken from [2], shows the stress distribution in a slice of a 3D FE model of the cylinder block with the main bearing cap, main bearings, all studs and a simplified representation of the cylinder head. In this application the critical point in fatigue is not in the steel stud rather in the threaded hole of the bulkhead and bearing cap, which are both made of cast Al-Si alloy.

To address the fatigue design of this threaded connection the following activities were performed and are reported: i) a simplified experimental test system was devised to provide reference fatigue data for a threaded hole in cast aluminum; ii) the test system was analyzed using the FE method to determine local stresses and strains in the threaded connection; iii) fatigue prediction based on the strain-life approach were checked against experimental tests.

1) Development of an experimental testing system

The bulkhead/bearing cap connection geometry and its actual loading condition are too complex for controlled fatigue experiments. A simplified but representative system, shown in Fig. 2a, was developed and tested in fatigue using a servo-hydraulic testing machine. It is made of a steel stud inserted in the threaded hole of a cast A356 cylinder. The M12 x 1.75 stud is initially tightened then inserted into the hydraulic grips of an MTS 810 test system and subjected to a cyclic force with a positive R-ratio to simulate axial preloading in actual applications. A sequence of fatigue tests was performed according to a reduced staircase method to estimate the fatigue strength of the threaded connection. Fatigue test that continued up to 2 10^6 cycles without failure were interrupted i.e. run-out. Fatigue strengths at 2 10^6 cycles for a given: i) type of stud mounting, ii) material combination and iii) preload were determined and used for assessing predictive fatigue methods. Fatigue cracks initiated at the root of the first engaged thread in cast A356.

2) Finite element stress analysis of test system

Compared to the realistic configuration of Fig. 1, the experimental system of Fig. 2a can be readily modeled using axis symmetric finite elements. The thread geometry can be represented in detail and a very fine mesh density specified to determine the local thread root stresses and strains. The contact pressure that develop among threads along the length of the engagement area is also computed. using the ABAQUS code capabilities, [3].The thread geometry, with special attention to the corner radius, was defined according to norm. Eight-node quadratic elements were applied for mesh development. A linear elastic behavior was assumed for the stud made of X8CrNiS18-9. A significant amount of plasticity was instead expected at the root areas of the threaded hole. Therefore the behavior of cast A356 was modeled as elastic-plastic with isotropic hardening. The monotonic properties were R_m= 240MPa, R_s=198 MPa, E= 76 GPa and cyclic curve data H=351MPa and n=0.088.

A typical axial stress distribution in the threaded connection under tensile load is shown in Fig. 2b. The local cyclic stress vs. strain cycles for three different loading cases, see Table 1, at most stressed thread root (i.e. the first in Fig. 2b) are presented in Fig. 3. Elastic shakedown is observed in the first two load cases. A hysteresis loop is associated to the third load case. FE elastic-plastic notch stresses and

strains were used to predict the fatigue life of the A356 threaded hole.

3) Fatigue prediction method

Different fatigue design approaches have been proposed for assessing threaded connections. Here the strain-life approach to fatigue crack initiation life and the Smith-Watson-Topper (SWT) empirical formula, [4], was used because the fatigue tests were characterized by a mean stress superposed to the local cyclic strain. The equation relating the local SWT parameter and the number of cycles to crack initiation is the following:

$$\sigma_{max}\varepsilon_a = \frac{(\sigma_f')^2}{E}(2N)^{2b} + \varepsilon_f'\sigma_f'(2N)^{b+c}$$

where $\sigma_{max} = \sigma_a+\sigma_m$ and ε_a are obtained from the computed local hysteresis loop, $2N = N_i$ is the number of cycles to initiation. The four material constants for the cast A356 are: $\sigma'_f = 666$MPa, $\varepsilon'_f = 0.09$; $b = -0.117$ and $c = -0.610$, [4].

The application of the method to the fatigue results is summarized in the Table 1, where the predicted crack initiation life vs. the observed total life is presented. The method captures the load dependence of the fatigue life although it apparently underestimates the total lives.

The microscopic observation of the thread shape after testing, see Fig. 4, demonstrates that i) the thread forming method (rolling) produces local micro structural distortion and ii) the load transfer from the rigid steel stud to the soft A356 thread produced plastic root straining with a reduction in sharpness and possibly crack initiation retardation in the experiments.

Table 1 – Fatigue lives of threaded connections

F_{min} (kN)	F_{max} (kN)	Predicted N_i	Observed Ave. N_f
3.0	11.7	$5.0\ 10^5$	$> 2\ 10^6$
3.0	13.7	$1.2\ 10^5$	$1.2\ 10^6$
3.0	16.5	$1.0\ 10^5$	$6.0\ 10^5$

References

[1] Bickford J. (1995) An Introduction to the Design and Behavior of Bolted Joints, Dekker,
[2] DeJack M. et al. (2002) ABAQUS Users' Conference.
[3] Anon., (2010) ABAQUS User's Manual
[4] Fatemi A., et al. (2005) Int. J. Fatigue, 27, 1040-1050

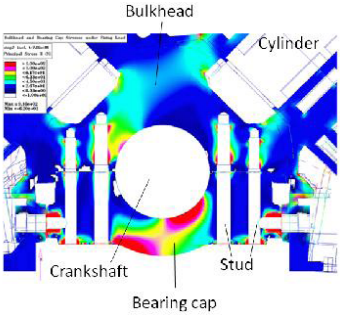

Fig. 1 Stress distribution in the bulkhead-bearing cap connection using studs, [2]

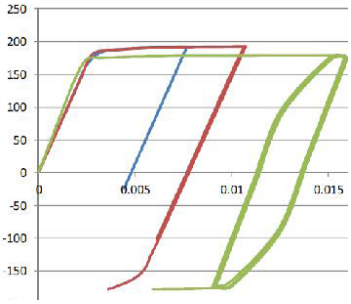

Fig. 3 Local stress-strain response at the thread root for three different loading conditions

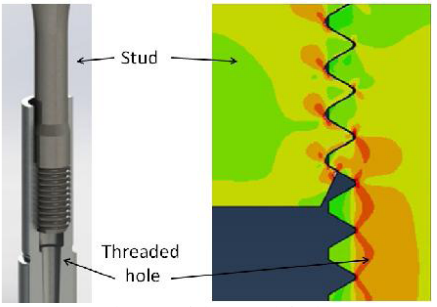

Fig. 2 a) Rendering of the simplified experimental system, b) elastic-plastic FE stresses in the engaged threads

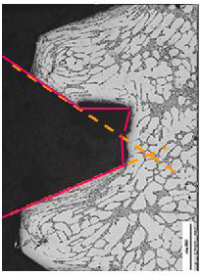

Fig. 4 Deformed thread root in cast A356 following engagement and load transfer (in yellow initial shape)

30th DANUBIA-ADRIA
Symposium on Advances in Experimental Mechanics
September 25-28, 2013 - Primošten, Croatia

5B36 122

MIXED MODE FRACTURE TOUGHNESS EVALUATION OF POLYURETHANE FOAMS

Dragoş A. Apostol[1], Dan M. Constantinescu[1], Liviu Marşavina[2], Emanoil Linul[2]

[1] University POLITEHNICA of Bucharest, Department of Strength of Materials, Splaiul Independentei nr. 313, 060042 Bucharest, ROMANIA. E-mails: apostolda@yahoo.com, dan.constantinescu@upb.ro

[2] POLITEHNICA University of Timişoara, Department of Mechanics and Strength of Materials, Bd. Mihai Viteazul nr. 1, 300222 Timişoara, ROMANIA. E-mails: msvina@mec.upt.ro, linul_emanoil@mec.upt.ro

1. Introduction

For experiments in mixed mode there are standard specimens, and one of the most common is the four-point bend specimen. This can create the pure mode I or II and the mixed modes I and II. The four-point bend specimen is loaded in two forms: symmetric and asymmetric. The symmetric bend specimen creates the pure mode I and the mixed mode, but the asymmetric specimen creates mode II in addition to the mixed modes I and II. In [1] a new fundamental reference solution is given for an infinitely long cracked specimen loaded by a constant shear force and the corresponding bending moment. Small corrections need to be applied for a finite four-point loading geometry. The geometry and loading conditions for another improved test configuration called the asymmetric semi-circular bend (ASCB) specimen is presented in [2]. In this case a semi-circular specimen that contains an edge crack emanating normal to the flat edge of the specimen is loaded asymmetrically by a three-point bend fixture. In order to use accurately the analytical solutions for these two testing configurations the loading points have to be sufficiently far from the crack.

2. Testing geometry

An asymmetric four-point bend specimen (A4PB) is used in these tests having the geometry presented in Fig. 1. All tested specimens had B = 12.5 mm, W = 25 mm, and $b_1 + b_2$ = 100 mm. Here are presented only results for b_1 = 40 mm, b_2 = 60 mm, and a/W = 0.5. Distance c was considered as being c = 0 mm, c = 5 mm, and c = 10 mm. For c = 0, Mode I should vanish according to the relations written bellow, from which one can calculate the stress intensity factors for a reference problem with an infinite specimen subjected to a force Q and a varying bending moment M, [1]

$$K_I^R = \frac{6cQ}{W^2}\sqrt{\pi a}F_I(a/W) \qquad (1)$$

$$K_{II}^R = \frac{Q}{W^{1/2}}\frac{(a/W)^{3/2}}{(1-a/W)^{1/2}}F_{II}(a/W)\,. \qquad (2)$$

The shear for Q which acts between the inner loading points is given by $Q = P\,(b_2 - b_1)/(b_2 + b_1)$ and $M = cQ$ are force and moment defined per unit thickness. The expressions to calculate $F_I(a/W)$ and $F_{II}(a/W)$ can be found in [1].

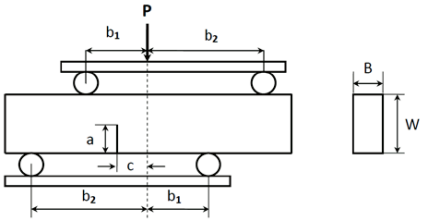

Fig. 1. Geometry of the specimen and loading configuration.

The reference solution of equations (1) and (2) is accurate (finite element results show this in [1]) as long as the distance of the nearest loading point is greater than $1.4W$. That is $(b_1 - c) > 1.4W$. For our b_1 value it results $c < 5$ mm, as to fulfill this condition. For loading points nearer to the crack, He and Hutchinson [1] established that a correction of the above relations is needed as these are valid only for a reference specimen. Such calculations were done for some geometries and further

discussions were presented in [3], as these authors introduced two more correction factors (one for each mode), besides the ones established in [1].

3. Results

In Mode I, 3PB tests were performed on closed-cell Necuron polyurethane foams of densities 100, 160 and 301 kg/m^3. Speed of testing was considered as 1, 10, and 100 mm/min. The obtained Mode I average critical toughness is given in Table I. Average values are obtained for each speed from 4 to 7 tests.

Foam density [kg/m^3]	Speed of testing [mm/min]	K_{Ic} [MPa$\sqrt{m}$]
100	1	0.0722
	10	0.0741
	100	0.0735
160	1	0.0797
	10	0.0881
	100	0.0861
301	1	0.341
	10	0.343
	100	not tested

Tab. 1. Mode I fracture toughness for three densities of polyurethane foam.

Loading was applied through loading cylinders having a diameter of 10 mm. In Fig. 2 is presented the failed specimen for $c = 0$. Due to the loading conditions the foam was crushed severely closer to the crack location and a secondary propagating crack developed.

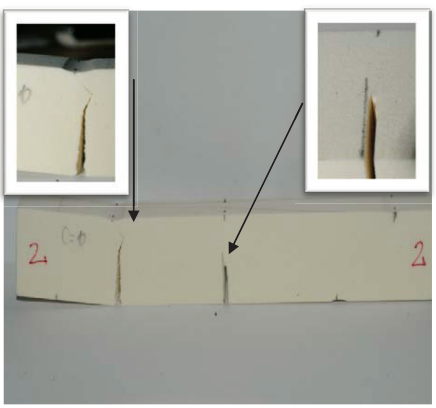

Fig. 2. Failure of A4PB specimen with $c = 0$.

This crack was the one which finally led to the failure of the specimen.

Almost the same behaviour of the tested specimen resulted when $c = 5$ mm, as presented in Fig. 3. This time the main crack propagated as being oriented towards the nearest loading point, and bifurcated close to the outer surface. One branch turned suddenly to the surface, while the other continued its path to the loading cylinder.

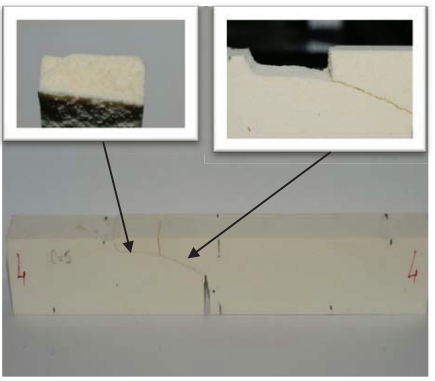

Fig. 3. Failure of A4PB specimen with $c = 5$ mm.

Although formally the condition $c < 5$ mm discussed previously was preserved, the local crushing of the polyurethane foam gave the undesired failure of the specimens. It is believed that the increase of the diameter of the loading cylinders and of the ratio a/W will lead to successful tests.

Acknowledgements

This work was supported by a grant of the Romanian National Authority for Scientific Research, CNCS – UEFISCDI, project PN-II-ID-PCE-2011-3-0456, contract number 172/2011.

References

[1] M.Y. He, J.W. Hutchinson, Asymmetric four-point crack specimen, J. Appl. Mech., **67**, 2000, pp. 207–209.

[2] M.R. Ayatollahi, M.R.M. Aliha, H. Saghafi, An improved semi-circular bend specimen for investigating mixed mode brittle fracture, Eng. Fracture Mech., **78**, 2011, pp. 110–123.

[3] A.R. Shahani, S.A. Tabatabaei, Computation of mixed mode stress intensity factors in a four-point bend specimen, Appl. Math. Modell., **32**, 2008, pp. 1281–1288.

30th DANUBIA-ADRIA
Symposium on Advances in Experimental Mechanics
September 25-28, 2013 - Primošten, Croatia

5B37 126

EXPERIMENTAL DETERMINATION OF CUTTING FORCES IN HARD TURNING OPERATIONS

Martin Obermair[1], Andreas Steininger[1], Friedrich Bleicher[1]

[1] Vienna University of Technology, Institute for Production Engineering and Laser Technology, Karlsplatz 13/311, 1120 Vienna, AUSTRIA. E-mails: obermair@ift.at, steininger@ift.at, bleicher@ift.at

1. Introduction

Over the last decade turning of hardened materials has become more and more interesting for the manufacturing industry due to rising requirements like high production flexibility and increasing cost pressure. Additionally the rapid development of new, highly wear-resistant cutting materials enables high performance cutting processes [1]. Compared to the sophisticated grinding processes of hardened materials chipping offers some essential advantages such as cheaper investments in machines, higher material removal rates and thus a significant reduction of processing times [2].

Besides these benefits, there are some aspects in hard turning processes that need to be considered. First of all, it is essential, that the stiffness of the machine tool is adequate due to the higher process forces compared to conventional turning. Furthermore, very high stresses and temperature gradients occur alongside the cutting edge, which cause highly abrasive wear and thus reduced tool lives and surface qualities of work pieces [3]. To achieve minimum wear of the cutting edge it is indispensable to choose appropriate process parameters such as feed rate, depth of cut and cutting speed, which are heavily depending on the cutting geometry, cutting material and work piece material.

However, beside an adequate machine tool and an ideal choice of process parameters, the run-out of the work piece seems to have a remarkable impact on the tool life. Hence, this paper is based on research work of the occurring process forces during hard turning and their influence on the tool's life.

Furthermore, this study focuses on roughing in order to match with the above mentioned requirement of high material removal rates. The used work piece material is hardened tool steel (1.2842, 60HRC). The material of the cutting inserts is Al_2O_3+TiCN ceramic. The cutting inserts are featured with a 25° negative chamfer to withstand the high process forces and ultimately to stabilize the cutting edge.

2. Experimental setup

2.1 Measuring setup

The core of the measuring setup is a piezoelectric dynamometer, consisting of four 3-component force sensors, e.g. Fig. 1. The physical principal of the piezoelectric effect contributes highly dynamic measurements. Hence the measuring series have been recorded with a sampling rate of 5 kHz.

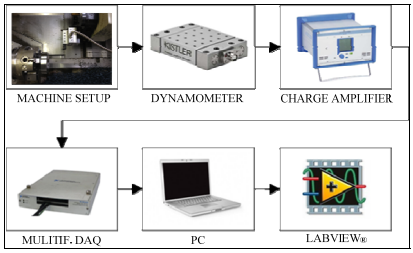

Fig. 1. Measurement chain

2.2 Machine setup

Due to the specific process requirements concerning the high cutting forces, a turning lathe with feasible machine rigidity has to be used for the machining investigations. Therefore, the measuring setup was adjusted to a HEID FS 300 CNC lathe with an incline bed, e.g. Fig. 2.

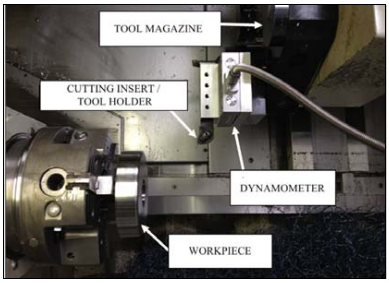

Fig. 2. Machine setup

3. Experimental results

3.1 Longitudinal hard turning operation

Several parameter sets have been tested to find an optimized process condition appropriate to the respective cutting edge geometry. Throughout the cutting processes the forces have been mapped in charts, e.g. Fig. 3. During the cut the cutting force and the feed force are the dominating components. No abnormalities seem to occur using the particular scaling of the x-axis shown in Fig. 3. However, when focusing on the start and end of the cut, as seen in Fig. 4 and Fig. 5, vibrations of all three force components have been measured.

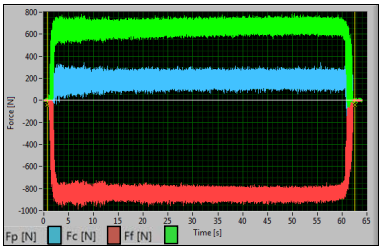

Fig. 3. Force chart, v_c=150m/min, f=0,11mm/U, a_p=2mm.

As seen in Fig. 4 the run-out of the work piece causes force peaks that occur with the rotational frequency of the spindle (ca. 5Hz). The reason for the peaks is the increasing area of the cut.

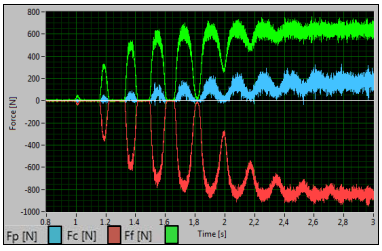

Fig. 4. Entering of cutting edge into material, v_c=150m/min, f=0,11mm/U, a_p=2mm.

Fig. 5 shows vibrations of the force components during the exit of the cutting edge. This effect was observed during all of the measurements with varying process parameters. Eventually these vibrations lead to a significant decrease of tool life.

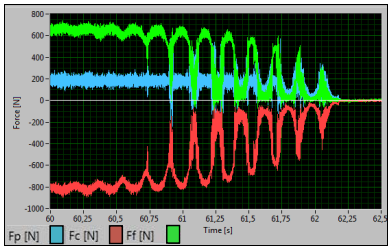

Fig. 5. Exiting of cutting edge from material, v_c=150m/min, f=0,11mm/U, a_p=2mm.

4. Conclusion

An essential negative impact on the tool wear was observed during longitudinal hard turning, especially when the cutting edge axially exits the material. Measurements show that this effect can be diminished by reducing the feed rate at the end of the cut. Moreover, when roughing miscellaneous contours, a carefully selected machining strategy can be the key to an enlarged tool life cycle, by avoiding numerous axial material exits of the cutting edge.

5. Acknowledgment

The authors are grateful to CORNET for approving the collective research project TEC - Total Efficiency Control and thus for the opportunity to work on this topic.

References

[1] Denkena, B., Tönshoff, H.K., Spanen, Springer-Verlag Berlin Heidelberg., 2011. p. 213.

[2] Matsumoto, Y., Barash, M.M., Liu, C.R., J. Eng. Ind., **108/3**, 1986. pp. 169-175.

[3] Ackerschott, G., Grundlagen der Zerspanung einsatzgehärteter Stähle mit geometrisch bestimmter Schneide, Dissertation, RWTH Aachen, 1989.

30th DANUBIA-ADRIA
Symposium on Advances in Experimental Mechanics
September 25-28, 2013 - Primošten, Croatia

5B38 142

EXPERIMENTAL APPROACH FOR CHARACTERIZING THE SHEAR FAILURE BEHAVIOR OF SHORT GLASS FIBER REINFORCED POLYPROPYLENE AND MICROMECHANICAL NUMERICAL IMPLEMENTATION

M. Reiter[1], A.M. Hartl[2], Z. Major[1]

[1] Johannes Kepler University Linz, Institute of Polymer Product Engineering, 4040 Linz, Austria. E-mails: martin.reiter@jku.at, zoltan.major@jku.at

[2] Johannes Kepler University Linz, Institute of Polymeric Materials and Testing, 4040 Linz, Austria. E-mail: anna.hartl@jku.at

1. Introduction

Short fiber reinforced polymers are widely used in automotive applications due to their superior mechanical properties and possibility of processing via injection molding which allows for application in mass production. To use these materials in crash relevant applications the deformation and damage behavior has to be adequately predicted.

The ultimate failure of the material can be predicted by use of various failure models (Tsai Hill, Tsai Wu, Puck, etc.) [1, 2]. These models were originally designed for unidirectional fiber orientations. Using the first pseudo grain failure (FPGF) model [3, 4] these failure criteria can be applied to complex fiber orientation distributions as they appear in injection molded components.

In order to determine proper parameters for the previously mentioned failure criteria axial and in-plane tensile tests as well as in-plane shear tests are an elementary input. In this study a methodology for shear testing is proposed and the results are compared to micromechanics based finite element simulations. Furthermore, critical failure stresses were extracted from the shear tests and parameters for a Tsai-Hill failure model [2] were determined.

2. Experimental

A commercial grade polypropylene (GD301FE from Borealis) with a fiber content of 32w% glass fibers was investigated. The material was provided as injection molded plate specimens (60mm x 60mm x 2mm) with a high fiber orientation.

2.1 Specimens

The plate specimens were milled as shown in Fig 1 in order to obtain a shear zone of 6mm x 2mm.

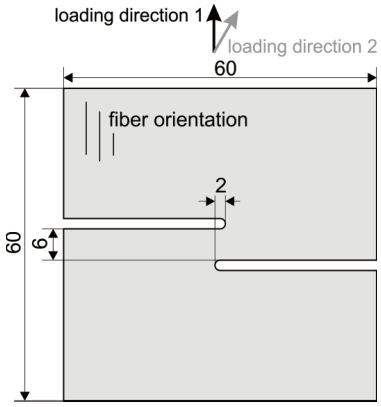

Fig. 1. Geometry of the milled shear specimens

2.2 Test Set-up

The specimens were tested on a tensile testing machine (Zwick Z020) under various monotonic loading rates (0.0002mm/s, 0.002 mm/s and 0.02mm/s). In addition a digital image correlation system (Aramis by GOM, Germany) was applied in order to measure the full strain field. This detailed strain information can be used to measure not only the nominal shear strains but also the true local shear strains, which allows for an effective validation of the simulation results.

Furthermore, the specimens were also loaded at different angles with respect to the shear zone. Thereby, different multiaxial strain states could be generated in addition to the shear strain, which provide additional points for the determination of the failure envelope. The critical failure stress was defined as the maximum shear stress.

3. Simulation

In order to perform finite element simulations an anisotropic material model based on the microstructure was set-up using a mean field homogenization method [4, 5]. The PP-matrix was modeled as elasto-viscoplastic and the fibers as linear elastic. Moreover, the whole specimen was meshed with the finite element software package Abaqus (Dassault Systems, France) and loaded as in the experiment.

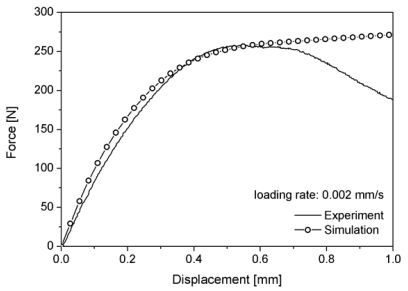

Fig. 2. Comparison of experimentally measured and simulated force-displacement curve of the shear test at 0.002mm/s loading rate

In Fig.2 a comparison of the experiment and the simulation is shown for an exemplary loading rate of 0.002 mm/s. As expected, the force signal shows a clear maximum in the experiment, whereas the simulation reveals a constantly increase in force due to lack of material damage.

In a consecutive step the parameters for a Tsai-Hill failure criterion were determined. The FPGF model together with the Tsai Hill criterion was implemented in the simulation in order to predict the point of damage.

4. Remarks

- Shear specimens were milled from injection molded plate specimens and tested under uniaxial loading. Critical shear failure stresses were extracted from those test results.
- A Tsai Hill failure criterion was determined using the critical shear stresses in combination with failure stresses derived from uniaxial tensile tests of specimens with 0° and 90° fiber orientation [6].
- A finite element simulation was set up in order to simulate the deformation behavior of the shear specimens. To predict the material damage this simulation was extended with a FPGF model with a Tsai Hill failure criterion.

Acknowledgements

The research work of this paper was performed in the K_{APMT} project with contributions by Borealis Polyolefine GmbH (Linz, A). The K_{APMT} is funded by the Austrian Government and the State Government of Upper Austria.

References

[1] S.-Y. Fu, B. Lauke, Y.-W. Mai, Science and engineering of short fiber reinforced polymer composites, Woodhead Publishing, Cambridge, UK, 206-219, 2009

[2] S.W. Tsai, Strength theories of filamentary structures fundamental aspects of fibre reinforced plastic composites, Wiley–Interscience, 1968, pp 3–11

[3] S. Kammoun et al., First pseudo-grain failure model for inelastic composites with misaligned short fibers, Composites Part A: Applied Science and Manufacturing, Vol. 42, I 12, pp 1892-1902, 2011

[4] Digimat, Linear and nonlinear multi-scale material modeling software, Tech. rep., e-Xstream engineering SA. ,Louvain-la-Neuve, Belgium, 2009

[5] I. Doghri et al., Mean-field based on a general incrementally affine linearization method, International Journal of Plasticity, 2010, Vol. 26, pp 219-238

[6] A.M. Hartl et al., Comparison of methods to characterize damage onset in short glass fiber filled polypropylene, ICCM19, 2013 Montreal, Canada

30th DANUBIA-ADRIA
Symposium on Advances in Experimental Mechanics
September 25-28, 2013 - Primošten, Croatia

5B39 053

VALIDATION OF ELASTIC AND IDENTIFICATION OF PLASTIC PARAMETERS OF JOHNSON-COOK LAW USING DIC

Zvonimir Tomičević[1,2], François Hild[2], Janoš Kodvanj[1], Stéphane Roux[2]

[1] University of Zagreb, Faculty of Mechanical Engineering and Naval Architecture, Ivana Lučića 5, HR-10000 Zagreb, Croatia. E-mail: zvonimir.tomicevic@fsb.hr, janos.kodvanj@fsb.hr

[2] LMT-Cachan, ENS Cachan/CNRS/UPMC/PRES UniverSud Paris, 61 Avenue du Président Wilson F-94235 Cachan Cedex, France. E-mail: hild@lmt.ens-cachan.fr, stephane.roux@lmt.ens-cachan.fr

1. Introduction

Nowadays, the identification and validation of constitutive laws with a high degree of reliability is an important demand from industry so as to apprehend safety factors in a rational manner. Full-field measurement techniques open the way to such an efficient and secure determination of constitutive parmeters. In the present case, nodular graphite cast iron was chosen as the studied material.

In this paper the identification of plastic parameters of Johnson-Cook law is performed from the analysis of biaxial tests. Two different loading paths are considered, namely, proportional equibiaxial and non-proportional "snail" histories. During the tests, images of the region of interest are taken. Displacement fields are measured via Digital Image Correlation (DIC). Boundary values of this measured displacement are prescribed in a FE modeling of the same test. Minimizing the difference between the measured and simulated displacement fields by tuning the plastic parameters is the strategy followed herein to identify the quasi-static part of Johnson-Cook's law.

2. Experimental procedure

Elastic properties of cast iron were determined from uniaxial tensile test on Messphysik Beta 50-5 screw-drive machine. The obtained mechanical properties are Young's modulus $E = 190$ GPa, Poisson's ratio $\nu = 0.3$, and yield stress $\sigma_{0.2\%} = 370$ MPa.

Biaxial tests were also conducted on the triaxial servo hydraulic machine ASTREE (Figure 1). Equibiaxial and "snail" loading paths were applied in load controlled mode with the loading rate of 0.5 kN / s. Cross-shaped specimens loaded under equibiaxial regime consists of loading and unloading along perpendicular axes at the same time and with the same load level. "Snail" history first (un)loads the specimen in one direction while the load in the other direction is kept constant. In the next (un)loading step the specimen is (un)loaded in the second direction while the load is held constant in the first direction, so that a single cycle follows a square in two-direction load plane.

During the test, one surface of the cross-shaped specimen was observed at the macroscale (picture definition 1024 × 1024 pixels, physical size of one pixel is 48 μm), which required to spray black and white paint with airbrush to enable DIC analyses.

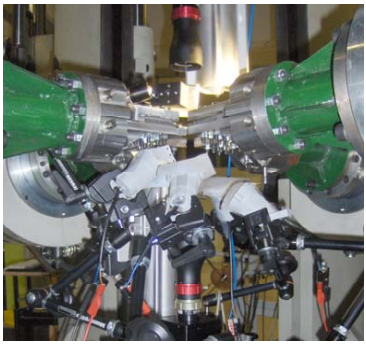

Fig. 1. Experimental setup

3. Identification procedure

The main identification tool is based on full-field measurements. In this study, a global approach to DIC is used. Three-noded triangles (T3) are chosen with a linear displacement

interpolation [1,2]. The identification process was conducted in several steps.

First, the 3D mesh is designed in the commercial FE code ABAQUS™. From the model surface nodes were extracted into a set that defines the 2D mesh that is imported in the T3-DIC code. The 2D mesh is adjusted and scaled (Fig. 2) to the macroscopic observation on the reference image of center part of the tested sample.

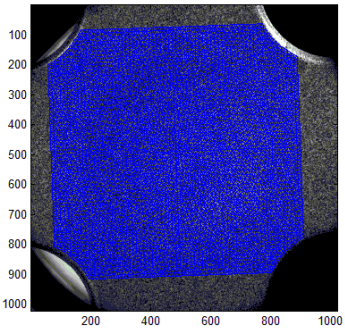

Fig. 2. Adapted mesh for T3-DIC analyses

The T3-DIC code provides the displacement fields. The in-plane nodal displacements on the boundary of the T3 mesh are extracted and prescribed to the 3D FE model. The same displacements were prescribed through the thickness along the edges (Fig. 3). Since the radii of the cross-shaped specimen are traction-free during the test they were treated as such and displacements were not prescribed in that region.

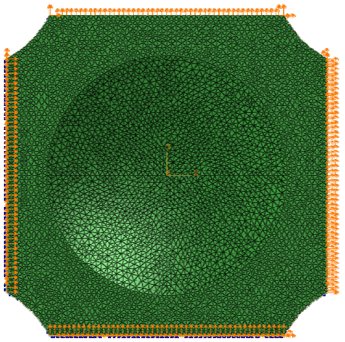

Fig. 3. Prescribed (measured) boundary conditions

In the FE simulations the material is described with an elasto-plastic law. To describe plastic hardening, a simplified version of Johnson-Cook's law is chosen

$$\sigma = \left[\sigma_0 + K\left(\bar{\varepsilon}^{pl}\right)^n\right], \qquad (1)$$

where σ is von Mises' equivalent stress, $\bar{\varepsilon}^{pl}$ the cumulative plastic strain, K the hardening parameter and n the hardening exponent to be indentified. The initial elastic and plastic parameters were determined from uniaxial test data (Table 1). Based on the minimization of the quadratic difference between measured and computed displacement fields, the elasto-plastic parameters are estimated.

Tab. 1. Initial elasto-plastic parameters

Young's modulus E [GPa]	Poisson ratio ν	Yield Stress σ_0 [MPa]	Hardening parameter K	Exponent n
193	0.33	360	3379	0.7363

4. Conclusion

An iterative method is implemented to update the finite element model by determining the sensitivity displacement fields, i.e., the displacement fields corresponding to a small change of the sought parameters δK and δn. Minimizing the least squares difference between the measured and calculated displacement fields allows us to tune the plastic parameters.

In this study, it was also noticed that without regularization of the measured displacement field [2] the stress profile on the boundaries of the FE model has a random distribution. Conversely, edge regularization yielded more appropriate stress profiles. While regularization enhances the displacement resolution [2], it also plays an important role for identification purposes.

Acknowledgements

This work was supported by an Eiffel scholarship from Campus France. ZT also thanks the International Affairs Bureau of École Normale Supérieure de Cachan for its support during his first stay at LMT-Cachan.

References

[1] Leclerc, H., Périé, J.-N., Roux, S. & Hild, F. in *MIRAGE 2009* Vol. LNCS 5496 (eds A. Gagalowicz & W. Philips), Springer (2009), 161-171

[2] Tomičević, Z., Hild, F. & Roux, S. to appear in J. Strain Analysis (2013).

6A01 135

TESTING METHODOLOGY FOR DETERMING VECTOR OF MAIN FORCE AND MAIN MOMENT OF THRUST VECTOR CONTROLLED ROCKET ENGINE

Marko Miloš[1], Jovan Isaković[2]

[1] University of Belgrade, Faculty of Mechanical Engineering, Kraljice Marije 16, 11120 Belgrade, SERBIA. E-mail: mmilos@mas.bg.ac.rs

[2] Military Technical Institute, 11000 Belgrade, SERBIA. E-mail: jovanisakovic@gmail.com

1. Introduction

Flaying vehicles which can not use control surfaces (fins, ailerons) to correct or change the position, must have some other type of attitude control systems. Focused to the missiles (object), solution for flight directional control is thrust delivered by propulsion system which must be deflected (vectored) to cause the object to pivot around its center of mass (center of gravity - CG) [1]. Generated lateral (side) force applied at some distance from the object's CG results in a control moment which change an object attitude. One of representatives of thrust vector control (TVC) mechanisms is movable nozzle (Fig.1.) where the lateral side force is generated by deflecting the main flow exhaust together with the nozzle [2][3]. In order to define three components of resulting force and three components of resulting moment, 6-component test bench (Fig.2.) needs to be used.

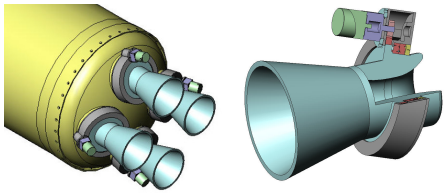

Fig.1. Rocket engine with 4 movable nozzles; Canted rotatable nozzle (single unit)

2. Testing methodology

The rocket engine is placed into horizontal position and constrained toward bench by six struts specifically located in three planes (Fig.2., Fig.5.). By measuring six forces in the struts and by applying appropriate mathematical calculation [4] vector of the main force together with the vector of the main moment can be obtained.

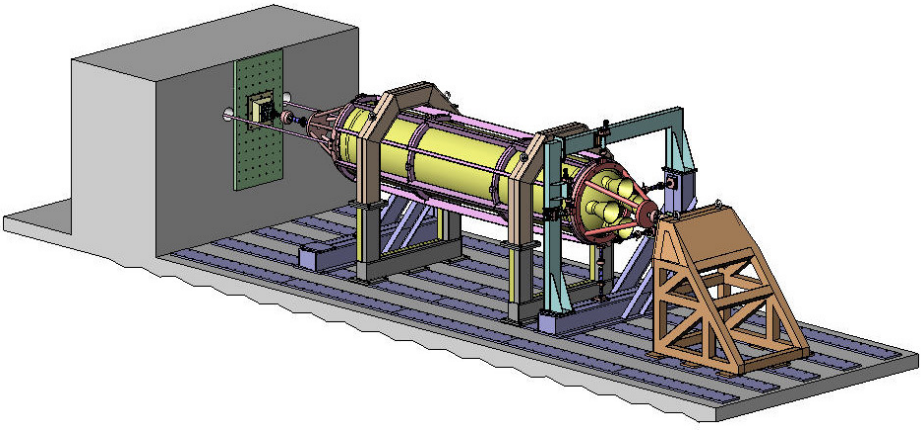

Fig.2. 6-component test bench & calibration system

3. Main components & calibration system

Each strut consists of force transducer, flexures, alignment subsystem and connections [5] (Fig.3., Fig.4.). Flexure separates cross influence of load cells. It is rigid in one plane and „soft“ in another.

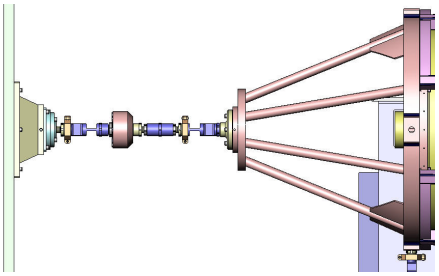

Fig.3. Axial Strut

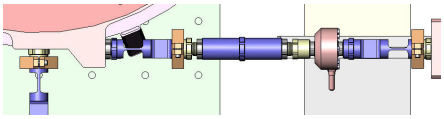

Fig.4. Moment strut in the aft plane

Cage (Fig.5.) is used to carry the motor and to prevent stresses caused by thermal rocket motor „growthing“ and „creeping“.

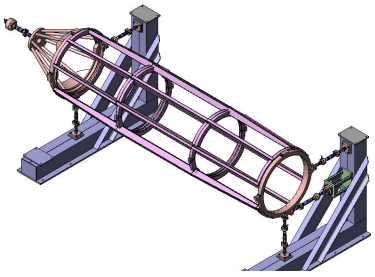

Fig.5. Motor cage and 6 struts

In order to define matrix of transformation for given main orthogonal system of the test bench, special calibration system is designed. It consists of calibration struts and rigid supports. Three calibration struts are shown on Fig.6. Beside previously mentioned parts, each calibration strut have a force source for generating load. In fact it is electromechanical actuator (Fig.7) which transforms rotation of the electromotor shaft to linear motion to push or pull certain point. Depending of the space, simulation of the axial force can be from top or from rear position.

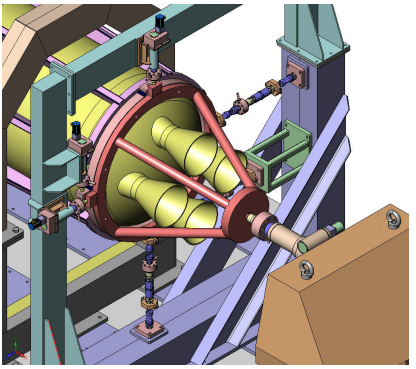

Fig.6. Part of the calibration system (actuator on the left, actuator on the top and actuator at the front)

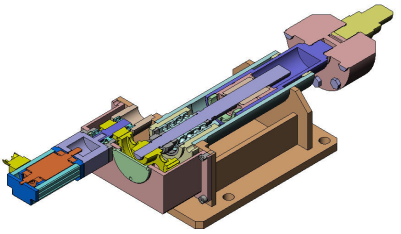

Fig.7. Actuator for simulation axial force

4. Conclusion

Presented testing methodology can be used as universal procedure. Own dimensions of the unit-under-test will define just mechanical details of the test bench.

Acknowledgements

The authors would like to express their great gratitude to Mr. Andrej Petric and to Mr. Mile Milisavljevic.

References

[1] Solid Rocket Thrust Vector Control turbines, NASA Monograph SP8114, 1974.

[2] Sutton, G., Rocket Propulsion Elements, 7th edition, John Wiley & Sons, Inc., NY, 2001.

[3] Rocket Basis, Thiokol Propulsion, US

[4] Lazić, R., Petrič, A., Šestokomponentni stolovi za ispitivanje raketnih motora, NTP, Vol. XXXIV, 6, 1984. pp. 3-10.

[5] Petrič, A., Lazić, R., primena savitljivih elemenata u ispitivanju raketnih motora, NTP, Vol. XXXIV, 6, 1984. pp. 3-10.

30th DANUBIA-ADRIA
Symposium on Advances in Experimental Mechanics
September 25-28, 2013 - Primošten, Croatia

6A02 061

IDENTIFICATION OF CAUSES OF DEGRADATION OF SHAFT FURNACE

Tadeusz Smolnicki[1)], Mariusz Stańco[1)], Damian Derlukiewicz [1)],

[1)] Wroclaw University of Technology, Faculty of Mechanical Engineering, Institute of machine Design and Operation, ul. Lukasiewicza 7/9, 50-371 Wroclaw, Poland

Corresponding author: tadeusz.smolnicki@pwr.wroc.pl; mariusz.stanco@pwr.wroc.pl; damian.derlukiewicz@pwr.wroc.pl

1. Introduction

Shaft furnaces (fig. 1) are used to melt copper. Their walls (caissons) are composed of segments made of steel with high heat resistance and are water cooled. Every 2 weeks the thermal load of the furnace is changing.

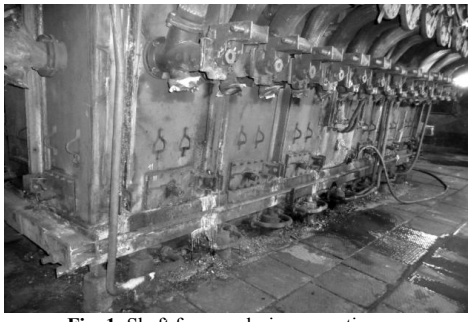

Fig. 1. Shaft furnace during operation

Technical problem during operation is the accelerated degradation of caissons due to the loss of geometric form (fig. 2).

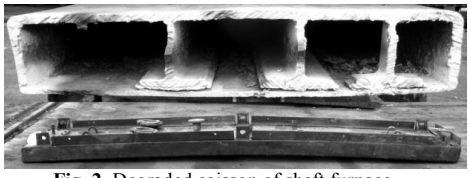

Fig. 2. Degraded caisson of shaft furnace

The boundary conditions of the furnace come from the process of operation and they are: the thermal loading caused by copper smelting, hydrostatic load of the charge weight, pressure and convection of cooling water. The support of the particular segments is statically indeterminate [1,2].

The aim of the analysis was to identify the causes of the damage occurrence.

2. Methodology

The measurements of deflection of selected segments of out of service were conducted. The measurement was performed using a laser level.

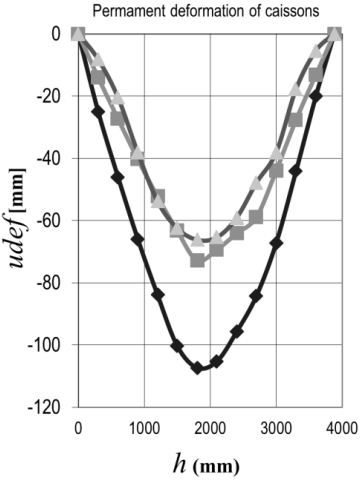

Fig. 3. Values of permanent deformation of caissons along their height

Selection of approximating function of a permanent deflection line by nonlinear regression analysis was performed. The good approximation of a quadratic function was stated. The measurement of the performance of the cooling water and the temperature of the input and output was conducted. On this basis, the heat balance of the furnace and the estimated value of the heat flux loading a single caisson was determined [4].

In next step, the FEM model of whole furnace, single segments (fig. 4) and their fragments was built. The thermal-displacement calculations were performed with use of FEM in the ranges of transient and steady state. The

nonlinear thermal characteristics of the material was taken into consideration.

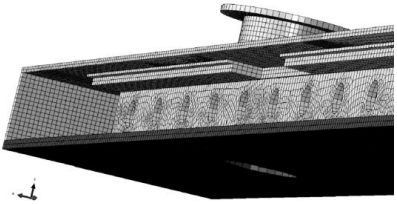

Fig. 4. Discrete model of caisson

3. Results

The contour lines of plastic strain and displacement after load decrease are shown on fig. 5. and fig. 6.

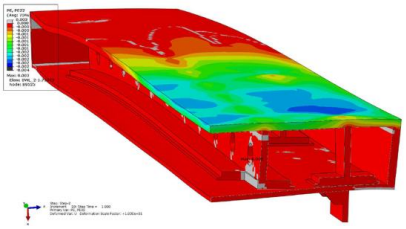

Fig. 5. Plastic strain after load decrease**.**

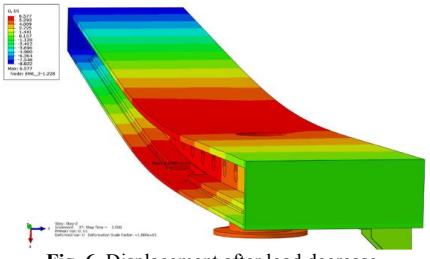

Fig. 6. Displacement after load decrease.

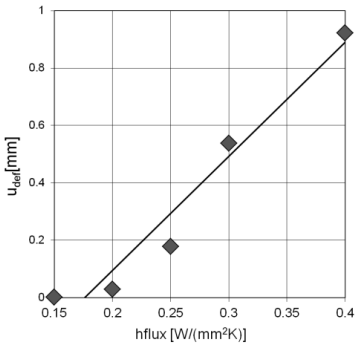

Fig. 7. Diagram of displacement increment – heat flux

The correlation between value of permanent deformation and the thermal load was also determined (fig. 7). The increase the accuracy of results, the numerical model was tuned based on the deflection measured experimentally [3].

4. Summary

Numerical models show a high sensitivity to the distribution and value of the thermal load [4]. Figure 8 shows the permanent deformation determined for different structural solutions of caissons (Fig. 8).

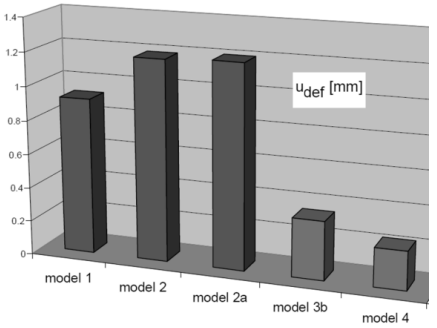

Fig. 8. Comparison of displacement after one load cycle for selected structural solutions of caisson

Based on the research the new design of caissons was proposed.

The main problem in solving the issue was the approximation of the distribution and the thermal loading.

References

[1] Smolnicki T.: Identification of Model of Change in Geometry of Large-Size Bearings on Flexible Supporting Structures (in Polish). Przegląd Mechaniczny 12/2001. (in Polish)

[2] Smolnicki T., Rusiński E.: Superelement-based modeling of load distribution in large-size slewing bearings. Journal of Mechanical Design. 2007, vol. 129, nr 4, s. 459-463

[3] Smolnicki T., Derlukiewicz, D., Stańco, M.: Evaluation of load distribution in the superstructure rotation joint of single-bucket caterpillar excavators. Automation in Construction. 2008, vol. 17, nr 3, s. 218-223.

[4] Derlukiewicz D.: Method of modelling the thermoelastic effects in laminar ceramic coatings , PhD Thesis, PWr 2006 PRE no 6

30th DANUBIA-ADRIA
Symposium on Advances in Experimental Mechanics
September 25-28, 2013 - Primošten, Croatia

6A03 086

EXPERIMENTAL VERIFICATION OF THE DYNAMIC MODEL FOR A WIND TURBINE TOWER

Jani Barle[1], Hinko Wolf[2], Predrag Đukić[3]

[1] University of Split, Faculty of Electrical Engineering, Mechanical Engineering and Naval Architecture, R. Boškovića 32, HR-21000 Split, Croatia. E-mail: barle@fesb.hr

[2] University of Zagreb, Faculty of Mechanical Engineering and Naval Architecture, Ivana Lučića 5, HR-10000 Zagreb, CROATIA. E-mail: hwolf@fsb.hr

[3] University of Split, Department of Professional Studies, Livanjska 5, HR-21000 Split, Croatia. E-mail: pdukic@oss.unist.hr

1. Introduction

Main issues in ensuring structural safety and optimal operational performance of a wind turbine as shown in Fig. 1. are: desired relatively long design life, sensitivity of structure on vibration and resonance, wind loads are non-deterministic with significant time variations and micro-location loads dependence. Failure or malfunction of control system which is trying to minimize stresses can result in overload or failure.

Load cases are well defined in [1] and [2] as essentially combination of external conditions (like wind speed, turbulence intensity, etc.) and wind turbine operational modes. Turbine operational modes are generally considered as normal (like: Power production, Start-up, Shut-down and Parked at extreme wind speeds) or fault (like: Generator short-circuit, Control system fault, Rotor emergency stop and Rotor overspeed)

Experimental procedure presented here is based on the [3]. Fig. 1 shows 1.5 MW turbine equipped with 5 dual-axis accelerometers, and 5 rectangular strain gage rossetes which allow measuring of accelerations and strains at defined locations. Strains further allow determination of internal forces: torsional and bending moments along the height of the tower. Following figures show a short time sequence of a detailed and long lasting monitoring record. In Fig. 2 control events sequence during a turbine emergency stopping with just 10 m/s wind speed is marked with red circles on the upper diagram's abscissa. Control events are correlated with bending moment at a height of 8.7 m: magnitude in the upper diagram, and corresponding longitudinal and transversal components with respect to the actual nacelle position in the lower diagram.

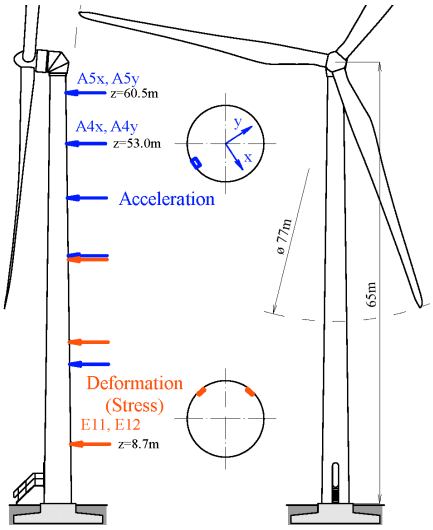

Fig. 1. Positions of used sensors.

Data similar to here presented can be used to verify design and/or its performance on the actual location. A great number of possible control sequences exists in reality, while their combinations with external loads are even more numerous. Control strategy, can be a solution of the problem of dynamic instability, as well as its cause.

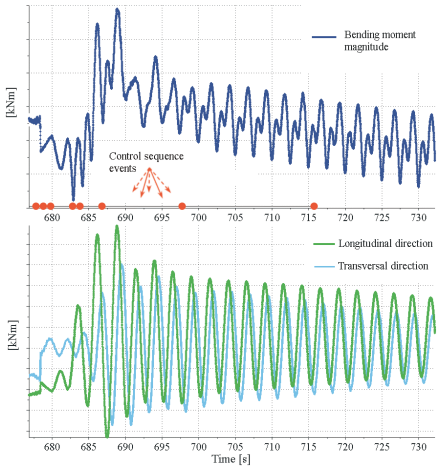

Fig. 2. Bending moment and control events during an emergency shutdown.

Using a complete structural model of the turbine to explain its dynamic behavior leads to enormous computational complexity resulting in huge amounts of data, with real possibility of missing the critical points. Solution is some simpler model of supporting structure, but complex enough to give a correct answer to the main questions.

2. Model of the supporting structure

Free-standing tubular steel tower is essential element which determines system dynamics and its model and verification follows

2.1 Experimental data

Analysis of the acceleration signals during idling phase with 3 m/s wind at last two levels yields first two eigenfrequencies of 0.402 Hz and 3.323 Hz. Minimum request set on the numerical model is to match those two frequencies and respective mode shapes.

2.2 Numerical model

A wind turbine conic tubular steel tower is modeled as a cantilever beam with 24 lumped masses (24 DOF-s) of 24 conical segments consisting the tower are determined in such a way that centers of gravity of conical segments match their actual position in the structure. Stiffness matrix of the cantilever beam with variable cross-section is obtained by numerical solving of differential equation of the beam elastic curve.

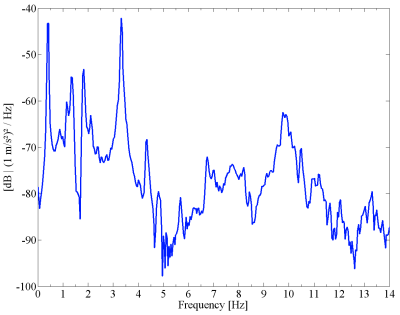

Fig. 3. Magnitude of spectral density between signals from A5x and A4x.

Figure 4 presents the first two mode shapes of the wind turbine tower. Circles indicate positions of the lumped masses i.e. the endpoints of conical segments. One can see that a very good agreement between the measured field data and the data obtained by considered simple numerical model has been obtained.

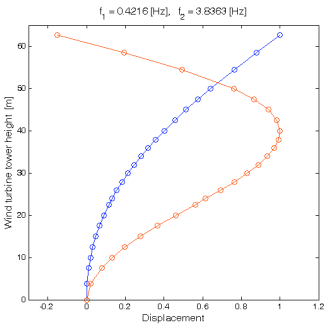

Fig. 4. First two mode shapes of the wind turbine tower

3. Conclusion

This paper reveals a need to have reliable experimental data of the wind turbine behavior. Since the described simple numerical model is validated it will be upgraded and used in further research to simulate response of the wind turbine tower subjected to external loads.

References

[1] EN 61400-01: Wind turbine generator systems - Part 01: Design requirements, 2010.
[2] Germanischer Lloyd, Hamburg, Germany: "Guideline for Certification of Wind Turbines", 2010.
[3] EN 61400-13: Wind turbine generator systems -Part 13: Measurement of mechanical loads, 2001.

30th DANUBIA-ADRIA
Symposium on Advances in Experimental Mechanics
September 25-28, 2013 - Primošten, Croatia

6A04 048

EFFICIENT LOAD AND STRESS DETERMINATION ON VEHICLES UNDER LONGTERM USAGE CONDITIONS

Andreas Rupp[1], Michael Städele[2], Andreas Küchler[2]

[1] University of Applied Sciences, Bahnhofstr. 61, 87435 Kempten, GERMANY.
E-mail: andreas.rupp@fh-kempten.de

[2] monalysis GmbH, Bahnhofstr. 69, 87435 Kempten, GERMANY.
E-mails: michael.staedele@monalysis.de, andreas.kuechler@monalysis.de

With the Durability Transfer Concept a efficient methodology is presented, in which the fatigue loading under operational conditions in all the different areas of a vehicle is determined based on the measurement of reference quantities, such as accelerations on the axle and transfer models. In a first step of the methodology short term measurements are performed with a vehicle equipped with sensors for the reference quantities, e.g. accelerometers on the suspension, and a large number of sensors for quantities of interest, such as wheel force transducers, strain gages in different areas e.g. the chassis or the body, displacement transducers and force transducers all over the vehicle. This instrumented vehicle is driven under well defined manoeuvres and on selected test tracks. The signals of the reference quantities are processed by band pass filters to virtual quantities with defined frequency content. Subsequently the virtual quantities and all other signals of the measured quantities are correlated to derive respective transfer functions. These durability transfer functions describe the complex load and stress conditions in different areas of a vehicle. The algorithms developed for this methodology are based on a perceptron first grade and is combined with physical boundary conditions of the vehicle dynamics. Subsequently measurements on many vehicles of the same type, measurements of only the reference quantities can be performed with only simple instrumentation very cost efficient and without measuring experts on board. The recorded reference quantities are finally processed by the identified transfer functions to the time histories of those quantities, which initially were identified but not measured during the long term campaign.

Effort and cost for the preparation, instrumentation, performance and processing of the long term measurements have been decisively reduced, since only the accelerations on the suspension are recorded, reduced and processed. Still the most valuable information about the damaging content of the load and stress conditions of parts and components in different areas of a vehicle are reliably gained.

Within this paper the methodology is described and results of multiple tests on passenger cars and heavy commercial vehicle for the proof of the reliability of the transfer method are presented. Examples of long term measuring campaigns in different missions are presented. The application of the methodology for the proof out of modern verhicles for well defined usage profiles is demonstrated as well as its potential for the monitoring of vehicle durability tests on proving grounds.

30th DANUBIA-ADRIA
Symposium on Advances in Experimental Mechanics
September 25-28, 2013 - Primošten, Croatia

6A05 134

DYNAMIC COUPLING STUDY BETWEEN SUBSTRUCTURES. APPLICATION TO THE CHASSIS-POWERTRAIN INTERACTION

A. El Hafidi, B. Martin, A . Loredo, B. Lay

DRIVE, EA 1859, Université de Bourgogne, France. E-mail: aehafidi@u-bourgogne.fr ; bmartin@u-bourgogne.fr ; aloredo@u-bourgogne.fr

1. Introduction

The design of vehicle powertrain and its mounting system is essential for improving the characteristics for noise and vibration. The powertrain vibration isolation from the rest of the vehicle is a problem often encountered in the design stage in the automotive field. Several methods have been developed to minimize the interactions between the powertrain and chassis. Most of these methods, which focus on the positioning and the design of resilient supports are based on decoupling rigid body modes from a grounded powertrain model with constant properties [1-5] or with characteristics that depend on the frequency or deflection [6,7]. Other methods have been developed in order to take into account the interaction between the chassis and the powertrain, but they considered that the chassis behaves like a rigid body.

The aim of this study is to present a method to predict the behavior of the chassis coupled to the powertrain. This method uses only the modal characteristics of the chassis and the vibration response of the grounded powertrain. The study is based on the vibrational coupling phenomenon between two subsystems: the chassis and the powertrain. A coupling matrix representing the influence of one system on the other is defined. The resolution of the problem is treated by using this coupling matrix. The method is applied to a city bus for which predominant excitations are assumed to be those of the powertrain. Usually, for such city buses, driving time is less than stop time and vibrations are low frequency with rather large amplitude.

2. Formulation of the coupling problem

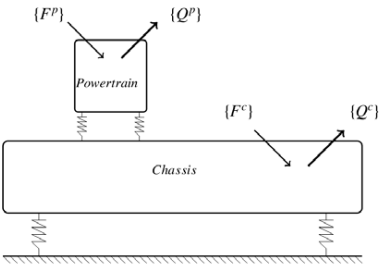

Figure 1: Powertrain coupled to the chassis

The equations describing the overall behavior can be obtained by considering that the vehicle is composed of three main parts: the powertrain which includes the engine and transmission, the engine mounts and the chassis with its suspension system. Figure (1) is a schematic representation of the model used in this study. the powertrain is modeled by rigid body with time-invariant mass and inertial matrix. It is supported by mounts on the vehicle chassis and it is modeled as a suspended body. The chassis is not considered as a rigid body, but it behaves like an elastic solid with its own characteristic frequencies.

Thus the response $\begin{Bmatrix} Q^p \\ q^c \end{Bmatrix}$ of the complete bus can be determined from equation 1 in which:

- $\{Q_0^p\}$ is the response of the powertrain (without the chassis) subjected to the force $\{F^p\}$. (see figure 2)
- $\{q_0^c\}$ is the response of the chassis (without the powertrain) subjected to the force $\{F^c\}$

- (D) is the coupling matrix obtained from the characteristics of the mount.

$$\begin{Bmatrix} Q^p \\ q^c \end{Bmatrix} = (I - D)^{-1} \begin{Bmatrix} Q_0^p \\ q_0^c \end{Bmatrix} \quad (1)$$

The principle of the method is shown schematically in Figure 2.

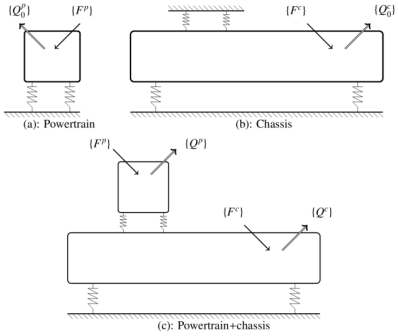

Figure 2. Principle of the method

3. Application for an industrial case

The studied structure is city bus manufactured by IVECO and operated by the Paris public transport company RATP (Régie Autonome des Transports de Paris). The bus has a length of 12 meters and a mass of 8008 kg. The powertrain is manufactured by IVECO (CURSOR 8 F2B) with a mass of 1147 kg

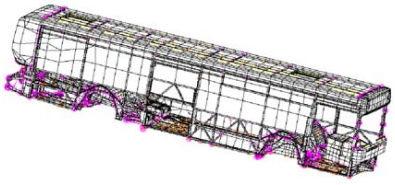

Figure 3: Finite element model used for the chassis

Figure 3 shows the mesh of the model used.

4. Results

A dynamic torque with a constant amplitude (220 Nm) was applied to the powertrain. The curves in figure 4 show the evolution of the vertical acceleration obtained near the driver's seat. The two curves are obtained by considering the full model and a condensed model thanks to the expansion to the second order of the coupling terms. One can see that the two curves are close over the frequency from which the convergence is verified (spectral radius<1).

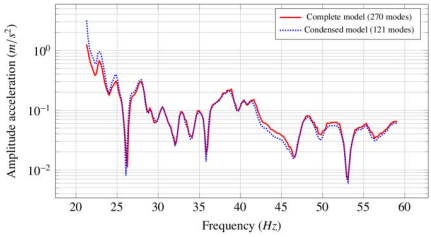

Figure 4: Acceleration v.s frequency for the full model and the condensed model.

References

[1] E. Courteille, F. Mortier L. Léotoing, and E. Ragneau. New analytical method to evaluate the power-plant and chassis coupling in the improvement vehicle nvh. European Journal of Mechanics-A/Solids, 24(6):929–943, 2005.

[2] Jae-Yeol Park and Rajendra Singh. E ect of non-proportional damping on the torque roll axis decou-pling of an engine mounting system. Journal of Sound and Vibration, 313:841–857, 2008.

[3] Taeseok Jeong and Rajendra Singh. Analytical methods of decoupling the automotive engine torque roll axis. Journal of Sound and Vibration, 234(1):85–114, 2000.

[4] J. A. Snyman, P. S. Heyns, and P. J. Vermrulen. Vibration isolation of a mounted engine through optimization. Mech. Math. Theory, 30(1):109–118, 1995.

[5] Ali ElHafidi, Bruno Martin, Alexandre Loredo, and Eric Jego. Vibration reduction on city buses: Determination of optimal position of engine mounts. Mechanical Systems and Signal Processing, 24(7)):2198–2209, 2010.

[6] Rajendra Singh Jae-Yeol Park. Role of spectrally varying mount properties in frequency coupling between powertrain motions under torque excitation. Journal of Sound and Vibration, 329:2895?2914, 2010.

[7] R.A. Ibrahim. Recent advances in nonlinear passive vibration isolators. Journal of Sound and Vibration, 314:371–452, 2009.

30th DANUBIA-ADRIA
Symposium on Advances in Experimental Mechanics
September 25-28, 2013 - Primošten, Croatia

6B01 131

STUDY OF MAGNETIC PROPERTIES OF SINGLE CRYSTAL NiMnGa ALLOY

Jerzy Kaleta[1], Daniel Lewandowski[1], Dajana Sawicka[1]

[1] Wroclaw University of Technology, Institute of Materials Science and Applied Mechanics, Wybrzeze Wyspianskiego 25-27, 50-370 Wroclaw, Poland.

E-mails: jerzy.kaleta@pwr.wroc.pl, daniel.lewandowski@pwr.wroc.pl, dajana.sawicka@pwr.wroc.pl

1. Introduction

NiMnGa alloy is a part of group of ferromagnetic shape memory alloys (FSMA) which are distinguished by large strains induced by magnetic field, high temperature or mechanical field. The material can elongate even up to 6% by the mechanism of twin boundary (TB) motion during the reorientation of magnetic domains [1,2,3]. The alloy is also characterized by magnetocaloric effect, temperature shape memory effect and harvesting properties.

This material has found an application in the construction of actuators, sensors and even energy harvesting devices.

2. Objectives

The aim of the study was an analysis of the magnetic properties of single crystal NiMnGa alloy. The magnetic parameters are required to understand the interaction of the material with a magnetic field. The obtained results enable to determine e.g. the range of working temperatures of the alloy.

3. Experimental results

The studied sample, which was provided by AdaptaMat, was a rectangular rod in the form of single crystal. Two kinds of studies were carried out: for determination of the magnetic properties and of the value of the magnetocaloric effect.

3.1 Magnetic properties

The chemical composition of the alloy was identified as $Ni_{46.4}Mn_{28.6}Ga_{24.0}$ using scanning microscopy with EDS detector. To measure the temperatures of the structural transformation the material was twice examined by differential scanning calorimetry (DSC) – Fig. 1, in the ranges of the -30°C÷80°C and 0°C÷110°C.

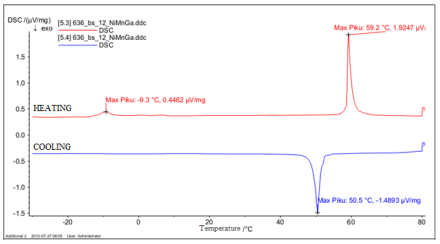

Fig. 1. DSC measurement with marked maximum peaks.

The calorimetric investigation shows that the temperatures of the structural transformation appear at 59.2°C and 102°C. The measured temperatures are similar to the results presented in other articles [4].

Based on the calorimetric analysis, the magnetic hysteresis loops were taken at two different temperatures, 325K and 340K, using Vibrating Sample Magnetometer (VSM) – Fig. 2.

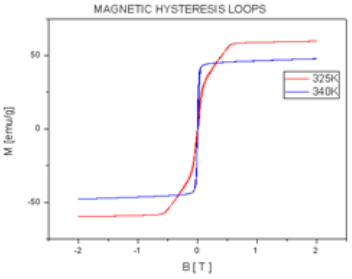

Fig. 2. Curves of the magnetic hysteresis loops

The shapes of the loops differ, which confirms the occurrence of the structural transformation at 59.2°C. The loops are very narrow, which suggests that the alloy is a soft magnetic material, suitable for working in an alternating magnetic field.

3.2 Value of the magnetocaloric effect

The magnetocaloric effect of the NiMnGa alloy was measured using the direct method. The results are depicted in Fig. 3.

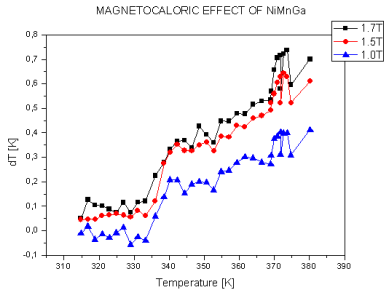

Fig. 3. Magnetocaloric effect measured by the direct method.

The value of the effect of 0.8K at 1.7T and 375K is significantly lower than for pure gadolinium – 4K at 1.5T and 297K.

The temperature hysteresis loop of the material was measured simultaneously – Fig. 4.

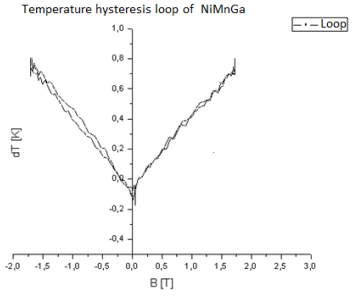

Fig. 4. Temperature hysteresis loop of the NiMnGa alloy.

The temperature hysteresis loop suggests that the studied alloy has a rapid reaction of the temperature to a variable magnetic field.

4. Conclusions

During the examination, the temperature of the austenite transformation of the alloy was determined at about 60°C and was additionally confirmed by the shape of the magnetic hysteresis loops.

The material was also found to be magnetically soft – it is easy to magnetize in a different direction.

NiMnGa is characterized by a narrow temperature hysteresis loop, thus a fast temperature reaction to a change in the magnetic field, but compared to pure gadolinium it has a much lower magnetocaloric effect, which makes it unsuitable for use as an active material in heat pumps.

The studied material, due to multiple characteristic features, did not yet find a precise field of application and is used in various kinds of devices.

References

[1] Murray, S.J., Marioni, M., Allen, S.M., O'Handley, R.C., Masachussetts Institute of Technology, Cambridge, Lagrasso, T.A., Ames Laboratory, United States Departments of Energy, Iowa State University, 6% magnetic-field-induced strain by twin-boundary motion in ferromagnetic Ni-Mn-Ga, Applied Physics Letters, vol. 77, num. 6, 2000.

[2] Chen, X., He, Y., Moumni, Z., Mechanical Engineering Unit, Materials and Structures Group, France, Twin boundary motion in NiMnGa single crystals under biaxial compression, Materials Letters 90, p. 72-75, 2013.

[3] Neudert, A., Wai Lai, Y., Shäfer, R., Kustov, M., Schultz, L., McCord, J., Magnetic Domains and Twin Boundary Movement of NiMnGa Magnetic Shape Memory Crystals, Advanced Engineering Materials, Vol.14, Issue 8, p.: 601-613, 2012

[4] Pagounis, E., Maier, M., Laufenberg, M., ETO MAGNETIC GmbH, Germany, Properties of large Ni-Mn-Ga single crystal with a predominat 5M-martensitic structure, IC FSMA'11, Dresden.

30th DANUBIA-ADRIA
Symposium on Advances in Experimental Mechanics
September 25-28, 2013 - Primošten, Croatia

6B02 114

MECHANICAL STIFFNESS AND STRENGTH TESTING OF CEMENT PASTES AT VERY EARLY AGES

Michal Hlobil[1,2], Philipp Karte[1], Roland Reihsner[1], Wolfgang Dörner[1], Josef Eberhardsteiner[1], Bernhard Pichler[1]

[1] Vienna University of Technology (TU Wien), Faculty of Civil Engineering, Institute for Mechanics of Materials and Structures, Laboratory for Macroscopic Material Testing, Karlsplatz 13/202, A-1040 Vienna, AUSTRIA. E-mails: Michal.Hlobil@tuwien.ac.at, Philipp.Karte@gmx.at, Roland.Reihsner@tuwien.ac.at, Wolfgang.Doerner@tuwien.ac.at, Josef.Eberhardsteiner@tuwien.ac.at, Bernhard.Pichler@tuwien.ac.at

[2] Double-degree PhD student, also enrolled at Czech Technical University in Prague, Faculty of Civil Engineering, Department of Mechanics, Thákurova 7, 16629, Prague 6, Czech Republic

1. Introduction

Reduction of CO_2 emissions motivates the cement and concrete industry to develop new binders, representing blends of classical cement clinker with supplementary cementitious materials such as fly ash and slag, or with fine-ground inert materials such as quartz and limestone. In order to be successful on the market, new materials have to perform similarly to their nowadays-available competitors. This implies that formworks should be removable one day after concrete production. Hence, compressive strength and material stiffness reached only 24 hours after production are of great importance. This raises the need for combined experimental-theoretical research.

We here focus both on non-destructive and on destructive uniaxial compression testing of young cement pastes using an electro-mechanical universal testing machine of type Walter & Bai LFM 150, designed for classical "quasi-static" testing of materials. We have developed procedures allowing us to reliably characterize both elasticity and strength of highly creep active and fragile cementitious materials at very early ages, with a very satisfactory level of reproducibility.

2. Methods

Macroscopic mechanical testing of cement pastes at early ages is a rather challenging task, because any imperfection will contribute to an increased scatter affecting the measurements of interest: either unloading displacements required for Young's modulus determination or the ultimate forces sustained by the sample. Therefore, it is important to analyze and to optimize every single element in the chain of actions from mixing the material up to the final test.

Concerning production of cement pastes with water-to-cement mass ratios resulting in initially rather stiff suspensions, intensive mixing is required as to achieve material homogeneity, followed by intensive vibration before and during casting, in order to effectively reduce the risk of air entrapment. As for casting, we let the material slide, under simultaneous dynamic vibration, over the surface of a funnel and over the inner surface of the formwork, rather than letting the material simply fall into the mold. After that, vibration intensity is reduced progressively, in the sense of a smooth fade-out. During subsequent curing at constant temperature, evaporation protection is very important, because even loss of only small amounts of water changes the effective water-to-cement mass ratio considerably, such that the tested mix would differ from the designed one.

In order to facilitate demolding, we use specially designed formworks consisting of two parts, such that they can be taken off the fragile specimen without applying notable forces. Subsequently, we remove the specimens' top layer which is typically affected by segregation effects. In order to achieve the desired plan-parallelity of the two opposite specimen surfaces, quasi-static scratching with a sharp Stanley knife turned out to be preferable to grinding with a belt slander,

because the latter dynamic action results in measurable damage of the fragile materials.

In order to obtain over-determined and, hence, redundant measurements of sample deformations during loading and unloading, we use five LVTDs instead of the minimum required three LVTDs. The LVTDs are evenly distributed around the specimen, measuring the relative displacement of two adapters that are clamped to the specimen such that they are in *continuous* contact with the specimen around its perimeter. The mean value of the five LVTD measurements together with the distance of the adapters allows for calculation of the normal strain in loading direction. The individual LVTD displacement fluctuations around the mean value, in turn, are related to bending, resulting mainly from load eccentricity.

In order to come as close as possible to a truly central application of the normal force, we use metal cylinders with bottlenecks, in a serial arrangement with the specimen. This way, the effective eccentricity of the applied normal force typically amounts to less than one percent of the specimen's diameter, reducing bending stresses very satisfactory to a reasonable minimum.

Poisson ratio's differences between sample and the adjacent metal cylinders result in inevitable self-equilibrated shear forces in the interfaces between specimen and adjacent loading cylinder. In order to minimize the influence of these undesired shear forces in destructive strength tests, we use two friction-reducing layers of Teflon in the mentioned interfaces, and we use cylindrical samples with a height-to-diameter ratio larger than 2. The observed failure mode (close-to-perfect axial splitting) underlines the success of this strategy. In case of non-destructive elasticity testing, we mount – inspired by Saint Venant's principle – the aforementioned LVTD-carrying adapters in a distance from the end of the specimens, which amounts to the one times the cylinder diameter, and we use slender specimens (typical height-to-diameter ratios amount to 5:1), in order to still guarantee a reasonable LVTD measurement length.

The sum of all described actions result in uniaxial compression experiments with very small scatter and a very high level of reproducibility, see, e.g. Fig. 1 for results from early-age strength testing on stoichiometric cement paste. Notably, both Young's moduli and uniaxial compressive strength values increase with increasing speed of loading/unloading. This can be explained by the pronounced creep activity of very young cementitious materials.

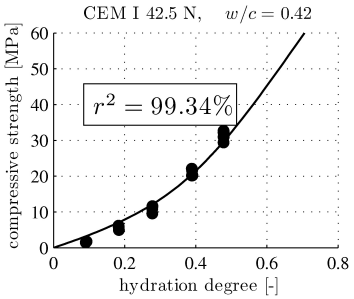

Fig. 1. Comparison of early-age strength values of stoichiometric cement paste, produced with a commercial CEM I 42.5 N, and comparison with a continuum micromechanics model prediction, after [1]

3. Results

Mechanical testing of young cement pastes is a challenging task, but a thorough analysis and optimization of every action from material production right up to the final mechanical test results in new standard procedures allowing us to achieve highly reliable and repeatable results regarding both early-age stiffness characterization and early-age strength determination. These results are starting points either for model development and or model validation activities; see, e.g., [1,2].

Acknowledgements

Funding of Michal Hlobil's double PhD degree at Vienna University of Technology and at the Czech Technical University in Prague, within core project 10 "Micromechanical analysis of blended cement-based composites" of the industrial-academic research network on cement and concrete "NANOCEM" (http://nanocem.org), as well as interesting discussions with Jaromír Wasserbauer and Ilja Fischer are gratefully acknowledged.

References

[1] Pichler B., Hellmich Ch., Eberhardsteiner J., Wasserbauer J., Termkhajornkit P., Barbarulo R., and Chanvillard G., Effect of gel-space ratio and microstructure on strength of hydrating cementitious materials: An engineering micromechanics approach, Cem Con Res, **45**, 2013, 55-68.

[2] Fischer I., Pichler B., Lach E., Terner C., Barraud E., and Britz F., Compressive strength of cement paste as a function of loading rate: experiments and engineering mechanics analysis, Cem Con Res, under review.

30th DANUBIA-ADRIA
Symposium on Advances in Experimental Mechanics
September 25-28, 2013 - Primošten, Croatia

6B03 100

EXPERIMENTAL INVESTIGATION OF MECHANICAL PROPERTIES OF OPTICAL FIBERS AND FBG SENSORS

Milan Dvorak[1], Milan Ruzicka[1], Lukas Horny[1]

[1] Czech Technical University in Prague, Faculty of Mechanical Engineering, Technická 4, Praha 6, 166 07, CZECH REPUBLIC.
E-mail: milan.dvorak@fs.cvut.cz, milan.ruzicka@fs.cvut.cz,lukas.horny@fs.cvut.cz

1. Introduction

This paper is focused on determination of mechanical properties of optical fibers that are used for manufacturing of Fiber Bragg Grating (FBG) sensors and also on calibration of strain and temperature sensitivity of chosen FBG sensors. The goal of the experimental testing is to choose a FBG sensor with primary coating material, which is suitable for embedding into the composite or into the adhesive joints of composite structures (ultralight aircraft wing or skeleton of a electric bus). Defining conditions for selection of FBG sensors are particularly max. temperature during the composite curing process (no more than 70 °C) and presumed level of max. mechanical strain in areas, where the FBG sensors will be installed (up to 6 000 μm/m). Another requirement was to use FBG sensors with central wavelength of 830 nm, because of available interrogators.

2. Primary coating materials

Three types of primary coating materials, which are commonly used for manufacturing of FBG sensors, were considered. Properties of commercially available FBG sensors (in the most common optical windows of 830 nm and 1550 nm) are listed in Tab. 1. FBG sensors with primary coating made of polyimide were not available in 830 nm, so sensor with acrylate and ORMOCER® coating were selected for experimental testing.

3. Experimental set-up

Experimental testing of tensile properties was carried out using the biaxial tensile testing machine Zwick/Roell. It was equipped with U9B HBM load cell (-250N to +250N, accuracy class 0.5). Longitudinal strain was measured by Messphysik video extensometer ME46, with minimum resolution 0.4 μm for vertical field of view 50 mm. Safibra FBGuard 2-channel interrogator (CW 830 nm, sampling frequency of 70 Hz) was used to measure signal from FBG sensors during the calibration tests.

prim. coating	acrylate	polyimide	Ormocer®
reflectivity [%]	>80% @ 10 mm [3] >90% @ 10 mm [4, 5]	>70% [2] >80% @ 10 mm [3] >90% @ 10 mm [4, 5]	>15% @ 8 mm [1]
coated fibre diamet. [μm]	255 [4]	145 - 165 [2] 165 [4]	195 [1]
strain sensit. [pm/μm/m]	1.2 [3, 4]	1.2 [2, 3, 4]	0.78 [1]
temp. sensit. [pm/°C]	11 [3]	9.9 [2], 11 [3]	6.5 [1]
strain limit [μm/m], tensile load at break	9 000 [3] 3 000 - 5 000 [4]	5 000 [2] 9 000 [3] 3000 - 5000 [4]	>50 000 [1] (> 50 N)
operational temperature range [°C]	- 270 to 85 [3] 5 to 120 [4] - 5 to 80 [5]	- 40 to 120 [2] - 270 to 300 [3] - 40 to 300 [4, 5]	- 180 to 200 [1]
manufacturing process	stripping & re-coating	stripping & re-coating	drawing

Tab. 1. FBG sensors properties.

4. Tensile properties of optical fibers

Specimens of optical fibers were about (80-90) mm long, with diameters of 0.255 mm (acrylate coating) and 0.195 mm (ORMOCER®). Both ends of each sample were glued into the woven string, using the cyanoacrylate glue. These strings were clamped in the loading grips of testing machine, ensuring a uniform force transfer into the fiber.

Pair of contrasting marks for video extensometer was glued to the center of the specimen. The goal of experiment was to obtain tensile force at break F_{MAX} (from the load cell), mechanical strain at break ε_{max} (from the video extensometer) and tensile modulus of optical fiber E (calculated from stress-strain curve), see Tab. 2. A total of seven specimens with acrylate coating were tested. Five of them were broken correctly, two of them was detached from the clamping string. A total of sixteen specimens with ORMOCER® coating were tested. Four of them were broken correctly, twelve of them was detached from the clamping string. High strength of this coting material is apparent from the prevailing number of unbroken specimens.

	F_{max}	ε_{max}	E
coating	[N]	[um/m]	[GPa]
acrylate	9.8	11644	17.5
calculated value			18.1
Ormocer®	48.6	49948	34.1
calculated value			31.2

Tab. 2. Mechanical properties of optical fibers.

Comparative tensile modulus of optical fibers was calculated using the simple rule of mixtures. Modulus E_{GLASS} = 73 GPa was taken from [6], $E_{ACRYLATE}$ = 0.7 GPa from [7] and $E_{ORMOCER}$ = 2 GPa from [8].

5. Calibration of FBG sensors

5.1 Temperature sensitivity coefficient

Coefficient was determined from the measured wavelength changes depending on temperature changes. The FBG sensor, protected by the steel tubing, was immersed in water. Gradual heating of water was measured using a PT100 thermocouple, connected to the HBM Spider8 measuring device.

5.2 Strain sensitivity coefficient

Coefficient was determined from the measured wavelength changes depending on changing mechanical strain of Bragg grating area (measured by external video extensometer).

5.3 Experimental calibration results

Calibration values of strain and temperature sensitivity was investigated (see Tab. 3). FBG sensors with ORMOCER® coating were chosen for further use, because of their ability to reach elongation of about 5 %, which is much more than the required value of 0.6 %. Moreover they can survive curing temperature up to 200 °C, which is enough even for the potential use of prepregs technology.

	acrylate	Ormocer®
temperature sensitivity [pm/°C]	5.70	6.30
strain sensitivity [pm/(μm/m)]	0.60	0.70

Tab. 3. Calibration values for FBG sensors.

6. Concluding remarks

- Tensile mechanical properties of optical fibers with two coating materials were tested. Limit values of load and strain at break were obtained, as well as tensile modulus.
- Calibration values of strain and temperature sensitivity for acrylate coated and ORMOCER® coated FBG sensors were measured.
- ORMOCER® was chosen as the most suitable coating material for embeddable FBG sensors, because of high mechanical and temperature durability.

Acknowledgements

The authors would like to thank the Ministry of Industry and Trade of the Czech Republic for supporting this research with project no. FR-TI1/290 and TA 02031296.

References

[1] http://www.fbgs.com/website/fbgs/assets/files/dtg-lbl-830_1550_datasheet.pdf

[2] http://www.micronoptics.com/uploads/library/documents/Datasheets/Micron%20Optics%20-%20os1100.pdf

[3] http://smartfibres.com/docs/SmartFBG.pdf

[4] http://www.fbg.com.cn/bare_fbg_8.html

[5] http://www.alxenses.com/FBG.html

[6] Dongsheng Li, Liang Ren and Hongnan Li (2012). Mechanical Property and Strain Transferring Mechanism in Optical Fiber Sensors, Fiber Optic Sensors, Dr Moh. Yasin (Ed.), ISBN: 978-953-307-922-6, InTech,

[7] Measures R.M., Structural Monitoring with Fiber Optic Technology (Academic Press, San Diego, 2001). ISBN 0-12-487430-4.

[8] http://www.ormocere.de/Property-profile.820.0.html?&L=1

30th DANUBIA-ADRIA
Symposium on Advances in Experimental Mechanics
September 25-28, 2013 - Primošten, Croatia

6B04 127

EXPERIMENTAL INVESTIGATION OF MATERIAL DAMPING IN POLYMER CONCRETE AND WELDED STEEL PARTS FOR MACHINE TOOL QUILLS

Thomas Mikats[1], Stephan Krall[1], Friedrich Bleicher[1]

[1] Vienna University of Technology, Institute for Production Engineering and Laser Technology, Landstraßer Hauptstraße 152, 1030 Vienna, Austria.

Corresponding author: mikats@ift.at

1. Introduction

In general mechanical structures of machine tools, especially those which are dedicated to high-precision machining purpose, show the need for high static stiffness characteristics and their dynamic behavior becomes of increasing importance. During machining, on the one hand the whole structure is excited by inertia forces due to the feed drives motion and the positioning movement of single axes. Furthermore deviations of the tool center point in reference to the workpiece occur due to the spindle rotation and unbalanced tools and rotors. Referring to this the engineer has to take care in the design of machine tools that this type of excitation does not meet one of the natural frequencies in order to avoid slightly damped vibrations in the kinematics structure elements. On the other hand the structure is loaded with an immediately rising force collective caused by transient reactions when the cutting edge gets into the cut. With respect to a typically fast change of forces and the requirements of precision and tolerances of workpieces it is important that the structure comes to a rest as soon as possible by an enhanced excited state deactivation. Thus the constructions material of machine tool components needs to offer an increased damping rate which is significantly influenced by the material damping characteristics.

In this regard a particularly very sensitive part of the machine tool is the last axis of serially arranged kinematic chains, mainly the quill where the main spindle is typically attached. At this axis it is always necessary to find a compromise between high stiffness and damping and low weight for high acceleration performance. A specifically challenging applications example can be located in the quill construction used in large milling centers with an increased stroke in the Z-axis. The design has to meet the requirements of a slim cross section area and a long but not guided length. As the mass, the stiffness and the natural frequencies of a structure can be calculated by FEM and optimized with advanced simulation techniques, it is hardly possible to make an indication of the damping performance of a structure without a measurement of the real part.

2. Test arrangement

The aim of the present work is to analyze the damping of structure parts usually used for a quill. As a first step two different designs have been compared. First a quill-construction consisting of welded steel plates. Second a quill with the same external dimensions build up with a thin steel plate coverage and filled with a composite material consisting of polymer concrete, like wet mix aggregate material and steel - called Hydropol. The following figure illustrates the test configuration.

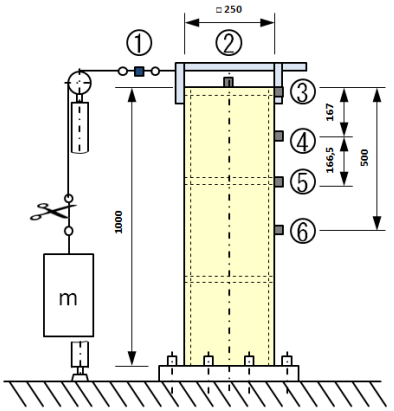

Fig. 1. Experimental setup.

The dimensions of the test parts have been defined by a ground view of 250 mm x 250 mm and by a height of 1000 mm as it is depicted in Fig. 1. To simplify the test arrangement the holes for the main spindle and for installation purpose like cables are disregarded. The steel test part shows a weight of 119 kg and the Hydropol test part has 211 kg. In order to enable a constant force and excitation on the structure the test is based on an experimental setup which is described in [1]. Fig. 1 shows the test implementation and the positions of the sensors. The used mass for excitation was selected with about 136 kg. This is equal to a force of 1340 N which was recorded with a load cell in Pos. (1) during the test. The acceleration sensor was placed at Pos. (2) to Pos. (6). The typical transient changeover of the force described in the time regime is presented in Fig. 3.

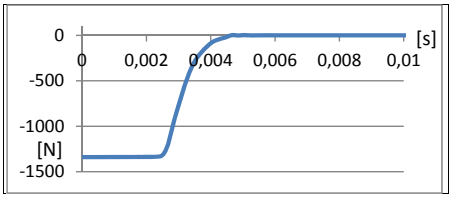

Fig. 2. Force-time-graph showing the changeover of excitation force.

3. Results

The experiment was repeated to check and to optimize the reproducibility. Different measurement positions have been investigated. Fig. 3 shows the measurement of the acceleration value against time of both the welded part and the Hydropol test part, measured on Pos. (5).

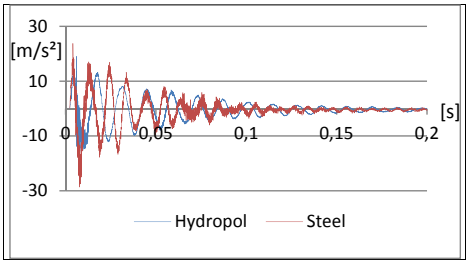

Fig. 3. Acceleration against time, measured on Pos. (5)

It can be depicted that the damping behavior in the experimental setup and test parts is almost equal. While the structure made of Hydropol shows rather constant characteristics at each of the measuring positions, the vibration in the dynamic behavior of the welded steel test part is significantly varying. Hence the acceleration against time graph illustrated in Fig.4 depicts that the acceleration value and with it the vibration effects of the steel test part rises at Pos. (4).

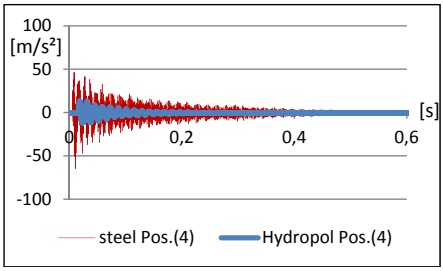

Fig. 4. Acceleration against time graph, measurement signals at Pos. (4)

The measuring signals show that the Hydropol test part has one dominating frequency at 87 Hz and almost no effects of harmonic components whereas the steel test part shows a basic frequency at 105 Hz and several natural harmonics at frequencies of about 870 Hz, 945 Hz and 1210 Hz. The attenuation factor by Lehr´s damping ratio can be determined in approximation for the given bending vibration using the logarithmic decrement. The evaluation for Hydropol material results in $D_H = 0{,}021$ and for steel $D_S = 0{,}11$. The latter can be regarded as a typical value for solid rigid material [2].

4. Conclusion

The experimental setup should help to gather data for damping characteristics of two different materials which can be used for designing machine tool frame parts. In evaluating the dynamic behavior of machine tools by FEM simulation the material characteristics become important. The materials investigated by the use of distinctive test parts show significantly different characteristics. The following step of material investigation will be the simulation of the experimental setup with the found material parameters. Furthermore, especially the test part connection to the foundation must be evaluated, because there is a wide influence of this connection on the stiffness and the natural frequencies.

References

[1] Weck M., Brecher C., Werkzeugmaschinen Band 5, Springer Verlag, 2006.pp. 367-368

[2] Hirsch A., Werkzeugmaschinen, Vieweg und Teubner Verlag, 2012.

30th DANUBIA-ADRIA
Symposium on Advances in Experimental Mechanics
September 25-28, 2013 - Primošten, Croatia

6B05 045

IMPACT OF THE SHAPE OF THE SAMPLE ON THE PLC INSTABILITIES - CONTRIBUTION OF DIGITAL IMAGE CORRELATION TECHNICS ON TENSILE TESTS

K. BOUABDALLAH [1], P. BALLAND[2], A. MANARI[3]

[1] Faculté de Technologie, Université de M'sila, Route de Chebilia, 28000, Algérie. E-mail: bouabdallahk@yahoo.fr

[2] Laboratoire SYMME, Université de Savoie. E-mail: pascale.balland@univ-savoie.fr

[3] Faculté de Technologie, Université de M'sila, Route de Chebilia, 28000, Algérie. E-mail : manariabdelmalek@yahoo.fr

1. Introduction

Simulation techniques are very powerful means of prospecting for mechanical behavior of materials. Their use needs, however, to be validated by appropriate experiments. In this article, the results of experiments on the behavior of an Al-Mg alloy with mechanical instabilities in the Portevin-Le-Châtelier effect (PLC) are presented. During a tensile test, the PLC effect is manifested, under certain conditions of temperature and strain rate, by the appearance of localization effects of plastic deformation zones that can spread throughout the body of the specimen. The deformation curves present then, at a certain rate of deformation, characteristic streaks that can occur until rupture. For a given alloy, the experimental results show that, while being interdependent, the characteristic parameters of the PLC instability are dependent on deformation conditions (strain rate, temperature, strain hardening rate). These features are revealed by the streaks on the stress-strain curve such as the shape of the step and the amplitude and frequency of stress drops.

Bibliographical references abound on the subject (see [1]) but few papers deal with the influence of specimen geometry on the characteristics of PLC bands.

In this article, the influence of specimen length and the presence of a notch on the characteristics of PLC bands during tensile tests on an Al-3.2 Mg is examined. A brief description of the experimental device and the used material will be given. The second part will be devoted to the presentation of experimental results and their analysis before ending with a conclusion.

2. Experimental device and material

Tensile tests on flat specimens of an Al-3.2 Mg alloy have been conducted at room temperature on a crosshead speed piloting machine (INSTRON). The test specimens with a notch of 1.1 mm width are obtained from a 1.1 mm thick sheet. The length used is 100 mm. The tests were conducted at constant imposed strain rate. The crosshead velocity, in mm/min, is determined by the expression:

$$V_T = \dot{\varepsilon}.L_0.60$$

where $\dot{\varepsilon}$ is the imposed strain rate (s^{-1}), and L_0 is the initial length of the specimen (mm).

The experimental setup (figure 1) comprises, in addition to a conventional traction device, an optical image acquisition system.

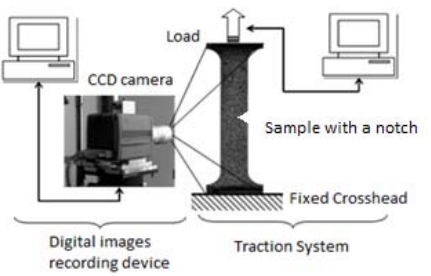

Fig 1: Experimental setup.

Sequences captured by the CCD camera are stored on a computer hard drive for further processing by the 7D software developed in the SYMME laboratory [2]. Image correlation on 7D can visualize and quantify the heterogeneity of deformation.

3. Results and analysis

The jerky flow associated with the PLC effect, is reflected in typical oscillations of the stress-strain curve ($\sigma = f(\varepsilon)$) (see figure 2).

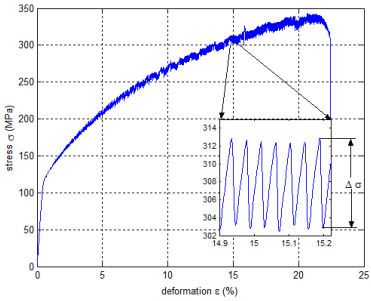

Fig 2: Stress-strain curve for a tensile test on Al-3, 2 Mg at room temperature ($\dot{\varepsilon} = 1.98.10^{-3} s^{-1}$).

Each serration corresponds to a location of the plastic deformation of the material (PLC band). The test conditions used in this study correspond to the area of occurrence of the PLC bands of type B. The heterogeneity of the plastic deformation is characterized in this case by quasiperiodic stress drop ($\Delta \sigma$) on the tensile curve. As it can be seen on figure 2, the amplitude of the stress drop is significant.

For different lengths of samples, the curves have the same overall look. The oscillation frequency of the curve is different, however.

Figure 3 shows a zoom on part of the stress-time curve for two samples. The curves were taken at the same strain rate (15%).

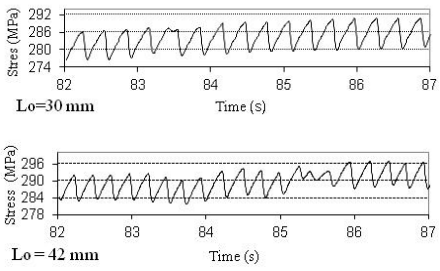

Fig 3: Deformation curves on a 5-second interval in the vicinity of 15% of strain rate for two samples of different lengths ($\dot{\varepsilon} = 1.98.10^{-3} s^{-1}$).

DIC techniques allow quantitative determination of the geometric and kinematic parameters of PLC bands (width, orientation, local deformation, velocity ...) [3,4]. Figure 4 shows two maps of the kinematic field relating to the times of occurrence of PLC bands which become blocked by the notch.

These maps clearly show that, step by step, the plastic deformation is localized not far from the notch of the specimen.

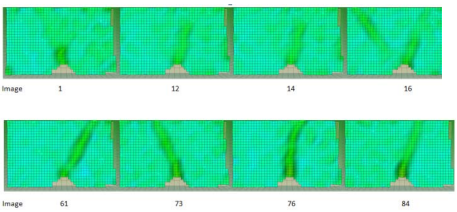

Fig 4: Cartography of kinematic fields showing the amplitude of the localization of longitudinal deformation in different moments from the tensile test on an Al-3.2 Mg ($\dot{\varepsilon} = 8.33.10^{-4} s^{-1}$).

Furthermore, and in association with changes in stress drop ($\Delta \sigma$) on the deformation curve, the kinematic field shows a clear increase in the strain amplitude within the PLC band during the test. The increment of deformation associated with each instability evolves during the global deformation of the sample.

The results of this work confirm that the PLC effect is an intrinsic property of the material and that the main features of the instability (appearance, mode of propagation and amplitude), for a given material, depend mainly on the strain rate imposed. The influence of the presence of a notch is also studied in this study (appearance, shape of the notch…).

References

[1] A. Yilmaz, The Portevin–Le Chatelier effect:a review of experimental findings, Sci. Technol. Adv. Mater. 12 (2011) 063001 (16pp)

[2] P. Vacher, S. Dumoulin, F. Morestin, S. Mguil-Touchal, Bidimensional strain measurement using digital images, Proc. Inst. Mech. Eng. 213 (1999) 811–817

[3] J. Zdunek and al, Digital Image Correlation investigation of Portevin - Le Châtelier effect in an aluminium alloy, Mat. Charact. Vol. 59, Issue 10, October 2008, Pages 1429–1433

[4] K. Bouabdallah, P. Balland, L. Tabourot, P. Vacher, Contribution of kinematic field measurements to the modelling of the Portevin - Le Châtelier effect by the image correlation method, The Journal of Strain Analysis for Engineering Design 42, 8 (2007) 589-594

30th DANUBIA-ADRIA
Symposium on Advances in Experimental Mechanics
September 25-28, 2013 - Primošten, Croatia

7A01 075

APPROACH IN SI ENGINE MISFIRE DETECTION

Jasmina Lozanovic Sajic[1], Sasa Petrovic[2]

[1] University of Belgrade, Faculty of Mechanical Engineering, Innovation Center, Kraljie Marije 16, Belgrade, SERBIA. E-mail: jlozanovic@mas.bg.ac.rs

[2] Ministry of Defense, Department of Logistics (J-4) of SAF Belgrade, Serbia, saskop@eunet.rs

1. Introduction

Increasing requirements for a fuel economy exhaust emissions and the output performance and also the complexity of the automotive engines necessitate the development of a new generation of the engine control functionality. Engine torque estimation function is an important function for an engine torque model, misfire diagnostics and dependability. The engine torque estimation function is based on monitoring of the cylinder individual fluctuations of the high resolution engine speed signal [1].

The engine speed signal is based on the measurements of a passage time between two subsequent teeth on a crank wheel. The passage time decreases as the rotational speed increases thus the time interval errors increase. Moreover, low frequency oscillations from the power train and high frequency oscillations due to the crankshaft torsion, together with vibrations induced by the road, act as disturbances on the crankshaft. These disturbances influence directly the performance of the engine speed signal and consequently the torque monitoring function. Many misfire diagnostic functions utilize a low rate sampling of the engine crankshaft speed. Typically, the crankshaft speed is sampled once per cylinder firing event. The engine speed can be approximated by a trigonometric polynomial due to the periodic nature of both engine rotational dynamics and combustion forces as functions of a crank angle [2]. Misfire is the state of an engine where the combustion does not occur due to the errors in fueling or ignition. As a consequence, such misfires affect long term performance of the exhaust emission control system. The misfires cause changes in the crankshaft rate of rotation, because the misfired cylinder is not able to provide the torque. Engine misfire diagnostic functions are based on monitoring of the cylinder individual fluctuations of the high resolution engine speed signal or a passage time between subsequent teeth on a crank wheel. The high resolution engine speed signal is calculated as a ratio of the length of the angular segment on the crank wheel and the passage time for this segment. The passage time becomes less as the rotational speed raises, thereby time interval errors rise. Usually, measured signal in most cases are transformed to frequency signal. In this paper we analyzed measured signal directly, without any transformation.

2. Problem Statement

As a rule, a passage time between two teeth on a crank wheel is measured in production engines. The high resolution engine speed signal is then calculated as a ratio of the length of the angular segment on the crank wheel and the passage time for this segment.

We prepare hardware for measurement signal value in voltage from engine crankshaft sensor on real engine. For this, we use universal measurement toll QUANTUM MX-840 and engine embedeed crank shaft speed sensor [3]. The sampling rate it's very high in interest for high resolution of measurement.

Suppose that there is a set of the Crank Angle synchronized data y_l, $l = 1,\ldots, n$ $(n < 15000)$ measured at the following points: x, $x_1 = \Delta$, $x_2 = 2\Delta$, $\ldots. x_n = n\Delta$, Δ=0,000417 s. Misfire state it is controlled manually, for any cylinder (1st to 4th).

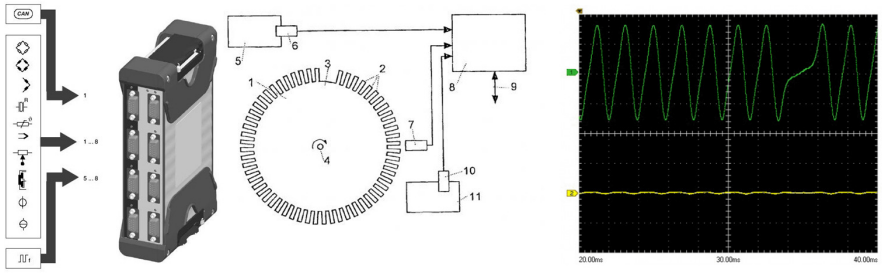

Fig. 1. The applied measuring system for data acquisition

normal state		1st cyl disabled		2nd cyl disabled		3rd cyl disabled		4th cyl disabled	
0	-0.34135	0	3.025295	0	-6.24184	0	-2.08619	0	-2.22722
0.000417	3.674666	0.000417	1.620199	0.000417	-11.3549	0.000417	-3.41265	0.000417	-5.53553
0.000833	0.289516	0.000833	-1.45069	0.000833	-2.03844	0.000833	-4.56775	0.000833	-3.39072
0.00125	-1.05096	0.00125	4.253419	0.00125	1.352602	0.00125	-0.94344	0.00125	-3.59625
0.001667	3.290856	0.001667	-0.63544	0.001667	10.69681	0.001667	-6.3695	0.001667	-4.99481
0.002083	0.85035	0.002083	1.482191	0.002083	3.597733	0.002083	-0.25947	0.002083	-2.19339
0.0025	-0.86523	0.0025	2.984	0.0025	2.470534	0.0025	-6.91866	0.0025	-6.96948
0.002917	3.151368	0.002917	-1.86904	0.002917	-3.30137	0.002917	-0.93836	0.002917	-0.89454
0.003333	1.211538	0.003333	3.738023	0.003333	3.078322	0.003333	-5.12115	0.003333	-7.48536
0.00375	-1.40347	0.00375	0.649114	0.00375	-2.19125	0.00375	-3.04726	0.00375	-0.53651
0.004167	3.067888	0.004167	0.193866	0.004167	0.889037	0.004167	-2.96356	0.004167	-6.83391

Tab. 1. Measured data

3. Verifying Data

First off all, we evaluated signal distribution for different samples [4]. Normal working condition are shown in Fig. 2.

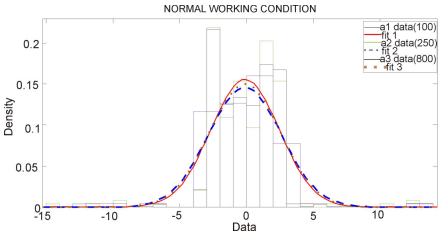

Fig. 2. *Analysis of different sample size (data)-function density for normal distribution*

4. Conclusions

Automotive makers are not published detailed engine onboard system for fault diagnosis. Complex algorithms for evaluation engine proper or improper work are secret, for reason of expensive development, researching and competition. It is known that engine revolution analysis is excellent tool for this purpose. Capability for capture real data in working conditions, and analyzing them with existing software (for example Matlab) in combination with simulating failures enabled possibility for education, scientific and other tasks. Measurement data (signal) can be analyzed, transformed, filtered, and combined with commercial software.

One of the key techniques used in this paper is the statistical techniques. A periodic nature of the engine rotational dynamics and a cycle-to-cycle variability allows the presentation of the engine signals as statistical signals utilizing such statistical variables as mean values and standard deviations. These statistical methods are the most future prospective methods for a new generation of robust engine functionality.

References

[1] U. Kiencke and L. Nielsen: Automotive Control Systems, For Engine, Driveline, and Vehicle, ISBN 3-540-23139-0.

[2] Alexander A. Stotsky: Automotive Engines, control, estimation, statistical detection, ISBN 978-3-642-00164-2, 2009

[3] T. Denton: Advanced Automotive Fault Diagnosis, ISBN-13: 978-0-75-066991-7.

[4] S.L. Kendal: An Introduction to Knowledge Engineering, ISBN 13: 978-1-84628-475-5.

[5] Allan W.M. Bonnick: Automotive computer controlled systems, ISBN 0 7506 5089 3.

30th DANUBIA-ADRIA
Symposium on Advances in Experimental Mechanics
September 25-28, 2013 - Primošten, Croatia

7A02 059

COMPARATIVE EXAMINATION OF THE MINING MACHINE OPERATOR PROTECTIVE STRUCTURE

Damian Derlukiewicz[1], Paulina Działak[1], Jacek Karliński[1]

[1] Wrocław University of Technology, Faculty of Mechanical Engineering, Institute of Machine Design and Operation, Lukasiewicza 7/9, 50-371 Wrocław, POLAND. E-mail: damian.derlukiewicz@pwr.wroc.pl; paulina.dzialak@pwr.wroc.pl; jacek.karlinski@pwr.wroc.pl;

1. Introduction

The main goal was to conduct comparative testing of the underground truck operator's compartment. The examination was made based on the computer simulation and experimental testing of the mining machine operator's protective structure. Computer simulations were conducted with the use of a finite element method in the range of dynamics, taking into consideration material and geometrical nonlinearity [2]. The experimental testing was taken by a competent certification unit INOVA – Technical Innovation Centre Ltd., within Lower Silesian Machine Factory ZANAM-LEGMET.

2. Examination methodology

The object of the studies was an operator's protective structure of the mining machine CB4_20TB (Fig. 1.)

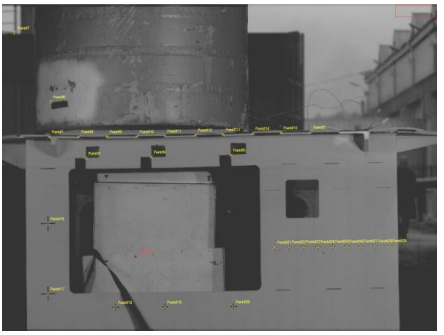

Fig. 1. Protective structure of the mining machine operator

Simulation included the strength test of the impact with the weight into protective structure according to norm PN-92/G-59001 (RSPS) „Self-propelled mining machines. Rock slide protective structures for operator – Requirements and Tests."[1]. Experiment was recorded with use of a specific camera for highly nonlinear transient dynamic phenomena (Fig. 2.).

Fig. 2. Camera PHANTOM V12

The picture was registered in a 800x600 dpi resolution, with the velocity of 11001 fps and with exposure time equal 91 μs.

All places, where the displacement measurement was taken (Fig. 1.) have the same location in case of the real and numerical model of the protective structure . This made the comparison of the results possible. The obtained picture was analysed to determine the values of the displacement and velocity from the specified test points. The picture analyses was performed using

the TEMA System. This was the base for carrying out the comparative tests.

The fundamental issue in this type of the studies is to determine the measuring error and precise its origin.

In order to perform the displacement measurement with the help of the photogrammetry, there was a necessity to execute a picture scaling at first (defining the number of the pixels per length unit). To do this, distance between two chosen points was measured (the longer distance the more accurate scaling is obtained). Precision of the points orientation on the recorded picture is conditional upon the method of their designation and brightness of the particular pixels [3,4].

The picture was registered in 255 shades of greyness. Minimal size of the point, where displacement measurement were taken, was 5 pixels. This was the base for determining the accuracy of the measurement, that equals 0.0007843 px. One pixel per 1.878 mm was obtained, so absolute error is equal 0.00147 mm.

Length of the section used for scaling is equal 0.9 m, what correspond to 478.74 pixels.

Generally, accuracy of the measurement is determined by the measuring error of the model section, equal in this case ± 1.5 mm (distance measurement was taken with the aid of the spring rule).

3. Results of the examination

Maximal absolute dynamic deflection obtained in the simulation was equal: f = 40.94 mm for t=15 ms. (Fig. 3.).

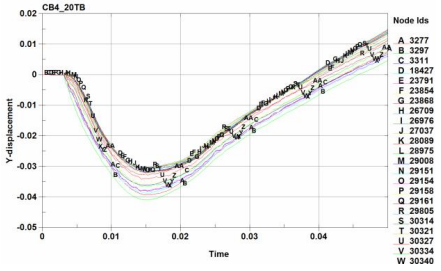

Fig. 3. Chart of the deflection values for specified points of the construction dependent on the time of the [mm-ms]

Figure 4 presents comparison of the deflection results received from numerical examination and the high-speed camera measurements, based on the picture analyses for the chosen point.

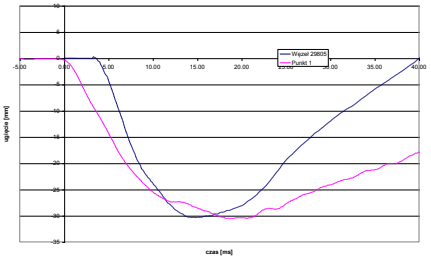

Fig. 4. Vertical displacement for the selected points of the protective structure (blue – computer simulation, pink – experiment)

4. Conclusion

- Performance of the displacement measurements during experimental testing with the aid of photogrammetry is very complicated and subjected to errors,
- While proper light conditions are maintained and adequately short exposure time and acuity is established, the error of the measurement is dependent on the measuring error of the model section distance,
- Proper choice of the shape and contrast of the test points is a substantial issue in this case.

Literature

[1] PN-92/G-59001 (RSPS) „Self-propelled mining machines. Rock slide protective structures for operator – Requirements and Tests."

[2] Derlukiewicz D., Karliński J., Iluk A., The Operator Protective Structures Testing for Mining Machines, Mechatronic Systems And Materials: Materials Production Technologies Book Series: Solid State Phenomena Volume: 165 Pages: 256-261., 2010

[3] Karlinski, J; Rusinski, E; Smolnicki, T. Protective structures for construction and mining machine operators, Automation In Construction Volume: 17 Issue: 3 Pages: 232-244 DOI: 10.1016/j.autcon.2007.05.008 Published: MAR 2008

[4] Karliński J.,Ptak M.,Działak P., Simulation tests of roll-over protection structure, Archives of Civil and Mechanical Engineering Volume 13, Issue 1, March 2013, Pages 57–63 DOI: 10.1016/j.acme.2012.12.001

30th DANUBIA-ADRIA
Symposium on Advances in Experimental Mechanics
September 25-28, 2013 - Primošten, Croatia

7A03 011

A SETUP PROCEDURE FOR A FLEXIBLE ROTOR/AMB SYSTEM WITH NON-COLLOCATION

Goranka Štimac[1], Sanjin Braut[1], Roberto Žigulić[1], Ante Skoblar[1]

[1] University of Rijeka, Faculty of Engineering, Vukovarska 58, HR-51000 Rijeka, CROATIA.
E-mails: gstimac@riteh.hr, sbraut@riteh.hr, zigulic@riteh.hr, askoblar@riteh.hr

1. Introduction

Contactless suspension of rotor dynamic systems is provided by means of active magnetic bearings (AMBs). Such systems offer many advantages over conventional bearings, such as no need for oil supply systems, absence of mechanical wear, lower maintenance costs etc. However, rotor/AMB systems are inherently unstable and require well tuned feedback control in order to ensure proper stabilization and required performance. Moreover, in a case of a flexible rotor, the dynamics of the rotor becomes significantly more complicated. One of the reasons is that, when the sensor and the actuator are non-collocated, there are always flexible modes with a zero vibrational displacement located between a sensor-actuator pair. If the frequencies of such modes lie within the bandwidth of the controller, then they represent a special problem on the stability of the system [1].

Current state-of-the-art in the control of AMB systems shows that PID controllers with associated filters are still the most widely used control strategy in industrial applications. The PID controllers ensure robustness in many applications but they can be implemented only as decentralized controllers which are not capable of addressing the non-collocation problems directly [2]. Moreover, this approach usually does not take into account the special requirements of complex rotor/AMB systems and therefore cannot guarantee their stability. To improve the efficiency of the controller and stabilize the system, notch filters need to be implemented.

A setup procedure for a flexible rotor/AMB system with non-collocation is presented in this paper. The system is controlled by four decentralized SISO controllers based on PID algorithm, each for one radial control axis (two per each AMB). Successful run up tests were carried out, which validated the efficiency of the presented procedure.

2. The setup procedure

Fig. 1 presents the mode shape of the first flexible mode of the rotor/AMB system. It is easily observed that this mode has a modal node lying between the sensor and the actuator axes. This implies that when the rotor vibrates with this mode shape at the corresponding natural frequency, the displacement measured by the sensor is out of phase with corresponding actuator.

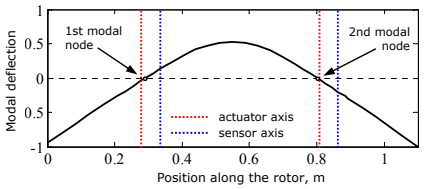

Fig. 1. Mode shape of the first flexible mode (related to the unstable rotor/AMB configuration)

In order to set up the rotor/AMB system and to resolve the system instability when the rotor passes the first critical speed, either advanced controller strategies (H_2, H_∞, μ-synthesis) should be implemented or, if PID control is applied, the mechanical components of the system should be adequately configured. For that purpose FE calculations are carried out in order to choose the locations of the discs and sensor/actuator positions along the rotor axis. A detailed modeling procedure of the rotor/AMB systems is presented in [3]. In accordance with the numerically selected configuration, the test rig is configured and assembled as shown in Fig. 2.

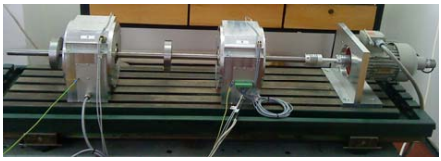

Fig. 2. Experimental test rig (from left to right): disk 1, radial AMB A, disk 2, radial AMB B, flexible coupling and electromotor

After placing the discs and AMBs at the proper locations along the rotor axis, the calibration of the inductive sensors of AMBs has to be carried out and the control system needs to be tuned. The controller parameters are determined based on an iterative approach. Moreover, the proper notch filter selection is of crucial importance for the stabilization of the higher order modes of the rotor, thus ensuring stable levitation. The frequencies of the notch filters, depending on the bearing, are set up to 10 Hz lower than the corresponding natural frequencies whose influence had to be eliminated. This means that the stabilization of the unstable modes is carried out by directly influencing the system phase, which is known as phase stabilization. Additionally, rotor balancing in two planes (for two discs) has been carried out.

3. Measurement results

The measured frequency responses from bearings AMB A and AMB B for the case of rotationless levitation are shown in Fig. 3 and Fig. 4. The location of the pole of the first flexible mode (peak) is located after the corresponding zero (valley) implying that the system can pass the first critical speed. The rotor was ran up to the speed of 6000 rpm during which the first critical speed (71,5 Hz) was passed.

Fig. 5 shows the lateral displacements of the disk 2 in the *y* direction, which proves the efficiency of the presented procedure.

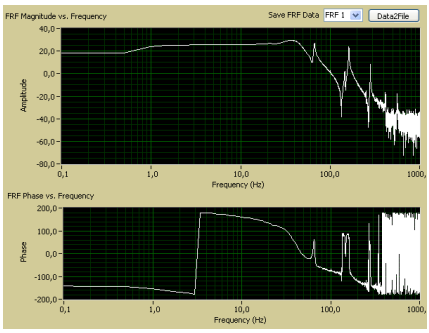

Fig. 3. Frequency response from the bearing AMB A

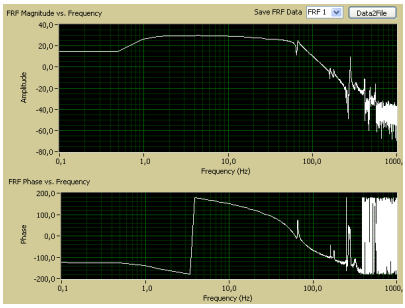

Fig. 4. Frequency response from the bearing AMB B

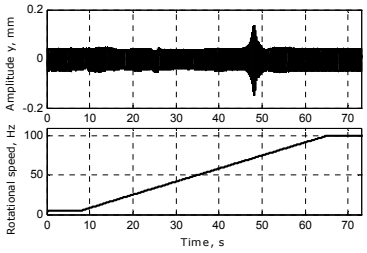

Fig. 5. Run up curve of lateral displacement in time domain (disc 2, *y*-direction)

4. Remarks

- In order to resolve the instability of the rotor/ AMB system with non-collocation, either advanced controllers should be implemented or the mechanical reconfiguration of the system should be adequately performed.
- Applying the proposed procedure, the stable performance of the rotor/AMB system was verified by experimental run up test using the PID control.

Acknowledgement

This work was supported by project IPA CBC /2nd/0127/AdriaHUB

References

[1] Schweitzer, G., et al, Magnetic Bearings: Theory, Design and Application to Rotating Machinery, Springer, 2009.

[2] Siegwart, R., Vischer, D., Larsonneur, R., Control concepts for active magnetic bearings, Proceedings of the 1st International Symposium on Magnetic Suspension Technology, Virginia, 1991, pp. 401-422.

[3] Štimac, G., Braut, S., Bulić, N., Žigulić, R., Modeling and Experimental Verification of a Flexible Rotor/AMB System, Special Issue of Compel, 2013. (in press)

30th DANUBIA-ADRIA
Symposium on Advances in Experimental Mechanics
September 25-28, 2013 - Primošten, Croatia

7A04 027

DYNAMICS OF THE VARIABLE MASS SYSTEM – EXPERIMENTAL AND NUMERICAL RESULTS

Tomasz Bartkowiak[1], Jakub Krzysztof Grabski[2], Jan Adam Kołodziej[2]

[1] Poznan University of Technology, Faculty of Mechanical Engineering and Management, Institute of Mechanical Technology, ul. Piotrowo 3, 60-965 Poznań, POLAND. E-mail: tomasz.bartkowiak@put.poznan.pl

[2] Poznan University of Technology, Faculty of Mechanical Engineering and Management, Institute of Applied Mechanics, ul. Jana Pawła II 24, 60-965 Poznań, POLAND. E-mails: jakub.grabski@doctorate.put.poznan.pl, jan.kolodziej@put.poznan.pl

1. Introduction

Dynamics of the variable mass systems has been received a lot of attention for many years. Some authors, in order to describe dynamics of the variable mass systems, used the Newton's second law in the form

$$\mathbf{F} = m(t)\frac{d\mathbf{v}}{dt} + \mathbf{v}\frac{dm(t)}{dt}, \qquad (1)$$

where **F** denotes the sum of the external forces acting on the particle of mass m, which moves at the velocity **v**. Plastino and Muzzio in [1] noticed that Eq. (1) is used erroneously in the case of an isotropic mass loss. They proposed to use the following form

$$m(t)\frac{d\mathbf{v}}{dt} = \mathbf{F} + \mathbf{u}\frac{dm(t)}{dt}, \qquad (2)$$

where **F** is the sum of the external forces, **v** is the velocity of the center of mass, m is the mass of the body and **u** is the relative velocity of the loss mass with respect to the center of mass of the body.

Nonetheless, in the literature publications where Eq. (1) is used for describing dynamics of a variable mass system still appear. The purpose of the paper is to propose the experiment, the results of which indicate that such approach to the mathematical description of variable mass system is wrong. The recommendable review article on the topic of variable mass systems was made by Irschik and Holl [2].

In the paper motion of the pendulum with variable mass was considered. The equation of motion was solved using fourth-order Runge-Kutta method. In addition, experimental and numerical results were compared.

2. Methods

In the paper we proposed to build the mathematical and physical model of the pendulum with variable mass consisting of the wire rope and the vessel with fluid. Two cases are studied: with and without reactive force.

2.1 Mathematical model

We proposed equation of motion for the pendulum with variable mass in the following form

$$I(t)\frac{d^2\varphi(t)}{dt^2} = M + M_r, \qquad (3)$$

where I denotes the moment of inertia, M is the moment of forces of the system and M_r is the moment of reactive force caused by the flow of the fluid out of the vessel. The moment of inertia of the system involves three elements (the moment of inertia of the fluid I_f, the moment of inertia of the vessel I_v and the moment of inertia of the wire rope I_l) and can be expressed by

$$I = I_f + I_v + I_l. \qquad (4)$$

The moment of forces of the system is represented by

$$M = M_{gf} + M_{gv} + M_{gl} + M_{Mv} + M_{Ml}, \qquad (5)$$

where M_{gf}, M_{gv} and M_{gl} denote the moments of the gravity – respectively of the fluid, the vessel and the wire rope; M_{Mv} and M_{Ml} are the moments of the

forces derived from Morisson equation – relevant for the vessel and the rope.

The equation of the motion in form (3) was solved using the fourth-order Runge-Kutta method.

The proposed model of pendulum and the fourth-order Runge-Kutta method was implemented in FORTRAN.

2.2 Test rig

In order to evaluate the presented mathematical model, test rig was designed and built (Fig. 1). The pendulum consists of steel rod which is wound around the ring. The oscillating mass is a vessel with the hole which the water flows through. The hole is located either on the side or the bottom of the vessel if cases with or without reactive are considered respectively. The ring rotates together with the mass and rope around the shaft. There is a ball bearing between the two elements in order to minimize the friction. The shaft is mounted firm on the frame.

Fig. 1. Test rig.

The angle of rotation is captured by the measurement system (Fig. 2) using rotary potentiometer.

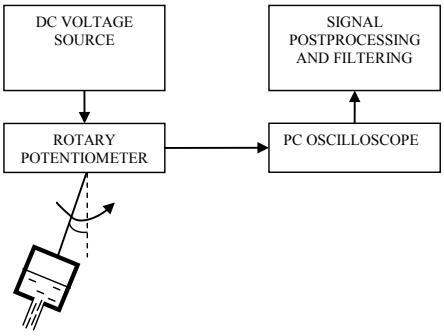

Fig. 2. Measurement system for measuring the dynamics of the variable mass system without reactive force.

3. Results

The numerical results were compared with experimental results.

3.1 Numerical results

The example results of the numerical experiment involving reactive force are presented in Fig. 3.

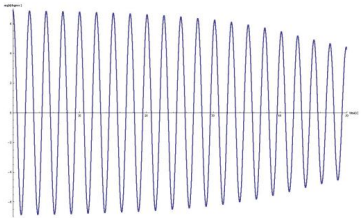

Fig. 3. Numerical results.

3.2 Experimental results

The example results of experiment involving reactive force are presented in Fig. 4.

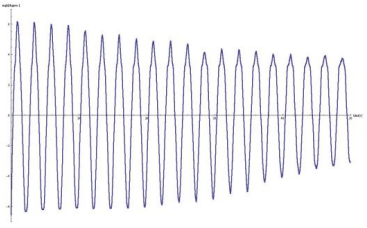

Fig. 4. Experimental results.

4. Remarks

- The amplitude of vibrations of the pendulum with variable mass declines faster than the amplitude of vibrations with constant mass.
- Numerical and experimental results present similar character of vibrations.

References

[1] Plastino, A.R., Muzzio, J.C., On the use and abuse of Newton's second law for variable mass problems, Celest. Mech. Dyn. Astron., **53**, 1992. pp. 227-232.

[2] Irschik, H., Holl, H.J., Mechanics of variable-mass systems-Part 1: Balance of mass and linear momentum, Appl. Mech. Rev., **57**, 2004. pp. 145-160.

30th DANUBIA-ADRIA
Symposium on Advances in Experimental Mechanics
September 25-28, 2013 - Primošten, Croatia

7A05 081

PROPERTY TESTING METHODOLOGY OF GEAR TRANSMISSION UNITS

Miloš Ristić[1], Milosav Ognjanović[1]

[1] University of Belgrade, Faculty of Mechanical Engineering, Kraljice Marije 16, 11000 Belgrade, SERBIA. E-mail: mristic@mas.bg.ac.rs, mognjanovic@mas.bg.ac.rs

1. Introduction

Increasing number and individualization of products force developers to develop products with predefined product behaviors. Product behavior is the result of product components properties and characteristics. Fig. 1 shows the V-model of gear drive unit design process obtained according to V-model in DIN-2206. Presented model includes application of various methods for design process realization, design parameters definition and indicators of gear unit's behavior indicators identification. All of these methods and procedures are based at experimental data. Without this data methodology can be useless. This contribution contains review of testing methods, procedures, features and characteristics which have to be tested and results involved in procedure in Fig.1.

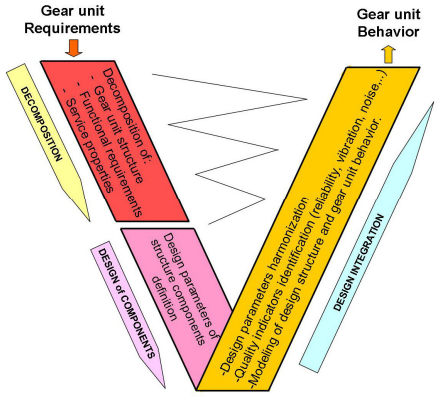

Fig. 1. V-model for gear units design

Gear transmission units are really a complex structure with various indicators of their behavior, such as the level of reliability, vibration and noise level, etc. These are result of properties and characteristics of components and machine parts. The property-based design methodology [1] needs precise definition of characteristics of material and characteristics and properties of parts and assemblies and their interaction in order to provide indicators of product behavior. In Fig.2 this interaction is presented for gear transmission unit using similar presentation in [1].

2. Parts properties testing

According to block diagram in Fig.2 the gear unit properties and gear unit behavior is predominantly the result of gear pairs and bearings properties and characteristics. Testing of these components can be specified as following.

- Testing of gear teeth surface fatigue endurance.
- Testing of gear teeth root fatigue endurance.
- Testing of gear teeth failure probability in relation of type of stress.
- Testing of load probability in exploitation (load spectrums).
- Testing of gear teeth geometry and effects of transmission errors at dynamic disturbances and vibration and noise generation.
- Testing of bearing load capacity and failure probability.

The most common is separate testing of presented properties. Also interaction is also very interesting for experimental research and failure process propagation [2]. Testing methodology is also wide area. For gear fatigue testing is common to apply FZG power circulation system [3]. For testing of teeth geometry imperfection are developed various methods including optical ones [4]. For vibration and noise testing [5, 6] are applicable closed and opens systems of power circulation with specific systems for measurement and data processing.

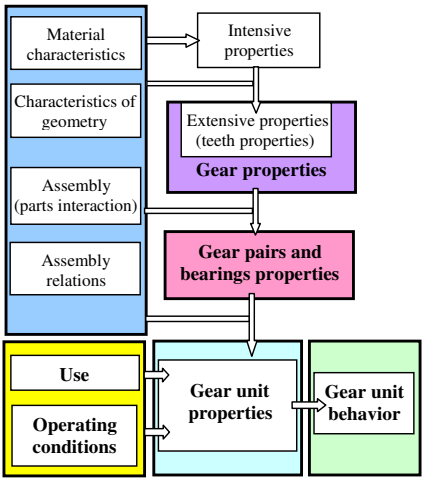

Fig. 2. Gear unit behavior based on characteristics and properties

3. Assembly properties testing

Gear unit examination includes observation of key parameters which describe gear unit behavior, such are reliability, vibrations, noise and gear unit heating. Material and geometry characteristics and gear pair and bearings properties affect a lot at gear unit behavior indicators.

Reliability of gear unit could be calculated based on components reliabilities. To obtain necessary data for calculations, it is usually performed testing by means of fatigue testing machines [7]. Also it is necessary to proof some of calculated results by reliability testing of complete gear unit. In combination with calculation this methodology is accelerated approach for gear unit identification.

Vibrations of the gear unit contains analysis of disturbance processes in gear and bearing assemblies and modal analysis and testing of gear unit housing modal behavior. Measuring and analysis of vibrations and noise is also complex area of gear units behavior testing, analysis and synthesis of various effects [8].

There is variety of method to obtain the temperature conditions of the gear unit. Analysis of heat sources inside of gear units (gear teeth meshes and bearings) including heat emission in surrounding is very important theoretical and experimental task. Various methodologies for local temperature testing inside of unit, oil temperature measurement, etc is available.

4. Conclusions

This contribution contains review of various methodologies, especially methodologies applied and developed by authors, for gear units and gear units components testing. This methods, properties and behavior indicators as the testing results are incorporated in models for gear units' development using actual trends in the area of product development.

Acknowledgements

This article is a contribution to the Ministry of Education and Science of Serbia funded project TR 035006.

References

[1] Krehmer H., Meerkamm H., Wartzack S., Monitoring a Property Based Product Development – From Requirements to a Mature Product, eProceedings of the 18th International Conference on Engineering Design 2011 (ICED11), Denmark, 2011.

[2] Lia C. J., Lee H., Gear fatigue crack prognosis using embedded model, gear dynamic model and fracture mechanics, Mechanical Systems and Signal Processing 19, 2005, pp 836–846.

[3] Aslantas K., Tasgetiren S., A study of spur gear pitting formation and life prediction, Wear 257, 2004, pp 1167–1175.

[4] Okuyama E., Kiyono S., Moritoki H., Investigation of an optical noncontact gear geometry measurement system: measurement of pitch errors and tooth profiles, Precision Engineering, April 1994, Vol. 16 No 2, pp 117-123.

[5] Mcfadden P. D., Cook J. G., Forster L. M., Decomposition of gear vibration signals by the generalised s transform, Mechanical Systems and Signal Processing, 1999, 13(5), pp 691-707.

[6] Belšak A., Prezelj J., Visualisation and analysis of noise sources of a gear unit, Engineering Failure Analysis 16, 2009, pp 1570–1578.

[7] Yang Q.J., Fatigue test and reliability design of gears, International Journal of Fatigue, 1996, Vol. 18, No. 3, pp. 171-177.

[8] Ćirić-Kostić S., Ognjanović M., The Noise Structure of Gear Transmission Units and the Role of Gearbox Walls, FME Transactions, 2007, Vol. 35, pp 105-112.

30th DANUBIA-ADRIA
Symposium on Advances in Experimental Mechanics
September 25-28, 2013 - Primošten, Croatia

7A06 105

AN EXPERIMENTAL DESIGNATION OF STRUCTURAL DAMPING COEFFICIENT OF ONE-DIMENSIONAL VIBRATING SYSTEMS

Marek Płaczek[1]

[1] Silesian University of Technology, Faculty of Mechanical Engineering, Institute of Engineering Processes Automation and Integrated Manufacturing Systems, Konarskiego 18A, 44-100 Gliwice, POLAND. E-mail: marek.placzek@polsl.pl

1. Introduction

Work presents results of an experimental designation of structural damping coefficient of one-dimensional, flexural vibrating mechanical system. Obtained results are juxtaposed with results of analytical methods of the considered system's analysis presented for example in [1-3]. In order to verify calculated characteristics of mechanical subsystems and mechatronic system with piezoelectric transducers used as passive vibration dampers or actuators it was necessary to carry out the experiment tests [1-4]. Only the part concerned with verification of assumed value of structural damping coefficient of the mechanical subsystem is presented in this paper. A laboratory stand was designed and build to carry out the test. The mechanical subsystem of mechatronic systems (a cantilever beam made of steel) was tested. Obtained results were juxtaposed.

2. Experimental and theoretical analysis of the system

The considered system is a cantilever bending beam that is excited by the externally applied harmonic force that operates on the free end of the beam, perpendicularly to the beam's axis. Strain of the beam's surface is measured using strain-gauges and the beam's deflection is calculated. The experimental test is realized on the designed and build laboratory stand with possibility to generate an electromechanical excitation of the beam with required frequency. Elements of the laboratory stand are presented in Fig. 1. It consists of:

- generator of signals with required frequency,
- laboratory power supply,
- electromagnetic inductors,
- structure with the possibility of mounting the tested piece,
- measuring amplifier MGCplus for strain gauge testing.

Fig. 1. The laboratory stand.

The excitation frequency is set to the value of calculated natural frequencies of the analysed mechanical system. Externally applied force is generated by a pair of electromagnetic inductors – see Fig. 2.

Fig. 2. A pair of electromagnetic inductors used for excitation of the analysed system.

The experimental works are realized parallel to the process of mathematical analysis of the flexural vibrating mechanical system using an approximate method. A dynamic flexibility of the considered cantilever beam was calculated using the Galerkin method. In this method a solution of the differential equation of motion is assumed as [1-3]:

$$y(x,t)=\sum_{n=1}^{\infty}\sin(k_n x)\cos(\omega t), \qquad (1)$$

where:

$$k_n=(2n-1)\frac{\pi}{2l}, \quad n=1,2,3... \qquad (2)$$

in agreement with boundary conditions of the considered beam.

A structural damping of vibration is being taking into consideration in mathematical model of the system using a Kelvin-Voigt model of the beam's material. It was introduced using a substitute Young's modulus of the beam E_b^* described by the equation [5]:

$$E_b^*=E_b\left(1+\eta_b\frac{\partial}{\partial t}\right), \qquad (3)$$

where η_b denotes structural damping coefficient of the beam. It was assumed as:

$$\eta_b=8\cdot10^{-5}[s]. \qquad (4)$$

Results obtained using the approximate Galerkin method are presented in Fig. 3. It is dynamic flexibility of the analysed beam presented on chart in a half logarithmic scale for the first three natural frequencies of the system.

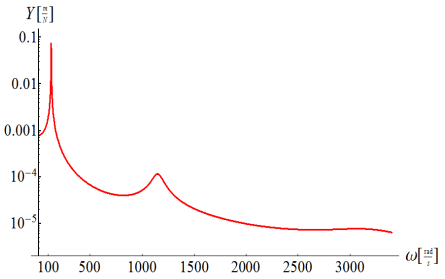

Fig. 3. Obtained dynamic flexibility of mechanical subsystem – analytical method

Introduction of the substitute Young's modulus causes that the assigned dynamic flexibility have limited values in resonance zones of the considered system. In the first step the value of the structural damping of the beam was assumed (based on literature review) in order to generate obtained characteristic of the system. In the next step, value of the structural damping coefficient was calculated on the basis of the experimental test. The true value of the coefficient was calculated taking into account values of the harmonic force applied to the system and its deflection. Obtained value was consistent with the value assumed in earlier calculations.

3. Conclusion

Knowing of the structural damping coefficient value is necessary to verify results of mechatronic systems analysis that was presented in the other author's works and to make the analysis more precise [1-3]. In those works systems with piezoelectric transducers used as passive vibration dampers were analysed and their dynamic flexibility was calculated. Obtained results were juxtaposed with the dynamic flexibility of the mechanical subsystem in order to verify efficiency of the piezoelectric shunt damping of vibrations.

Acknowledgements

Work supported by Polish Ministry of Science and Higher Education - National Science Centre - research project No. N501 064440 (2011-2013).

References

[1] Buchacz A., Płaczek M., Damping of Mechanical Vibrations Using Piezoelements, Including Influence of Connection Layer's Properties on the Dynamic Characteristic, Solid State Phenomena Vols. 147-149 (2009), pp. 869-875.

[2] Buchacz A., Płaczek M., The analysis of a composite beam with piezoelectric actuator based on the approximate method, Journal of Vibroengineering, Vol. 14, Issue 1 (2012), pp. 111-116,

[3] Buchacz A., Płaczek M., Wróbel A., Control of characteristics of mechatronic systems using piezoelectric materials, Journal of Theoretical and Applied Mechanics, Vol. 51 (2013), pp. 225-234.

[4] Hagood N. W., von Flotow A., Damping of structural vibrations with piezoelectric materials and passive electric networks, Journal of Sound and Vibration, Vol. 146(2) (1991), pp. 243-268.

[5] Pietrzakowski M., Active damping of beams by piezoelectric system: effects of bonding layer properties, International Journal of Solids and Structures, Vol. 38 (2001), pp. 7885-7897.

30th DANUBIA-ADRIA
Symposium on Advances in Experimental Mechanics
September 25-28, 2013 - Primošten, Croatia

7A07 106

RELIABLE MODEL OF MAXIMUM WIND LOAD AMPLITUDE

Predrag Đukić[1], Jani Barle[2], Vatroslav Grubišić[3], Dario Ban[2]

[1] University of Split, Department of Professional Studies, Livanjska 5, HR-21000 Split, Croatia. E-mail: pdukic@oss.unist.hr

[2] University of Split, Faculty of Electrical Engineering, Mechanical Engineering and Naval Architecture, R. Boškovića 32, HR-21000 Split, Croatia. E-mail: barle@fesb.hr ; darioban@fesb.hr

[3] Technical Consulting, 64354 Reinheim, Germany. E-mail: vatro.grubisic@gmx.de

1. Introduction

A lot of projects like serially built wind turbines or telecommunication towers are in a design or building phase. At the same time wind properties and intensity data at various locations of development projects are more and more available due to pre-building prospecting coverage. Still, even with data at hand main difficulty is how to obtain reliable structure load estimation. Procedure in [1] which establishes wind-to-load relationship uses a great number of heuristic parameters. Among those, the most important and basic parameter for the determination of wind actions on a structure is characteristic 10-minute mean wind velocity, irrespective of wind direction or season at 10 m above ground level on a terrain category II.

In the Fig. 1a there is a Bura wind speed distribution of an epoch. Record consists of one second samples for the duration of 6h 27min with maximum speed of v_{max} = 23.4 m/s. Wind was measured simultaneously on top of a 40 meter free standing telecomunication lattice tower and resulting bending moment in a foot of it, Fig. 1b. Similarity of the two patterns is high, leading to the question: How to establish a model of maximum bending moment amplitudes founded on maximum 10-minute wind speed. Method in [1], is to take average 10 minute windspeed and turbulence intensity, and then using tables or other suggestions from [1], calculate probable effects. The problem is that range of values in tables is very wide, and suggestions subject to designers personal opinion. Even then, [1] points to rarely available national annexes, or reccomends measurements.

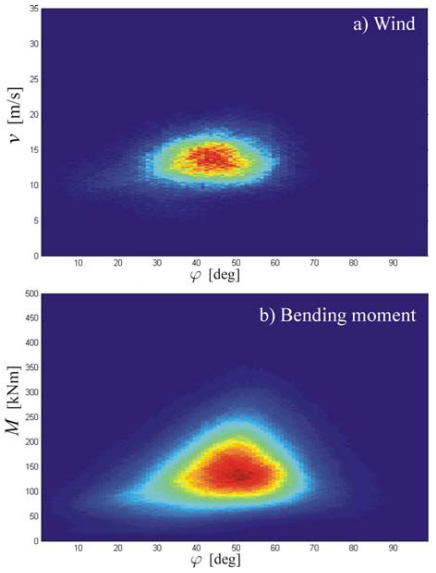

Fig. 1. Wind speed and bending moment spread of a Bura epoch.

2. Description of exprimental work

Experimental work which is source of real field data used here is a result of a project involving instrumentation and long term monitoring (1yr.+) of a telecommunication tower as described in details in [2]. From a collection of data, one 2.5 days epoch of Bura was chosen, segmented in series of 10-minute intervals, binned according to the maximum speed and then processed to get example spectra in Fig. 2. In Fig 2a there are 64

10-minute load spectra with maximum speed of 14-16 m/s and in Figure 2b 33 10-minute spectra with maximum speed of 18-20 m/s.

Figures clearly show considerable spread, graphed with *pdf* curves. Main task is establishing a direct link between maximum moment and maximum wind speed.

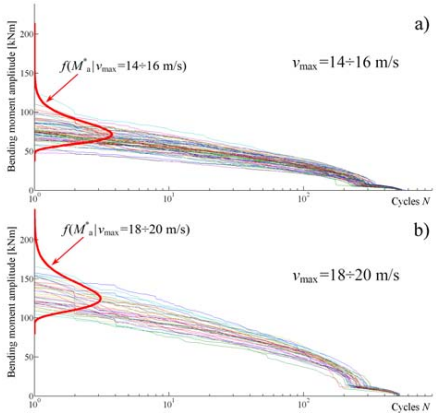

Fig. 2. Spectra of 10-min segments binned according to maximum wind speed.

3. Estimation of maximum bending moment amplitude

Analysis of M^*_a according to the Gumbel distribution,

$$f\left(M^*_a\right) = \frac{1}{\delta} exp\left[\frac{\lambda - M^*_a}{\delta} - exp\left(\frac{\lambda - M^*_a}{\delta}\right)\right], \quad (1)$$

is shown by Gumbel probability plots, Fig. 3. Every bin yields a pair of distribution parameters λ and δ. Further parameters p and q according to Eq. (2), introduce covariate v_{max} into the model Eq. (1).

$$\lambda = p{v_{max}}^2, \; \delta = q{v_{max}}^2, \quad (2)$$

In this example, parameters p and q are calculated by regression analysis (p=0.327, q= 0.0384) after which Eq. (1) changes form to $f(M^*_a|v_{max})$.

Resulting model as depicted in Fig. 4, show very good agreement between regression and empirical data.

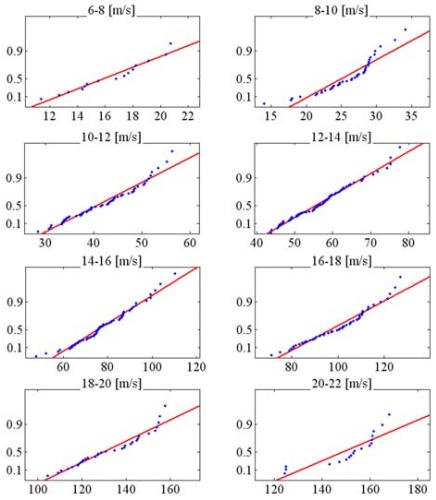

Fig. 3. Gumbel probability plots of M^*_a binned by v_{max}.

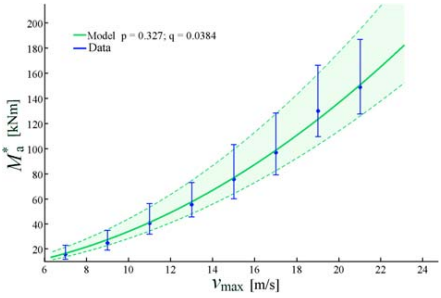

Fig. 4. Estimated and mesured bending moments vs max wind speed.

4. Conclusion

Here presented model matches closely with measured data. Therefore it is possible to estimate the bending moment to which the tower is subjected. Since model also follows stochastic nature of the process, extrapolation of standard 10-minute amplitudes to longer intervals up to the whole epoch duration of several hours is possible.

References

[1] European Committee for Standardization (CEN). Eurocode 1: Actions on structures – General actions Part 1-4: Wind Actions EN 1991-1-4, 2005.

[2] Dukic P.: Development of a Reduced Testing Method for Wind Loaded Line-like Structures, PhD thesis, Split, 2012.

7A08 012

SENSITIVITY OF THE MODAL DAMPING MEASUREMENT ON THE VIBRATION TESTING PROCEDURE

Ivan Tomac, Željan Lozina, Damir Sedlar

University of Split, Faculty of Electrical Engineering, Mechanical Engineering and Naval Architecture, Ruđera Boškovića 32, HR-21000 Split, CROATIA. E-mail: *ivan.tomac@fesb.hr*.

1. Introduction

Modal parameters are dynamical characteristic of mechanical system. They are: undamped natural frequencies, relative damping coefficients and mode shapes [1]. The modal parameters can be used for the assessment of structure condition [2]. In order to measure modal parameters, structure is exited: by an impact hammer, by a shaker, by ambient excitation [3], etc. In this paper we test sensitivity of modal damping to two different excitation methods: with a hammer and an electromagnetic shaker involving certain excitation strategy. Modal parameters from the IRFs are extracted using the continuous Wavelet Transform (WT) with Gabor Wavelet Function.

2. IRF measurement procedure

The test structure has two emphasized masses where accelerometers are applied.

For the measurement following equipment is used: 24bit – NI PXI-4472B data acquisition card, LabView measurement software. The H2 method was used in order to calculate IRFs. MMF type KS95B100 accelerometers are used.

2.1 Excitation procedure and equipment

The B&K impact hammer type 8206-001 with a rubber tip was used. Five measurements were acquired by exciting the second mass with sampling frequency f_s=1 kHz measuring collecting 8192 samples. WT of the second mass IRF is shown in Fig. .

Second set of measurements were acquired using the electromagnetic shaker TIRA S50009. Shaker was freely hanged and attached to the second mass through piezoelectric force sensor MMF type KF24 via thin stinger. System is excited with sine sweep in the frequency range 10-64Hz with duration of 8 s. Ten measurements were acquired with a sampling frequency of f_s=1024 Hz measuring 8192 samples. WT of the second mass IRF is shown in figure Fig. .

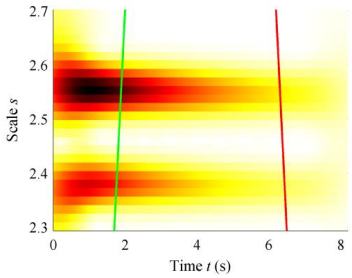

Fig. 1 WT of the second mass IRF, 5 averages

Signals were acquired with a sampling

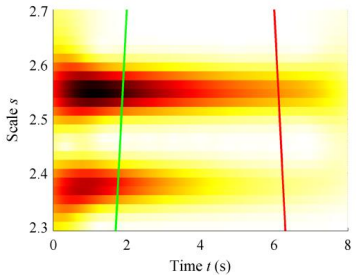

Fig. 2 WT of the second mass IRF, 10 averages

In order to have a better frequency resolution a longer duration of each measurement is required. So third set of measurements were acquired with 32768 samples leaving frequency range unchanged, but duration is set on 32 s. WT of the second mass IRF is shown in figure Fig.

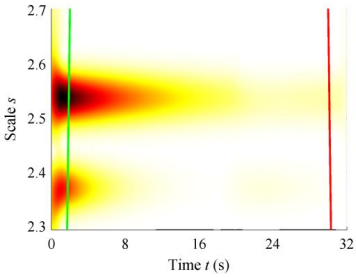

Fig. 3 WT of m_2 IRF, 10 averages, enhanced resolution

3. Identification results

Using the two different types of methods natural frequencies and relative damping coefficients are extracted from the calculated IRFs. Results are shown in tables 1-3.

	AV	f_1 [Hz]	ζ_1 [10^{-3}]	f_2 [Hz]	ζ_2 [10^{-3}]
Cross Section	1	19.69	2.00	21.12	1.96
	2	19.68	2.14	21.12	2.00
	3	19.68	2.11	21.11	2.00
	4	19.68	2.11	21.11	2.04
	5	19.67	2.16	21.11	2.10
Phase	1	19.68	1.38	21.12	1.31
	2	19.68	1.74	21.11	1.75
	3	19.68	1.79	21.11	1.86
	4	19.67	1.82	21.11	1.91
	5	19.67	1.82	21.11	1.94

Tab. 1 Identification results using an impact hammer as a source of the excitation. f_s=1000 Hz, N=8192 S

Modal parameters are extracted from the IRFs calculated with increasing number of averaged measurements.

	AV	f_1 [Hz]	ζ_1 [10^{-3}]	f_2 [Hz]	ζ_2 [10^{-3}]
Cross Section	1	19.66	1.53	21.1	2.68
	2	19.66	1.55	21.1	2.66
	4	19.66	1.54	21.1	2.67
	6	19.66	1.52	21.1	2.67
	8	19.66	1.49	21.1	2.63
	10	19.66	1.48	21.1	2.65
Phase	1	19.66	1.60	21.1	2.42
	2	19.66	1.60	21.1	2.56
	4	19.66	1.62	21.09	2.47
	6	19.66	1.60	21.1	2.60
	8	19.66	1.58	21.1	2.78
	10	19.661	1.59	21.1	2.62

Tab. 2 Identification results using an electromagnetic shaker as a source of excitation. f_s=1024 Hz, N=8192 S

Results show that with the increased number of averaged measurements relative damping coefficient is changing slightly. Natural frequencies are not affected.

	AV	f_1 [Hz]	ζ_1 [10^{-3}]	f_2 [Hz]	ζ_2 [10^{-3}]
Cross Section	1	19.76	1.07	21.09	2.24
	2	19.71	0.874	21.09	2.23
	4	19.71	0.874	21.09	2.30
	6	19.71	0.838	21.09	2.25
	8	19.71	0.811	21.08	2.35
	10	19.71	0.821	21.09	2.30
Phase	1	19.76	0.959	21.1	2.04
	2	19.71	0.862	21.09	2.09
	4	19.71	0.854	21.09	2.12
	6	19.71	0.829	21.09	2.13
	8	19.71	0.819	21.09	2.03
	10	19.7	0.821	21.09	2.06

Tab. 3 Identification results using an EM shaker with enhanced number of samples. f_s=1024 Hz, N=32768 S

With different excitation method a change in identified relative damping coefficient can be noticed.

4. Conclusion

Two excitation methods were used and three sets of measurements were acquired. IRFs were averaged increasing the number of measurements involved. The identification showed a discrepancy in the identified relative damping coefficients. This observed sensitivity should be reduced with the recommended procedures.

Acknowledgements

This work is supported in part by the Croatian Ministry of Science, Education and Sports, project number 023-0231744-1747, Inverse Procedures and Advanced Algorithms in Dynamics of Structures and Machine.

References

[1] D.J. Ewins, Modal Testing, Theory, Practice and Application. Research Studies Press, 2000.

[2] Sedlar, D., Lozina, Ž., Vučina, D., An implementation of structural change detection procedure based on experimental and numerical model correlation, Journal Of Sound And Vibration, **331**, 2012, pp. 3068-3082

[3] Le, T.P., Paultre, P., Modal identification based on continuous wavelet transform and ambient excitation tests, Journal of Sound and Vibration, **331**, 2012, pp. 2023-2037

30th DANUBIA-ADRIA
Symposium on Advances in Experimental Mechanics
September 25-28, 2013 - Primošten, Croatia

7A09 062

MODE COUPLING IN MULTI-CUTTER TURNING: SIMULATION AND EXPERIMENTS

Marta J Reith[1], Daniel Bachrathy[2], Gabor Stepan[3]

[1] Budapest University of Technology and Economics, Department of Applied Mechanics, Muegyetem rkp. 5., Budapest, HUNGARY. E-mail: reith@mm.bme.hu

[2] HAS-BUTE, Research Group on Dynamics of Vehicles and Machines, Hungarian Academy of Sciences, Muegyetem rkp. 5., Budapest, HUNGARY. E-mail: bachrathy@mm.bme.hu

[3] Budapest University of Technology and Economics, Department of Applied Mechanics, Muegyetem rkp. 5., Budapest, HUNGARY. E-mail: stepan@mm.bme.hu

1. Introduction

Manufacturing industry is facing a hard task, namely to increase accuracy and productivity simultaneously. Multi-cutter turning systems represent an excellent solution for the given problem, since they offer high material removal rates and ensure high feasible accuracy at the same time.

2. Theoretical background

Dynamics of turning operations, where more than one tool is cutting the same surface, can with reason be considered peculiar. If one takes into account the existing different coupling effects between the tools, the governing equation of motion will be intricate. In case the tools are cutting the same surface, a special form of coupling occurs, namely coupling via the regenerative effect. Investigation of this effect for one tool has a long history [1, 2]. Since the instantaneous value of the chip thickness is not only influenced by the instantaneous, but also by the previous tool displacement, the cutters are coupled through a delayed states. Beforehand, the corresponding theoretical model has been derived by the authors. Another way of coupling may also exist via the dynamics of the machine tool, since the two cutters are clamped in the same tool holder or at least in the same turret. This latter type of coupling is usually neglected [3].

2.1 Idealized multi-cutter turning system

Considering an idealized case, which is based on the fact, that the fixture is assumed to be much stiffer than the tools, the multi cutter turning system including n number of tools can be modeled by a minimum of n degree-of-freedom system. The corresponding equation of motion is assumed in the following form [4]:

$$M\ddot{x} + C\dot{x} + \mathrm{K}x = F_f, \tag{1}$$

where the vector $\mathbf{x} = [x_1\, x_2 \ldots x_i \ldots x_n]^{\mathrm{T}}$ contains the coordinates each of them representing the motion of a cutter in feed direction, **M** is the mass matrix, **C** is the damping matrix, **K** is the stiffness matrix. **M**, **C** and **K** are diagonal, containing mass, stiffness and damping of the tools respectively and $\mathbf{F}_{\mathrm{f}}$ is the feed cutting force.

2.2 Extended mathematical model for the multi-cutter turning system

Measurements have shown, that even when the tools are fixed into different tool holders with symmetric fixture, but in the same turret, the vibrations from one tool are transferred to the other tools via tool coupling. Thus the effect of the second type coupling through the physical contact of the fixture cannot be neglected. To improve the idealized mechanical model it can be extended by one additional degree of freedom representing the stiff fixture. The equation of motion is assumed in the same form as in the idealized case (see Eq. 1), but the matrices **M**, **C** and **K** have an extended size and structure. As a simple example, the system matrices for a multi-cutter turning system including two cutters can be written in the following forms:

$$M = \begin{matrix} m_1 & 0 & 0 \\ 0 & m_2 & 0 \\ 0 & 0 & M_3 \end{matrix}, \quad (2)$$

$$C = \begin{matrix} c_1 & 0 & -c_1 \\ 0 & c_2 & -c_2 \\ -c_1 & -c_2 & c_1+c_2+C_3 \end{matrix}, \quad (3)$$

$$K = \begin{matrix} k_1 & 0 & -k_1 \\ 0 & k_2 & -k_2 \\ -k_1 & -k_2 & k_1+k_2+K_3 \end{matrix}, \quad (4)$$

where c_1, c_2 are the damping coefficients, k_1, k_2 are the stiffness values and m_1, m_2 represent the modal mass of the two tools respectively. M_3, C_3 and K_3 represent the dynamical properties of the fixture, in which the tools are clamped in (see Figure 1).

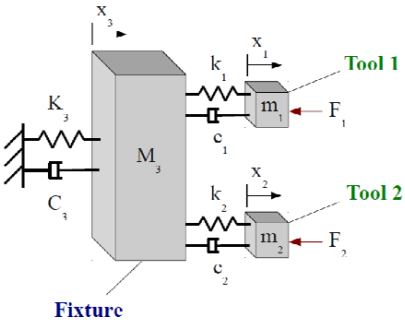

Fig. 1. Improved mechanical model of multi-cutter turning system

3. Methods

Numerical simulation and experimental investigation have been carried out to examine the different coupling effects. Furthermore, the simple mechanical model considering only tool coupling via the regenerative effect has been improved by taking into consideration the effect of the fixture represented by an additional degree-of-freedom.

4. Results

It is shown that the symmetric idealized system has qualitatively different mode shapes than the extended one. This system behaves differently compared to the idealized case - computed mode shapes are also completely different than the measured ones - due to the appearance of a beating phenomenon.

5. Remarks

- One might think that the theoretically computed mode shapes are completely different than the measured ones.
- The influence of this model modification on the stability properties of the cutting process is to be analyzed.

6. Acknowledgements

The academic and development work presented in this study has been developed within the framework of project "Talent care and cultivation in the scientific workshops of BME (Budapest University of Technology)". This project is supported by the grant TAMOP-4.2.2.B-10/1-2010-0009 and was also supported by the Hungarian National Science Foundation under grant no. OTKA K101714.

7. References

[1] Tobias, S.A. and Fishwick, W., The Chatter of Lathe Tools Under Orthogonal Cutting Conditions, Trans. of ASME, 1958. 80:1079-1088

[2] Tlusty, J., Polacek, M., The Stability of Machine Tools Against Self Excited Vibrations in Machining, Int. Research in Production Engineering, ASME, 1963. pp. 465 – 474.

[3] Ozturk E., Budak E, Modeling Dynamics of Parallel Turning Operations, Proceedings of 4th CIRP International Conference on High Performance Cutting, 2010.

[4] Stepan, G., Retarded dynamical systems, Longman Scientific & Technical, New York, 1989.

30th DANUBIA-ADRIA
Symposium on Advances in Experimental Mechanics
September 25-28, 2013 - Primošten, Croatia

7A10 006

ESTIMATION OF OVERHEAD TRANSMISSION LINE AEOLIAN VIBRATIONS

Hinko Wolf[1], Damir Semenski[1], Saša Korošić[1]

[1] University of Zagreb, Faculty of Mechanical Engineering and Naval Architecture, Ivana Lučića 5, HR-10000 Zagreb, CROATIA. E-mail: hwolf@fsb.hr

1. Introduction

Aeolian vibrations of overhead transmission line conductors are usually noticed at frequencies 5-100 Hz. These vibrations can cause the damage and breaking of the conductor due to material fatigue, and can significantly shorten its lifetime.

Very large differences among the numerical results obtained by different computational programs are frequently observed [1]. Two main reasons were identified for the large differences among the results. First, the aforementioned programs are based on several different models, i.e. different assumptions that are built into the models. Second, these programs use data from different sources that can differ significantly (wind power, data on the damper's mechanical impedance, mechanical characteristics of the conductor) [2].

Overhead transmission line Aeolian vibrations are in practice commonly estimated by using the Energy balance method (EBM) [1, 3] and the Modified energy balance method with using eigenfunctions (MEBM) [4]. In order to examine the accuracy of the developed computational programs, based on EBM and MEBM, as well as correctness of the estimation of the data used, results generated using the developed computer programs and data from field measurements using device VIBREC^{TM} 400 are compared in this paper.

2. Numerical methods

An overhead transmission line conductor is modeled here as an ideal taut string. All resonant frequencies of the string vibration model (without mounted dampers) are integer multiples of the resonant frequency corresponding to the first mode shape, which is of the order of magnitude of 0.1 Hz.

2.1 Energy balance method (EBM)

By using EBM relatively dense discrete spectrum of a conductor with Stockbridge-type vibration damper is approximated by the continuous spectrum of a semi-definite conductor. In that way the conductor vibration amplitude A can be simply determined using the non-linear algebraic equation for any given frequency without determining the natural frequencies and mode shapes

$$P_W(A) = P_D(A) + P_C(A). \tag{1}$$

$P_W(A)$ is the power of aerodynamic forces brought into the system, $P_D(A)$ is the power dissipated by the vibration damper, while $P_C(A)$ is the power dissipated by the conductor due to conductor self-damping.

2.2 Modified energy balance method with using eigenfunctions (MEBM)

From the boundary conditions at both ends of the each subspan, and from the force equilibrium at the clamps of the line fittings, one obtains a set of equations that leads to the eigenvalue problem. The spectrum of this eigenvalue problem is very dense and its numerical solution presents considerable numerical problem. After the complex eigenmodes are determined, one can formulate the energy balance by equating the wind power input over the whole span to the power disipated in all Stockbridge dampers and the power disipated in the cable due to cable's self-damping

$$\sum_{i=1}^{N+1} P_{Wi}(A_{\max}) = \sum_{i=1}^{N} P_{Di}(A_{\max}) + \sum_{i=1}^{N+1} P_{Ci}(A_{\max}). \tag{2}$$

$A_{\max}$ is here the variable to be determined by scaling the vibration amplitudes.

3. Field measurements

Field measurements of Aeolian vibrations are performed by vibration recorder VIBREC™ 400. Within the device, there is a microprocessor that records amplitudes, frequencies, wind velocity and surrounding temperature. A characteristic position of the VIBREC™ 400 is shown in Figure 1. The so-called Poffenberger-Swart formula [5]

$$\sigma_b = K_{pf}\, Y_b\,, \tag{3}$$

relates the stress in outer cable layer at the last point of contact between conductor and clamp (σ_b) and the measured shift of the cable Y_b (the so-called bending amplitude) at a certain distance c from the clamp edge. K_{pf} is the conversion factor that depends only on the characteristics of the conductor, conductor tension and the distance of the displacement transducer to the supporting clamp edge.

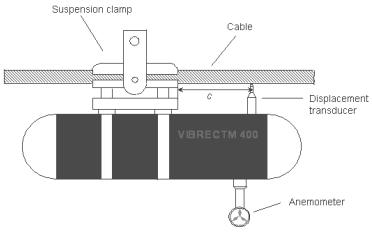

Fig. 1. Vibration recorder VIBREC™ 400.

Given the memory capacity limitations of the measurement device, the device doesn't record the amplitude and frequency of each observed vibration. Given the amplitude and frequency of each vibration, the observed data is classified into the appropriate class of the frequency-amplitude matrix. Each class encompasses an interval of frequencies and amplitudes.

4. Results

Results generated using the developed computer programs and data from field measurements are compared in Fig 2 (OPGW 18,1 mm, span length 425 m, 12 % UTS, Stockbridge damper position at 0.55 m from each suspension clamp). Classes of the frequency-amplitude matrix are shown in Fig. 2 with rectangles. Number inside the rectangle indicates the number of registered vibration cycles within the appropriate class of the frequency-amplitude matrix. Measurements of the span vibrations were conducted for 29 days. The measuring device was activated every 15 minutes and gathered data for 10 s. The total device working time was 7.63 hours.

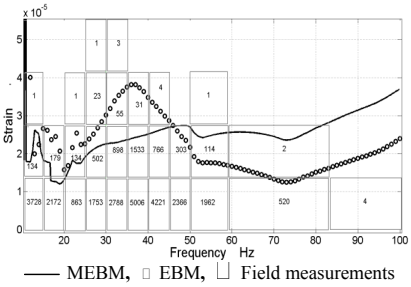

Fig. 2. Comparison of numerical results (EBM, MEBM) and data from field measurements.

5. Remarks

- A very high correlation between the measured field data and the data generated with the developed computer programs (EBM and MEBM) has been obtained.
- At several frequencies the measured vibration amplitudes are larger than those generated by developed computer programs. It should be noted that vibrations with these large amplitudes are very rare.

Acknowledgements

This work was supported by the National Science Foundation Grant No. 120-0362321-2198.

The data was collected using Dalekovod d.d. equipment and resources.

References

[1] CIGRE TF B2.11.01, Modelling of Aeolian Vibrations of a Single Conductor Plus Damper: Assessment of Technology, Electra **223**, 2005. pp. 28-36.

[2] CIGRE TF 22.11.1, Modeling of Aeolian Vibration of Single Conductors: Assessment of the Technology, Electra **181**, 1998. pp. 53-68.

[3] Hagedorn, P., Wind-Excited Vibrations of Transmission Lines: a Comparison of Different Mathematical Models, Mathematical Modeling **8**, 1987. pp. 352-358.

[4] Hagedorn, P., Mitra, N., Hadulla, T., Vortex-Excited Vibrations in Bundled Conductors: a Mathematical Model, Journal of Fluids and Structures **16**(7), 2002. pp. 843-854.

[5] CIGRE TF 22.11.2 1995, Guide to Vibration Measurements on Overhead Lines, Electra **163**, 1995. pp. 124-137.

30th DANUBIA-ADRIA
Symposium on Advances in Experimental Mechanics
September 25-28, 2013 - Primošten, Croatia

7A11 058

THE EXPERIMENTAL IDENTIFICATION OF EFFORT STATE OF TRUCK LOAD CARRYING FRAME

Mariusz Stańco[1], Mariusz Kosobudzki[2], Damian Derlukiewicz[1]

[1] Wroclaw University of Technology, Faculty of Mechanical Engineering, Institute of Machine Design and Operation, Łukasiewicza 7/9, 50-371 Wrocław,POLAND. E-mail:mariusz.stanco@pwr.wroc.pl, damian.derlukiewicz@pwr.wroc.pl

[2] Military Academy of Land Forces, Logistic Department, Czajkowskiego 109, 51 - 150 Wrocław,POLAND, E-mails:m.kosobudzki@wso.wroc.pl

1. Introduction

Truck that drives on unpaved roads is exposed to a number of loads, that must be carried by the main frame. Typically, these loads are dependent on the size of the traffic load and the type of surface on which the vehicle is moving [2,4]. However, the level of effort of the load carrying frame of the vehicle in addition to the above factors is also influenced by the way of the connection between the various elements of the frame and geometric dimensions. In trucks, the loading that comes from cargo is transferred to the main frame through the intermediate frame, which reduces the torsional compliance of the main frame [3]. These frames are often used as supporting frames and they increase the external load transfer capacity by stiffening the main frame. The experimental study of the truck was carried out in a static range by torsion the frame during the operation on sandy roads with big bumps in the ground. The study was conducted on a vehicle with 6x6 axle configuration designed for transporting the containers.

2. Measurement points

Based on the preliminary numerical calculations with use of finite element method [1], there were selected three points on the main frame of the vehicle and four points on the intermediate frame in which the strain gauges were glued (Fig. 1).

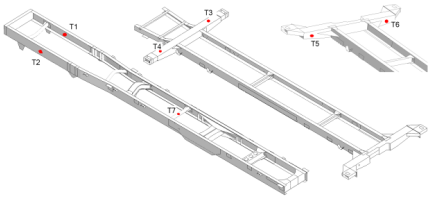

Fig. 1. Points of strain gauges location of main and intermediate frame.

To measure the strain of the frame the foil strain gauges were used with resistance of 350,5Ω±0,25%, constant k_{sg}=2,15 ±0,5% and type: TFpxy-5/350 and TFx-6/350.

Figure 2 shows an example of measurement point (T7) located in the middle cross-bar in main frame, that is characterized by the constant cross-section on the length and by the occurrence in the cross-bar of mainly torsion.

Fig. 2. Point T7

3. Measurements

Measurements were carried out in two stages. Initially, on the testing stand, the angle of rotation of the main frame, without intermediate frame by raising the opposite wheels was measured. In this way, the maximum angle of torsion of the main frame was determined. Then the vehicle with mounted both frames was twisted. This method of measurements allowed to determine the impact of stiffness of the intermediate frame on the torsional flexibility of the entire frame. Figure 3 shows the change of torsional stresses for the selected series of measurements in three measurement points installed on the main frame of the vehicle, while figure 4 shows the change of torsional stresses in the point T7 during measurements of torsion with installed intermediate frame.

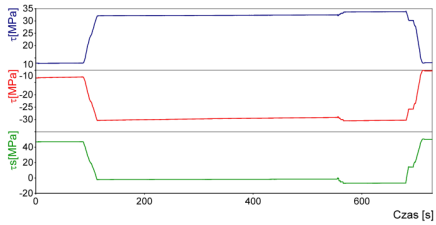

Fig. 3. The change of stresses in points T1, T2, T7 during torsion of the main frame

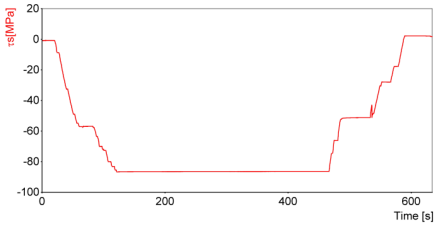

Fig. 4. The change of stresses in point T7 during torsion of the main frame together with intermediate frame

The vehicle load carrying frame due to lifting of the opposite wheels has been twisted by an angle of approximately 21°. However, after installing the intermediate frame the torsional flexibility of entire frame has been reduced, which affects the increase of its torsional rigidity. Then the torsional angle was reduced to the value of about 13°. The second stage of the measurements were the measurements of loading in the vehicle frame fully loaded during driving on uneven ground. The vehicle was moving at an average speed of about 20km/h. Figure 5 shows an example of changes of torsional stresses in point T7.

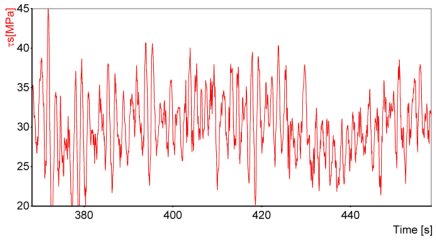

Fig. 5. The change of torsional stresses in point T7 during driving

While driving, the vehicle underwent torsion much less than those caused by the tests on the testing stand. The reason is that during testing in real conditions the vehicle was fully loaded by cargo, in the case by the rigid 20 foot container, that on the length of about 6000 mm has stiffen the main frame without allowing to its free torsion.

4. Conclusions

During the experimental measurements carried out on the test stand and during the operation of the vehicle the waveforms of stresses changes in the characteristic points of the frame were received. The maximum values of stresses ranged for the points T1 and T2 from 25 to 30MPa, for points T3-T4 from 50 to 90MPa, and at the point T7 the maximal values were about the half of the size of values measured at test stand and were about 50MPa. The mounted intermediate frame has caused that the angle of torsion of the main frame was reduced by 30%. However, in this type of vehicle that transports only a rigid container, such big torsional flexibility of the load carrying frame will never be used. Fellowship co-financed by European Union within European Social Fund.

References

[1] Rusiński E., Czmochowski J., Smolnicki T.: Zaawansowana metoda elementów skończonych w konstrukcjach nośnych, Oficyna Wyd. PWr, Wrocław 2000

[2] Kosobudzki M., Kowalczyk M., Stańco M., Akwizycja obciążeń dynamicznych działających na pojazd generowanych przez układ jezdny. Transport Przem. 4(30)/2007.

[3] Rusiński E.: Zasady projektowania konstrukcji nośnych pojazdów samochodowych. Oficyna Wydawnicza PWr., Wrocław 2002

[4] Jamroziak K., Kosobudzki M., Ptak J.: Assessment of the comfort of passenger transport in special purpose vehicles Maintenance and Reliability, 2013 vol.15 no.1

30th DANUBIA-ADRIA
Symposium on Advances in Experimental Mechanics
September 25-28, 2013 - Primošten, Croatia

7A12 084

TESTING METHODOLOGY OF GEAR TRANSMISSION WIND POWER PLANTS WITH SPEED CONTROL SYSTEM

Sanja Vasin[1], Milosav Ognjanović[1], Marko Miloš[1]

[1] University of Belgrade, Faculty of Mechanical Engineering, Kraljice Marije 16, 11120 Belgrade, SERBIA. E-mail: vasinsanja@gmail.com

1. Introduction

Wind turbines (WT) are multidisciplinary technical systems which convert wind energy into mechanical and then into electricity for ever growing need of power production. Common WT consists of rotor, gearbox, generator, nacelle and tower. Since output power production depends of wind speed which cannot be controlled, obtained electric power must be transformed into 50 Hz alternating current in order to be synchronized with electric net. These transformations significantly reduce WT system efficiency, comparing to direct synchronized electric generators at the electric net. For direct synchronization it is necessary to achieve a constant generator speed whether there is a sufficient wind power and speed or not. In the common WT design, gearbox transforms speed of rotation with the constant transmission ratio. The generator speed of rotation varies in relation of the rotor speed of rotation. To maintain generator speed at the constant level, it is necessary to provide gear transmission train with variable transmission ratio.

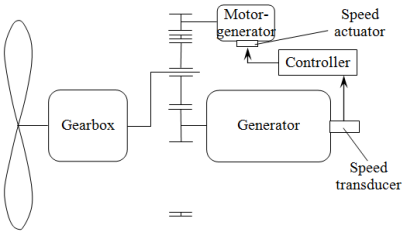

Fig.1. Wind turbine with controlled speed and with continual variation of gear train transmission ratio

Figure 1 shows possible kind of this design solution. Gear train transmission contains gearbox with constant transmission ratio and additional planetary gear set which can provide continual variation of transmission ratio. Ring of planetary gear set is toothed at both sides, inside and outside. An additional motor-generator with electronically controlled speed varies ring speed of rotation. If the wind is slow, motor-generator increases speed and vice versa keeping the constant speed of electric generator. Speed control of motor-generator is provided by controller.

2. Testing of mechanical components

The drive train consists of specific planetary gearbox with total transmission ratio i=25, and of one planetary gear set for variation of overall transmission ratio and keeping the constant speed of generator at 1500 rpm. The operating speed of rotor is 12 ÷ 16 rpm and generator output power is 1.5 MW. The main gearbox (Fig.1, i=25) is a specific conceptual design, without a sun gears. One inside toothed ring is input (drive) gear and another one is fixed, without rotation (Fig.2). The result is in reduced dimensions and increased systems reliability [1]. The average operating life of WT is about 20 years and for a gearbox it is 5 years.

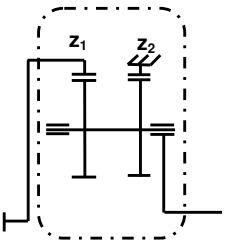

Fig.2. Conceptual design of gearbox

To provide functional requirements for components of complete gear train transmission, it

is necessary to carry out the next testing's of the system components [2].

- Testing of load capacity of complete gear train transmission. By use of specific design of testing rig with power circulation principle, it is necessary to identify the load capacity of gears for constant load (torque). It is possible to expect teeth flank failures at sun gear and at the central gear connected to generator. The ring toothed at both sides, during the test can be damaged by cracks in the teeth roots and in the ring body. For this purpose it is necessary to design and produce a specific testing rig for performance of this testing.
- Testing of bearings in gear train transmission. The bearings present potentially problematic components which can be damaged during operation. The tests can be carried out in the same time, during the gear testing at the testing rig.
- Dynamic testing of the gear train transmission vibration. In the course of load capacity test, vibrations at the chosen points will be measured and analyzed. Vibration can be caused by gear meshing and by natural vibrations disturbing of elastic and gear components with reduced masses.
- Modal analyses and modal testing of the whole gear train transmission and of complete system. Results obtained in this way have to be compared with results identified by measurement at the testing rig in order to harmonize design parameters and reduce vibrations.
- Measurement of vibrations in operating conditions using monitoring system. Monitoring process except vibrations has to contain monitoring of heating (oil temperature) and oil contamination by metal particles.
- Testing of load spectrum taking in consideration wind conditions in the course of the year dependence of the season. The load spectrum will be used for calculation and prediction of gear train transmission reliability.

3. Testing of electronic components

Due to the complexity of the system as a whole, testing of electronic components together with control software must be divided into parts as follows: testing of components, testing of subsystems and hardware-in-the-loop testing. Testing methodology will be subsequently defined but initially we'll focus our work on design of testing bed for each item needs to be tested.

- A lot of different types of sensors (such as strain gages, force, torque, pressure, temperature, speed, flow, heat-flux, level, oil contamination) will be incorporated into test beds which will be probably very complicated from mechanical point of view. Because of that - identification of static and dynamic characteristic of the testing system itself will be defined firstly. For that purposes, modular data acquisition system will be used together with activation units.
- We anticipate that control subsystem could consist of an onboard computer (OBC) with several DSP modules. One or two modules will be used for measurements other realizes control algorithm. Parameters of controller will be adjusted by many series of tests. OBC testing will be performed by additional hardware.
- Once, when testing of components and testing of subsystems will be finished, hardware-in-the-loop testing will be performed. Gear transmition train coupled with motor-generator and generator, together with control system, will be simultaneously activated by simulation of real load [3]. This test will prove proper work of the electrical as well as mechanical components of the whole system and control software too.

4. Conclusion

The testing methodology for the new type of wind turbine with controlled speed based on continual variation of gear train transmission ratio is suggested. Testing of mechanical components is oriented to identify potential failures and service life. Tastings' of electronic and other components in control loop are directed to provide reliable operation of control system.

Acknowledgements

This article is a contribution to the Ministry of Education and Science of Serbia funded project TR 035006.

References

[1] Höhn, B.R., Future transmissions for wind turbines, TU Munich, 2011.

[2] Lei, Y. at al., A method based on multi-sensor data fusion for fault detection of planetary gearboxes: Sensors., 12, 2012. pp. 2005-2017.

[3] Paunović, N., Kovačević, J., Rešetar, I, A methodology for testing complex professional electronic systems, Serbian journal of electrical engineering., 9, 2012. pp. 71-80.

30th DANUBIA-ADRIA
Symposium on Advances in Experimental Mechanics
September 25-28, 2013 - Primošten, Croatia

7A13 073

VIBRATION ANALYSIS OF POWER ENGINEERING EQUIPMENT

Jerzy Czmochowski[1], Michał Paduchowicz[1] Artur Górski[1]

[1] Wrocław University of Technology, Faculty of Mechanical Engineering, Institute of Machine Design and Operation, Lukasiewicza 7/9, 50-371 Wrocław, POLAND. E-mail: jerzy.czmochowski@pwr.wroc.pl; michal.paduchowicz@pwr.wroc.pl; artur.górski@pwr.wroc.pl;

1. Introduction

Cracking of elements working in the power industry is one of its main problems. One of the reasons may be occurring vibrations of these structures. Vibration measurement and verification based on numerical calculation methods allows sometimes to prevent effectively such phenomena at the stage of the design process [4]. The study is dedicated to the discussion of issues of power vibration analysis, based on selected devices of fluidized bed power boiler in power plant, such as convection chamber, primary and secondary air channels.

2. Experimental testing

The aim of the study was to determine the structure frequency and amplitude of vibration, which occur during their operation. Determination of these values enables subsequent assessment of the facility in terms of the possibility of resonance phenomena. Due to the reliability of the results of measurements an important issue is the selection of appropriate measurement points. One of the selection criteria is primarily the availability of the test object and the need to verify a specific area of the structure.

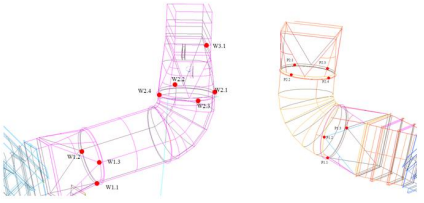

Fig.1 Distribution of acceleration sensors on the primary and secondary air channels

In figure 1, the measurement points at the channels of primary and secondary air and selected for testing are shown.

Another issue to be decided in the planning of measurement is the measuring equipment. To measure the voltage signals, depending on the value of the accelerations of elements of hermetic walls of convective chamber, the acceleration ICP sensors and capacitive sensors are used. In order to record the generated signal during the measurements, the sensors are connected to a multi-channel recorder equipped with a card to record measurements (Fig. 2).

Fig.2 Measuring equipment used in the measurements - multi-channel recorder

Obtained voltage signals were subjected to Fourier analysis. The result of such activity are the amplitudes spectra of acceleration. Figure 3 presents the examples of the result of Fourier analysis carried out for the selected measurement point at the convection chamber [1].

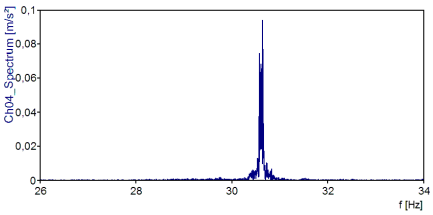

Fig.3. Amplitude spectrum of acceleration at the measurement point 04 - measurement 18

3. Numerical analysis

A key stage of research concerning the assessment of the durability of power equipment is the modal analysis with use of the Finite Element Method [2]. Consequently, the discrete models of convection chamber and the channels of the primary and secondary air were built (fig. 4).

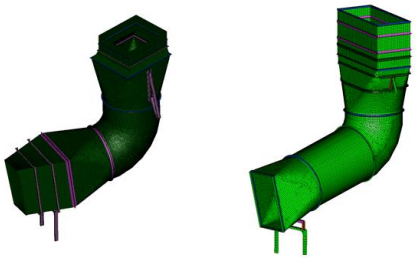

Fig.4. Discrete models of the channels of the primary and secondary air

To determine the free frequencies and their characters with use of the FEM the Lanczos algorithm was used [3]. It is used due to the fact that the results obtained are the most correspond to reality. Figure 5 shows the contours of normal modes of vibration for the selected vibration frequencies of primary and secondary air channels.

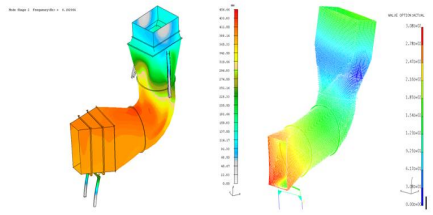

Fig.5. The modes of vibration for: a) primary air channel, free vibration frequency of f=4,15 Hz: b) secondary air channel, free vibration frequency of f=6,25 Hz

4. Conclusions

Comparing the vibration test of facilities of power plants to power block elements discussed above, it can be concluded that the combination of the actual object vibration measurements and numerical methods, FEM, is sometimes an effective way to determine the causes of cracks of their surfaces. This pattern was confirmed in the convection chamber. In this case, due to the similar values of free frequencies and the measured values of inputs, that could be found, probably we have to deal with the phenomena of resonance. However, in the case of the air channels, the phenomena of resonance should be excluded as a the reason of high-amplitude vibrations. The reason is, that the free frequency of these objects obtained by the FEM analysis are very different from those obtained from the measurements.

References

[1] Górski A., Iluk A., Rusiński E.: Diagnozowanie stanu odkształcenia ustroju nośnego komory paleniskowej fluidalnego kotła energetycznego. Prz. Mech. 2004 R. 63 nr 6 s. 11-16 (in Polish).

[2] Czmochowski J., Górski A., Smolnicki T.: *Wybrane problemy z obliczeń wytrzymałościowych ekranów komory paleniskowej kotła rusztowego wodnorurowego*. Systems 2004 vol. 9, s. 238-244 (in Polish)

[4] Czmochowski J., Górski A., *Analiza numeryczna stanu wytężenia bandaży kanału spalin kotła energetycznego*. Górnictwo Odkrywkowe 2003 R. 45 nr 4/5 s. 30-33. (in Polish)

[4] Koziołek S, Derlukiewicz D., Method of assessing the quality of the design process of construction equipment with the use of DFSS (design for Six Sigma). Automation in Construction. Vol. 22 , pp. 223–232, 2012

30th DANUBIA-ADRIA
Symposium on Advances in Experimental Mechanics
September 25-28, 2013 - Primošten, Croatia

7A14 107

ANALYSIS OF MECHANICAL PROPERTIES OF RESILIENT TRAM WHEEL SCREWS

Ivo Haladin[1], Damir Škrinjar[2], Ivan Duvnjak[1], Stjepan Lakušić[1]

[1] University of Zagreb, Faculty of Civil Engineering, Kačićeva 26, HR-10000 Zagreb, CROATIA. E-mail: ihaladin@grad.hr, iduvnjak@grad.hr, laki@grad.hr

[2] Zagreb Holding - Zagreb Municipal Transit System (ZET), Ozaljska 105, HR-10110 Zagreb, CROATIA. E-mail: damir.skrinjar@gmail.com

1. Introduction

Zagreb Municipality Transit System (ZET) runs 15 tram lines on a 116 km long tram track network, forming a backbone of Zagreb public transport. 176 tram units operate the network daily, servicing around 560 000 passengers. In recent years ZET has acquired 140 new low-floor trams TMK 2200 built by Croatian consortium – Crotram. New trams introduced new wheel type as well. Instead of monoblock wheels used on older tram units, the new trams run on resilient wheels Bochumer Verein BO 84, which consist of wheel tyre mounted on to the wheel body with resilient pads in between designed for vibration absorption. Two wheel components are bolted together using 24 high quality screws M22x58 and M16x60, 12 of each type, Fig. 1. The instructions provided by the tram manufacturer is to replace the screws after the second tyre refitting, hence after 200 000 km in operation. This procedure requires acquisition of 13400 new screws annually, which represents a significant expense for the tram maintenance. This fact has led to investigation of wheel screw behaviour over the exploitation period in order to examine their mechanical properties and to investigate if they are safe for further use, therefore saving valuable resources.

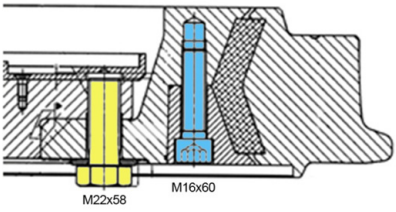

Fig. 1. Wheel BO 84 with marked screws

2. Visual inspection of screw geometry

In order to evaluate the geometry of used screws, a sample of 10 screws has been examined, 4 new ones, 4 taken after first refitting (100 000 km) and 2 after second refitting (200 000 km). Screws have been thoroughly cleaned and degreased in order to analyse screw body, thread surface, screw head and the washer. 100x magnification has been used in the process, Fig 2.

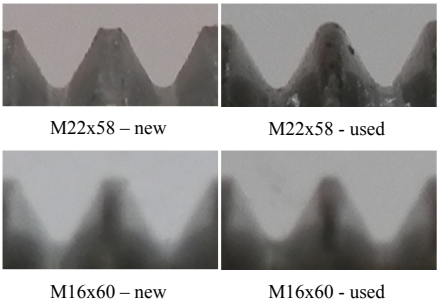

Fig. 2. Visual comparison of thread wear of new and used screws (100x magnification)

There were no identified significant wear changes on any of screw components.

3. Analysis of mechanical properties

As a part of mechanical properties analysis, screws have been processed on a turning machine in order to achieve test pieces according to ISO 6892-1 [1], i.e. round cross-section proportional test pieces. Two types of test pieces have been prepared, one from M22x50 and the other from M16x60 according to provided specification for proportional test samples, Fig. 3.

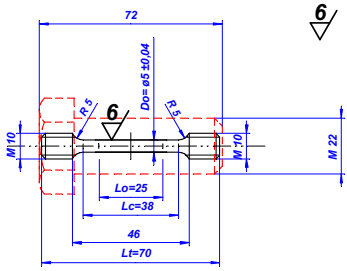

Fig. 3. Test piece extraction out of M22x58 screws

Tension testing has been performed on a universal testing machine Zwick Roell Z600. Total of 10 samples have been tested according to Table 1. Because of short reach of test machine clamps, special extensions for test samples have been machined as well.

Test sample	Screw type	Condition	Tensile strength (MPa)
DV01, DV02	M16x60	Unused	1108, 1113
DV11, DV12	M16x60	100 000 km	1072, 1074
DV21, DV22	M16x60	200 000 km	1081, 1108
KV01, KV02	M22x58	Unused	909, 945
KV11, KV12	M22x58	100 000 km	957, 834

Tab. 1. Test samples and tensile strength results

Tensile strength tests show no distinguishable difference between unused screws and screws after certain period of exploitation. All the samples fulfil the manufactures nominal tensile strength requirements (1000 - 1200 N/mm^2 for M22x58 and 800 – 1000 N/mm^2 for M16x60 according to [2]).

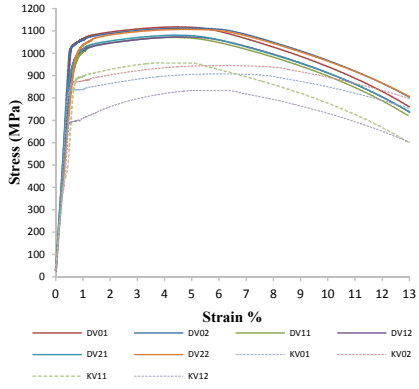

Fig. 4. Stress-strain record obtained during tensile test

Steel toughness is another mechanical property measured in order to evaluate exploitation influence. Toughness is ability of metal to deform plastically and to absorb energy in the process before fracture [3]. The good combination of strength and ductility of materials perform better toughness. To compare these tensile tests we use measure of toughness as the total area under stress-strain curve according to Eq. (1):

$$W = \int_0^{\delta} \sigma \, d\varepsilon \,, \qquad (1)$$

where δ is total strain up to the 13%. Values of specific work up to the 13% of strain are illustrated in Fig. 5.

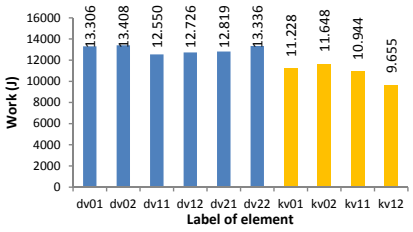

Fig. 5. Toughness values of test samples

Results of tensile test shows better behaviour according to strength and ductility for the longer screws compared to short ones, but at the same time there is no significant deviation for the same group of screws. According to results we can conclude the exploitation period plays no significant difference in any of the described material properties.

4. Conclusion

According to preliminary results of geometrical and mechanical properties examination of TMK2200 wheel screws, it is visible that exploitation period of the screws could be under evaluated. In addition, further fatigue testing could provide more insight into screw behaviour under the dynamic tram load.

If screws are to be used for a longer period of time, savings could be achieved, taking into account that 13 440 screwes are changed annualy. Ultimately the longer exploitation period should be evaluated in order to achieve economic benefits, yet having safe vehicle operation as a priority.

References

[1] ISO 6892-1 Metallic materials — Tensile testing —Part 1:Method of test at room temperature, 2009

[2] HRN M.B1.023-1983 – Bolts, screws and nuts with prescribed quality

[3] Krolo, J., Šimić, D., Mehanika materijala, Zagreb, 2011

30th DANUBIA-ADRIA
Symposium on Advances in Experimental Mechanics
September 25-28, 2013 - Primošten, Croatia

7A15 104

SYSTEM OF MONITORING BELT STATE OF BELT CONVEYORS

Paweł Maślak[1], Tadeusz Smolnicki[2],

[1] Wrocław University of Technology, Faculty of Mechanical Engineering, Wybrzeże Wyspiańskiego 27, 50-370 Wrocław, POLAND. E-mail: pawel.maslak@pwr.wroc.pl

[2] Wrocław University of Technology, Faculty of Mechanical Engineering, Wybrzeże Wyspiańskiego 27, 50-370 Wrocław, POLAND. E-mail: tadeusz.smolnicki@pwr.wroc.pl

1. Introduction

Belt conveyors are commonly used in the mining industry and each place, where the big amount of material need to be transported continuously. The belt conveyors are also used in open cast mining industry. The typical usage of belt conveyor is shown in figure 1. Overburden is transported from bucket wheel excavator to spoil tip or coal is being delivered to power plant [1, 2].

Fig. 1. Belt conveyor in Coal Open Cast Mine.

2. Typical damages of belt conveyors

Typically the wearing of the conveyor belt surface has been inspected visually, photographed, marked up where events observed, combined with thickness and hardness testing to project the expected life of the conveyor belt[3]. This service whilst accurate requires a significant amount of downtime of the target belt to be performed. Typical damages of belt are:

-mechanical failure of glued or steel belt joints shown in figure 2,

-cutting or delamination the belt: along the direction of moving or across, shown in figure 3,

-overheating idlers bearing, shown in figure 4,

-mechanical damage to electrical equipment built along the conveyor structure,

-excessive belt load bearing capacity in relation to the belt,

-overheating the rotating elements [4].

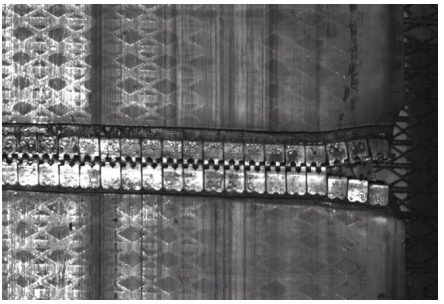

Fig. 2. Mechanical failure of steel belt joint[7].

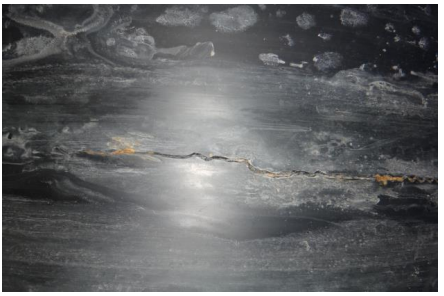

Fig. 3. Cutting the belt along the direction of moving.

Each of damage causes the stop of production and to mitigate the risk of catastrophic failure the monitoring systems are developed.

3. System of monitoring belt state

In the world there are plenty types of monitoring systems. Some of them use vision systems, others use X-ray or mechanical contact with the belt or belt equipment.in figure 4 is shown the magnetic system and in the figure 5 is shown the vision system.

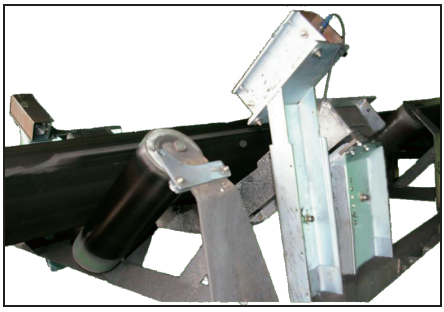

Fig. 4. Magnetic system to controling belt cord[7].

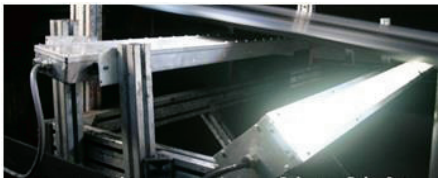

Fig. . Visionl system to control belt surfece defects [7].

The most important thing in those systems is identifying and monitoring steel links defects, surface damage, splice deterioration and tracking errors before they become serious problems [5,6] The condition of the belt is monitored continuously, providing immediate alarms of impending major failures, such as splice failure, belt tears, etc

New system should join two types of system: magnetic and vision system, because each of it has disadvantages. The research held in Wroclaw University of Technology try to join those two systems to make it more efficient and more reliable. New system consist of multiscan camera with laser lightening and the magnetic module to control belt with steel links.

4. Summary

Automatic belt conveyors monitoring systems are in common use, because they are reliable and allow to avoid human presence in dangerous environment. The dust and high humidity cause the very hard conditions for a human and make problems to identify the eventual damage of belt. Monitoring system always measures with the same precision at any time and any conditions. Monitoring system works 24 hours a day, 7 days a week and let the industry work well.

Acknowledgements

The research is co-financed by the European Union within the European Social Fund and Human Capital National Cohesion Strategy

HUMAN CAPITAL NATIONAL COHESION STRATEGY
EUROPEAN UNION EUROPEAN SOCIAL FUND

References

[1] Gładysiewicz L., Przenośniki taśmowe : teoria i obliczenia, Wrocław: Oficyna Wydawnicza Politechniki Wrocławskiej, 2003

[2] Antoniak J. – „Przenośniki taśmowe w górnictwie podziemnym i odkrywkowym". Wydawnictwo Politechniki Śląskiej, Gliwice 2007

[3] Gładysiewicz L., Król R. Bukowski J., Eksperymentalne badania oporów ruchu przenośnika taśmowego, Eksploatacja i Niezawodność-Maintenance and Reliability. 2011, nr 3, p. 17-25., 2011

[4] Biernat S. Hardygóra M., Górniak-Zimroz J., Król R.,Zimroz R., Propozycja budowy informatycznego systemu wsparcia podejmowania decyzji w obszarze zintegrowanych danych technicznych dotyczących procesów eksploatacji ciągłych systemów transportowych, Górnictwo i Geoinżynieria, R. 35, z. 3, p. 27-40., 2011

[5] Gorden T. Jemwa, Chris Aldrich, Estimating size fraction categories of coal particles on conveyor belts using image texture modeling methods Expert Systems with Applications 39 (2012) 7947–

[6] 7960Chuen-Shii Chou, Ching-Liang L., Wei-Chung C., Optimum conditions for vulcanizing a fabric conveyor belt with better adhesive strength and less abrasion, Materials and Design 44 (2013) 172–178

[7] *http://www.beltspy.com.au* 20.04.2013

30th DANUBIA-ADRIA
Symposium on Advances in Experimental Mechanics
September 25-28, 2013 - Primošten, Croatia

7A16 082

MEASURING OF RESULTANT AERODINAMYC FORCE ON VERTICAL TAIL OF THE TIP-JET HELICOPTER

Saša Damjanović[1], Predrag Miloš[2], Nikola Davidović[2], Branislav Jojić[1], Marko Miloš[1]

[1] University of Belgrade, Faculty of Mechanical Engineering, Kraljice Marije 16, 11000 Belgrade, SERBIA. E-mail: sasadamjanovic11@gmail.com, bjojic@gmail.com, mmilos@mas.bg.ac.rs

[2] EDePro, 11000 Belgrade, SERBIA. E-mail: nikola.davidovic@edepro.com, milos.predrag@edepro.com

1. Introduction

The purpose of this experiment is to measure resultant aerodynamic force on vertical tail surfaces of the tip-jet helicopter. One of the main advantages of the tip-jet helicopter is the lack of counter rotating moment. It means that tip jet helicopter has no need for tail rotor [1]. Still, some kind of vertical tail is needed for rotating the helicopter around Y-axis. It is important that tail surfaces are designed and positioned very carefully mainly because, in hovering, they use only airflow generated from the blades [2]. Larger tail surface area generates larger resultant aerodynamic force. If generated force is too large, helicopter is difficult to handle in forward flight. If the force is too small, helicopter won't be maneuverable in hovering.

2. Method of measurement

Measurement scheme is shown on **Fig. 1**.

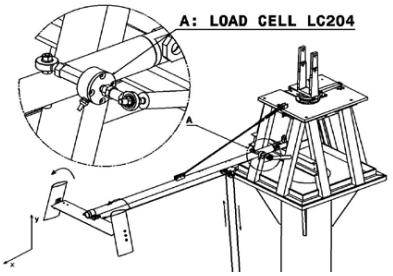

Fig. 1. Measurement scheme.

Vertical tail system and tail boom are attached on test stand beneath rotor blades. Aerodynamic force causes tail boom to turn around Y-axis. By preventing this turning, force can be measured with a load cell (see **Fig. 2**). Measurement starts when rotor head angular speed reaches 600rpm.

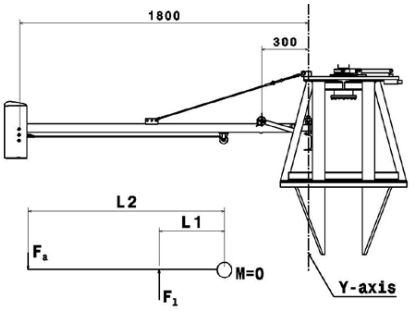

Fig. 2. Position of the load cell.

Load cell [3] is positioned 300mm from hinge axis. Resultant aerodynamic force is 1800mm from hinge axis.

$$\sum M = 0 \qquad (1)$$

$$F_a \cdot L_2 = F_l \cdot L_1 \qquad (2)$$

$$L_2 = 6L_1 \qquad (3)$$

$$\Rightarrow F_l = 6F_a \qquad (4)$$

Force measured on the load cell is six times greater than actual aerodynamic force on vertical tail surfaces (according to Eq. (1), (2), (3) and (4)).

Position of the load cell is determined by its capacity. For this measurement, we used OMEGA

LC 204 load cell, with capacity of 5 to 25lb (22 to 110N). Load cell is shown on Fig. 3. Expected aerodynamic force on tail surfaces is around 10N. That's why we positioned load cell in that way so it measures six times greater force.

Before measuring, load cell has to be calibrated. We calibrate load cell by adding known loads, starting from 30N, and then adding additional loads (5N each) until total load of 100N. After that we remove loads one by one until we get back to 0N. If a load cell shows actual value for each known load than it is calibrated.

Fig. 3. Load cell LC 204.

To produce movement of the vertical tail around X-axis we used MAXON step motor. Tail is turning ±30°, and that is the position when maximum force is expected. Change of sequences of the angular movement is shown on **Fig. 4**.

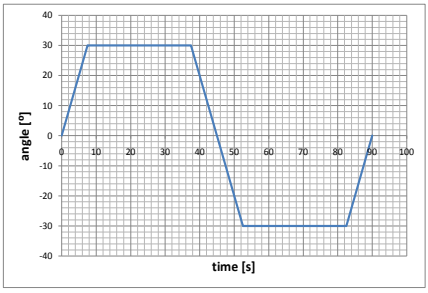

Fig. 4. Sequences of angular movement.

3. Results of measurement

Signal from the load cell is subsequently processed, and results are presented in MATLAB (see **Fig. 5**).

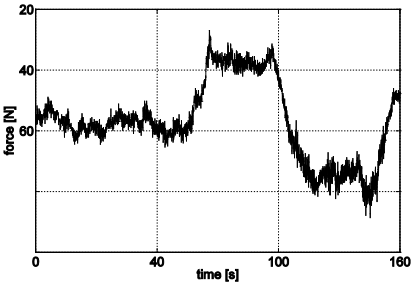

Fig. 5. Time-Force diagram presented in MATLAB.

As expected, maximum force of around 54N was measured in the ±30° position. It means that the actual resultant force on vertical tail is around 9N.

4. Conclusion

Calculations show that for 250kg helicopter, resultant aerodynamic force on vertical tail positioned 2000mm from axis of rotation should be 8-10.5N. Measured force is in that range, so we get to the conclusion that vertical tail area is enough for safe handling of the helicopter in hovering, and also in forward flight. Later that month, tail surfaces of the same area, were tested on helicopter in flight, and once again results were satisfying.

Acknowledgements

Tests were performed in EDePro d.o.o. facilities in Belgrade, as a part of the UAV tip-jet helicopter development program.

References

[1] John Watkinson, The Art of the Helicopter, Elsevier Butterworth-Heinemann, Oxford 2004.

[2] J. Seddon, Basic Helicopter Aerodynamics, BSP Professional Books, Oxford, 1990.

[3] William Bolton, MECHATRONICS A MULTIDISCIPLINARY APPROACH, Fifth Edition, Pearson Education Limited, Harlow, England, 2011.

30th DANUBIA-ADRIA
Symposium on Advances in Experimental Mechanics
September 25-28, 2013 - Primošten, Croatia

7A17 079

MONITORING OF ENGINE PARAMETERS IN TIP JET HELICOPTER TESTS

Nebojša Kosanović[1], Nikola Davidović[2], Predrag Miloš[2], Branislav Jojić[1], Marko Miloš[1]

[1] University of Belgrade, Faculty of Mechanical Engineering, Kraljice Marije 16, 11000 Belgrade, SERBIA. E-mail: nebkos@gmail.com, bjojic@gmail.com, mmilos@mas.bg.ac.rs

[2] EDePro, 11000 Belgrade, SERBIA. E-mail: nikola.davidovic@edepro.com, milos.predrag@edepro.com

1. Introduction

This paper presents the procedure for monitoring engine operation, health and performance in a tip jet helicopter [1] testing. In this case, engine is mounted on top of the rotor heat and it is rotating with helicopter rotor which represents a difficulty in data acquisition while monitoring engine performance.

For an effective operation of system it is necessary to reduce a number of sensors and communication lines between rotating helicopter driveline and stationary systems (external or located in fuselage).

2. Elements of the measuring system

The engine data measuring system used in this testing is a part of data acquisition system used to monitor all parameters needed in helicopter test. Measuring and control subsystem that is related to the engine is shown on figure 1.

To gather the data needed for appropriate performance monitoring, three essential parameters were measured: Engine speed of rotation (RPM), temperature on critical part of the engine and engine fuel flow.

2.1 Engine RPM measurement

Engine rotation velocity was measured using a proximity sensor. Proximity sensors [2] provide medium or low resolution sensing, depending on the number of pulses measured per revolution. The method of using a proximity sensor: to sense the teeth on a gear that is located on engine shaft. This type of sensing typically has pulses that are relatively clearly defined and symmetrical.

2.2 Temperature sensor

Temperature measurement is realised by means of thermocouple [3] which gives analog signal of 0.5-100 mV. That signal is then amplified and converted to signal interpreted by system as a temperature value.

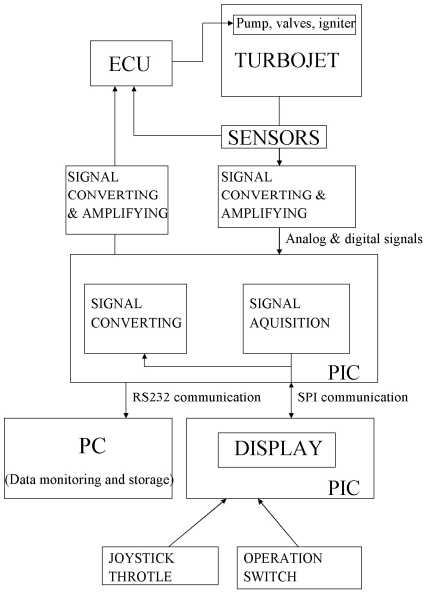

Fig. 1. Schematic representation of engine control and essential parameters measurement.

2.3 *Fuel flow*

Fuel flow is measured by turbine flowmeter. Turbine flowmeters [3] use the mechanical energy of the fluid to rotate a "pinwheel" (rotor) in the flow stream. Blades on the rotor are angled to transform energy from the flow stream into rotational energy. The rotor shaft spins on bearings. When the fluid moves faster, the rotor spins proportionally faster.

3. Results

Objective of testing was to achieve liftoff. During the test, it was important to have stable engine operation insuring thrust for lift force generation. Figure 2 shows engine RPM change during test. Engine was controlled by increasing the fuel flow which can be seen on figure 3.

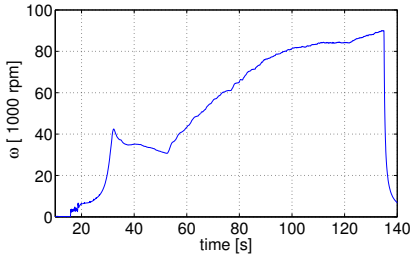

Fig. 2. Engine rotation speed diagram.

These two parameters are essential for monitoring of engine performance because they directly correlate with thrust and fuel consumption.

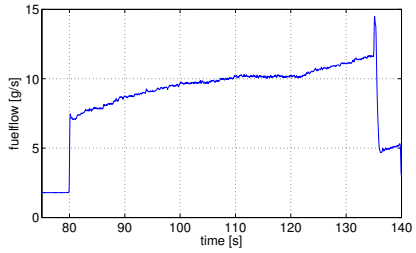

Fig. 3. Fuel flow diagram.

To prevent any damage to the engine it is necessary to prevent overheating. Figure 4 shows engine temperature during testing.

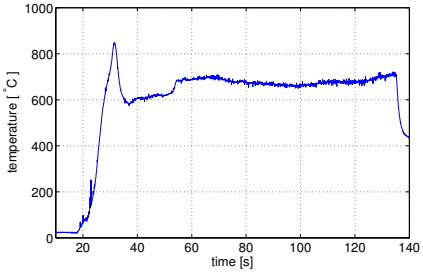

Fig. 4. Engine temperature diagram.

4. Remarks

Results of numerous numbers of tests that have been done with this measuring system show that this system provides sufficient data for effective engine monitoring.

During tests, engine performed stably and enabled measuring of relevant parameters of other parts of helicopter.

Data that is obtained from engine monitoring system will help in future development of helicopter systems and new engine, more suitable for this application.

Acknowledgements

Tests were performed in EDePro d.o.o. facilities in Belgrade as a part of UAV tip jet helicopter development program.

References

[1] John Watkinson, the Art of the Helicopter. Elsevier Butterworth-Heinemann, 2004.

[2] Robert H. Bishop, the Mechatronics Handbook. CRC Press LCC, 2002.

[3] William Bolton, Mechatronics – A Multidisciplinary Approach, Fifth Edition. Pearson Education Limited, 2011.

30th DANUBIA-ADRIA
Symposium on Advances in Experimental Mechanics
September 25-28, 2013 - Primošten, Croatia

7A18 080

EXPERIMENTAL DETERMINATION OF LIGHT HELICOPTER ROTOR LIFT CHARACTERISTICS WITH TIP-JET PROPULSION SYSTEM

Nenad Kolarević[1], Nikola Davidović[2], Predrag Miloš[2], Branislav Jojić[1], Marko Miloš[1]

[1] University of Belgrade, Faculty of Mechanical Engineering, Kraljice Marije 16, 11000 Belgrade, SERBIA. E-mail: nkolarevic1003@gmail.com, bjojic@gmail.com, mmilos@mas.bg.ac.rs

[2] EDePro, 11000 Belgrade, SERBIA. E-mail: nikola.davidovic@edepro.com, milos.predrag@edepro.com

1. Introduction

This paper presents the technical solution for reliable and precise measurement of lift force which acts on the rotor blades of tip-jet helicopter propulsion system [1].

The propulsion system consists of a teeter rotor and a turbojet engine with exhaust nozzles on the end of blades.

Measurement is done with an acquisition system which consists of:

- load cell for measuring the lift force of the rotor head;
- linear actuator with potentiometer for shifting and measuring of the collective step;
- tachogenerator [2] for determining angular velocity of the rotor head.

2. Measurement system

The measurement is based on the change of the rotor lift force which depends on the alternation of the rotor rpm and the collective step. Experimental testing is done on the test stand platform in real conditions. Figure 1 shows the setting up of the entire system on the test stand platform.

The control of propulsion group and collective step is done by the control panel with joysticks, and it is shown in Figure 2. Control and measured signals from the test stand platform are transmitted via telemetry.

To perform the collective step of blades one uses the linear actuator IDM 8A with incorporated potentiometer and the following characteristics: input voltage 12 VDC, load capacity 1500 N, static load 4500 N, stroke length 100 mm, speed at full load 27mm/s.

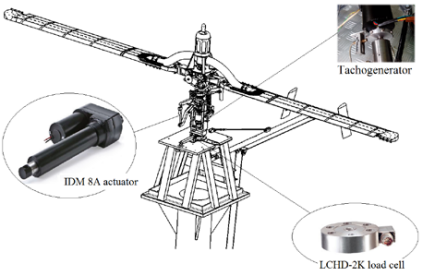

Fig. 1. Test stand platform and measurement system.

Fig. 2. Control panel.

Tachogenerator, developed for these measurement needs, is used for determining the rotor head rpm.

LCHD-2K load cell is employed for measuring the lift force, and it has the following

characteristics: excitation 10 Vdc, output 2mV/V ± 0.25%, linearity ±0.20% FSO, hysteresis ±0.10% FSO and load 9000N.

3. Results

Results of the measurement are shown in the following diagrams, which were obtained using the previously described methodology.

Figure 3 shows the measurement of the rotor head rpm vs. relevant period of time.

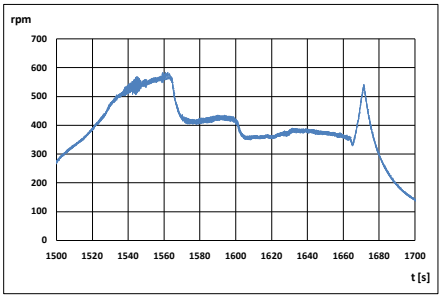

Fig. 3. Rotor head rpm.

Helicopter rotor lift force as a function of time is given in the Figure 4.

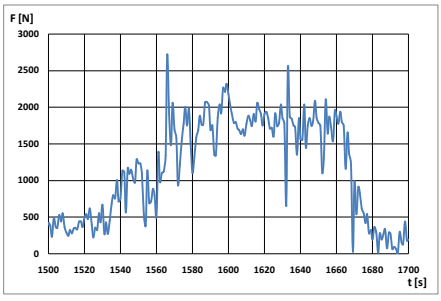

Fig. 4. Lift force.

Measurement of the collective step change is done indirectly, via linear movement of the actuator. This dependence of the collective angle of blades with the linear actuator movement directly correlates to the kinematic relation of rotor head element, as is described in this equation:

$$\theta = 0.0005 \cdot x^2 - 0.3662 \cdot x + 19.6160 \qquad (1)$$

where x is the linear movement of the actuator in *mm*, and θ is the angle in degrees.

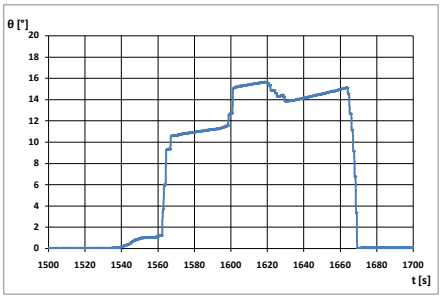

Fig. 5. Collective step.

4. Conclusion

The previously described measurement system is designed in order to figure out available performances of the propulsion system.

Figures 3, 4 and 5 show the results for the measured values. These values indicate that the maximum lift force around 1800 N was achieved during the continual work of the turbojet engine and the maximum values of the collective blades angle. This can be seen with nearly constant rotor head angular velocity in Figure 3. This lift force is enough for ultralight helicopters weighing up to 150 kg.

5. Acknowledgements

The tests were performed in EDePro d.o.o. facilities in Belgrade, as a part of the UAV tip-jet helicopter development program.

References

[1] John Watkinson, The Art of the Helicopter. Elsevier Butterworth-Heinemann, Oxford 2004.

[2] William Bolton, MECHATRONICS A MULTIDISCIPLINARY APPROACH. Fifth Edition, Pearson Education Limited, Harlow, England, 2011.

[3] J. Seddon, Basic Helicopter Aerodynamics. BSP Professional Books, Oxford, 1990.

[4] Alexander A. Nikolsky, Helicopter analysis. John Wiley & Sons, 1951.

30th DANUBIA-ADRIA
Symposium on Advances in Experimental Mechanics
September 25-28, 2013 - Primošten, Croatia

7A19 141

FRACTURE ANALYSIS OF PLATES UNDER LATERAL LOAD PRESSURE

Željko Božić[1], Damir Semenski[1], Hinko Wolf[1]

[1] University of Zagreb, Faculty of Mechanical Engineering and Naval Architecture, Ivana Lučića 5, HR-10000 Zagreb, CROATIA. E-mail: zeljko.bozic@fsb.hr

1. Introduction

In thin-walled structures such as the fuselages and wings of aircrafts or the deck and side structure of a ship, under cyclic loading fatigue cracks may initiate and further propagate, which can eventually lead to unstable fracture and result in structural failure. Sumi at al. [1] and Bozic [2] studied fracture mechanisms of stiffened panel specimens related to ship deck structure. Bozic [3] presented a procedure for determining the critical *J*-integral values associated with the onset of stable fracture in a centrally notched plate under tension loading. He related numerical results of the *J*-integral values to the experimentally observed crack tip opening displacement values associated with stable crack propagation onset.

In this paper is presented an experimental and numerical investigation of fracture occurring in damaged plates exposed to lateral pressure. The plate specimens notched with a central crack were subjected to increasing lateral pressure until fracture occurred. Pressurized test equipment was used for loading. The strains, the deflections, crack propagation and the applied pressure were measured during the experiment. Finite element analysis was carried out in order to investigate fracture onset conditions under Mode I type loading, taking into account both material and geometrical nonlinearity. The elastic plastic fracture mechanics concept was employed in the analysis. The critical pressures associated with the onset of stable fracture were determined based on the critical *J*-integral values J_c taken from [3].

2. Pressurized tests

The material of specimens was an aluminum alloy plate of thickness t=2mm, (JIS 5050 H32). The specimen is fixed along the edges to the pressurized tank by bolts. Two pressurized specimens were tested, PPR-1a I PPR-1b. The picture of the specimen after the test, depicting the geometry and locations of stain gages and crack gages is given in Fig. 1.

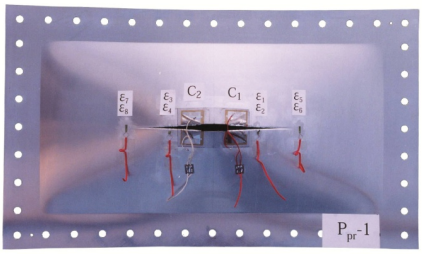

Fig. 1. Plate specimen with a central crack after the test.

Effective size of the specimen which is exposed to the loading pressure is 250x500mm. Initial crack, 2a=40mm, were machined by electric spark. Measured deflections of the plate at a point 25mm distant from the plate center and the crack, with respect to the applied pressure are shown in Fig. 2.

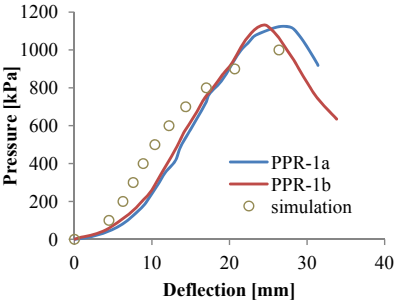

Fig. 2. Deflection of the plate versus the pressure.

The measured maximum pressures and the corresponding deflections for the two specimens

are very close indicating the reproducibility of the present experiment. Measured strains in the direction perpendicular to the crack line, at a point distant 125mm from the plate center in the crack line, with respect to the applied pressure is given in Fig. 3. The figure shows the membrane and total strains at the middle, top and bottom plate surface.

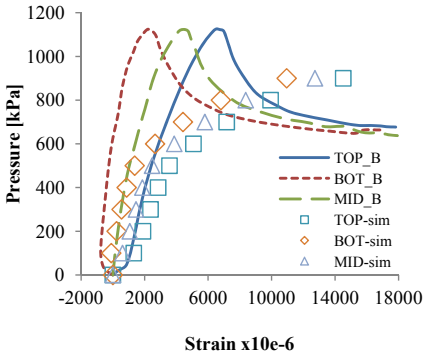

Fig. 3. Strains with respect to applied pressure.

From the experimental results one can see that the strains still increase after maximum pressure which means that the crack continues rapid propagation with depressurization until the driving force (oil pressure) is exhausted.

3. Numerical assessment of fracture onset

By using ANSYS program *J*-integral values with respect to applied pressure were calculated, as given in Fig. 4. For a centrally notched plate specimen it was estimated the critical value J_c = 360 MPa mm [3].

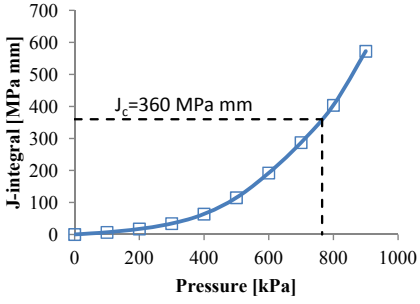

Fig. 4. Numerical estimation of the fracture onset.

Isoparametric eight-node shell elements were used in modeling the specimen. The crack tip was meshed by triangular non-singular elements, which are degenerated from quadrilateral elements having three nodes tight to one at the crack tip. The radial length of crack tip elements was 1/20 of the half crack length, which is proper for the evaluation of J-integral based on the contour integral procedure.

It can be expected that for specimens with different geometry having ligaments subjected primarily to tensile loading and under large scale yielding onset of stable fracture occurs at this critical point. According to Fig. 4 fracture onset occurs slightly before 800 kPa. In the experiment fracture onset was observed around 900kPa.

4. Discussion of results an conclusions

Experimental and numerical analysis of a plate with a central crack exposed to lateral pressure were carried out. The simulated deflections in Fig. 2 agree well experimental results in terms of shape, but the magnitudes are smaller than those measured in the experiment. This could be explained by a possible pull-in along the clamped edges, which could have occurred in the experiments. The edges of the specimen may slightly slip between the clamping frames due to the significant membrane force so that the membrane stiffness could be reduced, enabling larger deflections.

Finite element analyses including large deformations and elastic-plastic material behavior were carried out. The critical pressures associated with stable fracture were estimated. Slightly lower critical pressures were estimated which could be due to the above described reasons.

Acknowledgement

This work was supported by the National Science Foundation Grant No. 120-0362321-2198. The support is gratefully acknowledged.

References

[1] Y. Sumi, Z. Bozic, H. Iyama, Y. Kawamura, Fracture of a Stiffened Panel with Multiple Site Cracks under Lateral Pressure, *The Seventh International Symposium on Practical Design of Ships and Mobile Units*, Edited by M.W.C. Oosterveld and S.G. Tan, The Hague, The Netherlands, September 1998., pp.873-878, Publisher Elsevier Science B.V.

[2] Ž. Božić, Fracture Analysis of Stiffened Panels under Lateral Pressure, *Shipbuilding*, pp. 202-212, 2002.

[3] Ž. Božić, On Determination of the J_{Ic} Parameter using a CN Plate Specimens, *FAMENA*, 2000.

30th DANUBIA-ADRIA
Symposium on Advances in Experimental Mechanics
September 25-28, 2013 - Primošten, Croatia

7B21 094

EFFECT OF HARDENING AREA WIDTH ON RESIDUAL STRESSES IN LASER HARDENED STEELS

Kamil Kolařík[1], Nikolaj Ganev[1], Zdenek Pala[1], Jiří Čapek[1]

[1] Czech Technical University in Prague, Faculty of Nuclear Sciences and Physical Engineering, Department of Solid State Engineering, Laboratory of X – ray diffraction, Trojanova 13, 120 00 Praha 2, Czech Republic, email: kamil.kolarik@email.cz

1. Introduction

During interaction of laser beam with metal surface a time variable temperature gradient is present and consequently local changes of structure are generated. Diffraction methods offer information about phase composition of polycrystalline materials and numerous other structural parameters, such as residual stresses or crystallographic texture. Moreover, they embody a suitable tool for both analysis, and control of the surface quality due the non-destructive or semi-destructive character of the X-ray diffraction experiments. This contribution is focused on the issue of structure alterations brought about by laser hardening of steels and introduces possibilities of X-ray diffraction techniques in optimization of laser hardening treatment of machine parts.

2. Samples under Investigation

Two sides of steel sample of Czech grade 12050 (C45) with dimensions 190×50×20 mm^3 were analyzed (see Fig. 1). The effect of hardened area width was investigated. Width of hardening area on the first side was 20 mm and 30 mm on the other. As a source, 3.5 kW diode laser was used. The laser beam velocity was 3 mm/min. Hardening temperature was kept at 1200 °C by pyrometer.

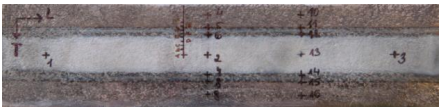

Fig. 1. Sample after hardening with measured areas.

3. Experimental Techniques

The residual stress measurements were performed with a θ - θ X'Pert PRO diffractometer in ω-arrangement with CrKα radiation. The line {211} of α-Fe phase was measured. The $\sin^2\psi$ method was applied to study the biaxial state of residual stresses (RS) and breadth of diffraction line (W) was determined [1]. In order to analyze the stress gradients beneath the samples surface, layers of material were gradually removed by electrolytic polishing in area 2, see Fig. 1.

4. Results

The back-reflection X-ray diffraction patterns, taken before performing residual stress measurements, correspond to diffraction of the spectral doublet $CrK\alpha_1\alpha_2$ on crystallographic planes {211} α-Fe, see Fig. 3. While the surface after temperature treatment shows isotropic fine-grained polycrystalline structure, i.e. the diffraction line is broad and continuous with homogeneous intensity around its perimeter, in the case of the origin surface, the diffraction line becomes narrow with a slight indication of discrete diffraction spots located uniformly around perimeter that gives evidence of non-existent preferred orientation. This is the reason why X-ray diffraction can be used for determination of the surface residual stress in the samples. The selected results of RS and W are in Tab. 1 and in Figs. 3 and 4.

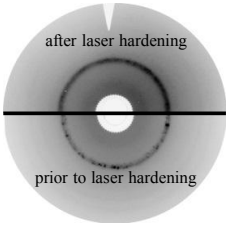

Fig. 2. Back-reflection X-ray diffraction patterns from the surfaces after and before laser hardening.

measured area (lasering area width)	$\sigma_L \pm \Delta\sigma_L$ [MPa]	$\sigma_T \pm \Delta\sigma_T$ [MPa]	<W> [deg]
1 (20 mm)	233±6	116±3	1.62
2 (20 mm)	302±14	143±5	1.62
3 (20 mm)	283±7	124±3	1.53
1 (30 mm)	177±3	235±2	1.44
2 (30 mm)	128±5	172±3	1.46
3 (30 mm)	110±3	203±4	1.45

Tab. 1. Values of surface macroscopic residual stresses σ_L, σ_T and breadth W of {211} α-Fe diffraction line obtained from surface hardened by 20 mm laser beam and 30 mm laser beam.

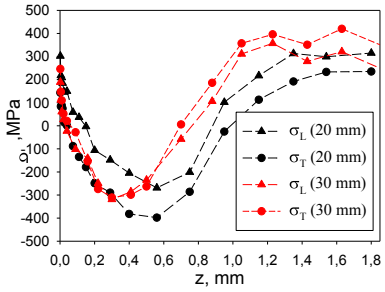

Fig. 3. The depth profiles of RS in surface layers of investigated areas.

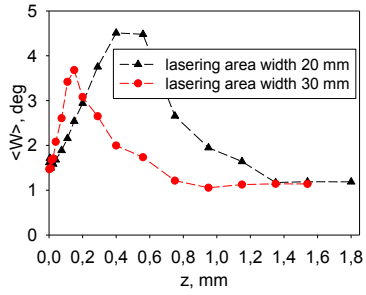

Fig. 4. The depth distributions of width of {211} α-Fe diffraction line.

5. Conclusions and discussion

It was found that both the laser hardened areas with widths of 20 and 30 mm have tensile surface RS exceeding 100 MPa which is most likely the consequence of inhomogeneous thermal deformations during cooling of even surface layers' partial melting [2 and 3].

Surface treated with narrower beam size shows higher values of parameter W. Increase of this parameter is due to existence of high concentration of dislocations after laser hardening and smaller crystallite size in structure which corresponds to higher hardness [4, 5].

RS depth distributions in Fig. 3 show that wider laser beam results in smaller maxima of compressive RS about 300 MPa which are found in shallower depth about 0.3 beneath the surface. Moreover, RS in both the measured directions are equal within the experimental inaccuracy which indicates centrally symmetric biaxial state of RS.

For narrower beam width, the maxima of σ_L and σ_T are found in larger depth of approx. 0.6 mm beneath the surface and RS in both the measured directions are not the same, namely $\sigma_T = -400$ MPa and $\sigma_L = -270$ MPa.

The shift in the position of RS maxima is also reflected in depth distribution of W parameter in Fig. 4. This indicates that smaller laser beam and, thus, smaller hardened volume, which is more effectively cooled by the adjacent material, results in deeper maxima of RS and thicker layer with compressive stresses.

During laser hardening two dominant mechanisms of residual stress generation are present. Phase transformation mechanism during sample cooling that introduces compressive RS and thermal deformation mechanism leading to tensile RS [2 and 3]. For the smaller beam size is, therefore, the phase transition mechanism more pronounced in comparison with wider beam.

Acknowledgements

This research was supported by the project FR-TI3/814 of Ministry of Industry and Trade of the Czech Republic.

References

[1] Kraus, I. Ganev, N., Residual Stress and Stress Gradients, In: Industrial Applications of X-Ray Diffraction. New York: Marcel Dekker, 2000, s. 793-811.

[2] Pilloz, M., Sahour, C., Vannes, B., Proc. 2nd Int. Seminar on Surface Engineering with High Energy Beams, Lisbon, 1989, 387-413.

[3] Freitas, M., Fereira, M.S., Michaud, H., Mat. Sci. Eng A167 (1993) 115-122.

[4] Benedek, J., Shachrai, A., Levin, L., Optics and Laser Technology 12 (1980) 247-253.

[5] Vilar, R., Colaço, R., Almeida, A., Optical and Quantum Electronics 27 (1995) 1273-1289.

30th DANUBIA-ADRIA
Symposium on Advances in Experimental Mechanics
September 25-28, 2013 - Primošten, Croatia

7B22 036

ANODIC OXIDATION OF TI-6AL-4V ALLOYS

Branislav Hadzima[1], Michal Bukovina[1], Filip Pastorek[1], Sylvia Dundeková[1]

[1] University of Žilina, Faculty of Mechanical Engineering, Dept. of Materials Engineering, Univerzitná 1, SK-01026 Žilina, SLOVAKIA. E-mail: branislav.hadzima@fstroj.uniza.sk; michal.bukovina@fstroj.uniza.sk; filip.pastorek@fstroj.uniza.sk

1. Introduction

Titanium and titanium alloys have many applications, notably as aerospace, cryogenic or biomedical materials [1]. For biomedical applications it has been widely used as artificial implant materials in dental, maxillofacial, bone replacement and orthopedic surgery due to their excellent mechanical, chemical properties and biocompatibility. However, as a bioinert metallic material, titanium implants cannot form direct bonds with living bone [2]

Several surface treatments have been proposed to improve important characteristics such as roughness, porosity, chemical composition and crystal structure, in order to promote a close bonding interface between implants and living bone. Thus, it is possible to transform the titanium surface into a bioactive one [3]. The rougher surfaces were obtained by methods such as plasma spraying, blasting, etching and sintering. Other techniques, such as sol gel processing, anodic plasma-chemical treatment, anodic oxidation under galvanostatic and potentiostatic mode and ion implantation, have been used recently to develop new surfaces [4] .

Anodic oxidation is an electrochemical method used to increase the thickness and the roughness of the titaniumoxide layer. The properties of the oxidized layer, such as thickness, microstructure, roughness, and concentrations of incorporated ions are controlled by adjusting the parameters (voltage, current, electrolyte composition, temperature, agitation velocity and processing time) during the oxidation process. The produced anodic film is well adhered on the substrate and presents suitable mechanical properties, notably the elastic modulus values, which can be lower than the Ti substrate and therefore closer to the bone values [3]. The high affinity that Ti has for oxygen results in several oxides of various crystalline structures. In a natural atmosphere the thermodynamically stable oxide is TiO_2 (1.5–10 nm thick), which can exist in three crystalline structures: anatase (tetragonal), rutile (tetragonal), and brookite (orthorhombic) [4]. The anodic films produced electrochemically are composed of two layers: the inner Ti oxide layer, which is composed of anatase crystals, and the outer Ti oxide layer formed at the film/electrolyte interface. The latter is composed of an amorphous oxide only and is morphologically homogeneous. Anodizing of Ti involves an amorphous-to-crystalline transition in the oxide structure at relatively low voltages [4]. Some authors have shown that the heat treatment after anodic oxidation increases the crystallinity of the produced titanium oxide layer and have discussed the role of the anatase and rutile phases on the surface bioactivity. They used sulfuric acid, phosphoric acid, sodium sulfate and calcium acetate and calcium phosphate [3] as electrolytes in order to make the new surface bioactive. The coloration of the oxide produced through anodic oxidation can be indicative of the thickness of the film. This relation between color and thickness of the oxide depends strongly on the anodization process and the nature of the electrolyte [4]. Anodizing can also result in the adsorption and incorporation of inorganic and organic, biologically important species, e.g. phosphate ions, into the oxide layer. Such surface layers, desirable for medical implants, are not only corrosion resistant in a biological environment, but also compatible with tissue response [5].

2. Experimental results and discussion

The tested material was titanium alloy (ASTM Grade 5) with chemical composition in Table 1 and microstructure in Fig. 1. Microstructure is bimodal consisting of alpha and beta phase

lamellae. The surface of tested alloy was mechanically and electrochemically treated. After surface grinding with emery papers with granularities of 200, 500 and 1000 the surface was anodized in 7 vol.% solution of sulfuric acid in distilled water with temperature of 12±2°C. Stainless steel electrode was used as a cathode and tested titanium alloy as working electrode (anode). Potential between anode and cathode was 65 V_{DC}. Different times of anodizing (2, 10 and 20 minutes) were used for surface treatment of the titanium alloy surface.

Component	Al	V	Fe	H	Ti
wt.%	6.46	4.27	0.19	<0.002	bal.

Tab. 1. Chemical composition of tested Ti alloy

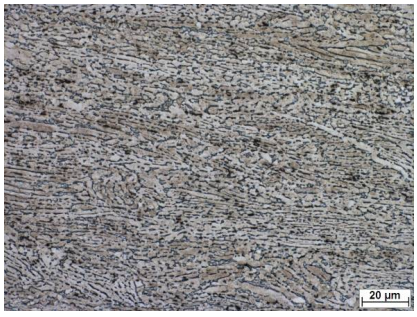

Fig. 1. Microstructure of Grade 5 Ti alloy, HNO3+HF+glycerine [6]

Anodized surfaces were evaluated by electrochemical impedance spectroscopy measurements in 0.1M NaCl solution. The platinum electrode was used as auxiliary electrode, saturated calomel electrode as reference electrode and anodized surface of Ti alloy was working electrode. The connection and measurement description was described elsewhere [7]. The results of the electrochemical tests in the form of Bode diagrams are in Fig. 2. The equivalent circuit method (equivalent circuit type – R_Ω+(CPE/(R_{CT}+Z_W)) was used for the analyses of measured curves. In the circuit the R_Ω is resistance of the solution, R_{CT} is charge transfer potential, Z_W is Warburg diffusion element and CPE is constant phase element of alloy surface. The results of the analyses are in Table 2. The corrosion resistance is characterized by active charge transfer resistance and by values of Warburg coefficient (the diffusion coefficient of ions in solution).

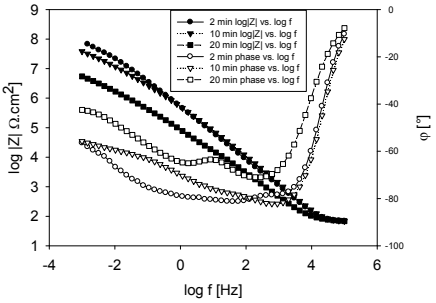

Fig. 2. Bode plots of various time anodized Ti alloy surfaces in 0.1M NaCl

Time of anodization	R_Ω [Ω.cm^2]	R_{CT} [kΩ.cm^2]	CPE [µF.s^{a-1}]	A_W [MΩ.s$^{-0.5}$]
0 min	63.7	36.54	34	-
2 min	63.0	132.05	0.33	8.69
10 min	62.7	66.42	0.23	2.41
20 min	64.7	20.08	1.65	0.38

Tab. 2. Electrochemical characteristics of Ti-6Al-4V alloy after anodization in 0.1 NaCl

3. Conclusion

On the basis of presented experiments and the analyses of measured curves, we concluded that the best electrochemical properties achieved the surface after 2 minutes of anodic oxidation (highest value of charge-transfer resistance and diffusion coefficient)

Acknowledgements

The research is supported by European regional development fund and Slovak state budget by the project ITMS 26220220048.

References

[1] Lewandowska, M. et. al: Thin Solid Films 515 (2007) 6460.

[2] Xie, Li. et al: J Mater Sci: Mater Med (2010) 21259.

[3] Szesz, E.M. et al: Thin Solid Films 528 (2013) 163.

[4] Kuromoto, N.K. - Simão, R.A. - Soares, G.A.: Mater. Charact. 58 (2007) 114.

[5] Krasicka-Cydzik, E.: Corr. Protect. XLII (1999) 48

[6] Janeček, M. – Nový, F. – Stráský, J. et al: J. Mech. Behav. Biomed. Mater 4 (2011) 417

[7] Vrátná, J. - Hadzima, B. - Bukovina, M. - Janeček, M.: J. Mater. Sci. 45 (2013) 4510

30th DANUBIA-ADRIA
Symposium on Advances in Experimental Mechanics
September 25-28, 2013 - Primošten, Croatia

7B23 021

CORRELATION BETWEEN MICROSTRUCTURE, HARDNESS AND FRACTURE TOUGHNESS OF HEAT-TREATED HIGH-SPEED STEEL

Franjo Cajner[1], Vojteh Leskovšek[2], Dragan Pustaić[1*]

[1] University of Zagreb, Faculty of Mechanical Engineering and Naval Architecture, Ivana Lučića 5, HR-10000 Zagreb, CROATIA. E-mails: franjo.cajner@fsb.hr, *dragan.pustaic@fsb.hr

[2] Institute of Metals and Technology, Lepi Pot 11, SI-1000 Ljubljana, SLOVENIA.

1. Introduction

The correlation between microstructure, hardness and fracture toughness of vacuum heat-treated high-speed steel AISI M2 was investigated. Our intention was to investigate the influence of microstructural parameters such as the volume fraction of undissolved eutectic carbides, their mean diameter, the mean distance between the carbides, as well as the volume fraction of retained austenite in the matrix, on the above mentioned mechanical and fracture properties. The experimental investigations were performed on the specimens which had the following chemical composition (mass content in %): 0.89% C, 0.20% Si, 0.26% Mn, 0.027% P, 0.001% S, 3.91% Cr, 4.74% Mo, 1.74% V and 6.10% W.

By means of heat treatment, the microstructure of high-speed steel can be changed. Due to secondary hardening under different tempering conditions, high-speed steels can obtain the same hardness but different microstructures and consequently different fracture toughness. Therefore, the optimization of the parameters of vacuum heat treatment of high-speed steels is a worthwhile task.

2. Description of vacuum heat treatment

The test specimens for investigating the fracture toughness K_{Ic} were heat-treated in a horizontal vacuum furnace *Ipsen VTTC-324R,* quenched with uniform high-pressure gas, using N_2 at a pressure of 5 bars. The graduate preheating (650 °C and 850 °C) was performed by rapidly increasing temperature (15 °C/min) to the austenitization temperature (between 1050 °C and 1230 °C). The homogenious gas quenching to a temperature of 80 °C was performed, and double-tempering on the temperatures of 500 °C and 540 °C in the same furnace in duration of 1h.

3. Test specimens for fracture toughness investigation of high-speed steel

In the frame of experimental work performed by the second author [2], circumferentially notched and fatigue pre-cracked tensile test specimen was used, machined to the dimensions indicated in Fig.1. Measurements of fracture toughness were

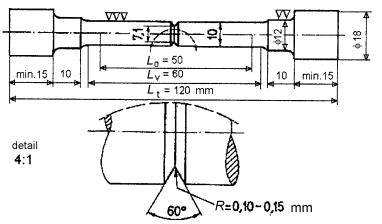

Fig. 1. Circumferentially notched and fatigue pre-cracked K_{Ic} test specimen.

performed, at room temperature, using an *Instron 1255* tensile testing machine. During the tests the tensile load/displacement relationship was recorded until failure of the test specimen occurred.

4. Microstructure investigation

The microstructural tests were performed on the individual groups of K_{Ic} test specimens using, firstly, optical microscope, and, secondly, scanning electron microscope (SEM). The microstructure investigation comprised the quantitatively determination the following parameters: the size of

the prior austenite grains, the mean diameter of the undissolved eutectic carbides, and the volume fractions of the individual microstructural phases, such as the undissolved eutectic carbides, the tempered martensite, and the retained austenite, Fig.2. The images of 11-16 visible fields, obtained on each of the metallographic specimens, were analysed by using *KS Lite V2.00* software for image analysis.

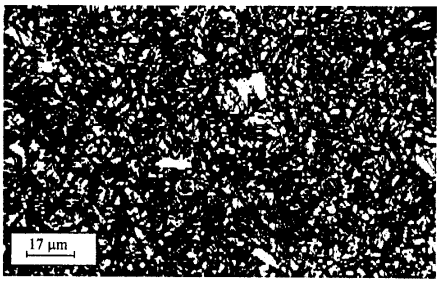

Fig. 2. Image of the undissolved eutectic carbides and the retained austenite (both white) taken by optical microscope; etched metallographic specimen.

5. Correlation between hardness and fracture toughness

The fracture toughness K_{Ic} is a very selective mechanical property and it is very sensitive to the change of the temperature of austenitization and to the temperature of tempering, as well. From the diagram in the Fig.3, it is clearly seen that, at higher austenitization temperatures (in a range from 1150 °C till 1230 °C), if the fracture toughness K_{Ic} increases, the hardness HRc remains almost constant at the temperature of tempering 500 °C. Generally, it could be said that with increase of austenitization temperature, the hardness HRc is also increased, while the fracture toughness K_{Ic} is decreased (at $\vartheta_t = 540°C$).

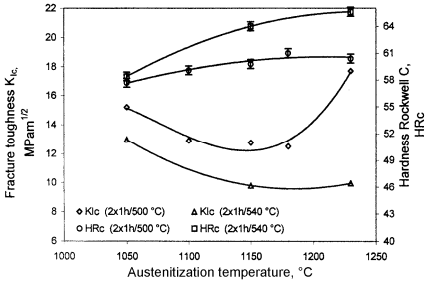

Fig.3. Influence of temperature of austenitization on the hardness HRc and fracture toughness K_{Ic} of the investigated high-speed steel.

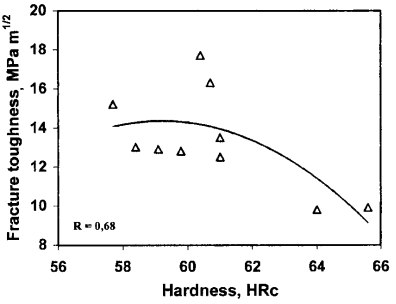

Fig. 4. Dependence of measured fracture toughness K_{Ic} upon the hardness HRc of investigated high-speed steel AISI M2.

6. Remarks

- The microstructure of investigated high-speed steel can be changed by vacuum heat treatment. The aim was to optimize the ratio between hardness and fracture toughness K_{Ic}.
- It has also been experimentally confirmed that different microstructural parameters, such as the volume fraction of retained austenite, the volume fraction of undissolved eutectic carbides, and the mean distance between the carbides have a significant effect on the measured fracture toughness K_{Ic}, [1-3].
- The second author has derived, in his Ph.D. thesis [3], a semi-empirical correlation between these parameters for calculating the fracture toughness K_{Ic} of the investigated high-speed steel AISI M2. The agreement between the measured and calculated values of fracture toughness was very good.

References

[1] Leskovšek, V., Ule, B., Liščić, B., Relations between fracture toughness, hardness and microstructure of vacuum heat-treated high-speed steel, J. of Mater. Proc. Tech., **127**, 2002. pp. 298-308.

[2] Ule, B., Leskovšek, V., Tuma, B., Estimation of plain strain fracture toughness of AISI M2 steel from precracked round-bar specimens, Engring. Fract. Mech. **65**, 2000. pp. 559-572.

[3] Leskovšek, V., Optimization of the vacuum heat treatment of high-speed steels, Ph.D. Thesis, University of Zagreb, 1999.

[4] ESIS P2-92: ESIS Procedure for determining the fracture behavior of materials, European Structural Integrity Society, ESIS, Delft University of Technology, 1992.

30th DANUBIA-ADRIA
Symposium on Advances in Experimental Mechanics
September 25-28, 2013 - Primošten, Croatia

7B24 096

USAGE OF RADIATIVE HEAT TRANSFER SIMULATIONS TO DETERMINE ALTERNATIVE REFLECTOR SHAPE

Jan Loufek[1], František Vlas[2]

[1] Technical University of Liberec, Faculty Faculty of Mechatronics, Informatics and Interdisciplinary Studies, The Institute of Mechatronics and Computer Engineering, Studentská 1402/2, 461 17 Liberec, Czech republic. E-mail: jan.loufek@tul.cz

[2] Technical University of Liberec, Faculty Faculty of Mechatronics, Informatics and Interdisciplinary Studies, The Institute of Mechatronics and Computer Engineering, Studentská 1402/2, 461 17 Liberec, Czech republic. E-mail: frantisek.vlas@gmail.cz

1. Introduction

The contribution presents some results achieved in the issue of numerical simulations of radiative heating of shell moulds that are used for the artificial leather production. In the process of moulds heating by set of emitters, it is necessary to heat up mould preferably equally.

To ensure uniformity of heat, it was necessary to design suitable algorithms for the mould heating control. To facilitate heating regulation, it was necessary to design alternative shapes of reflectors, which are more suitable for uniform heating of a mould. Requirement for heat emitters is to ensure spatially equal heat flow to irradiated surface as much as possible.

This article deals with utilization of radiative heat transfer simulation to optimize amount of heat transfer. Article presents two approaches. The first approach is focused on reduced two-dimensional task simulations. It can be used for determination of an alternative profile of reflector. The second one follows the results of two-dimensional task and extends it to three dimensions. The second approach involves several issues that make it difficult to solve.

2. Radiative heat transfer

In general, every part of an arbitrary system radiates continuously some electromagnetic energy. The energy amount depends on the temperature of the system part and its surface properties. The amount of energy emitted per square meter e_b (Wm^{-2}) by black body expresses the Stefan-Boltzmann law:

$$e_b = \sigma T^4 , \qquad (1)$$

where T (K) stands for absolute temperature and $\sigma = 5.670373 \times 10^{-8}$ $Wm^{-2}K^{-4}$ is Stefan-Boltzmann constant. The main issue in solving described problem is to determine view factor F_{i-j} (-). View factor F_{i-j} , which take the value between 0 and 1, represents the portion of energy emitted by surface i that strikes surface j.

$$F_{i-j} = \frac{1}{A_i}\int_{A_i}\int_{A_j}\frac{\cos\beta_i \cos\beta_j}{\pi r^2} dA_i dA_j \qquad (2)$$

In the term (2), r (m) stands for the length of particular points A_i and A_j join and β_i (rad) is the angle between the join and outer normal of A_i in the particular point of A_i.

3. Numerical model of infrared emitter

Our model of infrared emitter is designed to be able to figure heat flux distribution over any surface. The model is composed of a set of particle surfaces, whereas every particle surface has given particular properties (location, emittance and temperature).

3.1 Two-dimensional model

The implemented two-dimensional model uses Hottel´s crossed-strings rule [1] to determine view factors between particular surfaces of the whole system. The model was implemented as a simulation tool named IRE Designer. The tool has implemented several additional functionalities such as gradient optimization algorithm, which adjusts the shape of emitter reflector, to achieve better match between simulated and required tracing. For the sake of calibration, the tool enables the import of measurement results and subsequent comparison of measured a simulated values obtained for a particular real emitter. Fig. 1 shows an example of

simulation results obtained for a common emitter used in the process of artificial leather production.

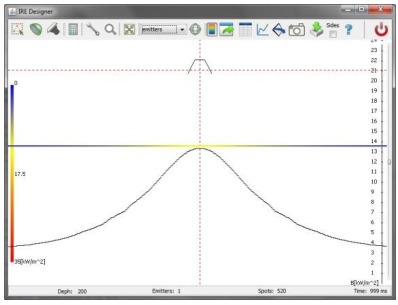

Fig. 1. IRE Designer.

Some results of the reflector optimizing are shown in Fig. 2.

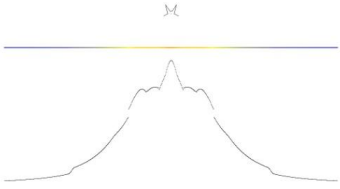

Fig. 2. Design of alternative reflector shape.

3.2 Three-dimensional model

The three-dimensional model was implemented as an extension of two-dimensional one. Taking into account of the third dimension implied two main problems to deal with: .

- Numerical solution of the term (1), which must be evaluated between every surface pair in every step of optimizing algorithm.
- Finding of suitable optimizing algorithm that can solve problem of searching alternative emitter shape in three-dimensional space in a real time.

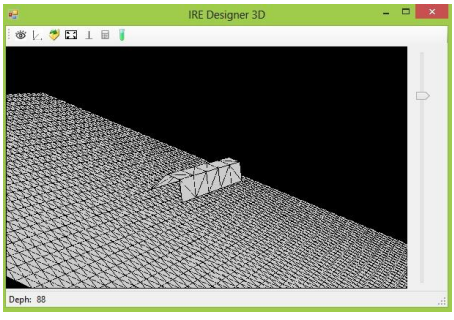

Fig. 2. IRE Designer 3D.

3.3 View factor calculation using the Monte Carlo method

Every plane is defined by three points, so we can speak about triangles in space. Let's reduce the problem to two triangles – emitter and receiver. As a first step we need to generate random points within emitter triangle. These random points are generated by randomize size of vectors computed from triangle points. Next step is to create random rays from these points in the direction of outer normal of the emitter. These rays are generated by random rotation (between $-\pi/2$ and $\pi/2$) of the emitter's normal vector. In this step the solution is focused on how to determine whether a particular ray intercepts the receiver. This task is solved by computing sum of triangles areas created by points of receiver and interception point (ray and plane defined by receiver triangle). If the computed area is same as the area of receiver, we can say, that the ray intercepts the receiver. After sending enough rays we can determine how much is the receiver affected by the emitter.

4. Conclusions

Represented numerical model is based on radiation heat transfer theory and its utilization for two-dimensional and three-dimensional cases. Results of the presented two-dimensional solution are used as basis for creation of the three-dimensional model with proper optimizing algorithm to achieve satisfying results.

Acknowledgements

This work is cofinanced from the student grant SGS 2013/78000 Progressive mechatronics, control and measurement systems with application of advanced simulation methods.

References

[1] Lienhard IV, J. H., Lienhard V, J. H., A heat transfer textbook. 3rd ed. Cambridge, Mass: Phlogiston Press, 2003. ISBN 09-713-8352-9.

[2] Siegel, R., Howell, J. R.. Thermal radiation heat transfer. 4th ed. New York: Taylor, 2002, 868 s. ISBN 15-603-2839-8.

[3] Loufek, J. Simulations of radiation heat transfer in design of alternative infrared emitters. In: XI. International Conference on the Theory of Machines and Mechanisms 2012. Liberec: Technická univerzita v Liberci, 2012.

30th DANUBIA-ADRIA
Symposium on Advances in Experimental Mechanics
September 25-28, 2013 - Primošten, Croatia

7B25 076

STRESS-STRAIN BEHAVIOUR OF LASER WELDED STAINLESS STEEL JOINTS

K. Colic[1], S. Petronic[1], A. Sedmak[2], I. Cekovic[1]

[1] Innovation Center, Faculty of Mechanical Engineering, Belgrade, Kraljice Marije 16, Serbia. E-mail: kbojic@mas.bg.ac.rs

[2] Faculty of Mechanical Engineering, University of Belgrade, Kraljice Marije 16, 11000 Belgrade, Serbia. E-mail: asedmak@mas.bg.ac.rs

1. Introduction

Stainless steel materials were analyzed in order to investigate the applicability of laser welding to the fabrication of biomedical devices. There are many stainless steel alloys available for use in biomedical applications, each with individual characteristics that make it a good solution to a certain problem [1]-[3]. During the last several decades, several stainless steel alloys have been developed for biomedical use, but the most often used steel alloy in biomedical applications is grade 316 L.

Implanted medical devices must function flawlessly and they must have an aesthetic quality that helps with sterilization and does not irritate the tissue. The welds on these implantable must be a hermetic seal very close to heat sensitive components and since the value of the component before welding is very high, the yield from the welding process must also be high. Laser welding meets these requirements, as this welding method produces a smooth hermetic seal. Laser welding of stainless steel biomaterials is used for all biomedical applications, where is of importance that parts must be joined with smooth welds without pores [4]. Laser welding is a high energy-density, low heat-input process with specific advantages over conventional fusion welding processes. These include high welding speed, narrow heat affected zone, low distortion, ease of automation, single-pass thick section capability and enhanced design flexibility.

The 316 L is easy to weld, does not crack easily, and does not corrode near the weld zone like other stainless steel alloys with higher content of carbon. However, under certain circumstances, even 316L stainless steels may corrode inside the body, e.g. in highly stressed and oxygen-depleted regions, such as contact points under the screws of the bone fracture plate. This steel is suitable for temporary implants, such as fracture plates, screws, and hip nails, and for manufacturing certain medical devices. Methods for surface modification, such as glow-discharge nitrogen implantation, anodization and passivation are often used to improve corrosion and wear resistance, and fatigue strength of 316L stainless steel. It has excellent forming and welding characteristics, thus it is commonly used for a variety of parts for applications in the industrial fields [5]-[6]. Formability and weldability of the S 316 L alloy are important factors for the fabrication and biomedical application of these components.

2. Experimental results

The experiment was carried out on stainless steel 316L sheets, heat treated by Annealing - heat to 1010-1120°C and cooled rapidly.

Grade 316L is the modified molybdenum-bearing grade, the low carbon version of 316, with a maximum amount of the carbon content of 0.03%, for better corrosion resistance to chloride solution and to minimize the sensitization. The minimum effective concentration of chromium is 11% to impart corrosion resistance in stainless steels. The maximum amount of 4% of molybdenum in this alloy, gives 316 better overall corrosion resistant properties than other austenitic stainless steels, particularly higher resistance to pitting and crevice corrosion in chloride environments.

Stainless steel 316L sheets were welded by pulsed Nd: YAG laser type HTS Mobile LS-P160 (OR Laser), without filler material. Mean laser power was 160 W, peak power was 7.5 kW, and max energy was 80 J. The parameters of the laser process were: laser energy 48J, pulse duration 6.0

ms and pulse frequency 5.5 Hz. (62 J, 5.0 ms, 6.0 Hz).

Specimens for the metallurgical and mechanical tests were sampled from the weld joints. Dimension of samples were 50x50x0.7 mm.

Tensile tests were carried out at room temperature according to relevant ISO specifications. Tensile testing machine used in this experiment was electro-mechanical type SCHENCK TREBEL RM 400, and parameters that were determined were tensile strength, yield strength and elongation.

Detailed investigation of microstructural changes was performed by optical microscope -model KEYENCE VH-Z100, scanning electron microscopes (SEM) model: JOEL JSM-5800, as shown in [7]. Tensile specimen fracture surfaces were observed using a scanning electron microscope (SEM).

Examination of various aspects of pulsed laser welding of steels and superalloys show that through proper control of welding parameters, especially with pulse heat tailoring and manipulation of plasma location, weld seam shape and thermal history may vary.

The aim of our investigation was to find optimal parameters of laser welding process that would produce crack-free weld seam and good mechanical properties. In this paper are presented results for two different specimens, welded with different laser welding process parameters.

Mechanical properties of welded joint for sample 1 and 2 were determined by tensile test. Results of tensile tests for the welds are presented in Figures 1 and 2, and they show load–displacement curves for various tensile specimens.

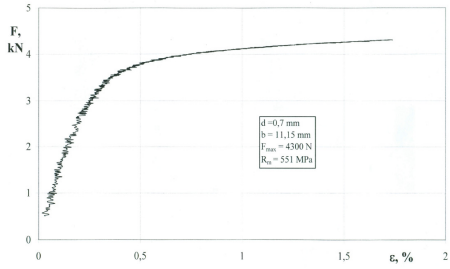

Fig. 1. Diagram of tensile tests for sample 1.

Figure 1 indicates maximum load of 4300 N (tensile strength 551 MPa) for the optimal welding process parameters used for sample 1, whereas Fig. 2 indicates maximum load of 3856 N (tensile strength 502 MPa) for badly chosen welding parameters, used for sample 2. The experimental results have confirmed both the expected tensile properties of austenitic stainless steel, and the effect of welding parameters, contributing to the complete understanding of its stress-strain behavior.

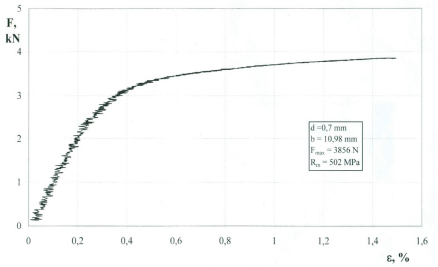

Fig. 2. Diagram of tensile tests for sample 2.

The experimental study performed in this paper has confirmed Grade 316L outstanding welding characteristics. Post-weld annealing is not required when welding thin sections.

Acknowledgements

This work was supported by the Ministry of Science of the Republic of Serbia under contract number TR-35040.

References

[1] Park, J.B., Lakes, R.S., Biomaterials An Introduction. Plenum Press, New York, 1992.

[2] Niinomi, M., Fatigue characteristics of metallic biomaterials, Int. Journal of Fatigue, **29**, 2007. pp. 992–1000.

[3] Milne, I. et al., Com. Structural Integrity 9, Elsevier Ltd, Oxford, 2003.

[4] Klages, K. et al., Laser Beam Micro Welding of Dissimilar Metals, Proc. of SPIE, **5063**, 2003. pp. 303-307.

[5] Hirokazu Yamada et al., Re-weldability tests of irradiated 316L(N) stainless steel using laser welding technique, Jour. of Nuclear Mat., **307–311**, 2002. pp. 1584–1589.

[6] Kazuyuki Furuya et al., Mechanical properties of F82H/316L and 316L/316L welds upon the target back-plate of IFMIF, Jour. of Nuclear Mat., **386–388**, 2009. pp. 963–966.

[7] Colic, K. et al., Laser Welding Process of Stainless Steel Used for Biomedical Applications, Welding and Material Testing, **20/3**, 2011. pp.16-19.

30th DANUBIA-ADRIA
Symposium on Advances in Experimental Mechanics
September 25-28, 2013 - Primošten, Croatia

7B26 070

DETERMINATION OF STRESSES LEVEL IN THE WELDED JOINT OF THE ECCENTRIC PRESS FRAME

Damian Derlukiewicz[1], Jacek Karliński[1]

[1] Wrocław University of Technology, Faculty of Mechanical Engineering, Institute of Machine Design and Operation, Lukasiewicza 7/9, 50-371 Wrocław, POLAND. E-mail: damian.derlukiewicz@pwr.wroc.pl, jacek.karlinski@pwr.wroc.pl

1. Introduction

The object of the analysis was the welded joint in the eccentric press frame (fig. 1), with the load to 12.5 MN. The press consists of a frame, inside which there is transmission with shafts of the entire stamping mechanism. The frame is supported by the supporting pillars that rest on the basis fixed to the foundation.

Fig. 1. Eccentric press

2. Kinematic calculations of press drive

In order to determine the loading characteristics that act on the press frame during stamping process it was necessary to evaluate the kinematic model of the press drive [1]. This will be used to estimate the effort state of investigated joint. For that reason the complete model of press transmission and numerical simulation of transmission kinematic was performed with use of CAD software (fig. 2).

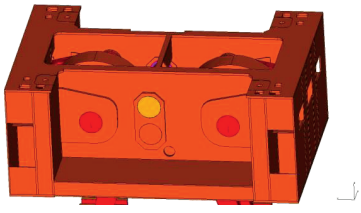

Fig. 2. 3D model of eccentric press frame

The model was used to determine the forces acting on the individual kinematic pairs during pressing of the force of 12.5 MN at a constant rotational speed of the drive shaft. The complete stamping mechanism is shown in fig. 3.

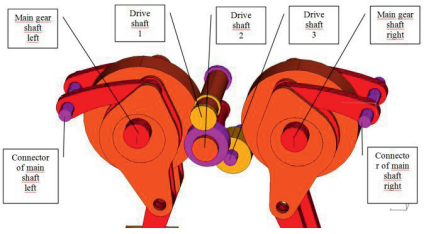

Fig. 3. Kinematic model of stamping eccentric press drive, components - kinematic pairs

The constant speed of the drive shaft due to nominal discharge cycles equivalent to 12 turns per minute. The calculations take into account the weight of the tool of 31.4 Mg. It is also assumed that the stamping power increases linearly from the minimum to the maximum value of 12.5 MN. Determination of forces acting on the body of the press frame has been done for several different computational cases to see how the work unevenness affects the value of these forces and, consequently, on the effort state of the press frame [2,3]. The results of the kinematic analysis allowed to determine the course of the forces and moments variation as a function of changes in the position angle of the drive shaft and the selected diagram is presented in fig. 4.

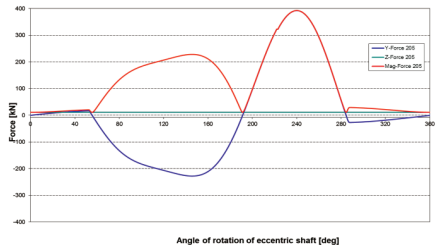

Fig. 4. Forces in the shaft connecting the left main wheel with frame

3. Strength calculations

The strength calculations take into account the characteristic load values that occur during a single cycle and were done with use of FEM. The boundary conditions are defined on the basis of kinematic and dynamic analysis of press power system. The press frame strength calculations give the results in the form of equivalent stress contours by Huber-Mises hypothesis. The analysis allows to determine the stress level of area of investigated welded connection that equals 120MPa (fig. 5).

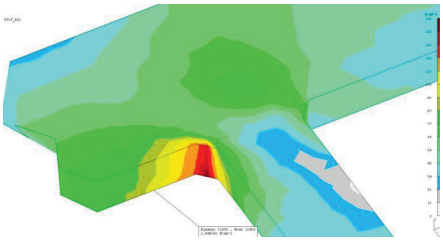

Fig. 5. Stress contour lines in welded joint [MPa]

4. Experimental testing

Additionally to confirm the stress level of analyzed joint the experimental measurements were done with the use of strain gauges. The measurements were conducted for number of cycles of press stamping at the same loading as for the FEM calculations. The measurement allows to receive the waveforms of stresses in the selected points, similar that in FEM analysis (fig 6).

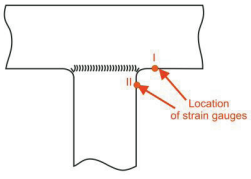

Fig. 6. Location of strain gauges for experimental testing

On the basis of the stress waveforms the ranges of stress levels at loading cycles in measurement conditions during press operation were determined [4]. Table 1 presents the maximal values of equivalent stresses at the maximal press loading.

Experiment designation	Stress [MPa]
Point I	118
Point II	60

Tab. 1. Values of maximal stresses in measurement points I and II

The results of experimental testing shows a very good accuracy of numerical simulations.

5. Conclusions

The strength calculations of the press frame including welded joint allows to determine the stress level of the area of the joint during the stamping process. The experimental verification confirms the accuracy of FEM results.

These kind of determination of stresses of selected welded joint can be an initial stage to the future fatigue analysis. The presented results of performed FEA can be used in the method of Hot Spot in order to determine the fatigue strength of the selected joint.

References

[1] Rusiński E., Czmochowski J., Smolnicki T.: Advanced Finite Element Method for Load-carrying Structures of Machines (in Polish), Oficyna Wydawnicza PWr., Wrocław 2000.

[2] Rusiński Eugeniusz, Smolnicki Tadeusz, Karliński Jacek: Simulation Studies of Mining Machine Protective Cabin Safety (in Polish), Prz. Mech. 1998 Vol.. 57, No. 15, pp. 20-25, 12 figs, 8 refs, sum.

[3] Smolnicki T., Rusiński E.: Superelement-based modeling of load distribution in large-size slewing bearings. Journal of Mechanical Design. 2007, vol. 129, nr 4, s. 459-463.

[4] Rusiński E., Moczko P., Czmochowski J., Numerical and experimental analysis of a mine's loader boom crack, Automation in Construction, 2008, vol. 17, no 3, 271-277

30th DANUBIA-ADRIA
Symposium on Advances in Experimental Mechanics
September 25-28, 2013 - Primošten, Croatia

7B27 009

INFLUENCE OF FILLER MATERIAL ON DYNAMIC MECHANICAL BEHAVIOUR OF OPEN-CELL METAL FOAM

Lovre Krstulović-Opara[1], Matej Vesenjak[2], Zoran Ren[2], Željko Domazet[1]

[1] University of Split, Faculty of Electrical Eng., Mechanical Eng. and Naval Architecture, R. Boškovića 32, HR-21000 Split, CROATIA. E-mails: Lovre.Krstulovic-Opara@fesb.hr, Zeljko.Domazet@fesb.hr

[2] University of Maribor, Faculty of Mechanical Engineering, Smetanova 17, SI-20000 Maribor, Slovenia. E-mails: matej.vesenjak@um.si, zoran.ren@um.si

1. Introduction

Open-cell metal foams [1] with high degree of porosity are materials with particular investigation potential due to their advantageous characteristics such as high energy absorption capabilities, lightweight, insulation and fire resistance. These characteristics make them of particular interest for transport industries, aerospace, protection of objects, etc.

The initial idea of introducing filler material to regular open-cell cellular structures investigated in [2-4] was applied to irregular open-cell aluminum metal foam produced by m.pore GmbH. The filler material was a two component silicon rubber 2K-Z1010, described in [2, 4], enabling de-bonding of silicon from foam structure. The proper filling of foam interior was enabled by vacuum curing.

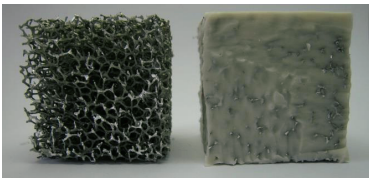

Fig. 1. Cellular structure specimens without (left) and with (right) silicone pore filler.

The infrared thermography based on high speed cooled middle-wave camera was used to trace plastification zone in material and evaluate the plastification mechanism of the base material. The 320 Hz frame rate enabled acquisition of dynamical loading process presented herein.

2. Compression tests

The compression tests were performed on 40x40x40 mm specimens on servo-hydraulic dynamic loadframe at speed of 284 mm/s, achieving the deformation rate of 15 s^{-1}.

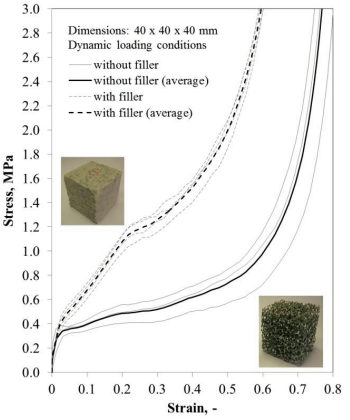

Fig. 2. Dynamical response of foam with and without filler included.

The surface under curves represents the absorbed energy density. Introduction of the filler material increases absorbed energy capacity by 97.2% in comparison to the foam specimen without filler. The drawback of filler is increase of mass by 92.9%.

3. Infrared evaluation of plastification mechanism

As plastic yielding is accompanied by significant heat energy dissipation, the thermal imaging enables visualization of plastification mechanism.

Figure 3 depicts deformation process and formation of yielding zone (stress plateau) where stain localization and plastification front propagates from movable lower loading palate towards upper fixed plate until total densification. The whole compression process is characterized by layer-wise collapse of intercellular struts. After one layer comes in the self-contact, plastification wave propagates towards the next layer. This collapse mechanism is described in [5].

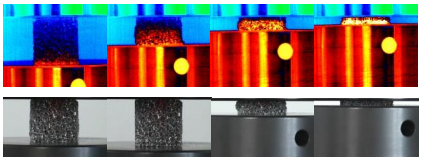

Fig. 3. Infrared and video loading sequence of metal foam without filler material.

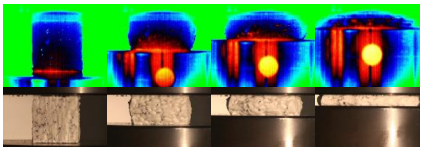

Fig. 4. Infrared and video loading sequence of metal foam with filler material.

Figure 4 depicts deformation process of metal foam with filler material. The incompressible filler material causes different mechanical behavior. For the case without filler, the foam was compressed without significant transversal deformation.

In case of the metal foam with the filler material, a layer-wise collapse is not detected. Formation and transition of hot front proves that there is a conical front propagating from moving compression plate towards upper fixed plate. Self-contact of struts is prevented by filler material. The incompressibility of silicone causes different stress distribution. There is significant transverse deformation that causes transverse tension in metal foam. The composite material (foam and filler) is significantly influenced by the contribution of filler material. The filler material causes tangential shear bends, what is depicted in cross-section of the compressed specimen (Fig. 5).

Fig. 5. Cross-section of compressed specimen showing conical deformation distribution

4. Remarks

- The Influence of filler material significantly increases energy absorption capabilities of metal foams, with drawback of losing the lightweight characteristics of cellular materials.
- Introduction of filler materials shifts plastification mechanism from flat propagating front to formation of conical of shear bends.
- The infrared thermography based on cooled middle-wave infrared camera is an appropriate method for evaluating dynamical loading of cellular materials.

Acknowledgements

Financial support from the Ministry of Science, Education and Sports (project ‘‘Fatigue strength of constructions and materials‘‘) and from the Slovenian Research Agency is gratefully acknowledged.

References

[1] Gibson, L.J, Ashby, M.F., Cellular solids: structure and properties, Cambridge University Press, Cambridge, 1997.

[2] Vesenjak, M., Krstulović-Opara, L., Ren, Z., Öchsner, A., Domazet., Ž., Experimental Study of Open-Cell Cellular Structures with Elastic Filler, Material. Exp. Mech., **49**, 2009. pp. 501-509.

[3] Vesenjak, M., Öchsner, A., Ren, Z., Characterization of open-cell cellular material structures with pore fillers, Mater. Lett., **62**, 2008. pp. 3250-3253.

[4] Vesenjak, M., Krstulović-Opara, L., Ren. Z., Characterization of photopolymer cellular structure with silicone pore filler, Polymer Testing, **31**, 2012. pp. 705-709.

[5] Pampolini, G., Del Piero, G., Strain localization in open-cell polyurethane foams: Experiments and theoretical model, Journal of Mechanics of Materials and Structures, **3**, 2008, pp. 969-981.

30th DANUBIA-ADRIA
Symposium on Advances in Experimental Mechanics
September 25-28, 2013 - Primošten, Croatia

7B28 051

EFFECT OF PRECIPITATION AND PLASTIC DEFORMATION ON THE HARDNESS OF AZ 61 ALLOY

Soviarová Andrea[1)], Dresslerová Zuzana[1)], Palček Peter[1)], Blažek Dalibor[2)]

1) University of Žilina, Faculty of Mechanical Engineering, Department of Material Engineering, Univerzitná 8215/1, 010 26 Žilina, Slovakia
2) VŠB - Technical University of Ostrava, Nanotechnology Centre, 17. Listopadu 15, 708 33 Ostrava - Poruba, Czech Republic,
Corresponding author: andrea.soviarova@fstroj.uniza.sk

1. Introduction

Nowadays we are challenging a large demand for an effective use of materials based on magnesium. Due its specific weight, corrosion resistance, density and strength, magnesium alloys are very interesting materials for applications in different industries. [1]

Magnesium and its alloys have a hexagonal close-packed crystal structure. For plastic deformation it is needed at least five independent slip systems. In each grain of magnesium there are only two independent active slip systems thus plastic deformation in magnesium is limited only to the basal slip planes at the room temperature. Additional slip systems are activated after increasing of the temperature and deformation at prismatic and pyramidal slip systems occurs in this case. [2-4]

The contribution is focused on increasing of the hardness of AZ 61 magnesium alloy by precipitation and plastic deformation.

2. Experimental Results

Material used for experimental study was magnesium alloy AZ 61 which was manufactured by squeeze casting. The test specimen was annealed for 22 hours at 420 °C and then cooled in a 60 °C water.

After homogenisation annealing all segregated phases were dissoluted. The microstructure after annealing is created by polyedric grains and the grain boundaries are clearly visible. (Fig.1).

The Vickers hardness method HV0.5 was used for experimental measurements which were carried out on Zwick / Roell Indentec ZHμ hardness tester.

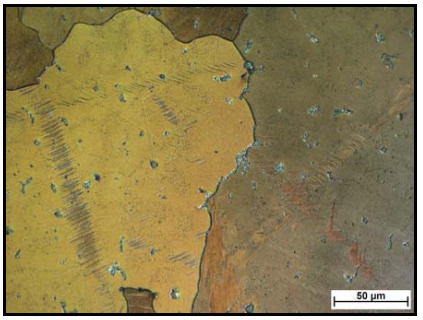

Fig. 1 Microstructure of magnesium alloy AZ 61 after homogenization annealing, etch. Nital 1%

Precipitation hardening

The precipitation hardening was carried out at a temperature of 200 °C at predetermined time intervals. The average hardness of the annealed material was 60 HV. From the obtained hardness values it is clear, that the hardness of the alloy AZ61 was not increasing with increasing time of precipitation hardening (Fig. 2).

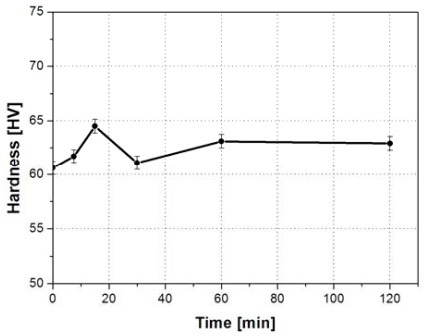

Fig. 2 Dependence of hardness on aging time

During the aging up to 120 min. the hardness didn´t significantly changed.

Compression plastic deformation

The test specimen had the shape of a cuboid with a length of 20 mm, width of 13 mm and height of 10 mm. The specimen was after homogenisation annealing as in previous case. Before the compression test a special lubricant was placed between the faces of the specimen and the ram which prevented unwanted specimen deformation caused by shear strain. The specimen was step by step loaded with a higher compression force and the surface hardness and plastic deformation were measured among each loading (Fig.3).

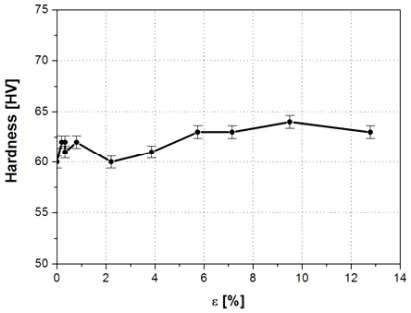

Fig. 3 Dependence of surface hardness on compression deformation

Uniaxial compression plastic deformation did not cause significant increase of hardness.

Plastic deformation by shear stress

The specimen used for this measurement has the same geometry and dimensions as in previous test. The surface was plastically deformed by sliding friction. This plastic deformation caused highest hardness increase. After this, the surface hardness increased from the original value of 60 HV0.05 to 112 HV0.5.

Plastic deformation by shear stress caused creation of plastically deformed surface layer, increase of the dislocation density and grain crushing in the surface and subsurface layers of material (Fig. 4). These facts resulted in increasing of the surface hardness of the magnesium alloy.

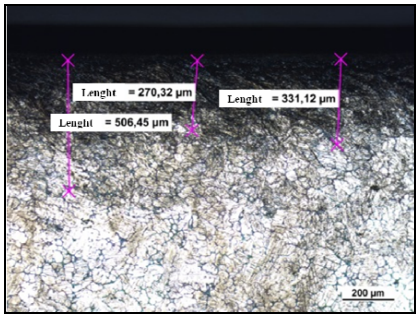

Fig. 4 Deformed surface layer

Conclusions

From obtained results can be concluded:

• continuous precipitation does not affect the hardness of AZ 61 alloy,

• uniaxial compression loading does not cause any significant hardness increase on the surface,

• the surface hardness increased from 60 HV up to 112 HV by shear plastic deformation.

Acknowledgements

This work has been supported by Scientific Grant Agency of Ministry of Education of Slovak republic and Slovak Academy of Sciences Nº1/0797/12 and project SK-PL-0083-12

This work was supported by IT4Innovations Centre of Excellence project (CZ.1.05/1.1.00/02.0070), by "New creative teams in priorities of scientific research" (CZ.1.07/2.3.00/30.0055) and the Grant Agency of the Czech Republic (No. P205/11/2137).

References

[1] AVEDESIAN, M. M.; BAKER, H. *Magnesium and Magnesium Alloys*. Materials Park OH: ASM International, 1999. 298 s. ISBN 0-87170-657-1.

[2] BLAŽEK, D. Analýza spektra vnútorného tlmenia horčíkových zliatin. Dizertačná práca. Žilina. 2012.

[3] KRUML, T.; MICHEL, J.-P. Úvod do teorie dislokací. Brno : Vysoké učení technické v Brně, 2009. 59 s. ISBN 80-214-0576-3.

[4] PLUHAŘ, J., PUKÁR, A., KOUTSKÝ, J., MACEK, K., BENEŠ, V. Fyzikální metalurgie a mezní stavy materiálu, Praha: SNTL, 1987. 418s.

30th DANUBIA-ADRIA
Symposium on Advances in Experimental Mechanics
September 25-28, 2013 - Primošten, Croatia

7B29 047

DUCTILE CAST IRON MICROSTRUCTURE AND ITS INFLUENCE ON MECHANICAL PROPERTIES

Predrag Čanžar[1], Zdenko Tonković[2]

[1] Končar – Electrical Engineering Institute, Inc., Fallerovo šetalište 22, HR-10002 Zagreb, CROATIA. E-mail: pcanzar@koncar-institut.hr

[2] University of Zagreb, Faculty of Mechanical Engineering and Naval Architecture, Ivana Lučića 5, HR-10000 Zagreb, CROATIA. E-mail: ztonkov@fsb.hr

1. Introduction

The vast majority of modern structural components used in industry and power generation are made of ductile cast iron. One such kind of nodular cast iron is EN-GJS-400-18-LT which is especially used for the manufacture of dynamically loaded structural components. Due to fatigue loading, damage accumulates preceding in crack initiation and propagation which contributes to the overall failure of the structure. Well known fact is that the content of certain phases, i.e. ferritic and pearlitic as well as the size and shape of the graphite nodules influences significantly fracture toughness and fatigue life.

Since the object of this paper is the cast iron grade EN-GJS-400-18-LT, its nodules or graphite spheroids in a ferritic matrix provide large ductility and fatigue strength [1]. In order to prevent component failure with catastrophic consequences it is especially important to investigate the influence of the microstructure on the before mentioned material.

2. Materials and specimens

Four types of cast iron EN-GJS-400-18-LT produced by different technologies are considered. For producing nodular cast iron, one nonstandard technique (type 100) and three standard techniques (Flotret − type 200, Tundish − type 300, and Inmould − type 400) are used. The graphite morphology of the casting types is shown in Fig. 1.

As it can be seen, material produced by the Flotret process has significantly larger nodules with low density distribution than the other three types of nodular cast iron. Besides that, Flotret material has graphite nodules with the lowest circularity (irregularly shaped nodules) and lower content of pearlitic grain.

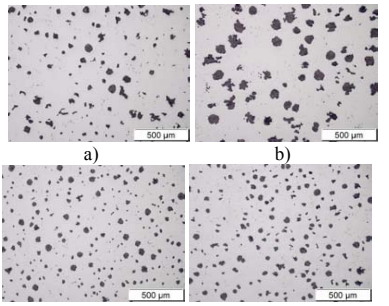

Fig. 1. Microstructure of the nodular cast iron for: a) type 100; b) type 200; c) type 300 and d) type 400.

All uniaxial (monotonic and cyclic) as well as fatigue tests are conducted at room temperature on a Walter Bai servohydraulic testing machine with a load capacity of ±50 kN. Fig. 2 illustrates the schematic shape and geometry of specimens used for experimental part of research.

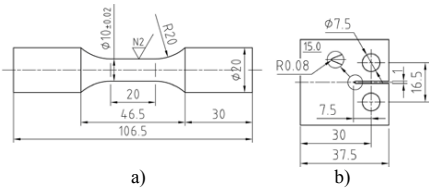

Fig. 2. Shape and dimensions of specimens: a) cylindrical specimen for monotonic and cyclic testing and b) CT specimen.

It comprises a smooth polished cylindrical specimens used for monotonic and cyclic symmetric and unsymmetric tests as well as

compact tension (CT) specimens for fatigue crack growth according to the standards ASTM E606 and ASTM E647.

3. Experimental investigation

Mechanical properties as well as Ramberg-Osgood's material parameters of nodular cast iron grade EN-GJS-400-18-LT are systematically presented in Tab. 1 as well as in Fig. 3 depicted by true stress– strain curves.

Material Series	σ_y [MPa]	σ_u [MPa]	E [GPa]	K [MPa]	n
Nonstandard	286.4	435.1	163.4	700.4	0.1726
Flotret	244.0	385.8	180.0	630.4	0.1809
Tundish	250.0	402.0	215.9	666.7	0.1869
Inmould	255.8	417.2	199.9	691.3	0.1868

Tab. 1. Mechanical properties of nodular cast iron grade EN-GJS-400-18-LT.

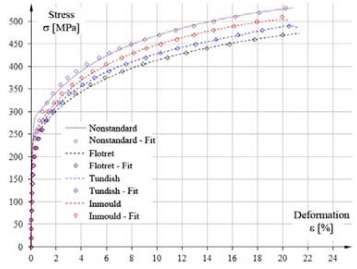

Fig. 3. Monotonic tensile tests (true stress– strain curves) for four different types of nodular cast iron grade EN-GJS-400-18-LT.

Representative cyclic symmetrical test ($\Delta\varepsilon/2=\pm0.8\%$) is presented in Fig. 4 due to conciseness of this paper. More data can be found in [2]. As one can see, significant cyclic hardening is observed.

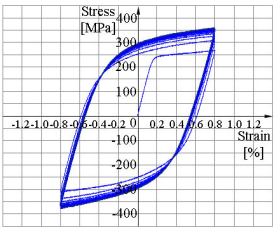

Fig. 4. Representative symmetrical stress–strain hysteresis loops.

Cyclic tests are carried out with the constant strain rate of 10^{-3} s^{-1} limited by applied strain amplitude ($\Delta\varepsilon/2$). For symmetric cyclic test, different strain amplitude is applied from the 0.2% up to the 1.2% with the increment of 0.2%. In these tests mean strain is always equal to zero. In each test, 40 stress–strain hysteresis loops are obtained which is more than enough to achieve a stabilized material behaviour; in fact stabilization of material is achieved after approximately 15 cycles, which was evident from decreased difference between two adjoining stress ranges. Monitoring and recording of crack length during the tests is performed by an optical measuring system Aramis [3]. The tests are conducted on the compact tension (CT) specimens (Fig. 2b).

Fig. 5 shows that Tundish type of material (blue curve) can withstand the largest number of loading cycles till the final fracture, while the Flotret type (black curve) of material shows the least resistance for crack propagation.

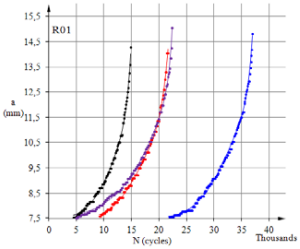

Fig. 5. Number of cycles vs. crack length for R=0.1

4. Conclusion

Experimental results show that size, shape and distribution of the graphite nodules has no significant influence on cyclic hardening of the material but they play a great role in the crack initiation and propagation process. It is shown that the larger irregularly shaped nodules reduce mechanical properties as well as fracture toughness and fatigue strength.

Acknowledgements

The investigations described in this paper are part of the project ''Development of Fatigue Analysis Procedure for Wind Turbine Components'' (TP-09/0120-55) supported by the Croatian Institute of Technology and KONČAR - Electrical Engineering Institute, Inc.

References

[1] Hübner P., Schlosser H., Pusch G., Biermann H., International Journal of Fatigue Vol. 29 (2007), p. 1788–1796.
[2] Čanžar P., Tonković Z. and Kodvanj J., Mat. Sci. & Eng. A Vol. 556 (2012), p. 88-99.
[3] Čanžar P., Experimental and Numerical Modelling of Fatigue Behaviour of Nodular Cast Iron, Doctoral Thesis, University Of Zagreb, Croatia, Faculty of Mechanical Engineering and Naval Architecture, Zagreb, 2012.

30th DANUBIA-ADRIA
Symposium on Advances in Experimental Mechanics
September 25-28, 2013 - Primošten, Croatia

7B30 042

EFFECT OF MODIFICATION BY STRONTIUM ON RECYCLED AL-SI-MG CAST ALLOY

Eva Tillová[1], Mária Chalupová[1], Lenka Hurtalová[1]

[1] University of Žilina, Faculty of Mechanical Engineering, Department of Materials Engineering, Univerzitná 8215/1, 010 26 Žilina, Slovak Republic. E-mail: eva.tillova@fstroj.uniza.sk, maria.chalupova@fstroj.uniza.sk, lenka.hurtalova@fstroj.uniza.sk

1. Introduction

The hypoeutectic Al-Si-Mg based alloys are the most popular alloys of the casting industry worldwide with a highly desirable combination of characteristics, such as excellent castability, weldability, low thermal expansion coefficient, good corrosion resistance, and machinability. Addition of Mg results in good mechanical properties after heat treatment. These properties lead to the application of Al-Si-Mg alloys in automotive industry, especially for wheels, structural castings and suspension parts requiring moderate to high strength and good ductility [1].

Mechanical properties are principally controlled by the cast structure. Microstructure evolution of hypoeutectic Al-Si-Mg alloys during solidification is in two stages: primary dendrite Al phase formation (α-matrix), and the subsequent eutectic transformation (eutectic Si particles in α-matrix) The important influence on mechanical properties of Al-Si-Mg alloys has the morphology of the eutectic silicon [2]. Silicon is a faceted phase and makes the Al-Si eutectic an irregular eutectic. The brittleness of Si-crystals, of course, is the main reason responsible for the poor properties of Al-Si alloys since the large eutectic silicon particles lead to premature crack initiation and fracture in tension conditions [2]. It has been proven that modification of eutectic silicon plays an important role in improving the mechanical properties of hypoeutectic Al-Si alloys. Therefore, many efforts have been made in the modification of casting Al-Si alloys in order to achieve fine silicon phase with beneficial shapes and distribution. The eutectic silicon in Al-Si alloy can be modified using chemical (addition of specific elements), quenching (rapid freezing), outfield or superheating modification [3-4].

Chemically induced modification results in a fibrous or fine flake-like structure. In most foundry applications it occurs by adding small concentrations of elements such as Sr, Na, and Sb. The refinement of scale and distribution of the silicon phase leads to a substantial improvement in mechanical properties. Alloys which are commonly modified generally fall in the 5 - 12 % Si range [3].

The present study is a part of larger research project, which was conducted to investigate and to provide a better understanding microstructure quality control of recycled Al-Si-Mg cast alloys. The main objective of this work was to demonstrate the modification effect by Sr on microstructure and mechanical properties of AlSi10MgMn cast alloy.

2. Material and experiment

As an experimental material was used secondary near-eutectic AlSi10MgMn cast alloy (11 % Si, 0.15 % Fe, 0.42 % Mg, 0.066 % Mn, 0.034 % Cu, 0.076 % Ti and Al balance). The secondary alloy (prepared by recycling of aluminium scrap) was received in the form of 12.5 kg ingots. The melting process and the modification were carried out in a graphite melting crucible in a resistance oven. For the grain refinement process was used refining by AlCuAB6 salt and it was carried out while overheating the metal bath to 730 °C ± 5 °C. Sr was added to the melt in the form of AlSr10 master in the range 0, 0.05 %, 0.1 % and 0.15 %.

In the experimental cast alloy, which has 11 % Si, the microstructure (Fig. 1) consists of eutectics (eutectic Si particles in α-matrix), α-phase and variously type's intermetallic phases. Fig. 1 shows three-dimensional morphology of the eutectic Si after Sr-modification. The microstructure seen in

Fig. 1a reveals plate-like eutectic silicon. It is obvious in Fig. 1b, Fig. 1c and Fig. 1d that the eutectic Si platelets after addition of Sr changes morphology from compact plate-like to fine stick. Si-sticks in samples with 0.1 % and 0.15 % Sr coarsen (first of all at the edge of α-matrix) probably as a result of over-modification.

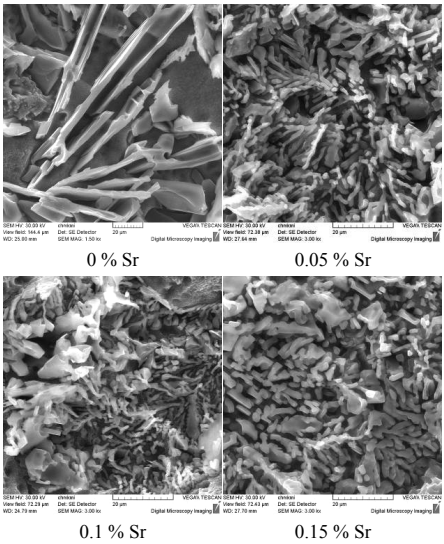

Fig. 1. The morphology of eutectic Si, deep etch. HCl

In practice, quantity of introduced Sr amounts to about 0.04 - 0.07 % [4]. However, there are existing different opinions concerning optimal additives of Sr introduced to Al-Si alloy, which should assure complete and stable effect of structure modification, and owing to it - high mechanical properties. Too high contents of Sr in the modified alloy is not required, because except intensive susceptibility of the alloy to gassing, in its structure can appear releases of brittle Al_2SrSi_2 phase, confirmed during metallographic tests as early as above 0.06 % of Sr contents, what deteriorates mechanical properties of the castings, first of all ductility (Fig. 2) [1, 4].

The effect of Sr-amount to tensile strength and ductility is shown in Fig. 2 and Fig. 3. Values of ultimate tensile strength are determined by the average of value of three test bars. Fig. 2 shows that increasing amount of the modifying element increases tensile strength from 146 MPa to 183 MPa. A remarkable increase in the strength is observed in samples modified by 0.15 Sr (cca 25 %). Ductility for alloy modified with 0.05 % Sr increases from 2.2 % to 4.3 % (about 95 %). Higher amount of modifier (above 0.15 % Sr) has led to a decrease of ductility.

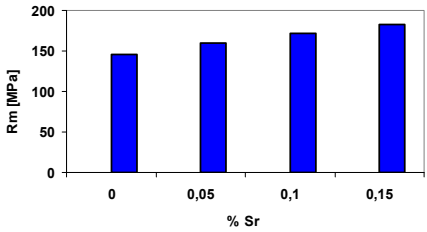

Fig. 2 Effect of Sr-modification to tensile strength

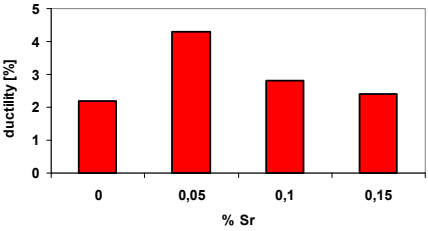

Fig. 3 Effect of Sr-modification to ductility

3. Conclusion

Morphology of eutectic Si changes from compact plate-like (0 % Sr) to fine stick (after modification). Si-sticks in samples with 0.1 % and 0.15 % Sr coarsen probably as a result of over-modification.

Increasing amount of the Sr increases tensile strength and ductility. Higher amount of Sr (above 0.15 %) has led to a decrease of ductility.

In the last analysis (morphology of Si, mechanical properties) probably amount 0.05 % Sr it will by optimal.

Acknowledgements

The authors acknowledge the financial support of the VEGA project N°1/0841/11 and Education project EÚ - OPV - ITMS: 26110230052.

References

[1] Tillová, E., Chalupová, M., Štruktúrna analýza zliatin Al-Si, EDIS Žilina, 2009 (in Slovak).

[2] COMALCO, Technical report No. 4, Comalco Aluminum Limited. Brisbane, Australia, 1997.

[3] Kósa, A., Gácsi, Z., Dúl, J., Materials Science and Engineering, Vol. **37**, 2, 2012, pp. 43-50.

[4] Pezda, J., Archiwes of Foundry Engineering, Vol. **9**, 3, 2009, pp. 121-124.

30th DANUBIA-ADRIA
Symposium on Advances in Experimental Mechanics
September 25-28, 2013 - Primošten, Croatia

7B31 041

CHANGES OF MATRIX MICROHARDNESS IN ALUMINIUM CAST ALLOYS DURING HARDENING

Lenka Hurtalová[1], Eva Tillová[1], Mária Chalupová[1]

[1] University of Žilina, Faculty of Mechanical Engineering, Department of Materials Engineering, Univerzitná 8215/1, 010 26 Žilina, Slovak Republic. E-mail: lenka.hurtalova@fstroj.uniza.sk, eva.tillova@fstroj.uniza.sk, maria.chalupova@fstroj.uniza.sk

1. Introduction

Is know that 1 kg of aluminium in a car reduces CO_2(eq) emissions by 19 kg during its whole lifecycle. In addition, 5 - 7 % fuel savings can be realized for every 10 % weight reduction by substituting aluminium for heavier steel through appropriate design. The application of aluminium in passenger vehicles and light trucks manufactured in 2006 will lead to potential savings of approximately 140 million tons of CO_2(eq) emissions and to energy savings of equivalent to 55 billion litres of crude oil over the lifecycle of these vehicles. With the climate change of concern and also due to the energy costly process of the production of primary aluminium alloy, involving bauxite mining, purification of alumina and a molten salt electrolyte based on cryolite (Na_3AlF_6) is increasing interest in the use and production of secondary aluminium alloys [1].

The alloys of the Al-Si-Cu system have become increasingly important in recent years, mainly in the automotive industry that uses recycled (secondary) aluminium in the form of various motor mounts, pistons, cylinder heads, heat exchangers, air conditioners, transmissions housings, wheels, fenders and so on due to their high strength at room and high temperature [2].

To this end, was studied hypoeutectic secondary Al-cast alloy - AlSi9Cu3. This material has good mechanical properties and casting characteristics. Cu addition makes this alloy heat treatable and hence improves its mechanical properties by forming finer hardening phase (Al_2Cu precipitate). Therefore the mechanical properties depend of the microstructure (will change as the microstructure changes) and changes in microstructure depend of heat treatment, the objective of this study is to understand the role of structural parameters (α-matrix, Si-particles, Fe-rich phases, secondary dendrite arm spacing - SDAS) on the mechanical properties (especially Vickers microhardness) during heat treatment [3].

2. Material and experiment

The experimental secondary Al-alloy (prepared by recycling of aluminium scrap) was received in the form of 12.5 kg ingots. Experimental material was molten into the chill (chill casting). The melting temperature was maintained at 760 °C ± 5 °C. Molten metal was purified with salt AlCu4B6 before casting and was not modified or grain refined. The chemical analysis of AlSi9Cu3 cast alloy was carried out using an arc spark spectroscopy and the chemical composition was: Al-9.4Si-2.4Cu-0.24Mn-0.9Fe-0.28Mg (wt. %). In the experimental cast alloy, which has 9.4 % Si, the microstructure (Fig. 1) consists of eutectics (eutectic Si particles in α-matrix), α-phase and variously type's Fe-rich (needle-like Al_5FeSi phase, skeleton-like $Al_{15}(FeMn)_3Si_2$ phase) and Cu-rich (Al-Al_2Cu-Si) intermetallic phases.

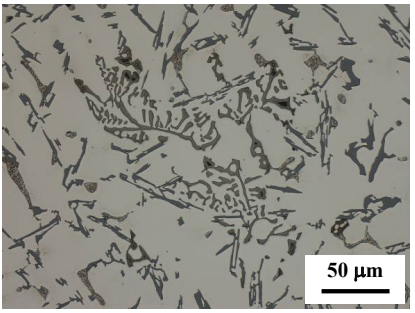

Fig. 1. The microstructure of AlSi9Cu3 cast alloy in as-cast state, etch. Dix-Keller.

The different intermetallic phases are concentrated mainly in the interdendritic spaces. The experimental material was not modified or grain refined therefore eutectic Si was observed in a form needles on scratch pattern of as-cast samples (on deep-etcher samples in a form of large hexagonal platelets) [4].

Experimental cast samples were given a age-hardening, that consist of solution treatment by 515 °C with holding time 4 hours, water quenching at 40 °C and artificial aging by different temperature 130, 150 and 170 °C with different holding time 2, 4, 8, 16 and 32 hours. After age-hardening were samples subjected for micro-hardness test (HV 0.01) and microstructure observation.

2.1 Effect of age-hardening on structure

Due to solution treatment the needles of eutectic Si were fragmentized and spheroidised into smaller round particles. Size of these particles was not affected with different temperature of artificial aging. The temperature of artificial aging 130 °C and 150 °C caused only small changes in morphology of intermetallic phases. Major changes in morphology of intermetallic phases have been reported after temperature of artificial aging 170 °C. In as-cast samples had the Fe-rich intermetallic phase a compact skeleton-like morphology. During heat treatment compact phase dissolved and fragmented to smaller skeleton particles. The Fe-rich needles was shorted and narrowed after age-hardening into small needles phases. The Al-Al_2Cu-Si phase without heat treatment (as-cast state) occurs in form compact oval troops. After heat treatment compact Al-Al_2Cu-Si phase disintegrates to separates Al_2Cu particles and redistributed within α-matrix. Cu also creates dispersed intermetallic precipitates and increases the overall matrix strength by a mechanism called the precipitation strengthening effect. Unfortunately, because these precipitates are very fine, their area fractions can not be quantified using image analysis combined with light optical microscopy and scanning electron microscopy [4].

2.2 Vickers microhardness

The matrix (α-phase) Vickers microhardness was measured in HTW Dresden. The micro-hardness measurements of the samples were performed using a MHT-1 microhardness tester under a 1g load for 10 s (HV 0.01) at the room temperature. Twenty measurements were taken per sample and the median microhardness was determined. Fig. 2 shows the change of α-phase Vickers microhardness during age - hardening. It can be found that the highest Vickers micro-hardness was by temperature 170 °C with holding time from 16 to 32 hours (176 HV 0.01).

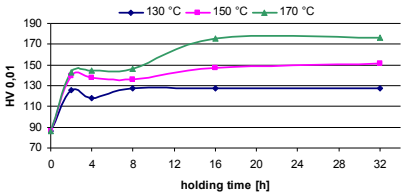

Fig. 2. Effect of age-hardening on α-phases Vickers microhardness.

The first aging peak for each temperature of artificial aging was observed after holding time 2 hours. At intermediate stage of aging, after a little decrease the microhardness increases again and reaches the potential second peak. The final stage of aging, when the hardness decreases as a result of over-aging, was not observed. For temperature 130 and 170 °C was observed hardness high plateau. The microhardness on samples aged at temperature 150 °C gradually increase. These changes in microhardness related with changes in micro-structure and substructure of samples.

3. Conclusion

Changes in structure and substructure of materials led to increasing of α-phase Vickers microhardness. The „optimum" schedule for mechanical properties is as follows: T6 - solution treatment: 4 h at 515 °C; water quenching at 40 °C; artificial aging: 16 h at 170 °C. This will produce the following properties: Vicker microhardness of α-phase = 176 HV 0.01 in compare with as-cast state was of 44 % higher (78 HV 0.01).

Acknowledgements

This work has been supported by Scientific Grant Agency of Ministry of Education of Slovak Republic and Slovak Academy of Sciences, No1/0841/11 and Education project EÚ - OPV - ITMS: 26110230052.

References

[1] Cui, J., Roven, H. J., Transactions of Nonferrous Metals Society of China, **20**, 2010, pp. 2057 - 2063.

[2] Rios, C. T., Caram, R., Acta Mikroscopica, **12**, N°1, 2003, pp. 77-81.

[3] Gao, Y.X., Yi, J.Z., Lee, P.D., Lindley, T.C., Acta Materialia, **52,** 2004, pp. 5435 - 5449.

[4] Tillová, E., Chalupová, M., Hurtalová, L., The Scaning Electron Microscope. INTECH, 2011, pp. 411-438.

30th DANUBIA-ADRIA
Symposium on Advances in Experimental Mechanics
September 25-28, 2013 - Primošten, Croatia

7B32 083

MODERN APPROACH EXPERIMENTAL VERIFICATION OF NUMERICAL MODELS FOR TENSILE TESTS OF WELDED SPECIMENS

Simon Sedmak[1], Uros Tatic[1], Nenad Mitrovic[2], Ratko Jovicic[2], Tasko Maneski[2], Aleksandar Sedmak[2], Milos Milosevic[1]

[1] University of Belgrade, Innovation center of Faculty of Mechanical Engineering, Kraljice Marije 16, 11000 Belgrade, SERBIA. E-mail: mmilosevic@mas.bg.ac.rs, ssedmak@mas.bg.ac.rs, utatic@mas.bg.ac.rs, rrajkovic@mas.bg.ac.rs, jasmina.perovic84@gmail.com

[2] University of Belgrade, Faculty of Mechanical Engineering, Kraljice Marije 16, 11000 Belgrade, SERBIA. E-mail: nmitrovic@mas.bg.ac.rs, asedmak@mas.bg.ac.rs,

1. Introduction

The subject of this paper is the behavior of a welded specimen subjected to tensile forces, with the purpose of confirming results obtained by experimental methods (digital image correlation) using numerical simulation by finite element method. The 3D optical strain and displacement analysis using Digital image correlation represents a useful experimental approach that helps to better understand full displacement/strain fields of loaded materials and structures [1,2,4].

During these experiments, numerous problems are encountered, often involving the equipment used, as well as the geometry and the inhomo–geneity of the specimen [1].

The results obtained by numerical simulations were then compared to the existing ones, in order to determine how well the strain distributions in both cases comply with each other, i.e. to deter–mine if the largest strains would occur in appro–ximately same locations. In addition, the purpose of this numerical simulation was to determine the stress field for the whole specimen [1,2], including locations that were not measured experimentally.

2. Methods

The experimental measuring was performed using DIC. For this purpose, ARAMIS software (GOM, Braunschweig, Germany) was used. The specimen was subjected to tension and the resulting displacement was used as input data for the numerical model. Two materials were used in the real specimen, Č0361 steel for the base metal, and VAC 60 as the weld metal. The welded joint is overmatched, i.e. its yield strength is noticeably greater than that of the base metal [3]. As a result, plasticity occurred in the base metal.

The simulation was performed in ABAQUS CAE (Dassault, France). Due to the specimen symmetry along two planes, a quarter of the model was used for the simulation. The load was given in form of displacement control, with maximum value of 18 mm, at the rate of 3mm/minute. The geometry of the specimen is given in figure 1.

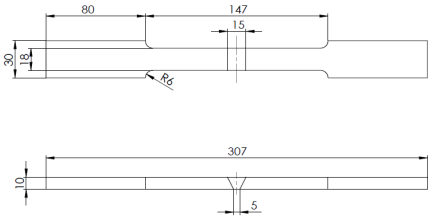

Fig. 1. Geometry of the specimen used in the experiment.

Boundary conditions were defined in accor–dance with the experiment and the fact that the model geometry was approximated as a quarter of the real specimen. Along the symmetry planes, displacement was constrained in the direction perpendicular to them. Additional constraints were made on the parts of the upper and the lower surfaces (figure 2) to simulate the grip surfaces of the real specimen.

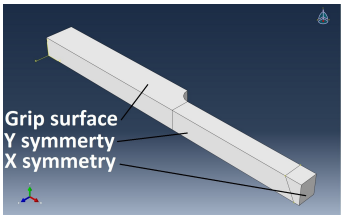

Fig. 2. Boundary conditions

Due to high plasticity occurring in the model, a mesh made of 20 node quadric brick elements (C3D20) was used. Non-linear geometry option was used for the same reason.

3. Results

The model was made simpler since in the experiment, only one side of the specimen yielded, due to structure flaws, and also in order to reduce the total number of elements, and therefore make the calculation simpler and faster [2,3].

Experimental displacement, obtained by DIC, in longitudinal direction is presented in figure 3.

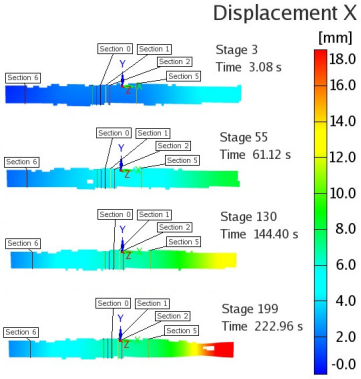

Fig. 3. Experimental results for displacements

Numerical results are given in the figure below. Figure 4 shows the equivalent plastic strain distri–bution at stage 130, along with the displacements.

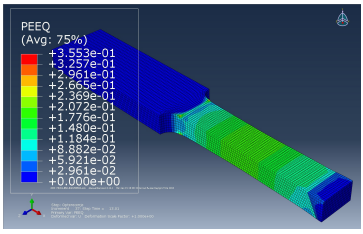

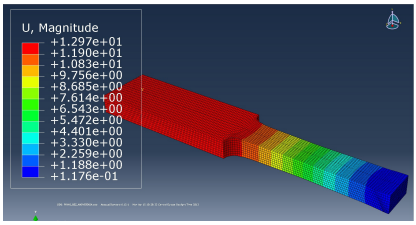

Fig. 4. Plastic strain and displacement at stage 130

The above figure shows that highest plastic strain occurs at the expected location. Displa–cements in both cases are very similar as well.

4. Conclusion

Numerical and experimental results have shown good compliance, especially regarding the distri–bution of plastic strain, i.e. both specimens started yielding at the approximately same time and position. Experimental measuring using DIC, along with numerical simulation using FEM gave us insight into stress distribution and was con–firmed as a reliable method for obtaining results for displacements and strain in welded specimens. Use of a simple model (quarter of the specimen), as well as the correct choice of elements used in the mesh has greatly improved the results obtained.

5. Acknowledgements

The study was carried out within the Project TP - 36027 and Project TP – 35040, financed by the Ministry of Education, Science and Technological Development, Republic of Serbia.

References

[1] Jovicic R., Sedmak A., Colic K., Milosevic M., Mitrovic N.: ”Evaluation of the local ten–sile properties of austenite-ferrite welded joint”, Chemicke Listy 105, s754-s757, 2011.

[2] Sedmak A., Milosevic M., Mitrovic N., Petrovic A., Maneski T.: “Digital image correlation in experimental mechanical analysis”, Integritet i vek konstrukcija (Structural Integrity and Life), Vol.12, No1, pp.39–42, 2012.

[3] Dobrojevic, M., Sedmak, A., Argob, E., Popovic, O.: “The analysis of geometry and welded joint heterogeneity effect on Charpy specimen beha–viour”, Integritet i vek konstrukcija (Structural Integrity and Life), Vol 3, No 2, pp. 73-83, 2003

[4] Mitrovic N., Milosevic M., Sedmak A., Petrovic A., Prokic-Cvetkovic R.: „Application and Mode of Operation of Non-Contact Stereo–metric Measuring System of Biomaterials“, FME Transactions, Vol. 39, No 2, p 55-60, 2011

30th DANUBIA-ADRIA
Symposium on Advances in Experimental Mechanics
September 25-28, 2013 - Primošten, Croatia

7B33 039

EVALUATION OF PLASTIC DEFORMATION PROCESS IN AZ61 ALLOY

Ivana HLAVÁČOVÁ[1)], Peter PALČEK[1)], Mária CHALUPOVÁ[1)]

[1)] University of Žilina, Faculty of Mechanical Engineering, Department of Materials Engineering, Univerzitná 1, 010 26 Žilina, Slovak Republic

Corresponding author: ivana.hlavacova@fstroj.uniza.sk

1. Introduction

Magnesium alloys are attractive as structural light-weight materials in the automotive and aerospace industries for their extremely low density, good cast ability and recyclability [1]. Recently, there has been a strong demand from industries for the development of high strength casting and wrought magnesium alloys. A great amount of research has been performed to enhance the strength level of the conventional wrought magnesium alloys such as Mg–Al and Mg–Zn based alloys. Despite this progress, the highest strength of the ordinary cast Mg alloys reported so far is no more than 414 MPa [2, 3, 4].

Deformation of Mg alloys at normal temperatures causes that each grain is deformed to the shape determined by nearby grains. The preferred plane of Mg alloys for the formation of twins is $\{1\ 0\ 1\bar{2}\}$ in the slip direction $[1\ 0\ 1\bar{1}]$ [5, 6]. Due to the slip deformation, which tends to occur easily on the Mg basal plane at a low critical shear stress, crystal orientation with his basal plane on the surface negatively influences the wear-resistance [7, 8]. As is already known the AZ61 alloy has good plastic properties, toughness and it is used in multiple applications, replacing other Mg alloys [9]. The aim of this study is to identify the influence of plastic deformation on strength characteristics of AZ61 Mg alloy with the addition of Ca by the pressure deformation.

2. Experiments and Results

The semi product AZ61 alloy with addition of 0.5 wt. % Ca was manufactured by squeeze - casting in the form of a square plate. The experimental material was heat treated to achieve full polyhedrization of grains with almost complete phase dissolution of the dendritic structure. Heat treatment consisted of dissolution annealing at temperature 490°C for 32 h and fast cooling to 60°C by water. After cooling, the specimens were annealed for 5 h at 200°C in order to obtain a stable microstructure. After heat treatment, the specimen were prepared from experimental material. The specimens were of square cross-section 15 x 15 mm with length of 25 mm. One side of surface was metallographically prepared and etched so it was possible to identify all structural components of the studied alloy. After heat treatment, the microstructure was formed by solid solution of aluminum and zinc in magnesium (phase δ) and other phases based on Al-Ca-Mg, Al-Mn-Mg. In the polyhedral grains precipitated particles of $Mg_{17}Al_{12}$ (γ phase) [9].

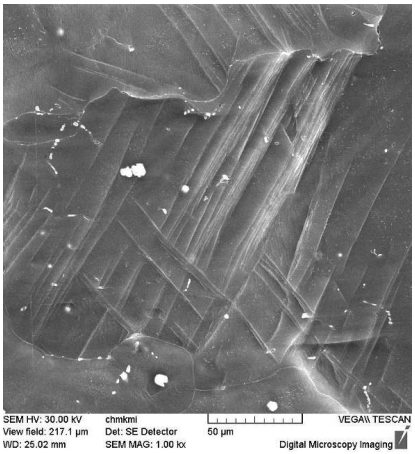

Fig. 1: Plastic deformation realized by screw and slip dislocations; (SEM)

After microstructure evaluation, a steel indentor was pressed perpendicular to the metallographically prepared surface. Consequently, there was created a network of slip bands, deformation twins and some grains were shifted due the plastic deformation on the surrounding area. The steel roller had a diameter of 1 mm and the used strength was

3800 and 7800 N. By the stress release in the surrounding of the indentor there were formed small cracks in several directions and some of them, due to their propper orientation, formed one or more magistral cracks.The change of the direction of plastic deformation propagation occured due to the presence of undissolved phases in grains and also on grain boundaries, which were present in the microstructure even after heat treatment. The plastic deformation was characterized by a combination of screw and edge dislocation slip, formation of deformation twins and fine cracks in the areas of the highest tension stress during loading (Fig. 1). The plastic deformation intensity was caused by improper crystallographic orientation of grains. In these grains, the process is not so intensive to cause significant plastic deformation of the grain surface. After polishing of the deformed surface, there was measured microhardness HV 0.1, so that the change of the plastic deformation intensity was

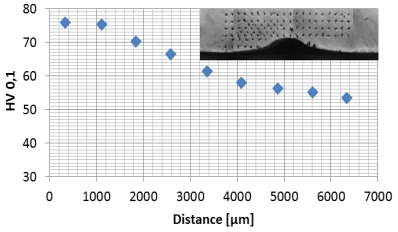

Fig.2: The gradual change of hardness with increasing distance from the bottom of the indentation

documented in all the affected surface. The gradual change of hardness with increasing distance from the bottom of the indentation place is shown in Fig. 2 (the points were obtained as the average of 5 measurements). By comparing of the hardness course and the surface deformation relief it is possible to state that there is a good correlation between them and the hardness measurement is a suitable method for evaluation of the plastic deformation range in Mg alloys.

Conclusions

Based on experimental work it can be concluded:

- the compression loading of experimental specimens after heat treatment leads to slip and twinning plastic deformation,
- in the surrounding area of the indentation were created cracks and also cracking of intermetallic phases present in the microstructure was present ,
- changes in the intensity and distribution of plastic deformation was caused by deformation strengthening and shifting of grain boundaries,
- measuring of the microhardness showed increase of hardness in the places with the highest plastic deformation in loading area.

Acknowledgement

The research was supported partially by SK VEGA grant No. 1/0797/12, No. 1/2594/12 and project SK-PL-0083-12. Authors gratefully acknowledge this support.

References

[1] POLMEAR, I. J.: *Light Alloy*, 2006, Australia, pp. 237 – 296, ISBN 0-7506-6371-5

[2] HE, S. M.: *Study on the Microstructural Evolution , Properties and Fracture Behavior of Mg-Gd-Y-Zr(-Ca) Alloys*, PhD Thesis, Shanghai Jiao Tong University, 2007

[3] HE, S. M., ZENG, X. Q., PENG, L. M. et al. *Microstructure and Strenghthening mechanim of High Strenght Mg-10Gd-2Y-0.5Zr Alloy,* In Journal of Alloys and Compounds, 2007, China, pp.316-323, ISSN 09258388

[4] HOSHIKAWA, H., MAKI, S., KAMADO, S. et al.: *Realization on Excellent mechanical properties in Mg-Gd-Ag-Zr and Mg-Gd-Cu-Zn-Zr Casting Alloys Containning LPSO Structure*, Proceedings of 2nd Asian Symposium on Magnesium Alloys, Fukuoka International Congress Center, 2007, Japan, pp. 136 -137

[5] WANG, Q., CHEN, J. et al.: *Microstructure and Super High Strenght of Cast Mg-8.5Gd-2.3Y-1.8Ag-0.4Zr Alloy*, In Material Science and Engineering, 2010, China, pp. 323-328

[6] BARNETT, MR.: *Twinning and the Ductility of Magnesium Alloys: Part II.—Contraction Twins*, Materials Science and Engineering A, 2007

[7] RAUCH, M., LEGROS, M. et al.: *Small Volume Investigation of Slip and Twinning in Magnesium Single Crystals*, Universtitéde Grenoble, 2011

[8] TROJANOVÁ, Z., SZÁRAS, Z., et al. Magnesium Alloys Based Composites. In: Magnesium Alloys - Design, Processing and Properties. Publisher: In Tech, Rijeka, Croatia, 2011, p. 501-526. ISBN 978-953-307-520-4

[9] PALČEK, P., HLAVÁČOVÁ, I. et. al.: Influence of AZ61 Structure on the Plastic Deformation Around a Crack. In: 29th DANUBIA-ADRIA : Symposium on Advances in Experimental Mechanics : September 26 – 29, 2012, Planeta Print : Belgrade, Serbia - 2012. p. 134-135. - ISBN 978-86-7083-762-1

30th DANUBIA-ADRIA
Symposium on Advances in Experimental Mechanics
September 25-28, 2013 - Primošten, Croatia

7B34 128

A MEASUREMENT TECHNOLOGY TO DEFINE THE QUALITY OF MACHINED FRP

Richard Zemann, Roland Fürbacher, Friedrich Bleicher

Vienna University of Technology, Institute of Production Engineering and Laser Technology, Landstraßer Hauptstraße 152, 1030 Wien, AUSTRIA. E-mail: zemann@ift.at

1. Introduction

Fibre reinforced polymers (frp) are more and more used in different industrial branches like the transportation, the sport or the medicine industries. The variety of different compositions consisting of fibre and bedding matrix to a composite and the following variety of characteristics is one of the biggest advantages for this material class. This variety allows on the one hand, defining an appropriate composite with partially very specific behaviour for different uses. But on the other hand, the grade of complexity for this material class is getting higher with every new composite.

The finishing, like the drilling of holes or the milling of grooves, is a very common process step in the production of frp parts. Due to the construction of these materials consisting of the matrix system and the fibre material, the cutting is very demanding. The problematic is consisting in the fact that you have to machine two different materials with different characteristics. For example, young's modulus of a common resin system (=matrix) is around 3 GPa [1] and the value for a common industrial fibre (toray T300) is 230 GPa [2]. Complicating the matter is the fact that the young's modulus of this fibre is depending on the load direction. The resulting problem is a short tool life time in comparison with the machining of metallic materials and defects on the machined surface. These defects can be classified in:

- delamination
- fraying
- splintering

The practical problem for the industry is that there are no regulations for the definition of the mentioned defects. Furthermore, there is no measuring method defined, so that anybody who has to qualify the result of a finishing operation has to find a useful way to do so. This subjective way of working leads to misunderstandings and different points of view in case of business.

The Institute of Production Engineering and Laser Technology (IFT) of the Vienna University of Technology is dealing with this topic. Measurement technologies to define the quality of machined frp as well as appropriate quality indices were developed.

2. Occurring defects

In the following, the occurring defects while machining frp products are described. In Fig. 1. a schematic view of a machined hole is shown. In this figure the green section is the cross section of a drill. The orange areas indicate delamination, the reds fraying and the yellow ones splintering.

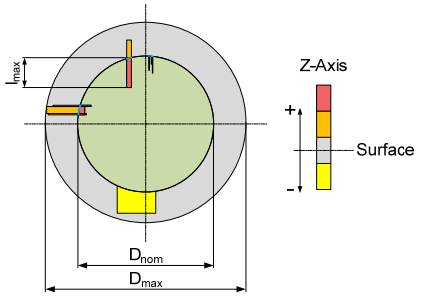

Fig. 1. left: schematic view of a machined hole and the associated defects; right: legend of contour levels

2.1 Delamination

The delamination occurs mostly at the top or bottom layer of a structure. It also occurs in the laminate, for example at the boundary of different materials. These layers delaminate because of a transgression of the maximum interlaminate

bonding force. While finishing frp such a transgression is based on the machining force. The geometric definition of a delamination for the measurement is a local increase of the topological behaviour of a surface. Additional attendance while measuring has to be given to the roughness and the global waviness of the part to avoid influences of the result.

2.2 Fraying

The fraying of fibres is again a defect at the top or bottom layer. The strong fibres move away from the cutting edge. Frayed material stays in the machined volume after the process.

2.3 Splintering

Splintering is also a defect at the surrounding layers of a composite. The angle from the delaminated section to the part surface of the ply, increases during the machining process so that these section splinters. Such a defect after a drilling process is indicated in Fig. 2.

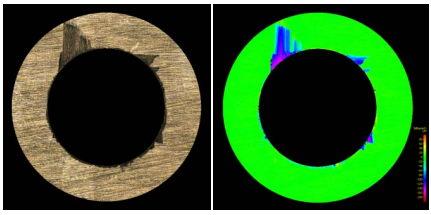

Fig. 2. splintering, left: photo via measurement device, right: wrong colour photo.

3. Quality indices

The defects occurring after finishing operations in the production process of frp parts have to be measured in that way, that you get information about the size of a defected area and about the specific type of a defect at an area. The representation of this principle is based on the work of Mohan [3]. At the IFT an Alicona Infinite Focus 4G and a Nikon Nexiv VMR 2520 are used for the investigations. The machine supported measurement increases the objectivity and the precision of the process. Very important is that the measuring parameters are defined and stay constant for every measuring process.

To qualify a machining result and to compare different results together, a criterion has to be defined. For that reason three quality indices for every type of defect were developed. In Tab. 1. the fraying quality index is shown. This index is generated with two digits. The first digit indicates the longest fraying in comparison to the tool diameter of a machined structure. The amount of fraying at the circumference of the structure is represented by the second digit. The percentile ranges are based on the standard line R8. The index goes from 11, for the worst result, to 99 for the best possible result. The quality of a machined structure can now be determined.

FQI - Fraying Quality Index									
longest fraying in comparison to the tool diameter	amount of fraying at the circumference								
	0% ≤ y ≤ 1%	1% ≤ y ≤ 2%	2% ≤ y ≤ 3%	3% ≤ y ≤ 6%	6% ≤ y ≤ 10%	10% ≤ y ≤ 18%	18% ≤ y ≤ 32%	32% ≤ y ≤ 56%	56% ≤ y ≤ 100%
0% ≤ x ≤ 1%	**99**	**98**	**97**	**96**	**95**	**94**	**93**	**92**	**91**
1% ≤ x ≤ 2%	**89**	**88**	**87**	**86**	**85**	**84**	**83**	**82**	**81**
2% ≤ x ≤ 3%	**79**	**78**	**77**	**76**	**75**	**74**	**73**	**72**	**71**
3% ≤ x ≤ 6%	**69**	**68**	**67**	**66**	**65**	**64**	**63**	**62**	**61**
6% ≤ x ≤ 10%	**59**	**58**	**57**	**56**	**55**	**54**	**53**	**52**	**51**
10% ≤ x ≤ 18%	**49**	**48**	**47**	**46**	**45**	**44**	**43**	**42**	**41**
18% ≤ x ≤ 32%	**39**	**38**	**37**	**36**	**35**	**34**	**33**	**32**	**31**
32% ≤ x ≤ 56%	**29**	**28**	**27**	**26**	**25**	**24**	**23**	**22**	**21**
56% ≤ x ≤ 100%	**19**	**18**	**17**	**16**	**15**	**14**	**13**	**12**	**11**

Tab. 1. FQI matrix

The classification for the delamination and splintering indices uses the same two digit principle as the fraying one. With the information of these three indices a machining process can be qualified completely.

4. Results

With the possibility to use a regulation to define the quality of a machined structure, companies can produce parts with defined characteristics and avoid conflicts with partners. The R&D society gets the necessary basis to compare results as well. Such comparison is most fundamental for any improvements in the process, like the development of new tools, machining strategies and so on.

References

[1] N.N., TCR Composites Resin Selector Guide, TCR DS-0011, Rev. 13, October 2012

[2] N.N., Torayca T300 data sheet, technical data sheet No. CFA-001, http://www.toraycfa.com/pdfs/T300DataSheet.pdf, 2013

[3] Mohan N., Kulkarni S., Ramachandra A., Delamination Analysis in Drilling Process of Glass Fiber Reinforced Plastic Composite Materials, Journal of Materials Processing Technology, Nr. 186, 2007

30th DANUBIA-ADRIA
Symposium on Advances in Experimental Mechanics
September 25-28, 2013 - Primošten, Croatia

7B35 037

SURFACE TREATMENT OF BIOCOMPATIBLE MAGNESIUM ALLOYS

Filip Pastorek[1], Branislav Hadzima[1], Otakar Bokůvka[1]

[1] University of Žilina, Faculty of Mechanical Engineering, Dept. of Materials Engineering, Univerzitná 1, SK-01026 Žilina, SLOVAKIA. E-mail: filip.pastorek@fstroj.uniza.sk; branislav.hadzima@fstroj.uniza.sk

1. Introduction

Investigation of the materials for fabrication of the parts for using in human body is very important theme because of life style changing and average age of life increasing. Metallic materials continue to play an essential role as biomaterials to assist with the repair or replacement of bone tissue that has become diseased or damaged [1].

Magnesium has been suggested as a revolutionary implant material to overcome the limitations of the current metallic materials being used. Mg is light in weight and low in density, and exhibits high strength/weight ratio [2]. Mg also has the advantage of degradation, and thus if corrosion rates are controlled, the material would slowly degrade, removing the necessity for second removal surgeries, thereby decreasing health risks, costs and scarring. Additionally, in contrast to the metals currently utilized, the wear products of which can be potentially toxic or otherwise harmful to the patient [3, 4], the corrosion products of Mg have been shown to be potentially beneficial to the patient [5].

Calcium phosphates have extensively been studied due to its biocompatibility, chemical stability and similarity in composition with the mineral phase of teeth and bone and use as bone substitutes in biomedical industry.

Aim of this study is to electrodeposit calcium phosphate layer on magnesium alloy AZ31 surface and to improve its corrosion properties by this way.

2. Experimental results and discussion

The tested AZ31 magnesium alloy was continually casted at Brandenburgische Universität in Cottbus, Germany. The chemical composition is in Tab. 1. The microstructure (Fig. 1) is created by polyedric grains of supersaturated solid solution of aluminium, zinc and other alloying elements in magnesium. The average grain size is 220 μm.

Component	Al	Zn	Mn	Si	Mg
wt.%	2.96	0.828	0.433	0.004	bal.

Tab. 1. Chemical composition of tested Mg alloy

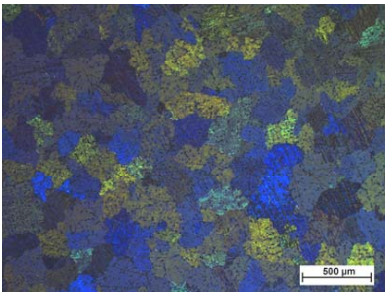

Fig. 1. Microstructure of AZ31 alloy, polarized light, etch. picral [6, 7]

For the evaluation of calcium phosphate surface treatment influence on electrochemical characteristics the sample surfaces (2x2 cm²) were grinded with 1000 grit SiC paper, then degreased with ethanol, and dried using a stream of hot air. The calcium phosphate was deposed on the samples' surfaces. Treatment electrolyte solution was prepared with 0.1M $Ca(NO_3)_2$, 0.06M $NH_4H_2PO_4$ and 10 ml.dm^{-3} of 50 vol.% H_2O_2. Sample was used as cathode. Electrodeposition was performed with constant current density -0.5 mA.cm^{-2} for 1 hour.

The surface morphology of the treated specimens was assessed in the laboratories of the Department of Materials Engineering, FME, University of Žilina, by a stereomicroscope Nikon

AZ100 with a digital camera using NIS Elements software. Electrodeposition under specified conditions led to the creation of a thin layer of calcium phosphate (Fig. 2).

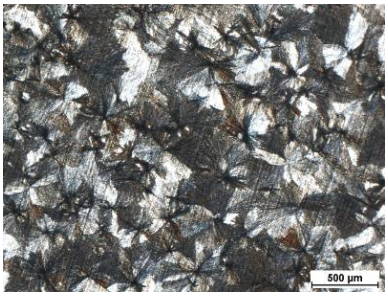

Fig. 2. Morphology of CaP layer on AZ31 Mg alloy surface

The corrosion characteristics of the untreated and CP-coated AZ31 magnesium alloy samples were evaluated by potentiodynamic polarization tests. The corrosion experiments were performed at 22 ± 1 °C in 0.9% NaCl with the time exposure 5 minutes. A saturated calomel electrode and a platinum electrode served as the reference and auxiliary electrodes, respectively. Treated and untreated AZ31 samples formed the working electrode in such a way that only 1 cm² area of the working electrode surface was exposed to the electrolyte solution in corrosion cell. Potentiodynamic polarization tests were carried out from -200 to + 500 mV vs SCE with respect to the OCP at a scan rate of 1 $mV.s^{-1}$. Measured potentiodynamic curves were analysed using Tafel fit by EC-Lab software.

Fig. 4 shows the measured potentiodynamic curves of untreated and treated AZ31 Mg alloy samples using current controlled electrodeposition of CaP. Curves of both surfaces demonstrated a transition between a passive state and active state. Short steady state was measured on both surfaces that is corresponding with passive behavior of the surfaces in testing media.

More positive corrosion potential (E_{corr})value (-1.518 V) is observed on samples with the surface covered by CaP. Just grinded AZ31 magnesium alloy samples show the corrosion potential value -1.604 mV. Surface covered by CaP is electrochemically nobler and hence thermodynamically more stable.

In terms of kinetics the samples coated by CaP show significantly lower values of corrosion current density (i_{corr}). Untreated samples achieve the i_{corr} value of 34.421 $\mu A.cm^{-2}$, while samples with CaP achieve 0.484 $\mu A.cm^{-2}$ that represents 71-fold reduction. This finding is very important for assessing the kinetics of corrosion, since corrosion current density is directly related to the corrosion rate and therefore tells us about the intensity of the ongoing corrosion process in the specific electrolyte.

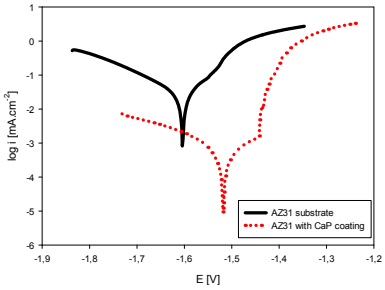

Fig. 3. Potentiodynamic curves of tested alloys in 0.9% NaCl solution

3. Conclusion

On the basis of performed experiments, analysis of the results and their interpretations, we concluded that the surface of AZ31 alloy with CaP coating reaches better electrochemical corrosion characteristics from thermodynamic (more positive values of E_{corr}) and from kinetic (lower i_{corr} values) point of view also.

Acknowledgements

The research is supported by European regional development fund and Slovak state budget by the project ITMS 26220220048 (call OPVaV-2008/2.2/01-SORO).

References

[1] Niinomi, M.: Met Mater Trans A, **33**, 2002; pp.477–86.

[2] Mordike, B. – Ebert, T.: Mater Sci. Eng A, **302,** pp. 37–45.

[3] Albrektsson, T: Crit. Rev. Biocomp. **1**, 1985, pp. 53–84.

[4] Black, J.: J. Bone Joint Surgery **70,** 1988, pp. 517-519.

[5] Touyz, R.M.: Front Biosci. **9**, 2004, pp. 1278–1293.

[6] Nový, F. et al: Int. J. Mater. Res. 100 (2009): 288-291

[7] Pastorek, F. – Hadzima, B.: Mater. Eng – Mater. inž. **20**, 2013, pp.54-63.

30th DANUBIA-ADRIA
Symposium on Advances in Experimental Mechanics
September 25-28, 2013 - Primošten, Croatia

7B36 145

STATISTICAL ANALYSIS OF ZIRCONIUM DIOXIDE 3-POINT BENDING RESULTS

Mateusz Wirwicki[1], Tomasz Topolinski[1]

[1] University of Technology and Life Sciences in Bydgoszcz, Faculty of Mechanical Engineering, Department of Biomedical Engineering, Al. Prof. Kaliskiego 7, 85-796 Bydgoszcz, POLAND. E-mail: wirwicki@utp.edu.pl

1. Introduction

Testing new biomaterials, including dental composites or fully-ceramic framework, to a large extent, covers determining their material characteristics. An important element of the evaluation of the material used is testing the mechanical strength which gets extended by the analysis of probability and reliability based on the use of the Weibull distribution. The Weibull distribution module *m*, namely the shape parameter, provides characteristics of the variation in material strength. It is assumed that the higher the value of that module, the greater the operational reliability. The biomaterial tested in the paper is zirconium dioxide which, has been applied for dental purposes, since the 1990s. It seems that one of the problems of common application is an excessively expensive workmanship of the dental crown or bridge and a later development of a reliable method of gluing to earlier-prepared – teeth filed down in oral cavity. However, much interest in that material is due to the fact that it is very easy to model the patient's support in the CAD system and to map it in the material applying machining with a specialist CNC milling machine. The shape created in that way gets baked – synterised at the temperature of 1500°C. Yet another element is baking porcelain onto the support; porcelain which will not differ in colour from the other teeth in the patient's oral cavity. Dental supports prepared and made in that way demonstrate not only expected shapes and dyes, but also show high strength properties, including a high value of the elastic modulus, as well as good biocompatibility.

2. Materials and method

Static 3-point bending tests were performed compliant with the PN-EN 843-1 norm. The tests involved the use of the Zircon Lava material provided by 3M company; the material is used to make dental crowns and bridges. The material supplied by the manufacturer was cut with the circular saw Buehler ISOMET 5000 (Poland) into slices 25mm x 16mm x 2.5mm in size. The elements received in that way were exposed to laser cutting using the Alfalas WS device (Poland) setting the cutting parameters in a way which would not allow for material overheating. With cutting performed in that way about 6 samples 1.87mm x 1.87mm x 15mm in size were made. The specimen sizes consider the contraction accounting for about 20%, which occurs during material synterisation. Fig. 1 presents the specimens geometry.

3-point bending tests were performed using the strength testing machine Instron 8874. The tests

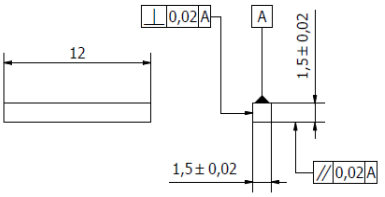

Fig. 1. Specimens geometry

involved the use of dynamometer with a maximum measurement scope of ± 5kN and the upper arm dislocation was 0.5 mm/min.

3. Results

Static 3-point bending tests were made for 30 specimens 1.5mm x 1.5mm x 12mm in size. The analysis with the Weibull distribution assumed the results for 23 specimens. Results rejection was made according to the guidelines provided for in PN-EN 843-5 norm where the number of the results cannot exceed 30 and extreme results must be rejected. Single test results for respective samples exposed to the analysis in the order of increasing values of maximum bending stress are provided in Fig. 2, which was supplemented with the regression line plotted-in together with the value of the coefficient of determination R^2.

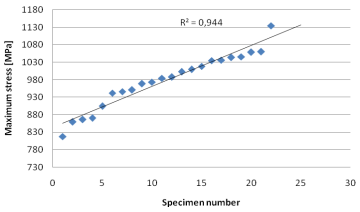

Fig. 2. Graphic representation of 3-point bending results

The analysis of reliability of the material investigated involved the use of the two-parameter Weibull distribution in a form of:

$$P_f = 1 - exp\left[-N\left(\frac{\sigma - \sigma_u}{\sigma_0}^m\right)\right] \quad (1)$$

$$P_f = \left(\frac{n}{N+1}\right) \quad (2)$$

Equation 1 can be compared to, having been logarithm-transformed, to linear equation $y = ax + b$:

$$\ln\left(ln\left(\frac{1}{P_s}\right)\right) = m\ln(\sigma) - m\ln(\sigma_0) \quad (3)$$

where P_s stands for the probability of specimen survival, P_s equals 1-Pf.

The linear approximation after logarithm-transformation of the testing results for bending strength and regression equation and the coefficient of determination are given in Fig. 3.

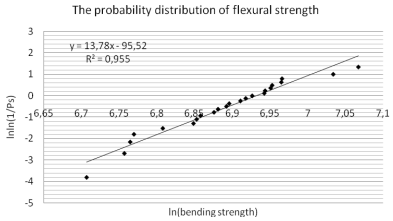

Fig. 3. Approximation of the distribution of probability for bending strength of Lava zirconium dioxide.

It should be noted the fact that the Weibull modulus m for the material has a low value. In the literature, a low Weibull modulus authors interpreted as the result of a big distraction structural defects in the samples, equivalent to its poor reliability.

References

[1] P.G. Coelhoa, N.R. Silvab, E.A. Bonfantea, P.C. Guessc, E.D. Rekowd, V.P. Thompsona Fatigue testing of two porcelain–zirconia all-ceramic crown systems, Dental Materials 25 (2009) p. 1122 - 1127

[2] Andr´e R. Studart, Frank Filser, Peter Kocher, Ludwig J. Gauckler Fatigue of zirconia under cyclic loading in water and its implications for the design of dental bridges, Dental Materials 23 (2007) p. 106 - 114

[3] Susanne S. Scherrer, Maria Cattani-Lorente, Eric Vittecoq, Francois de Mestral b, Jason A. Griggs, H.W. Anselm Wiskott, Fatigue behavior in water of Y-TZP zirconia ceramics after abrasion with 30µm silica-coated alumina particles, Dental Materials 27, (2011) p. 828 - 842

[4] A. M. Niewczas, D. Pieniak, P. Ogrodnik, Analiza niezawodnościowa wytrzymałości kompozytów stomatologicznych poddanych zróżnicowanym procedurom fotopolimeryzacji, Eksploatacja i niezawodność, Vol 14, No. 3, (2012) p. 249 - 264

30th DANUBIA-ADRIA
Symposium on Advances in Experimental Mechanics
September 25-28, 2013 - Primošten, Croatia

7B37 147

EXPERIMENTAL SETUP FOR DIRECT MEASUREMENTS OF DYNAMIC BULK COMPLIANCE OF POLYMERS

Alen Oseli[1], Igor Emri[2]

[1] Institute for Sustainable Innovative Technologies, EEIG, Pot za brdom 104, SI-1000 Ljubljana, Slovenia. E-mail: alen.oseli@isit.si

[2] Faulty of Mechanical Engineering, University of Ljubljana, Aškerčeva 6, SI-1000 Ljubljana, Slovenia. E-mail: igor.emri@fs.uni-lj.si

1. Introduction

The use of polymers has significantly increased, in the past decades on many engineering areas. In the production phase and later on during utilization polymers are exposed to different environmental conditions (i.e., different temperatures, pressures, humidity) that affect their volumetric behavior. Understanding such behavior is important on numerous engineering processes (e.g., high pressure polymer processing technologies) and applications (e.g., noise and vibration reduction applications).

Often it was assumed that volumetric response was time or frequency independent. However increasing demands for higher material performance at elevated temperatures and pressures do not allow such simplification, consequently pointing out potential need for more careful characterization of time or frequency dependant volumetric (bulk) response of polymers.

Due to modern industrial requirements a novel measuring system for investigation of dynamic bulk behavior of polymers was developed based on previous research works of McKinney and Belcher, 1963 [1]; Deng and Knauss, 1997 [2,3] and Sane and Knauss, 2001 [4,5]. The newly developed measuring system can simultaneously measure real (storage) component $B'(\omega)$ and imaginary (loss) $B''(\omega)$ component of the dynamic bulk compliance, $B^*(\omega)$.

This paper represents the measuring capabilities and optional upgrades of an apparatus for the characterization of viscoelastic bulk characteristics under harmonic excitation.

2. Experimental methodology

2.1 Measuring principle

Measurement of dynamic bulk compliance $B^*(\omega)$ takes place in the cavity of a pressure chamber, filled with an incompressible medium (oil), where there is uniform hydrostatic pressure. Sinusoidal signal in the form of AC voltage at respective frequency excites a piezoelectric disk (transducer), which acts as an actuator and causes compression waves that travel through the transmitting medium and a polymeric sample. A second piezoelectric disk, which acts as a pressure sensor, perceives compression waves in the form of amplitude and phase (phase is shifted due to measurements of time-dependant materials) [1,2].

Such method allows direct measurements of volume change under sinoidal hydrostatic pressure at the time of volumetric deformation of the polymeric sample. However, the following assumptions must be taken into account:

1. length of the cavity must be much smaller than the wave length of compression wave; this ensures that pressure is uniform (constant) inside the cavity;
2. force transferred to the sample is essentially hydrostatic pressure;
3. complex compliances (compressiblities) of piezoelectric disks, cavity, wires, sample and transmitting medium are additive (can be summed);
4. process is taking place in ideal rigid body;
5. transmitting medium by which the polymeric sample is excited is incompressible.

2.2 *Experimental setup*

Experimental setup for measuring dynamic bulk compliance $B^*(\omega)$ of time-dependant materials can be divided in 3 major subsystems. These subsystems are hydraulic, electronic and thermal subsystem.

Hydraulic subsystem is needed to supply transmitting medium into the pressure chamber and also to pressurize hydraulic subsystem. Electronic subsystem ensures generation of the signal, transmission, filtering and acquisition of the signal. Thermal subsystem contains isolation chamber, which enables measurements at constant room temperature.

2.3 *Procedure and materials*

Apparatus is in the prototype state and can measure dynamic bulk compliance $B^*(\omega)$ at the following boundary conditions: room temperature ± 1 °C, pressure range from 1 to 100 bar ± 1,5 bar and frequency range from 100 to 1000 Hz. Measurements were carried for two different materials, i.e., polyvinyl acetate (PVAc) and thermoplastic polyurethane (TPU).

3. Results

Figure 1 presents results of dynamic bulk storage $B'(\omega)$ and loss $B''(\omega)$ compliances for two different materials; PVAc and TPU. Measurements were conducted at room temperature, atmospheric pressure and frequency range from 100 Hz to 1000 Hz. Volume of the samples was 0,0128 cm^3. For both materials (PVAc and TPU) it is clear that storage and loss components of complex dynamic bulk compliance $B^*(\omega)$ are constant within the whole frequency range, no transition is observed. Storage component $B'(\omega)$ of TPU has higher value (approximately 1,1 GPa^{-1}) than PVAc, which means it is more compressible. Loss components $B''(\omega)$ for both materials are almost zero, which means that materials do not cause damping at particular boundary conditions.

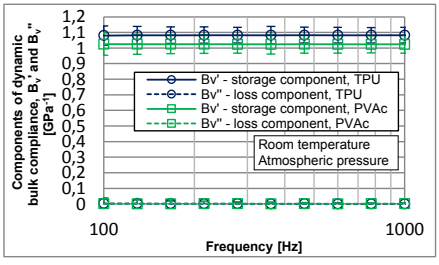

Figure 1: Dynamic bulk storage and loss compliance of PVAc and TPU

4. Concluding remarks

Novel measuring system was developed for measuring dynamic bulk compliance $B^*(\omega)$ of time-dependant materials. Apparatus in current state can directly measure mentioned material property at room temperature, at pressures up to 100 bar and frequencies from 100 Hz to 1000 kHz. Measurements were conducted on two different materials (PVAc and TPU) at room temperature, atmospheric pressure and frequencies from 100 Hz to 1000 Hz.

Dynamic bulk storage $B'(\omega)$ and loss $B''(\omega)$ compliance exhibit constant values within frequency range, no transition was observed. Obtained data reflects general functionality of apparatus although apparatus has certain limitation regarding boundary conditions.

Future work will include upgrading of the apparatus to allow measurements of dynamic bulk compliance in a wider range of temperatures pressures and frequencies. Device structure will also allow measurements of mentioned material function in the molten state.

References

[1] J. E. McKinney, H. V. Belcher, Dynamic compressibility of poly(vinyl acetate) and its relation to free volume, Journal of Research of the National Bureau of Standards – A. physics and chemistry, Vol. 67A, No. 1, 1962

[2] T. H. Deng, W. G. Knauss, Measurements of the dynamic bulk compliance of polymers, PhD thesis, California Institute of Technology, 1997

[3] T. H. Deng, W. G. Knauss, The temperature and frequency dependence of the bulk compliance of poly (vinyl acetate): A re-examination, Mechanic of Time-Dependant Materials, Vol. 1, No. 1, 1997

[4] S. Sane, W. G. Knauss, Time-dependant compressibility of poly(methyl methacrylate) (PMMA): An experimental and molecular dynamics investigation, PhD thesis, California Institute of Technology, 2001

[5] S. Sane, W. G. Knauss, The time-dependant response of poly (methyl methacrylate), Mechanic of Time-Dependant Materials, Vol. 5, No. 4, 2001

30th DANUBIA-ADRIA
Symposium on Advances in Experimental Mechanics
September 25-28, 2013 - Primošten, Croatia

7B38 148

COMPARISON OF PIEZO AND RESISTIVE STRAIN GAUGE IN HIGH AND LOW FREQUENCY LOADING

Witold Rządkowski[1], Michał Kowalik[1], Marcin Obszański[1], Karol Suprynowicz[1], Paweł Pyrzanowski[1]

[1] Warsaw University of Technology, Institute of Aeronautics and Applied Mechanics, Faculty of Power and Aeronautical Engineering,; Nowowiejska 24, 00-665 Warsaw, Poland, E-mails: wrzadkowski@meil.pw.edu.pl, mkowalik@meil.pw.edu.pl, mobszanski@meil.pw.edu.pl, ksuprynowicz@meil.pw.edu.pl, pyrzan@meil.pw.edu.pl

1. Introduction

In recent years there is a need to increase development of smart and low weight and low energy consumption sensors and actuators for engineering applications. Sensors which are independent from external energy sources, or their energy consumption is negligible are desired. These requirements can be met by piezoelectric materials. When mechanical force is applied to piezo-material, due to the direct piezoelectric effect, an electrical voltage is generated. Although due to inverse piezoelectric effect it can induce force, when electric field is applied. Different application of piezoelectric materials makes them appropriate for the development of systems that such sensor-active vibration damper [1]. Unfortunately, such a sensor records measurements only when the load changes, so the measurements may be flawed depending on the frequency of excitation.

2. Methods

Specimen was made form aluminum alloy and dimensions was 350x40x1mm. On two sides piezo and resistive (for correlation) strain gauge were bonded (Fig. 1.).

Fig. 1. Resistive strain gauge (on left) and piezo sensor (on right) bonded to aluminum alloy sample.

Piezo strain gauge material is PZT5AH1 Navy Type II with longitudinal active part, and transverse electrodes [2]. Size of sensor is 28x7x0.3mm. Data acquisition was performed with National Instruments software and hardware. Piezo data was amplified by MMF M68D1 charge amplifier. Large electrical noise appeared during measurements, got rid of them by using battery power for piezo amplifier, instead of the power supply.

Fig. 2. MMF M68D1 piezo charge amplifier.

3. Results

The main issue was to determine the behavior of the piezo sensor when forcing with a low frequency, or between cycles is the steady-state. Result were obtained in several loading function applied with different parameters (e.g. amplitude, frequency, steady state time). Only some of them are presented below.

3.1 Unit step function

First unit step function were applied, there has been a change from 0N in 0.25s and force was detained at a constant level. Piezo sensor has not hold the state, in contrast to the resistive strain gauge (Fig. 3.). This experiment can be very useful to determinate transmittance of sensor.

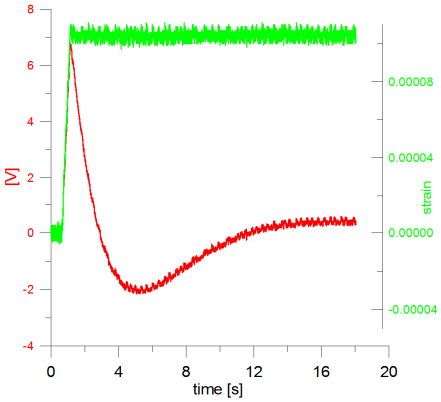

Fig. 3. Results obtained in unit step function loading. Red line represents results from piezo sensor.

3.2 Subsequent step function

Model was loaded by 5 consecutive step units, with 15 seconds break after each other, where load was locked in constant position. Here, loss of load history is very clear. On piezo graph there is no difference between each step, while resistive strain gauge in every step has increased observed value (Fig. 4.).

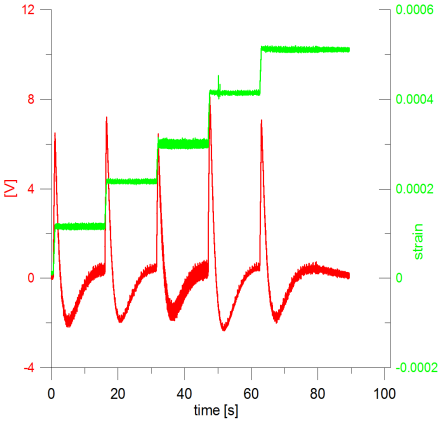

Fig. 4. Results obtained in subsequent step function loading. Red line represents results from piezo sensor.

3.3 Sinusoidal function

5 Hz frequency excitations were investigated in that case. In contrast to previous experiments, the history of the load is not lost when loading frequency is high enough (Fig. 5.).

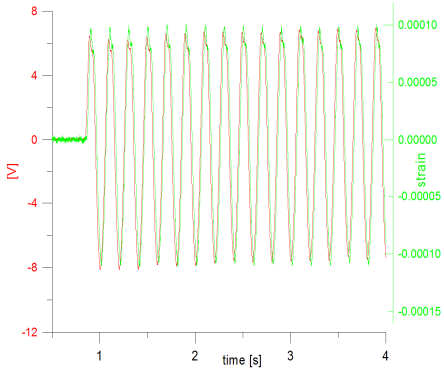

Fig. 5. Results obtained in sinusoidal function loading. Red line represents results from piezo sensor.

4. Remarks

- The sensor responds very well to a high-frequency loading,
- The low-frequency excitations measurements have to be updated about the history of model load, due to the loss of signal in the steady state,
- Determine transmittance of sensor is necessary to correct obtained data by loading history, especially for slow cycles.

Acknowledgements

Financial support of Structural Funds in the Operational Programme - Innovative Economy (IE OP) financed from the European Regional Development Fund - Project "Modern material technologies in aerospace industry", Nr POIG.01.01.02-00-015/08-00 is gratefully acknowledged.

References

[1] R. Paradies, P. Ciresa, Active wing design with integrated flight control using piezoelectric macro fiber composites, Smart Materials and Structures 18, 2009.

[2] N. Hagood, R. Kindel, K. Ghandi, P. Gaudenzi, Improving Transverse Actuation of Piezoceramics using Interdigitated Surface Electrodes, Smart Structures and Intelligent Systems, 1993. pp. 341-352

30th DANUBIA-ADRIA
Symposium on Advances in Experimental Mechanics
September 25-28, 2013 - Primošten, Croatia

7B39 149

FATIGUE DAMAGE DEVELOPMENT IN NICKEL-BASED SUPERALLOY WITH THE ALUMINA LAYER

Dominik Kukla[1], Paweł Grzywna[1], Ryszard Sitek[2], Maciej Szwed[2]

[1] Institute of Fundamental Technological Research, Department for Strength of Materials, A. Pawińskiego str. 5B, 02-106 Warszawa, Poland; E-mails: pgrzywna@ippt.gov.pl, dkukla@ippt.gov.pl

[2] Faculty of Materials Science and Engineering, Warsaw University of Technology, Woloska 141 Str., 02-507 Warsaw, Poland; E-mails: rsitek@inmat.pw.edu.pl, mszwed@inmat.pw.edu.pl

1. Introduction

The operating conditions of the aircraft engine turbines, made from e.g. nickel-based super alloys, require high mechanical load resistance in high temperature. To improve the parameter, protective layers are applied. They increase the heat resistance of alloys but are likely to reduce the fatigue strength. In this work the impact of the aluminide layer, deposited on the samples made from Inconel 740 alloy in a chemical vapor deposition process (CVD), on the fatigue parameters is assessed. A comparative analysis was carried out for the damage development mechanisms in both sample types. The damage parameter was defined as the sum of the strains and its plot in the function of the number of cycles. The results obtained were correlated to the factual studies of fractures.

2. Research methodology

The studies carried out were of the high-cycle test nature. Basing on the results obtained in a static tension test, the range of values for the load amplitude was defined, being 350 - 500 MPa for In740 samples and 500 - 650 MPa for In 740_Al samples. The studies were carried out for two batches of samples (4 with the layer and 4 without it) displaying axial symmetry with a narrowing in the measured section. The strain was measured by transverse extensometer, checking the narrowing values in (fig. 1)

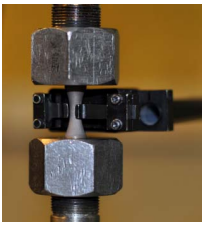

Fig. 1. A fixed sample with the extensometer.

The results obtained were used for developing the relationship between the damage parameter defined as the sum of average strain and the strain amplitude to the number of cycles, in accordance with the following formula:

$$\phi = \varepsilon_a + \varepsilon_m$$

where:

ε_w - width amplitude of the cycle hysteresis loop:

$$\varepsilon_w = \frac{\varepsilon_{min}^{F=0} - \varepsilon_{max}^{F=0}}{2}$$

ε_m - average strain in the cycle, defining the location of the hysteresis loop for a given cycle in the strain axis, expressed by:

$$\varepsilon_m = \frac{\varepsilon_{min}^{F=0} + \varepsilon_{max}^{F=0}}{2}$$

The principle of determining the damage parameter φ is presented also in the diagram in Fig.3.

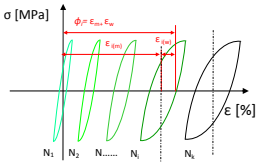

Fig. 2. Diagram showing the strain development in consecutive fatigue cycles

Thanks to describing the strain development in this way, it was possible to assess the changes in the fatigue damage dynamics in the samples with the layer and without it in the extensive amplitude range.

3. Results

Presenting the results in the form of Wohler curve (Fig. 2) enables to detect a clear increase (by about 100 MPa) in the fatigue strength of Inconel alloy with Al layer in a wide range of stress values.

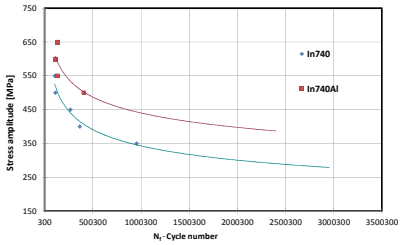

Fig. 3. Wohler diagram depicting the influence of Al. layer on the fatigue strength of In 740 alloy.

Basing on the determined fatigue damage parameters, the strain development in consecutive cycles was analyzed. Figure 4 presents the matching of these data for both sample types subject to the load with the amplitude of 500 MPa. With a significantly higher resistance (the number of cycles before breaking was 4 times greater) for the sample with the layer, a similar plot of the damage development can be observed for both samples, characterized with three stages.

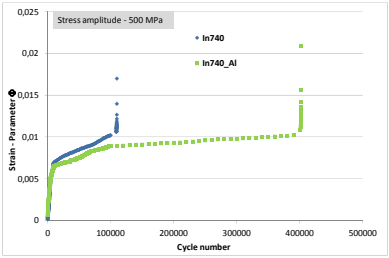

Fig. 4. Changes in φ parameter in consecutive cycles.

The first stage was a dynamic increase in the damage in over ten cycles. The second stage was a stable increase which ends earlier for the sample without the layer, leading to the third stage, connected with the crack initiation and development. The final strain level measured for both samples is similar.

The reasons for the increased fatigue strength of the samples given the surface treatment were sought in factual studies. Figure 5 presents selected fracture images. Besides various traces of cyclic load in the form of ribs, it is possible to assess the layer thickness (about 30 μm) and its diffusive nature, as well as strong integration with the substrate. However, this can hardly be used for explaining such a clear improvement of fatigue properties. Due to the function of aluminum layers which in principle can create heat barriers for nickel alloys, the results obtained should be explained rather in the context of heat-activated processes, accompanying the layers' deposition and not their presence as such.

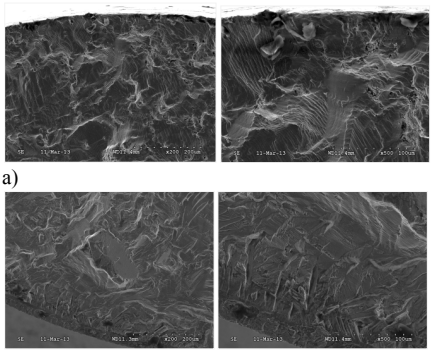

a)

b)

Fig. 5. Fatigue fractures for In740 samples without the layer (a) and with the Al layer (b)

Acknowledgements

The studies were carried out within the project no. 178781 financed from the National Centre for Research and Development.

References

[1] R. Sitek, D. Kukla, K.J. Kurzydłowski; Structure and Properties of the CrN+QlrNi3 Layer Produced on Inconel 740 by Pulse Plasma Ion Nitriding at a Frequency of 10kHz, Plasma Application and Hybrid Functionally Materials vol. 22 March 2013

30th DANUBIA-ADRIA
Symposium on Advances in Experimental Mechanics
September 25-28, 2013 - Primošten, Croatia

7B40 153

SAVART SHEARING INTERFEROMETER FOR SLOPE CONTOUR DETERMINATIONS

Shyh-Tsong Lin

Department of Electro-optical Engineering, National Taipei University of Technology, 1, Sec.3, Chung-Hsiao East Road, Taipei 10608, Taiwan. E-mail: f10402@ntut.edu.tw

1. Introduction

Due to the common-path design, the shearing interferometers are with the feature of anti-vibration, they therefore have been widely used in the testing of optical components [1-3]. To enhance their precision and automation, the phase-shifting technique realizing by rotating a birefrigent prism [4], moving a reflecting mirror [5], shifting a wedge prism [6-7], changing the retardation of a LCD [8, 9], or using a polarization phase-shifter [10,11] was proposed. They however require a light source with ideal wavefront, the optical elements used in the interferometers are hence expensive and the alignment for generating the illuminating beam is time consuming.

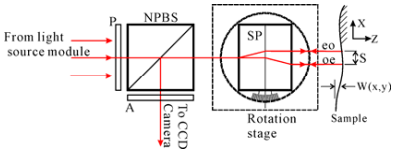

Fig. 1. Schematic diagram of the proposed shearing interferometer.

2. The interferometer

A novel shearing interferometer is therefore proposed as that shown in Fig. 1. It is composed of a polarizer (P) with a transmitting axis at 0 deg, a non-polarizing beam-splitter (NPBS), a Savart plate (SP) [3, 12, 13], a rotation stage having a rotation axis parallel to the Y-axis, a sample to be examined, an analyzer (A) with a transmitting axis at 0 deg, and a CCD camera. Where the SP is placed on the rotation stage, the principal section of the left plate of the SP is with an angle of 45 deg measured from the X-Z plane, and the surface normal of the SP makes a small angle of $\Delta\alpha$ with respect to the Z-axis.

Now assume a light beam, which has a center wavelength of λ, passing through the polarizer and NPBS is incident into the SP at a direction of the Z-axis, it would be laterally sheared into two parallel beams (oe and eo beams) which lie on the X-Z plane and have a shear distance of **S**; the sheared beams travel to the sample and then return to the SP to get recombined; and the recombined beams are finally guided to propagate through the analyzer to generate a shearing interference pattern on CCD camera which can be explicitly expressed as

$$\mathbf{I = I_0[1+\cos(\phi-\Phi)]}. \tag{1}$$

The term Φ happens when the interference beams pass through the SP twice (i.e., forwards or backwards), it is constant over the X-Y plane, but it is linearly proportional to $\Delta\alpha$. The relation between Φ and $\Delta\alpha$ is given by [12,13]

$$\Phi = \frac{4\pi}{\lambda} S\Delta\alpha. \tag{2}$$

Whereas the term ϕ comes from the wavefront distortion due to the profile of the sample, i.e., $\mathbf{W(x,y)}$; ϕ is linearly proportional to $\partial\mathbf{W(x,y)}/\partial\mathbf{x}$ (i.e., the sample slope), and they are governed by [4]

$$\phi(x,y) = \frac{4\pi}{\lambda}\frac{\partial W(x,y)}{\partial x} S. \tag{3}$$

From Eqs. (1-3), it is obviously found that the rotation of the Savart plate can be adopted as the phase shifter of the interferometer, and a $\Delta\alpha$-rotation of the Savart plate causes the interference pattern a phase-shift of Φ. Let $\mathbf{I_1(x,y)}$, $\mathbf{I_2(x,y)}$, $\mathbf{I_3(x,y)}$, $\mathbf{I_4(x,y)}$, and $\mathbf{I_5(x,y)}$ be the interference patterns corresponding to 0^o, 90^o, 180^o, 270^o, and 360^o phase-shifts, respectively, [14] gives

$$\phi(x,y) = \tan^{-1}\left[\frac{2(I_4 - I_2)}{(I_1 + I_5) - 2I_3}\right]. \tag{4}$$

In other words, once $I_1(x,y)$ to $I_5(x,y)$ mapped on the CCD camera are captured, the proposed interferometer is able to extract the slope of the sample by using Eqs. (3) and (4). Note, because the standard arctan function is with principal value in the range ($-\pi/2$, $\pi/2$], the atan2 function [15] is

adopted to replace the acrtan function in Eq. (4). The solved $\phi(x,y)$ is however still with 2π discontinuities, and it is referred to as the wrapped phase map. Therefore, a phase unwrapping technique [16] is also employed during the process of retrieving $\partial W(x,y)/\partial x$.

3. The experimental results

A setup was constructed to verify the proposed interferometer, where the sample was a circular diaphragm loaded by a central force, the wrapped phase map is shown in Fig. 2(a). By using Fig. 2(a), the slope contour of the diaphragm was obtained and is displayed in Fig. 2(b), which demonstrates that the proposed interferometer is capable of slope contour determinations.

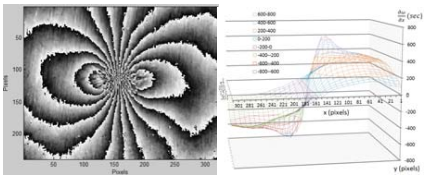

(a) (b)

Fig.2. (a) The wrapped phase map ; (b) the measured slope contour of the sample

4. Conclutions

In summary, this paper has presented a novel phase-shifting shearing interferometer capable of slope contour measurements. A setup was constructed to realize the interferometer; and the experimental results from the use of the setup validate the feasibility of the proposed interferometer.

Acknowledgments: The support of the National Science Council, Taiwan, Republic of China, under grant NSC 101-2221-E-027-103 is gratefully acknowledged.

References

[1] J. B. Song, Y. W. Lee, I. W. Lee, and J. U. Lee, "Optical test of aspheric lenses using instantaneous wedge plate phase shifting lateral shearing interferometer," Proc. of SPIE, 5638, 902 (2005)

[2] Y. H. Lo, A.R.D. Somervell, and T.H. Barnes, "Wavefront measurement with a phase-shifting lateral-shearing Sagnac interferometer operating in broadband light," Opt. Lasers Eng., 43, 33(2005)

[3] D. Malacara, in *Optical Shop Testing*, 3rd Ed. (Wiley 2007), pp 104-106, 122-184.

[4] S. T. Lin, S. H. Shih, H. N. Feng, and T. C. Tsai, "Phase-shifting Savart shearing interferometer," Opt. Eng., 45, 125602 (2006)

[5] E. Mihaylova, M. Whelan, and V. Toal, "Simple phase-shifting lateral shearing interferometer," Opt. Lett., 29, 1264 (2004)

[6] H.H. Lee, J. H. You, and S. H. Park , "Phase-shifting lateral shearing interferometer with two pairs of wedge plates," Opt. Lett., 28, 2243 (2003)

[7] J. B. Song, Y. W. Lee, I. W. Lee, and Y. H. Lee, "Simple phase-shifting method in a wedge-plate lateral-shearing interferometer," Appl. Opt., 43, 3989 (2004)

[8] D. W. Griffin, " Phase-shifting shearing interferometer," Opt. Lett., 26, 140 (2001)

[9] S. T. Lin, K. T. Lin, and Y. C. Liao, "Shearing interferometer using low-coherent light source and calcite prism," Opt. Commun., 276, 201 (2007)

[10] X. Guo, A. Zeng, and H. Huang, "Spatial phase-shifting lateral shearing interferometer," Proc. of SPIE, 7160, 71602D-1 (2009)

[11] L. Wang, L. Liu, Z. Luan, J. Sun, and Y. Zhou, "Polarization phase-shifting Jamin shearing interferometer," Optik, 121, 358 (2010)

[12] C. Zhang, B. Zhao, B. Xiangli, Y. Li, and Z. Peng, "Birefringent laterally Sheared Beam Splitter – Savart polariscope," Proc. of SPIE, 6150, 615001 (2006)

[13] http://www.halbo.com/sav_plat.htm

[14] P. Hariharan, B. F. Oreb, and T. Eiju, "Digital phase-shifting interferometry: a simple error-compensating phase calculation algorithm," Appl. Opt., 26, 2504(1987)

[15] http://en.wikipedia.org/wiki/Atan2

[16] W. W. Macy, Jr., "Two-dimensional fringe pattern analysis," Appl. Opt., 22, 3898(1983).

Author Index

Đ

E

F

G

H

M

N

O

P

R

S

S

T

U

V

W

Y

Z

Z

UNDER THE AUSPICES OF

Croatian Academy of Science and Arts
www.hazu.hr

SPONSORS

Ministry of Science, Education and Sports of the Republic of Croatia

IPA Project Adria HUB

TRC, Ljudmila Ličen s.p., Kranj, Slovenia

Croatian Chamber of Economy

Faculty of Mechanical Engineering and Naval Architecture, University of Zagreb

KONČAR - Electrical Engineering Institute Inc., Zagreb

KONČAR - Distribution & Special Transformers Inc. (Končar – D&ST), Zagreb

Neptun Sub d.o.o., Šibenik

AKNOWLEDGEMENTS

The Organizing and Scientifc Committees would like to express their gratitude to all institutions and firms for supporting scientifc and social events of the

30th DANUBIA-ADRIA Symposium on Advances in Experimental Mechanics